MONASH University

The Design of an L-/Ku- band shared aperture phased array for passive airborne remote sensing

Jiewei Feng
Master of Advanced Electrical Engineering

Bachelor of Engineering (with Honours) in the field of Electrical and Computer Systems

A thesis submitted for the degree of *Doctor of Philosophy* at
Monash University in 2024
Department of Electrical and Computer Systems Engineering, Faculty of Engineering

Copyright notice

New page

Abstract

Soil moisture is a key parameter for agriculture applications, climate modelling and forecasting, as well as flood and drought prediction. However, the usefulness of soil moisture information in those applications is currently limited by the low spatial resolution space borne radiometer results. While multi-frequency radiometer-based approach for enhancing spatial resolution could be a good candidate for the next satellite design concept, very limited number of field experiments and no single radiometer system could facilitate the demonstration of this concept; especially in the airborne platform, which is an essential component for satellites validation, calibration and algorithm development.

In this regard, this research work has the main focus on the simulation design of an L- (1.4 GHz) and Ku- (18.7 GHz) band shared aperture patch antenna phased array which is ultimately to be deployed onto the airborne platform to simulate satellite missions. This antenna shall have the capability to generate scanning footprints in an overlapping manner for high-resolution soil moisture downscaling measurements. With microstrip patch antenna array being the best candidate to meet the requirements of compactness for installation, shared aperture and beam scanning capability at the same time, this research work can be strategically divided into the following stages (*in collaboration with the radiometer research team for phase shifters and single element patch antenna designs):*

1. *The development of a Low-cost 4x4 L- phased array, and a complete phased array antenna system has been fabricated, assembled and tested with satisfactory measurement results at the end of this stage*
2. *The design of a Ku- band phased array. Upon a successful simulation design of an L-/Ku- band shared aperture fixed beam array, a 6x6 array configuration in Ku-band is found to be optimum with the 4x4 L- band array for a balance of design complexity, pattern distortion and footprint resolution requirements. Thereby, a*

compact 6x6 Ku- band phased array with irregular three-way unequal power dividers have been designed in an intricate feed network, this antenna is able to generate 15 antenna scanning patterns (which can cover the L- band one-dimensional scanning footprints) while maintaining low side lobe level and acceptable main beam efficiency.

3. *The design of an unprecedented L-/Ku- band shared aperture phased array. This stage is to combine the design results of the previous two stages, and the simulation design has been divided into two parts: (a) simplified shared aperture simulation at the Ku- band channel: satisfactory result and only minor radiation pattern distortion can be observed (b) full shared aperture simulation at the L- band channel: notable radiation distortion caused by the extended Ku- band phased array feed network which interferes with the energy coupling between the L- band patch and feedline layer. Radiation pattern distortion can be minimised by moving the Ku-band array from the 4x4 L- band array centre to the side the array, leading to overall satisfactory results with the trade-off of a minor level of asymmetry in the antenna radiation patterns and impedance matching characteristics when scanning in one dimensional across track direction.*

The outcomes of this study are (1) the completion on proof of concept and simulation design work of a novel L-/Ku- band shared aperture phased array antenna to be deployed in the airborne platform, its Ku- band phased array has the capability to generate overlapping high-resolution footprints to cover the low-resolution across track L- band footprints, which is to demonstrate the first-stage shared aperture phased array design for passive soil moisture remote sensing, and potentially to facilitate the simulation a new satellite design concept. (2) A compact low-cost L- band phased array antenna system with the benefit of two dimensional scanning capability, as compared to the state of art L-band airborne radiometer with one dimensional scanning.

New page (standard thesis only)

Declaration

This declaration is to be included in a standard thesis. Students should reproduce this section in their thesis verbatim.

This thesis is an original work of my research and contains no material which has been accepted for the award of any other degree or diploma at any university or equivalent institution and that, to the best of my knowledge and belief, this thesis contains no material previously published or written by another person, or any use of generative artificial intelligence technologies, except where due reference is made in the text of the thesis.

Signature: ……

Print Name: Jiewei Feng…….

Date: 09 May 2024…….

Publications during enrolment

1. K. T. Trinh, **J. Feng** and N. C. Karmakar, " Transferring PhD Research Outcome into Tertiary Teaching Laboratory in Electrical Engineering Education," in *33rd Australasian Association for Engineering Education Conference (AAEE2022)*

2. T. K. Ho, **J. Feng**, F. Bilawal, S. Shehab, K. T. Trinh, Y. Yang, C. Rüdiger, J. Walker and N. Karmakar, "Lightweight and compact radiometers for soil moisture measurement: A review," in *IEEE Geoscience and Remote Sensing Magazine*, vol. 10, no. 1, pp. 231-250, March 2022, doi: 10.1109/MGRS.2021.3082179.

3. K. T. Trinh, **J. Feng** and N. C. Karmakar, "18.7 GHz 4-Bit PIN Diode Reflection Type Phase Shifter for Radiometer Phased Array Antenna," *2021 2nd International Conference on Robotics, Electrical and Signal Processing Techniques (ICREST)*, 2021, pp. 504-509, doi: 10.1109/ICREST51555.2021.9331208.

4. S. H. Shehab, **J. Feng**, N. Karmakar, E. M. Amin and J. Walker, "Improved wideband phase balancing SIW unequal power divider design for the low side-lobe array antennas," in *IET Microwaves, Antennas & Propagation*, vol. 15, no. 2, pp. 115-122, 2020, doi: 10.1049/mia2.12027.

5. F. Babaeian, **J. Feng** and N. Karmakar, "Realisation of a High Spectral Efficient Chipless RFID Tag using Hairpin Resonators," *2019 IEEE Asia-Pacific Microwave Conference (APMC)*, 2019, pp. 114-116, doi: 10.1109/APMC46564.2019.9038844.

6. G. Khadka, **J. Feng** and N. C. Karmakar, "Chipless RFID: A Low-cost Consumer Electronics in the Retail marketplace for Moving Item Detection," *2019 IEEE 8th Global Conference on Consumer Electronics (GCCE)*, 2019, pp. 618-621, doi: 10.1109/GCCE46687.2019.9015239**.**

7. K. T. Trinh, **J. Feng**, S. H. Shehab and N. C. Karmakar, "1.4 GHz Low-Cost PIN Diode Phase Shifter for L -Band Radiometer Antenna," in *IEEE Access*, vol. 7, pp. 95274-95284, 2019, doi: 10.1109/ACCESS.2019.2926140.

8. S. H. Shehab, **J. Feng** and N. Karmakar, "Trends on Remote Sensing Technology: Receiver Architectures and Antenna Systems," *2019 International Conference on Robotics, Electrical and Signal Processing Techniques (ICREST)*, 2019, pp. 227-232, doi: 10.1109/ICREST.2019.8644361.

9. S. H. Shehab, **J. Feng** and N. Karmakar, "Ka-band Radiometer System Design Incorporated with SIW Slot Antenna for Soil Moisture Sensing," *2018 IEEE International Symposium on Antennas and Propagation & USNC/URSI National Radio Science Meeting*, 2018, pp. 1153-1154, doi: 10.1109/APUSNCURSINRSM.2018.8608564.

10. **J. Feng,** S. Hasan Shehab, Y. Yang, N. C. Karmakar and S. Gupta, "A Design and Implementation of an Ambulatory Electrocardiogram (ECG) Acquisition Circuit for Emergency Application," *2018 12th International Symposium on Medical Information and Communication Technology (ISMICT)*, 2018, pp. 1-6, doi: 10.1109/ISMICT.2018.8573705.

Acknowledgements

I would like to express my utmost gratitude to my main supervisor Professor Scott Tyo for his kind support, patience, and guidance towards the completion of my PhD study. His supportive attitude, dedication and constructive suggestions to a great extent helped me continuously make improvements as an academic researcher, such as to make realistic timelines and stay focus, put my best effort to improve details and keep learning even at the very late stage of my PhD journey. I would like to thank my associate supervisor Professor Jeffrey Walker for his valuable insights, and detailed feedback on my research work. His advice has been most helpful for me to broaden my knowledge in the area of passive soil moisture remote sensing, and deepen my understanding on the context and uniqueness of this study. I truly feel it is a privilege to complete my PhD journey under their guidance. I would like acknowledge that this study would not be possible without previous supervision from Associate Professor Nemai Karmakar who provided precious opportunities, resources and guidance for me to grow and overcome countless challenges, and Dr. Ali Mohammadi who motivated and guided me to pursue my PhD journey. I would also like to thank Dr Lilian Khaw for her encouragements and academic support from the beginning to this stage of my PhD study.

This study is supported by Australian Research Council Discovery Project DP160104233 (Airborne passive radiometer for high resolution soil moisture monitoring). I would also like to acknowledge all the financial support from Monash University in the form of both tuition fees scholarship and stipend scholarship.

In here, I would like thank Dr. Shahriar Hasan Shehab for his technical guidance, academic collaborations and countless long discussions to help me step into the fields of radiometer and antenna engineering, make contributions to this radiometer project and publish academic papers. I am also grateful for all the kind help and knowledge sharing from my colleagues of Monash Microwave, Antennas, RFID and Sensor (MMARS) Laboratories, Dr. Grishma Khadka, Dr. Kim Tuyen Trinh, Dr. Muhsiul Hassan, Dr. Shuvashis Dey, Dr. Mazyar Forouzandeh, Dr. Fatemeh Babaeian, Dr. Larry Arjomandi, Ms. Shahreen Hassan, Mr. Wan Muhammad Imran Wan Mohd Zamri, Dr. Dong Huu Nguyen, Dr. Guanghui Ma, and the list goes on. I am truly thankful for the supports from the professional staff from Department of Electrical and Computer Systems Engineering (ECSE), sincerely to Ms. Emily Simic, Mr. Daryl Gaspero, Mr. Ian Reynolds, Mr. Rob Jackel, Mr. Andrew Linzner, Mr. Martin Linzner, Ms. Roslyn Rimington, Mr. Geoff Binns.

At last, I would like thank the unconditioned support from my family, my father Zhaojin Feng, mother Lan Liu, elder sister Qianyi Feng, and brother-in-law Ang Li. I believe it would not be an overstatement to consider my PhD candidature as a journey full of joy, but also challenges, uncertainties, and at times pain and frustrations. Without them, I could not even image myself going through so many hurdles and now stepping into the finish line.

Table of Contents

Table of Figures

List of Tables

List of Abbreviations

1D	One dimensional
2D	Two dimensional
2D-STAR	Two-Dimensional Electronically Scanning Thinned-Array Radiometer
3D	Three dimensional
A	Ampere
AACES	Australian Airborne Cal/val Experiments for SMOS
AC	Alternating current
ACPA	Aperture coupled patch antenna
ADC	Analogue to digital converter
AMSR	Advanced Microwave Scanning Radiometer
AMSR 2	Advanced Microwave Scanning Radiometer 2
AMSR-E	Advanced Microwave Scanning Radiometer - Earth Observing System
APMIR	Airborne Polarimetric Microwave Imaging Radiometer
ARC	Australian Research Council
BPF	Band pass filter
CIMR	Copernicus Imaging Microwave Radiometer
cm	Centimetre
CST	Computer Simulation Technology
dB	Decibel
dBi	Decibels relative to isotropic
dBm	Decibel milliwatts
DC	Direct current
ED	Environment Canada
FR	Flame retardant
GHz	Gigahertz
GLOWS	Global L-band Observatory for Water Cycle Studies
GPIO	General-purse input/output
HUT-2D	Helsinki University of Technology 2D Radiometer
IF	Intermediate frequency
KHz	Kilohertz
kΩ	Kiloohm
LFMC	Live fuel moisture content
LNA	Low noise amplifier
mA	Milliampere
mAh	Milliampere-hour
MHz	Megahertz
ms	Millisecond
mV	Millivolt
NASA	The National Aeronautics and Space Administration
PALS	Passive Active L- and S-band Sensor
PCB	Printed Circuit Board
PKSR	Polarimetric K-band Scanning Radiometer
PLMR	Polarimetric L-band Multibeam Radiometer
PPMR	Polarimetric P-band Multibeam Radiometer
PSR/CX	Polarimetric Scanning Radiometer - C/X Band

RF	Radiofrequency
RFI	Radio frequency interference
S	Second
SFIM	Smoothing Filter-based Intensity Modulation
SIW	Substrate integrated waveguide
SLAP	Scanning L-band Active Passive
SMA	SubMiniature version A
SMAP	Soil Moisture Active Passive
SMAPEx	Soil Moisture Active Passive Experiments
SMAPVEX12	Soil Moisture Active Passive Validation Experiment 2012
SMD	Surface Mount Device
SMOS	Soil Moisture and Ocean Salinity
SPDT	Single Pole Double Throw
SSB	Single side band
SSL	Side lobe level
STARRS	Salinity, Temperature, and Roughness Remote Scanner
V	Volt
W	Watt
Ω	Ohms
$M\Omega$	Megaohm
μS	Microsecond

Chapter 1. Introduction

1.1 Overview

This thesis presents the stage-by-stage design of a novel L-/Ku- band shared aperture phased array radiometer antenna system for airborne remote sensing. Working in a team towards the completion of an ARC Discovery Project which aims to develop a revolutionising tri-band shared aperture antenna array with beam scanning capabilities, the design work presented in this thesis consists of four stages: (1) Fundamental studies of aperture-coupled antenna arrays; (2) Development of a low-cost L- band phased array with integration of phased shifters developed by collaborating researchers, and a radiometer receiver frontend prototype; (3) Simulation design of a Ku- band phased array, which was developed from the in-house initial patch element and phased shifters; (4) Simulation design of an L-/ Ku- band shared aperture phased array. The outcomes of these four stages of design work complete the antenna design work required for an unprecedented high-resolution dual-band airborne simulator (for satellite missions), which demonstrates the first-stage shared aperture phased array design for passive soil moisture remote sensing. A beam scanning proposal for a Ka- band phased array to demonstrate the design concept of tri-band beam scanning, which is the blueprint to meet the essential requirements of this ARC Discovery Project will also be presented in this thesis.

In this chapter, a general background on radiometric soil moisture sensing will be presented, followed by an overview of the current development of spaceborne radiometers for soil moisture applications. Thereby, the research problem statement, and sequentially the driven research focus with specific aims for each stage will be elaborated. Finally, the structure of this thesis will be outlined

1.2 General background and merits of passive soil moisture remote sensing

Soil moisture plays a critical role in the earth system. Soil moisture interacts with the atmosphere through evapotransporation and precipitation [1, 2]. It influences the earth's water balance by controlling the process of infiltration and water runoff partitioning of rainfall. Moreover, with saturated soil conditions, heavy rainfall could be transformed into a flood. Therefore, soil moisture information

is an essential element in climate modelling and weather forecasting, as well as flood and drought prediction [1, 2, 3, 4]. Recent studies also showed that soil moisture is strong predictor of live fuel moisture content (LFMC) which is a critical factor of the vegetation flammability, hence could facilitate to predict fire danger because of its better availability of data as compared to the optical based LFMC products [5]. In the agricultural aspect, soil moisture plays a vital role for vegetation growth [3]. Water shortage is a major limiting factor for agriculture production. On the other hand, excess watering could to insufficient oxygen in soil hence slow growth, and also in some cases yield reduction [6, 7]. Therefore, it is the soil moisture dynamics that are most important, and this information on its evaluation is required for optimal water management [8]. Agriculture applications occupy the largest proportion of water usage in Australia, and so saving even just 10% of water in this sector would be equivalent to water saving from 1/3 of the total water consumption by Australian capital cities [9]. Accordingly, accurate and dynamic soil moisture information would be essential for optimum water management.

Remote sensing, in this regard, has been considered as an advancement in agriculture because of its capability to monitor over a large area in a systematic and efficient manner [10, 11]. Optical, thermal and microwave are the main categories of remote sensing, and microwave remote sensing is widely viewed as being the most promising approach for soil moisture measurement. Compared to thermal and optical sensing which are highly affected by cloud cover and atmospheric effects, microwave sensing has virtually all-weather capability. Microwave sensing also has a more direct relation with the soil water content via the effective dielectric constant, as compared to skin temperature from thermal infrared sensing [3, 9, 12]. The sensing depth of microwave sensing is up to 5 cm from L- band (1.4 – 1.425 GHz) passive measurements, and has been shown to achieve an accuracy better than 0.04 $\mathrm{m}^3/\mathrm{m}^3$ for land with vegetation water content with up to 5 kg m^{-2}, which corresponds to 65% of the non-frozen land over the world [13].

Within the category of microwave remote sensing approaches, passive sensing measures, amplifies and converts the natural thermal radiation from soil to brightness temperature for soil moisture retrieval. Therefore, this approach eliminates the need for high power signal transmission, as well as more complex electronics and signal processing for back scattered signals of radars (i.e. active

sensing). Moreover, active remote sensing suffers speckle effect from coherent summation of random scattering, and is highly impacted by surface roughness and vegetation cover; resulting in noisy data and thus larger uncertainty in the derived soil moisture [3, 9].

With the advancement of technology, remote sensing is now a feasible approach for global soil moisture mapping [14]. For global scale measurement, spaceborne remote sensing is the only approach [3]. Thus far, there are two dedicated space-borne radiometer-based missions providing soil moisture information in a global scale with 2-3 days revisit time: The Soil Moisture Active Passive (SMAP) and the Soil Moisture and Ocean Salinity (SMOS). Both satellite instruments utilise L- band radiometers with a native spatial resolution of around 40 x 40 km for brightness temperature measurement. However, this coarse resolution is of limited use for regional weather forecasting and water resource management. Further, this resolution cannot meet the very high spatial resolution requirements (< 100 m) needed for improving agricultural irrigation [11, 15]. Accordingly, researchers have been exploring a variety of techniques to enhance the spatial resolution of spaceborne sensors [16, 17]. Recently studies also reported promising performance of using an L-band radiometer for very high-resolution proximal sensing [18], and particularly demonstrated the novel concept of a smart irrigation system by mounting an L- band radiometer into a linear irrigator for real time soil moisture mapping at a spatial resolution of 5m [15]. As compared to drone-based proximal sensing, this smart irrigation system also minimises the required effort to synchronise and communicate between sensors and irrigators [11].

1.3 Research problem statement

Thus far, there is no single satellite mission that is able to implement accurate radiometric-based soil moisture measurement with a native spatial resolution better than 40 x 40 Km. This resolution is of limited use for regional flood and precipitation prediction [19]. In this sense, the research problem can be divided into two aspects:

While multi-frequency radiometer-based approach for enhancing spatial resolution could be a good candidate for a next satellite design concept, existing airborne systems could facilitate the demonstration of this concept. Accordingly, it is important to develop and demonstrate this capability utilising especially an airborne platform, which is an essential component for satellites

concept development and evaluation, and for maturing the associated algorithm development. Apart from the tests using data from different satellites, with important differences in overpass dates and times, there has been limited work done on developing this approach. The only airborne study utilising simultaneous L- and Ku- band observations for multi-frequency radiometer-based downscaling experiments has been conducted by the Civil Engineering Department of Monash University [20], however, in those experiments, the L- band and the Ku- band radiometer measurements were made using separate systems. The L- band system used a patch array antenna while the Ku- band radiometer adopted a mechanical one-dimensional scanning.

With agriculture being the largest water use sector in Australia, the demonstration of the smart irrigation system in [15] used the L- band radiometer ELBARA system that is initially design for ground and tower-based measurements [18], hence it is large in size and requires over 45 W of power [21], making it cumbersome to be deployed onto the irrigator boom. Therefore, it is envisioned that a low-cost, low profile, solar-power-compatible radiometer system to be developed and integrated with linear irrigators for monitoring the soil moisture content in real time, and so that farm managers can make intelligent decisions relating to their irrigation needs could help so as to reduce water use, as well as to achieve high production [15].

1.4 Aims of this research

Given the current limitations, this research can be progressively divided into two goals:

The first goal of this research is to develop a standalone low-cost L- band phased array antenna system. Along with a lightweight, low-power radiometer receiver front end as the key components for the above-mentioned sensor to improve agricultural irrigation.

Being the main focus of this thesis, the second goal is to complete the design work of an L- (1.4 GHz) and Ku- (18.7 GHz) band shared aperture patch antenna phased array. Although measurements at L- band have promising sensing depth because of its long wavelength, large antenna sizes limit the spatial resolution of measurements. In contrast, the antenna array sizes are much smaller at Ku- band; however, Ku- band measurement results are not as accurate due to a lack of sensing depth [22]. In this sense, this phased array shall have the capability to generate

overlapping footprints in such manner that the low-resolution L- band radiometer measurements can be combined with information from the higher resolution Ku- band radiometer measurements in order to derive a high-resolution and high accuracy soil moisture mapping. Being sensitive to the top layer of canopies, Ku- band observations are also able to estimate vegetation water content and surface temperature as important ancillary parameters for soil moisture retrieval [23, 24]. As compared to the conventional separate radiometer systems with bulky mechanical scanning parts, the proposed shared aperture electronic scanning design can also notably reduce airborne payload and hence make rooms for other sensors. In consideration of PhD timeframe, the scope of the research presented in this thesis is to complete the proof the concept and simulation design work.

In collaboration with the radiometer research team for phase shifters and single element patch antenna designs, this research work can be strategically divided into a few components to ultimately produce an airborne simulator of a potential new satellite concept:

1.4.1 L- band aperture-coupled patch antenna phased array and low-cost radiometer receiver frontend design

This stage starts with L- band uniform aperture-coupled patch antenna element and array designs. Careful design considerations on antenna gain, impedance matching, cross-polarisation level, total antenna loss and fabrication cost are required.

Once satisfactory designs for uniform L- band antenna arrays were realized, the next stage was to design and integrate antenna feed networks with non-uniform distribution. This is to suppress antenna radiation side lobe level for meeting the stringent requirements of radiometer antenna beam efficiency being better than 90%.

With sufficiently low side lobe level, the next step was to incorporate low loss L- band phase shifters (developed by Dr. Kim Trinh [25]) for (1) beam scanning plan (2) integration feed network design, and (3) phased array simulations for performance optimisation. Upon obtaining satisfactory simulation results for all the beams, the next stage was to design driving electronics for controlling the states of each phase shifter bit, fabrication files preparation; and finally, antenna support structure design, multi-layer assembly, Arduino programming and phased array antenna

measurements for each beam.

As for the other part of this component, the radiometer receiver front end design starts from (1) system level simulation of radiometer receivers, (2) commercial components selection for optimum cost and compactness, (3) passive and active RF circuits design, (4) fabrication, system blocks testing and validation, and (5) finally system integration and initial laboratory experiments.

1.4.2 Ku-band phased array and fixed beam L-/Ku- band shared aperture array design

Provided the initial Ku- band single element aperture-coupled patch antenna designed developed by Dr. Muhsiul Hassan [26], this component has a few design phases:

(1) Design concept testing of the L-/Ku- band shared aperture array with setting a discrete port for each Ku- band and L- band patch antenna.

(2) Fixed beam Ku- band feed network design with non-uniform distribution, and integration with the fixed beam L- band antenna array for an L-/Ku- shared aperture fixed beam radiometer antenna array

(3) Overlapping L- and Ku- band antenna beam scanning plan; design of the Ku- band feed network to integrate with the Ku- band phase shifters designed by Dr. Kim Trinh [27]; iterations of phased array simulations for performance optimisation in terms of pointing angle accuracy, total antenna loss and beam efficiency

1.4.3 L-/ Ku- band shared aperture phased array design

This component is the combination of the successful results from the earlier two components. Considering running the full simulation design model at Ku- band will take approximately one month, which is not practical, this component will also be divided into a few parts:

(1) Instead of running a 4x4 L- band /6x6 Ku- band shared aperture phased array simulation at Ku- band, a simplified 2x2 L- band/ 6x6 Ku- band model is designed. with both models simulated with a discrete port setting to feed each patch, allowing the simulation to be compared for consistency to validate that the simplified model could represent the antenna radiation pattern at Ku- band.

(2) With the simplified model found to be consistent at Ku- band, the simplified model was simulated to model the shared aperture antenna at Ku- band with simulation time of around 1 week, which is a significant reduction as compared to running a full simulation.

(3) For the antenna beams of the L- band 4x4 array, a full model was simulated at L- band.

(4) This research was concluded when the results from parts (3) and (4) were analysed to be sufficient

1.4.4 Research outcomes

The successful outcomes of this research, combined with contributions from other aspects of the research collaboration, are:

(1) a low-cost L- band radiometer phased array antenna system with 2D scanning capability. Further, a low-cost L- band radiometer receiver frontend was developed by the author. This antenna system and receiver frontend are aimed to be deployed onto linear irrigators for real time soil moisture monitoring

(2) a novel dual band planar radiometer phased array antenna being compatible for multi- band downscaling airborne field experiments. With the existing airborne platform and Ka- (36.5 GHz) band mechanically scanning radiometer at Monash Civil Engineering department, this outcome can facilitate the demonstration of Ka-, Ku- and L- band concurrent radiometer sensing for high resolution soil moisture mapping. This shared aperture L-/Ku- band phased array could also be a demonstration for the next space-borne radiometer design concept.

1.5 Structure of thesis

The remaining chapters of this thesis are organised as follows:

Chapter 2 presents an overview of moisture mapping, followed by a review of current space-borne radiometers that are dedicated to soil moisture monitoring and also downscaling approaches for generating high-resolution soil moisture products. The second half of the chapter presents an extensive review of existing satellite multi-frequency sensors and airborne radiometers, with focus

on radiometer antennas. The discussion is thereby extended to suitable antenna types for planar shared aperture phased array design with a review considering shared aperture and beam scanning capability. Finally, the driven research gap is defined.

Chapter 3 starts with the design principle of an aperture patch antenna, then expands to design considerations for radiometer antenna arrays. At the first stage of planar array designs, low-cost and low-loss 4x4 and 8x8 antenna arrays with uniform excitation are developed. The next half of the chapter discusses the design of non-uniform antenna arrays to suppress radiation side lobe level. Starting from excitation allocation design, breakdown of each unequal power divider branch for meeting power division and phase balance requirements, and finally a combination of unequal power dividers and simulation with the full antenna models. In this chapter a 4x4 and 8x8 L- band antenna array with high main beam efficiencies are designed following the above procedures.

Chapter 4 presents the design of an L- band phased array radiometer antenna targeted to provide multi-track scanning capability for the above-mentioned smart irrigation system [15]. This chapter starts from beam pattern planning, design integration and simulations in CST. The next part presents the driving electronics prototyping and design. Finally, this layered phased array antenna has been fabricated and assembled, with satisfactory measurement results.

Chapter 5 presents the design of a Ku- band 6x6 phased array, and the combination work towards an unprecedented L-/Ku- band shared aperture phased array. This chapter starts from fixed beam Ku- 6x6 array design, and integration with an L- band 4x4 array for the first stage evaluation of coupling and pattern distortion in a shared aperture structure. The next half of the chapter presents the design of a 6x6 Ku- band phased array, and sequentially integration with a 4x4 L- phased array. In consideration of practical simulation duration, the final simulations are divided into two parts, one being a full model at L- band, and other being a simplified model at Ku- band. Overall, demonstratable simulation results have been obtained from both simulations as a proof of concept to conclude this study. At last, Chapter 6 presents the conclusions of this study, and recommendations of future work.

As part of the future work discussed in Chapter 6, Appendix A is an expansion of the L- and Ku-

band overlapped scanning design concept presented in the main body of this thesis. This document presents a beam scanning proposal for the additional Ka- band phased array using two-bit phase shifters to complete the design concept of tri-band beam scanning.

Appendix B presents the design of the radiometer receivers. This is a complementary document to the main body of the thesis which has the focus on radiometer antennas. In the first half of the appendix, an overview of commonly used receiver topologies followed by a system-level simulation design of a Ka- band Dicke type radiometer receiver is presented. The working principles of a Dicke type radiometer will be discussed stage-by-stage with this simulation example. The second half of the chapter presents the development of a low-cost L- band radiometer receiver frontend PCB design. Each phase of this hardware design workflow, from system simulations, filters and PCB design, and finally fabrication and testing are discussed.

Considering the nature of this study requires teamwork towards the completion of a larger ARC Discovery project, there will be various collaborative components throughout the thesis. For clarification, Table 1. 1 summarises the collaborative components and contributions of the author for each technical chapter.

Table 1. 1 Summary of collaborative components and the author's contributions

Technical Chapter	Collaborative components and the author's contributions
Chapter 3 L- band Aperture Couple Patch Antenna Array Design	**Sole contribution**
Chapter 4 L- band phased array design	**Collaborative components:** 1.4 GHz phase shifters developed by Dr. Kim Tuyen Trinh [25]
	The author's contributions: patch element, beam scanning scheme, feedline integration with phase shifters, phased array system simulation, control circuit and programming, support structure design, fabrication process (manufactured

	by an external vendor), soldering, assembly and antenna measurements
Chapter 5 L-/Ku- band shared aperture phased array design	**Collaborative components:** 18.7 GHz phase shifter developed by Dr. Kim Tuyen Trinh [27], initial Ku- band antenna patch element developed by Dr. Muhsiul Hassan [26]
	The author's contributions: Modification of the Ku- single patch element, Ku- band feed networks design for both fixed beam and integration with phase shifters, L- band phased array with all TLX-8 substrate material, shared aperture configuration design, simplified model design and verification, shared aperture phased array system simulations at L- and Ku- band
Appendix A. Ka- band phased array beam scanning proposal	**Collaborative components:** Initial Ka- band antenna patch element developed by Dr. Muhsiul Hassan [28], initial phase shifter specifications provided by Dr. Trong Khoa Ho [29]
	The author's contributions: Modification of the single patch element, bean scanning design to fulfil tri- band overlapped requirements, beam efficiency and phase shifter dimension trade-off analysis.
Appendix B. Radiometer receiver simulation, fabrication and testing	**Sole contribution**

Chapter 2. Literature Review

2.1 Overview

This chapter starts with the essential requirements for high-resolution global soil moisture mapping, followed by a review of the current development of space-borne radiometers for soil moisture sensing and downscaling approaches. Being a critical platform for satellite sensor design validation and calibration, the existing reported airborne radiometers in the past two decades are reviewed. The section is followed by a specific focus on radiometer antennas, and a discussion and review on planar antenna arrays being most suitable for dual-band overlapped beam scanning radiometer antenna. Thereby, the driven research gap in shared aperture radiometer phased array antenna is defined, and the research methodology and scope is established.

2.2 Requirements for high resolution global soil moisture mapping

Soil moisture content varies rapidly in both time and space [30], and this creates difficulties for global measurement and application [4]. While the current state-of-the-art resolution of 40 x 40 km is sufficient for many global climate modelling applications [4, 12], a resolution of 10 x 10 km or better would be required for numerical weather prediction at mesoscale and practical urban hydrological modelling and hydrometeorological applications such as flood prediction [4, 31, 32]. This requirement is based on the typical resolution of convective rain cells being on-order of 10 km [33, 34]. In terms of temporal resolution (i.e. revisiting time), to accommodate the wetting and drying sequences of rain events, Ref. [30] suggests that 2-3 days for revisiting the same site would be adequate.

2.4 Development of global soil moisture mapping and overview of downscaling approaches

Currently two satellites are dedicated for soil moisture sensing that work at L-band with sufficient temporal resolution. These are Soil Moisture and Ocean Salinity (SMOS) [12] and Soil Moisture Active Passive (SMAP) [35]. The L- band radiometers in both SMOS and SMAP have a footprint size of around 40 x 40 km, where the footprint is defined as the -3dB antenna beamwidth [36]. SMOS provides radiometric results with resolution of 40 x 40 km, and SMAP planned to generate results with 10 x 10 km resolution by combining noisy high-resolution Radar results (3 km) and the accurate

coarser radiometric results (40 km) [9]. Unfortunately, the radar of SMAP ceased operation a few months after launch due to an anomaly in the radar's high-power amplifier used is to boost the radar transmitting power strength for an accurate measurement of scattered energy from the Earth's surface [37]. As a result, the native radiometric resolution of SMAP is not better than 40 km.

2.5 Overview of downscaling approaches

Upon the anomaly of radar in SMAP, generating high quality 10 km resolution soil moisture data has been of great research interest in recent years. Alternative approaches include modelling, fusing with geoinformation data, combining radiometric results with different sensors, and merging multi-frequency radiometric results [38, 39, 40, 41].

Among those approaches, the oversampling approach of Backus-Gilbert optimal interpolation has been used as official enhanced 9 km data for SMAP [42], and fusing SMAP with another radar Sentinel -1 to generate 3 km resolution is also officially available as a Beta-release [43]. Considering the satellite AMSR2 carries C-, X- and Ka- band radiometers, smoothing filter-based intensity modulation (SFIM) has been adopted to downscale the coarse results from C- and X- band with finer Ka- band measurements, this generates 10 km x 10 km data that are officially available from NASA [44, 45].

However, each of the downscaling solutions has its limitation for high resolution soil moisture mapping. As for combining Sentinel -1 radar results with SMAP, the temporal resolution is reduced to 6-12 days due to the limited overlapping coverage of the two satellites [46], which could not meet the revisit time requirement. In terms of the Backus-Gilbert optimal interpolation technique adopted by SMAP, reference [36] suggests that its accuracy in highly heterogeneous sites and very local conditions (e.g. a single 9 km resolution) is yet to be examined, and this implementation is rather complex with ancillary information required, such as antenna pattern information [47, 48]. Fusing X- and Ka- band would not give as accurate results as that from L- band satellites sensors due to the lack of soil penetration depth, this is based on the comparison in a few studies that SMAP has better accuracy as compared to AMSR2 [49, 22, 50]. The alternative of combining passive radiometer results with optical sensors results in the loss of the all-weather capability [39]. Modelling approaches are overall limited to area-specific or certain types of terrain characteristics rather being able to be

applied globally [40].

Among the current solutions, the approach of fusing multi-frequency radiometric data is one of the promising concepts for the next satellite design, because of the all-weather availability and high-resolution capability without the need for active sensing. Moreover, the combination algorithm has the beauty of keeping the penetration depth of the low frequency measurement while improving the resolution to that of the higher frequency measurement [47]. To date, there is ongoing research on fusing spaceborne L- band radiometric results with higher frequency observations such as those from AMSR2 [39, 46, 51, 52]. Those reported studies are examined with historical reference data in limited sites, and/or the downscaled results are based on combined results with likely time or overpass difference which results in reduced availability of data, rather than field experiments with concurrent multi-frequency measurement over different conditions. Overall, these studies report improved spatial correlation, and the performance of SFIM is at least reasonable and better than that of fusing radar data. However, the sensitivity of high frequency radiometric measurements (in those studies Ka- band results) can be reduced by precipitation [32, 41, 51].

2.6 Review of multifrequency spaceborne radiometer missions and frequencies

The study of enhancing L- band spaceborne radiometric spatial resolution with higher frequency radiometric measurement is fundamentally limited by the lack of concurrent higher frequency radiometers on the same satellite platform. Provided that both SMOS and SMAP equip only L- band channels, Table 2. 1 summarises the operational status and the onboard radiometers equipped in multi-frequency spaceborne missions. Although the listed missions in Table 2. 1 are capable of providing radiometric measurements in the order of 15 km at Ku- band, and 10 km at Ka- band, owing to the primary objectives of those missions are not for soil moisture mapping, L- band radiometers are not equipped onboard. In addition, the channels at 23.8 GHz are not included in the discussion since this frequency is primarily for water vapor measurement, and similarly 89 GHz is prone to atmospheric influences such as water vapor and effects of wind [53, 54].

Aiming for $>$ 95% global coverage every day and at least two daily revisits in the arctic regions, the first Copernicus Imaging Microwave Radiometer (CIMR) is expected to launched in 2029 [55, 56].

This satellite mission equips multifrequency radiometer with L- band footprint < 60 km resolution; C- and X- band ≤ 15 km; Ku- band < 5.5 km and Ka- band ≤ 5 km [56, 57]. Given that the primary parameters of this mission are high-resolution Sea Ice Concentration and Sea Surface Temperature; while soil moisture is listed as a secondary mission objective and not a driving factor for the instrument design [56], CIMR targets to provide daily Level 2 soil moisture product at < 60 Km resolution, with provision to enhance product spatial resolution by using on board C- and X- band measurements [58]. While supporting study for enhancing L- band spatial resolution with C- band radiometric measurements has been demonstrated [59], no information enhancing L- band measurements with the onboard Ku- or Ka- band > 10 km observation has been proposed or reported at this stage.

Table 2. 1 Frequency and footprint of multi-frequency space borne radiometer

Satellite	C – band Bandwidth and -3 dB footprint size	X – band Bandwidth and -3 dB footprint size	Ku – band Bandwidth and -3 dB footprint size	Ka – band Bandwidth and -3 dB footprint size	Operation status
WindSat [60]	6.8 GHz with 125 MHz bandwidth	10.7 GHz with 300 MHz bandwidth	18.7 GHz with 750 MHz bandwidth	37 GHz with 2000 MHz bandwidth	End of life [61]
	71 x 39 (km x km)	38 x 25 (km x km)	27 x 16 (km x km)	13 x 8 (km x km)	
AMSR [62]	6.925 GHz with 350 MHz bandwidth	10.65 GHz with 100 MHz bandwidth	18.7 GHz with 200 MHz bandwidth	36.5 GHz with 1000 MHz bandwidth	Solar panels stopped
	70 x 40 (km x km)	46 x 27 (km x km)	25 x 14 (km x km)	14 x 8 (km x km)	
AMSR-E [62]	6.925 GHz with 350 MHz bandwidth	10.65 GHz with 100 MHz bandwidth	18.7 GHz with 200 MHz bandwidth	36.5 GHz with 1000 MHz bandwidth	Stopped rotating
	75 x 43 (km x km)	51 x 28 (km x km)	27 x 16 (km x km)	14 x 8.2 (km x km)	
AMSR-2 [62]	6.925 GHz and 7.3 GHz with 350 MHz bandwidth in each	10.65 GHz with 100 MHz bandwidth	18.7 GHz with 200 MHz bandwidth	36.5 GHz with 1000 MHz bandwidth	Operating
	62 x 35 (km x km)	42 x 24 (km x km)	22 x 14 (km x km)	12 x 7 (km x km)	

The thermal emission from soil at microwave wavelengths is a result of combining upwelling radiation from all depths in soil [63].In this thesis, provided that the real part of soil dielectric constant is relatively constant for frequencies below 5 GHz at various moisture levels [64], it is the imaginary

part of soil dielectric constant that leads to frequency dependent attenuation on upwelling radiation, such that longer wavelengths provide information of a deeper layer of soil [65]. In this sense, with L-band positioned at the long wave section of the microwave spectrum, and 1.4-1.427 GHz being a protected bandwidth for radio astronomy [66], making this particular bandwidth promising for soil moisture remote sensing.

While low frequency observation is more sensitive to soil moisture, observations at high frequencies may be more suitable for vegetation cover and surface temperature [67], both being essential information for soil moisture retrieval along with brightness temperature from low frequency measurements. Furthermore, the higher frequency systems provide better spatial resolution for the same aperture size, since resolution scales like λ/D, where D is the size of the antenna system. Several well-defined studies have been conducted for deriving surface temperature (T_S) from microwave observations, with a strong linear relationship between T_S and brightness temperature at 37 GHz having been observed [68, 69]. As for multi-frequency application, Li et al. have integrated Ka-, Ku- and X- band for vegetation water content, surface temperature estimation using a maximum likelihood method [23]. X- and Ka- band data from AMSR 2 has also been used for computing polarisation indices for vegetation biomass estimation [52, 70]. However, X- band is reported to be contaminated by RFI in Japan and Europe, such as the urban areas of Italy along with C- band [52], while Ku- and Ka- band observations were reported to be free of RFI [60]. Also, Ku- and Ka- have been commonly used in satellite missions since 1970 [68].

2.7 Review of radiometer antennas in the airborne platform

Since land surfaces are rather heterogeneous, the measured brightness temperature could be attributed to many factors [71], such as vegetation density, rain events, and surface roughness. Field experimentation with ground truth measurements is therefore essential for design concept validation over a diverse set of land cover and climatic conditions to ensure robust algorithm development [14]. Among the commonly used methodologies for field campaigns, airborne measurement is a crucial component as it enables the validation over a large area and a wide range of conditions, while avoiding biases that may be induced at a particular location (due to local surface peculiarities) in ground-based measurement [72].

Airborne measurement is a relatively low cost and efficient platform for high resolution soil moisture measurement. With equivalent cost from that by ground-based measurement, airborne soil moisture measurement could cover an area two orders of magnitude larger in just a few hours with higher resolution and accuracy [9, 73]. It is also a platform for understanding the linkage between satellite footprints and in situ measurements, and examining the satellite design concept over a variety of vegetation and soil conditions [74]. Before launching SMAP, a series of airborne field experiments such as the Soil Moisture Active Passive Validation Experiment 2012 (SMAPVEX12) in Canada [75] and Soil Moisture Active Passive Experiments (SMAPEx) in Australia, particularly SMAPEx-1/-2 and SMAPEX-3, were conducted for simulation of integrating radar and radiometer observations, as well as retrieval algorithm development [14, 74, 76]. As for the Post-launch of satellites, SMEX03 was performed to validate and calibrate the brightness temperature of the Japanese Advanced Microwave Scanning Radiometer (AMSR-E), as well as to support algorithm development [77]. EuroSTARRS was conducted to support the development of soil moisture retrieval algorithm from multi-angular and multi-frequency observation for SMOS [78]; followed by the Australian Airborne Cal/val Experiments for SMOS (AACES) for the validation and calibration of SMOS brightness temperature and soil moisture products covering at least 20 independent SMOS pixels [79]. SMAPEx-4/5 were preformed to evaluate the in-orbit performance of SMAP, and SMAPVEx16 were conducted with the priority to investigate the large errors in SMAP Level 2 Passive Soil Moisture product over agricultural landscapes in Lowa, America and Manitoba, Canda [80, 81, 82].

Table 2. 2 lists some important airborne radiometers that have been used for soil moisture measurement and the validation/calibration of satellite measurements since 2000 [74].

Table 2. 2 Airborne radiometers used for field campaigns in the past decade

Microwave radiometer	Measurement Frequency	Antenna type
PPMR [20]	P band (742-752 MHz)	4x4 Microstrip patches antenna array with passive electronic beam scanning for one dimensional 4 beams
PLMR [20, 83]	L band (1401-1426 MHZ)	8x8 Microstrip patch antenna array with Butler Matrix for 6-

		beam configurable across track or push-broom one dimensional scanning
STARRS [78, 84]	L- band (1401 – 1425 MHZ) C- band (5.18, 5.65, 5.85, 6.21,6.60,7.05 GHz)	L- band: 8x8 Microstrip Patch Array Antenna with Bulter Matrix for 6-beam one-dimensional push -broom scanning C- band: Fixed beam nadir looking
EMIRAD [85]	L band (1400-1427 MHZ)	Two large Potter horns with 2 bulky waveguide Ortho Mode Transducers (OMTs), fixed angle for one pointing at nadir, the other at 40° aft
CAROLS [86, 87]	L- band (1400-1427 MHZ)	Two large Potter horns and OMTs, fixed angle for one pointing at nadir, the other point at right side with 30° incidence angle
PALS [88, 89, 90]	L- band (1403-1423 MHz)	Dual-band (1.413 GHz for radiometer and 1.26 GHz for sactterometer) 4x4 stacked-patch microstrip patch antenna array, with a rotor for mechanical scanning
SLAP [91]	L- band (1.4 GHz) same as the SMAP at 1.4015-1.4255 GHz [92]	Dual-band (1.4 GHz for the Radiometer and 1.2 GHz for the scatterometer) microstrip patch antenna array, with mechanical conical scanning at 40° incidence angle
PSR/CX [93, 94, 95]	106, 6.6, 6.92, 7.32, 10.64, 10.69, 10.70, 10.75 GHz	Dual-band lens/feedhorn antenna (10° and 70° beamwidth at C- bands and X- bands respectively) in a mechanical scanhead for

		azimuth scanning and up to 70° elevation view angle
APMIR [96, 97]	6.6, 6.8, 7.2, 10.7, [18.7 and 23.8 GHz for WindSat] or [19.35 and 22.23 GHz for SSMIS], and 37 GHz	Separate Lens-loaded horns with elevation and azimuth mechanical rotation in a gimbal system
PKSR [20, 98]	Swappable RF front-end plates working at either Ku-band (18.7 GHz) or Ka- band (36.5 GHz) at a time	a reflector with scalar feed horn antenna in each RF front-end plate, and a programmable motor system for one dimensional scan
Environment Canada (EC) Radiometers [99, 100]	Separate systems at 1.4, 6.9, 19, 37, 89 GHz installed on different parts of the airplane	6.9, 19, 37 and 89 GHz antennas have a fixed incidence angle at 53°, 1.4 GHz antenna has fixed incidence angle at 40°. The 19 GHz and 37 GHz antennas are lensed type, and the 89GHz antenna is a corrugated horn
Hut-2D [101, 102]	L- band (1.4 GHz with 8 MHz bandwidth)	36 aperture coupled microstrip patch antennas with 36 radiometer receivers in a U-shaped configuration for two dimensional aperture synthesis
2D-STAR [103]	L- band (1.413 GHz with 24 MHz bandwidth)	21 patch antennas with 21 receivers for two dimensional aperture synthesis

Among above listed airborne radiometers, EMIRAD and CARLOS use two large Potter horns, each with a total length of over 150 cm (including the orthomode transducer). This, in turn, typically requires modifications to install on an aircraft, especially the precise design of the interface between the horn antenna and aircraft, as shown in Figure 2. 1. Furthermore, the radiometer receivers are bulky as depicted in Figure 2. 2. The installation of PSR/CX also required modification, while the

radiometers were housed within the scan head as shown in Figure 2. 3 [93], the overall structure including the gimbal mount is bulky as depicted in [104], and the weight of the positioner itself is 215 kg. Although this radiometer is capable of two-dimensional scanning, including conical scanning, the minimum scanning cycle is on the order of 10 seconds [94]. The EC radiometer antennas are mounted on different locations of Twin Otter aircraft with modification with fixed look angles. Although aperture-synthesis techniques have the capability to generate multangular measurements without heavy mechanical moving parts, the trade-offs are a large number of receivers required and reduced radiometric sensitivity [105].

Figure 2. 1 Antenna Installation of (a) EMIRAD [85] *(b) CARLOS in an air plane* [106]

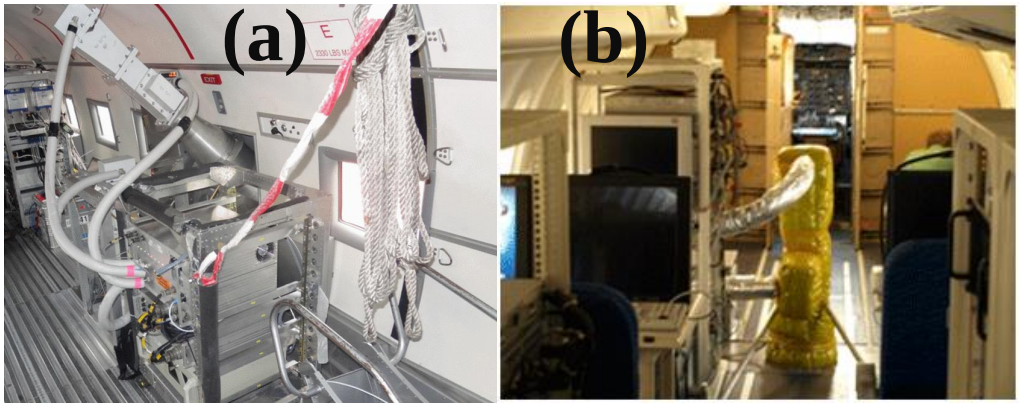

Figure 2. 2 Receiver of (a) EMIRAD [85] *(b) CARLOS in an airplane* [106]

Figure 2. 3 Scanning head installation of PSR/CX [94]

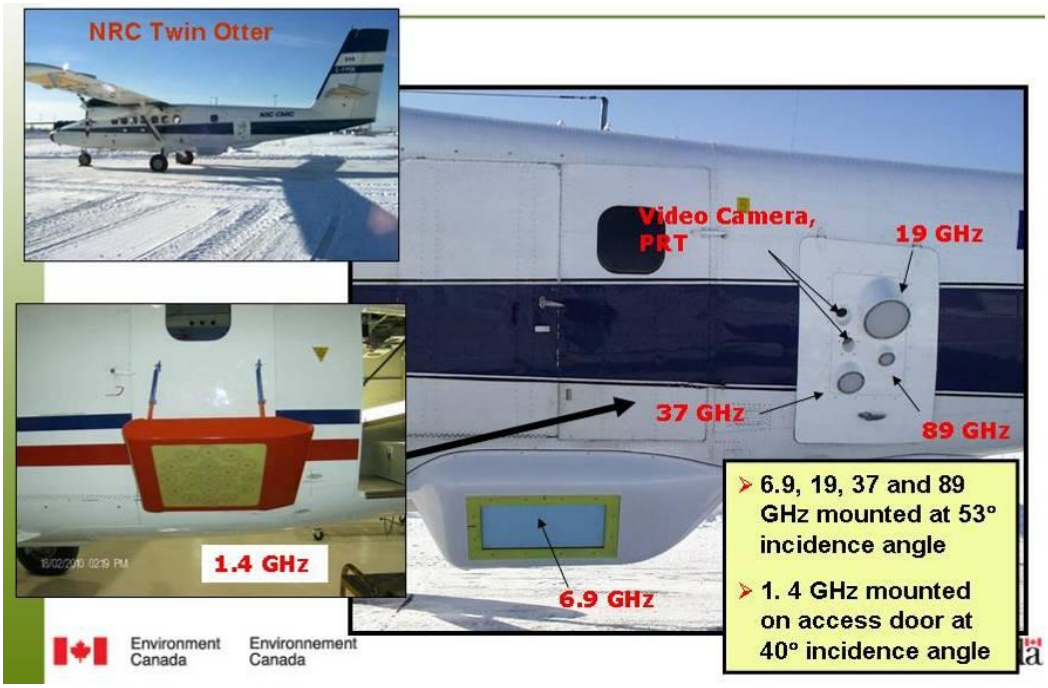

Figure 2. 4 Installation of EC Radiometer on Twin Otter airplane [99]

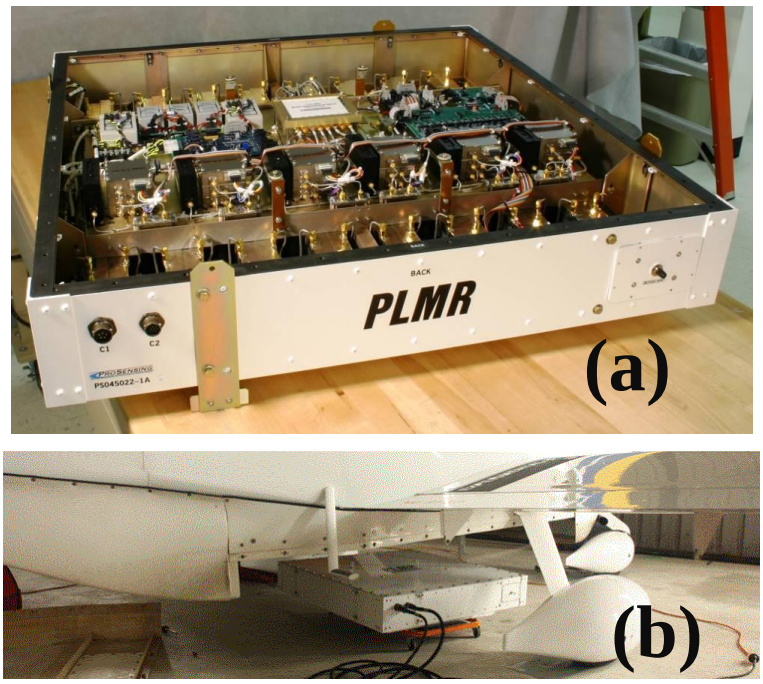

Figure 2. 5 (a) PLMR Radiometer [107] *(b) PLMR retrofitted to an aircraft* [108]

In comparison, compact planar structure radiometer such as the PLMR antenna has a total height of only 15 cm for the entire system, making it easier to be retrofitted into a small aircraft. Likewise, the large horn antennas earlier deployed in the PALS radiometer were substituted by a planar 4x4 patch antenna array, enabling the system to be operated on small aircraft [90]. In addition to reducing the form factor in the aircraft platform, planar antenna arrays could also be a potential alternative feed (as compared to using traditional horn antennas) to a large lens antenna or reflector antenna in the satellite platform, and this could reduce the overall weigh by three times and length by as much as six times with a similar performance [105, 109]. This feed concept is also adopted in [110] to significantly improve the packing factor of the next L- band spaceborne sensor - the Global L-band Observatory for Water Cycle Studies (GLOWS)

2.8 Suitable types of antenna arrays

As discussed in the previous section, antenna arrays with planar structures are highly attractive for future airborne radiometer sensors to simulate satellite missions. Two types of planar antenna arrays, namely Substrate Integrated Waveguide (SIW) arrays and patch antenna arrays are to be discussed in terms of form factor, capability of shared aperture design and two-dimensional design.

2.8.1 Substrate Integrated Waveguide antenna

SIW slot antenna is a planar form of waveguide type structure. Its effective waveguide characteristic is implemented by incorporating two rows of vias connecting the top and bottom metal layer of a planar substrate to form the electric field shield, while its radiation characteristic is controlled by careful slot design [111, 112, 113]. An example of a single element SIW antenna designed in [111] is depicted in Figure 2. 6.

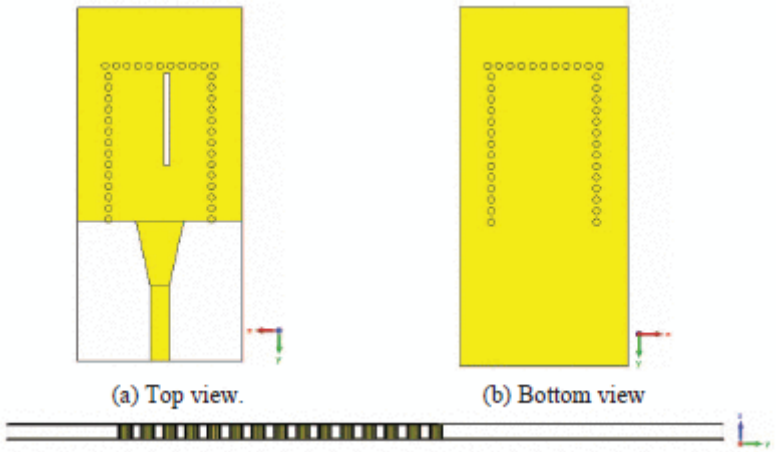

Figure 2. 6 Single element SIW slot antenna designed by Dr. Shahriar Shehab [112]

There are recent studies on substrate integrated waveguide being a strong candidate for future radiometer antennas [114]. In [115], a low-loss Ka- band 1x8 SIW slot array antenna with over 1 GHz bandwidth and low cross-polarisation level is reported. In [113], a Ku- band 1x8 SIW array antenna has been developed using a novel design approach to improve antenna co-phase bandwidth while suppressing antenna side lobe level to -27 dB, leading to a high beam efficiency of 97% to meet the stringent requirement for radiometer antennas.

As compared to the aperture coupled patch antenna (ACPA) phased arrays discussed below, SIW arrays have the merit of implementation in a single layer, while ACPA arrays require multilayer structures. However, a single-layer SIW design has the capability of scanning only in 1D [116]. To realise 2D scanning similar to the patch antenna arrays, multiple layers with much higher complexity are required for an SIW, for example studies in [117, 118, 119]. One example of the complex 2-dimensional butler matrix design in [118] is depicted in Figure 2. 8, while further design challenges were presented for integration with the antenna array. Although a recent study [120] demonstrated a comparably simple structure for 2D beam steering by controlling the radiation of slots with pin

diodes, this design has trade-offs as some antenna elements being equivalently deactivated (resulting in lower antenna gain) and higher side lobe levels.

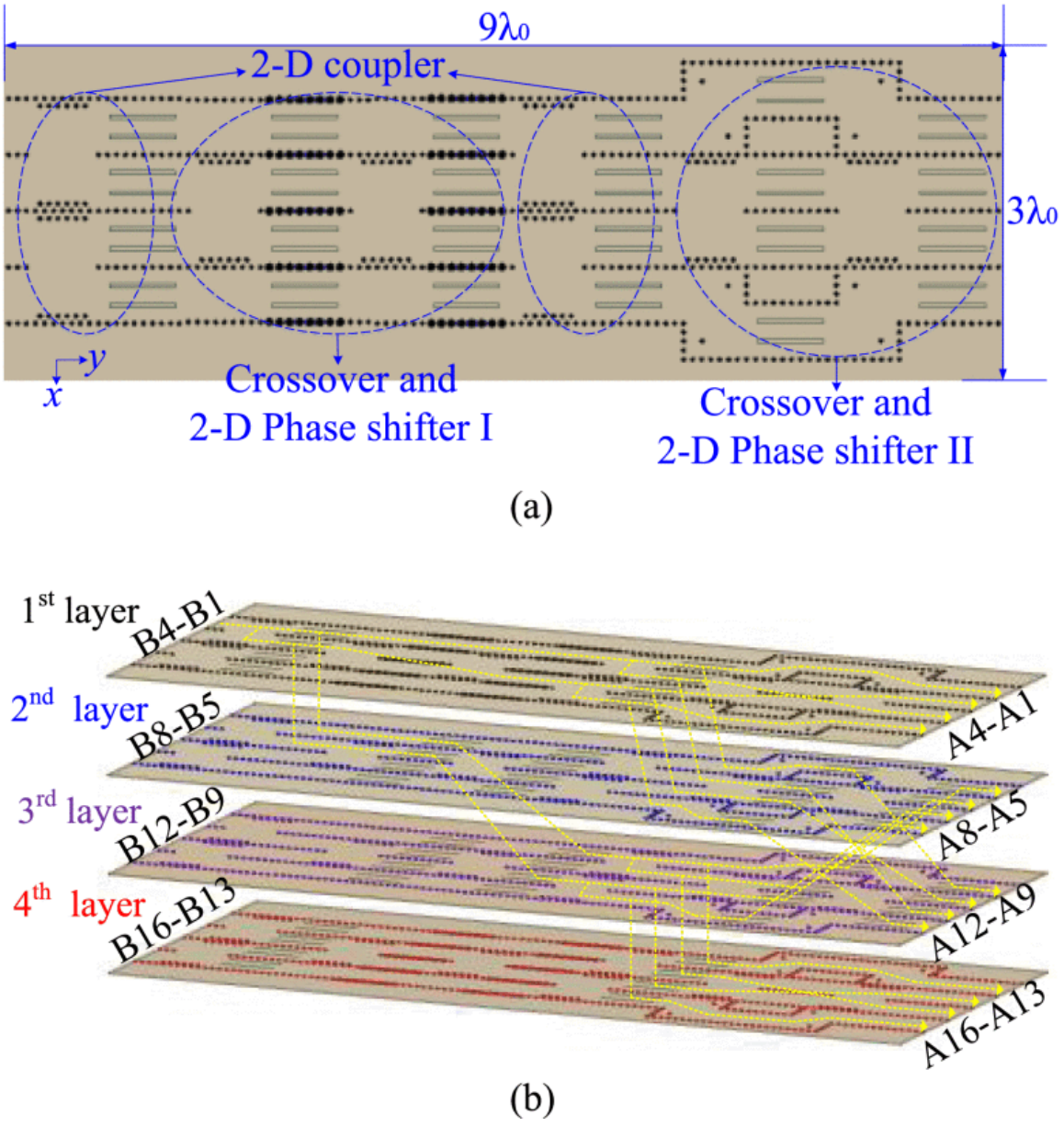

Figure 2. 7 SIW 2-Dimensional Beam-forming network reported in [118]

In terms of shared aperture capability, the study in [121] reported a Ku/Ka band shared aperture with SIW feedline for the Ku- band dipole radiator; while using waveguide antenna for Ka- band in a structure reuse topology and exhibits high isolation and beam scanning capability, as depicted in Figure 2. 8. However, the overall structure is complex, while manual work is required to install two different feed networks rather than being electronically controlled. In [122], a 60 GHz 12 x 12 SIW array is integrated with a 3.5 GHz single patch antenna. This design exhibits high isolation with a large frequency ratio of 17. Reference [123] reports a shared aperture dual-polarized antenna

integrating 60 SIW arrays with a 2.4 GHz patch antenna, yielding a larger frequency ratio of 25. However, beam scanning was not considered in both works.

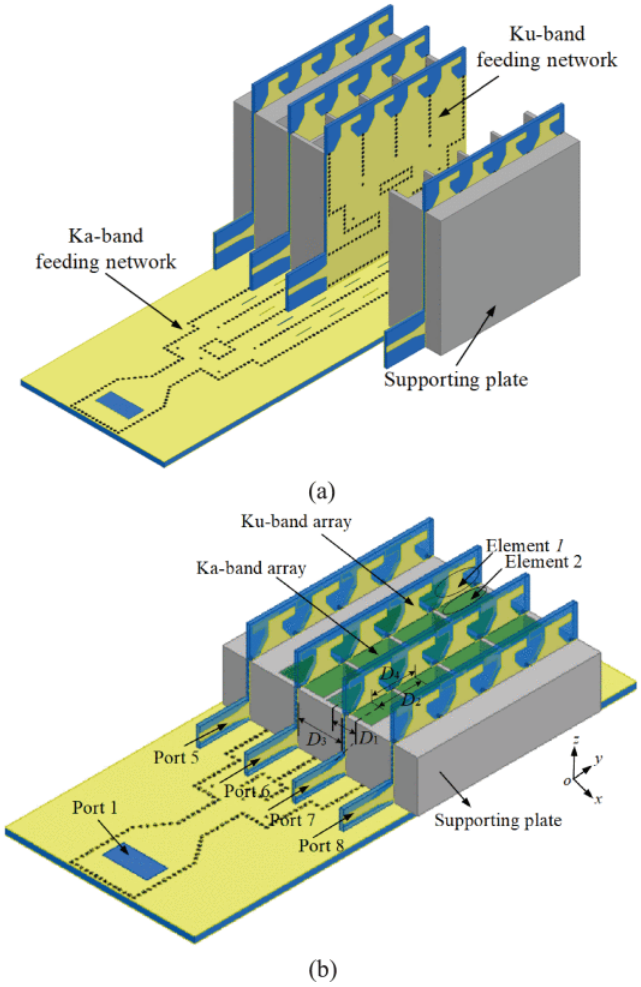

Figure 2. 8 The Ku-/ Ka- band shared-aperture beam scanning antenna array reported in [121] *(a) Explosive view (b) Integrated view*

Overall, although recent studies show that SIW arrays have the merit of low profile since they are mostly single layer designs, and promising capability of structural reuse for shared aperture design. More complex structure would be required for two-dimensional scanning. Moreover, by far there is limited research on shared aperture beam scanning SIW array. Therefore, in the author's perspective, SIW arrays are not the optimal choice for L-/Ku- band shared aperture phased array to meet structural compactness, shared aperture and 2-D beam scanning requirements at the same time.

2.8.2 Shared aperture patch antenna array with electronic beam scanning capability

Vigorous research has been conducted in the development of shared aperture phased array in microstrip patch array antennas. In [124], a 4x4 probe feed X- band array is integrated with a matameterial-based stacked S- band mushroom antenna in a novel structural reuse approach. With 11 of S- band elements configured in triangular arrangement and correspondingly a 8x 16 X- band array, this shared aperture is able to archive ±50° of scanning at both bands in a low profile design with high channel isolation. The layered antenna structure is depicted in Figure 2. 9. However, power dividers and phase shifters have not been integrated with the antenna in this work.

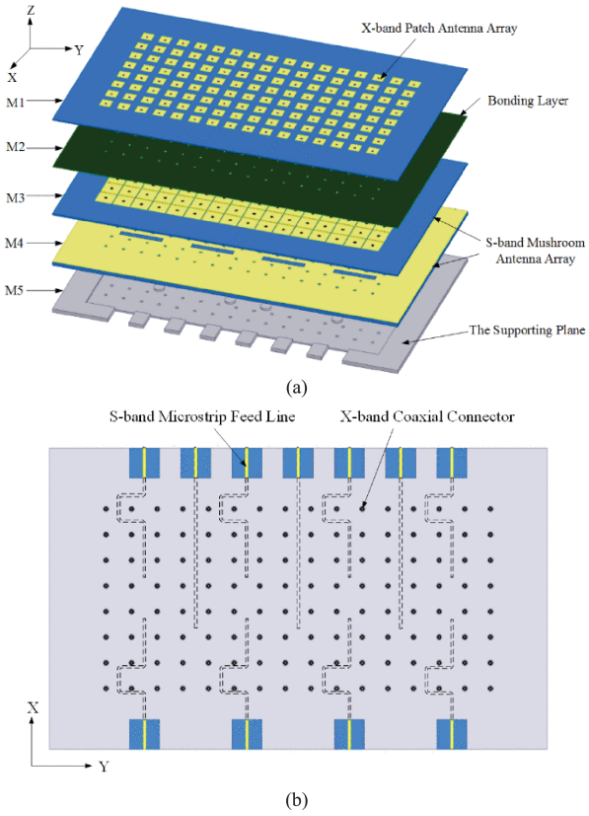

Figure 2. 9 Layered design of the S-/X- band shared aperture phased array antenna reported in [124] *(a) Exploded view (b) Bottom view*

In [125], a perforated approach has been applied in the L- band patch element, such that one L-band element is surround by a 4x4 C- band array. This design exhibited very low cross polarisation, and demonstrated beam scanning capability. However, phase shifters are not integrated with the antenna feed network, and only limited beam scanning capability has been demonstrated.

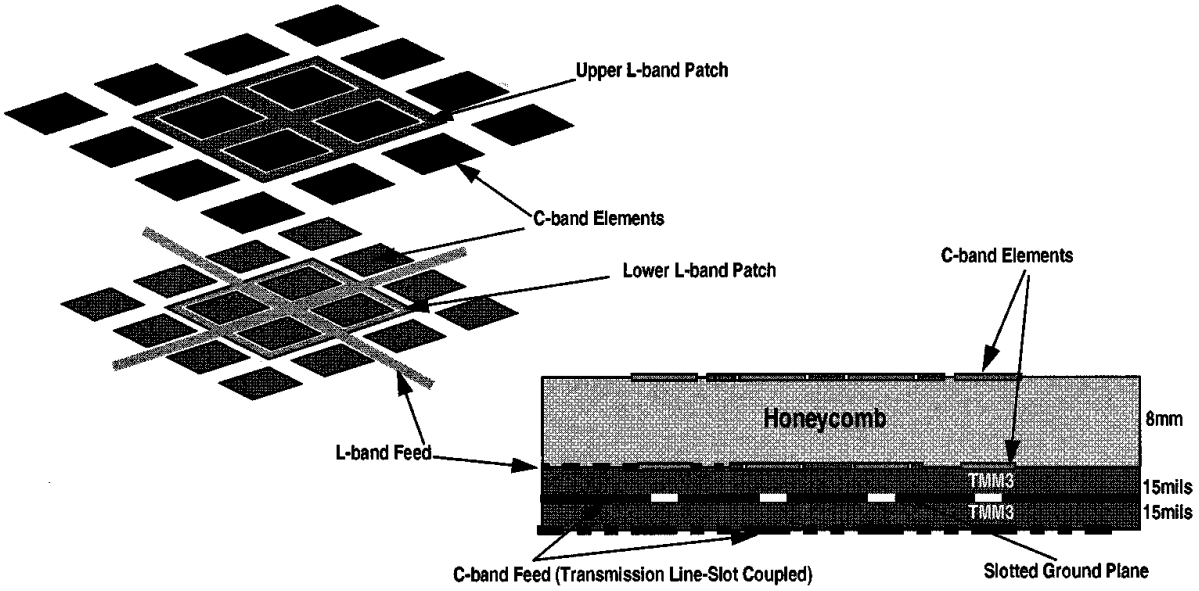

Figure 2. 10 Perforated L-/C- band shared aperture array design reported in [125]

Reference [126] reports a shared aperture Ku/Ka- band array integrating Ku- band Patch-Dipoles and 832 Ka- band patch antenna elements with multi-layer feeding. This design adopts metal shielding vias for coupling suppression and bracket-shape defected ground structure for improve scanning range. Further, with inter-element distance of 0.55λ in both Ku- and Ka- band, as well as adopting the Taylor weighted distribution, this array demonstrated side lobe level of -21.2 dB and a wide scanning range of $\pm 45°$. However, each antenna element is feed with a separated tiny electrical connector and the array is connected to an external T/R module for beam scanning, which could incur high implementation cost.

2.9 Research gap and methodology

To date, to the best of the author's knowledge, there is no single airborne radiometer system that works concurrently at L-, Ku- and Ka- band. Although separate systems are available as discussed in Section 2.7, those systems are generally bulky, and generally require modification on the aircraft due to the large system size and non-planar antenna design. Further, owing to stringent requirements of radiometer antennas which will be discussed in detail in Chapter 3, there is no report of a planar shared aperture fixed beam array combining L- band with Ku- or Ka- band for the application for passive soil moisture remote sensing. Furthermore, none of the existing literature discusses electronic beam scanning, a capability that is only afforded by phase array technology.

To design a planar, multi-band shared aperture antenna array with electronic beam scanning for a revolutionary high-resolution airborne simulator as a prototype for next satellite design concept, microstrip patch antenna array would have the best potential for meeting the requirements of shared aperture, beam scanning and side lobe suppression at the same time. Along with the availability of the Ku- band patch antenna element [26], as well as the L- and Ku- band PCB-based phase shifters [25, 27]developed by research team members (Dr. Muhsiul Hassan and Dr. Kim Tuyen Trinh respectively) [127], this research focuses on the design work of microstrip patch antenna arrays with integration of the developed phased shifters to complete the proof of concept and simulation of an unprecedented L-/ Ku- band shared aperture phased array with specific aims of each stage explained in Chapter 1.

2.10 Chapter Summary

This chapter has presented the high-resolution requirements of global soil moisture information for hydrometeorological applications. Following the anomaly of the onboard radar in the SMAP spaceborne sensor, rigorous research has been conducted for alternatively downscaling approaches. Among the downscaling methods, the radiometer-based downscaling approach fusing L- band with higher frequencies radiometric results using the SFIM technique has been reported to perform better than radar-based downscaling methods, along with the virtually all-weather capability.

However, the studies of SFIM with L- band spaceborne radiometric measurements have been limited by the lack of an L- band radiometer onboard with higher frequency high resolution radiometers in the existing multi-frequency spaceborne sensors. With a review on the commonly used radiometric frequencies, Ku- band and Ka- band are found to be best higher frequency channels because of the fine spatial footprints, capability of providing ancillary parameters for soil moisture retrieval and relatively free of RFI.

With the airborne platform being vital for the design concept simulation and calibration/validation of spaceborne radiometers, in the second half of the chapter, the radiometer antennas installed in the reported airborne simulators for soil moisture experiments since 2000 have been reviewed. With no single airborne radiometer system works concurrently at L-, Ku- and Ka- band being reported as

a prototype to facilitate the next multi-frequency satellite design concept, flat structure antenna arrays with beam scanning capability are most suitable for future airborne radiometer simulators because of the compactness and easier installations as compared to that of conventional horn antennas and/or mechanical scanning parts. In this regard, two types of printable planar arrays, namely SIW and microstrip patch antenna arrays have been reviewed in terms of shared aperture and beam steering capability. It is found that multi-frequency microstrip patch antenna arrays have the best potential to meet the stringent requirements of radiometer antennas with compact shared aperture structure and 2-dimensional beam scanning at the same. Along with the in-house Ku-band single patch element design, as well as L- and Ku- band phase shifters, the scope of this study focuses on the complete simulation design of an unprecedented L-/Ku- band shared aperture microstrip patch antenna phased array, while a blueprint (initial simulation proposal) of tri-band beam scanning will also be presented at the end of the study.

Chapter 3 L- band Aperture Couple Patch Antenna Array Design

3.1 Overview

As discussed in chapter 2, microstrip patch antenna array is found to be the best candidate for planar, dual-band, shared aperture radiometer antenna with beam steering capability. Thereafter, this chapter presents the fundamental studies of microstrip patch antenna arrays using the aperture-coupled feeding approach.

This chapter starts with a brief review of microstrip patch antennas for radiometric applications then moves on to the discussion of feeding approaches with a focus on the aperture coupled feeding. The next part of the chapter presents the design of an L- band -coupled patch antenna array with uniform phased and excitation. Three subsections are to be covered, namely single element design, multi-section power dividers and materials selection. The next stage discusses the suppression of array side lobe levels, for which a non-uniform amplitude distribution is discussed and applied. Design details will be reported in the second half of the chapter. At the end of the chapter, an 8x8 L- band aperture coupled microstrip patch antenna array with fixed uniform phase allocation is presented, as well as a 4x4 array which will be further developed with in-house phase shifters to an L- band phased array in the next chapter.

Overall, the main objective of this chapter is to build the foundations of microstrip patch antenna arrays design using conventional approaches and structures. More challenging designs of phased arrays and shared aperture arrays will be built upon this fundamental study, and be presented in chapter 4 and 5.

3.2 Brief review of microstrip patch antennas

3.2.1 Microstrip patch antenna arrays for radiometric applications

Being lightweight and planar, microstrip patch antenna arrays are gaining popularity for use with airborne radiometers, including systems deployed on unmanned aerial vehicles (UAVs). Chapter 2 listed the microstrip patch antennas deployed in aircraft, and examples of microstrip patch antennas in UAVs are reported in [128, 129, 130].

3.2.2 Aperture coupled feeding with air gap and metal back reflector

There are four most widely used feeding approaches for microstrip patch antennas: probe feeding, microstrip inset feeding, proximal feeding and aperture coupled feeding.

Microstrip inset feeding has the advantage of being easy to fabricate. However, this method could cause spurious feedline radiation because the feedline is in the same layer with the radiation patch above the back plane. The method of coaxial probe feeding is also easy to fabricate and has low spurious radiation. The drawbacks of this method are that each coaxial feed must be physically underneath each patch, leading to a large number of coaxial connectors required and complex wiring in a large array.

Proximity feeding and aperture coupling feeding methods are rather similar. The proximity method directly energises the antenna patch by the strip line underneath, while in aperture coupling, the feedline is positioned behind a metal ground plane, with a slot (aperture) to couple energy from the feedline to the patch. The slotted ground in the aperture coupled antenna serves for two main purposes:

(1) Selectively create room for the feedline underneath to couple energy to the radiating patch on top. Without this slot, the bare copper ground plane (e.g. similar to a metallic back reflector) will prevent the feedline from coupling to the patch, and hence block the patch from radiating.
(2) Prevent spurious radiation from the feedline for radiation pattern shaping and polarisation purity, since only a selected area of radiation can reach the top patch through the slot.

Although it is the most difficult to fabricate, the aperture coupled feeding method with air gap is selected for this study because of the following merits:

(1) With the feedline and the patch being in different layers, different substrate materials can be selected for optimal cost
(2) Phase shifters and bias lines can be integrated in the feedline layer to reduce substrate surface congestion
(3) Optimal spurious radiation suppression and polarisation purity

(4) Provided that the feedline for each frequency band can be designed and positioned in a different layer, it is possible to design a compact shared aperture multi-band patch antenna array in this method.

The layered design of a single element aperture coupled patch antenna is depicted in Figure 3. 1 (a). The coupling slot is cut out in the top layer ground plane of the second substrate, and centred right below the patch. As illustrated in Figure 3. 1 (c), instead of using the conventional single microstrip feed line, a dual offset design with 100-ohm stubs at each end is selected for high polarisation purity and hence low cross polarisation level [26]. Further, the feedline radiates in an omnidirectional pattern, which can cause a significant back lobe and therefore poor front-back ratio. A solid metal back reflector has been placed directly under the feedline to suppress back lobe radiation [26, 131, 132], with the trade-off of an added layer and increased structural complexity.

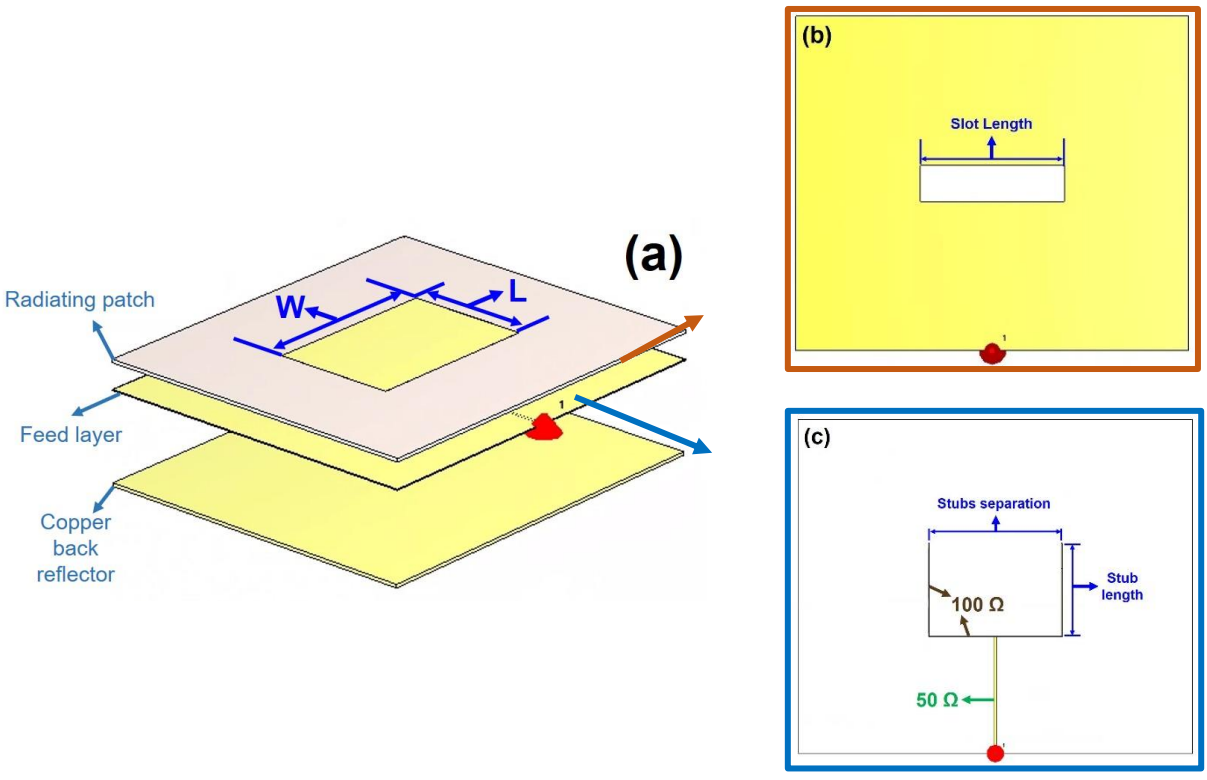

Figure 3. 1 An aperture coupled microstrip patch antenna with key tuning parameters labelled in blue (a) Overall structure (b)Feed layer top layer (c)Feed layer bottom layer

3.3 Uniform aperture coupled patch antenna arrays design

3.3.1 Design requirements and flow chart

The target of this stage is to design an 8x8 array in uniform phase and amplitude within a total antenna loss of -2 dB as an achievable goal for a low-cost radiometer antenna with microstrip feed network. As illustrated in the design flow chart Figure 3. 2. To minimise the fabrication cost, the design procedure started with the lost-cost material FR-4 for each part of the antenna, beginning with a single element design and progressively expanding to an 8x8 array. For each design step, careful analysis was conducted to ensure reflection coefficient is at no worse than -10 dB, while the radiation loss was minimum.

Through three iterations of design as summarised in Table 3. 1, the final 8x8 uniform array exhibited -2.034 dB radiation loss with Fr-4 for the radiating patch substrate and Taconic TLX for the feedline layer. Three design aspects, namely substrate materials single patch design and uniform arrays design are to be discussed in the following sections.

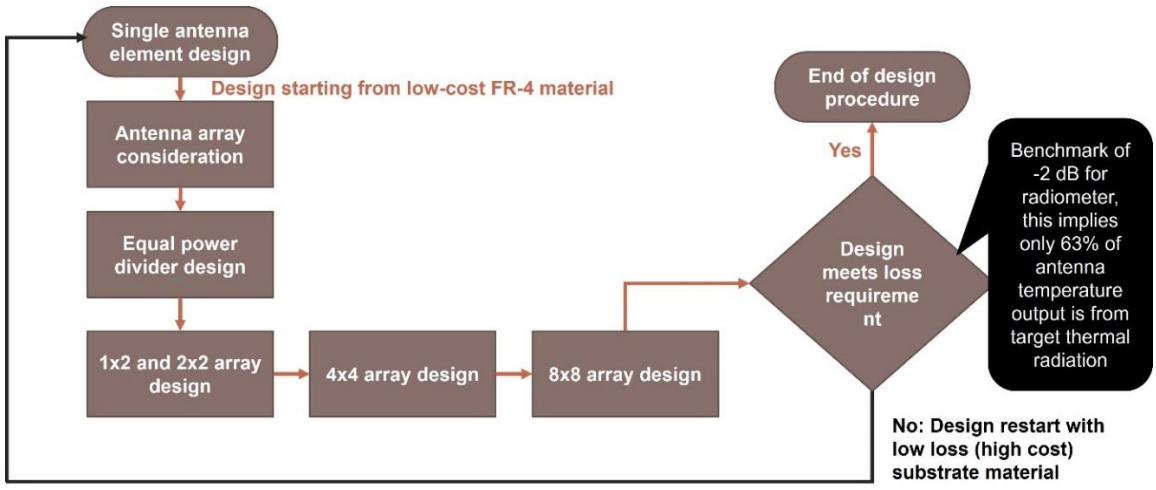

Figure 3. 2 Design flow chart of the L- band uniform patch antenna array

Table 3. 1 Iterations of uniform patch antenna array design

Iteration	1st	2nd	3rd
8x8 antenna radiation loss	-10.28 dB	-3.5 dB	-1.997 dB
Patch substrate	1.0mm FR-4	1.0mm FR-4	1.6mm FR-4
Feed layer substrate	1.0mm FR-4	0.5 mm Taconic TLX-8	0.5 mm Taconic TLX-8
Power divider topology	T-junction with a quarter-wave transformer at each branch	T-junction with a quarter-wave transformer at each branch	Two-way power divider

3.3.2 Substrate materials

The primary factors in the substrate materials selection are material cost and antenna radiation loss. One important parameter is dielectric loss tangent ($tan\delta$), which quantifies electrical energy being dissipated as heat in a dielectric material. The lower the dielectric loss tangent the lower dielectric loss, and hence higher antenna radiation efficiency. Table 3. 2 lists the important parameters of two substrate materials in this design cycle.

Table 3. 2 Substrate Materials

Material	ε_r	$tan\delta$
Fr-4	4.3	0.025
Taconic TLX-8	2.55	0.0019

Fr-4 is a low-cost material widely used in commercial applications. Due to high loss tangent of 0.025, careful design is required to minimise loss for applications above 1 GHz such as minimizing field enhancement regions inside the substrate. Although the antenna efficiency improves with higher

substrate thickness as conductor loss and dielectric loss generally decrease with thicker substrate due to the reduced field strengths, at the same time fabrication cost increases.

Taconic TLX-8 is a much lower loss material with loss tangent at 0.0019, but the trade-off in this case is that the fabrication cost is about 6-7 times the cost of Fr-4. It also worth mentioning that a smaller relative dielectric constant lead to lower surface wave loss, but a large antenna element size [133].

3.3.3 Single element patch element design

The key tuning parameters for the single element design are illustrated in Figure 3. 1. The resonant frequency of a single element is primarily determined by the antenna patch dimensions and patch substrate material, while the feedline substrate material and aperture size control the coupling factor. For maximum coupling, the aperture shall be positioned centred below the patch, which also leads to symmetric excitation and hence high polarisation purity. The impedance matching is controlled by fine tuning the slot length, stub length and the separation between two stubs. The detailed effect of each parameters and design procedures are well explained in [134, 135, 136]

The electric field distribution of the patch is illustrated in Figure 3. 3. The electric field varies sinusoidally along L direction with the lowest intensity at the centre, and the field strength is uniform along W direction. This antenna is in fundamental TM_{010} mode of the cavity created by the patch over the ground plane. The equations for the initial rectangular patch dimension in the fundamental mode are [137]:

$$f = \frac{c}{2(L+h)\sqrt{\varepsilon_e}} \qquad (3.\ 1)$$

Where:

f is the patch resonant frequency

c is the light speed

L is the patch resonant length

h is substrate thickness

W is the patch width

and ε_e is the effective dielectric constant of the substrate to be computed based on the relative effective dielectric constant ε_r of the substrate material as followed:

$$\varepsilon_e = \frac{\varepsilon_r + 1}{2} + \frac{\varepsilon_r - 1}{2}\left(1 + \frac{12h}{W}\right)^{-\frac{1}{2}} \qquad (3.\ 2)$$

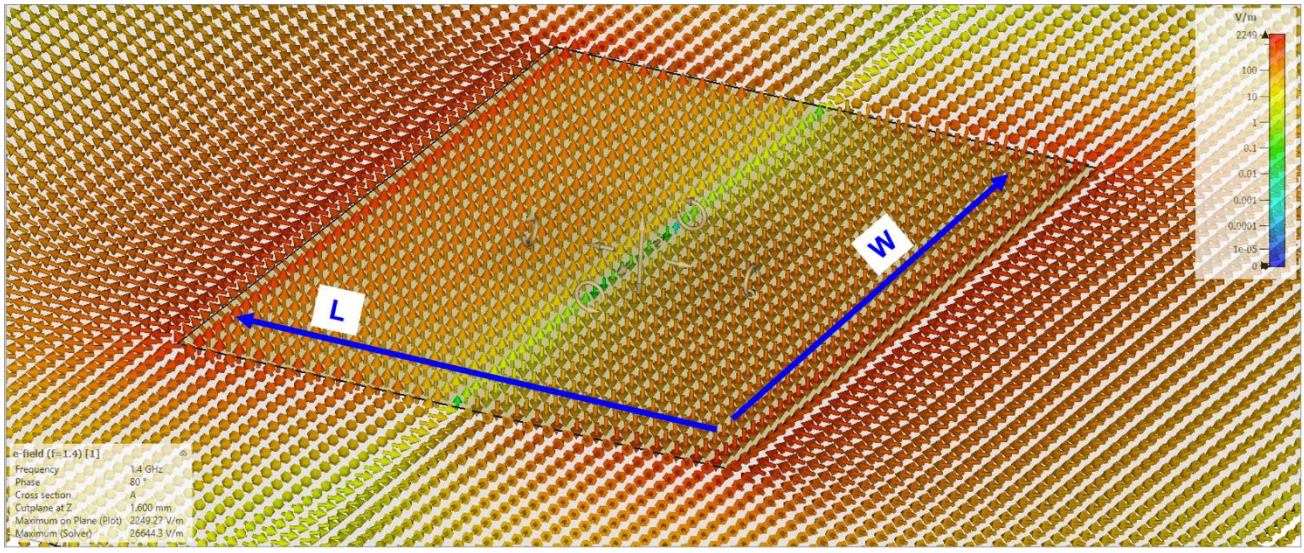

Figure 3. 3 Electric field distribution of a single element in TM010 mode

The finalised single patch design is shown in Figure 3. 4. Through iterations of optimisation, this design has a directivity of 9.533 dBi, and total efficiency of -0.40 dB with |S11|=-25 dB at 1.4 GHz. The radiation pattern at Phi=0° and Phi=90° cut planes are shown in Figure 3. 6 and Figure 3. 7 respectively, the half power beam width is 60° and the back-lobe level is at -22 dB level.

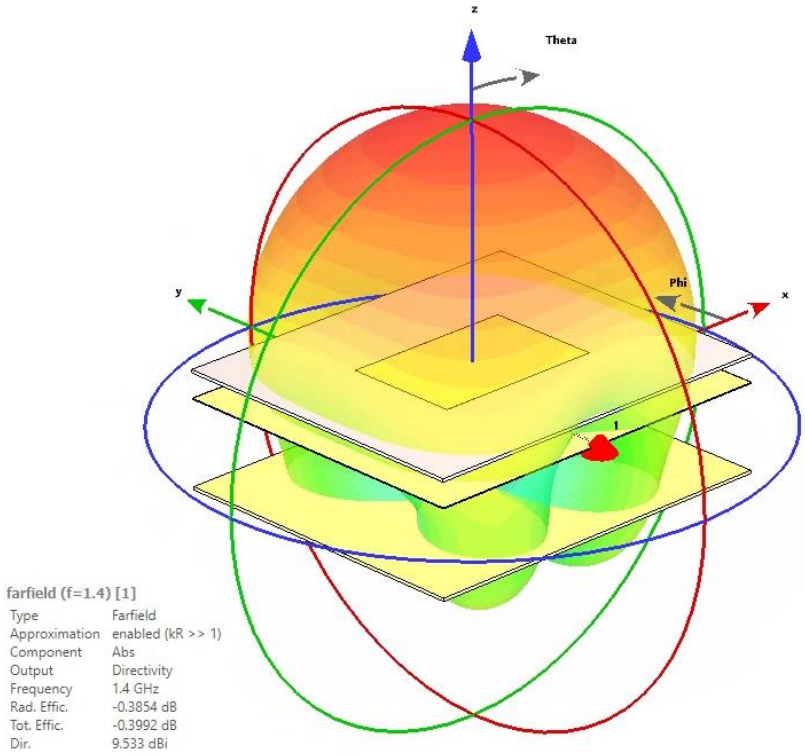

Figure 3. 4 Three-dimensional far field of the single patch design

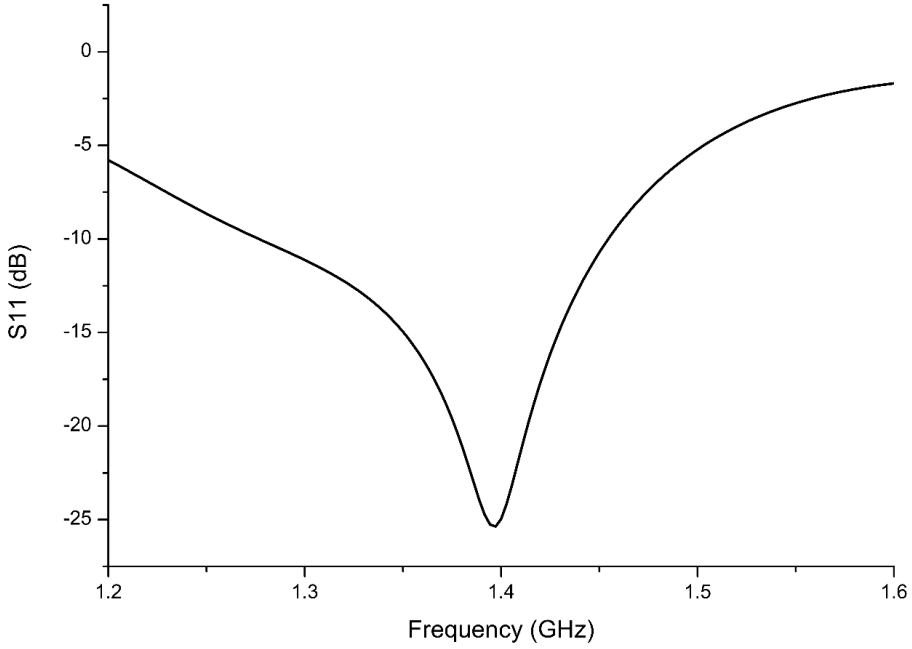

Figure 3. 5 Impedance matching of the single patch design

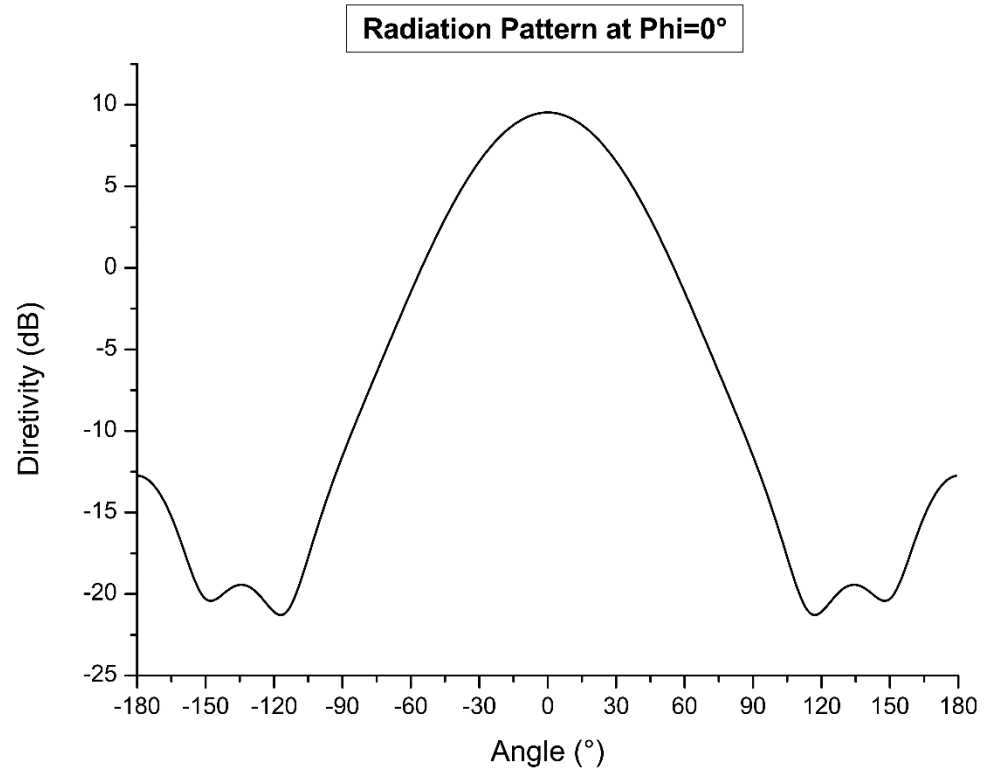

Figure 3. 6 Radiation pattern of the single element at Phi=0° cut plane

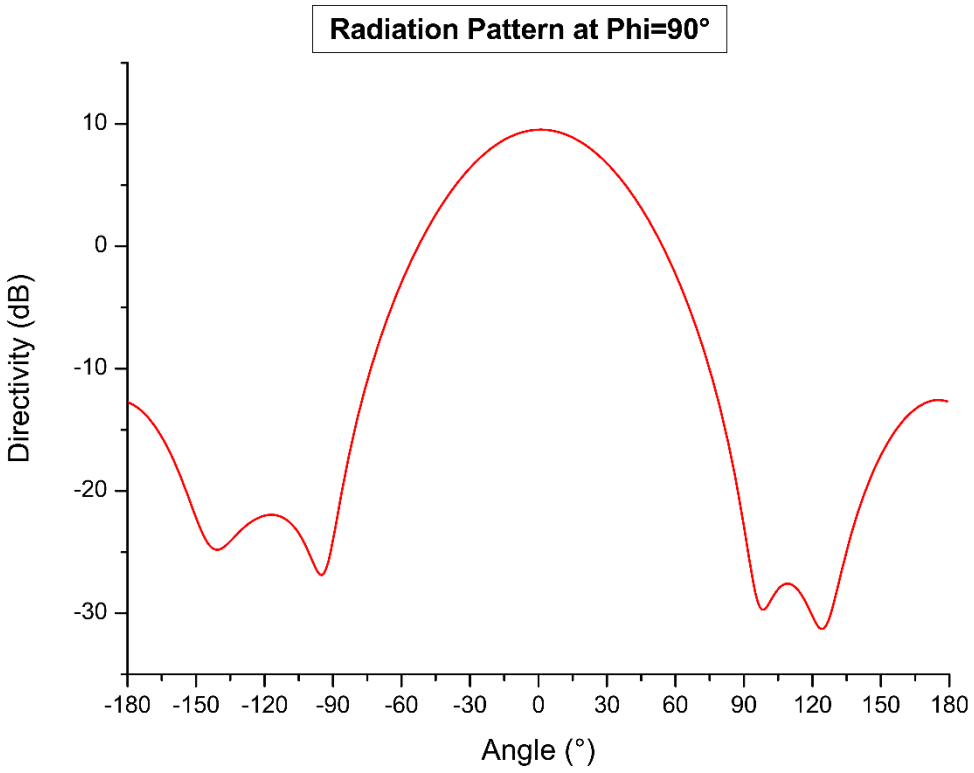

Figure 3. 7 Radiation pattern of the single element at Phi=90° cut plane

3.3.4 Uniform array design

Upon the completion of a single patch element design, the next step is to design a uniform antenna array. For this study, the main driving factors for using the array are beam shaping for higher spatial resolution and beam steering capability. These factors naturally lead to the preference of a corporate feed network. This is because a series feed network is limited to a fixed-beam and hence frequency scanning of the antenna, owing to any change to one element will propagate in a series feed network. In contrast, the phase and amplitude in a parallel feed network can be adjusted without affecting other elements.

Throughout this research, each radiation element in the array is designed identically, hence the total radiation field of an array is multiplication of the single element radiation field and array factor as [137]:

$$E_{array} = [E_{single\ element}] \times [Array\ Factor] \quad (3.\ 3)$$

Where E is the antenna radiated electric field and the array factor is the multiplying factor controlled by parameters such as the number of elements and shape of the array (e.g. circular, rectangular), inter-element distance, amplitude and phase of each element. The last two parameters are the primary focus of this study.

The inter-element distance of the array was selected to be 144.65 mm, which is 0.675 λ_0 (free space wavelength) at 1.4 GHz, this is to consider the size of each 2-bit phase shifter is 59.3x59.5mm for later integration in Chapter 4. While this spacing is larger than 0.5λ, and results in grating lobes in the array factor, the element pattern suppresses these grating lobes within the scan angle of the array. A test on mutual coupling has also been conducted [133]. Figure 3. 8 shows the test configuration where each antenna element is terminated by a discrete port, and only Port 1 is energised throughout the test. By varying the interelement distance between each element, the amount of coupling in terms of transmission coefficients $|S21|$, $|S31|$ and $|S41|$ are computed and plotted in Figure 3. 9. It can be observed that $|S21|$ and $|S31|$ drop at a higher rate passing beyond

$0.575\,\lambda_0$, and $|S41|$ is below -24 dB from $0.525\,\lambda_0\ to\ 0.725\,\lambda_0$. At the point of $\lambda_0 = 0.675$, the maximum amount of amount is at Port 3 with -17.41 dB level, hence the effect of mutual coupling is considered to be minor for this design.

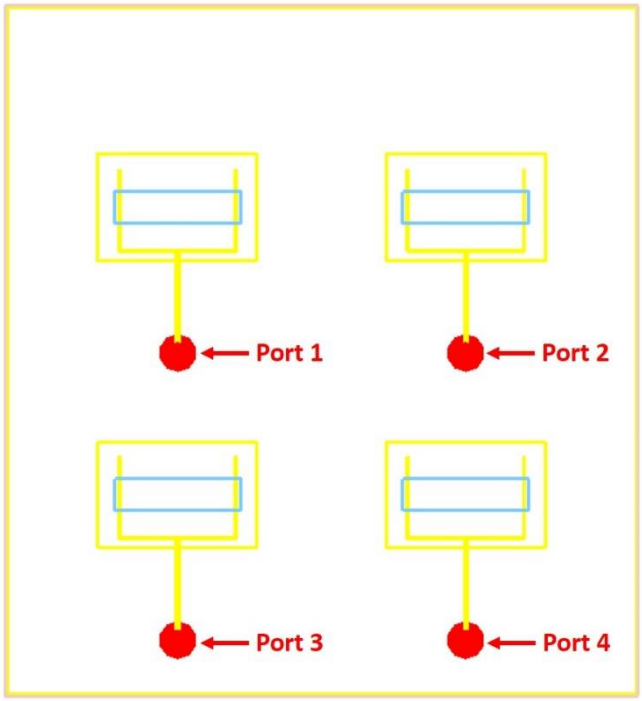

Figure 3. 8 Test configuration of mutual coupling

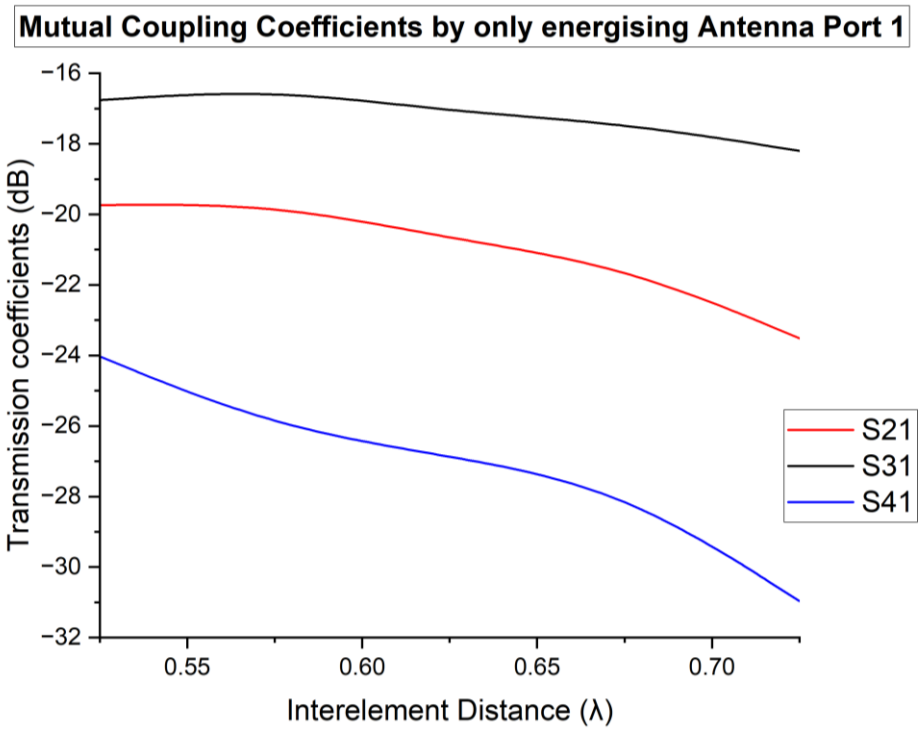

Figure 3. 9 Mutual Coupling Coefficient by varying interelement distance

In the design process, two types of power divider have been tested. The first type is T-junction power divider; the second type is two-way power divider.

For an equal power division from a 50Ω input, each dividing branch has a characteristic impedance of 100 Ω in a T-junction power divider. For impedance matching, quarter-wave transformers are adopted with the required impedance Z_2 in the length of 90° effective wavelength [135]. The structure is illustrated in Figure 3. 10, and Figure 3. 11 shows the implementation.

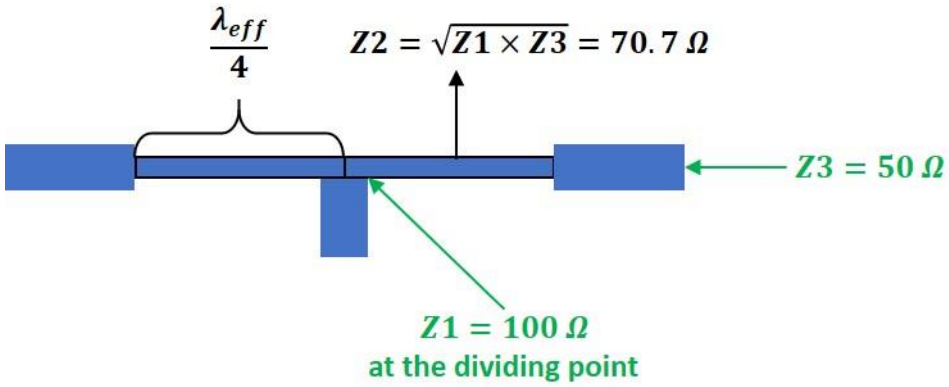

Figure 3. 10 Structure of a -3dB power divider with a quarter wavelength transformer at each side

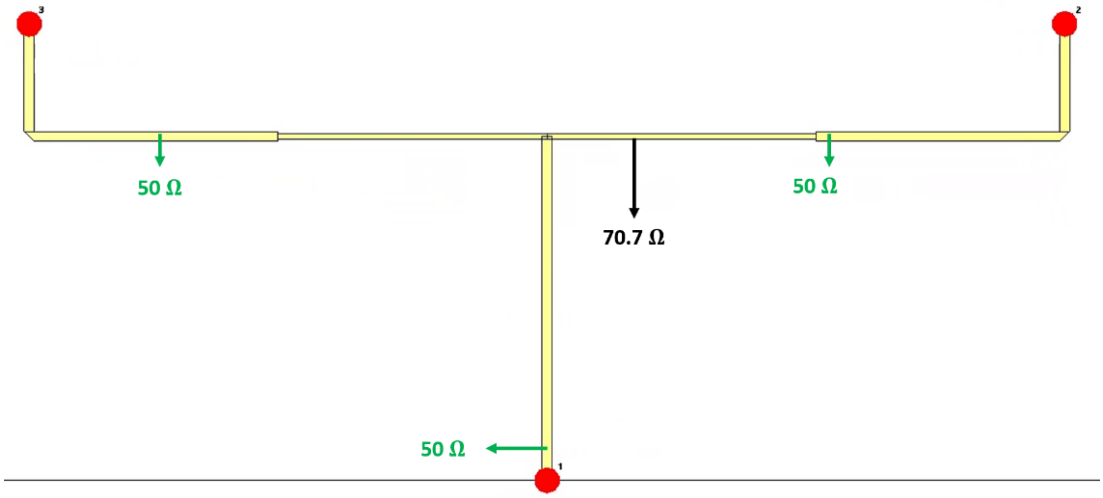

Figure 3. 11 Implementation of a T-junction power divider with a quarter-wave transformer at each branch

However, although being easy to design, one drawback of this topology is the long, thin 70.7Ω line which results in high insertion loss. The alternative method for impedance matching is the two-way power divider as illustrated in Figure 3. 12.

The fundamental design equations for the two-way power dividers are computed as per equations

(3. 4) to (3. 6). At this stage $Output\ Power\ 2\ =\ Output\ Power\ 3$, following equations (3. 4) and (3. 5) $\frac{Z_2}{Z1} = \frac{Z_3}{Z_1} = \frac{1}{2}$; and for the best matching to the antenna input, $Z_2 = Z_3 = 50\Omega$. Accordingly, as equation (3. 6), $Z_1 = 25\Omega$. A quarter-wavelength transformer has also been adopted between Z1 and the input feedline for impedance matching as depicted in Figure 3. 13. The improvement in insertion loss is summarised in the 2nd and 3rd iterations of Table 3. 1, along with increasing the patch substrate thickness, replacing with equal two-way power divider reduced the total radiation loss from -3.5 to -2.034 dB in a large 8x8 array.

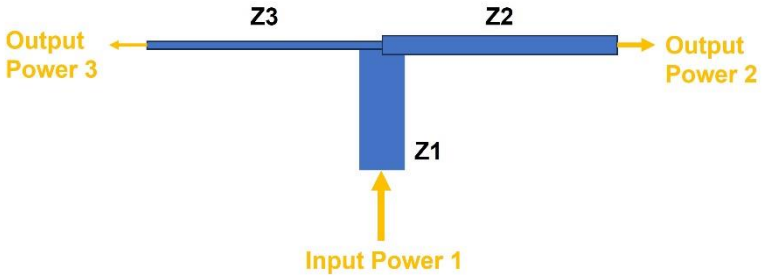

Figure 3. 12 Basic Microstrip two-way unequal power divider modified from [8]. Due to the thin feedline widths, angled cut off was not considered in the design

$$Output\ Power\ 2 = \left(\frac{Z1}{Z2}\right) \times Input\ Power\ 1 \qquad (3.\ 4)$$

$$Output\ Power\ 3 = \left(\frac{Z1}{Z3}\right) \times InputPower\ 1 \qquad (3.\ 5)$$

$$Z1 = \frac{Z2 \times Z3}{Z2 + Z3} \qquad (3.\ 6)$$

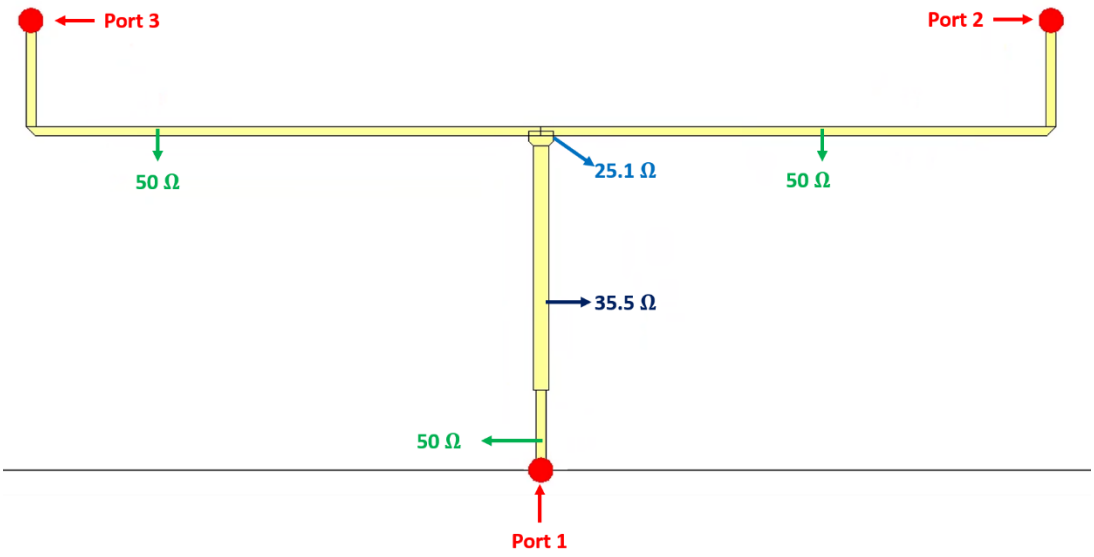

Figure 3. 13 Implementation of a two-way power divider with a quarter-wavelength transformer between Input and Z1

By assigning 50 Ω ports as labelled in Figure 3. 13, this equal power exhibits moderate matching with |S11| better than -18.4 dB within 1.4-1.425 GHz. Since each branch has the same transmission line widths and path lengths, the receiving power at port 2 and port 3 should be the identical in both amplitude and phase, this is reflected in Figure 3. 15 and Figure 3. 16.

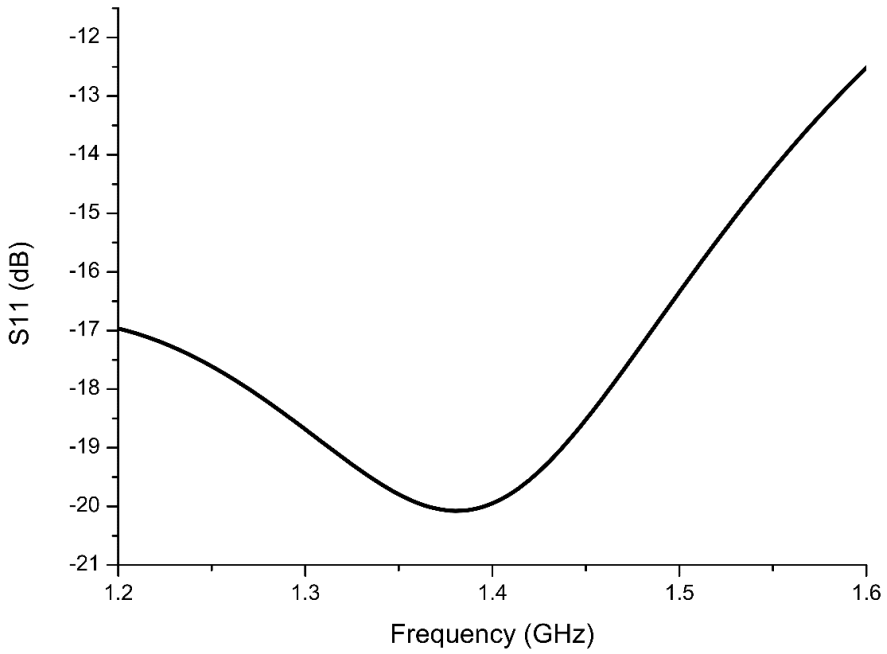

Figure 3. 14 Input impedance matching of the equal two-way power divider

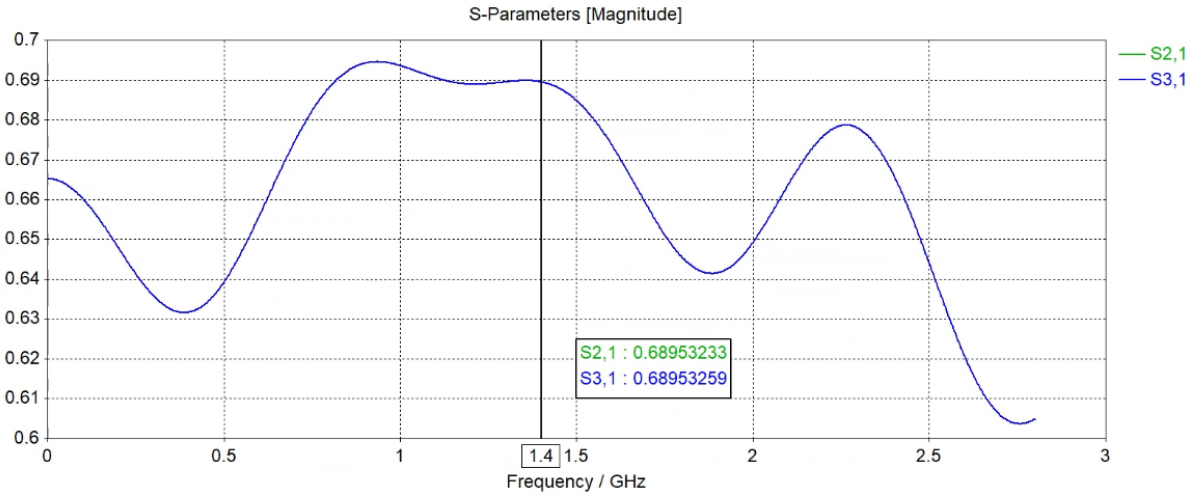

Figure 3. 15 Voltage ratio of the equal two-way power divider

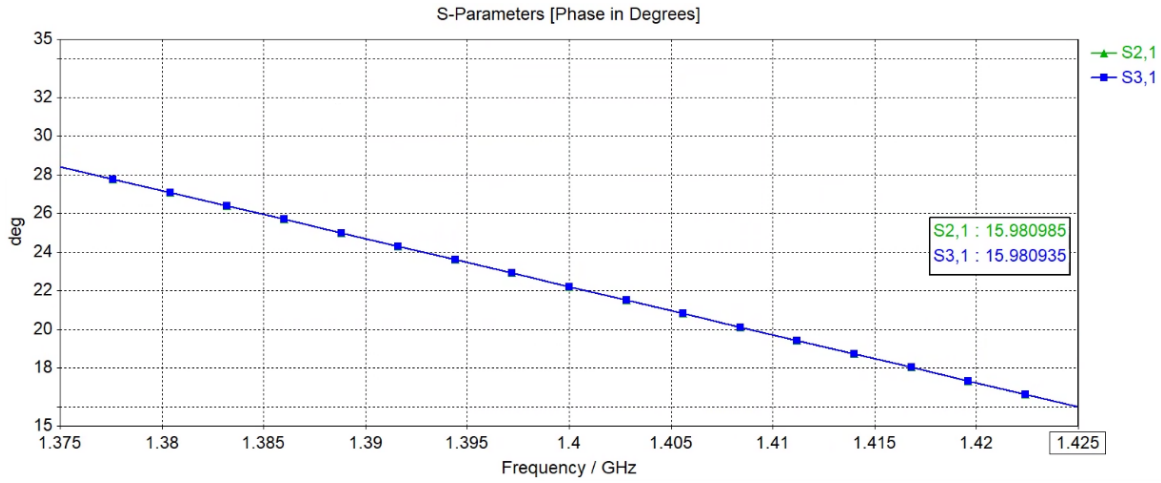

Figure 3. 16 Phase balance of the equal two-way power divider

Using the equal two-way power divider in uniform arrays design with 0.675 λ_0 inter-element distance, the radiation patterns of a 2x2, 4x4 and 8x8 are plotted in Figure 3. 17 and Figure 3. 18 as simulated in CST Microwave Studio, and Table 3. 3 summarises the key characteristic parameters of each array. Doubling the size of an array in each direction would increase the antenna directivity by approximately 3 dB [133], depending on the element spacing. Radiation loss increases with the array size mainly due to insertion loss in more and longer transmission lines of the power dividers. This is more pronounced with high loss substrate materials as indicated in Table 3. 1, where radiation loss is as high as -10.28 dB with Fr-4 as the substrate material. It can also be observed that the half power beam width narrows with larger array size as a result of increasing the effective array aperture to achieve high spatial resolution. A side lobe is defined as any antenna radiation pattern lobe other

than the antenna main lobe in the same hemisphere, and side lobe level (SLL) is defined as the power level difference between peak of antenna main lobe and side lobe. As summarised in Table 3. 3, the highest side lobe level is at -10.6 to -13.2 dB level because of uniform excitation and 0.675 λ_0 spacing.

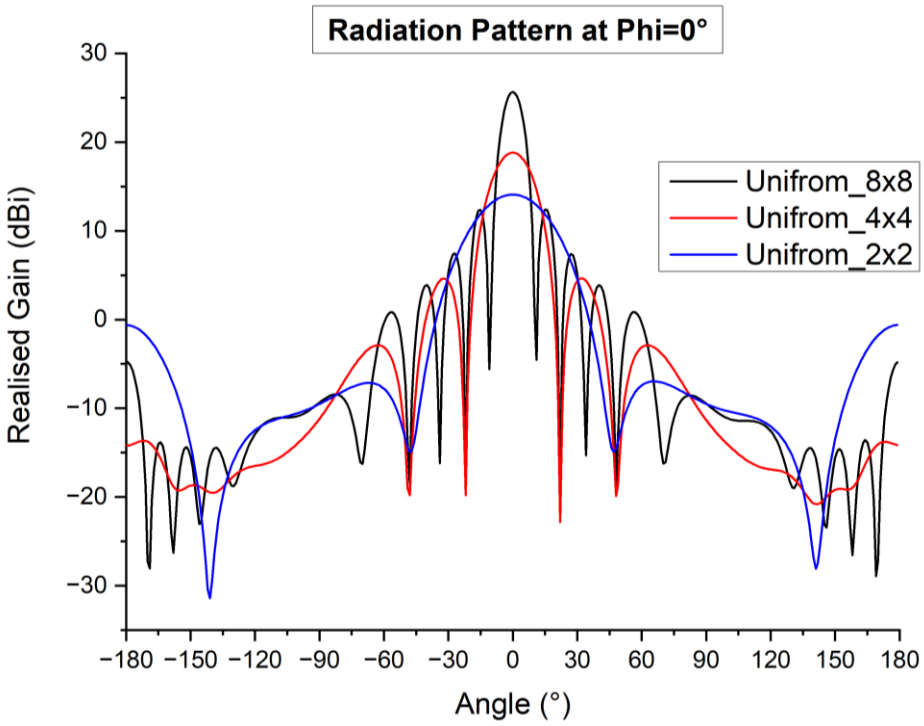

Figure 3. 17 Radiation Pattern of Uniform 2x2, 4x4 and 8x8 Array at Phi=0° cut plane

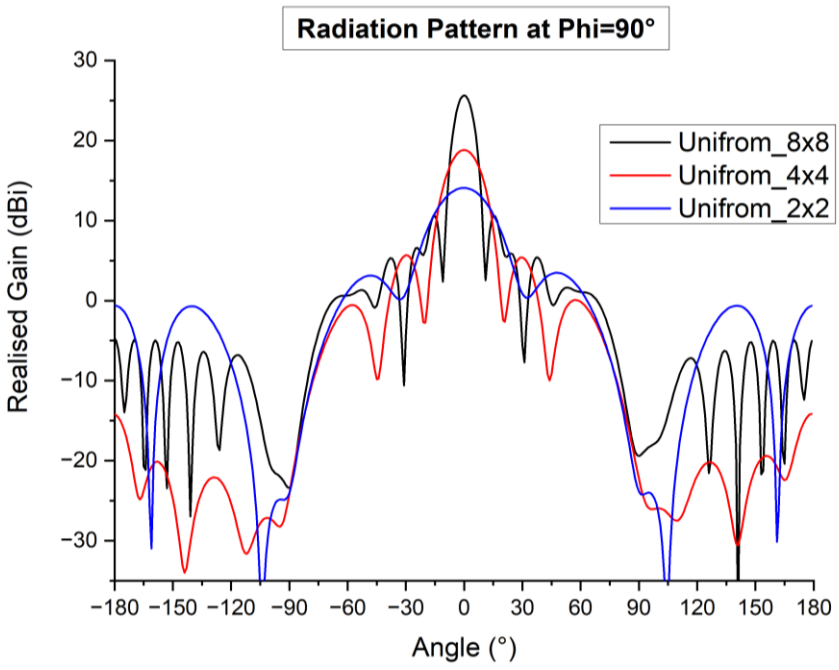

Figure 3. 18 Radiation Pattern of Uniform 2x2, 4x4 and 8x8 Array at Phi=90° cut plane

Table 3. 3 Key parameters of Uniform 2x2, 4x4 and 8x8 array

Array size	Directivity (dBi)	Radiation loss(dB)	Half Power Beam width (°)	Highest Side lobe level (dB)
2x2	14.73	-0.629	35	-10.6
4x4	19.9	-1.09	18.9	-13.1
8x8	25.64	-1.997	9.4	-13.2

3.4 Side lobe suppression with non-uniform excitation

3.4.1 Beam efficiency requirements for radiometer antennas

For radiometer applications, very high main beam efficiency in the range of 90% is required [137].Main beam efficiency can be understood as the ratio of energy received by the main beam to that of the total energy collected by all the antenna radiation lobes (i.e. main lobe and all the minor lobes), and can be expressed as equation (3. 7) [137, 138].

$$BE(\theta_1) = \frac{\int_0^{2\pi}\int_0^{\theta_1} D(\theta,\phi)sin\theta d\theta d\phi}{\int_{\phi=0}^{2\pi}\int_{\theta=0}^{\pi} D(\theta,\phi)sin\theta d\theta d\phi} \quad (3.\ 7)$$

where:

$$D(\theta,\phi): Directivy\ of\ the\ antenna\ in\ every\ direction$$

$$\theta_1 : Main\ beam\ axis\ to\ first\ null.$$

An antenna collects thermal radiation from the entire radiation pattern and sums up according to each lobe weighting in the form of brightness temperature $T_{Antenna}$. Since the antenna main lobe usually has the largest weighting to the resultant brightness temperature, $T_{Antenna}$ can be expressed in the form of equation (3. 8) [34, 137].

$$T_{Antenna} = T_{Main\ lobe} \times BE_{\theta_1} + T_{Minor\ Lobes}[1 - BE_{\theta_1}] \quad (3.\ 8)$$

Where:

$T_{Main\ lobe}$: *the equavalent brightness temperature observed by the antenna main beam*

$T_{Minor\ Lobes}$: *the equivalent brightness tempearture observed by the antenna minor lobes*

As illustrated in Figure 3. 19 (a), now consider a scenario where the antenna main beam is collecting thermal radiation from soil with brightness temperature $T_B = 200° K$. However, the target soil is surrounded by water with much lower emissivity and hence lower brightness temperature (e.g. $T_B = 100° K$), which will be picked up by the antenna side lobes. By assuming negligible contribution from the antenna back lobe, a SLL of -14 (in a typical uniform 8x8 array) and the corresponding main beam efficiency of 80% could cause an error of $20°K$ as illustrated in Figure 3. 19 (b) , while suppressing the SLL down to -20 dB increases the main beam efficiency to 90% and reduces the error to $10°K$ as in Figure 3. 19 (c). Although it is unlikely that the only a footprint size of soil is surrounded by water in practice, for soil moisture remote sensing applications with precision requirement of $1°K$, endeavours to improve main beam efficiency are required.

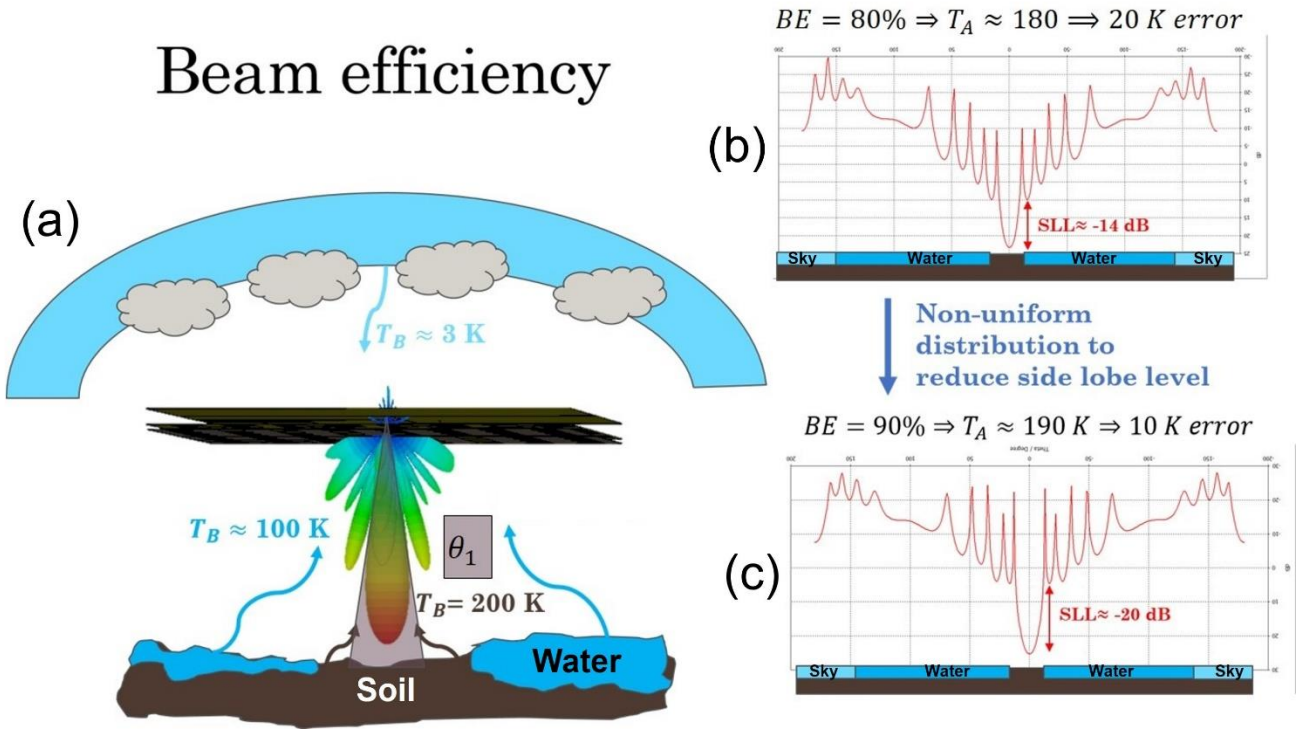

Figure 3. 19 Illustration of antenna beam efficiency (a) 3D scenario of the scene (b)2D Phi=0° cut-plane view of the scene from -180° to +180° with uniform excitation (c) 2D Phi=0° cut-plane view of the scene from -180° to +180° with tapered excitation

3.4.2 Dolph-Tschebysheff coefficients

There are various amplitude tapering methods for side lobe suppression [139], such as binomial array [137], Taylor distribution [140] and Staircase Power Distribution [141]. In this study, the Dolph-Tschebysheff method [142] has been selected for both the 4x4 and 8x8 designs because this method provides the degree of freedom to compute excitation coefficients according to a specified side lobe level, or adjust the best side lobe level according to practical design limitations (e.g. microstrip feedline width). This method was first introduced by Dr. Dolph to optimise side lobe level and main beam width of a broadside array by fitting Tschebysheff polynomials into antenna array factor weighting. Figure 3. 20 plots the zero order and odd orders of the Tschebysheff polynomials of the first kind [143], where the 3rd,5th and 7th order polynomials will be used for fitting the excitation coefficients of 1x4, 1x6 and 1x8 arrays in this study. It can also be observed that each polynomial has equal amplitude of oscillation ($T_n(z) = \pm 1$) within $-1 \leq z \leq +1$, leading to equal side lobe levels in the corresponding array factor and minimum main beamwidth [137, 144].

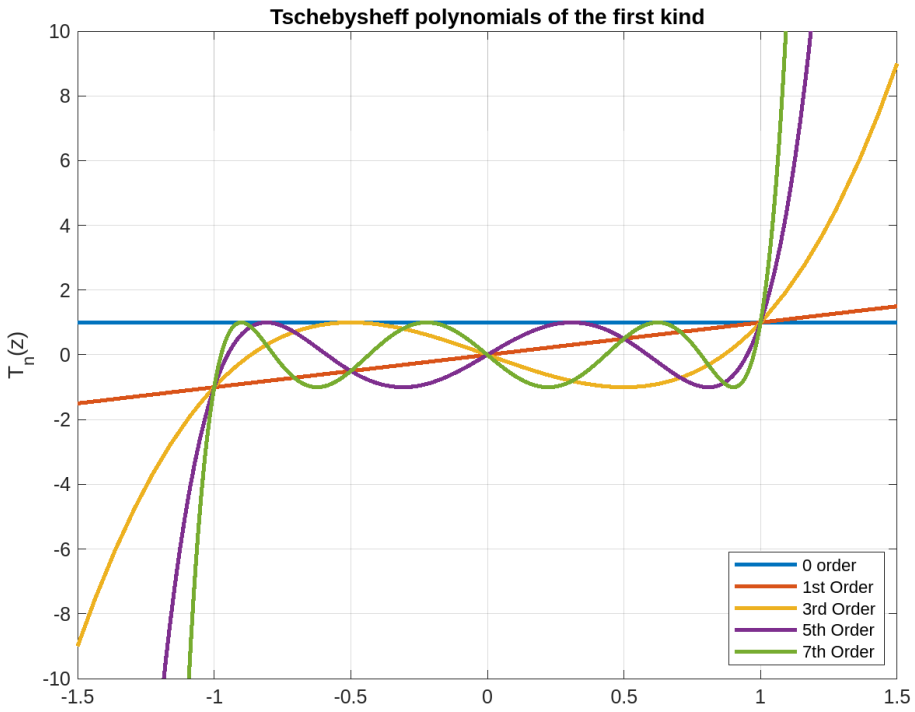

Figure 3. 20 Plots of the Tschebyscheff polynomials of the first kind

3.4.3 A 4x4 L- band ACMPA array with side lobe suppression

3.4.3.1 Excitation coefficient

As a starting point for side lobe suppression, a -20 dB side lobe level was selected as an achievable

goal. The computation of coefficients in terms of current ratio are computed following the fitting procedures in [137], Figure 3. 21 shows the excitation coefficients plot for a linear 1x4 array.

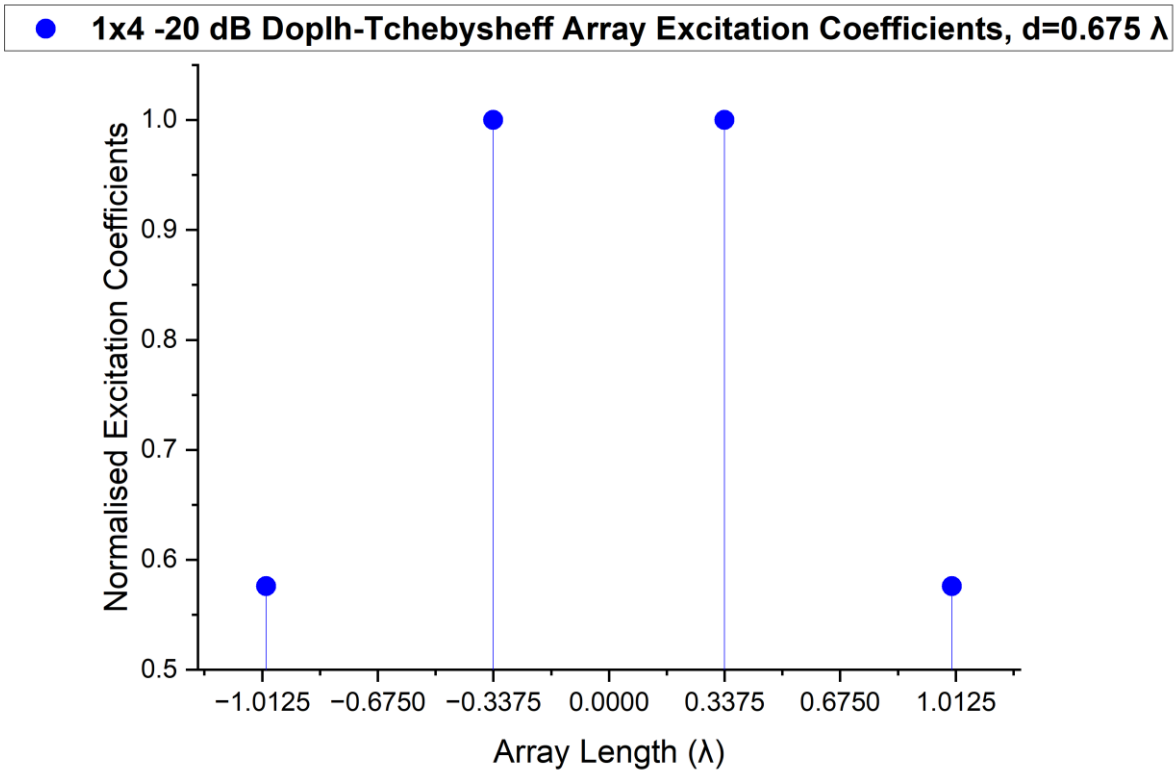

Figure 3. 21 -20 dB Doplh-Tchebysheff Array Excitation Coefficients for a linear 1x4 Array

Accordingly, to apply side lobe suppression in both X- and Y- direction, the current distribution for a 4x4 array is listed Table 3. 4. It is apparent that the lowest coefficient 0.332 in the top right corner has both vertical and horizontal suppression hence $0.576^2 = 0.332$. Because each quadrant of the table is symmetrical, the main work is to complete one quadrant of the required 2x2 power division. The current division of the top right quadrant is illustrated in Figure 3. 22. Thereafter, the design work breaks down to

(1) The design of the horizontal unequal power divider

(2) The design of the vertical unequal power divider

Table 3. 4 Excitation coefficients for a 4x4 -20 dB Dolph-Tschebysheff array

0.331	**0.576**	**0.576**	**0.332**
0.576	**1**	**1**	**0.576**
0.576	**1**	**1**	**0.576**
0.331	**0.576**	**0.576**	**0.331**

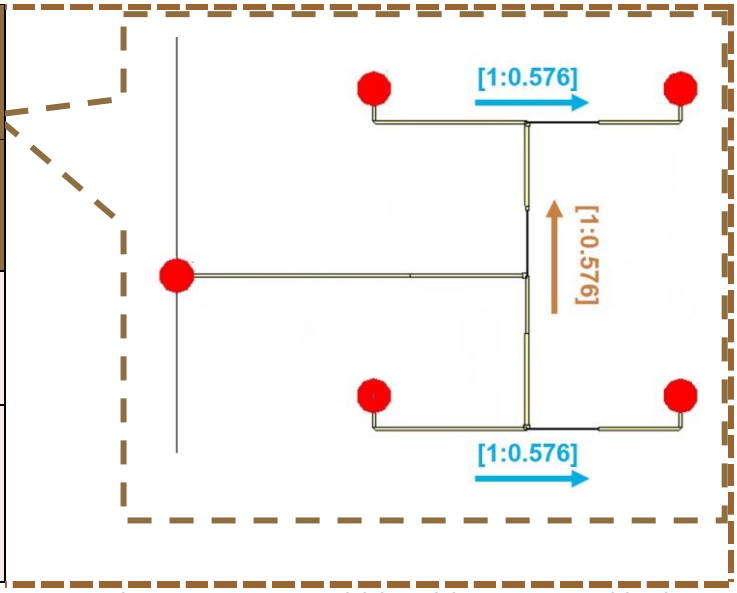

Figure 3. 22 Current Division of the 2x2 unequal feed network

3.4.3.2 Unequal power dividers design

For the implementation of unequal current division, a two-way unequal power divider was selected to be modified from the earlier stage two-way power divider. Accordingly, the modified design for a horizontal [0.575:1] power divider is shown in Figure 3. 23. In this case, unequal power division requires different branch impedances and hence different transmission line widths W which is a controlling factor of effective dielectric constant as in *Equation 3.3,* resulting in different phase propagation constants in each transmission line section. Therefore, a phase difference was introduced between Port 2 and Port 3. In here, Z_2 was 50 Ohm for the higher power arm, the length of the lower power arm has been carefully tuned to match the current division requirement and minimise phase imbalance at the same time. As depicted in Figure 3. 24, this power divider exhibits good impedance matching with |S11| better than -31dB from 1.4 to 1.425 GHz. The linear voltage division (in Figure 3. 25) is [0.492: 0.846] which can be normalised to [0.58: 1] to be acceptably close to the requirement; while the phase imbalance is less than 0.8° within the 25MHz bandwidth as in Figure 3. 26.

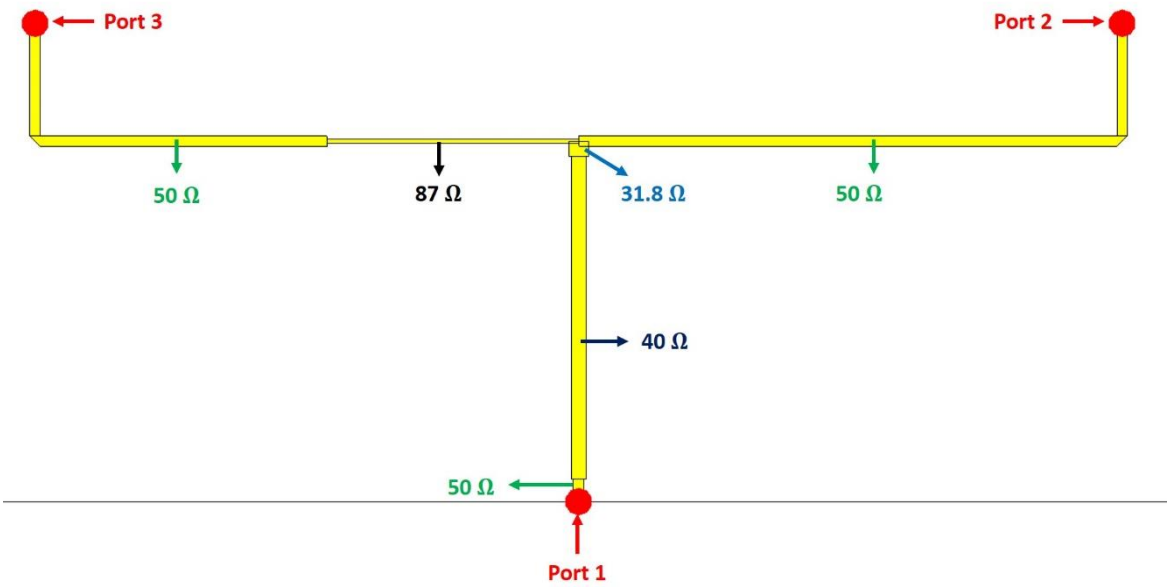

Figure 3. 23 Implementation Horizontal [0.575:1] two-way power divider

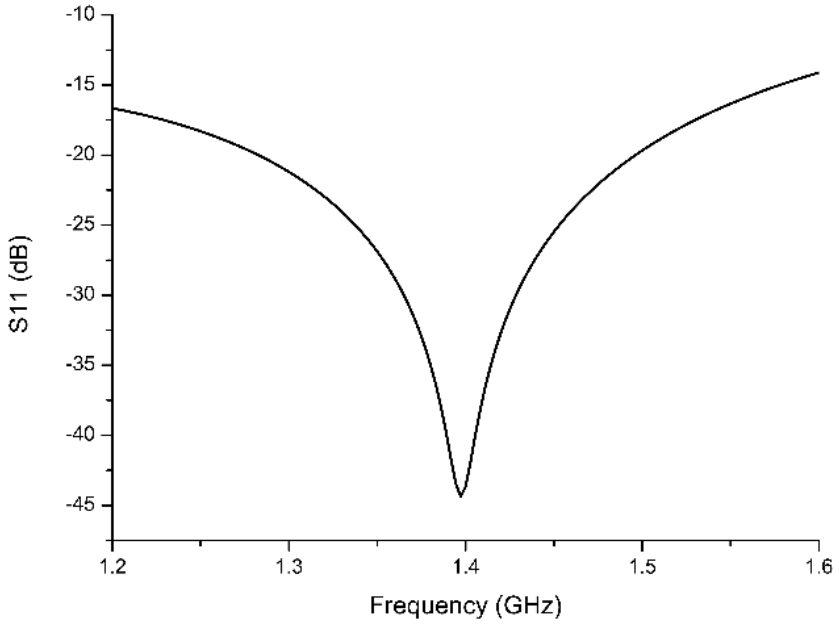

Figure 3. 24 Input impedance matching of the horizontal [0.575:1] power divider

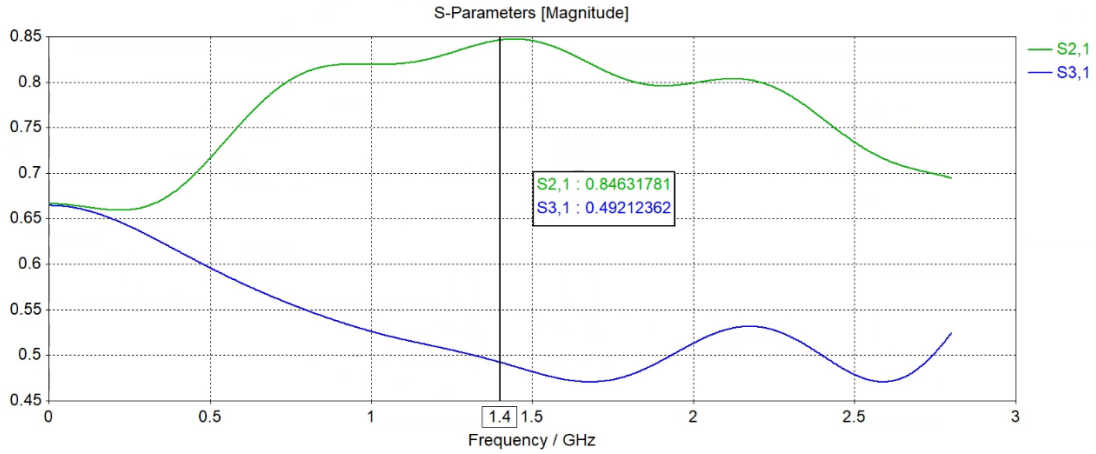

Figure 3. 25 Linear voltage division of the horizontal [0.575:1] power divider

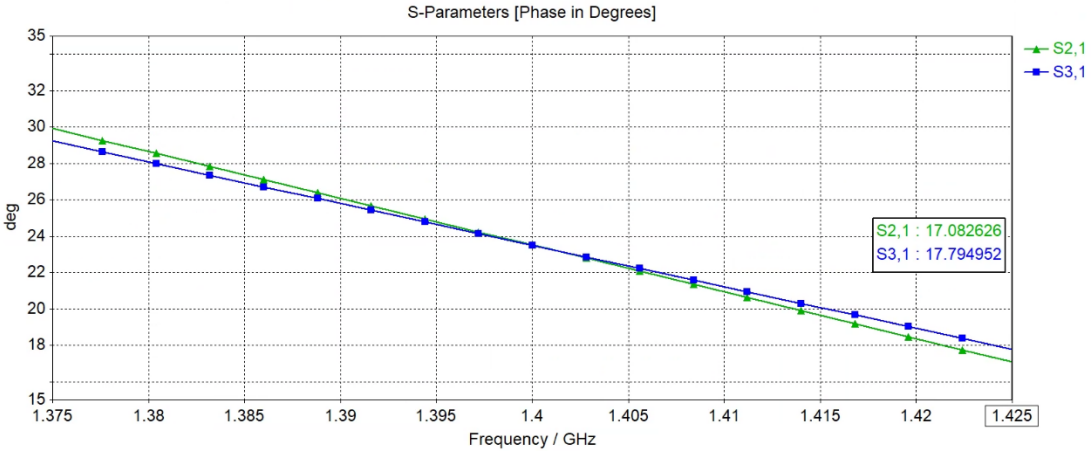

Figure 3. 26 Phase difference of the horizontal [0.575:1] power divider

Upon the successful design of the horizontal power divider, the next step is to design the vertical unequal power divider which connects two horizontal [0.575:1] power dividers. Figure 3. 27 shows the impedance stages of the power divider, while the width of the thin 99.3 Ω line predominantly controls the power ratio, the length of the 50 Ω and 40 Ω microstrip lines at each top and bottom branch controls the phase balance, iterations of optimisation had taken place to meet the power ratio, phase balance and impedance matching at the same time.

As depicted in Figure 3. 28, the simulated reflection coefficient is better than -36.6 dB at port 1. The linear voltage ratio in Figure 3. 29 is [0.489: 0.841], equivalent to [0.58: 1] after normalisation, and the phase imbalance is less than 0.5° referring to Figure 3. 30.

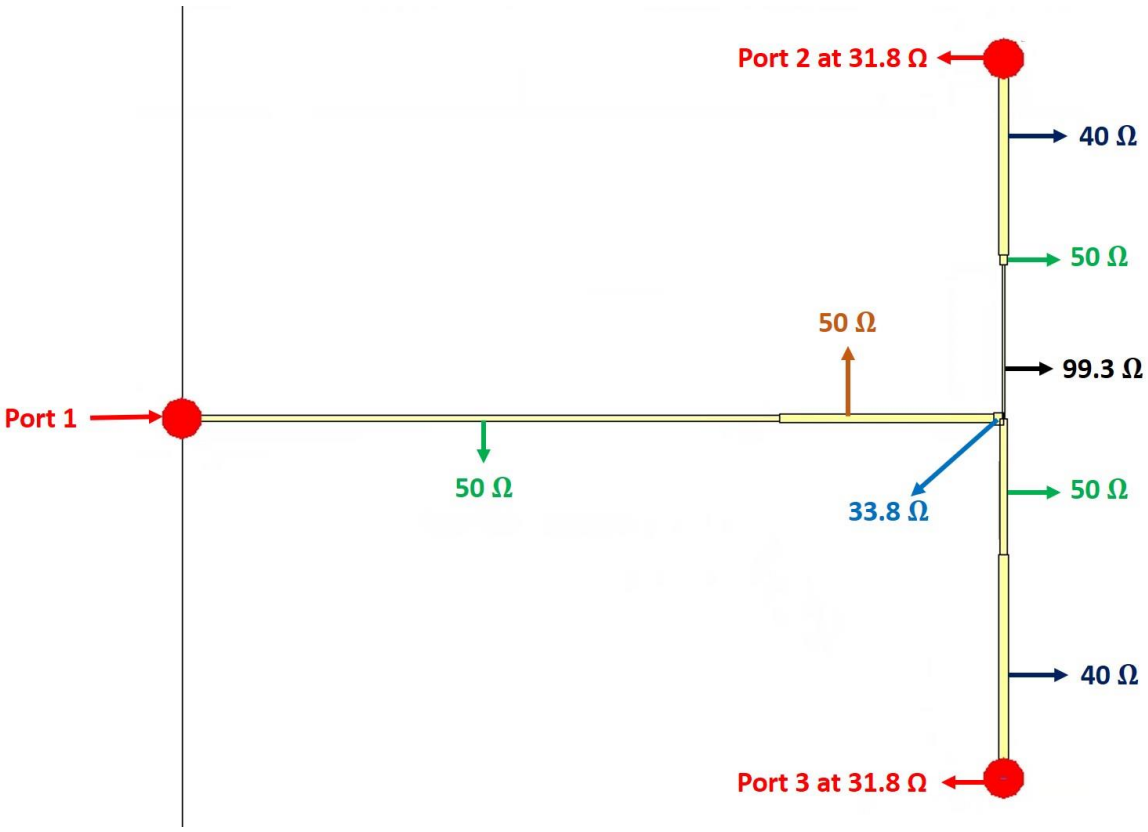

Figure 3. 27 Vertical [0.58:1] two-way power divider

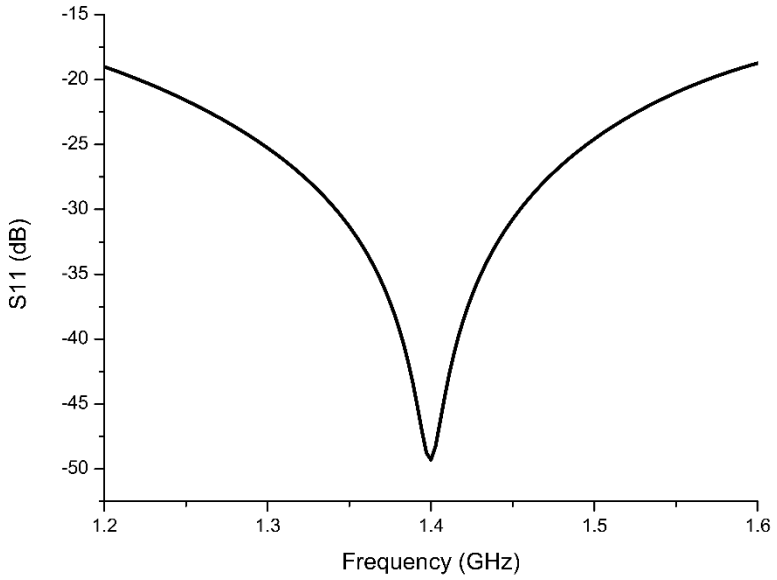

Figure 3. 28 Input impedance matching of the vertical [0.58:1] power divider

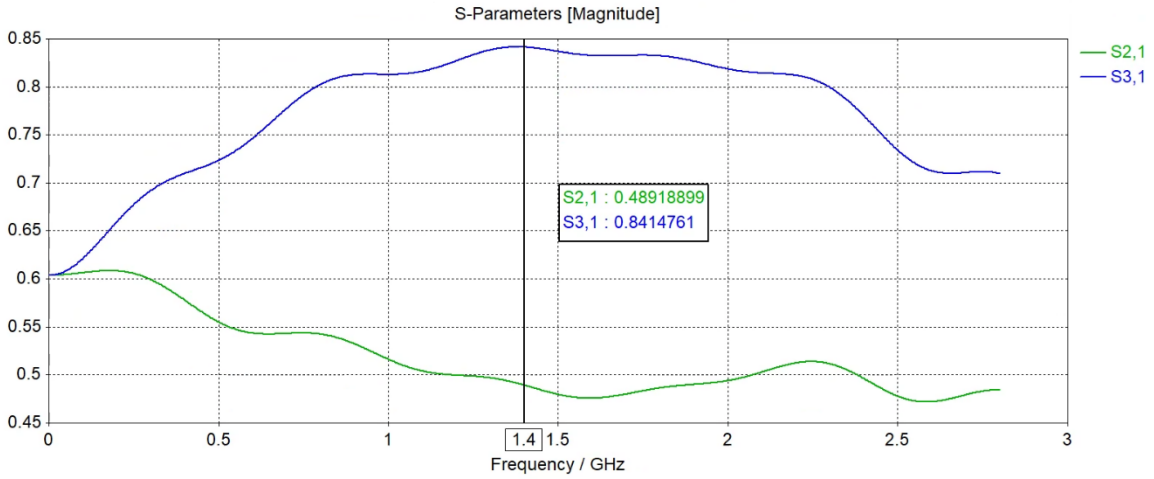

Figure 3. 29 Linear voltage ratio of the vertical [0.58:1] power divider

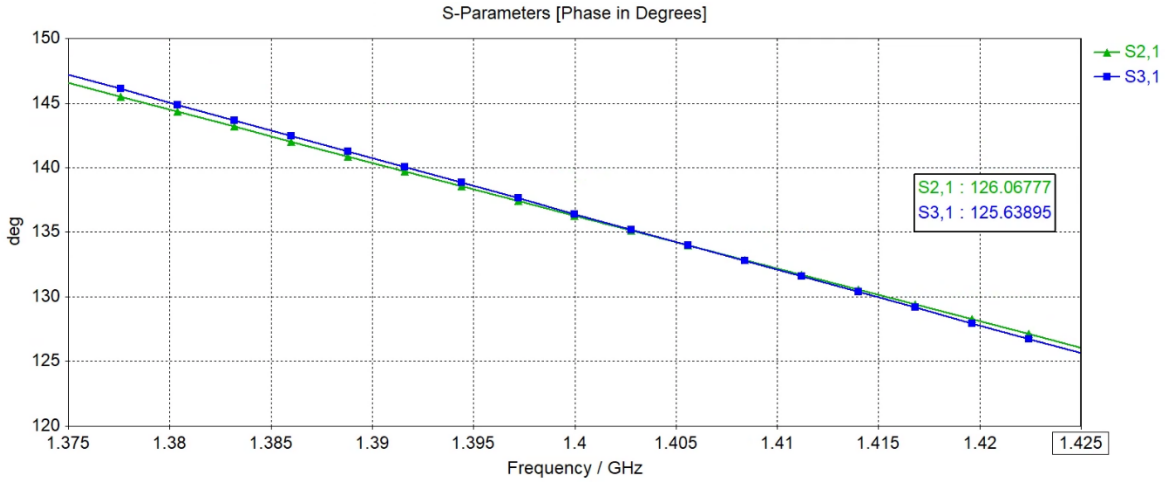

Figure 3. 30 Phase difference of the vertical [0.58:1] power divider

3.4.3.3 Integration and simulation validation

The next step was to combine the horizontal and vertical unequal power dividers as in Figure 3. 31. Overall, with slight adjustment of the 41.1Ω transmission line of the vertical power divider for input impedance matching, the 2x2 unequal power divider exhibits |S11| better than -24 dB as depicted in Figure 3. 32. The linear voltage ratio and phase imbalance of each port is plotted in Figure 3. 33 and Figure 3. 34 respectively, and also summarised in Table 3. 5, where the maximum amplitude error is 0.01, and phase imbalance is 1.6°

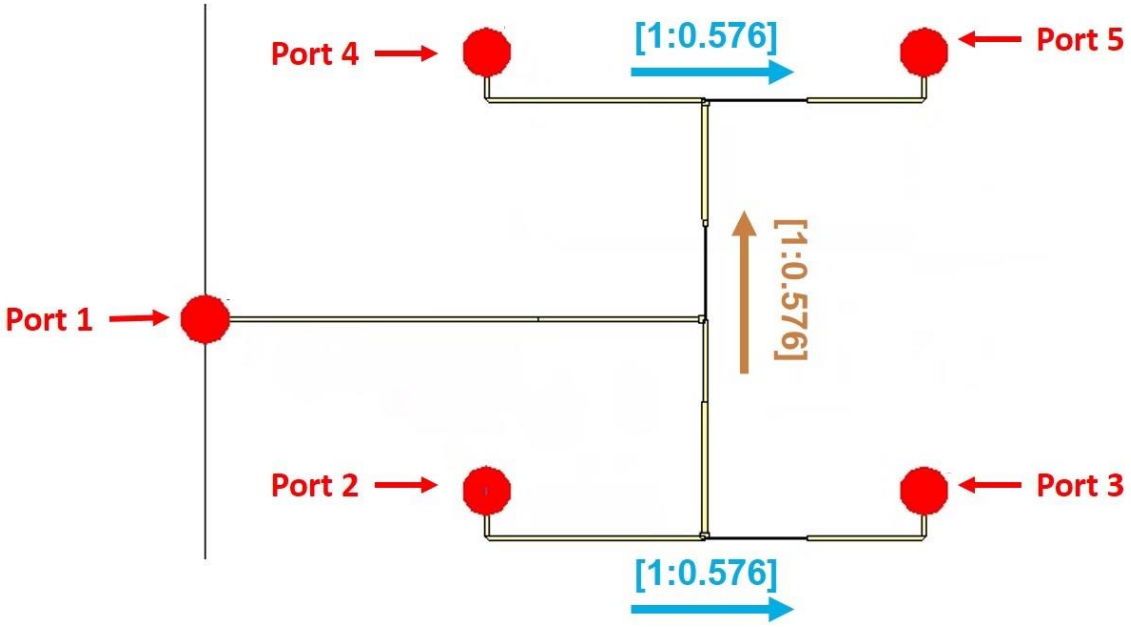

Figure 3. 31 Two by two unequal power divider

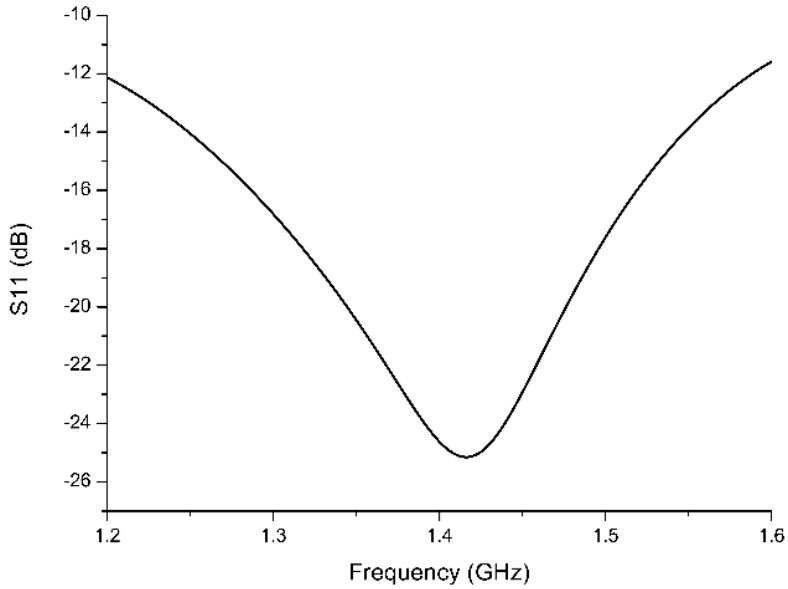

Figure 3. 32 Input impedance matching of the two by two unequal power divider

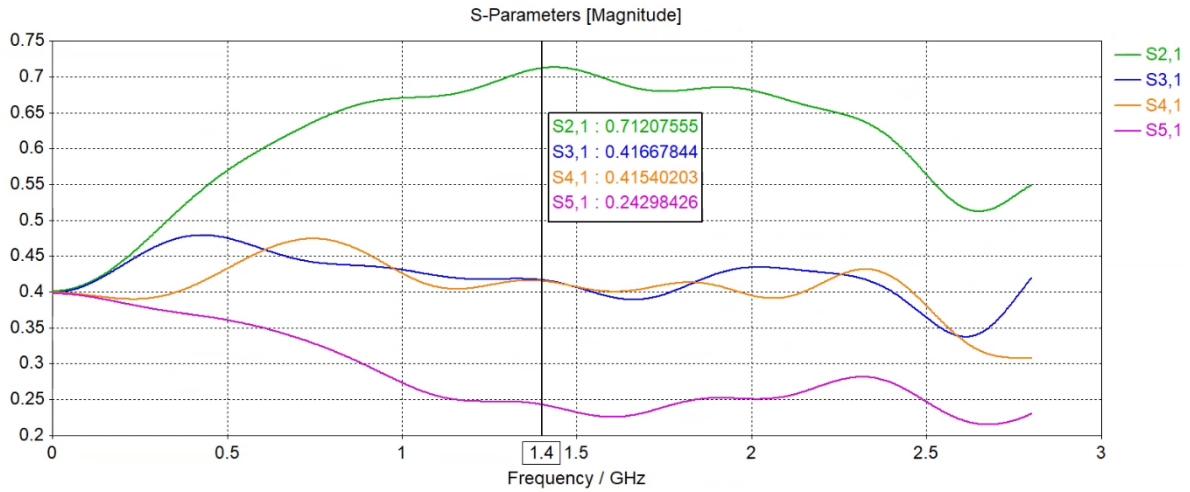

Figure 3. 33 Linear voltage ratio of the two by two unequal power divider

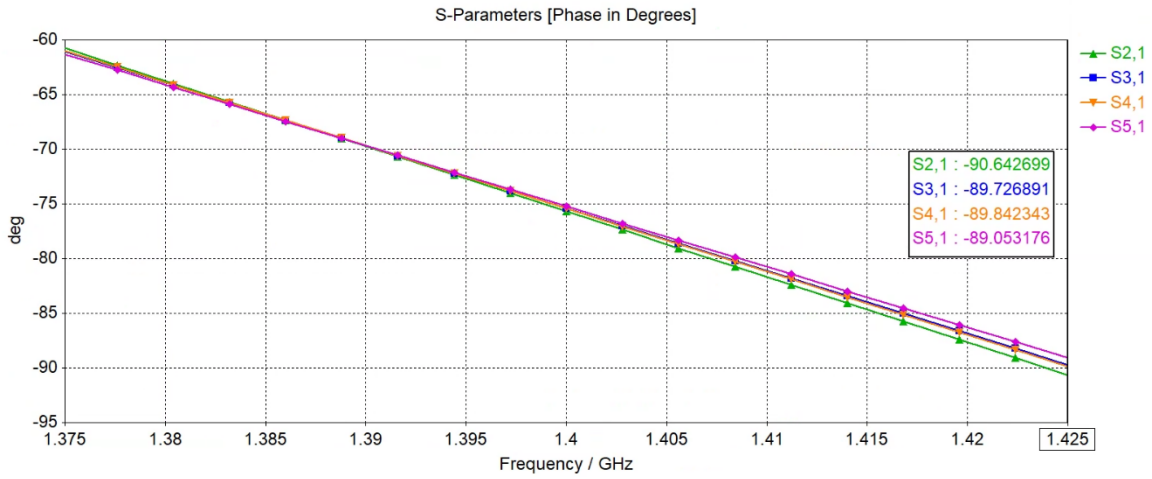

Figure 3. 34 Phase difference of the two-by-two power divider

Table 3. 5 Summary of the two-by-two unequal power divider network

Port	Nomalised Voltage ratio	Maximum Phase difference (°)
Port 2	1 (reference)	0 (reference)
Port 3	0.585	0.91
Port 4	0.583	0.8
Port 5	0.341	1.6

The 2x2 unequal power divider was then integrated into the 4x4 feed network of the antenna array as illustrated in Figure 3. 35. Thereafter, Figure 3. 36 depicts the three-dimensional radiation

pattern of the 4x4 array, it can also be observed that radiation loss has slight increased from -1.09 dB with uniform excitation to -1.235 dB due to thinner transmission lines adopted for unequal power division. This tapered array exhibits |S11| better than -22.81 dB as depicted in Figure 3. 37, and side lobe level at -21.9 dB as shown in the radiation pattern plots in Figure 3. 38 and Figure 3. 39. This results in an improvement of three-dimensional main beam efficiency (as per *Equation 3.7*) from 84.41% in a uniform array to 97.74% in this tapered array.

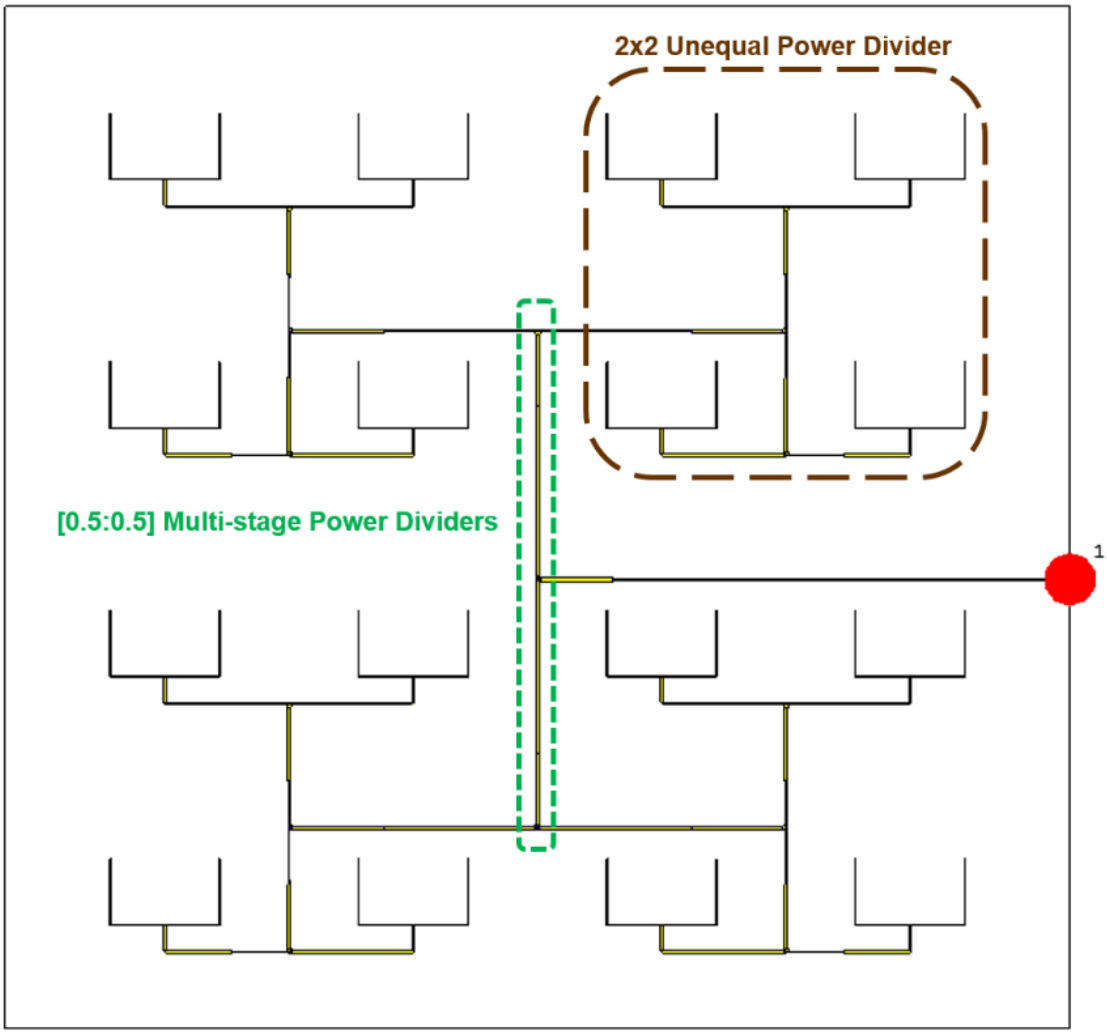

Figure 3. 35 Integrated 4x4 feed network

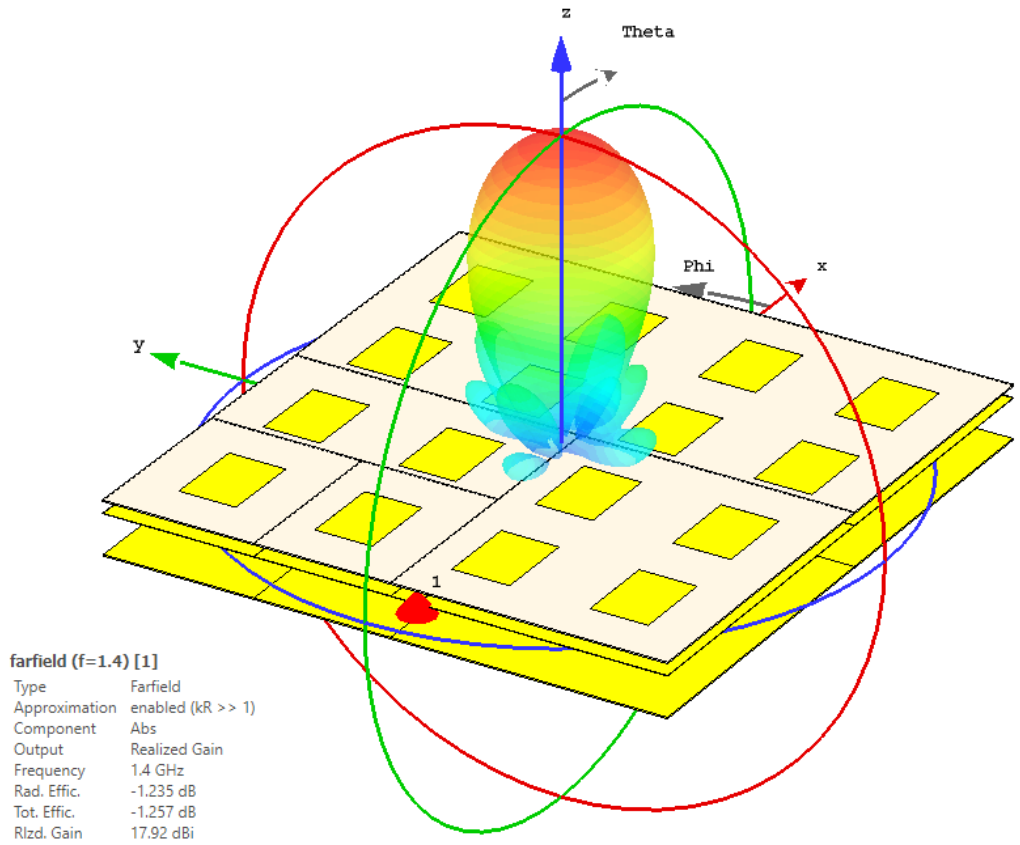

Figure 3. 36 Three-Dimensional Far-field result of the 4x4 array with tapered excitation

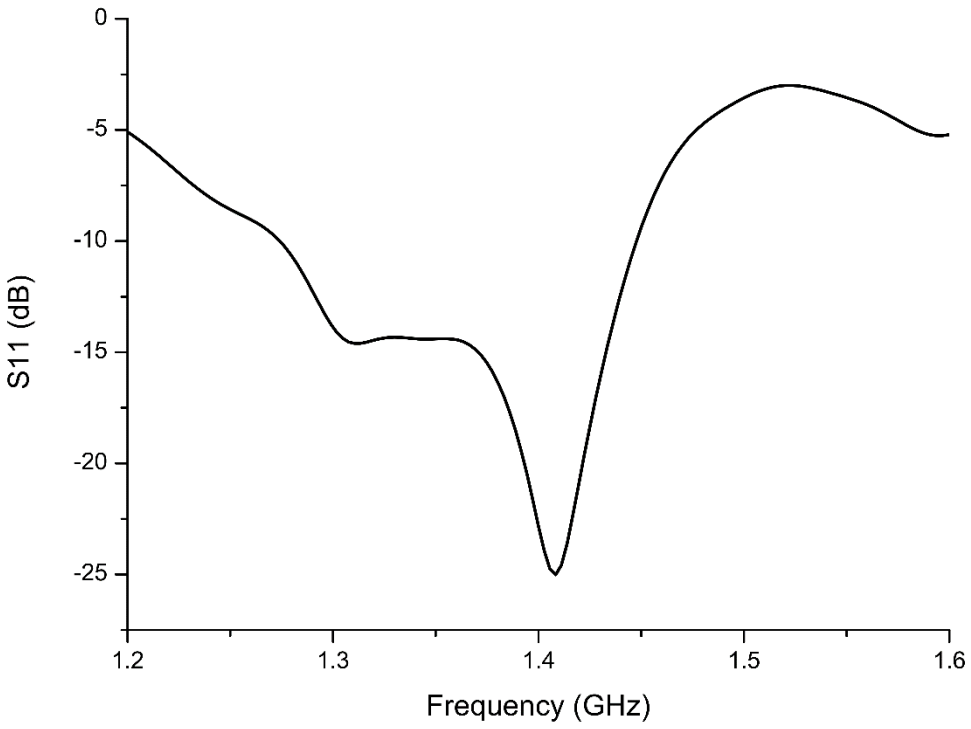

Figure 3. 37 Impedance matching of the tapered 4x4 array

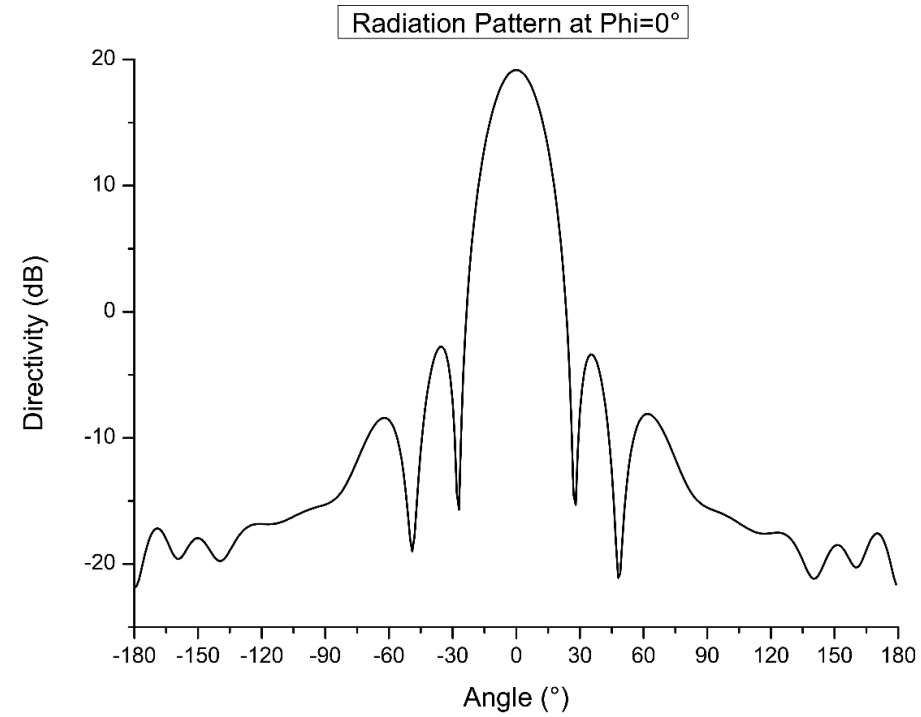

Figure 3. 38 Radiation pattern of tapered 4x4 array at Phi=0° cut plane

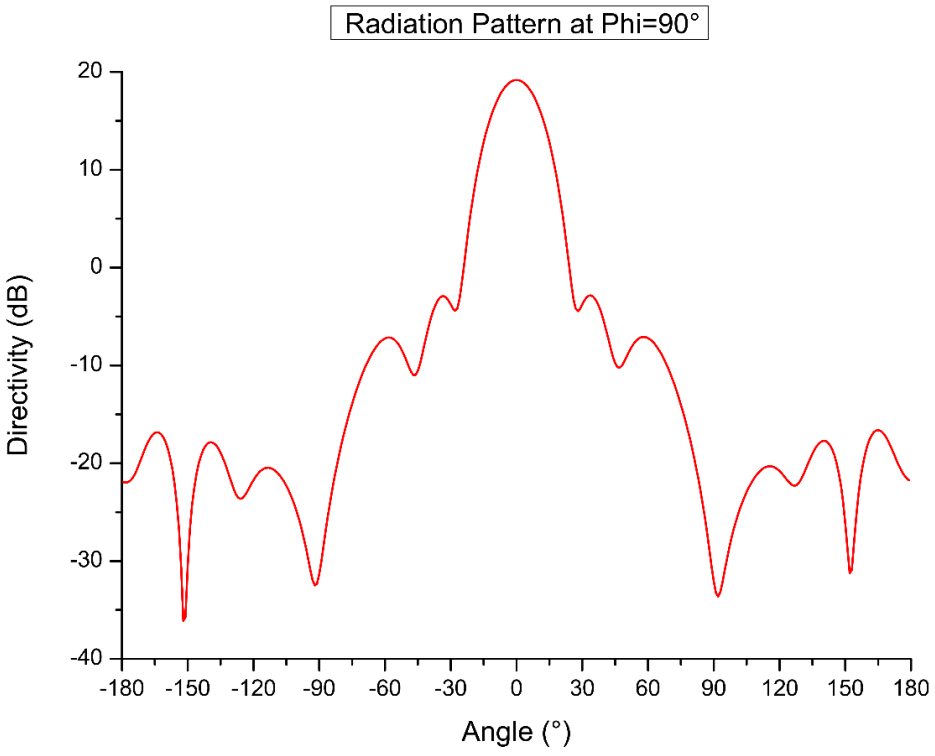

Figure 3. 39 Radiation pattern of tapered 4x4 array at Phi=90° cut plane

3.4.4 An 8x8 L- band ACMPA array with side lobe suppression

3.4.4.1 Excitation coefficients

For the 8x8 array, a -35 dB side lobe level was selected. Likewise, the excitation coefficients are computed as per [137]. The normalised excitation coefficients for a linear 1x8 array are plotted in Figure 3. 40, after which the current distribution for an 8x8 -35 dB Dolph-Tschebysheff array is computed in Table 3. 6.

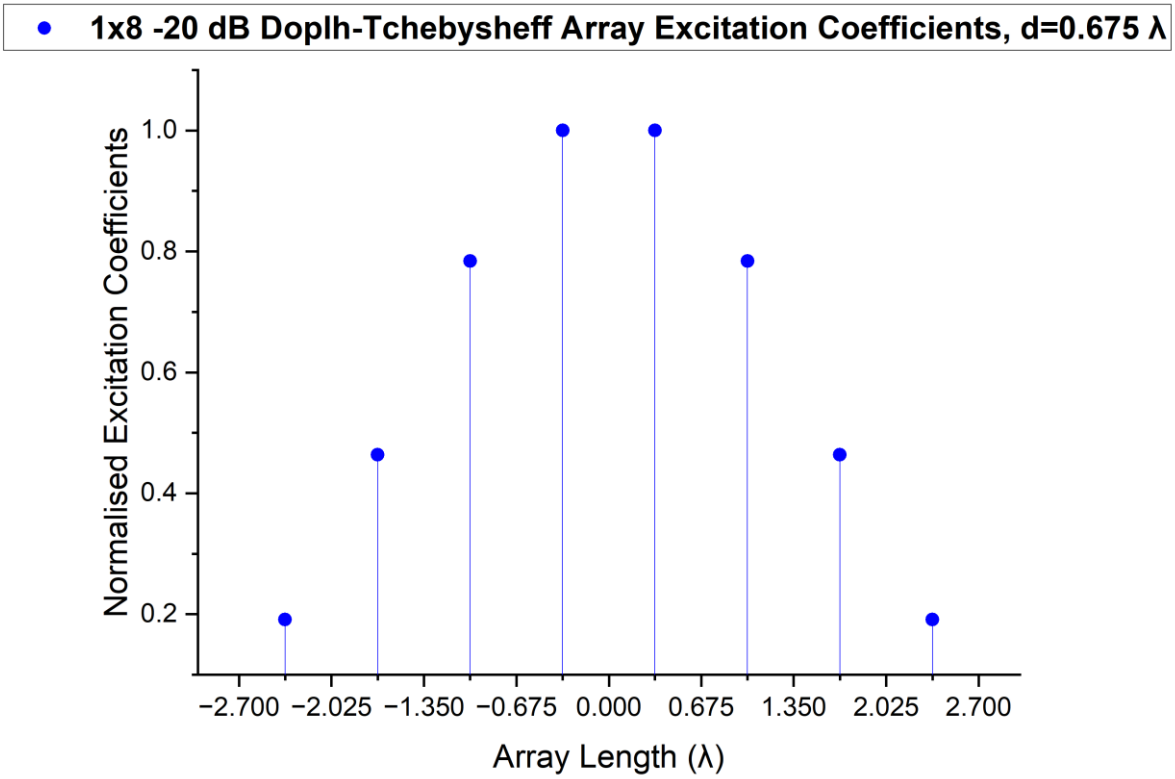

Figure 3. 40 -25 dB Doplh-Tchebysheff Array Excitation Coefficients for a linear 1x8 Array

Table 3. 6 Excitation coefficients for an 8x8 -35 dB Dolph-Tschebysheff array

0.0367	**0.0888**	**0.1502**	**0.1915**	**0.1915**	**0.1502**	**0.0888**	**0.0367**
0.0888	**0.2149**	**0.3636**	**0.4636**	**0.4636**	**0.3636**	**0.2149**	**0.0888**
0.1502	**0.3636**	**0.6151**	**0.7843**	**0.7843**	**0.6151**	**0.3636**	**0.1502**
0.1915	**0.4636**	**0.7843**	**1.0000**	**1.0000**	**0.7843**	**0.4636**	**0.1915**
0.1915	**0.4636**	**0.7843**	**1.0000**	**1.0000**	**0.7843**	**0.4636**	**0.1915**
0.1502	**0.3636**	**0.6151**	**0.7843**	**0.7843**	**0.6151**	**0.3636**	**0.1502**
0.0888	**0.2149**	**0.3636**	**0.4636**	**0.4636**	**0.3636**	**0.2149**	**0.0888**
0.0367	**0.0888**	**0.1502**	**0.1915**	**0.1915**	**0.1502**	**0.0888**	**0.0367**

3.4.4.2 Unequal power dividers design

The same design procedures for unequal power dividers as explained in section 3.4.3 were implemented for the 8x8 array. Figure 3. 41 shows the combined four-by-four unequal power divider with current division according to the highlighted quadrant of Table 3. 6.

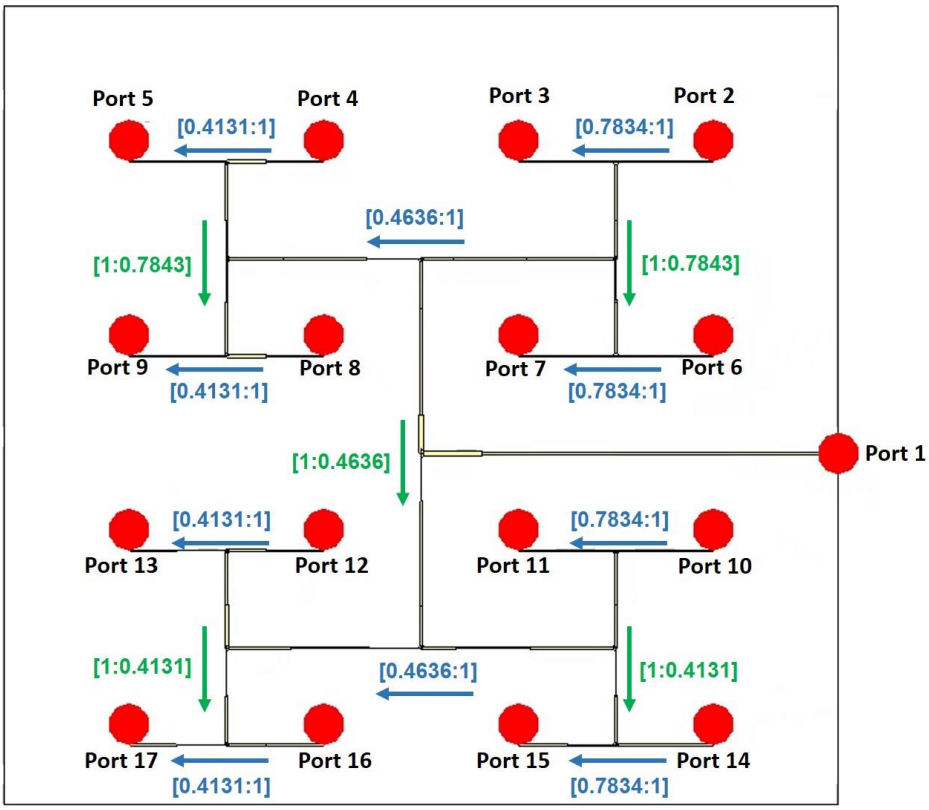

Figure 3. 41 Four-by-four unequal power divider

The power divider has an acceptable reflection coefficient of -11.4 dB at 1.4 GHz as depicted in Figure 3. 42. The linear voltage division and phase imbalance of each port are plotted in Figure 3. 43 and Figure 3. 44 respectively; with port 2 as the reference, the voltage ratio and phase difference of each port is summarised in Table 3. 7. Overall, the split ratios are slightly better than the computed -35dB array coefficients, and phase error is less than 6° within the bandwidth of 1.4-1.425 GHz.

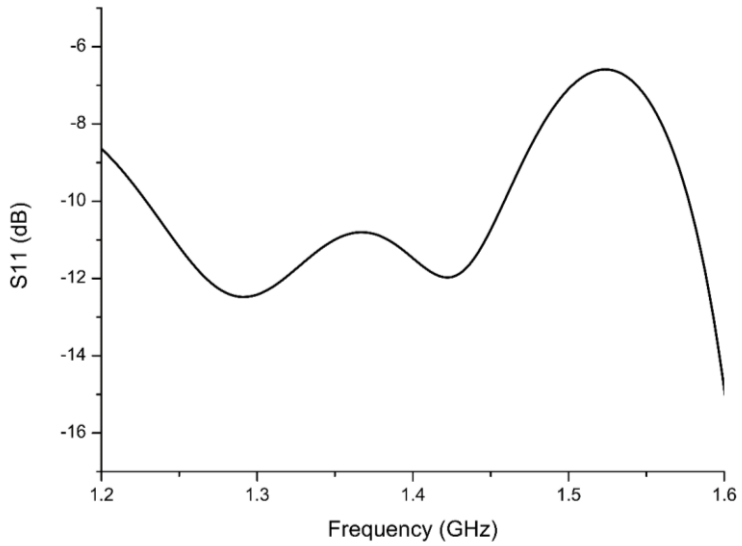

Figure 3. 42 Input impedance matching of four-by-four unequal power divider

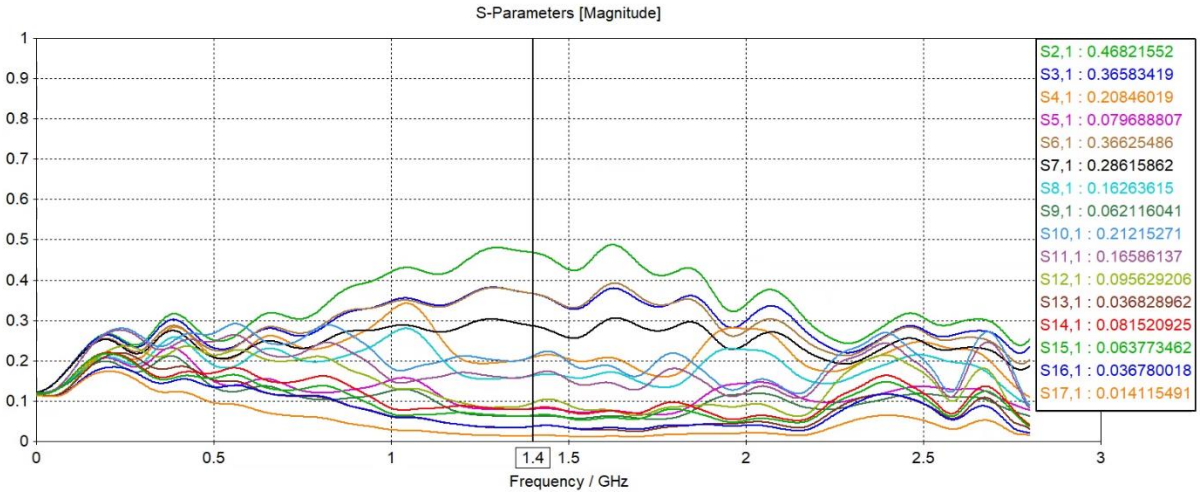

Figure 3. 43 Linear voltage ratio of the four-by-four unequal power divider

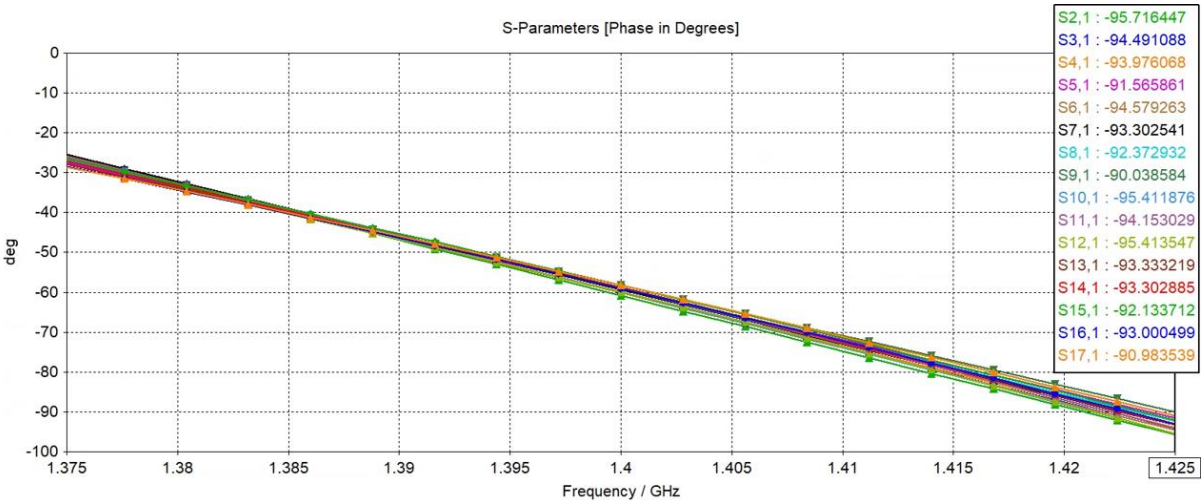

Figure 3. 44 Phase difference of the four-by-four unequal power divider

Table 3. 7 Summary of the four-by-four unequal power divider network

Port	Nomalised Voltage ratio	Maximum Phase difference (°)
Port 2	1 (reference)	0 (reference)
Port 3	0.782051	1.23
Port 4	0.444444	1.74
Port 5	0.17094	4.15
Port 6	0.782051	1.14
Port 7	0.611111	2.42
Port 8	0.348291	3.35
Port 9	0.132479	5.68
Port 10	0.452991	0.31
Port 11	0.354701	1.57
Port 12	0.205128	0.31
Port 13	0.07906	2.39
Port 14	0.175214	2.42
Port 15	0.136752	3.59
Port 16	0.07906	2.72
Port 17	0.029915	4.74

Likewise, the 4x4 unequal feed network was integrated into the 8x8 antenna array as illustrated in Figure 3. 45. The resulting tapered 8x8 array has an acceptable matching as depicted in Figure 3. 46, with |S11| better than -11dB from 1.4 to 1.425 GHz. It can be observed from the three-dimensional radiation pattern in Figure 3. 47 that the antenna side lobes have been notably suppressed. From a closer look at the radiation pattern plots in Figure 3. 48 and Figure 3. 49, side lobe level is observed to be better than -31.5 dB, where phase imbalance could be one contributing

factor for not meeting the -35 dB target. However, the tapered array still exhibits a three-dimensional beam efficiency of 99.6% as compared to 81.44% for a uniform array.

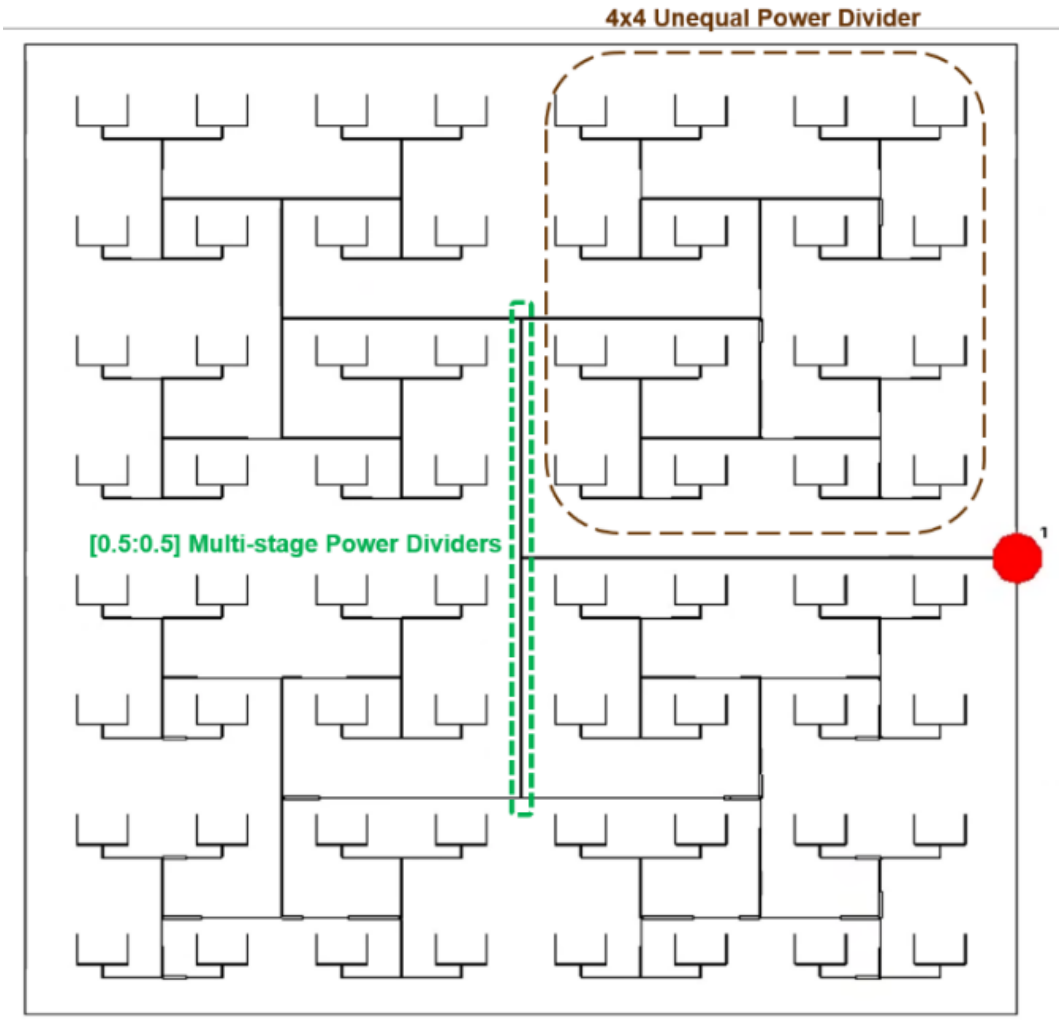

Figure 3. 45 Integrated 8x8 Feed Network

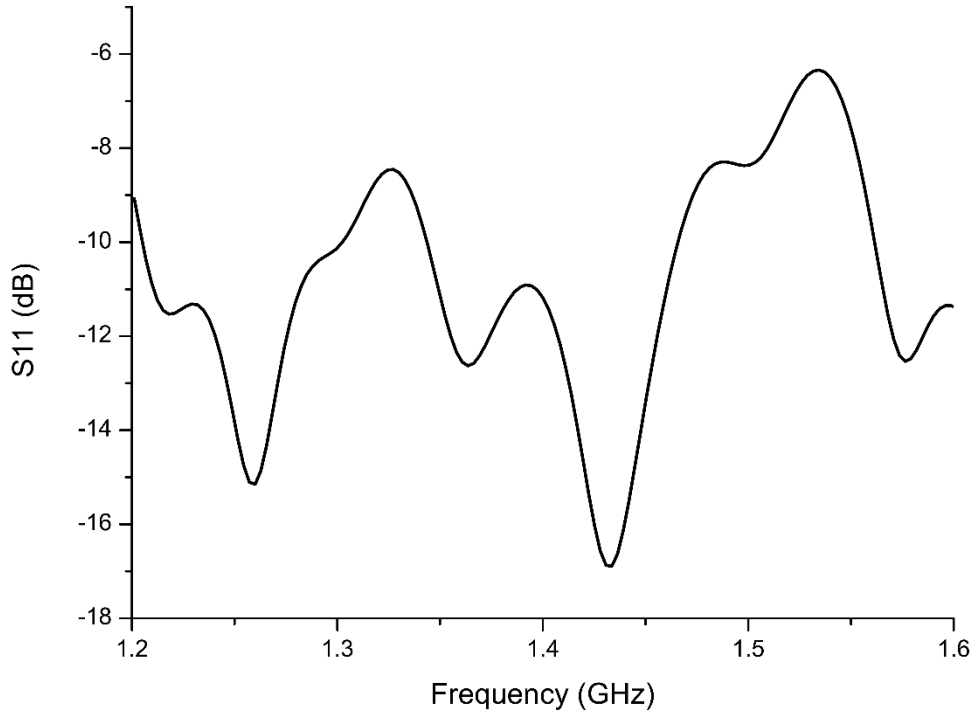

Figure 3. 46 Impedance matching of the tapered 8x8 array

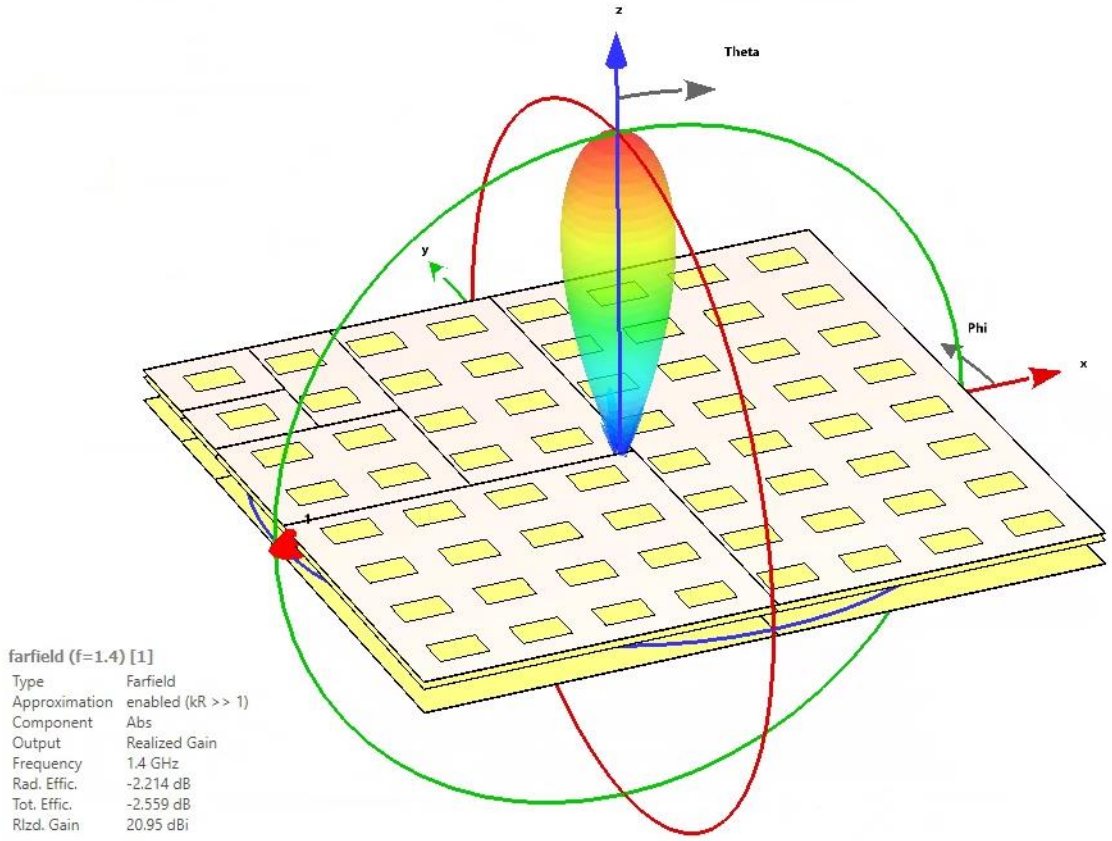

Figure 3. 47 Three-Dimensional Far-field result of the 8x8 array with tapered excitation

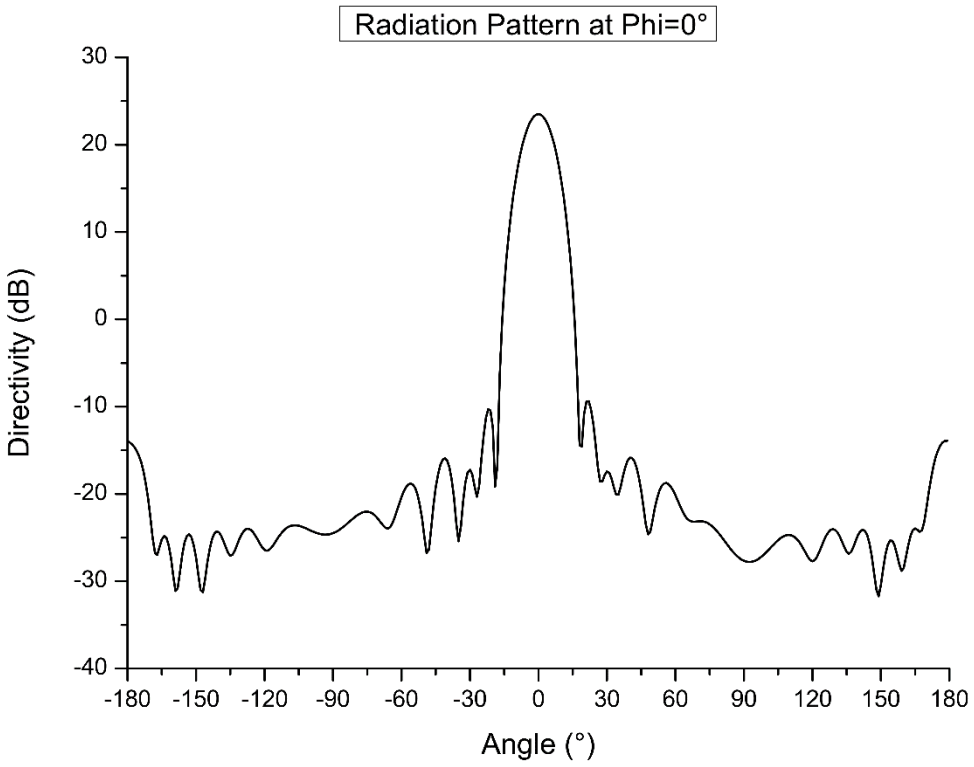

Figure 3. 48 Radiation pattern of tapered 8x8 array at Phi=0° cut plane

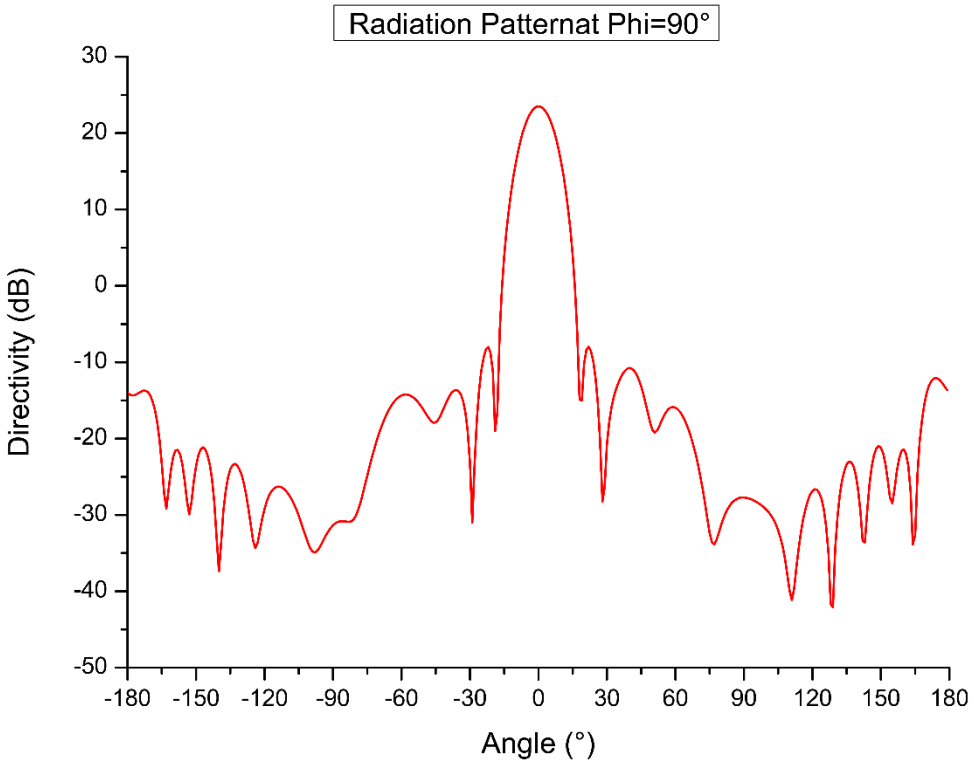

Figure 3. 49 Radiation pattern of tapered 8x8 array at Phi=90° cut plane

3.5 Chapter summary

In this chapter, the fundamental design principles for fixed-beam aperture-coupled microstrip patch antenna arrays have been discussed, from single patch design, uniform array to tapered array to meet the requirements for radiometric applications. The importance of this chapter is to provide foundations for more challenging designs further down this thesis, the 4x4 tapered array was integrated with phase shifters to develop a 2-dimensional scanning phased array in next chapter, and the design principles of two-way unequal power dividers has been applied to design irregular 3-way unequal power dividers at Ku- band in chapter 5.

Chapter 4 L- band phased array design

4.1 Introduction

Following the initial 4x4 L- band fixed beam array with high main beam efficiency in chapter 3, this chapter focuses on the further development of a low-cost L- band 4x4 phased array. The array is integrated with phase shifter elements developed by Dr. Kim Tuyen Trinh [25]. The primary targeted application for this phased array is to provide multi-track scanning capability to the novel smart irrigation system [15], the design concept is illustrated in Figure 4. 1. This design also provides a foundation for the more complex Ku- band and L-/Ku- band shared aperture phased arrays discussed in chapters 5 for airborne applications.

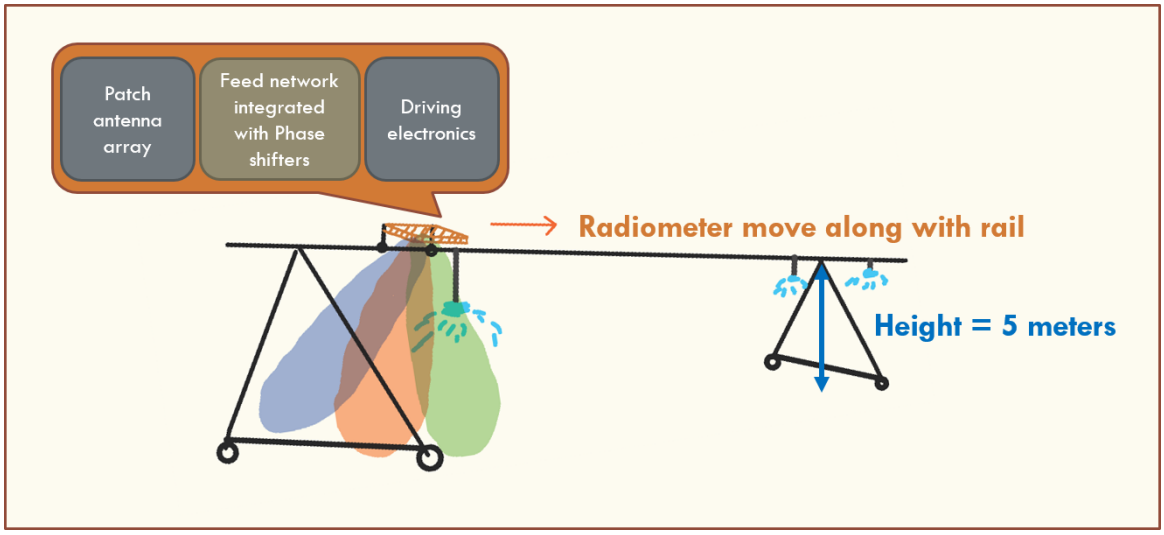

Figure 4. 1 Design concept of the low-cost L- band phased array

This chapter starts with a beam scanning plan with consideration of requirements for scanning angle and requirements for bits of phase shift resolution, followed by the design details carried out in CST Microwave Studio from feed line compensation to final combined simulations and tuning. The chapter goes on to describe the development of the driving electronics from simple switch simulation models to breadboard prototype and then to PCB design. Finally, the support structure was designed, and the antenna system was fully assembled for radiation pattern measurements in an anechoic chamber, which are presented at the end of the chapter.

4.2 Beam scanning plan

4.2.1 PathWave System Design and CST array synthesis

The array synthesis process started with an initial set up to activate the Farfield Array function in CST Microwave Studio Suite using the L- band single element designed in Chapter 3.3.3, with the 4x4 side lobe suppression coefficients presented in Table 4. 1. As depicted in Figure 4. 2 and Figure 4. 3, this resulted in side lobe level of -23 dB and a main beam efficiency of 98.23%. The half-power beamwidth is 21° and the full main beam width is 54°.

Table 4. 1 Excitation coefficients for the initial set up

0.341	**0.583**	**0.583**	**0.341**
0.585	1	1	**0.585**
0.585	1	1	**0.585**
0.341	**0.583**	**0.583**	**0.341**

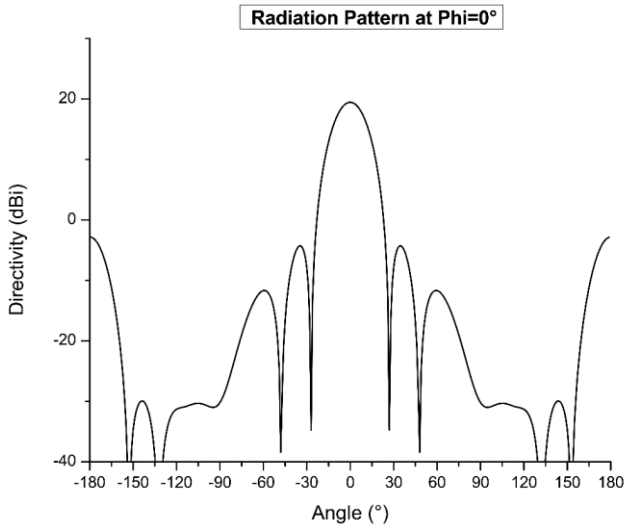

Figure 4. 2 Radiation pattern of the synthesised 4x4 array at Phi=0° cut plane

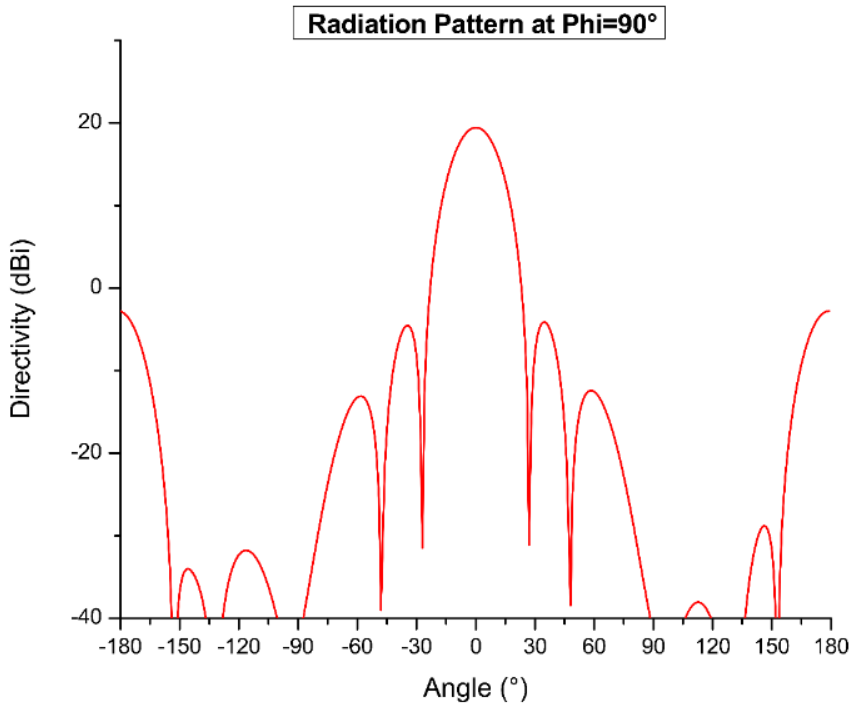

Figure 4. 3 Radiation pattern of the synthesised 4x4 array at Phi=90° cut plane

As compared to a single line measurement from a fixed beam antenna array, a scanning array can significantly improve the soil moisture mapping efficiency by measuring multiple tracks across the flight direction from a single aircraft flight line [34] as illustrated in Figure 4. 4. Alternatively, as depicted in Figure 4. 5, it can also measure multiple beams along track for multi-angular soil moisture retrieval [145].

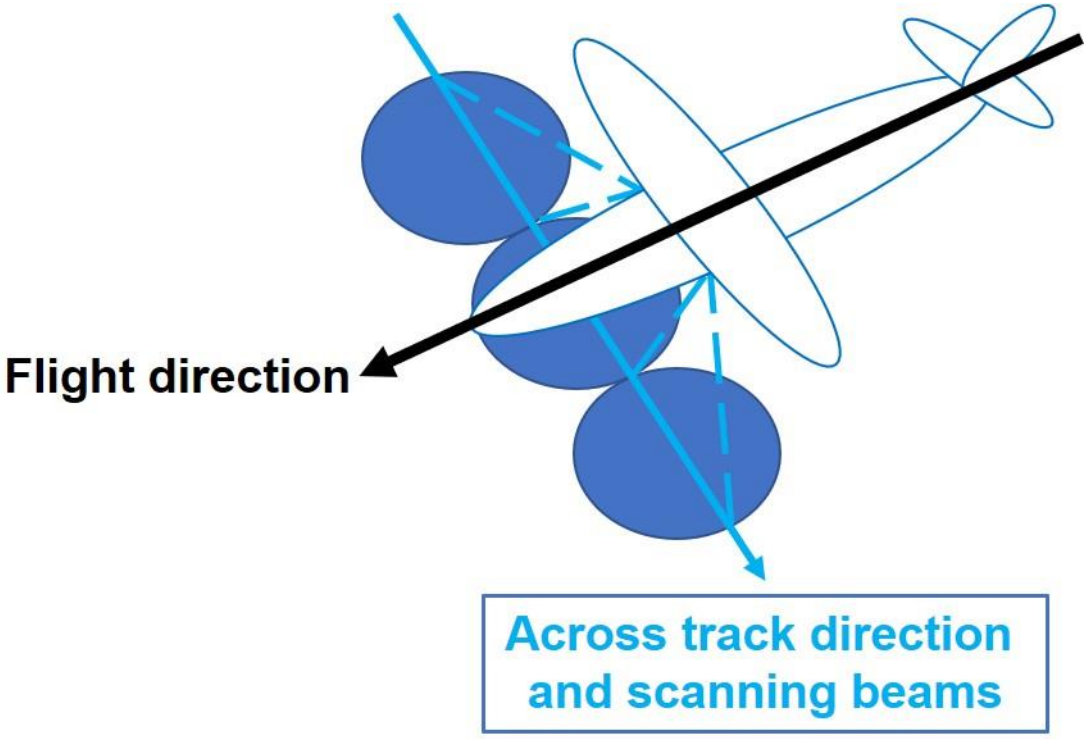

Figure 4. 4 Illustration of across track scanning

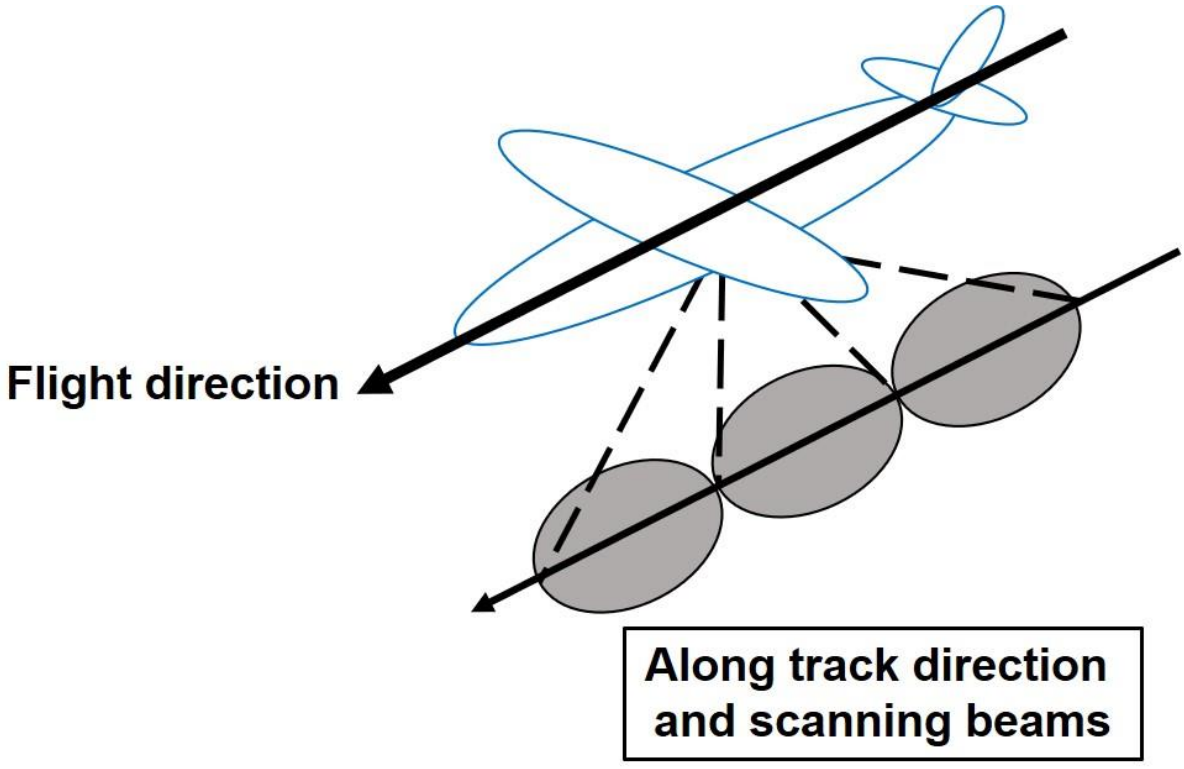

Figure 4. 5 Illustration of along track scanning

Electronically steering the antenna beam from the broadside direction is accomplished by controlling the progressive phase difference β between the radiating element along the scanning direction (of either along track or across) as [137]:

$$\beta = -\mathrm{kd}\cos\theta_0 \qquad (5.1)$$

where:

- k is the wave number
- d is the interelement distance along the scanning direction
- θ_0 is the pointing angle from the axis of the array (resulting in a pointing angle of $90° - \theta_0$ from nadir)

As the ultimate goal of this study is to develop phased array antennas to be deployed on an airborne platform, learning from examples of Polarimetric L- band Multibeam Radiometer (PLMR) and Polarimetric P-band Multibeam Radiometer (PPMR), each scaning footprint shall be spaced at intervals equal to the half power beamwidth for a balance between coverage area and the limited sampling time from a flying plane. In this sense, given the half power beamwidth of the 4x4 array is 21°, the most ideal pointing angles shall be [-63°, -42°,-21°,0,+21°,+42°, +61°].

The phase shifters to be integrated into the 4x4 L- band phased array have been developed by Dr. Kim Tuyen Trinh [25]. The developed phaseshifter has 4 independent digital bits with nominal phase shifts of [180°, 90°, 45°, 22.5°]. By controlling the on and off states of all 4 bits, a highest angular resolution of 22.5° from 0° to 360° can be achieved. If only the first two digital bits are used [180°, 90°], the result is an angular resolution of 90°, leading to only 4 states as [0°,90°,180°,270°]. There is a tradeoff to be considered between better resolution and greater complexity afforded by four bits:

1.Higher space consumption given each bit requires a size of approximately 26 mm x 60 mm. This size is significant because the space between each antenna input port to the corresponding power divider centre is about 72 mm x 71 mm which favours using only the first 2 bits, and challenging tranmission line designs (e.g. bends and long lines) will be required to integrate over 3 phase shifters bits into the feed network.

2. Each bit has a maximum insertion loss of about -0.5 dB and around -0.3 dB at minimum. In this sense, cascading more bits will lead to higher insertion loss in each phase state and higher amplitude imbalance between states.

Therefore, a comparison of using 4 bit, 3 bits, and 2 bits for the targetted pointing angle has been conducted to evaluate the trade-offs. The scanning directions of patch antenna arrays in this study are defined in Figure 4. 6. With the primary purpose to obtain multiple track measurements across the flight line, the array synthesis focuses on X- direction across track.

To begin the process, the initial phase allocations were obtained from Keysight PathWave System Design phased array module (as illustrated in Figure 4. 7) and recorded in the following tables (Table 4. 2 to Table 4. 8), after which the phase of each element was updated in the Farfield Array synthesis function of CST Microwave Studio accordingly. For example, as per Table 4. 2, the top left element shall have 0° phase, and the next element along X- direction shall have 157.5° phase shift and so forth. It can also be observed that the required phase allocation only varies in the X-direction, while each element in the same column has the same phase allocation (i.e. no phase variations in Y- direction are needed for one-dimensional across track scanning).

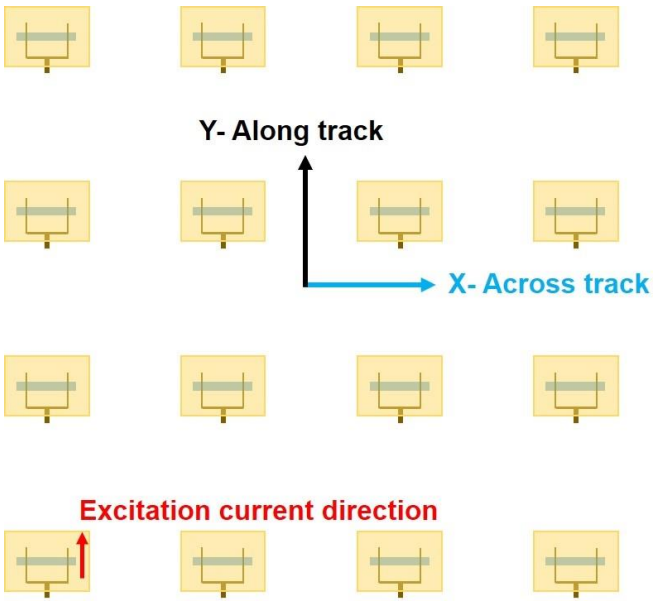

Figure 4. 6 Illustration of scanning directions in the 4x4 patch antenna array

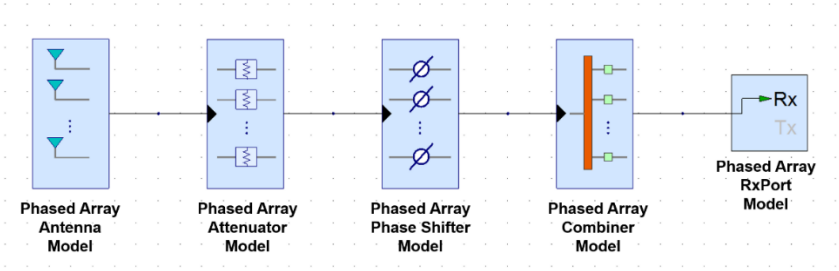

Figure 4. 7 Phased array module in Keysight PathWave System Design

The following subsections **4.2.1.1 60°** to **4.2.1.3 30°** present the phase allocation and radiation pattern of each targeted angle using 4, 3 and 2 bits, and also the synthesised radiation pattern at Phi=0° cut plane with standard axes for comparing both side lobe and pointing angles as shown in Figure 4. 8. For an effective side lobe levels comparison at Phi=90° cut plane, the axes have been tilted to aligned with the main beam direction as illustrated in Figure 4. 9 . After which, a summary of results will be present in **4.2.2 Results summary and final plan**.

4.2.1.1 60°

Table 4. 2 Phase allocation for 60° using 4 bits in a 4x4 array

0	157.5	315	112.5
0	157.5	315	112.5
0	157.5	315	112.5
0	157.5	315	112.5

Table 4. 3 Phase allocation for 60° using 3 bits in a 4x4 array

0	135	315	90
0	135	315	90
0	135	315	90
0	135	315	90

Table 4. 4 Phase allocation for 60° using 2 bits in a 4x4 array

0	180	0	90
0	180	0	90
0	180	0	90
0	180	0	90

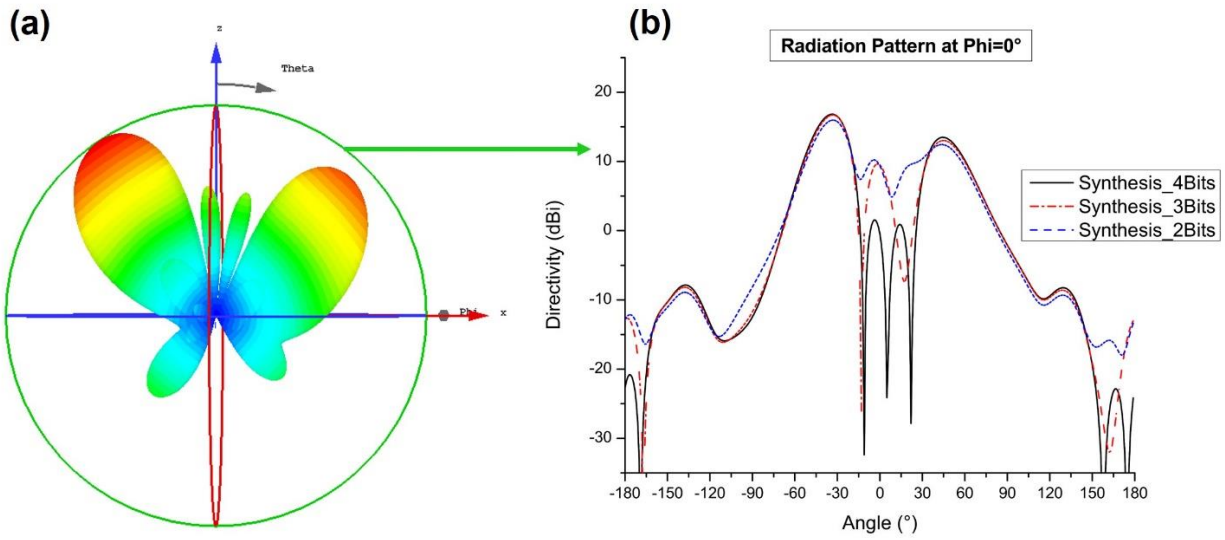

Figure 4. 8 Radiation pattern of the synthesized 4x4 array (a) 3D radiation pattern with standard axes (b) radiation pattern at Phi=0° cut plane (green circle) with target angle of 60°

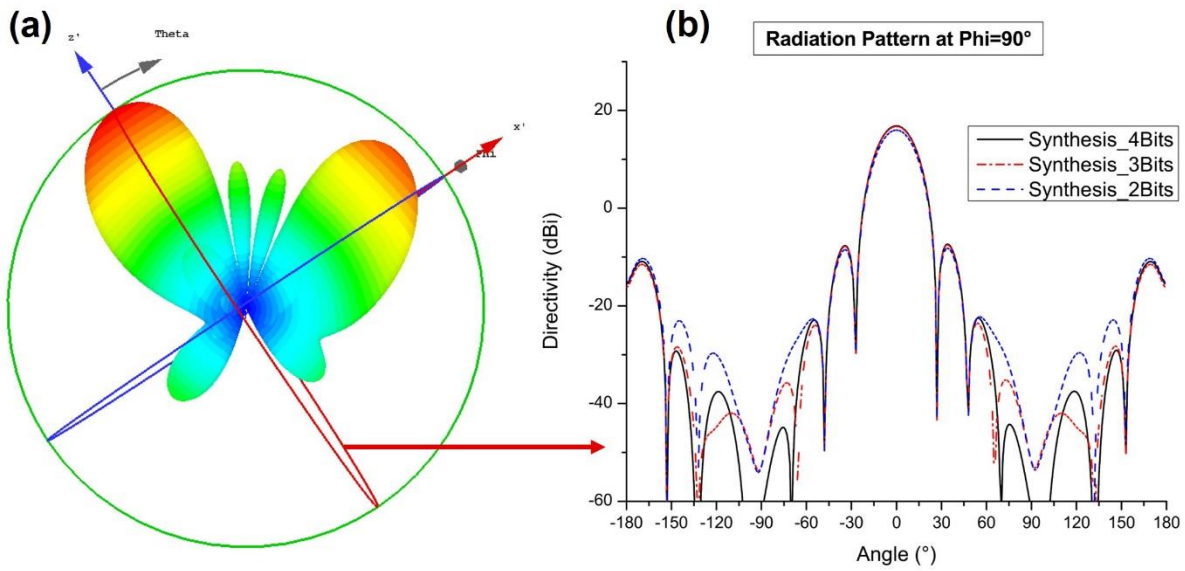

Figure 4. 9 Radiation pattern of the synthesis 4x4 array (a) 3D radiation pattern with main beam aligned axes (b) radiation pattern at Phi=90° cut plane (red circle) with target angle of 60°

4.2.1.2 40°

Table 4. 5 Phase allocation for 40° using 4 bits in a 4x4 array

0	112.5	225	337.5
0	112.5	225	337.5
0	112.5	225	337.5
0	112.5	225	337.5

Table 4. 6 Phase allocation for 40° using 3 bits in a 4x4 array

0	135	225	0
0	135	225	0
0	135	225	0
0	135	225	0

Table 4. 7 Phase allocation for 40° using 2 bits in a 4x4 array

0	180	270	90
0	180	270	90
0	180	270	90
0	180	270	90

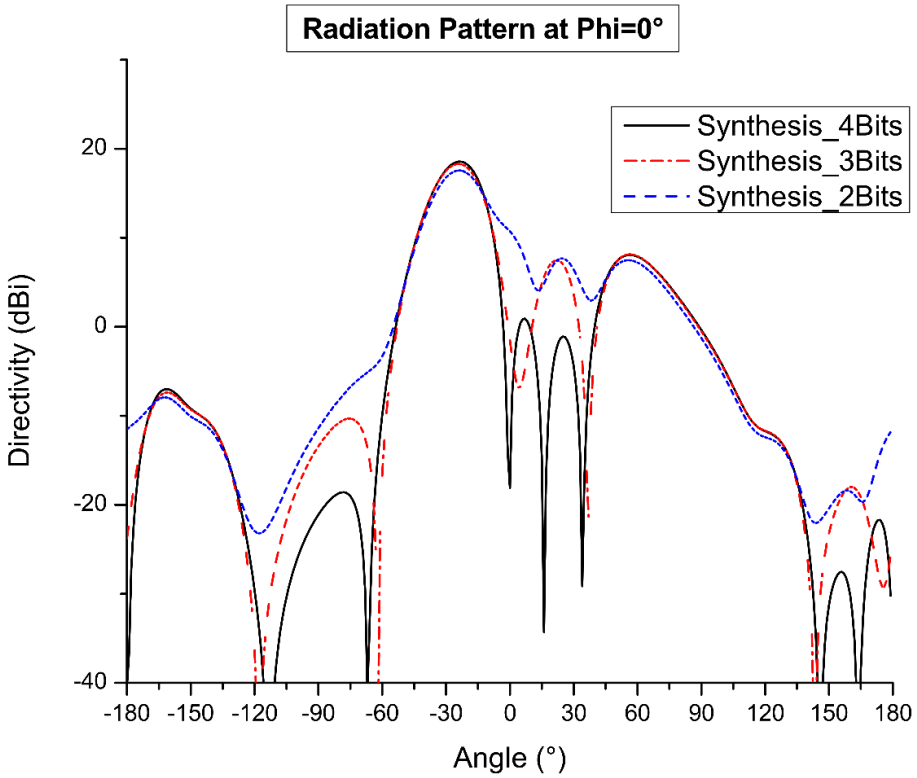

Figure 4. 10 Radiation pattern of the synthesis 4x4 array at Phi=0° cut plane with target angle of 40°

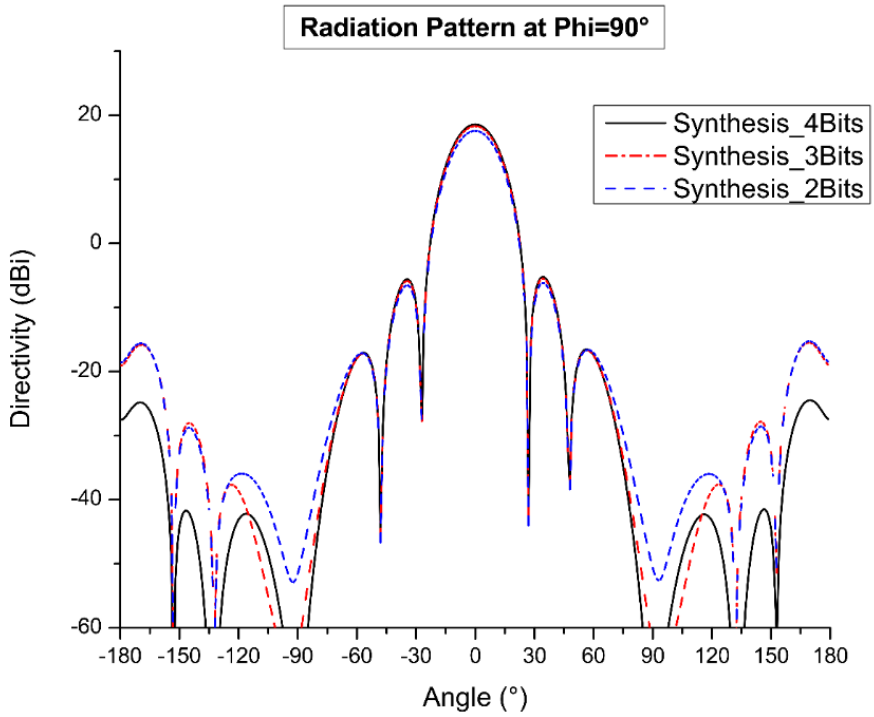

Figure 4. 11 Radiation pattern of the synthesis 4x4 array at Phi=0° cut plane with target angle of 40°

4.2.1.3 30°

Since the phase allocation for 30° is the same for using 4,3 and 2 bits, only one table (Table 4. 8), and the resultant radiation pattern plots Figure 4. 12 and Figure 4. 13 are presented.

Table 4. 8 Phase allocation for 30° using 4,3 and 2 bits in a 4x4 array

90	180	270	0
90	180	270	0
90	180	270	0
90	180	270	0

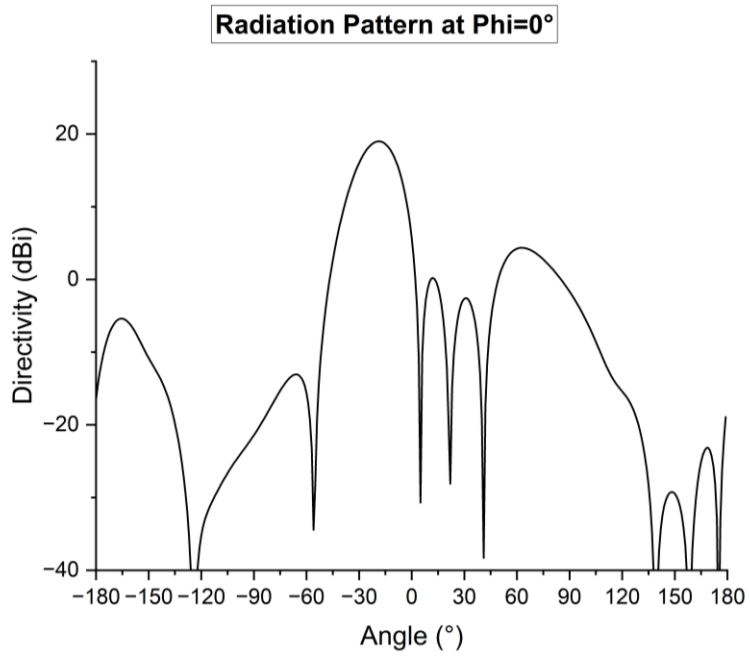

Figure 4. 12 Radiation pattern of the synthesis 4x4 array at Phi=0° cut plane with target angle of 30°

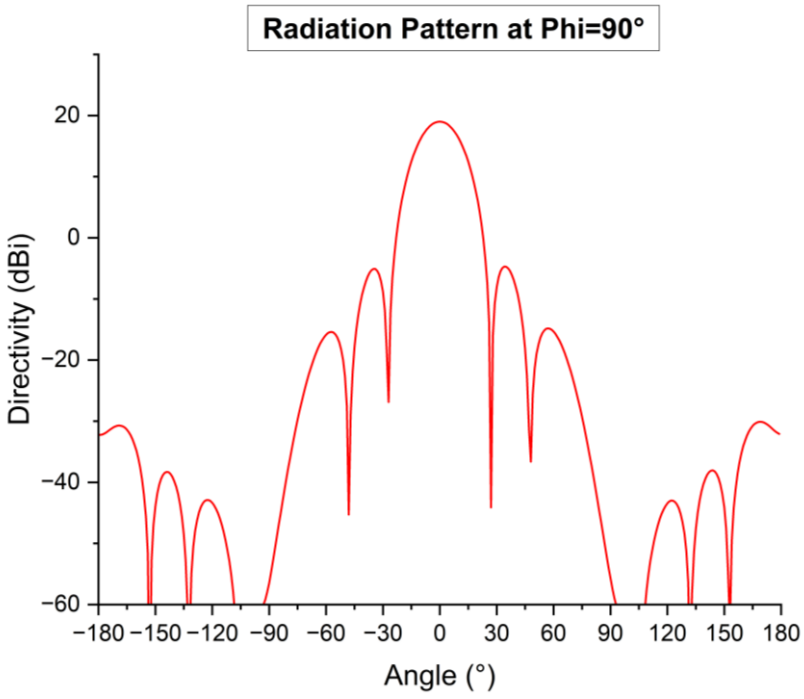

Figure 4. 13 Radiation pattern of the synthesis 4x4 array at Phi=90° cut plane with target angle of 30°

4.2.2 Results summary and final plan

Table 4. 9 Summary of pointing angles using 4 bits,3 bits and 2 bits

	4 bits pointing angle	3 bits pointing angle	2 bits pointing angle
60°	34°	33°	33°
40°	24°	24°	24°
30°	19°		

Table 4. 9 summarises the pointing angles using all 4 bits, the first 3 bits and the first 2 bits of digital phase shift, and it can be observed that due to the limitation in the array size and number of bits, the pointing angle errors are similar for all three cases. Furthermore, the maximum pointing angle is approximately 34°. In this aspect, a 4-bit phase shifter may not bring any extra benefit beyond that of 3 bits. In addition to angular error, for a phased array radiometer antenna, main beam efficiency must be compared between these three cases, as it can be observed from Figure 4. 8 and **Error! Reference source not found.** that the 4 bits design shows notable improvements in side lobe levels. Accordingly, the 3-dimensional main beam efficiencies over the scanning angles for these three cases have been plotted in Figure 4. 14.

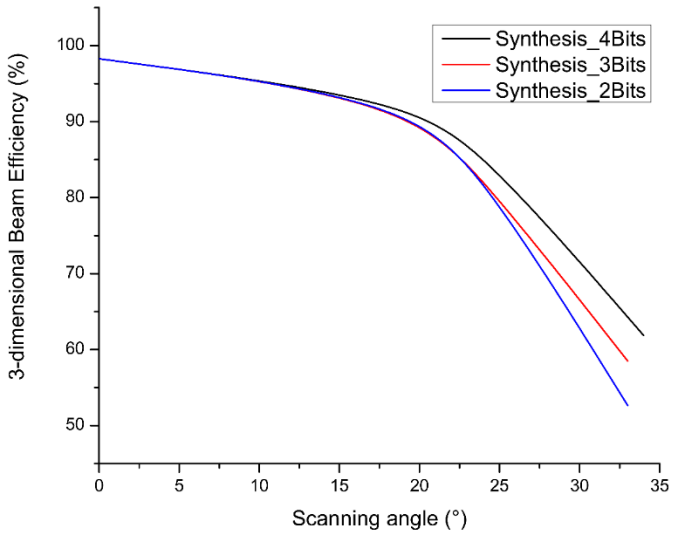

Figure 4. 14 Beam efficiency vs Scanning angle for 2,3, and 4 Bits

According to the plot, it could be also observed that the beam efficiency drops rapidly with increasing main angle beyond 20°. Although using 4 bits has the slowest decaying curve due to lower side lobes in large scanning angles, the overall improvement is insignificant as the resultant main beam efficiency falls below 80% for scanning angle larger than 27°. Considering using 4 bits or 3 bits phase shifter could not significantly improve either the main beam angular error or beam efficiency, it would be viable to utilise 2 bits phase shifter for space requirement and reducing antenna loss.

4.3 Phased array simulation design

4.3.1. Importing Phase shifter measurement results into CST

The phase shifters are reflection type phase shifters, using the phase difference between the forward and reverse bias states of a PIN diode along with carefully tuned reflective loads. It is worth mentioning that the RF characteristics of the diode on/off states were also considered as equivalent lumped components in the reflection load design, rather than just being considered as switches in conventional reflection phase shifters design [25].

To begin the process in CST Microwave Studio, the measured results of the 180° and 90° phase shifter bits were recorded in the form of S2P text files to store phase, transmission and reflection

information. These were then imported into CST as simplified circuit elements in schematic mode as illustrated in Figure 4. 15. In here, off state stands for PIN diodes are in reversed biased state; while on stands for PIN diode are in forward bias state. For Simplicity, off state is considered to contribute 0° phase shift, therefore 0° phase state stands for both bits are in off state; and 90° phase state stands for the 90° bit is in on state while the 180° bit is in off state and so forth.

The results for the two-bit phase shifters are depicted in and summarised in Table 4. 10. As depicted in Figure 4. 16, all four states exhibit good input impedance matching with reflection coefficient less than – 21 dB within the 1.4 -1.425 GHz bandwidth. This is also shown in Figure 4. 17 where the input impedance curve of each phase state moves well within the blue -10 dB reflection coefficient circle, and close to the Smith Chart centre from 1.4- 1.425 GHz. It should also be noted from the markers that each phase shifter has a different input impedance, which is an important design factor for later integration with the two-way power dividers. Table 4. 10 summarises the insertion loss and phase information from Figure 4. 18Figure *4. 19* Figure 4. 19, it can be observed that the maximum amplitude imbalance is 0.41 dB between 0° and 270° phase states for all PIN diodes being reversed biased and forward biased respectively; and the phase shifter module has the maximum phase error of 2.4° at 180° state at 1.4 GHz.

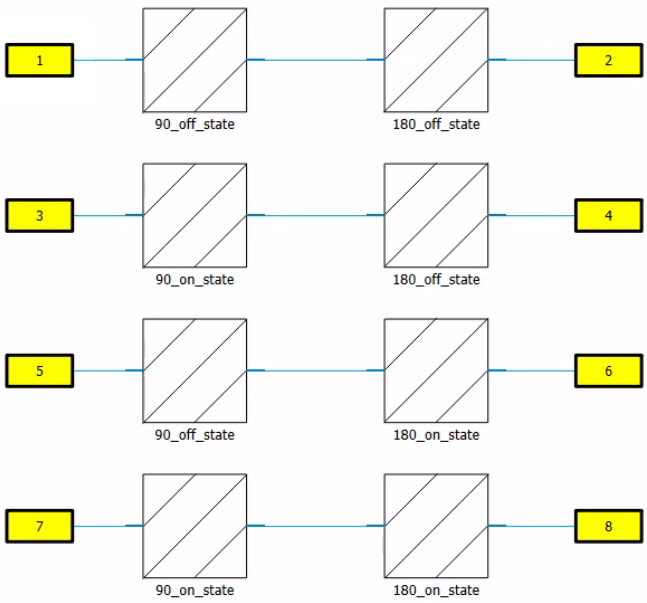

Figure 4. 15 Schematic mode for importing Phase shifter results into CST

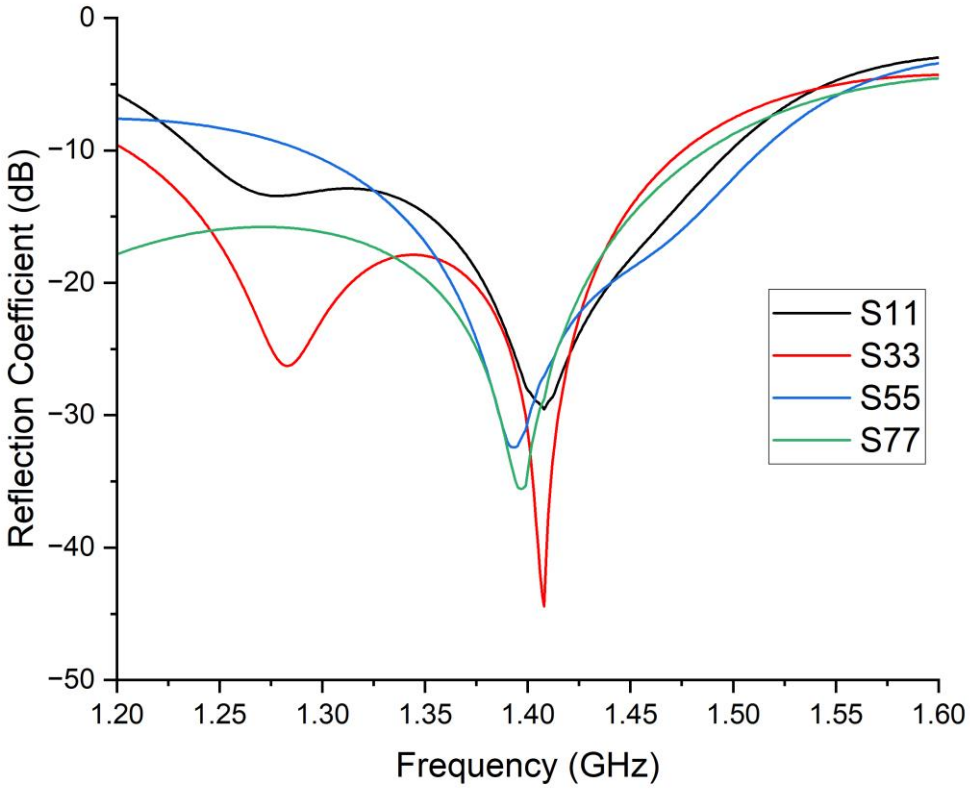

Figure 4. 16 Input impedance matching of each phase shifter state

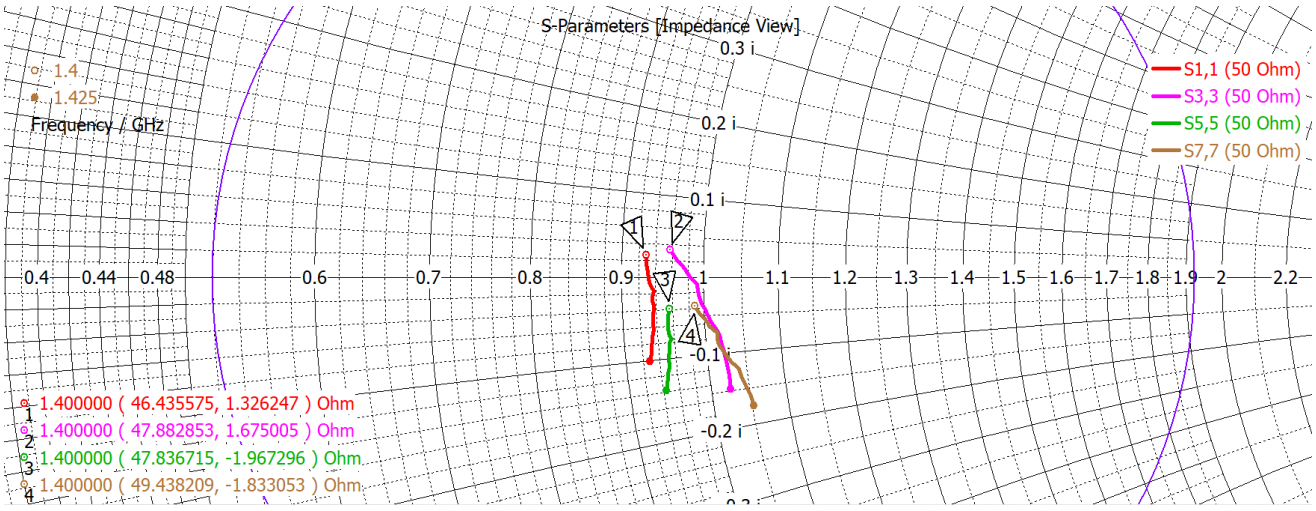

Figure 4. 17 Input impedance of each phase shifter state

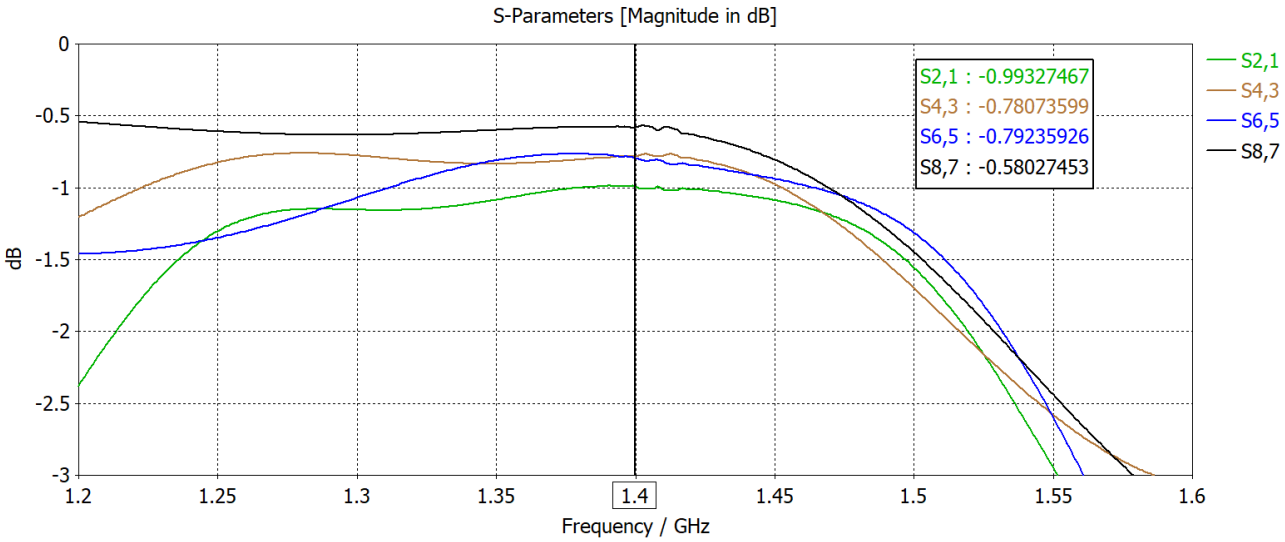

Figure 4. 18 Insertion loss of each phase shifter state

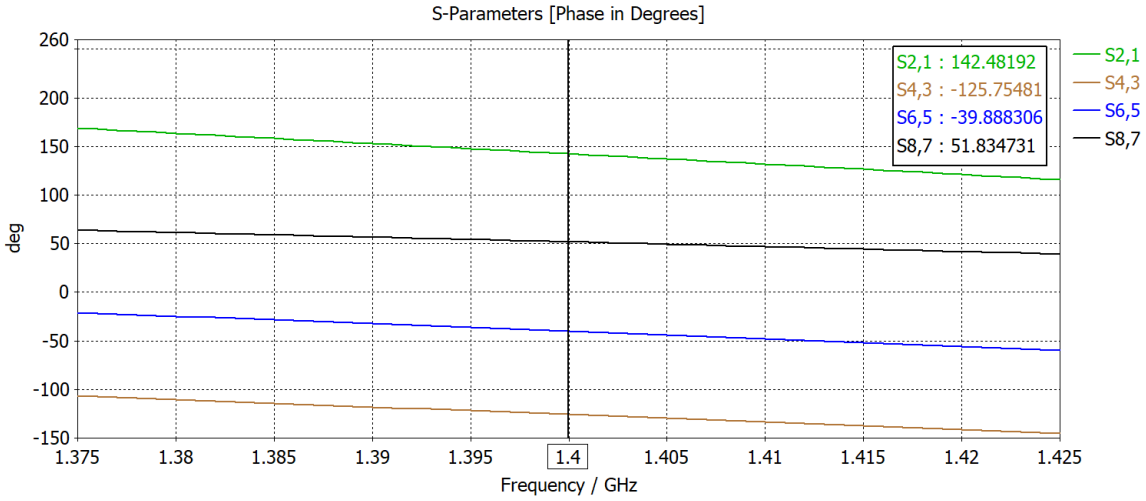

Figure 4. 19 Phase shift of each phase shifter state

Table 4. 10 Summary of phase shifter performance

90° Bit	180°Bit	Phase shift (°)	Insertion loss (dB)
Off	Off	0 (reference)	-0.99
On	Off	91.77	-0.78
Off	On	177.63	-0.79
On	On	269.35	-0.58

4.3.2. Power divider design for phase shifter integration

For an initial test of the integration, the 50 Ω transmission line sections of the two-way unequal power divider (discussed in Chapter 3) have been removed. Considering the S2P files are the measurement results with 50 Ω RF ports at each end, all ports in are assigned at 50 Ω in Figure 4. 20, and the phase shifters are considered as black boxes to connect from port 4 to port 5 and port 6 to port 7 in schematic mode as illustrated in Figure 4. 21. Geometries of the phase shifters were not included in the simulation to avoid duplicating effects of transmission attenuation and phase shifting (mostly in consideration of the hybrid coupler in the structure).

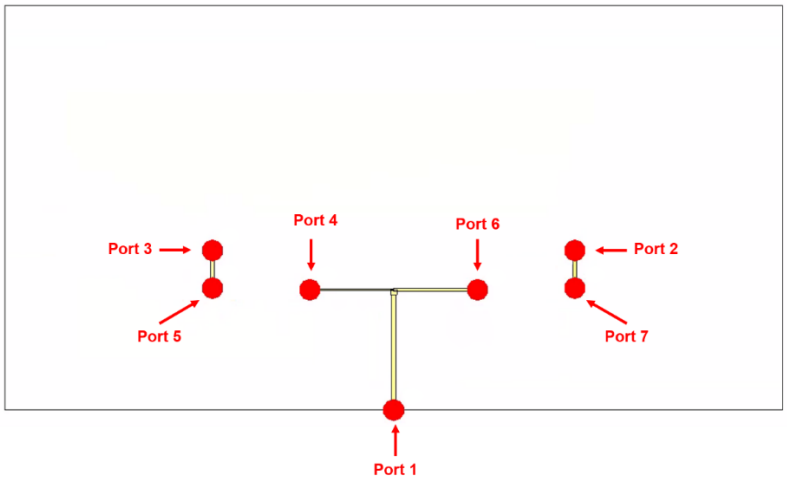

Figure 4. 20 Initial power divider test with phase shifters

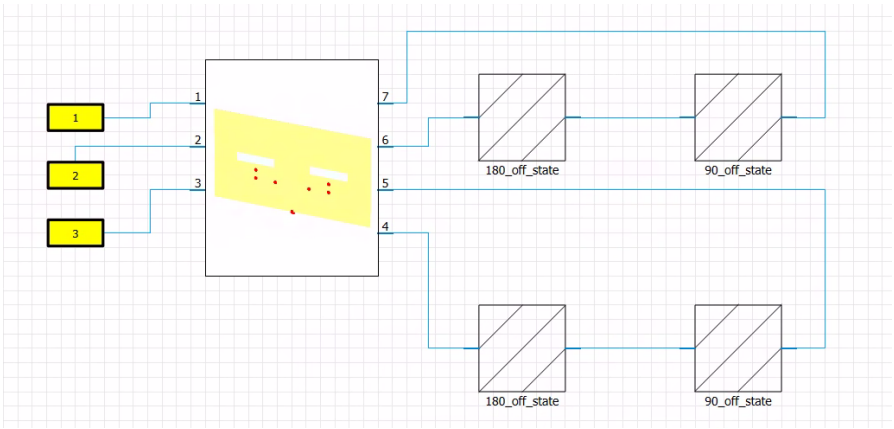

Figure 4. 21 Schematic mode for test connection

The initial test started with 0° at each branch, as shown in Figure 4. 22 and Figure 4. 23, the split ratio is 0.58:1 with a phase error of 1.05° at 1.4 GHz which are acceptable results. However, once

each power divider output port is simulated with a different phase state, the results are vastly different.

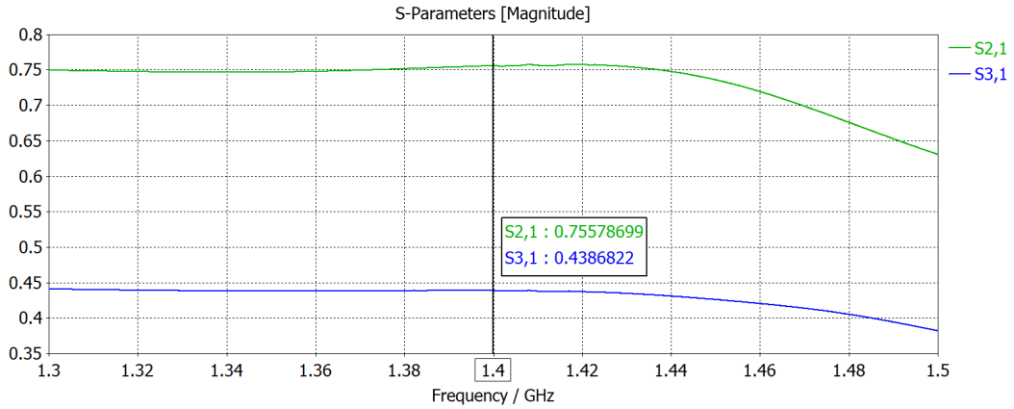

Figure 4. 22 Linear voltage division of the initial integration with phase shifters

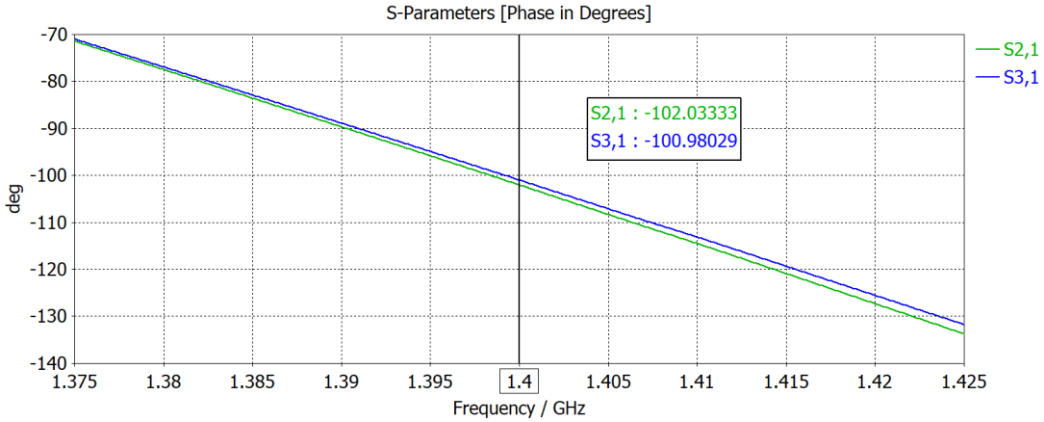

Figure 4. 23 Phase difference of the of the initial integration with phase shifters

In here, two cases for beam steering of 19° (as per Table 4. 8) are considered with results summarised in Table 4. 11, where the split ratio is either larger or much smaller than the required 0.58:1 ratio with a maximum error of 0.172. This is because the two-way power dividers have poor isolation (less than -10 dB) between the output ports [134], hence any change of impedance matching at one output end will affect the ratio of split power to the other end [146]. Provided that each phase shifter state has different input impedance (as summarised in Figure 4. 17), this will lead to uneven changes in impedance matching at the output ends when the power divider is paired with different phase shifters states. Along with poor isolation (and difference in insertion loss of each phase state as a smaller factor), these results in notable amplitude imbalance.

Table 4. 11 Summary of initial integration with different phase shifter states at 1.4 GHz

Cases	0.58 Branch	1 Branch	Split Ratio	Phase error (º)
1	90°	180°	0.752:1	3.39
2	0°	270°	0.411:1	8.15

To examine the effects of large amplitude errors, an initial phased array has been simulated to observe the resultant phase distortion. The simulation was set up with port allocation as labelled in Figure 4. 24 and schematic connections illustrated in Figure 4. 25. As shown in the simulation results in Figure 4. 26 and Figure 4. 27, the large amplitude errors lead to a high side lobe level of -4.7 dB, which in turn leads to poor 3-dimensional beam efficiency of 71.84%, as well as unsatisfactory impedance matching with |S11| being -9dB at 1.4 GHz as depicted in Figure 4. 28.

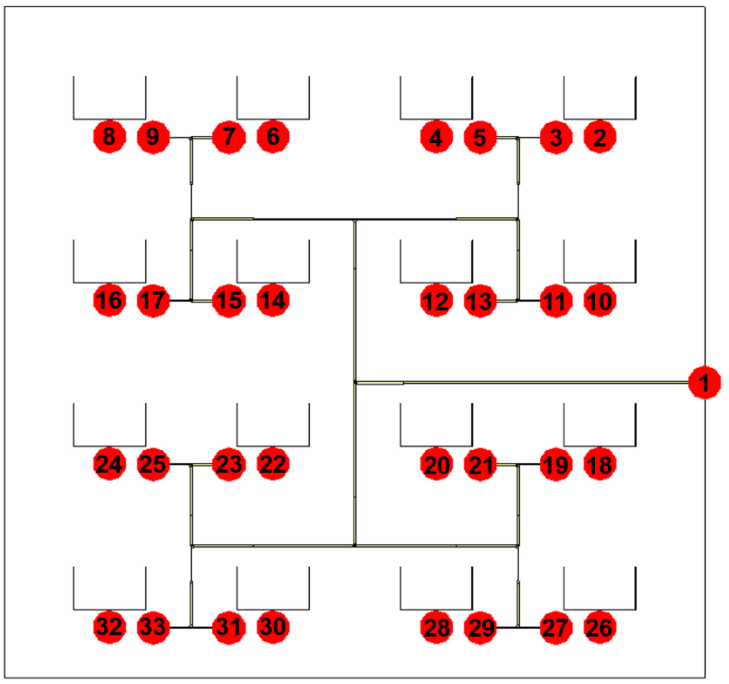

Figure 4. 24 Ports label for the initial phased array

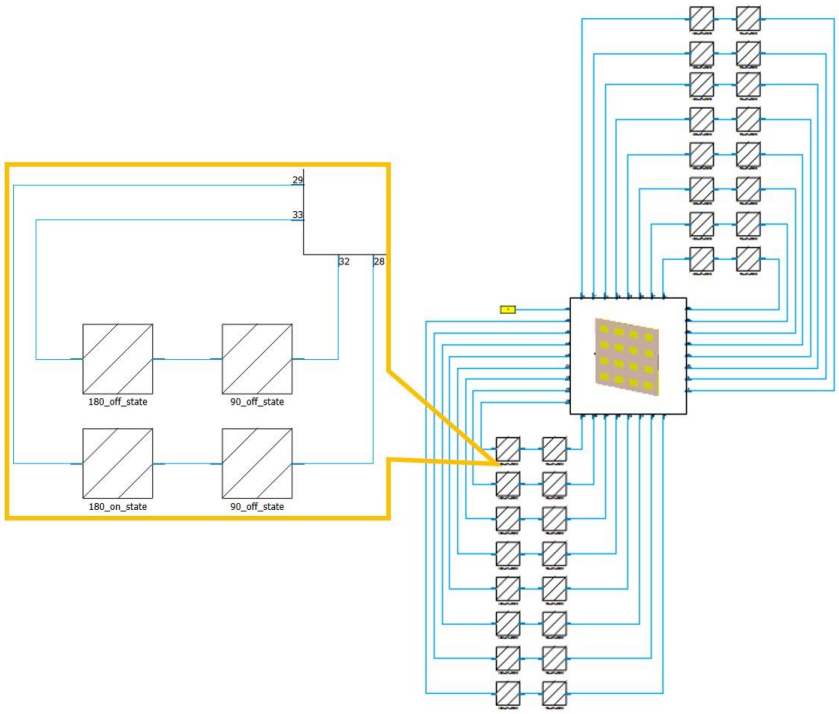

Figure 4. 25 Schematic connection for the initial phased array

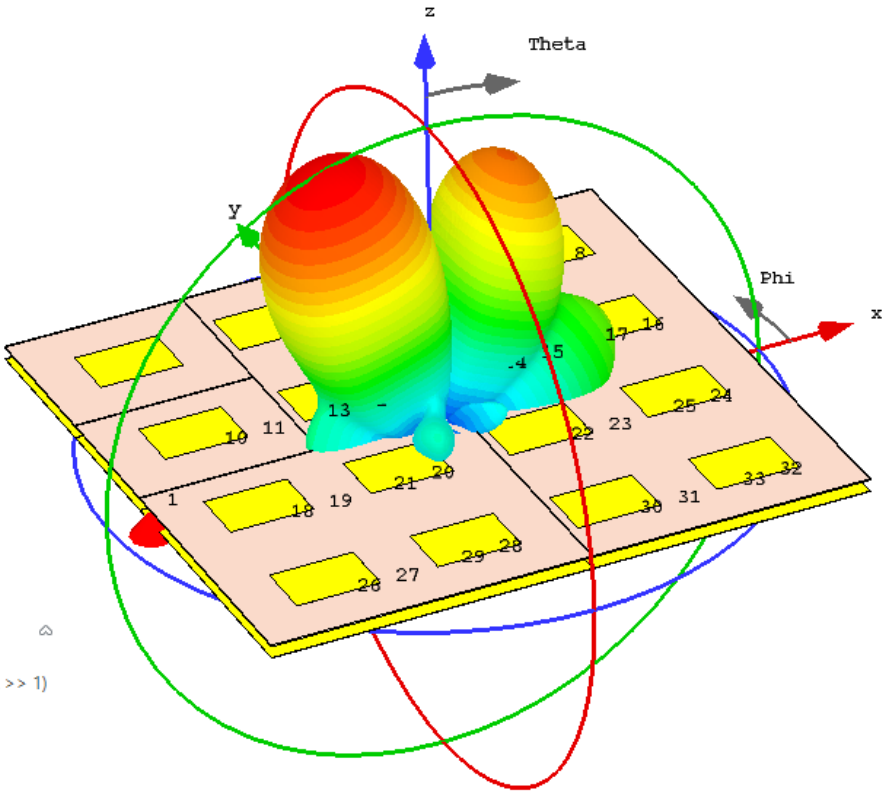

farfield (f=1.4) [AC1]

Type	Farfield
Approximation	enabled (kR >> 1)
Component	Abs
Output	Directivity
Frequency	1.4 GHz
System Rad. Effic. [AC1]	-2.718 dB
System Tot. Effic. [AC1]	-3.300 dB
Dir.	17.74 dBi

Figure 4. 26 Farfield pattern of the X-20° Beam in the initial phased array

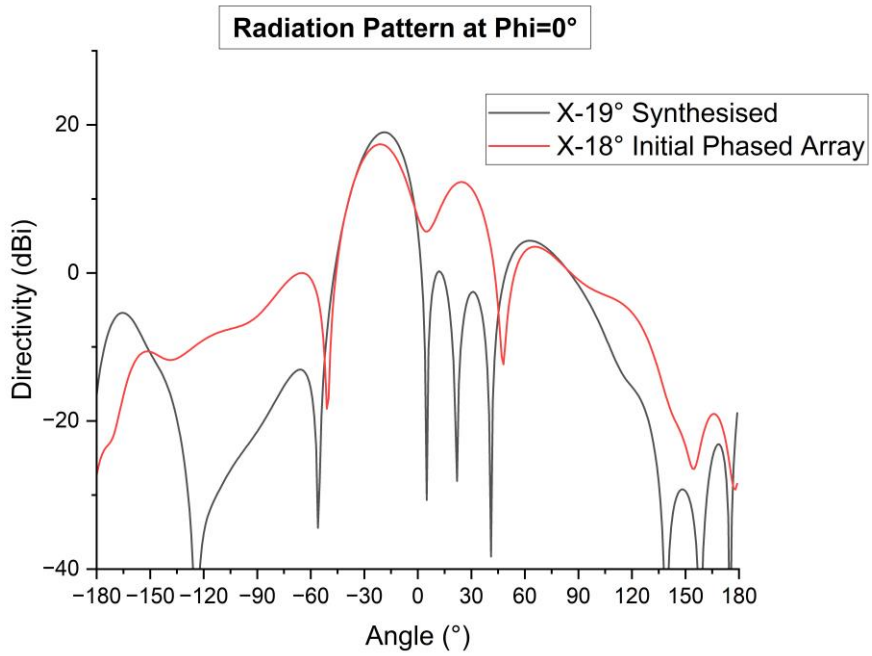

Figure 4. 27 Comparison radiation plot of 20° Initial array and Synthesis array

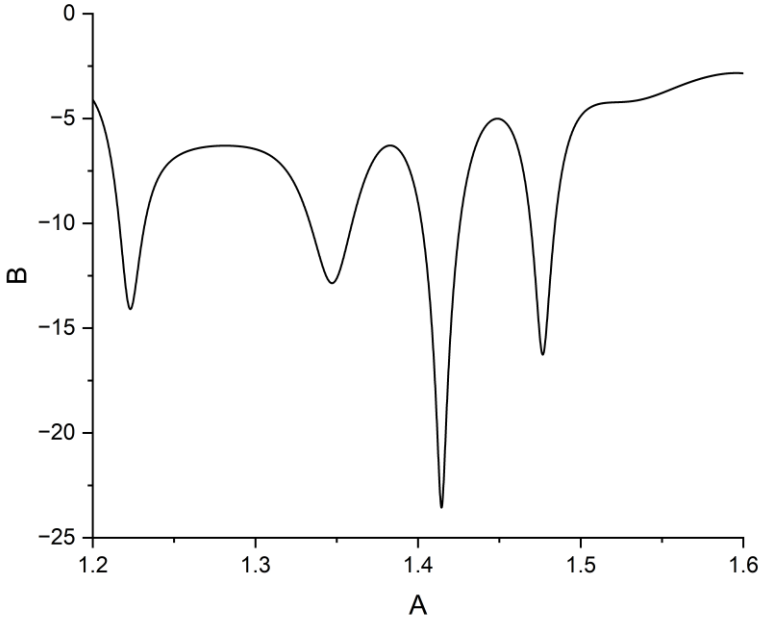

Figure 4. 28 |S11| of the initial phased array

Due to space constraints, one simple way to reduce amplitude errors is to insert 50-ohm transmission lines before adding the phase shifters. This is to improve the impedance transition especially from the 87Ω power divider end to the phase shifter input with varying impedances, and

also keep consistent connecting impedance to be 50Ω at both ends of the power divider. The 3D model is illustrated in Figure 4. 29.

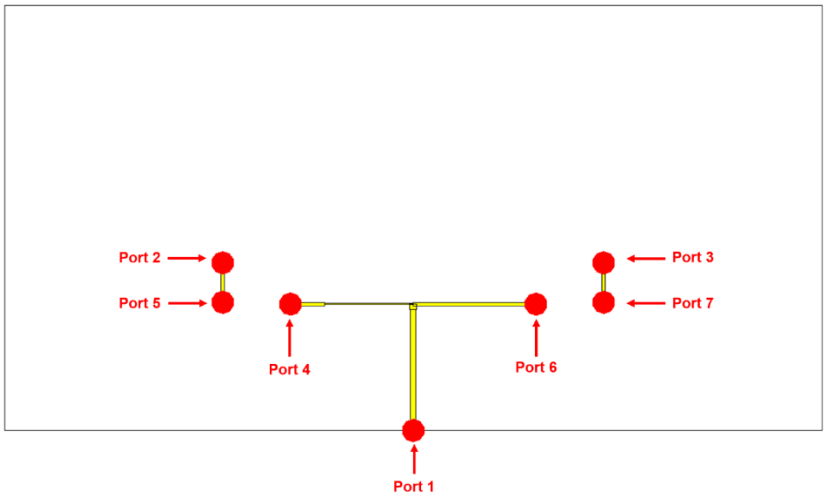

Figure 4. 29 Two-way power divider with an extra 50-ohm section at each end

It can be observed from Table 4. 12 that the inserted 50Ω transmission line reduced amplitude errors to a large extent. Considering the input impedances of each phase shifter state is not exactly at 50Ω, this extra 50Ω transmission line section caused further microstrip discontinuity [133, 147], resulting in additional phase error up to 10° and could lead to minor pointing error in the phased array. From a further array synthesis using the Farfield Array synthesis function of CST Microwave Studio, these phase errors result in the pointing angle increased from 19° to 20°. However, provided that the half power beamwidth of this 4x4 array is 21°, 20° pointing angle is still efficiency for scanning in an airplane, hence this is less concerning as compared to high side lobe levels.

Comparing to the full 50 Ω branch in the right, the 0.58 branch on the left has a phase lag because of the thinner microstrip line (for unequal power division). Provided that Taconic TLX-8 is a low loss material, one potential approach to reduce phase errors is to finely reduce the length of the full 50 Ω branch on the right to compensate for the phase lag, while keeping the split ratio close to [0.58:1].

Table 4. 12 Summary of the compensated power divider at 1.4 GHz

Cases	0.58 Branch	1 Branch	Split Ratio	Phase error (º)
1	90°	180°	0.587:1	10.2
2	0°	270°	0.580:1	18.1

Upon success with suppressing amplitude errors, the next step is to bend the transmission lines to fit for phase shifter integration. Figure 4. 30 shows the finalised power divider design with meandered transmission lines, and the amplitude and phase results are summarised in Table 4. 13 with impedance matching plot in Figure 4. 31. It can be observed that the amplitude errors are slighter larger due to the excess capacitances caused by multiple 90° bends of the transmission line [133], but still limited to 0.03. By slightly adjusting the junction impedances before power splitting, this power divider also exhibits good impedance matching as |S11| is better than -16 dB for both cases within the 1.4-1.425 GHz.

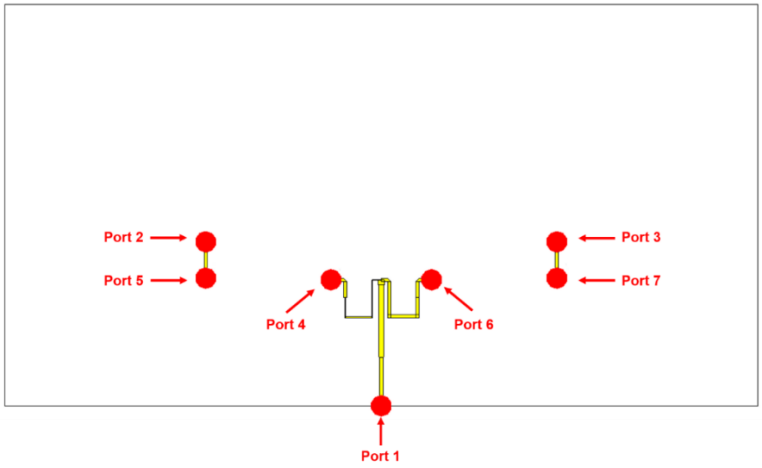

Figure 4. 30 Compensated power divider with meandered transmission line

Table 4. 13 Summary of the final power divider at 1.4 GHz

Cases	0.58 Branch	1 Branch	Split Ratio	Phase error (º)
1	90°	180°	0.563	10.2
2	0°	270°	0.611	17.9

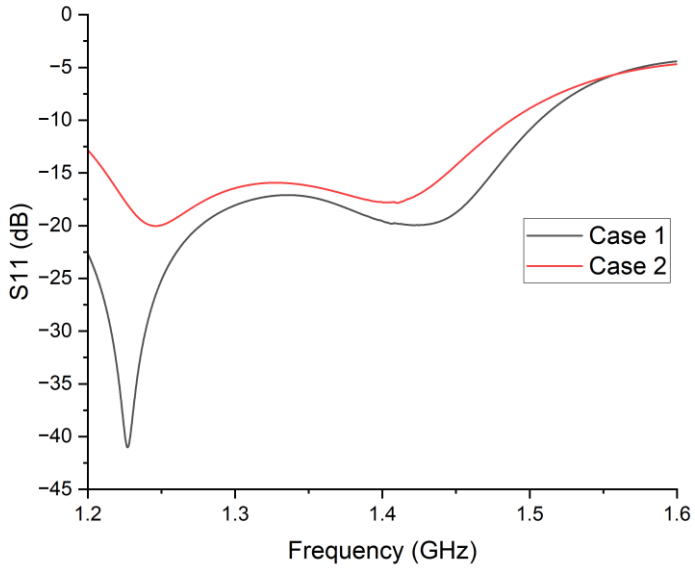

Figure 4. 31 Reflection coefficients of the final power divider

4.3.3 Combined simulation and tuning, final results

The final version of the power divider was then integrated into the 4x4 array by fine tuning the separation distance for adjusting resonant frequency and the stub length for matching reactance [28]. When this was done the antenna exhibited sufficient impedance matching results. Then the PCB for driving electronics and the DC bias lines (both will be discussed later in this chapter) were designed and integrated in the final simulation. Since the results with and without the DC bias lines are very similar, only the final simulation results with the whole system (as depicted in Figure 4. 32) are summarised in the following sections. In here, the driving electronics PCB was integrated into the metal back reflector.

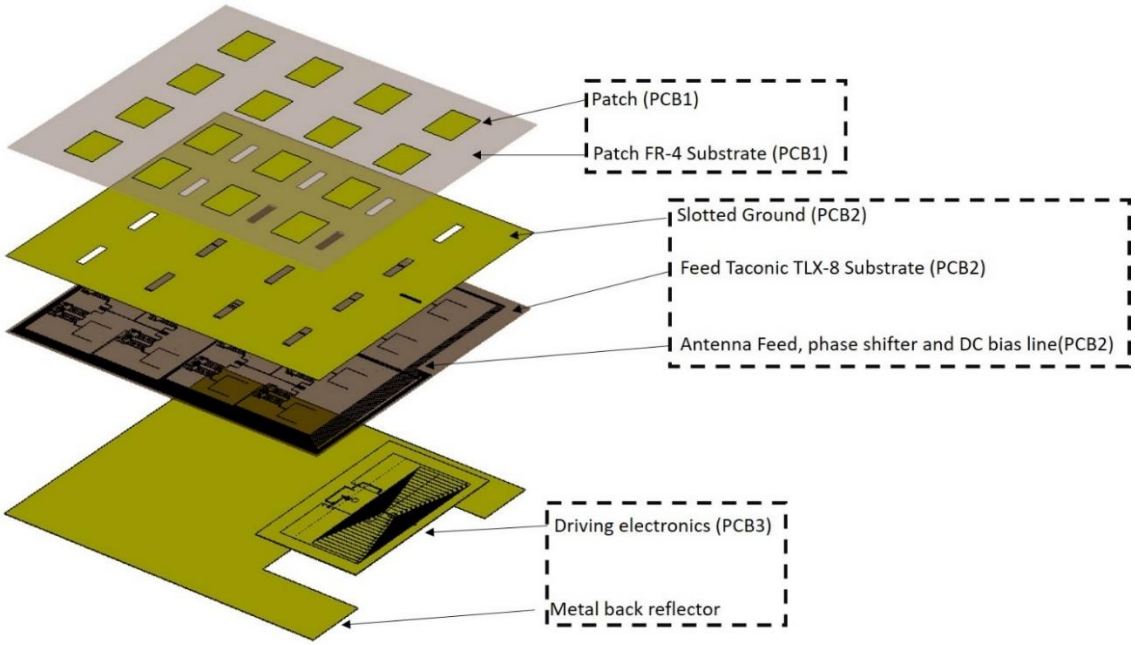

Figure 4. 32 Layered diagram of final L- band phased array simulation model

The following subsections **4.3.3.1 X- direction** to **4.3.3.3 Diagonals** present the phase allocation, impedance matching and radiation patterns of the antenna beams in each direction, followed by the results analysis and summary in **4.3.4 Results analysis and summary**.

4.3.3.1 X- direction

To change the scan direction from X-20° to X+20°, the phase allocation is effectively reading the X-20° table (Table 4. 8) in reverse direction (i.e. from Right to Left) to Table 4. 14. Symmetrical results can be observed both in terms of impedance matching in Figure 4. 33, and radiation patterns in Figure 4. 34 and Figure 4. 35.

Table 4. 14 Phase allocation for X+20° beam (table for X-20° beam can be referred to Table 4. 8) in a 4x4 array

0	270	180	90
0	270	180	90
0	270	180	90
0	270	180	90

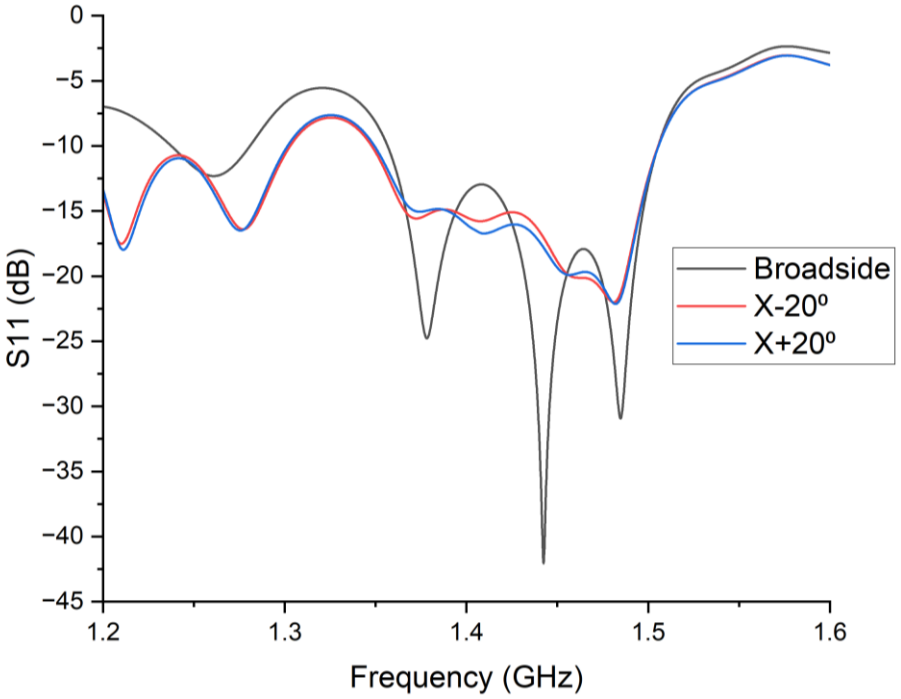

Figure 4. 33 |S11| of the X- direction beams of the finalised 4x4 array

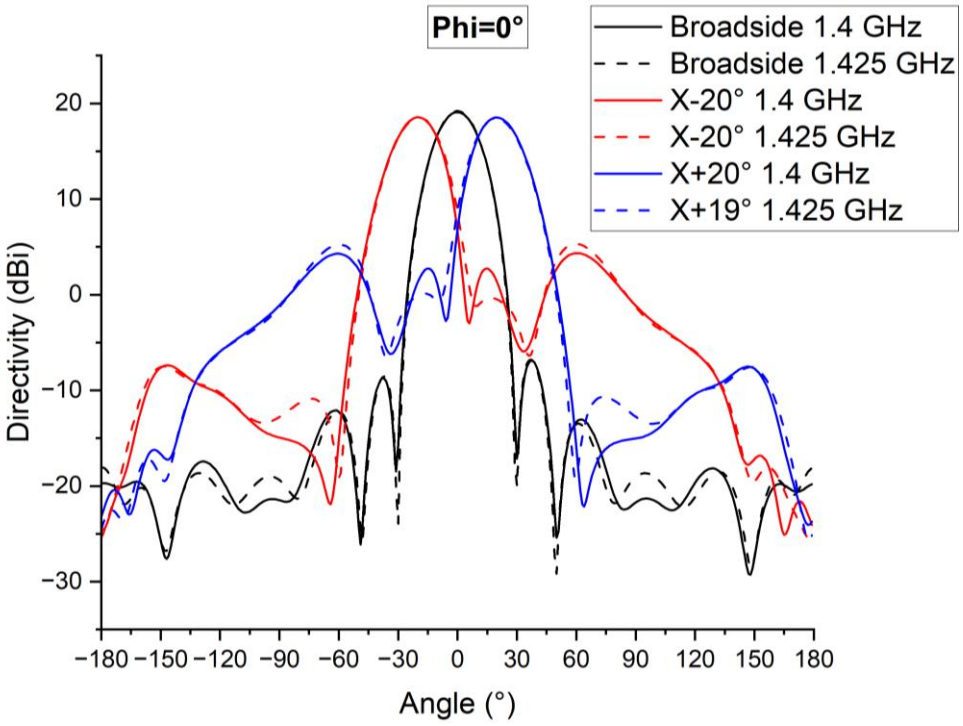

Figure 4. 34 Radiation patterns of X- direction beams of the finalised 4x4 array at Phi=0° cut plane

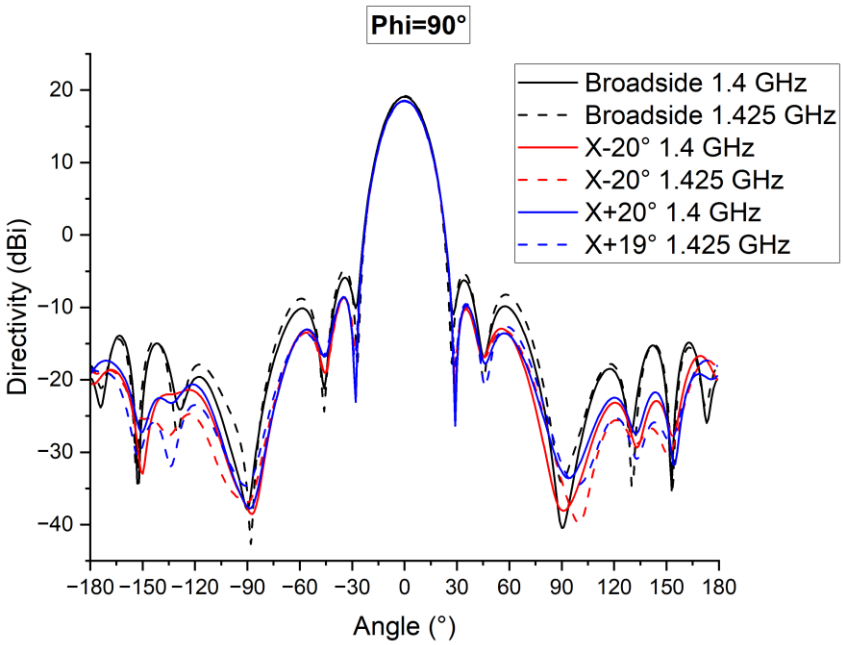

Figure 4. 35 Radiation patterns of X- direction beams of the finalised 4x4 array at Phi=90° cut plane

4.3.3.2 Y- direction

Likewise, for beam scanning in Y- direction, phase variation can only be observed in Y- (i.e. column) direction as shown in Table 4. 15 and Table 4. 16. Highly symmetrical impedance matching can be observed in Figure 4. 36, and also in the radiation patterns depicted in Figure 4. 37 and Figure 4. 38.

Table 4. 15 Phase allocation for Y+20° Beam in a 4x4 array

90	90	90	90
180	180	180	180
270	270	270	270
0	0	0	0

Table 4. 16 Phase allocation for Y-20° Beam in a 4x4 array

0	0	0	0
270	270	270	270
180	180	180	180
90	90	90	90

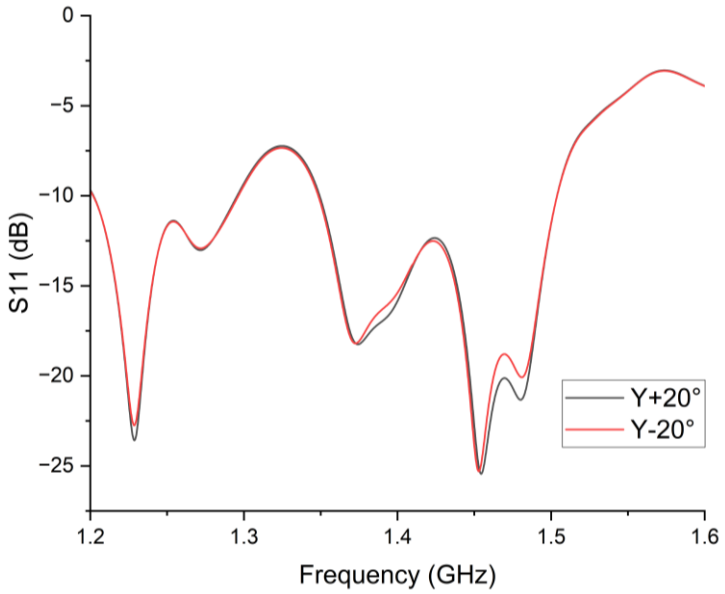

Figure 4. 36 |S11| of the Y- direction beams of the finalised 4x4 array

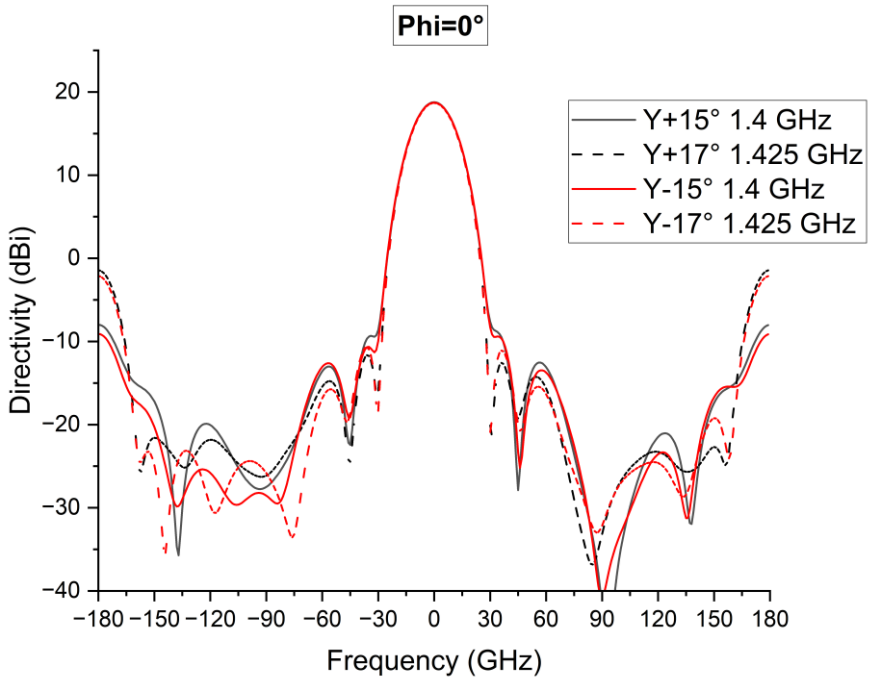

Figure 4. 37 Radiation patterns of Y- direction beams of the finalised 4x4 array at Phi=0° cut plane

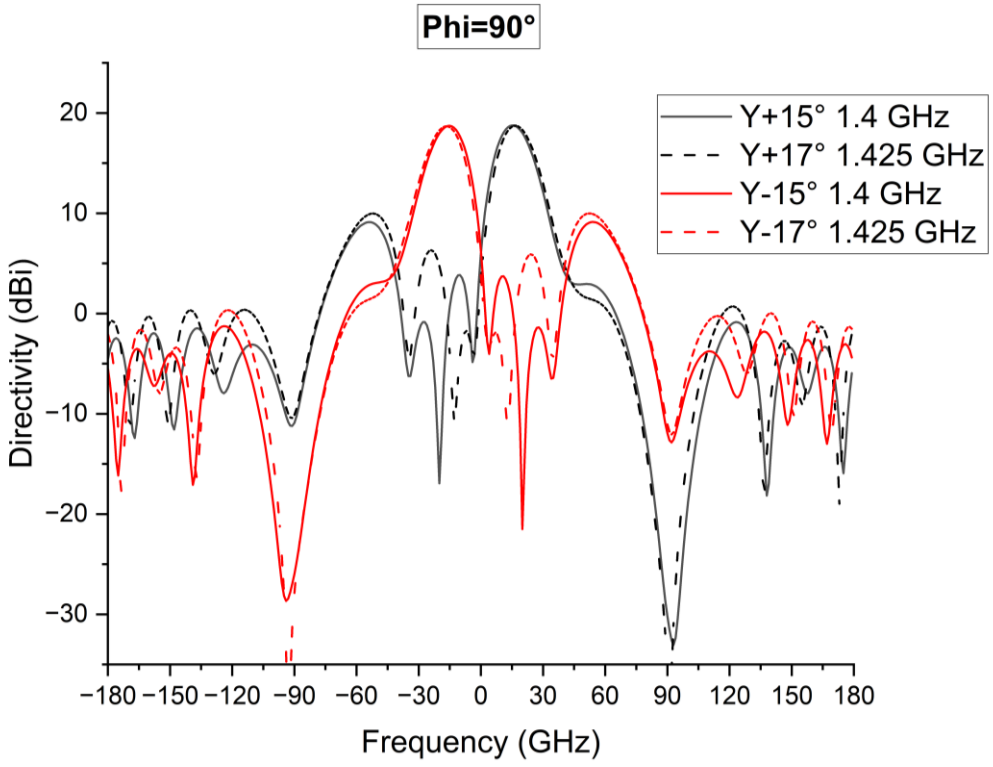

Figure 4. 38 Radiation patterns of Y- direction beams of the finalised 4x4 array at Phi=90° cut plane

4.3.3.3 Diagonals

For diagonal scanning, phase shall vary in both X- and Y- directions. The diagonal scanning phase allocation is effectively the phase allocation summation from each direction, for example, Table 4. 17 is the phase summation of Table 4. 8 and Table 4. 15, but with an additional 180° added to each element for optimal results, and so forth for Table 4. 18 to Table 4. 20. Detailed discussion of phase allocation will be presented later in **5.3.3.1 Phase allocation optimisation**. In here, as this phased array is highly symmetrical in both X- and Y- direction, the impedance matching results are also rather consistent for all four diagonal beams as shown in Figure 4. 39, so are the pointing angles and overall radiation patterns in Figure 4. 40.

Table 4. 17 Phase allocation for [X-19°, Y+17°] beam in a 4x4 array

0	90	180	270
90	180	270	0
180	270	0	90
270	0	90	180

Table 4. 18 Phase allocation for [X+19°, Y+17°] beam in a 4x4 array

270	180	90	0
0	270	180	90
90	0	270	180
180	90	0	270

Table 4. 19 Phase allocation for [X-19°, Y-17°] beam in a 4x4 array

270	0	90	180
180	270	0	90
90	180	270	0
0	90	180	270

Table 4. 20 Phase allocation for [X+19, Y-17°] beam in a 4x4 array

180	90	0	270
90	0	270	180
0	270	180	90
270	180	90	0

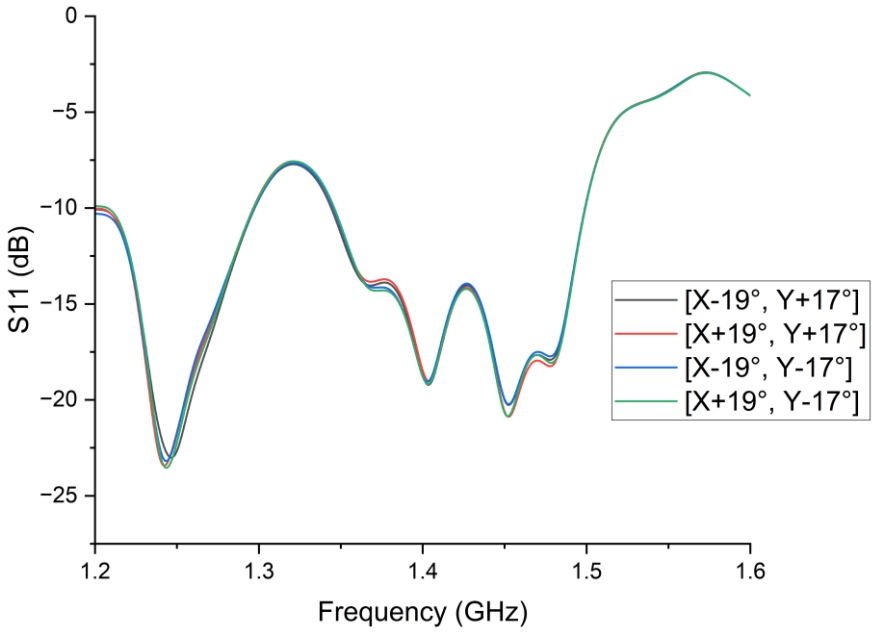

Figure 4. 39 |S11| of the diagonal beams of the finalised 4x4 array

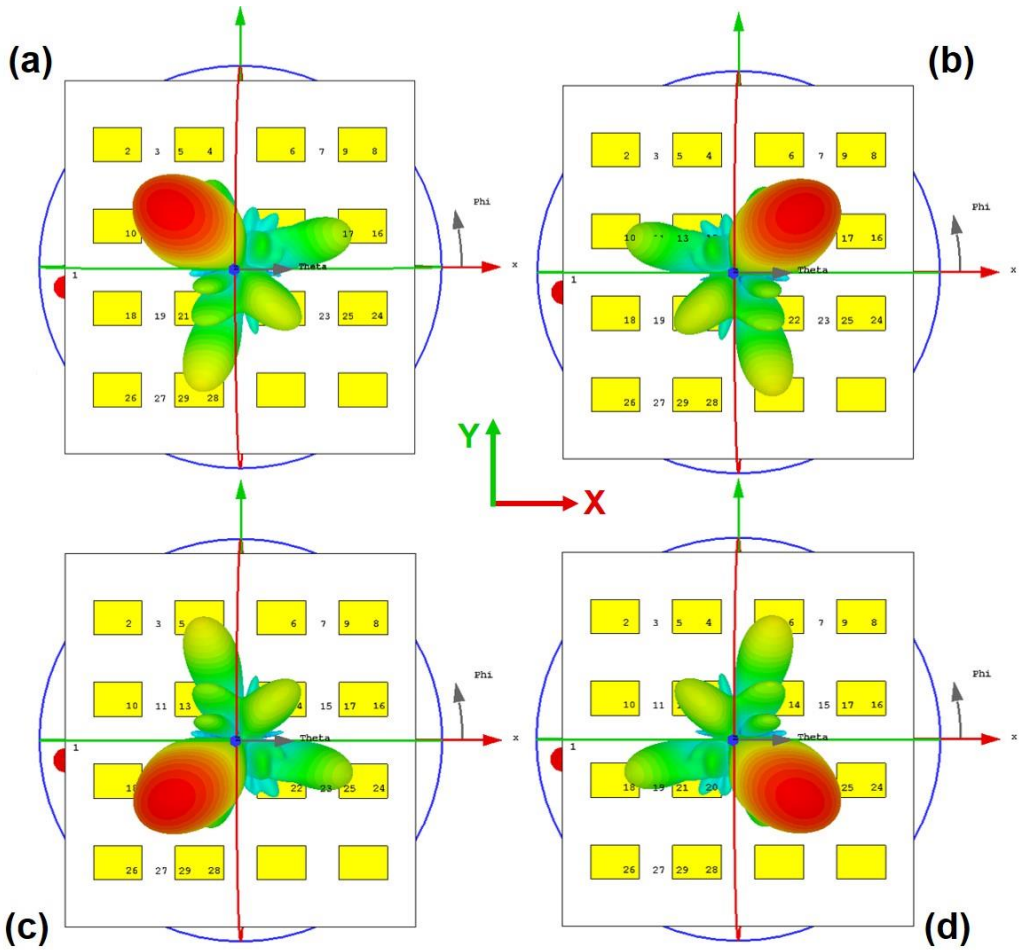

Figure 4. 40 Diagonal beams far field patterns of the finalised phased array at 1.4 GHz

4.3.4 Results analysis and summary

Table 4. 21 Radiation pattern results summary at 1.4 GHz

Beam	Total loss (dB)	3-Dimensional Main Beam Efficiency (%)	Highest side lobe (dB)
0°	-2.093	98.97	-25
X-20°	-1.748	90.86	-14.2
X+20°	-1.734	90.89	-14.3
Y+15°	-1.782	82.26	-9.6
Y-15°	-1.796	83.26	-9.6
[X-19.32°, Y+17.40°]	-1.806	77.58	-10.8
[X+19.32°, Y+17.40°]	-1.825	77.77	-10.9
[X-19.32°, Y-17.40°]	-1.807	78.47	-10.9
[X+19.32°. Y-17.40°]	-1.812	78.33	-10.9

Table 4. 22 Radiation pattern results summary at 1.425 GHz

Beam	Total loss (dB)	3-Dimensional Main Beam efficiency (%)	Highest side lobe (dB)
0°	-2.027	98.88	-24
X-20°	-1.829	91.41	-13.2
X+19°	-1.792	91.33	-13.2
Y+17°	-2.084	78.22	-8.8
Y-17°	-2.069	78.52	-8.7
[X-19.32°, Y+17.40]	-2.058	77.33	-11.3
[X+19.02°, Y+17.73°]	-2.066	77.31	-11.4
[X-19.32°, Y-17.40°]	-2.066	77.61	-11.3
[X-19.32°, Y-17.40°]	-2.056	77.56	-11.2

To summarise the results, the total efficiency of each beam is better than -1.825 dB at 1.4 GHz, and -2.084 dB at 1.425 GHz; by using 2-bit phase shifter with loss from -0.58 to -0.99 dB at 1.4 GHz, and -0.65 to -1.02 dB at 1.425 GHz. Given that the 2-bit phase shifter does not have significantly higher loss at 1.425 GHz, the lower total antenna efficiency could be due to matching (S_{11}) at 1.425 is over 3dB worse than at 1.4 GHz for most of the beams (except Left/Right 20°). In addition, this antenna has better radiation efficiency at 1.4 GHz for all of the beams. In terms of 3-dimensional beam efficiency, all the one-dimensional beams have efficiencies better than 82.26% at 1.4 GHz. Notably those for the Left/Right 20° beams are over 90%. The diagonal scanning beams have efficiency around 77%.

Overall, the simulation results are considered to be sufficient for fabrication. The next two sections present the design of driving electronics and the phased array fabrication, assembly and measurement.

4.4 Driving electronics design

4.4.1 Overview and objectives

The objective of driving electronics development is to control each of the 32 individual phase shifter elements for implementing beamforming. Although this part of the work only involves low frequency control logic and DC voltages, it is not an easy task, and a few stages of design work are required to fully develop a stand-alone control network. Those stages include:

Stage 1: Build up fundamental hardware and understanding for a $+5V/-15V$ breadboard switch circuit and develop a breadboard prototype for controlling the 2-bit phase shifter element.

Stage 2: Once the design concept was demonstrated in stage 1, the system was tested with switching performance, and make further optimisation if required. The other goal of this stage is to develop power supply for the Arduino Mega, so that the whole system can be fully stand-alone with only battery supply. The proof of concept and breadboard prototype concludes at the end of stage 2.

Stage 3: The final stage is to select low profile (preferably SMD) and low power consumption

components and design a PCB for controlling all 32 phase-shifter elements.

4.4.2 Breadboard prototype for controlling 2-bit phase shifters

The overall system schematic is depicted in Figure 4. 41. The system consists of a +5V line and a -15V line sourced from the battery supply, while the Arduino Mega provides the +5/0V digital control signal. The output of the PNP transistor switch is either +5V or -15V to control the forward and reverse biased state of the diodes in the phase shifter element respectively, and hence implement the controlled phase difference at its output.

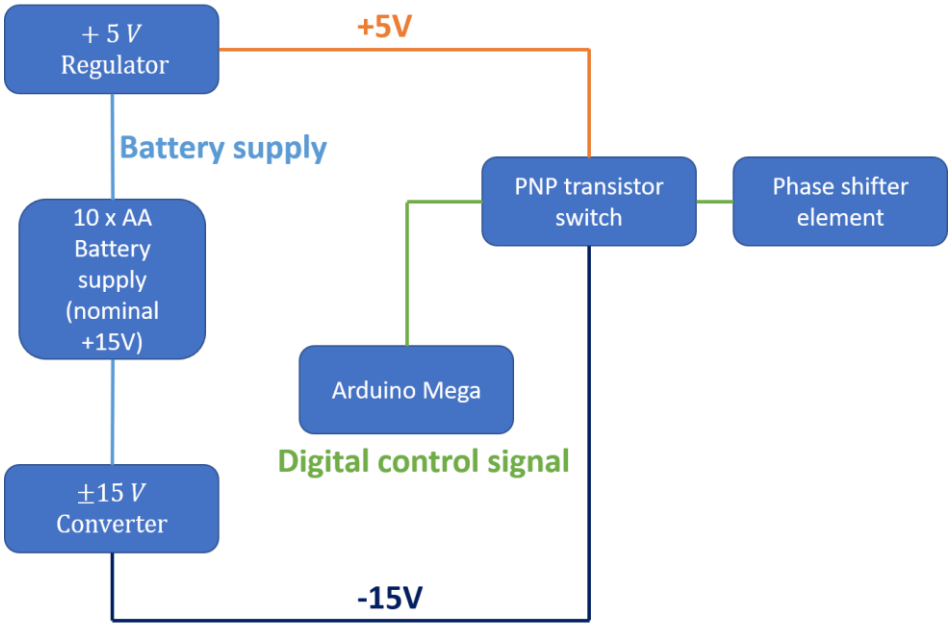

Figure 4. 41 System schematic for controlling a single phase-shifter element

4.4.2.1 ±15V converter, 10 x AA Battery supply and +5V Regulator

In the whole control system, the -15V line is the less commonly used part and usually provided by the laboratory DC supply machine rather than being integrated in the system. In this design, -15V is required to be generated from a battery supply to be stand-alone, and the DC/DC converter M7886 is selected to provide -15V output from a DC source with 9-36V [148], while its +15V output is not utilised in this design. The wide input voltage range of 9-36V ensures the system can be easily powered by batteries, and based on the minimum voltage requirement of 9V, a 10 x AA battery supply (and hence +15V nominal voltage) is selected to ensure the system works for a long duration before the supply voltage drops below 9V. For the generation of +5V, the regulator 7805CT (with input voltage ranges from 7 to 35V) [149] is selected because of immediate

availability for proof of concept, and it is used as the voltage/current source for the phase shifter forward state. As for the phase-shifter forward state, 17 mA will be drawn by two BA682 diodes in the phase shifter circuit. Due to this high current consumption, Arduino Mega is only used for +5/0V logic signal control, rather than supplying current directly to the phase shifters. Further details will be discussed in the 4.4.2.2 Arduino Mega and PNP transistor switch sections below.

4.4.2.2 Arduino Mega and PNP transistor switch

In this design, the 180° and 90° phase shifter bits shall be integrated with each patch (out of total $4 \times 4 = 16$ patches), which in turn requires $2 \times 16 = 32$ independent logic controls. It can be argued that each column has the same phase assigned for X- directional scanning (as per Table 4. 8 and Table 4. 14), and thus only $2 \times 4 = 8$ independent controls are needed. However, proceeding in this way will lose the possibility of implementing 2-dimensional scanning in the future, and will even lose the flexibility of selecting which single dimension to scan (e.g. the antenna can only scan in X- direction but not Y- direction by limiting the number of limiting the number of control elements to 8). Therefore, this loss of future flexibility outweighs its benefit of reducing the control requirements.

Based on the requirement of 32 independent logic controls, the micro-controller shall have at least 32 programmable digital outputs, which makes ATMega2560 (with 54 Digital pins) [150] a suitable candidate. Due to availability, the ATMega2650 with Wi-Fi [151] is selected.

In order to use the 0V Low logic signal from the Arduino Mega to output -15V for reverse bias, and +5V High logic signal to control the +5V voltage source for forward bias, a PNP transistor would be a more practical option as compared to an NPN transistor. For the case of using an NPN transistor, it would be easy to produce -15V output, since connecting either +5V or 0V to the base the transistor would suffice (as $V_B > V_E(15V) + V_{BE(sat)}$) to turn on the switch, this is also shown in simulation result Figure 4. 42. However, as indicated in Figure 4. 43, it would be rather difficult to produce 5V output, as it requires a negative base voltage $V_B < V_E + V_{BE(sat)} = -15 + 0.7(typical) = -14.3\,V$ in order to turn off the switch. In short, both the +5V/0V logic outputs could only drive the NPN to the same state (i.e. output of -15V), while additional -14.3V supply and

switching is required for controlling the NPN to produce +5V. Therefore, a single NPN switch is not a suitable candidate in this context.

In contrast, a PNP switch fits in this application. By applying 5V to its base, as depicted in Figure 4. 44, since $V_B > V_E - V_{BE(on)}$ the switch is shut-off hence -15V output could be obtained. Figure 4. 45 shows the simulation result when 0V is connected to the base of this PNP transistor, as $V_B < V_E - V_{BE(on)}$ in this case, the switch is on and effectively V_E is connected to the resistor R_1, hence the transistor output is +5V. In short, the +5V/0V logic output is able to drive a single PNP to Off/On stage and thus output -15V/+5V. Therefore, a PNP transistor is an appropriate choice for this design.

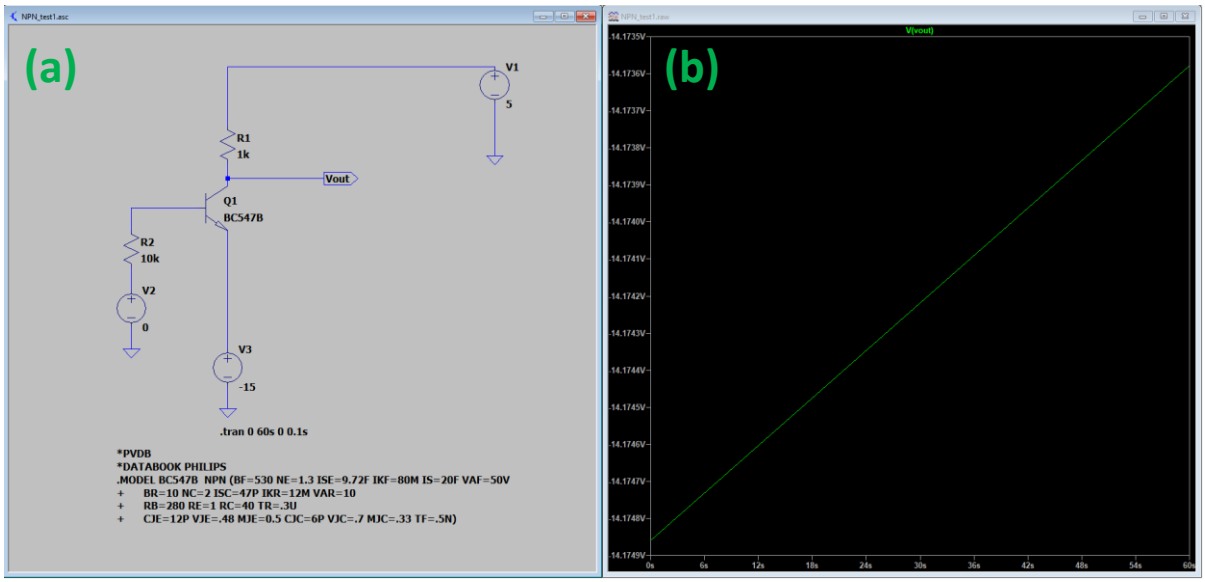

Figure 4. 42 NPN transistor On-state (a) Circuit diagram with V_B=0V (b) Open collector output of -14.2V

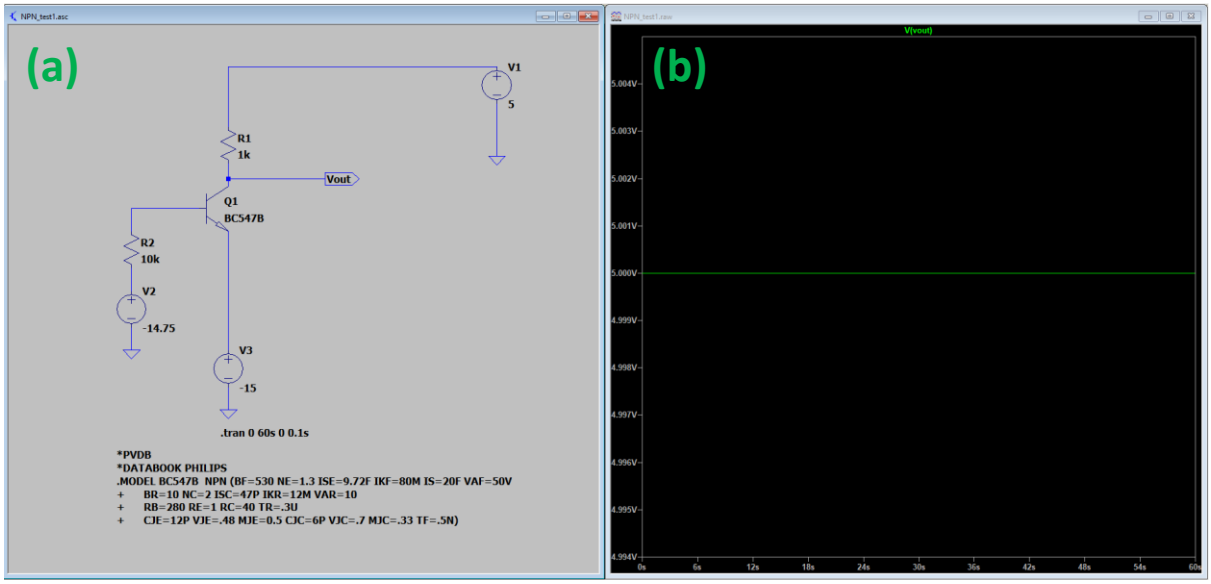

Figure 4. 43 NPN transistor Off-state (a) Circuit diagram with V_B=-14.75V (b) Open collector output of +5V

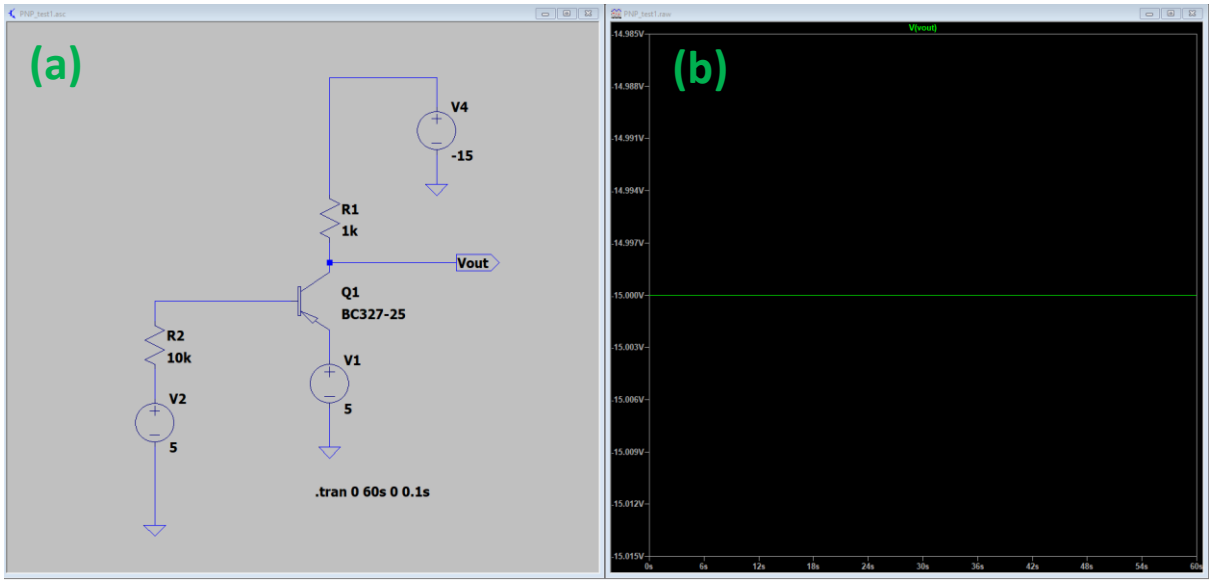

Figure 4. 44 PNP transistor Off-state (a) Circuit diagram with V_B=5V (b) Open collector output of -15V

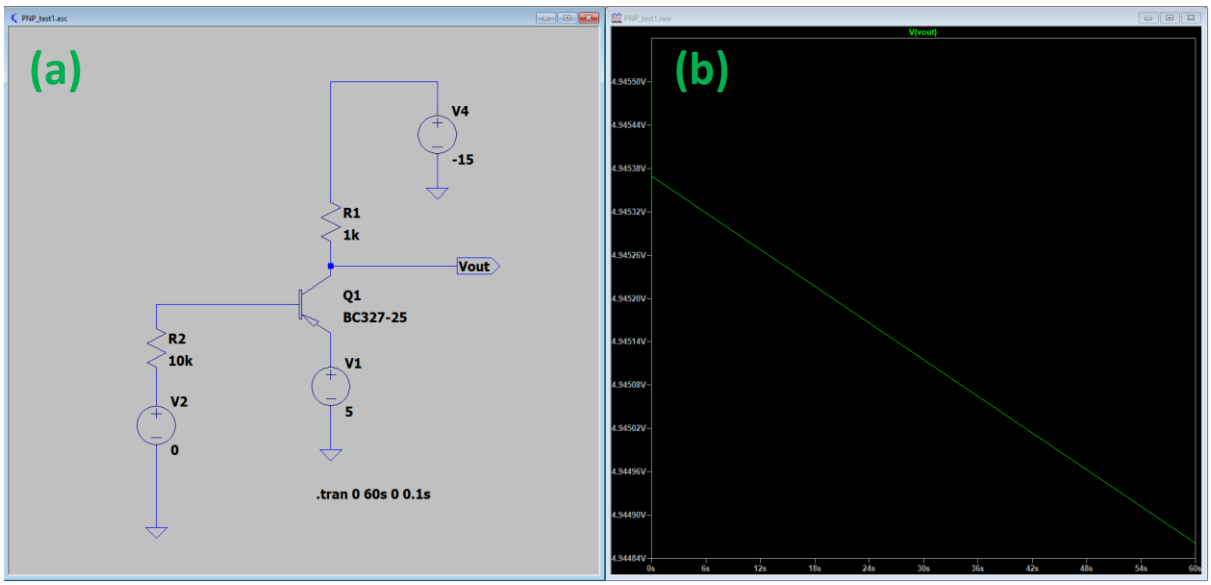

Figure 4. 45 PNP transistor On-state (a) Circuit diagram with V_B=0V (b) Open collector output of 5V

Based on the successful control of +5V Forward/-15V Reverse bias control voltage. The next stage is to design the transistor circuit closely to meet the following criteria:

1. For the circuit protection point of view: To draw minimum current from the microcontroller. To meet this criteria, two factors needs to be considered:
    a. Considering each phase shifter circuit consists of two diodes in parallel with a 470Ω resistor for each to provide forward current, the current flow though the PNP collector (I_C) is required to be $\frac{5}{470/2} \approx 21mA$. It is given that $V_{CE} = -15 - 5 = -20V$. As indicated in the datasheet of PNP transistor BC327 [152], $I_B = 0.5\,mA$ is a good operating point to transfer $I_C > 20mA$ with high current gain ($\beta > 100$), while V_{CE} of -20V would be sufficient to drive the transistor to saturation region.
    b. Consequently, even if the extreme that all 32 phase-shifter are in forward-biased state, the total required current will be $0.5 \times 32 = 16\,mA$. Given that the maximum safe current for the microcontroller is 200mA [153], this current requirement is well within the limit. In the meantime, because only at maximum 0.5 mA current will be drawn from each pin, optocouplers are not necessary for additional protection. In the design perspective, standard optocouplers require more than 2 mA turn-on current [154], while low-current optocouplers are costly (if 32 units required); the demand of

space and soldering workload will also increase if optocouplers are adopted. Therefore, due the only low current requirement for the microcontroller and high cost of using optocoupler, the additional layer of optocouplers was not considered.

Based on these two factors, $R_2 = 10\ k\Omega$ is designed to keep $I_B = \frac{0-5}{10\times1000} = 0.5\ mA$ when the transistor is turned on.

2. From the power saving criteria: To draw minimum current from the battery supply, we should keep the voltage outputs sufficient for driving the diodes. Likewise, two factors are to be considered:

    a. During the transistor on state, resistor R_1 is connected in parallel with the phase shifters, the approximate circuit model is depicted in Figure 4. 46. Therefore, the value of R_1 would not have much impact on the diode forward voltage as long as $R_1 > 470\ \Omega$ (otherwise it might affect the current gain requirement). However, R_1 could directly affect the power consumption of the system as current of $\frac{20}{R_1} A$ will be drawn during transistor on state. Considering the current drawn by R_1 would not affect the phase shifter performance, it is favoured to make the current consumption as small as possible.

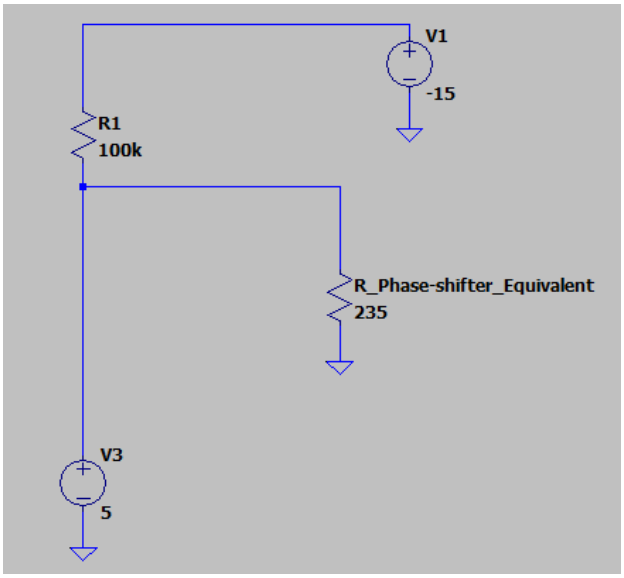

Figure 4. 46 Approximate circuit model when the PNP switch is on/ Diodes forward biased

    b. During the transistor off state, resistor R_1 is connected in series with the phase shifter

(as in Figure 4. 47). In this regard, R_1 shall be designed such that most of the voltage drop ($\approx -15V$) goes across the diode, thus R_1 shall be relatively small as compared to diode's reverse resistance.

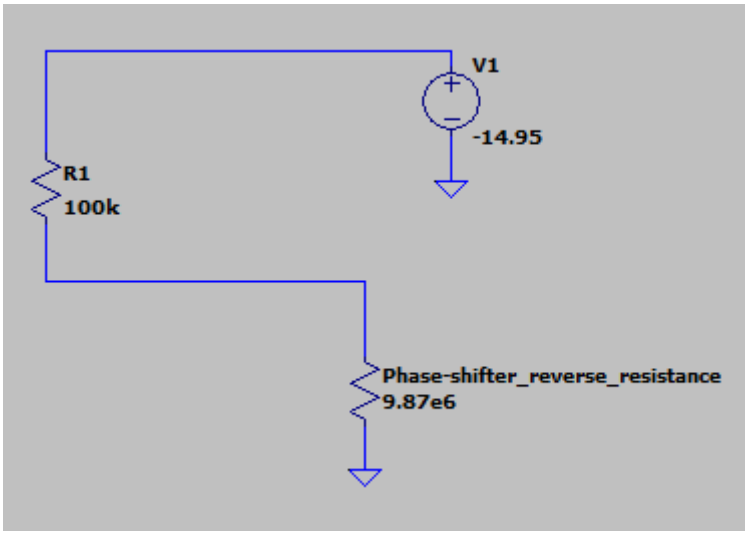

Figure 4. 47 Equivalent circuit model when PNP transistor is off/ Diodes reverse biased

This resistance could be estimated by changing R_1 values and measuring the corresponding voltages across the phase-shifter circuit (V_{ps}), Table 4. 23 records the measured values. By voltage division rule, the phase-shifter reverse resistance (R_{psr}) can be computed as:

$$R_{psr} = \frac{(R_1 \times V_{ps})}{14.95 - V_{ps}} \qquad (5.\ 2)$$

Table 4. 23 Diode reverse resistance test

R1 Resistance ($k\Omega$)	Voltage across the phase-shifter (V)
100	-14.8
57	-14.87
28.5	-14.91

Based on this equation, R_{psr} is approximated to be $9.87\ M\Omega$.

By considering the above-discussed factors, R_1 is design to be 100K Ω to limit the forward parallel current to $\frac{5}{100\times1000} = 0.05mA$; while keeping its resistance small as compared to the diode's reverse DC resistance.

4.4.3 Stage 1 testing

Upon the completion of the first-stage circuit design, the system is tested with the 2-bit phase shifter elements for proof of concept.

Figure 4. 48 shows the sample test setup and stage 1 breadboard prototype, during this testing, a few parameters shall be looked closely:

1. Battery current: This would indicate how much current consumed when all the phase-shifter elements are in different states, and accordingly calculate current consumption for each phase-shifter.
2. Microcontroller current: This could indicate how much current needed to turn on a PNP transistor, and the overall power consumption (as later on the system will be powered solely by batteries)
3. Relative phase shifter (reference to 0°): This directly shows how effective is the control circuit, and the resultant phase accuracy

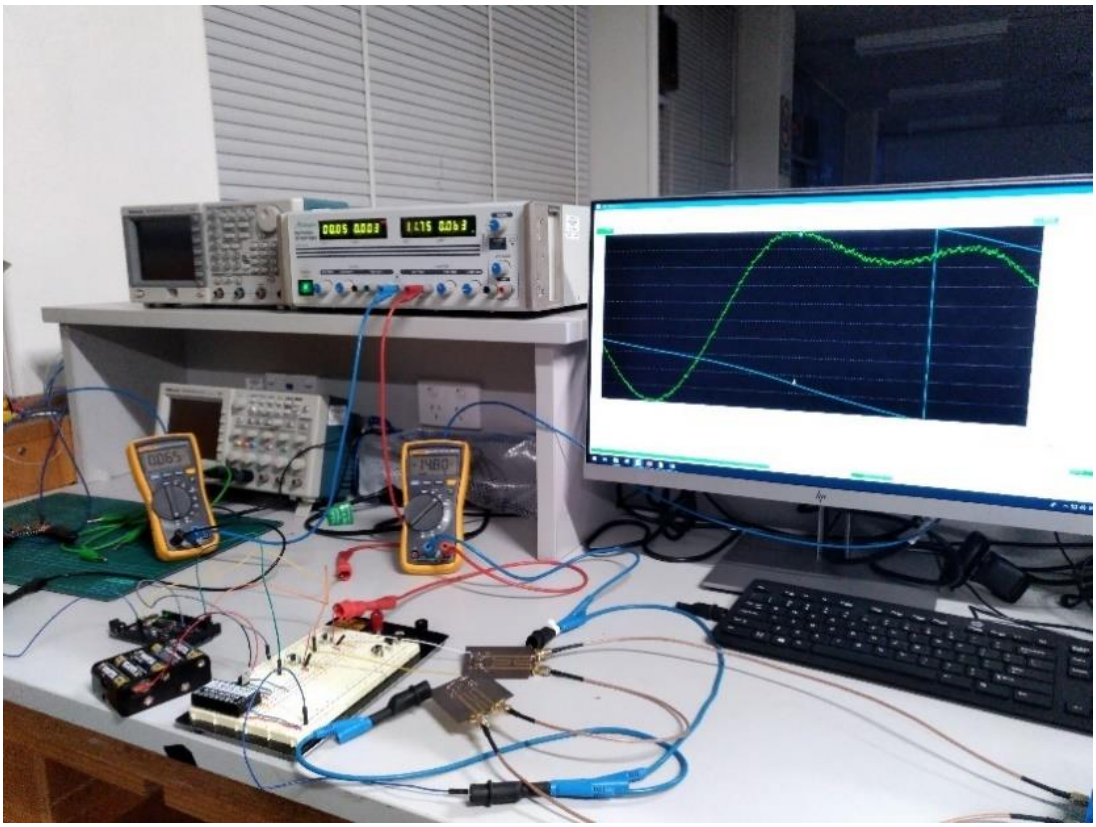

Figure 4. 48 Sample setup for Stage1 test

Table 4. 24 records the system key parameters, it can be observed that

a) each phase-shifter consumes around 18 mA battery current, this result is consistent with the earlier discussion in the preceding two sections

b) No measurable difference in the Microcontroller current even when both PNP transistors are on, this implies each transistor draws little current in the current design. Therefore, the total current shall be well within the safety limit of 200 mA even all 32 transistors are turned on.

c) The phase shift error is within $10°$. This could be attributed to minor design error in the phase-shifter element prototype, as well as miniVNA Tiny measurement error. Overall, this performance is sufficient for demonstrating the required control capability.

Table 4. 24 Stage 1 system measurement results

	0°	90°	180°	270°
Battery current (mA)	25	44	44	62
Microcontroller current (mA)	62	62	62	62
Relative phase shift (reference to 0°)	0°	92.88°	189.35°	280.84°

As can also be observed from Figure 4. 48, the driving voltage for phase-shifter reverse state is -14.8V rather than -14.95V because of voltage division by R_1. Considering the phase shift accuracy is rather sensitive to the reverse bias voltage [25], to examine if -14.8V would have any impact of the phase-shifter performance, a separate test with voltage of -14.95V (by directly connect the phase shifter to the -14.95V line) has been conducted, Table 4. 25 compares the results of these two cases. It can be observed that the phase difference between two cases is less than $0.1°$, hence it can be concluded that voltage deviation within 0.2V does not cause significant accuracy error. In conclusion, the current design meets the criteria of controlling phase shifters, protecting the microcontroller, and drawing minimal current from the battery supply.

Table 4. 25 Phase shift comparison between bias voltage of -14.8V and -14.95V

	0°	90°	180°
-14.8V driving Relative phase shift	0° (−125.92° absolute)	92.88°	189.35°
-14.95V driving Relative phase shift	0° (125.83° absolute)	92.82°	189.28°

4.4.4: Switching test, optimisation and integration

4.4.4.1 Switching test

Since acceptable DC/static performance has been obtained from stage 1, as advised by [154], the next step shall be testing the switching capability of the system and making further necessary modifications. In this test, a function generator is adopted to generate 1 KHz pulse signal with 5/0V for high/low logic level, considering there are 3 primary used beams ([X-20°, 0°, X+20°]) to be switched, the duty cycle of the pulse is set to be 33%. An oscilloscope is used to monitor the function generator signal, as well as the PNP transistor output, Figure 4. 49 shows the sample captured results. In this figure, the yellow line shows the function generator signal, while the blue line shows the PNP output. It can be seemed that the rise time of the blue time (from -15V to 5V) is rather short that a sharp transition can be observed, while it takes about 100mS from the output to fall from 5V to -15V. This rather large fall time could be attributed to the large value of R1 and the rather large capacitance of the diode off-state. These two factors lead to a large time constant and hence slow down the switching. In order to reduce the fall time, R1 has been tested with different resistance values, and the corresponding fall time has been recorded and plotted in Figure 4. 50. It can be observed that the transistor output fall time is proportional to the resistance value of R_1. Considering the typical integration time of an L- band radiometer is in the order of milliseconds to tens of milliseconds [20, 85, 128], R_1 value has been selected to be around 57 kΩ for reducing the fall time to around 52 μS (which is even less than 5% of the radiometer integration time), while keeping the current consumption low. During the measurement, both 180° and 90° phase shifter has been tested separately, the switching performance of them are very similar. Even when they

are connected in cascade, the switching performance is not affected, this may because of the large SMD DC blocking capacitor integrated in the phase-shifter circuit.

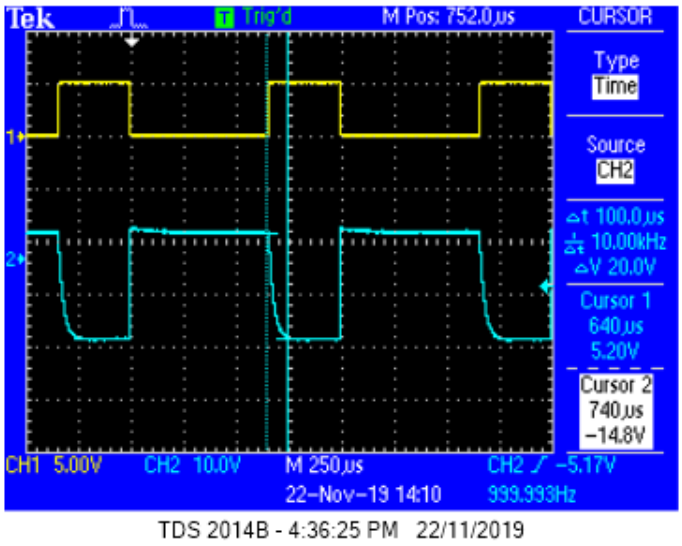

Figure 4. 49 Sample measurement result from the Oscilloscope: Yellow: Input test signal; Blue: Transistor output

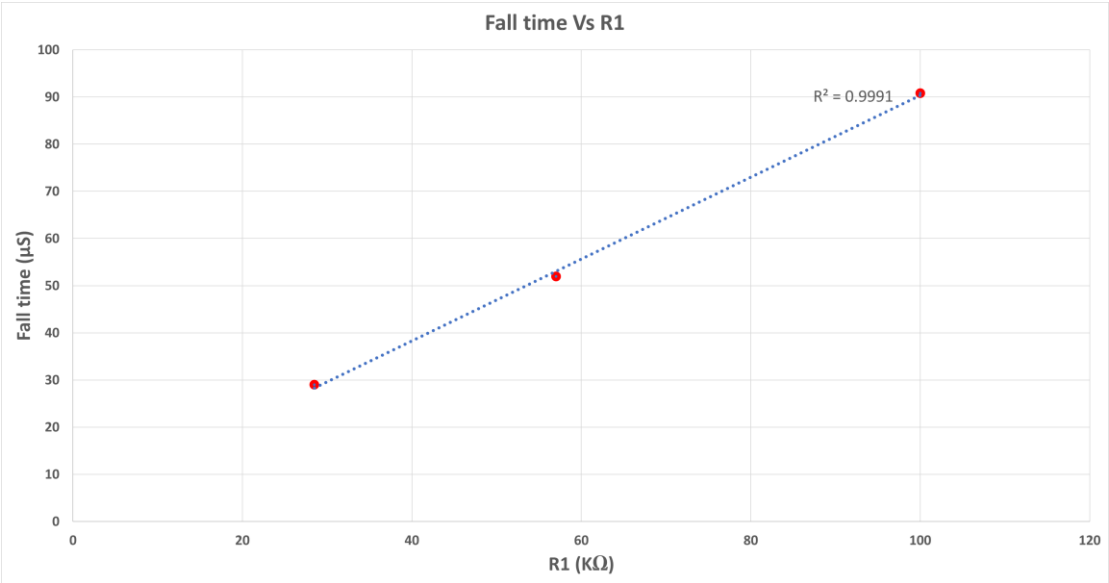

Figure 4. 50 Transistor output fall time vs R1

4.4.4.2 12V System integration

After obtaining acceptable phase control capability and switching performance, the final step of breadboard prototype is to make the whole system stand-alone. As suggested by [150], the supply voltage to the Arduino shall be 7 to 12V for a stable operation and prevention of regulator overheat. In this context, simply changing the battery holder (supply) from 10XAA to 8xAA would suffice.

Considering the micro-controller is connected in parallel with the regulators and transistors circuit, directly connect it to the power supply should not have concern on overcurrent.

To further reduce the current consumption, the PNP base resistor R_2 has been modified to 20 KΩ, the whole system has been tested as in Figure 4. 51. Table 4. 26 and Table 4. 27 summarise the system key parameters and estimations on power consumption.

As suggested by the project chief investigator, this radiometer antenna shall be able to work at least 5 hours per run. Considering the overall system current consumption will be around 724 mA when all 32 phase shifters are in on-state (which is the extreme case), lithium batteries would be better options as they could provide high voltage and high capacity at the same time (rather than series 8x AA batteries with equivalent capacity of a single 3000mAh AA battery [155]). ANAMANN 2447-3050 would be a good candidate because of its sufficient voltage (11.1V) and high capacity of 5.2Ah (which in terms could supply the system for over 7 hours), as well as its compact size and easy-to-use wire leads [156].

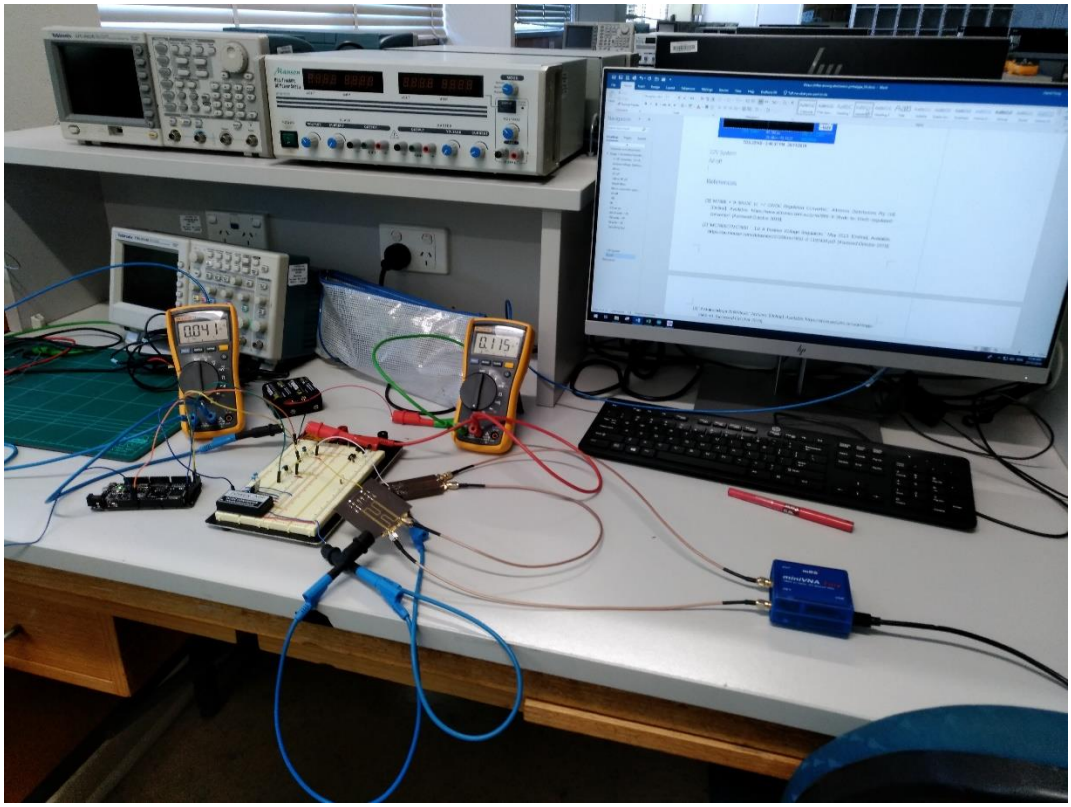

Figure 4. 51 Sample stand-alone system test to conclude stage 2

Table 4. 26 System key performance

	0°	90°	180°	270°
System current (mA)	116	134	135	153
Microcontroller current (mA)	41	42	42	43
Relative phase shift (reference to 0°)	0°	89.41°	189.58°	276.66°

Table 4. 27 System complementary details and estimation

PNP on state voltage	$4.929V$
PNP off state voltage	$-14.86V$
Current consumption per phase shifter on state	$18mA$
Current drawn per transistor on state	$<= 1mA$
Estimated microcontroller current when all 32 transistors are on	$<= 73mA$
Estimated system current when all 32 transistors are on	$<= 724\ mA$

In summary, at the end of Stage 2, the system is integrated to be stand-alone with optimised switching performance and power consumption. This power consumption is still feasible with careful lithium battery selection for meeting the continuous run time requirement (i.e. 5 hours) of the project. Proof of design concept concludes at this point; the final stage is to develop a PCB for controlling all 32 phase-shifters.

4.4.5 PCB Design and fabrication

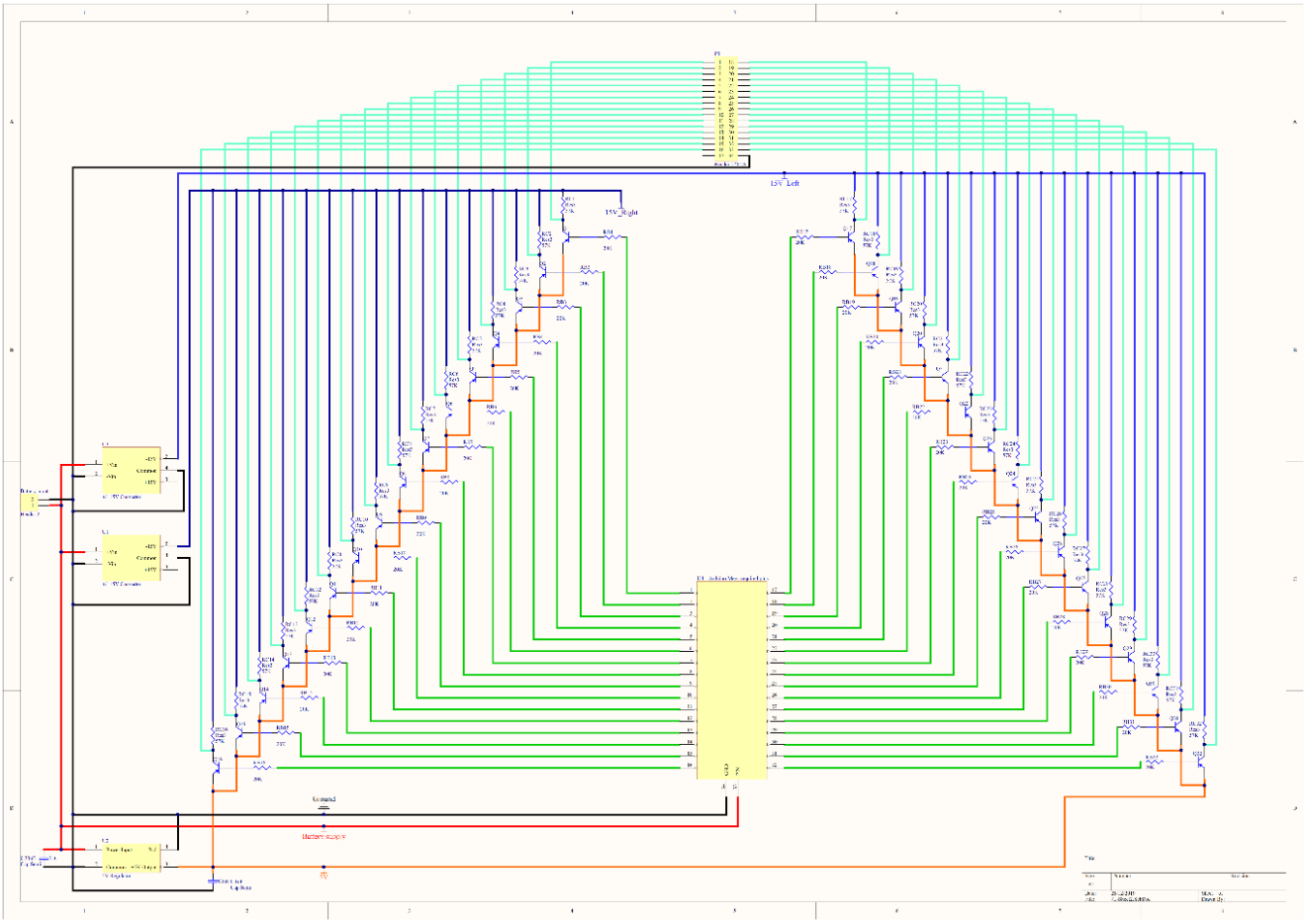

Figure 4. 52 Schematic diagram of the driving electronics PCB design

In the final PCB Design the 5V regulator MC7800 has been selected for a low-profile design, and the selection of other components remained unchanged. Figure 4. 52 shows the schematic diagram of the final PCB design. The final PCB is fabricated in FR-4 material with 1.6 mm for low cost and sturdy structure. Figure 4. 53 to Figure 4. 56 shows the fabricated design layers. Being a soft metal material, aluminium plate was selected as the metal back reflector for the ease of modification.

The voltage output of each transistor is then connected to the 34-pin header of the feedline layer, with thin 0. 254mm thin DC bias lines connecting from each pin to phase shifter bit. Figure 4. 57 shows the connections from each pin to each corresponding phase shifter bit. Accordingly, basic Arduino programs to produce digital high/low output to control the off/on state of each PNP

transistor, hence reverse/forward biased state of each phase have been completed for each radiation pattern.

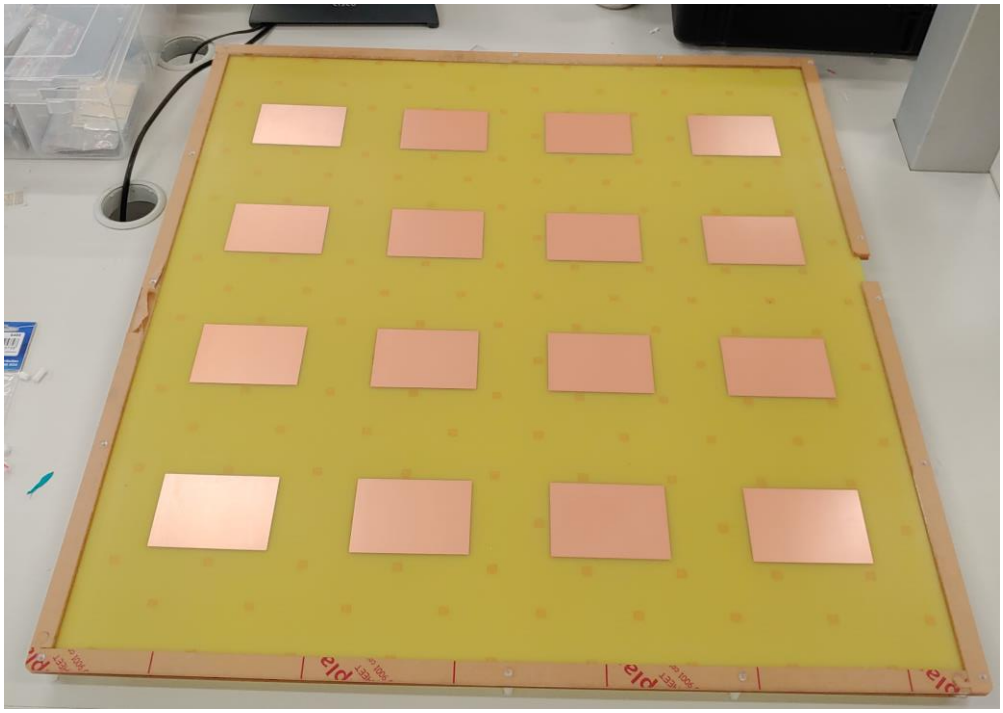

Figure 4. 53 Fabricated Radiating Patch layer

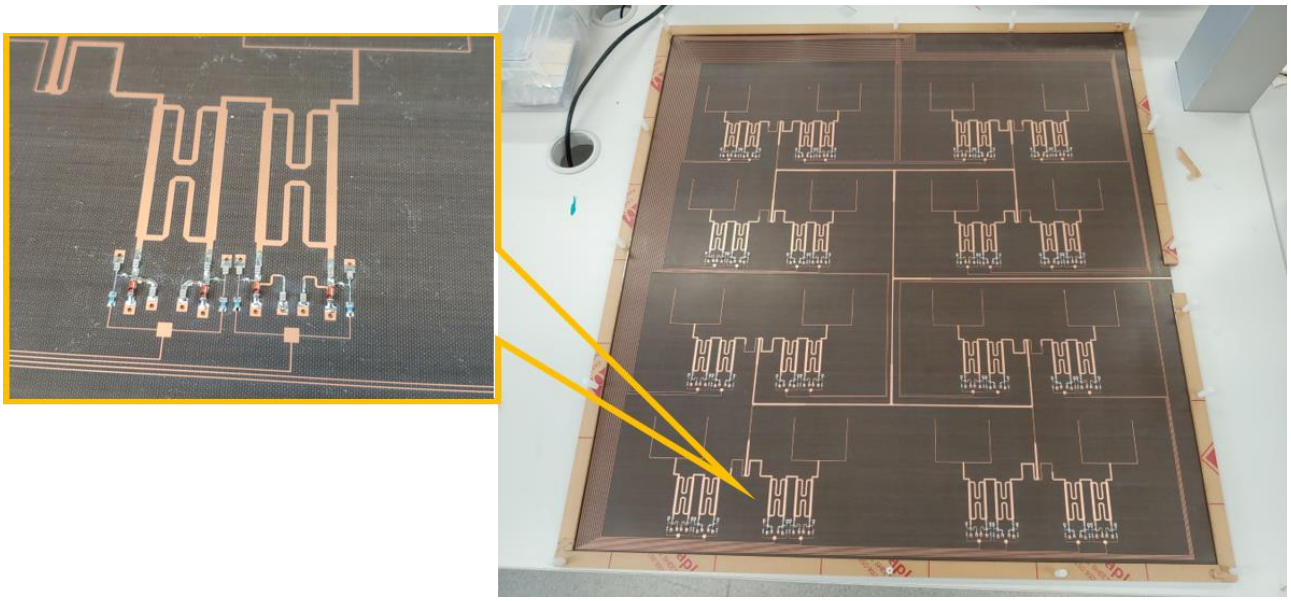

Figure 4. 54 Fabricated Feedline layer

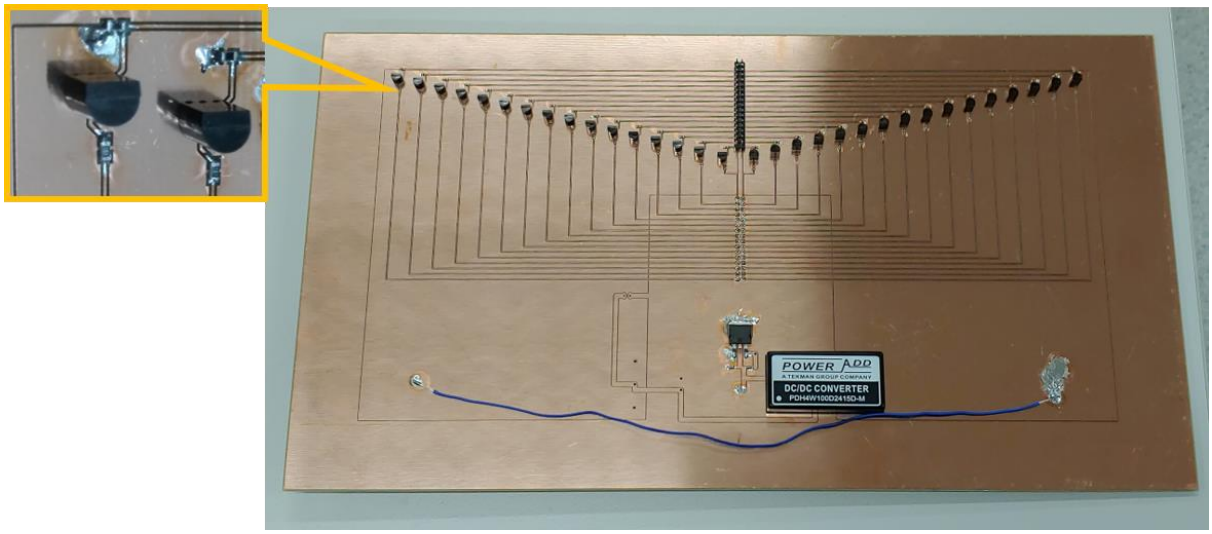

Figure 4. 55 Fabricated Driving Electronics Circuit

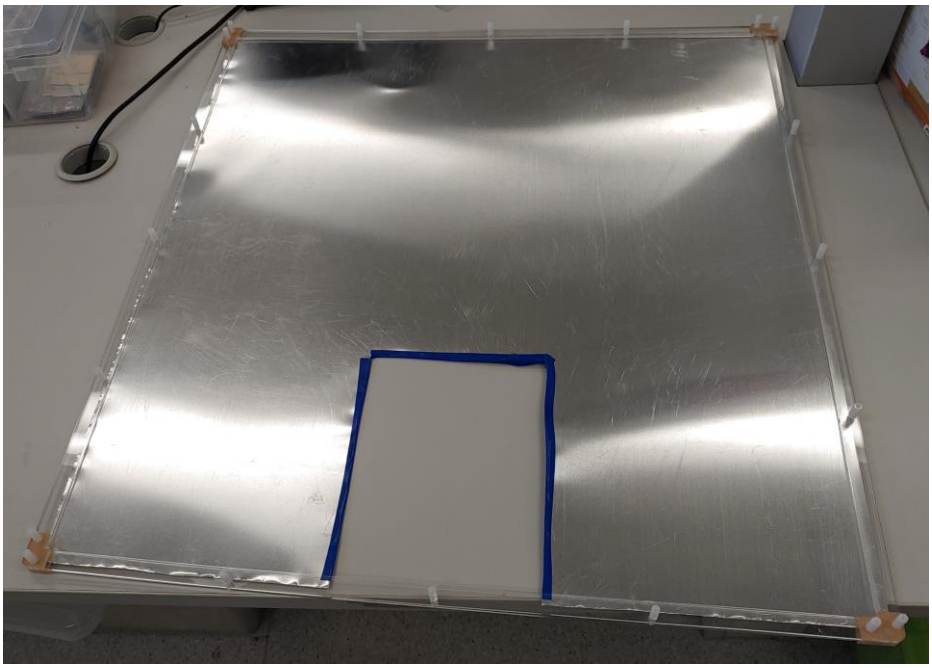

Figure 4. 56 Aluminium back reflector

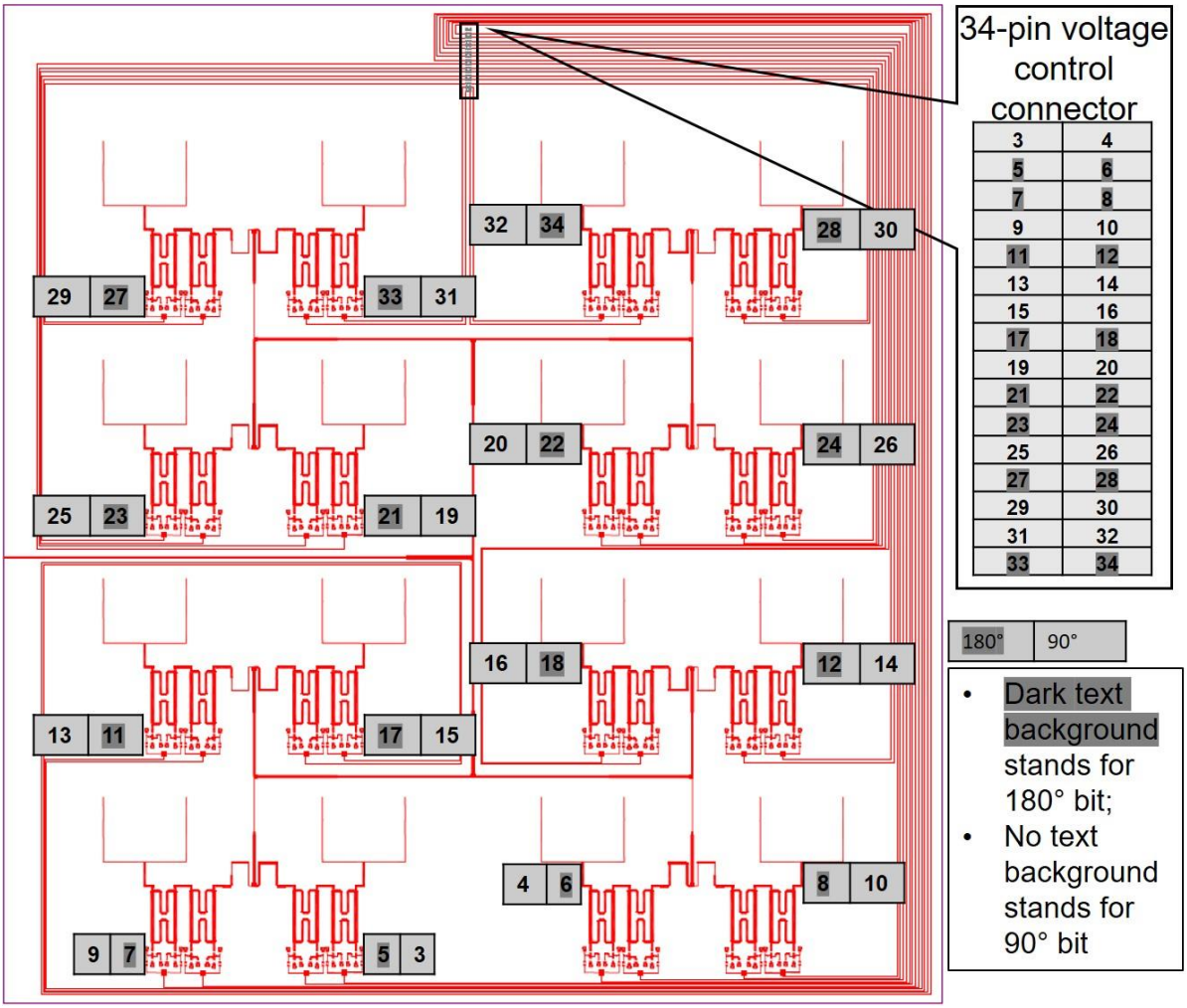

Figure 4. 57 Pin allocation for each phase shifter bit

4.5 Assembly and measurements (600)

4.5.1 Assembly and Measurements set up

To assemble the phase array, support structures were designed in multiple parts with two-directional lockers connecting each part as illustrated in Figure 4. 58, and fabricated in 3mm acrylic with the help from Monash ECSE CAD CAM centre. The spacing of each antenna substrate was supported by nylon spacers on each mounting hole. Figure 4. 59 shows the assembled phased array.

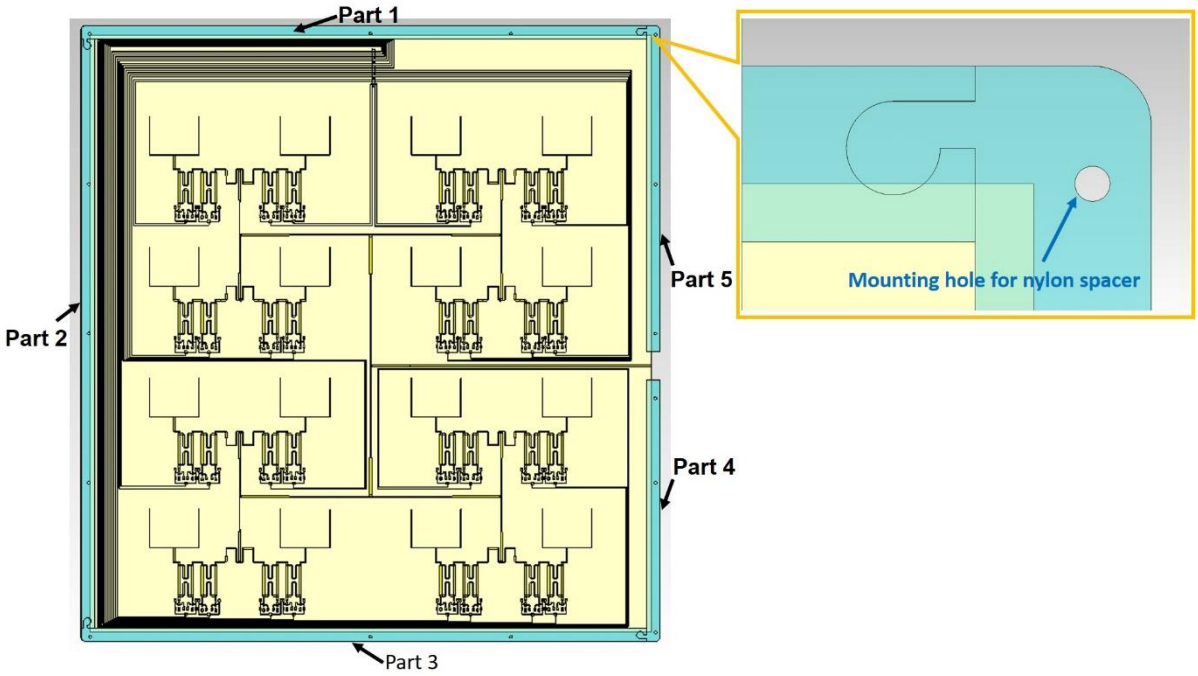

Figure 4. 58 Assembly support structure design

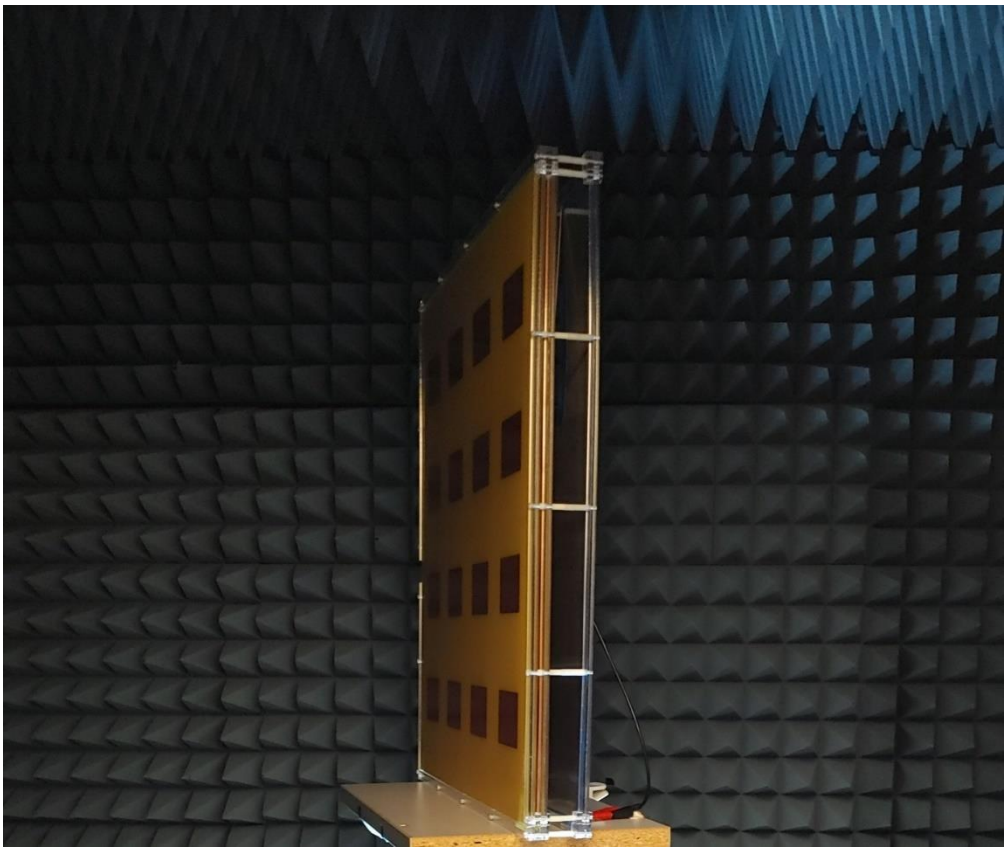

Figure 4. 59 Assembled L- band phased array

The radiation pattern measurements of the antenna were conducted in an anechoic chamber with RF absorber to suppress signal reflection. Figure 4. 60 shows the measurement set up. In these

tests, a broadband horn antenna LB-8180 with around 8 dBi gain at 1.4 GHz was used as the transmitting antenna connected with a Rodhe & Schwarz SM300 Signal Generator. The assembled L- band phased array was set on a test platform for rotation, and it was connected to a Rodhe & Schwarz FSV40-N signal analyser. The distance between these two antennas was 5.10 meters which is larger than the far-field distance of both antennas. To closely monitor the current consumption for connections checking, a DC supply machine was used to power up the phased array.

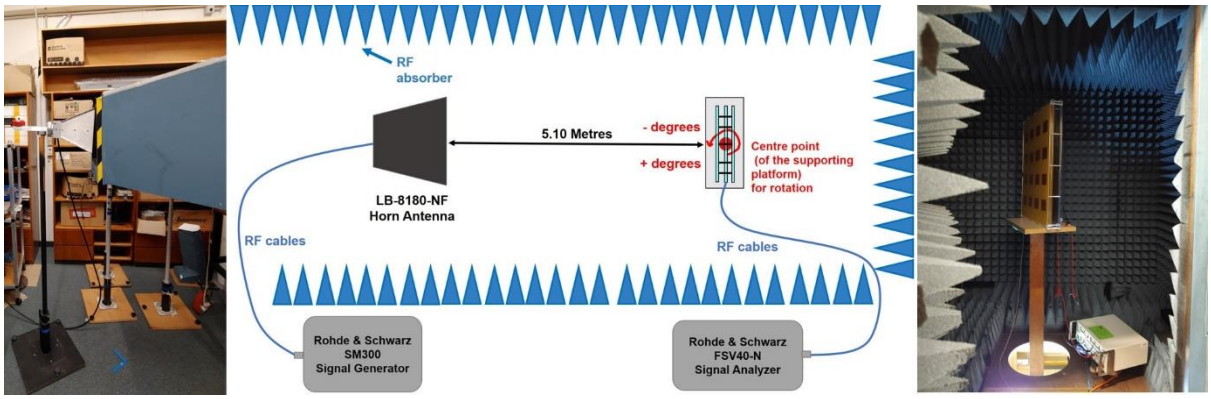

Figure 4. 60 Phased array measurement set up

4.5.2 Measurement results at 1.4 GHz

The impedance matching of each beam was measured using miniVNA Tiny during the early stage of the assembly and measurements, the results are summarised in Figure 4. 61. Overall, the assembled antenna exhibited acceptable matching with reflection coefficient better than -12 dB with the radiometric bandwidth of 1.4-1.425 GHz.

The measured radiation patterns results are plotted in Figure 4. 62 and Figure 4. 63 for antenna beam along X- and Y- axis respectively, simulation results are included in dotted lines for comparisons. In terms of the overall patterns and pointing angles, the measurement results are rather consistent with those from simulations. The side lobe suppression of all the measurements results are not as good as the simulations predicted. In spite of this, the highest sidelobe level for the boresight beam is -18.7 dB, while the other side lobes are below -20 dB hence overall exhibits overall acceptable beam shaping. As for the scanning beams, the highest sidelobe level is found to be -8.5 dB in the Y+20° beam (as illustrated in blue solid line in Figure 4. 63), and all other

scanning beam has satisfactory side lobe level under -10 dB. By considering RF cables loss to be -2dB, the measured peak gain of the boresight beam is 17.92 dBi; the peak gain for X-20° and X+20° is 18.23 dBi and 17.89 dBi respectively. For the Y- axis beams, the measured peak gain is 17.14 dBi for the Y-20° beam, and 17.23 dBi for the Y+20 beam. The measured antenna gains are in close agreements with the simulation calculation.

The differences between simulation and measurement results could be caused by the following factors: (1) Fabrication tolerance and soldering imperfections over hundreds of soldering points in the feedline layer and driving electronics; (2) limited accuracy of the simulation, especially due to the absence of phase shifter geometries which could cause spurious radiation in the hybrid coupler, input and output microstrip lines. Overall, the measurement results are considered to be satisfactory.

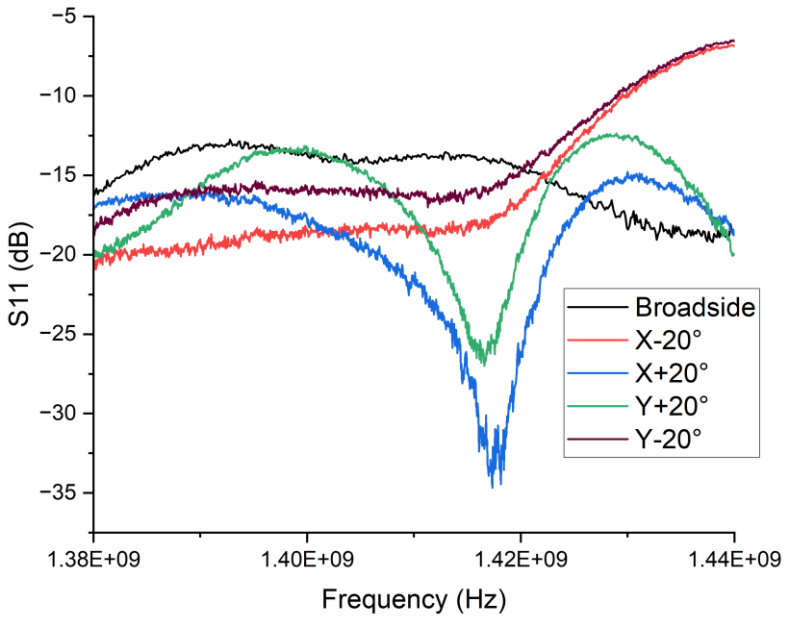

Figure 4. 61 |S11| of each beam during early stage measurements

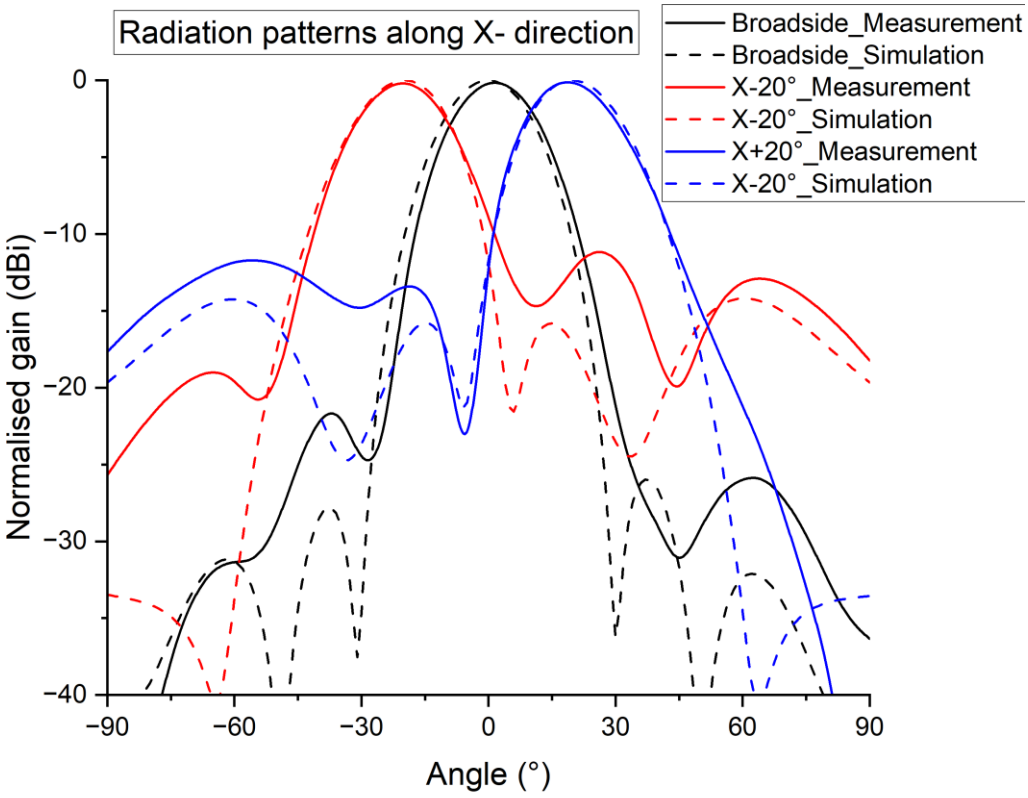

Figure 4. 62 Radiation patterns measurement results along X- axis in comparison with simulation results

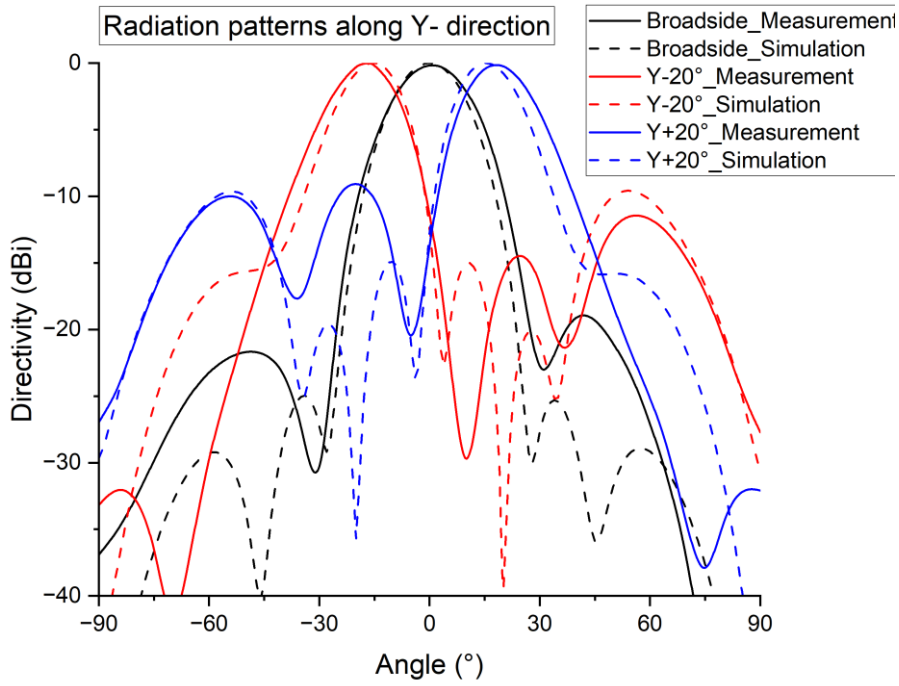

Figure 4. 63 Radiation patterns measurement results along Y- axis in comparison with simulation results

4.6 Chapter summary

This chapter presents the design of a low-cost L- band 4x4 phased array, covering the details of beam scanning plan which leads to an optimum choice of using 2-bit phase shifters to scanning beams of [X-20°, 0°, X+20°]; power divider design to suppress amplitude errors caused by pairing different phase shifter states and final integration for phased array simulation. In the next part of the chapter, design details for driving electronics from single switch model to breadboard prototypes then PCB design and fabrication are discussed. At last, the design of supporting structures to assemble the phased array, measurement setup, as well as sufficient impedance matching results and radiation pattern measurement results are presented.

As compared to the state of art PLMR radiometer which has the capability to scan 6 beams [±7°, ±21.5°, ±38.5°] in one dimension by adopting Butler Matrix Beamforming network [20, 83], this design is capable of two dimensional scanning in X- and Y- direction, but with a smaller scanning angle up to 20° in each direction, leading to 9 beams in total (referring to 4.3.4 Results analysis and summary

Table 4. 21 and Table 4. 22). By integrating 2-bit phase shifters into the feed network, the design is more compact as compared to using Butler Matrix which would require either switch or multiple receivers (with benefit of push broom capability) for beam scanning. As compared to designing the whole array in Taconic TLX-8 material, using FR-4 as the substrate material for the radiating patch layer also reduces the fabrication cost for about $900 AUD per 600mm x 600mm board. The design principles of beam scanning plan and phase shifters integration presented in this chapter also provides strong foundation for more intricated simulation designs of the Ku- and L-/ Ku- band shared aperture phased array in Chapter 5.

Chapter 5

5.1 Introduction

This chapter presents the simulation designs of a more intricate planar Ku- band phased array, as well as the design for an unprecedented L-/ Ku- band shared aperture phased array, which was the ultimate goal of this research. The chapter starts with feed network design of a 6x6 fixed beam Ku-band array using unequal three-way power dividers with irregular shapes. For the first stage shared aperture design focusing on fixed beam array, an L- band 4x4 fixed-beam array has also been re-designed solely in Taconic TLX-8 substrates to integrate with the 6x6 Ku- band array, this is to initially evaluate coupling and pattern distortion in the shared aperture configuration. The next part of the chapter focuses on the design of a Ku- band phased array. Two types of three-way power dividers have been designed from the fixed beam network to fit into the very congested area where phase shifters occupy most of the space, making the unequal power dividers very challenging to design. One notable coupling issue causing the asymmetry power division in vertical direction has also been investigated. Optimisation on phase allocation to minimise antenna loss has also been conducted.

After obtaining sufficient simulation results from the Ku- band phased array, the final part of the chapter discusses the integration of the 6x6 array with a re-designed 4x4 array to form an L-/Ku-band shared aperture phased array. The simulations were divided into two parts: L- band simulations and Ku- band simulations. Overall, simulation results have been obtained from both bands as a proof of concept to conclude this study.

5.2 Fixed beam arrays design

5.2.1 Single element patch antenna modification

Following the design procedures discussed in Chapter 3, a Ku- band single-polarisation, single element aperture coupled patch antenna has been designed by modifying Dr. Muhsiul Hassan's dual polarised antenna design [26]. Figure 5. 1 shows the farfield pattern at 18.7 GHz. Since both the radiating patch layer and the feedline layer are in low loss Taconic TLX-8 substrate, this antenna exhibits good radiation efficiency of -0.1093 dB. Its reflection coefficient |S11| is better than -17.5 dB within the Ku- band radiometric bandwidth of 18.6-18.8 GHz as shown in Figure 5. 2. The 3dB beamwidth is 68° and 60.1° at Phi=0 and Phi=90 cut plane, and plotted in Figure 5. 3 and Figure 5. 4 respectively with back lobe at -26dB level, being similar to the L- band single element discussed in Chapter 3.

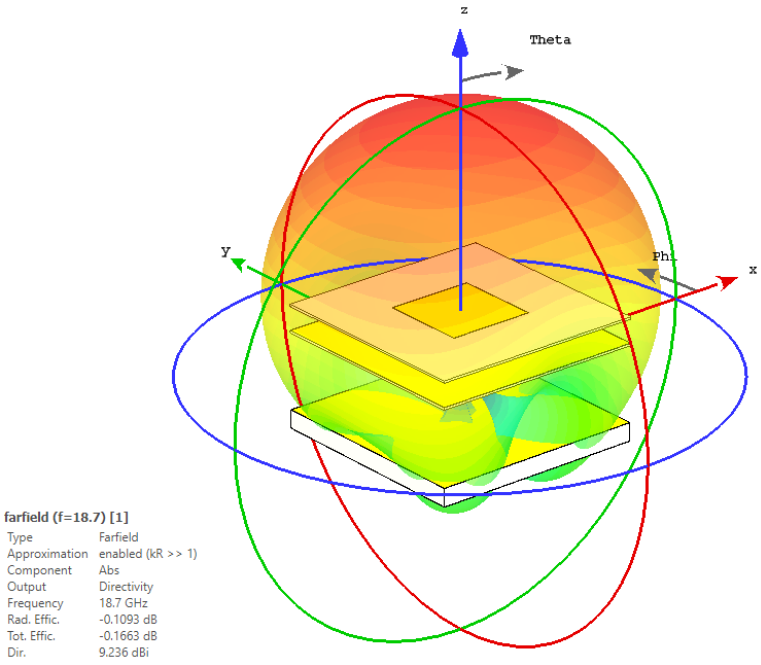

Figure 5. 1 Three-dimensional farfield pattern of the Ku- band single polarised antenna design

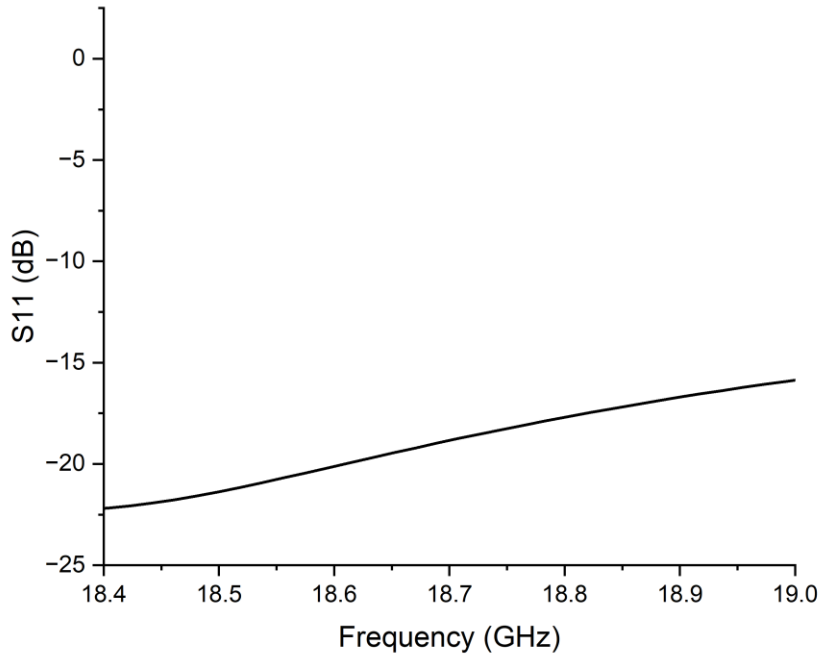

Figure 5. 2 Impedance matching of the Ku- band single element antenna

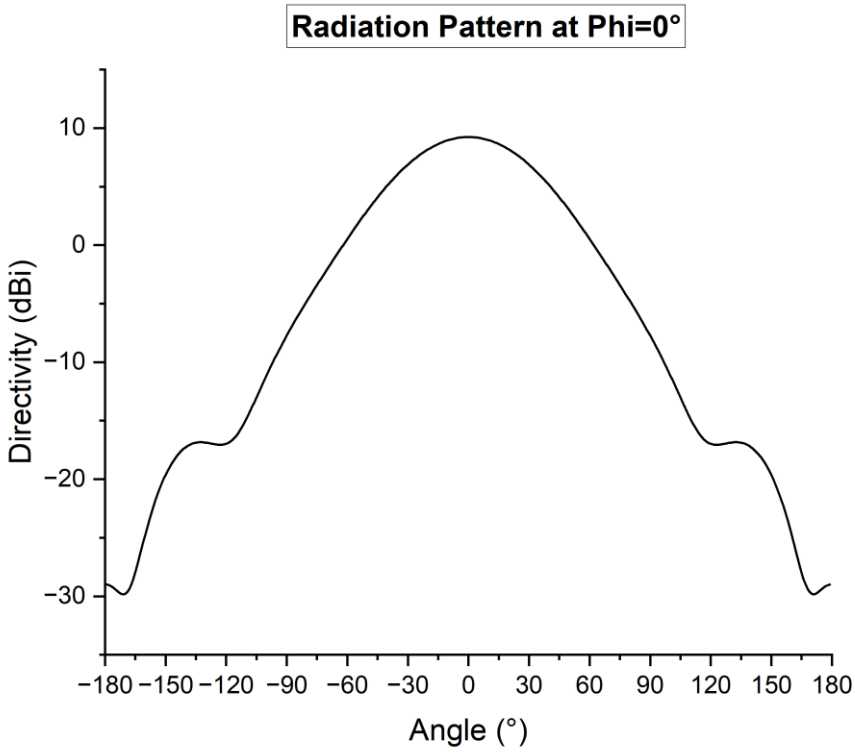

Figure 5. 3 Radiation pattern of the Ku- band single element at Phi=0° cut plane

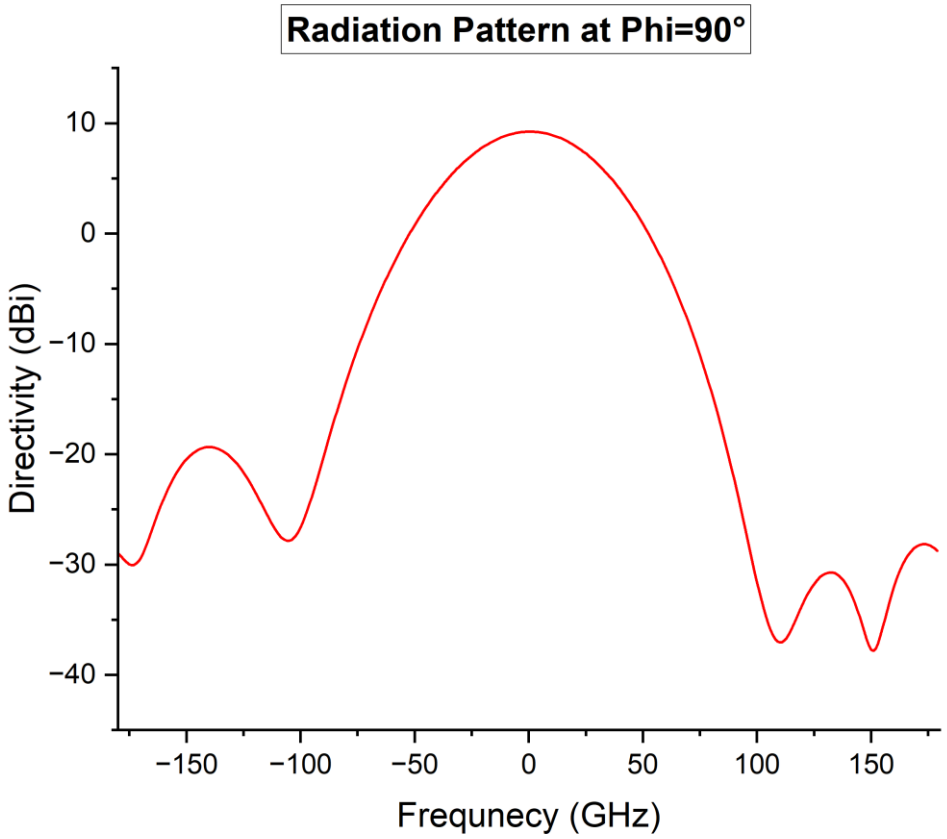

Figure 5. 4 Radiation pattern of the Ku- band single element at Phi=90° cut plane

5.2.2 Array consideration

For the design of the Ku- band array, three factors have been be considered:

(1) Interelement distance

The inter-element distance of the Ku- band array is set to be 12mm, which corresponds to 0.75 λ at 18.7 GHz. This distance is in consideration of the minimum size requirement of 12.7mm x 5.5 mm for the 2-bit phase shifter developed by Dr. Kim Tuyen Trinh [27]. This in turn leads to the edge-edge distance of each square Ku- band patch to be 6.8 mm in both X- and Y- direction. The inter element distance between the L- band patch is 144.65 mm, resulting in edge-edge distance of 58.85 mm in the X- direction and 78.65 mm in the Y-direction. As illustrated in Figure 5. 5, it can be observed that the edge-edge distance in Y- distance is the major limiting factor for the Ku- band array, as any expansion beyond 6 Ku-elements in the Y- direction would require perforations in the L- band patches.

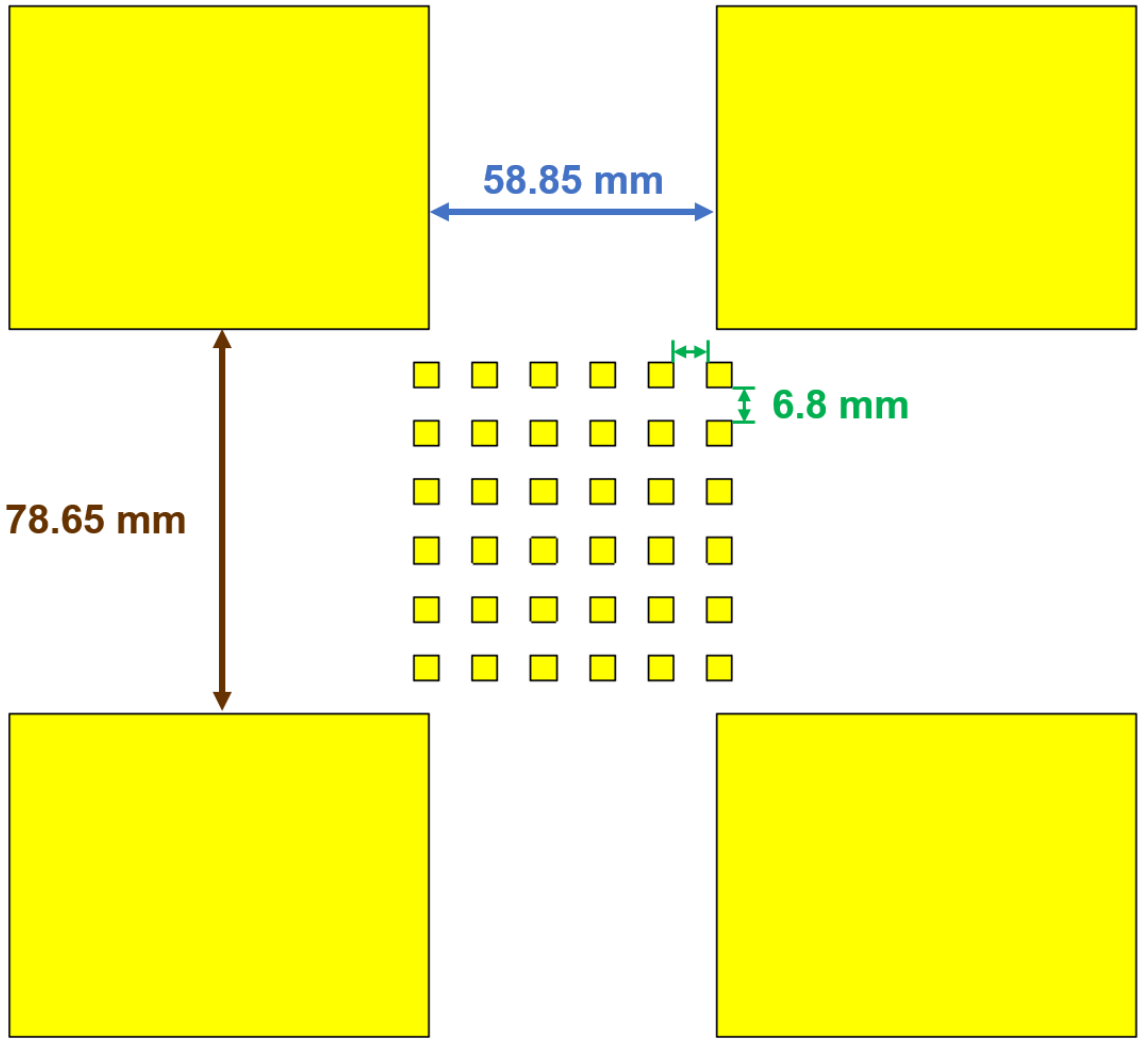

Figure 5. 5 Illustration of Ku- band array size, and the edge-edge distances of the L- band and Ku- band patch

The other factor to be considered is the Ku- band footprint size. By synthesising a 6x6 -20dB Ku-band array following Table 5. 1, Figure 5. 6 and Figure 5. 7 shows the antenna beam width comparison between the 6x6 Ku- band and 4x4 L- band array. It can be observed that the Ku-band array has a half power beamwidth of approximately 13°, which is 62% of the L- band array beamwidth at 21°. The Ku-band array is hence able to generate approximately twice the resolution of the L- band in the same aperture, which is sufficient for the first stage demonstration.

Table 5. 1 Excitation coefficients for 6x6 -20 dB Dolph-Tschebysheff array

0.2922	0.4199	0.5406	0.5406	0.4199	0.2922
0.4199	0.6034	0.7768	0.7768	0.6034	0.4199
0.5406	0.7768	1	1	0.7768	0.5406
0.5406	0.7768	1	1	0.7768	0.5406
0.4199	0.6034	0.7768	0.7768	0.6034	0.4199
0.2922	0.4199	0.5406	0.5406	0.4199	0.2922

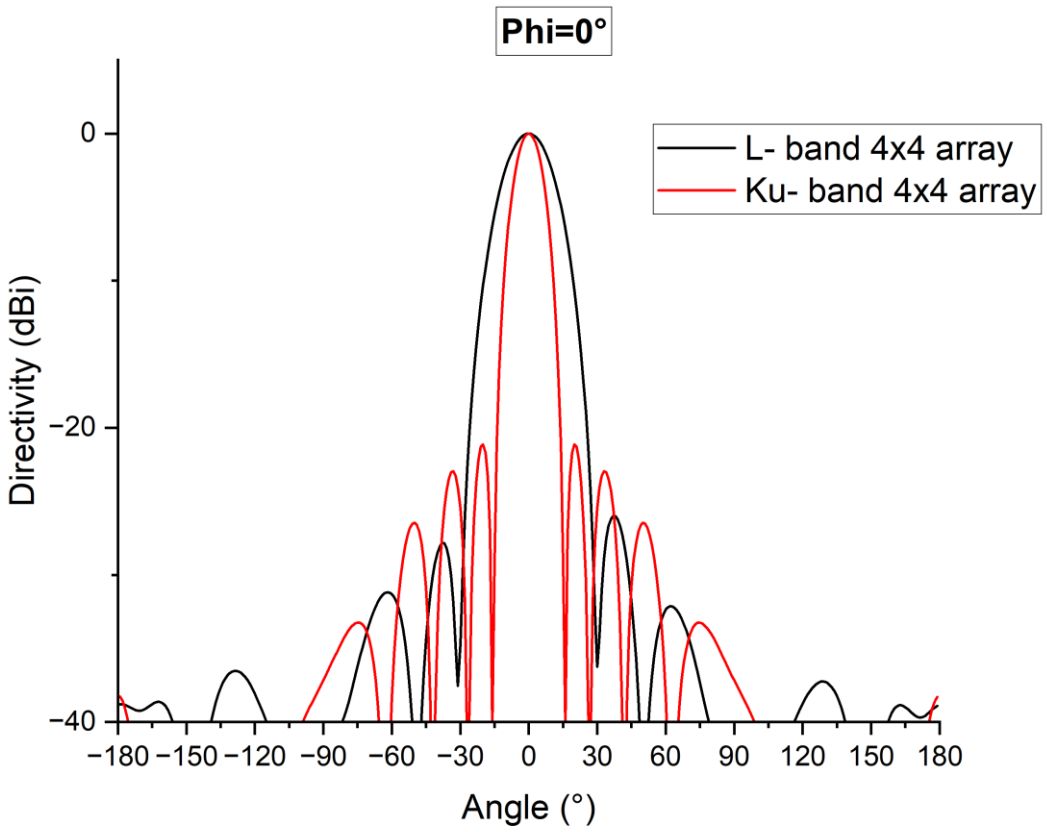

Figure 5. 6 Normalised radiation pattern of the L- band 4x4 phased array and synthesised 6x6 array at Phi=0° cut plane

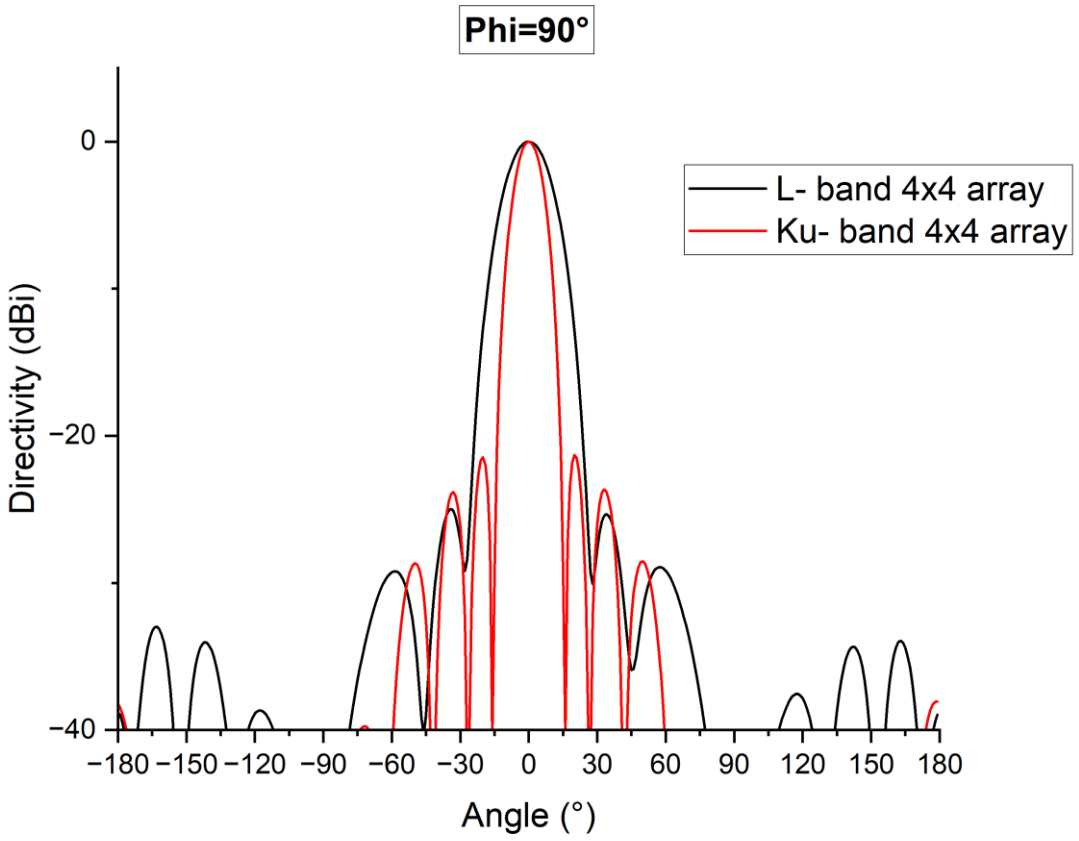

Figure 5. 7 Normalised radiation pattern of the L- band 4x4 phased array and synthesised 6x6 array at Phi=90° cut plane

Overall, considering a 6x6 array has adequately high resolution, the further design complexity of perforation of the L-band patches can be avoided. It is the optimum size for the Ku- band array to share radiation aperture with the 4x4 L- band array.

5.2.3 Power dividers design for the tapered 6x6 Ku- band array

5.2.3.1 Feed network configuration

For the feed network of the 6x6 array, horizontal and vertical 3-way power dividers (as illustrated in Figure 5. 8) are chosen over 2-way power dividers (in both Figure 5. 9 and Figure 5. 10). This is because 3-way power dividers only require 3 levels of power dividers while the other two cases require 4 levels as illustrated in different colours in the corresponding figures. This results in minimum space required and total transmission line length, thereby reducing feedline loss.

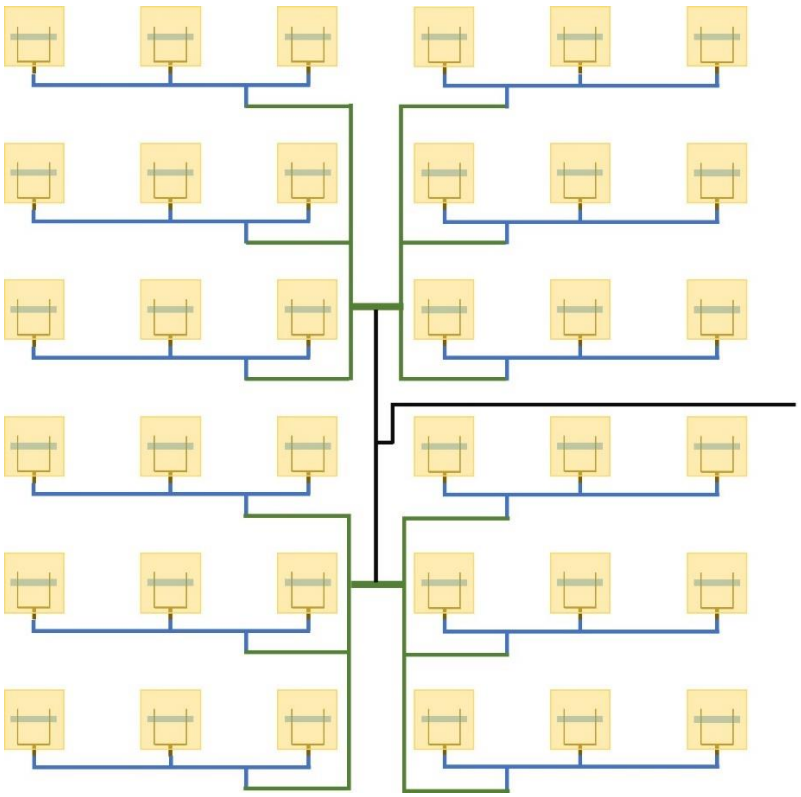

Figure 5. 8 6x6 Feed network case 1 using irregular 3-way power dividers

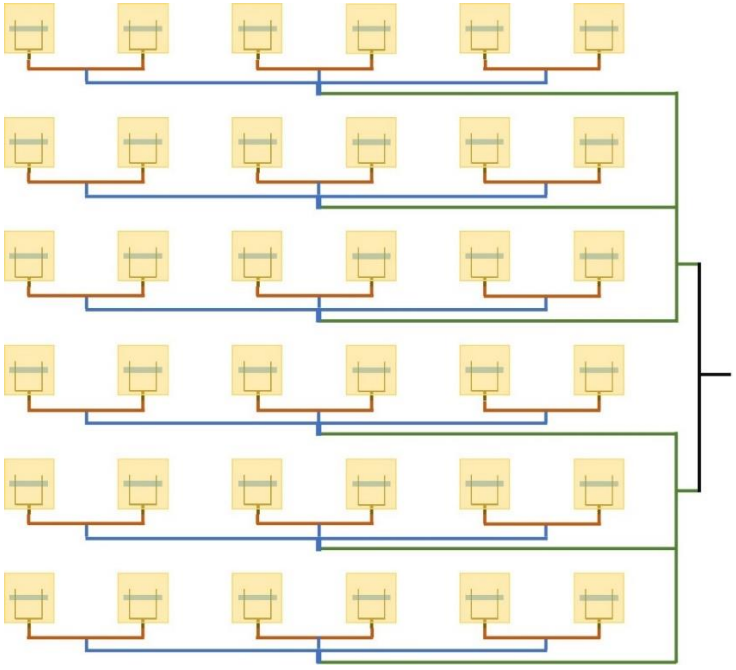

Figure 5. 9 6x6 Feed network case 2 using two-way power dividers at the antenna feed end

Figure 5. 10 6x6 Feed network case 3 using three-way power dividers at the antenna feed end

5.2.3.2 Horizontal power divider

The implementation of the irregular horizontal three-way power divider is depicted in Figure 5. 11. The design of this power divider is derived from the conventional three-way power divider with the input branch offset from the centre toward the higher power branch, this is to help achieve the required split ratio without needing an excessively thin feedline width. For the target [0.54:0.78:1] voltage division ratio, using the conventional three-way power divider will required microstrip line width under 0.1 mm (for characteristic impedance over 90 Ω) hence notably higher fabrication cost. Although this design is able to reduce the power level at the lower end, the position of the input branch must be carefully tuned for phase balancing.

As shown in Figure 5. 12, the power divider has moderate impedance matching with |S11| better than -13.5 dB within the radiometric bandwidth of 18.6-18.8 GHz. As per Figure 5. 13 and Figure 5.

14, this power divider exhibits a linear voltage ratio of [0.527 0.777 1] which is well within the required split ratio, while the maximum phase imbalance is 6.02°.

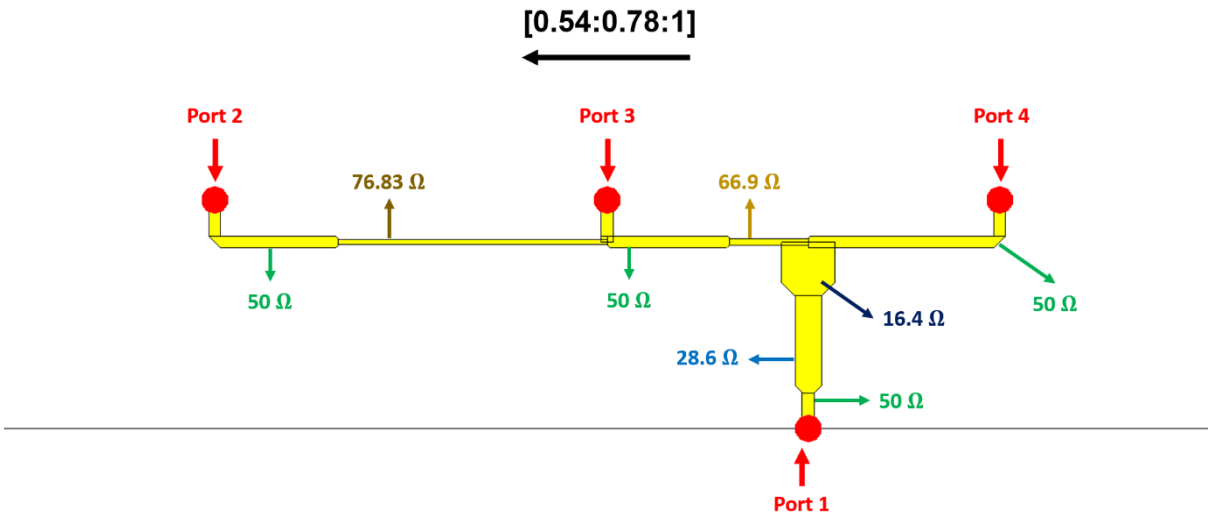

Figure 5. 11 Implementation of the Horizontal [0.54:0.78:1] three-way power divider

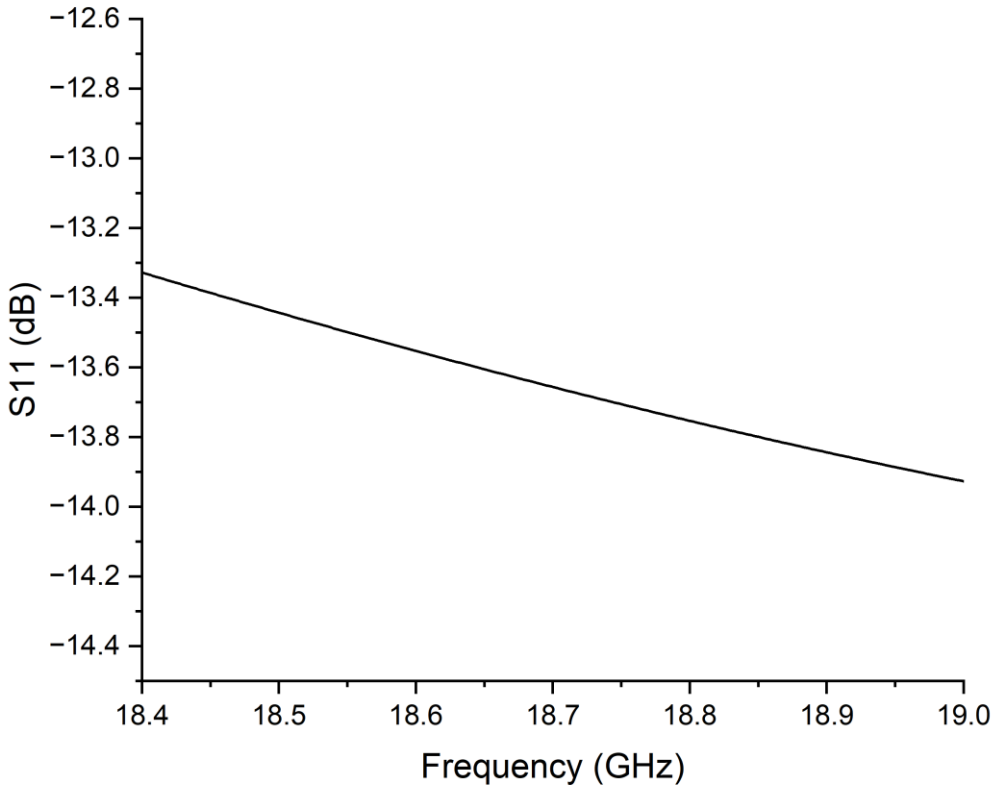

Figure 5. 12 Input impedance matching of the Horizontal [0.54:0.78:1] power divider

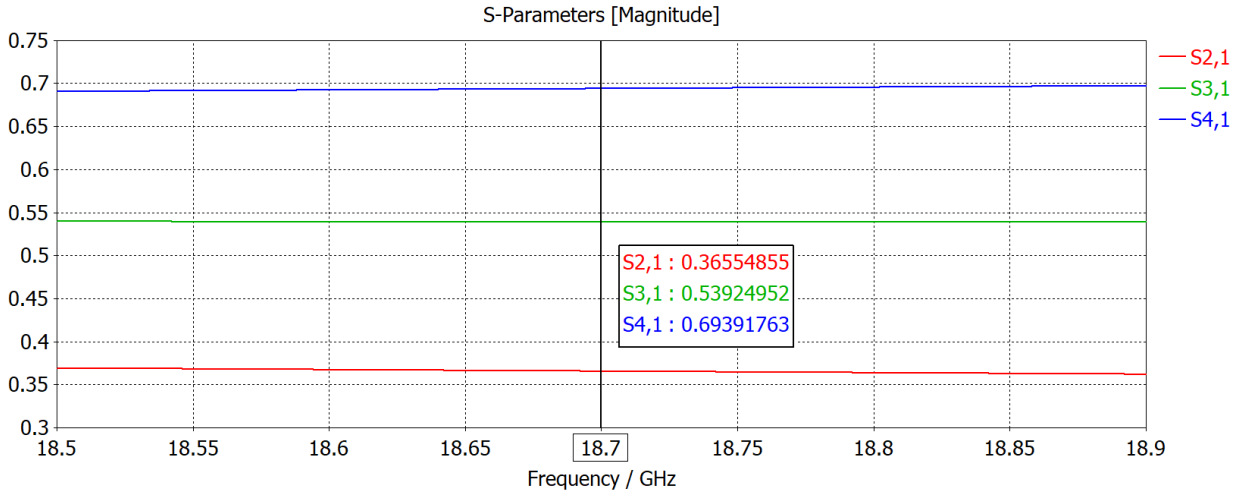

Figure 5. 13 Linear voltage division of the Horizontal [0.54:0.75:1] power divider

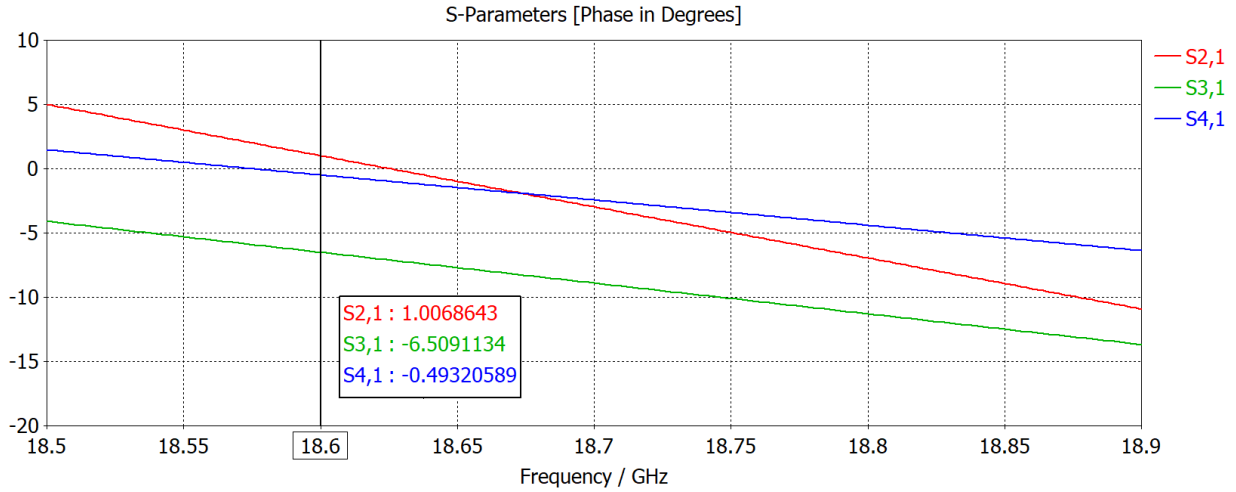

Figure 5. 14 Phase difference of the Horizontal [0.54:0.75:1] power divider

5.2.3.3 Vertical power divider

Likewise, the vertical [0.54:0.78:1] power divider has been developed as shown in Figure 5. 15, with |S11| better than -12.3 dB within the 200 MHz Ku- band radiometric bandwidth in Figure 5. 16. As per Figure 5. 17 and Figure 5. 18, the corresponding split ratio is [0.546 0.776 1] which is 0.06 over the requirement at port 4 but considered as acceptable, while the maximum phase imbalance is -8.83°.

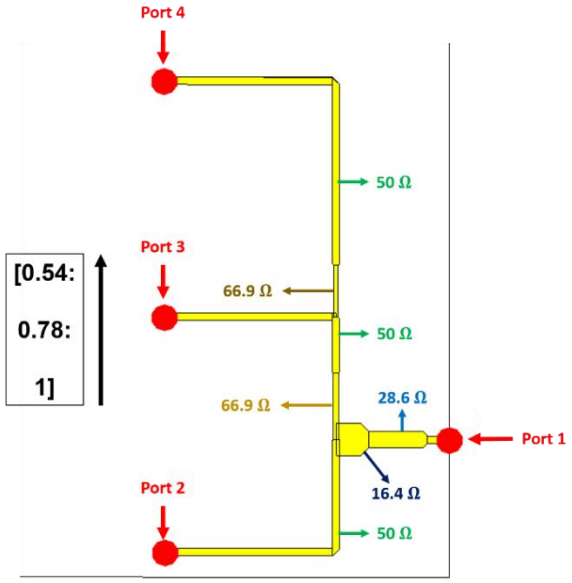

Figure 5. 15 Implementation of the Vertical [0.54:0.78:1] three-way power divider

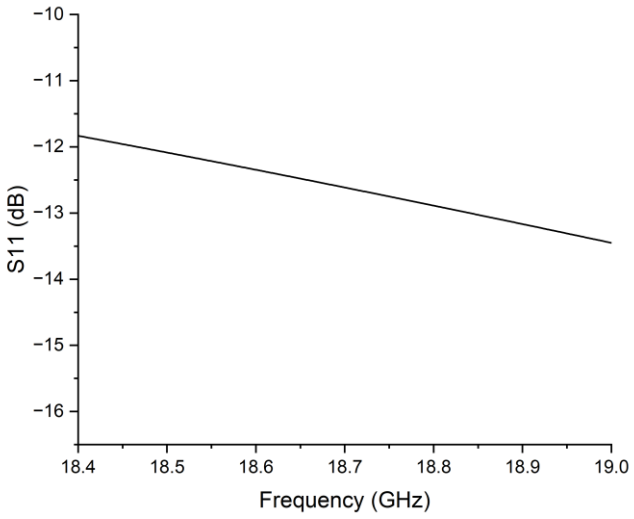

Figure 5. 16 Input impedance matching of the Vertical [0.54:0.78:1] power divider

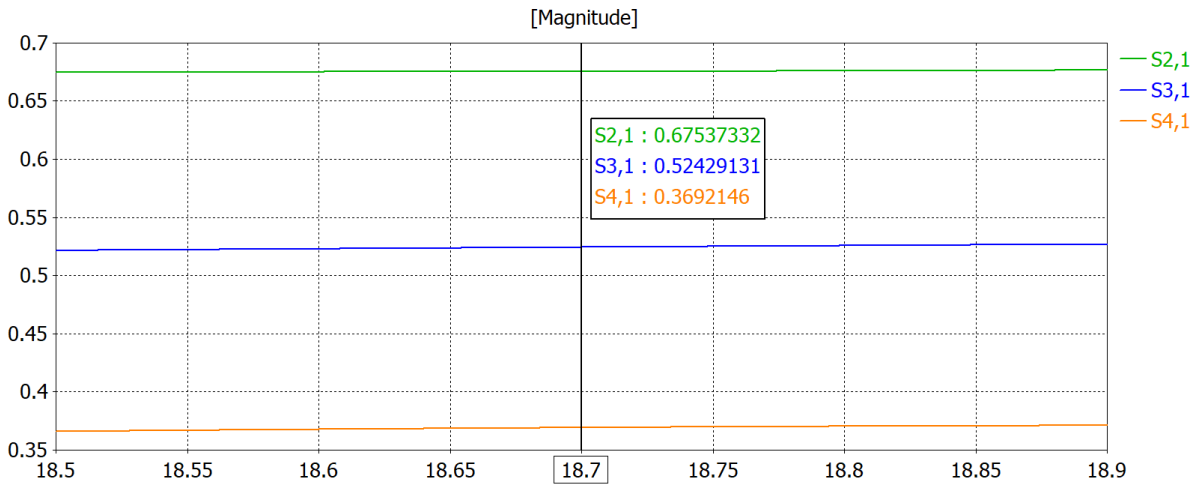

Figure 5. 17 Linear voltage division of the Vertical [0.54:0.75:1] power divider

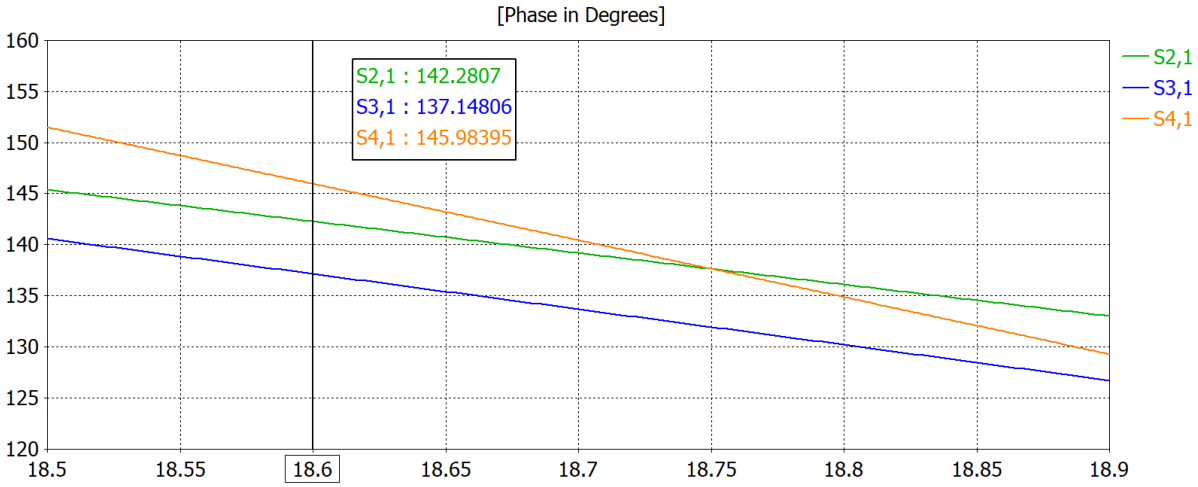

Figure 5. 18 Phase difference of the Vertical [0.54:0.75:1] power divider

5.2.3.4 3x3 unequal feed network and integration

The horizontal and vertical power dividers were then combined as depicted in Figure 5. 19. Overall, with slight tuning, the 3x3 unequal power divider exhibits |S11| better than -10.9 dB from 18.6 to 18.8 GHz as depicted in Figure 5. 20. The normalised voltage ratio (Figure 5. 21) and phase differences (Figure 5. 22) are summarised in Table 5. 2, with only Port 5 exceeding the amplitude split requirement by 0.0031, and the overall maximum phase imbalance is 14.32°

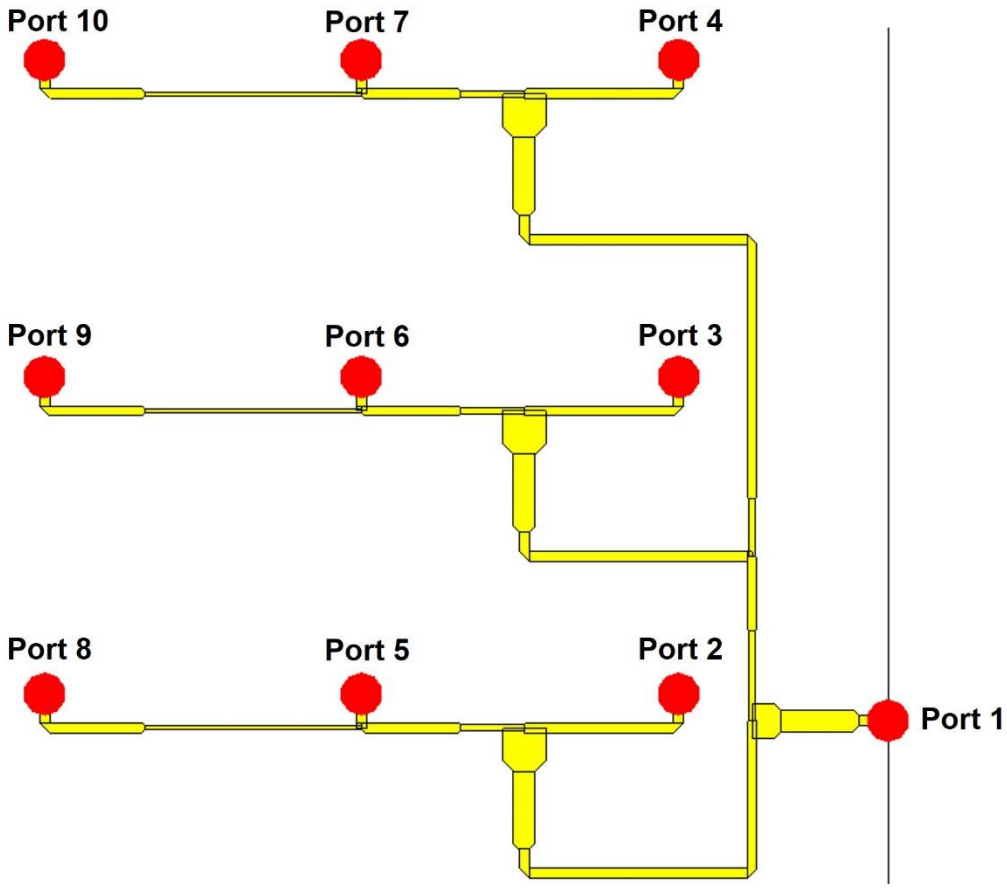

Figure 5. 19 Three-by-three unequal power divider

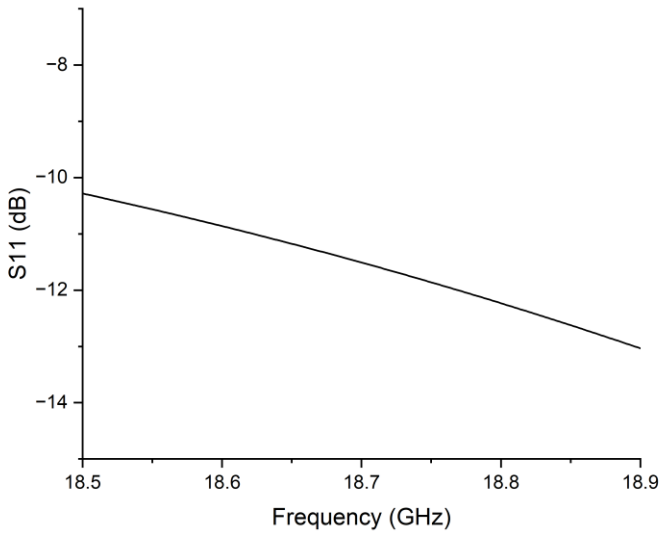

Figure 5. 20 Input impedance matching of the three-by-three unequal power divider

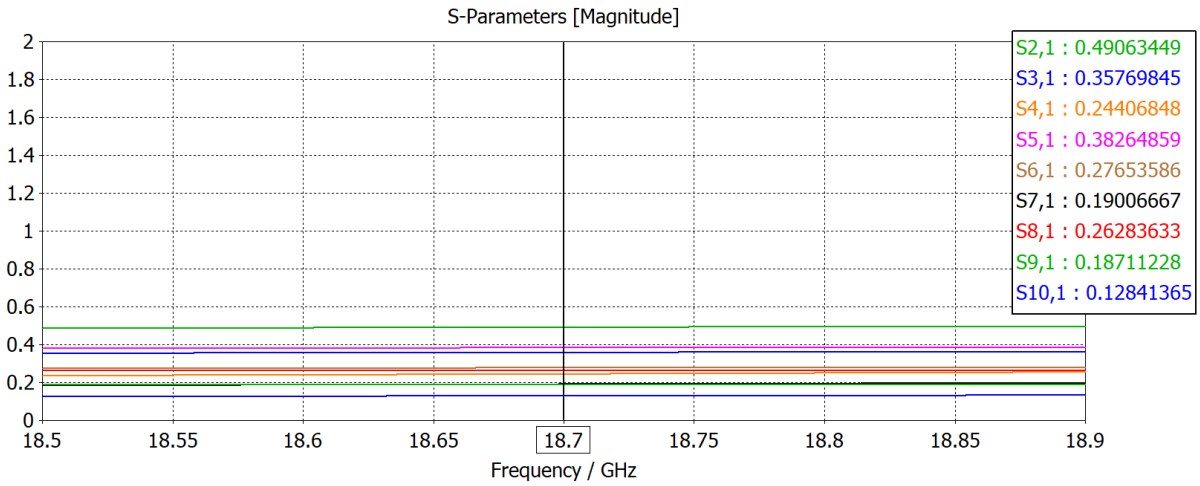

Figure 5. 21 Linear voltage ratio of the three-by-three unequal power divider

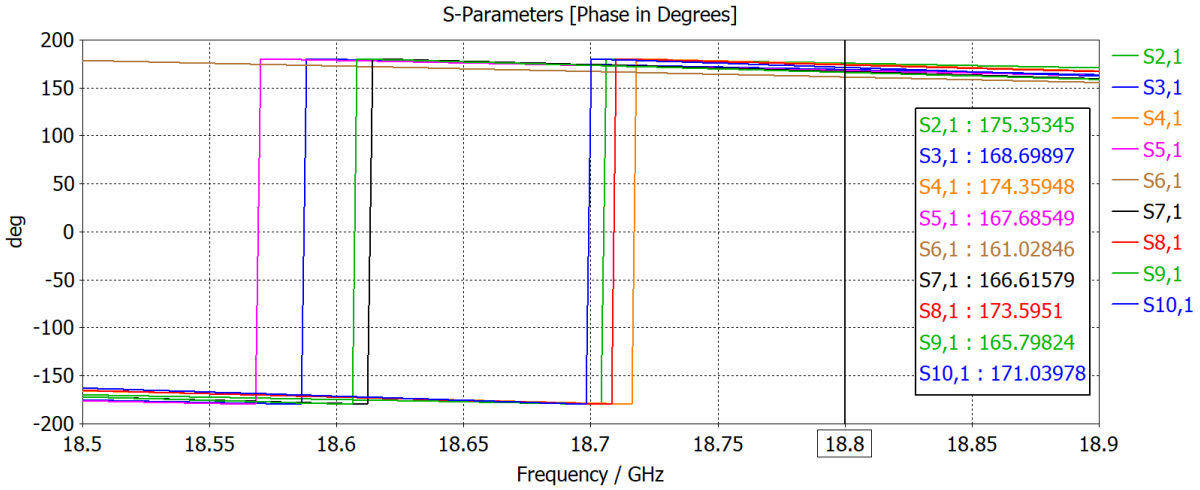

Figure 5. 22 Phase difference of the three-by-three unequal power divider

Table 5. 2 Summary of the three-by-three unequal power divider network

Port and the required voltage division	Normalised Voltage ratio	Maximum phase difference (°)
Port 2	1 (reference)	0 (reference)
Port 3 [0.7768:1]	0.7291	4.31
Port 4 [0.5406:1]	0.4976	9.55
Port 5 [0.7768:1]	0.7799	2.53
Port 6 [0.6034:1]	0.5636	8.73
Port 7 [0.4199:1]	0.3875	14.32
Port 8 [0.5406:1]	0.5357	7.66
Port 9 [0.4199:1]	0.3814	2.72
Port 10 [0.2922:1]	0.2617	6.65

The 3x3 unequal power divider was then integrated into the 6x6 feed network of the antenna array as illustrated in Figure 5. 23. This tapered 6x6 array exhibits |S11| better than -11.76 dB as shown in Figure 5. 24. From a closer analysis of the 3D radiation pattern in Figure 5. 25, the side lobe level is at -21dB as shown in the radiation patterns plots in Figure 5. 26 and Figure 5. 27. The asymmetric sidelobes in the Phi=90° cut plane (in Figure 5. 27) could be attributed to coupling effects between the input feedline and the upper half of the vertical power divider.

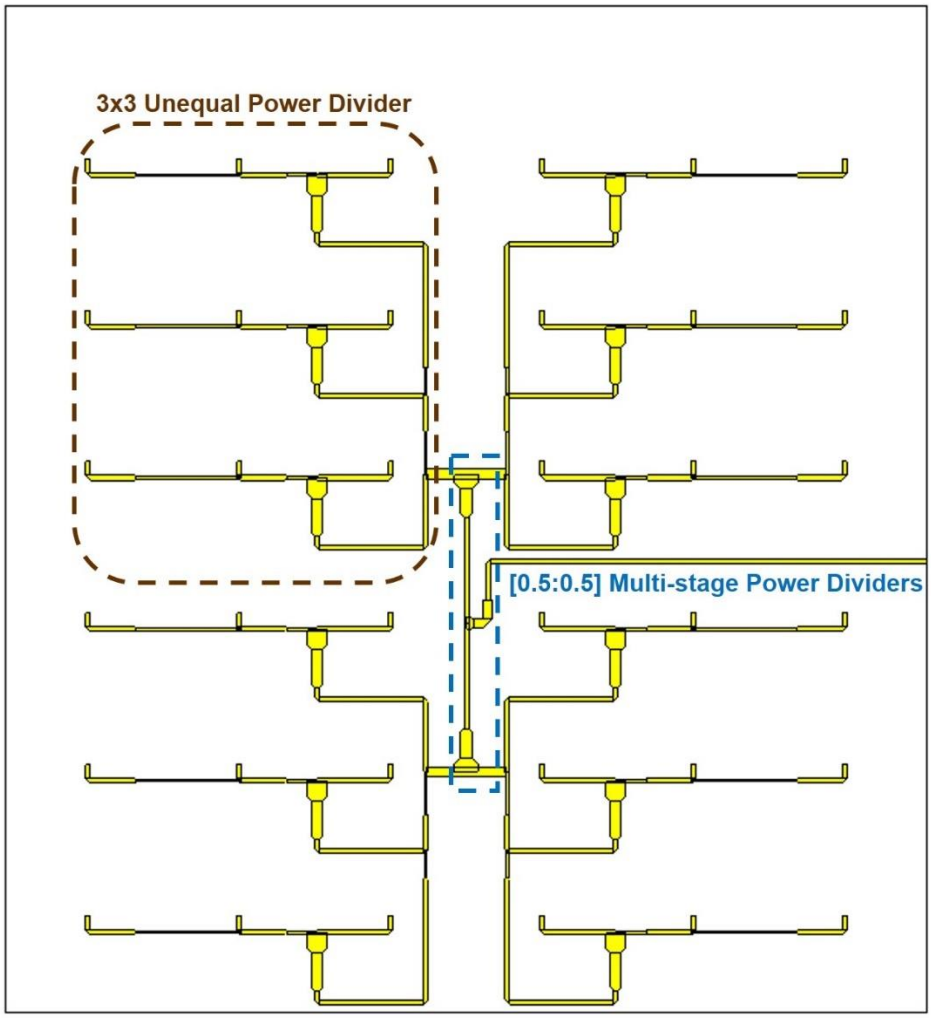

Figure 5. 23 Integrated 6x6 feed network

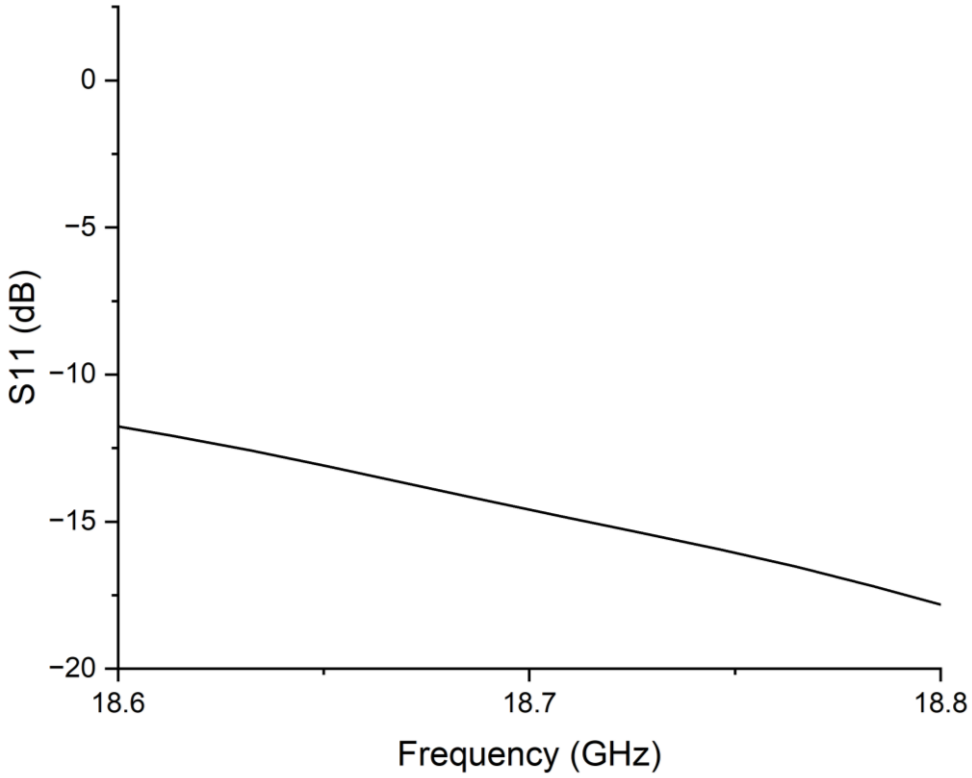

Figure 5. 24 Impedance matching of the tapered 6x6 array

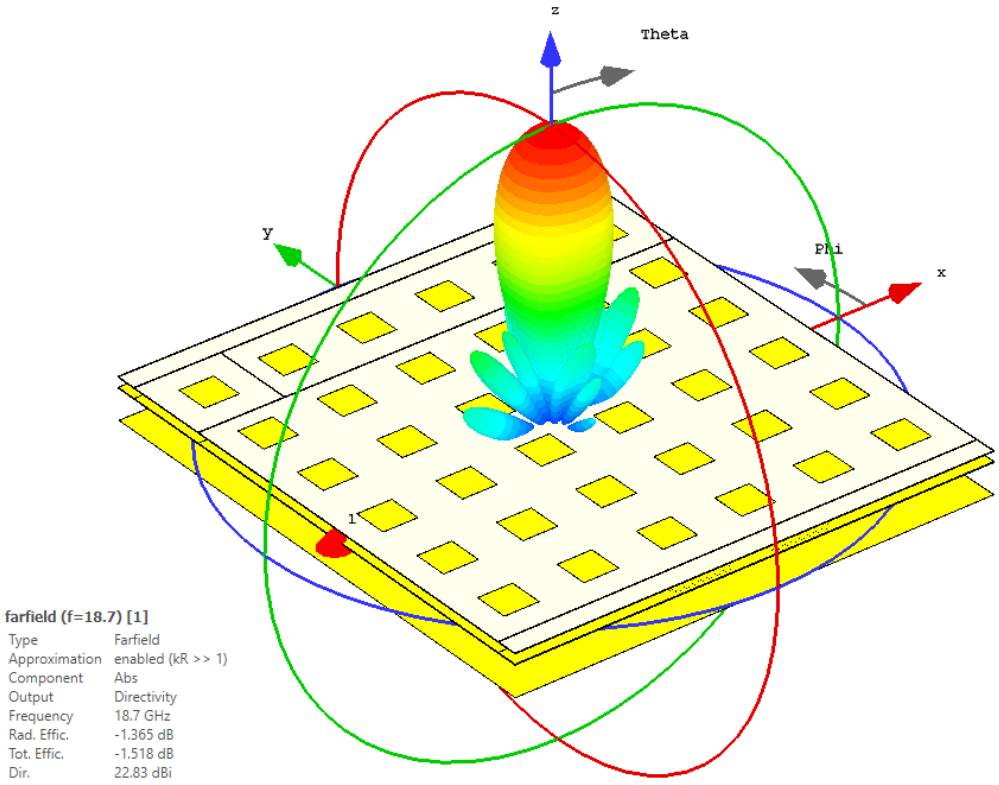

Figure 5. 25 Far-field result of the 6x6 fixed beam array with tapered excitation

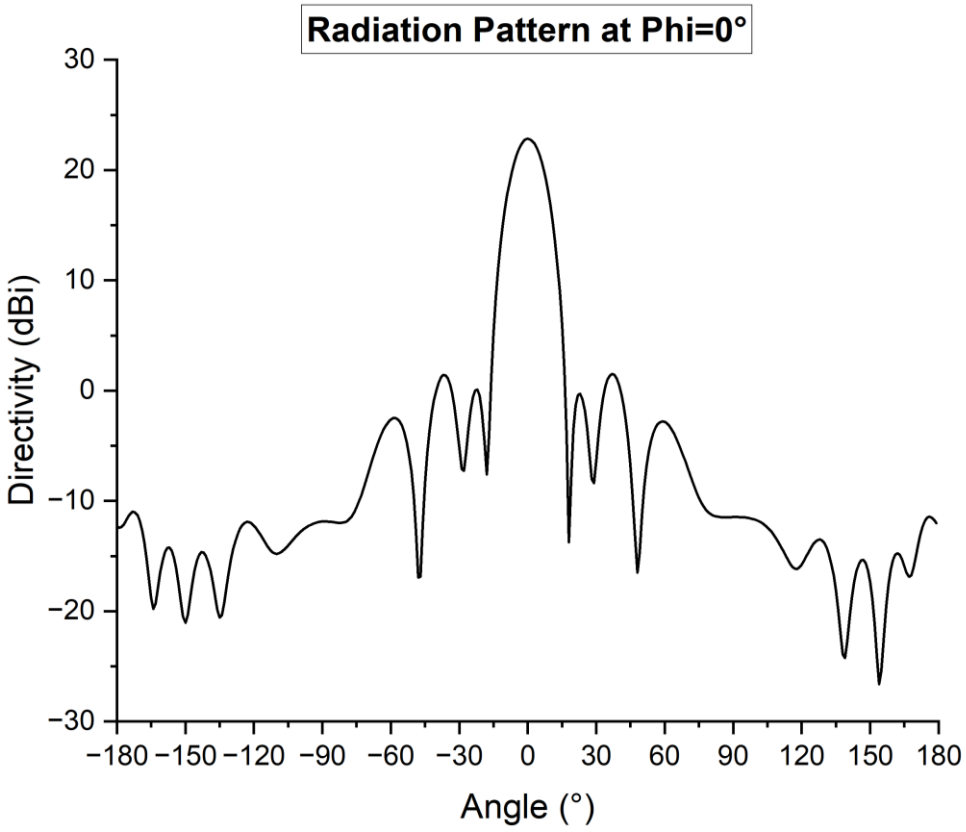

Figure 5. 26 Radiation pattern of tapered 6x6 array at Phi=0° cut plane

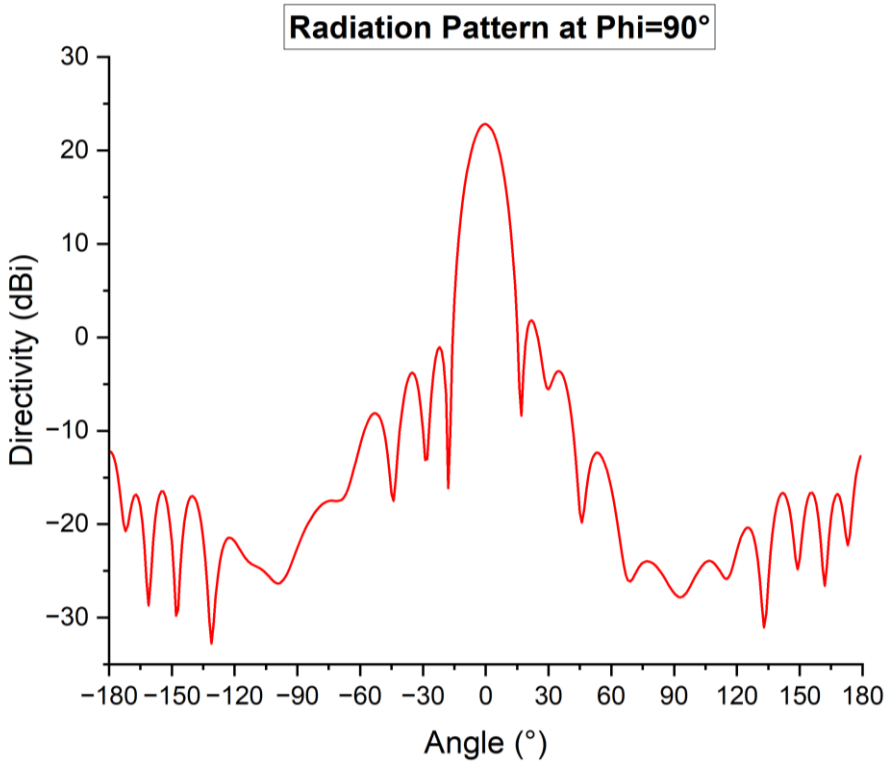

Figure 5. 27 Radiation pattern of tapered 6x6 array at Phi=90° cut plane

5.2.4 L-/Ku- band shared aperture fixed beam array

The layered drawing of the L-/Ku- band shared aperture fixed beam array is illustrated in Figure 5. 28. In this design, the tapered 4x4 L- band fixed beam array discussed in Chapter 3 has been redesigned on a Taconic TLX-8 substrate. For the integration with the Ku- band array, the Ku- patch are place in the middle of the 4x4 L- band patches as depicted in Figure 5. 29, while the Ku- band feedline layer is positioned in between the radiation patch and L- band feedline layer, so that the ground plane of the L- band array also acts as the metal back reflector of the Ku- band array. The other advantage of using separate feedline layers is to avoid excessively large feed line substrate for the Ku- band array which could cause significant radiation pattern distortion due to surface wave effects [157].

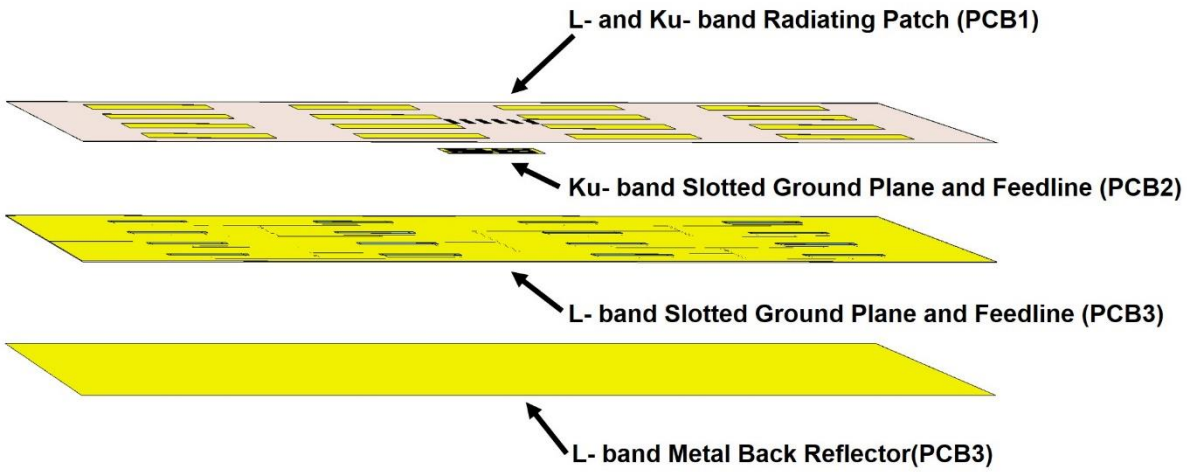

Figure 5. 28 Layered drawing of the L-/Ku- band shared aperture fixed beam array

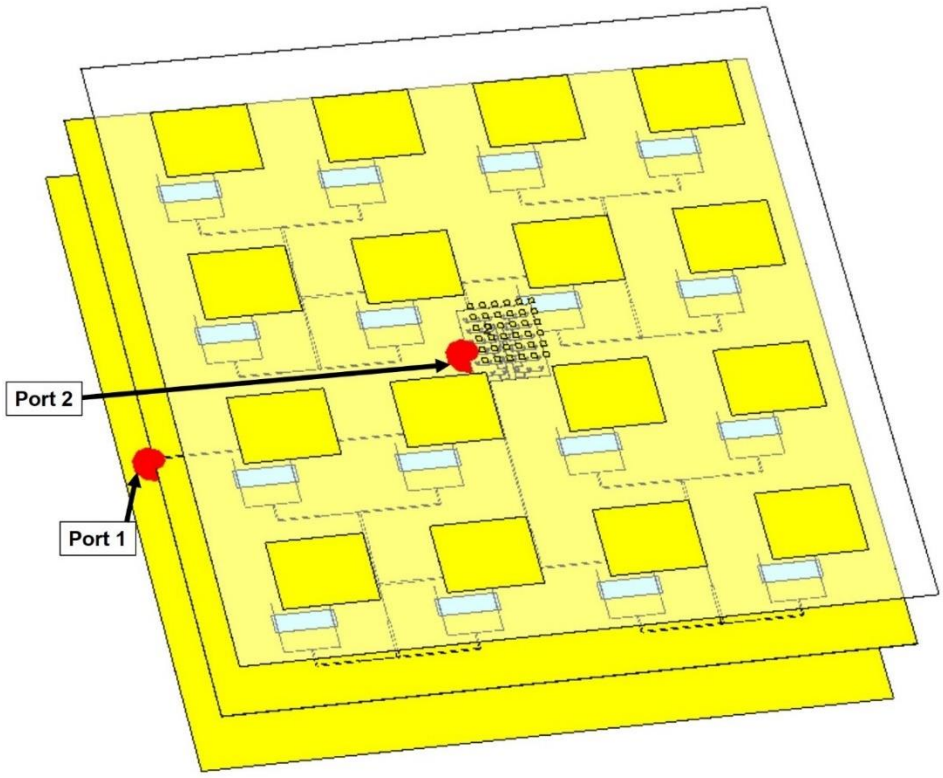

Figure 5. 29 Ports illustration of the L-/Ku- band shared aperture fixed beam array

It can be observed from Figure 5. 30 and Figure 5. 31 that by using separated ground planes, both channels exhibit excellent isolation (better than -67 dB), implying negligible coupling between the L- and Ku- band feedlines. The impedance matching curve of the Ku- band array (in this case |S22|) is very similar to that of Ku- band fixed beam alone (in **Error! Reference source not found.**), while reflection coefficient is better than -11. 7 dB for the L- band channel.

As per Figure 5. 32 and Figure 5. 33, radiation pattern distortion at L- band is observed to be minor, owing to the relatively much smaller fixed beam Ku- band feedline layer positioned in between the radiating patch and L- band feedline. Minor pattern distortion can be observed at Ku- band in Figure 5. 34 and Figure 5. 35, implying negligible interference with the L- band patches on the same aperture.

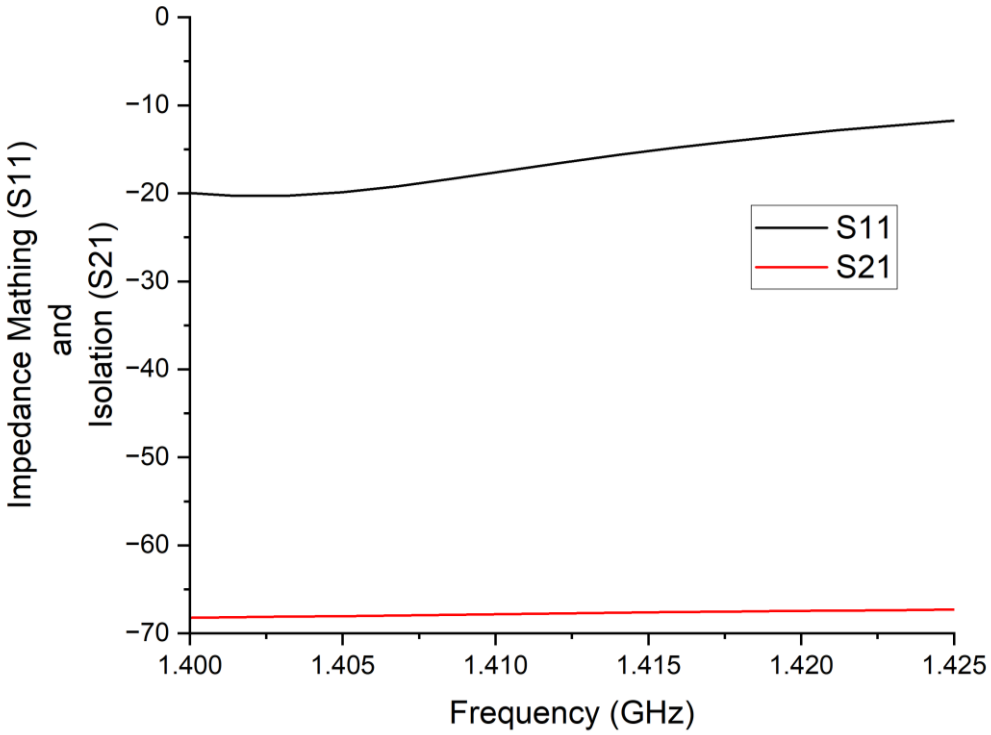

Figure 5. 30 Impedance matching and isolation of the L- band channel at Port 1

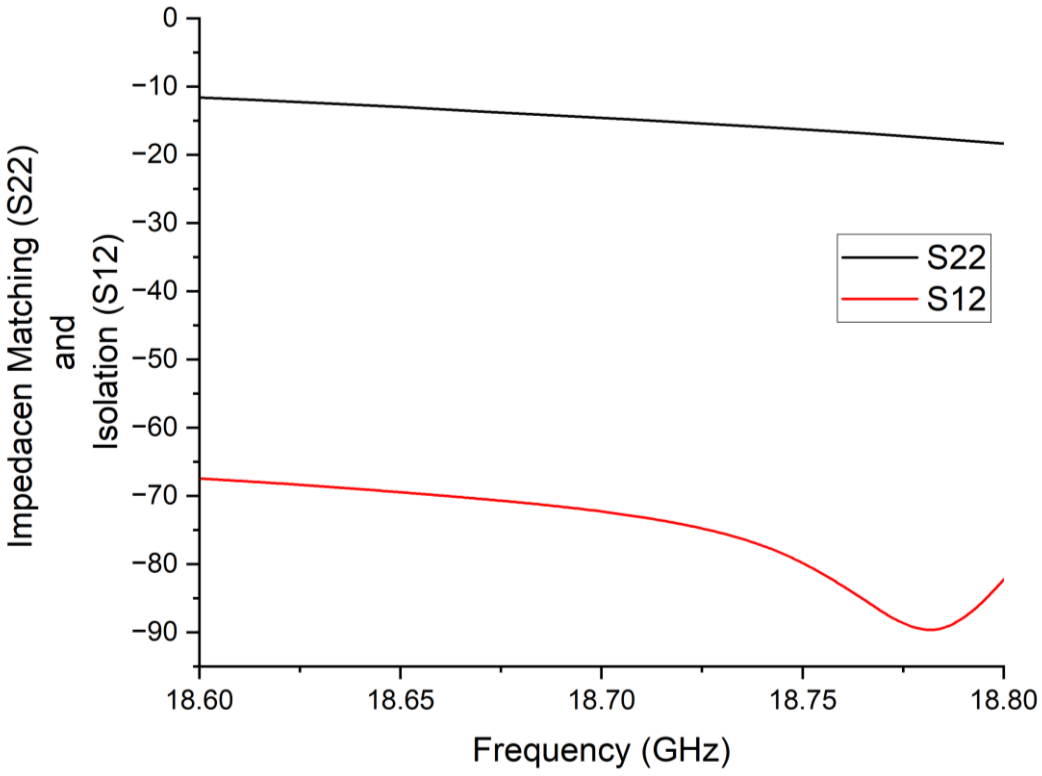

Figure 5. 31 Impedance matching and isolation of the Ku- band channel at Port 2

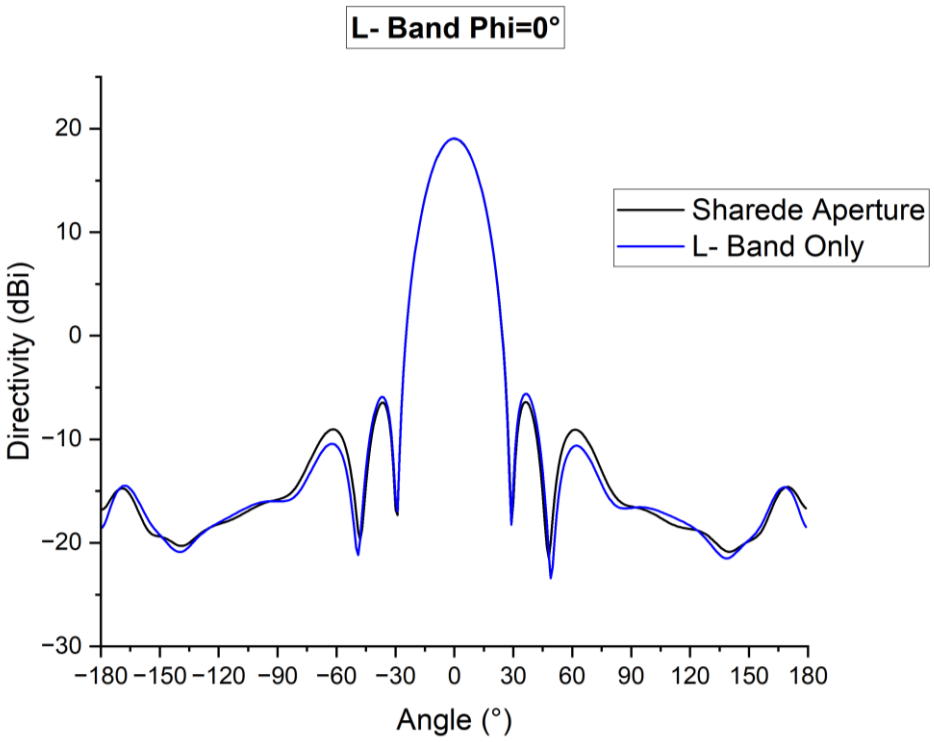

Figure 5. 32 Radiation patterns of the 4x4 L- band array at Phi=0° cut plane

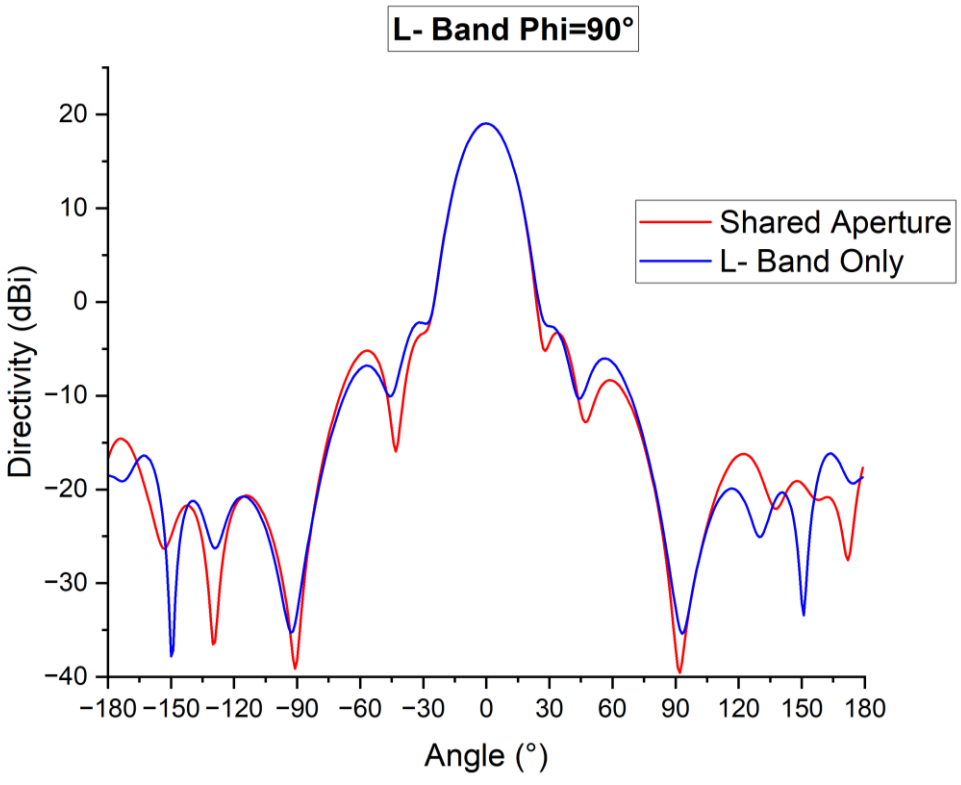

Figure 5. 33 Radiation patterns of the 4x4 L- band array at Phi=90° cut plane

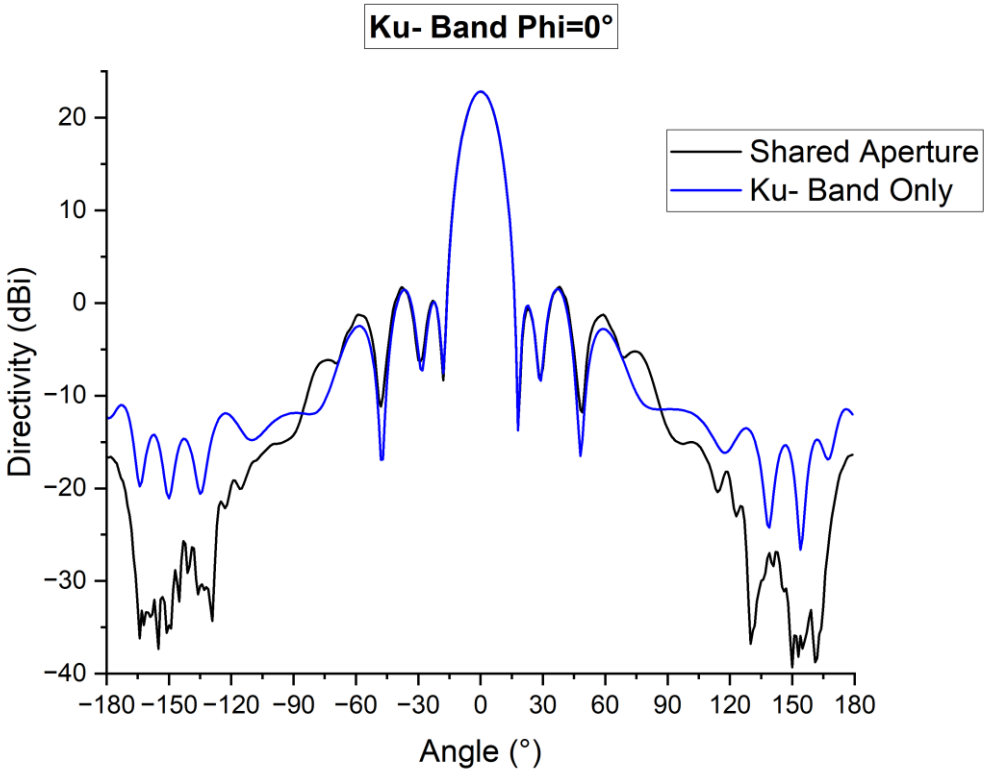

Figure 5. 34 Radiation patterns of the 6x6 Ku- band array at Phi=0° cut plane

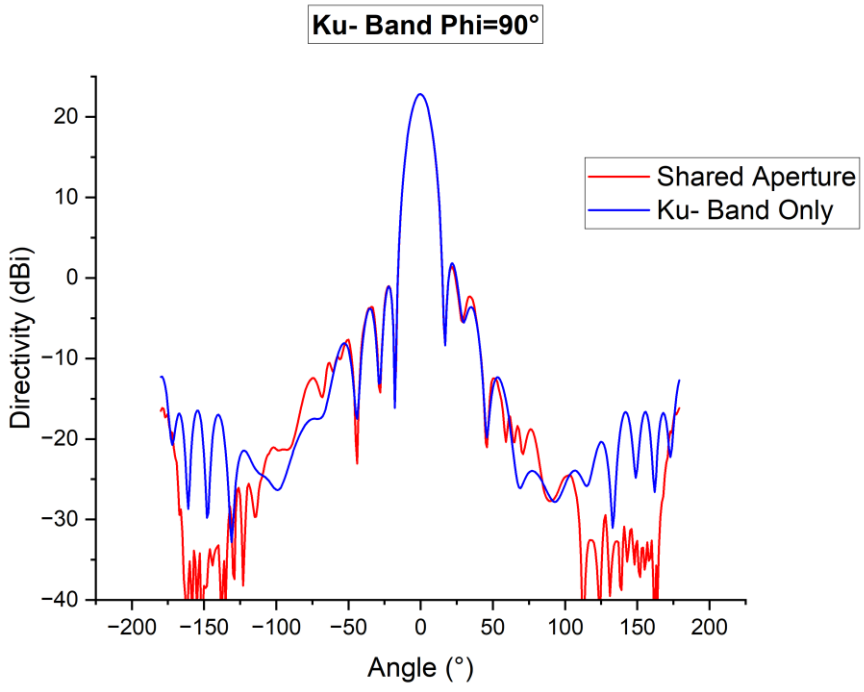

Figure 5. 35 Radiation patterns of the 6x6 Ku- band array at Phi=90° cut plane

5.3 Ku- band Phased array designs

5.3.1 Feed network implementation

Due to space constraints, it is challenging to design tapered feedlines to integrate with the phase shifters. The feedline line design starts from a sketch to find out possible ways to connect the phase shifters as illustrated in Figure 5. 36. Thereafter, the three-way unequal power dividers developed in Section 5.1.3.2 and 5.1.3.3 have been modified by following the same design principles in Chapter 4 for amplitude tapering and phase balancing. Figure 5. 37 shows the implementation of the power divider network integrated with two-bit phase shifters, and Figure 5. 38 shows the power divider details of one quadrant of the array.

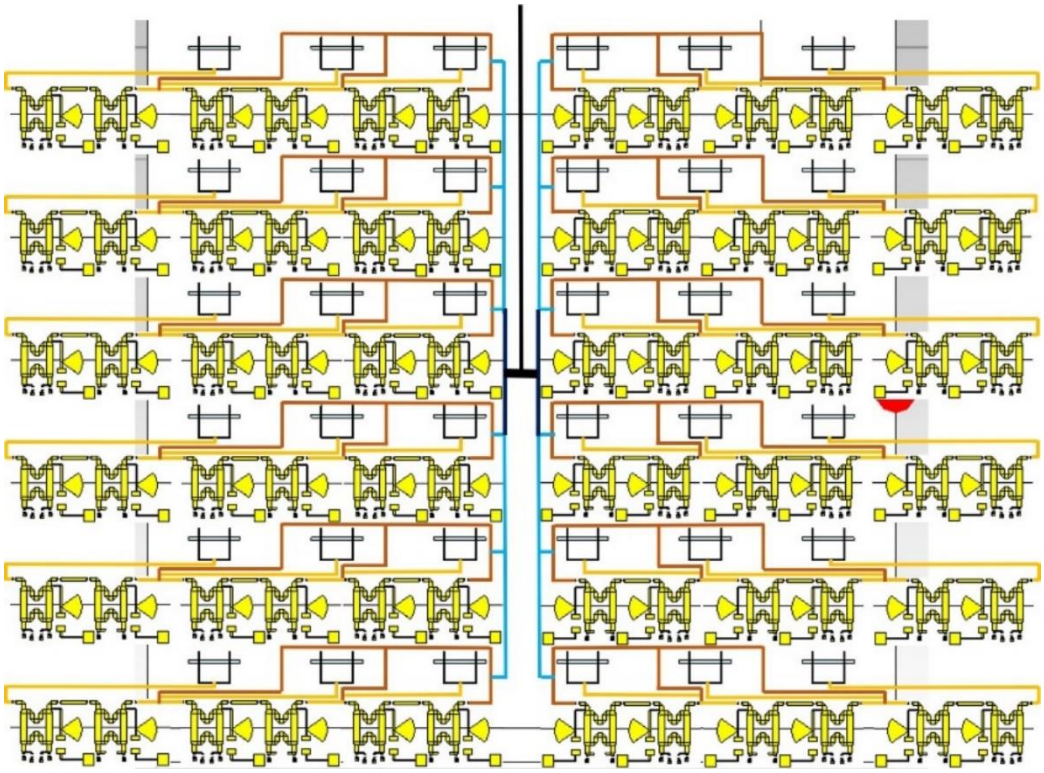

Figure 5. 36 Sketch drawing of feedlines for the 6x6 Ku- Band phased array

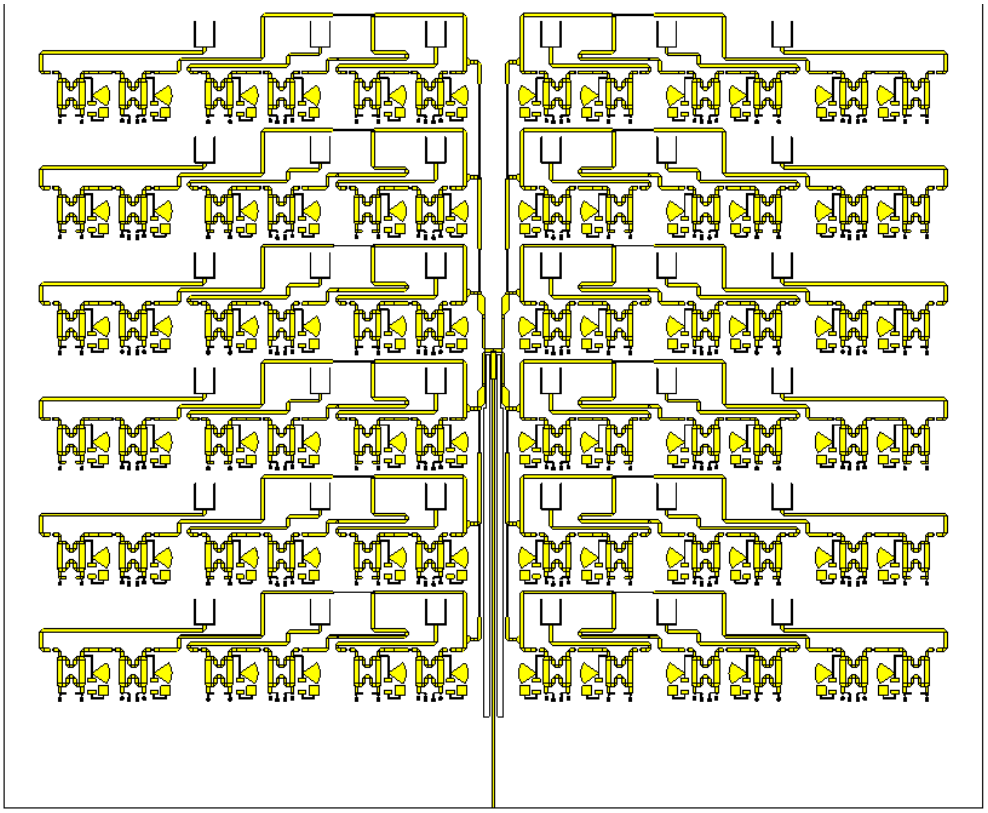

Figure 5. 37 Implementation of the feed network for the 6x6 Ku- Band Phased Array

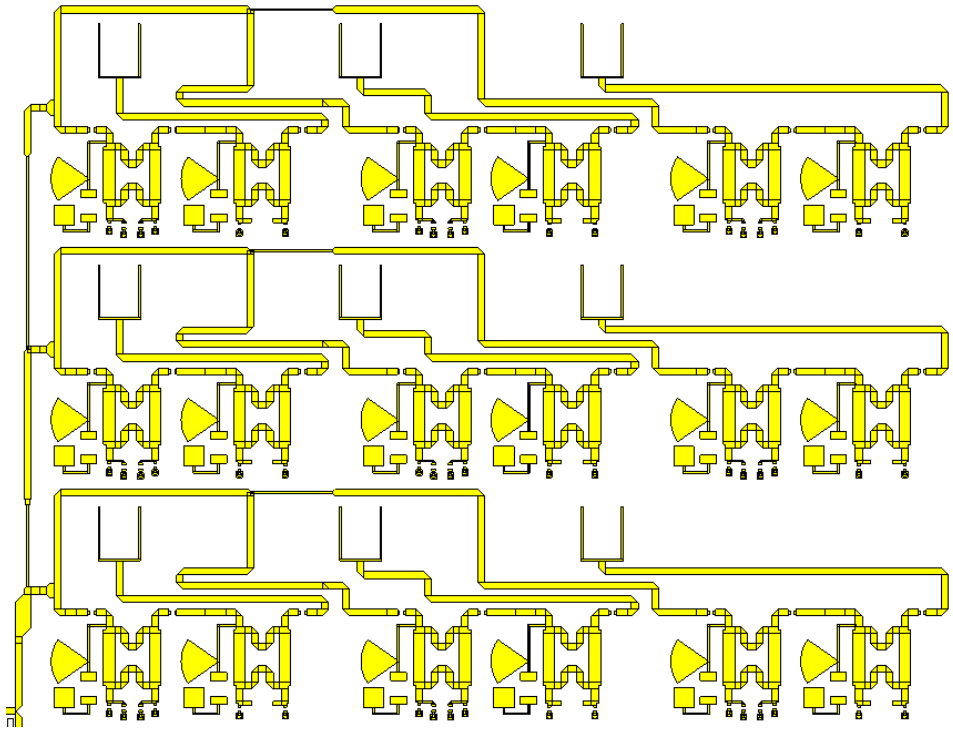

Figure 5. 38 Detailed view for one quadrant of the feed network

5.3.2 Coupling issue in the vertical power divider

Before finalising the phased array design, one issue to be addressed is port imbalance in the vertical feedline. In the initial design (as shown in Figure 5. 39), severe port imbalance between Port 8 and Port 4 was observed. As illustrated in Figure 5. 40, this was because the power flows from Port 1 to the centre of the power divider, while Port 4 has the exact opposite power flow direction and has only 10% of the input power. Therefore, even only a small portion of radiation from the input divider could significantly distort the amplitude and phase of Port 4. This in turn causes amplitude imbalance of 5.4 dB and 34.1° phase imbalance, as shown in the dotted lines of Figure 5. 41 and Figure 5. 42 respectively.

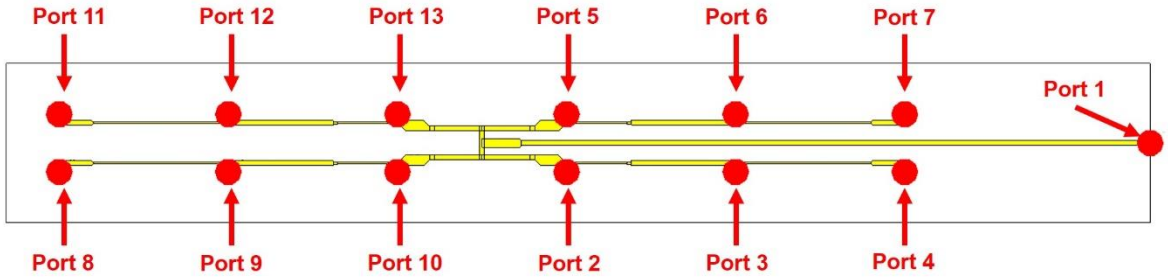

Figure 5. 39 Implementation of the initial 2x6 vertical power divider

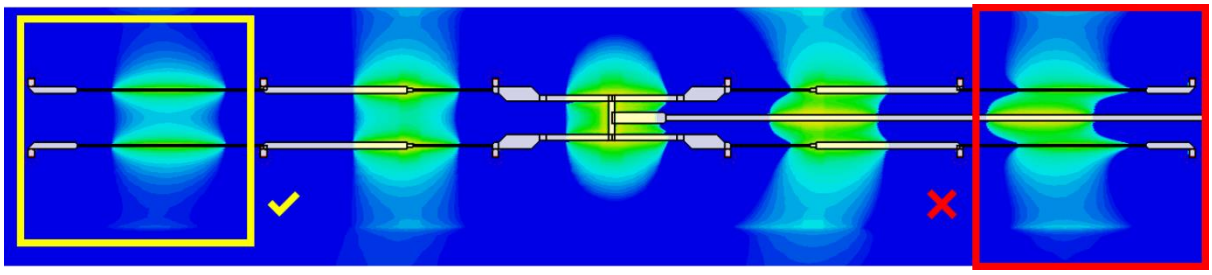

Figure 5. 40 Electric field distribution at the initial 2x6 vertical power divider

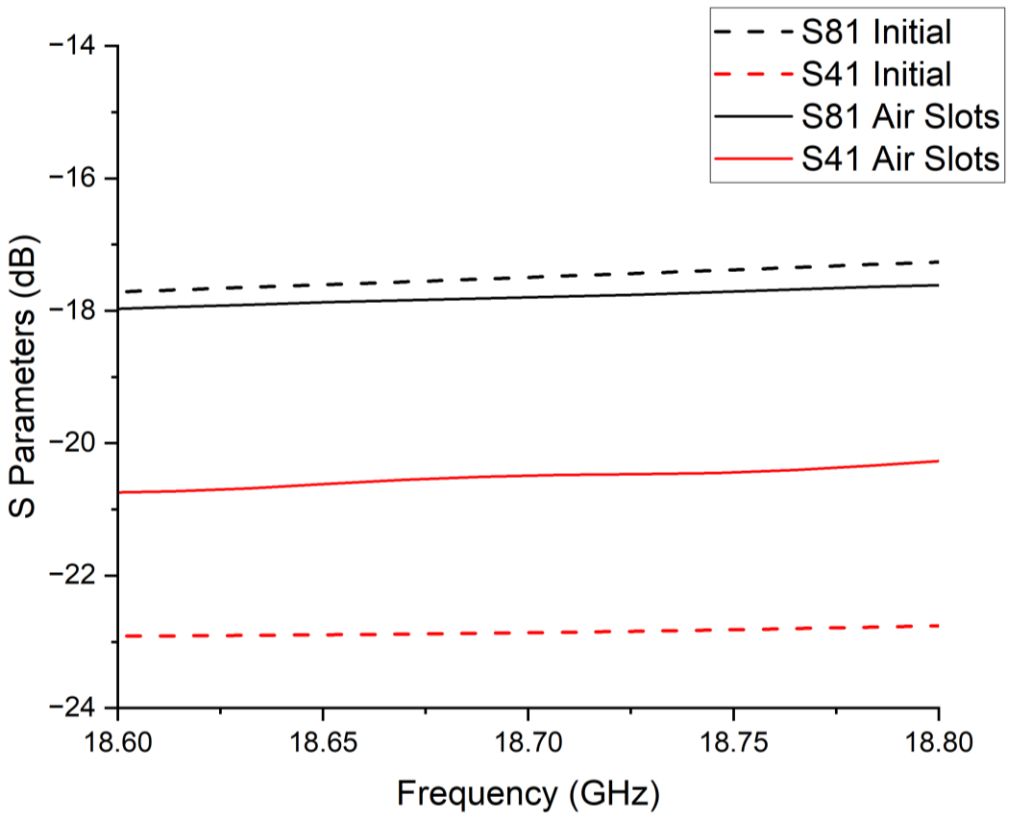

Figure 5. 41 Amplitude imbalance between Port 4 and Port 8 of the vertical power dividers

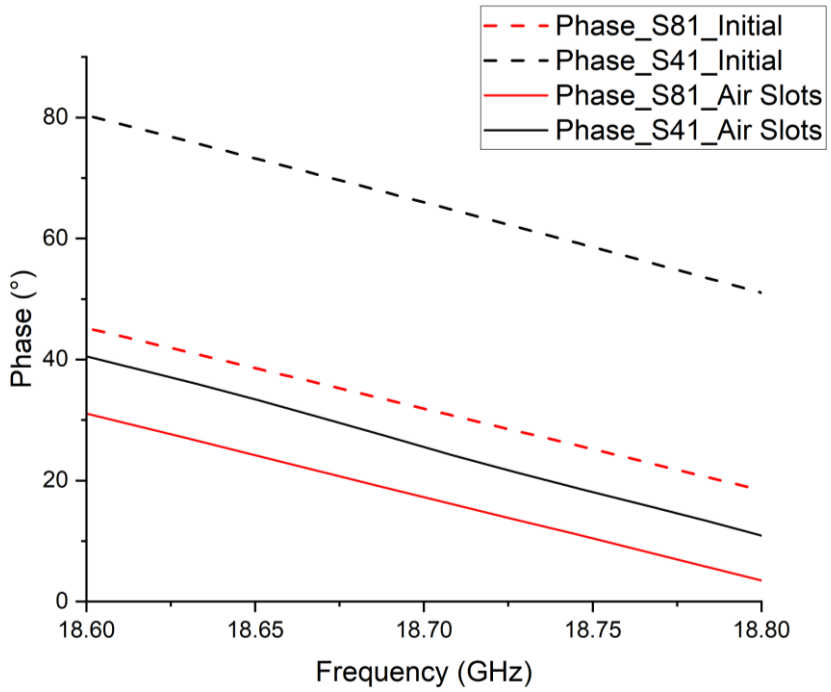

Figure 5. 42 Phase imbalance between Port 4 and Port 8 of the vertical power dividers

One effective way to alleviate the imbalance without manual work to is to cut out air slots around the input feedline to attenuate the radiation, as depicted in Figure 5. 43, so that the amount of

coupling can be reduced. As a result, the amplitude imbalance has been reduced to 2.7 dB, and phase imbalance suppressed down to 8.3° as illustrated by the solid lines of Figure 5. 41 and Figure 5. 42. Although the reduced amplitude imbalance still causes the vertical power divider to be asymmetric, which will also be reflected in the later beam steering patterns, the suppressed phase imbalance helps to reduce antenna pointing errors.

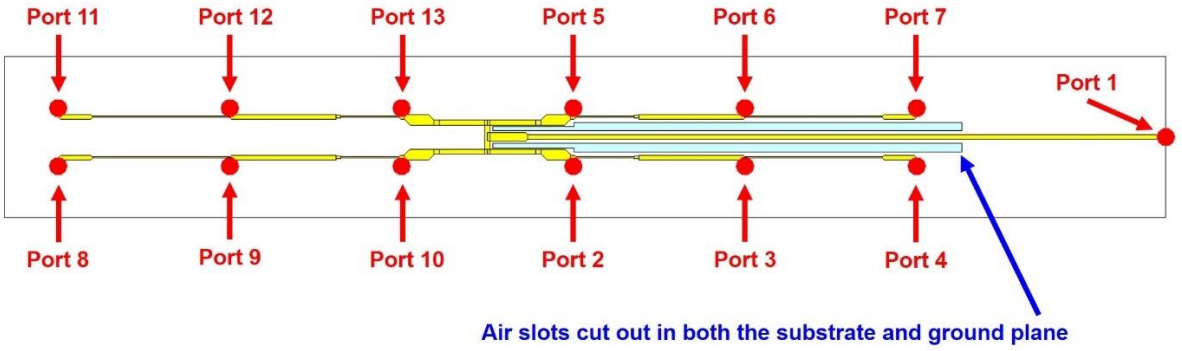

Figure 5. 43 Implementation of the 2x6 vertical power divider with air slots cut off in both the substrate and ground plane

To examine the effect of the reduction in port imbalance, 2x6 antenna arrays have been simulated and compared, with the 3D fan-beam radiation shown in Figure 5. 44. Thereafter, Figure 5. 45 shows the main beam and the first and second side lobes on both the left and right side, and it can be observed that the maximum amplitude difference between the presented side lobes is 4.17 dB in the initial design, and down to 3.16 dB with air slots cut out. The pointing angle has also been corrected from 1° in the initial design to 0° by cutting out air slots. These improvements are important to the later 6x6 phased array.

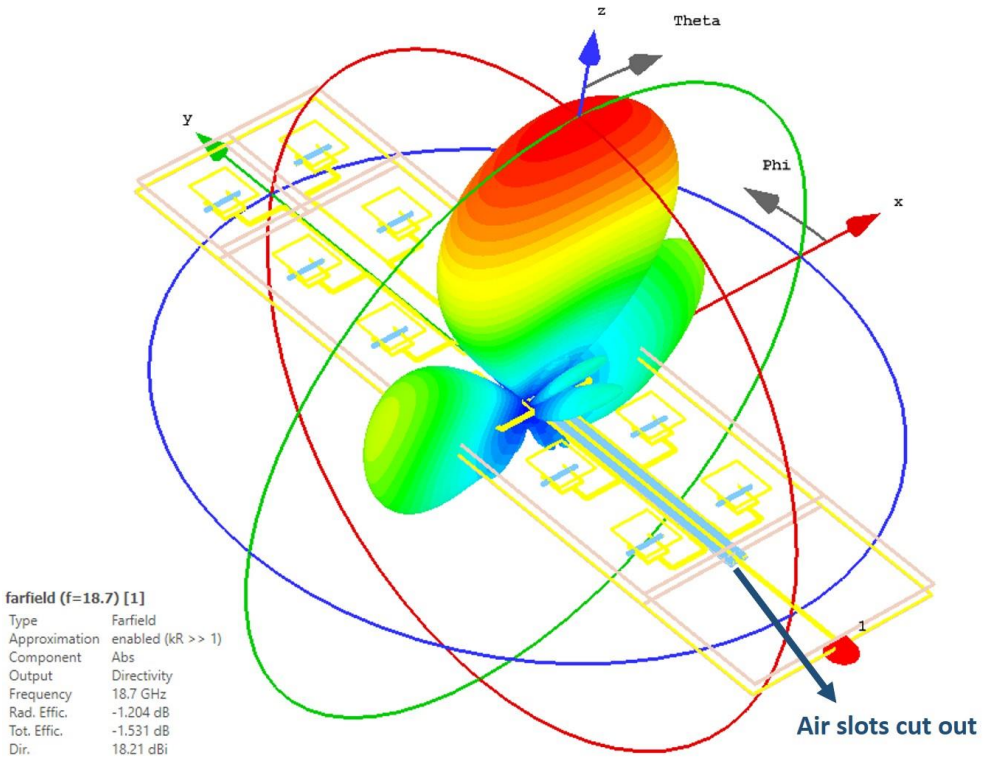

Figure 5. 44 Farfield pattern of the 2x6 array with air slots cut out

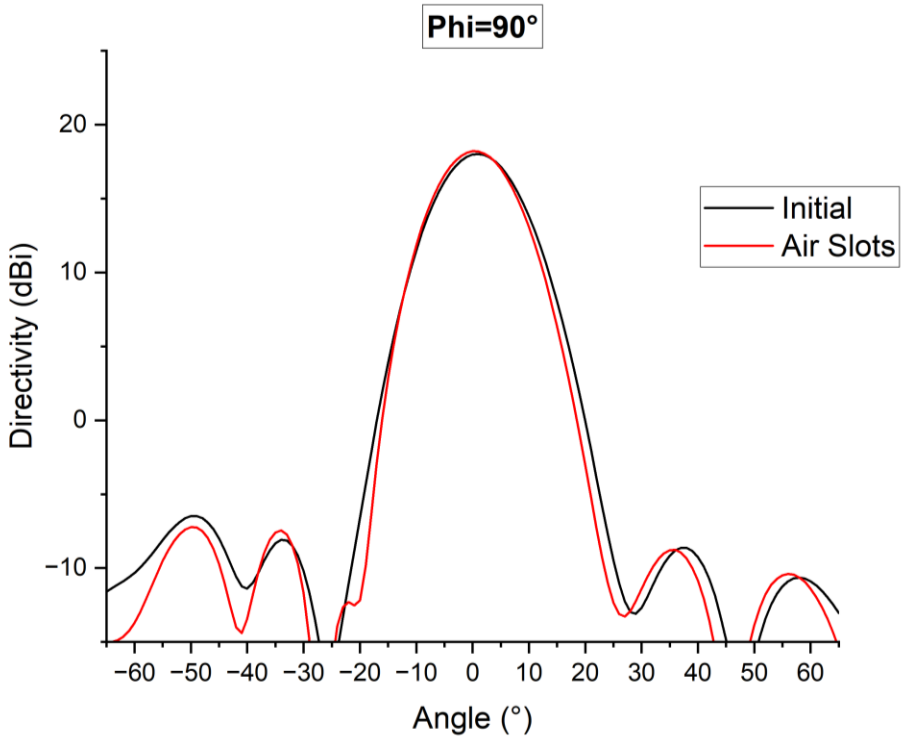

Figure 5. 45 Radiation patterns comparison of the 2x6 Ku- band array at Phi=90° cut plane showing the main beam and the first two side lobes on both the left and right side

5.3.3 Ku- band phased array

5.3.3.1 Phase allocation optimisation

Regarding the phase allocation for beam steering, according to [27], the 180° bit has the largest difference in insertion loss, which is about 1.3 dB between on and off state at 18.6 GHz as illustrate in Figure 5. 46. Provided that the centre elements of the tapered phased array have the higher power splits, for optimum radiation efficiency, care must be exercised to avoid using 180° and 270° states in the centre part of the array.

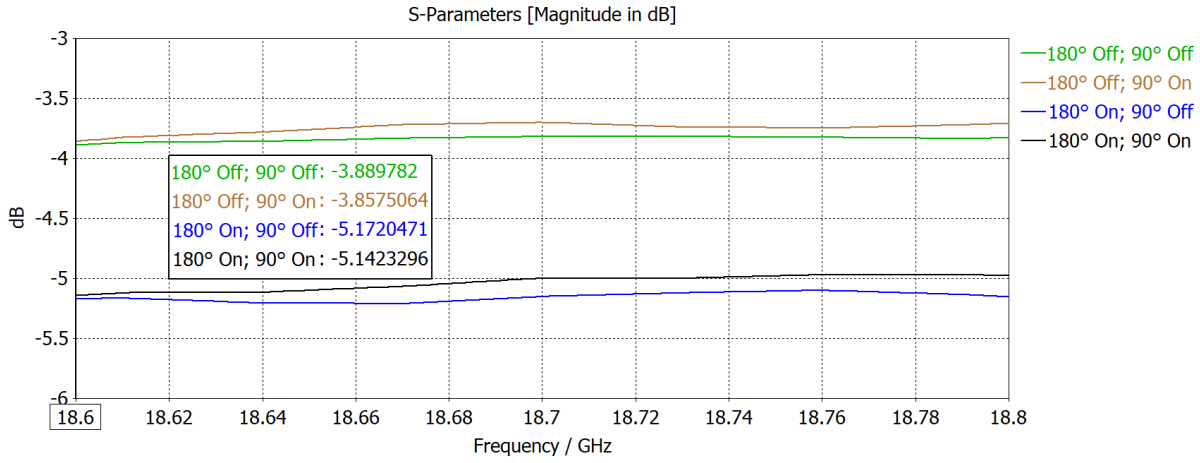

Figure 5. 46 Insertion loss of each two-bit phase shifter states

To demonstrate, by using the phase allocation in Table 5. 3 for beam scanned 20° in the X-20°direction (e.g. the top left element shall have 180° in phase, and the next element along X-direction shall have 0° phase shift and so forth), this leads to low radiation efficiency of -6.158 dB at 18.6 GHz. To improve the radiation efficiency, given phase shift the result of relative phase difference between elements (e.g. if every element in an array is allocated to 180°, the resultant phase shift is 0°), 180° is added to each allocation. As listed in Table 5. 4, this results in low loss states being allocated in the centre and high loss state at the edge. In this example, the radiation efficiency has been improved from -6.158 dB (in Figure 5. 47) to -5.509 dB (in Figure 5. 48) while the pointing angle is very similar. Likewise, phase allocation for other beams has been optimised following the same principle.

Table 5. 3 Initial phase allocation for X-20° in a 6x6 array

180°	0°	270°	180°	90°	0°
180°	0°	270°	180°	90°	0°
180°	0°	270°	180°	90°	0°
180°	0°	270°	180°	90°	0°
180°	0°	270°	180°	90°	0°
180°	0°	270°	180°	90°	0°

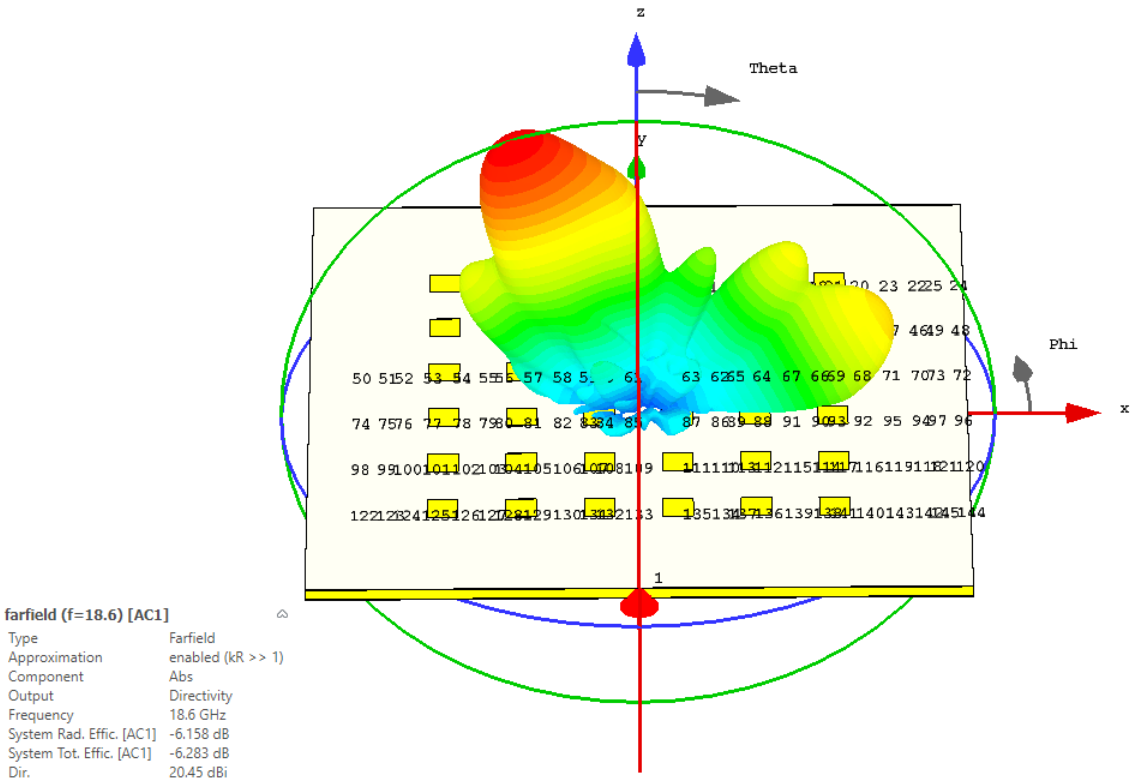

Figure 5. 47 Fairfield pattern of the 6x6 Ku- band at X-20° beam using the initial phase allocation

Table 5. 4 Improved phase allocation for X-20° in a 6x6 array

0°	180°	90°	0°	270°	180°
0°	180°	90°	0°	270°	180°
0°	180°	90°	0°	270°	180°
0°	180°	90°	0°	270°	180°
0°	180°	90°	0°	270°	180°
0°	180°	90°	0°	270°	180°

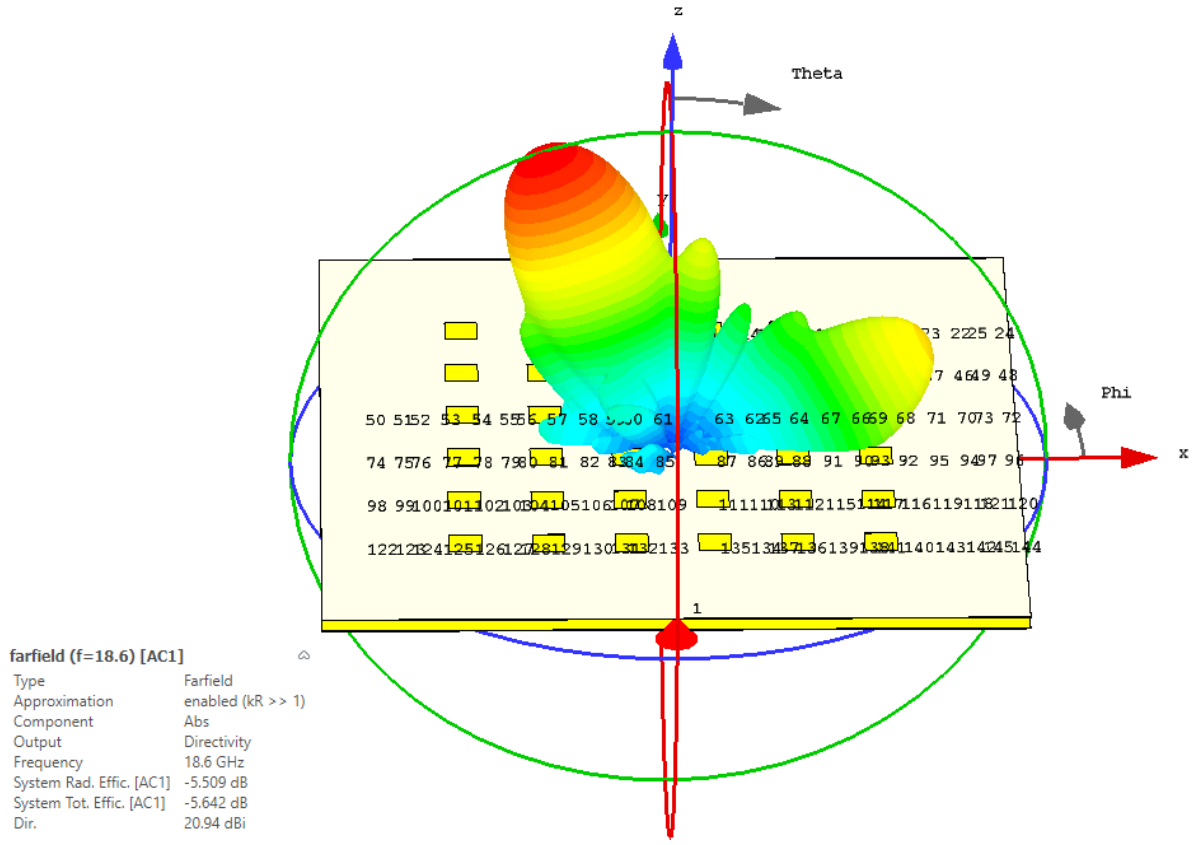

Figure 5. 48 Fairfield pattern of the 6x6 Ku- band at X-20° beam using the improved phase allocation

5.3.3.2 X- direction

From Figure 5. 49, it can be observed that all X- direction beams exhibit good impedance matching with |S11| better than -13.1dB from 18.6 to 18.8 GHz. Along with the highly overlapping |S11| curves of pair X±6° and X±21°, the pointing angles and overall patterns of these two pairs are mirrored in Figure 5. 50 and overlapped in Figure 5. 51. Therefore, it can be concluded that the Ku-band phased array is highly symmetrical in the X- direction.

Table 5. 5 Phase allocation for X+7° in a 6x6 array

0°	0°	90°	90°	90°	180°
0°	0°	90°	90°	90°	180°
0°	0°	90°	90°	90°	180°
0°	0°	90°	90°	90°	180°
0°	0°	90°	90°	90°	180°
0°	0°	90°	90°	90°	180°

Table 5. 6 Phase allocation for X-7° in a 6x6 array

180°	90°	90°	90°	0°	0°
180°	90°	90°	90°	0°	0°
180°	90°	90°	90°	0°	0°
180°	90°	90°	90°	0°	0°
180°	90°	90°	90°	0°	0°
180°	90°	90°	90°	0°	0°

Table 5. 7 Phase allocation for X+20° in a 6x6 array

180°	270°	0°	90°	180°	0°
180°	270°	0°	90°	180°	0°
180°	270°	0°	90°	180°	0°
180°	270°	0°	90°	180°	0°

180°	270°	0°	90°	180°	0°
180°	270°	0°	90°	180°	0°

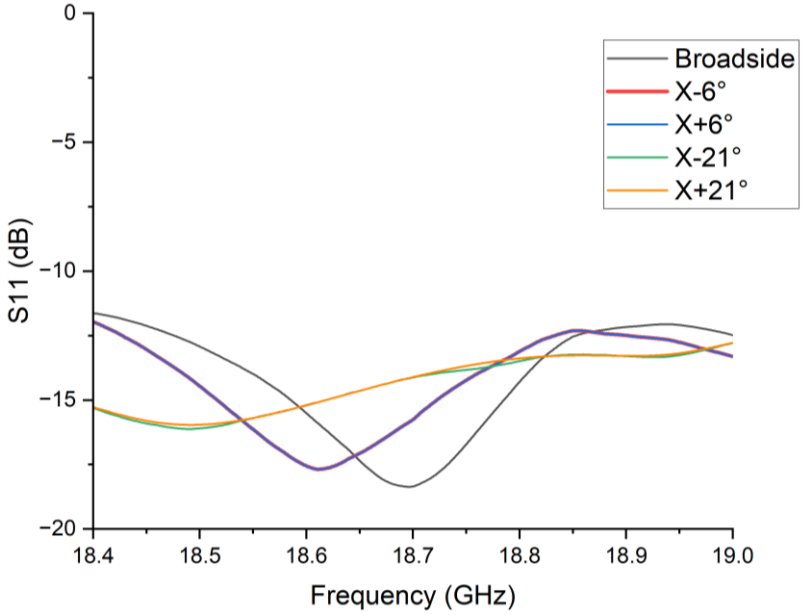

Figure 5. 49 |S11| of the X- direction beams of the finalised 6x6 Ku- band array

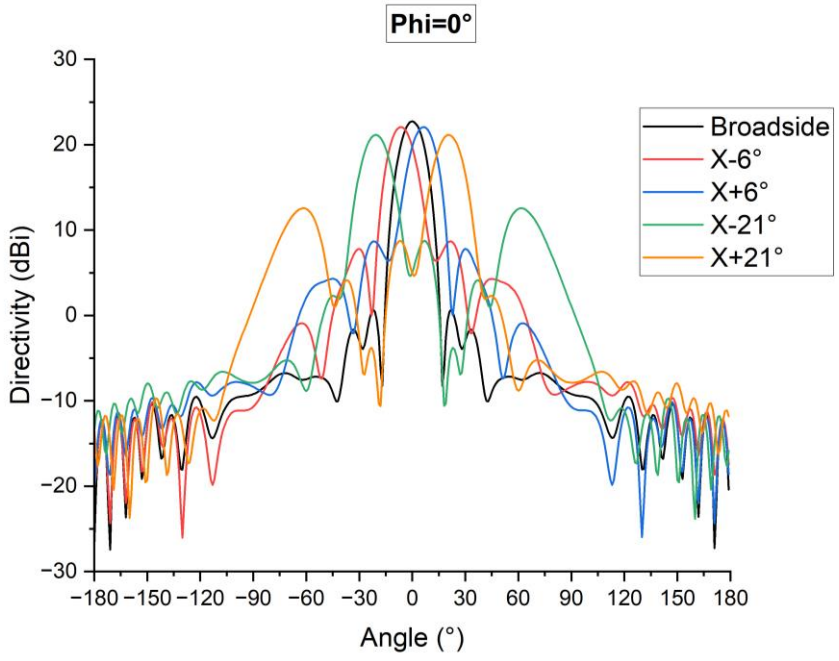

Figure 5. 50 Radiation patterns of X- direction beams of the 6x6 Ku- band array at 18.7 GHz and Phi=0° cut plane

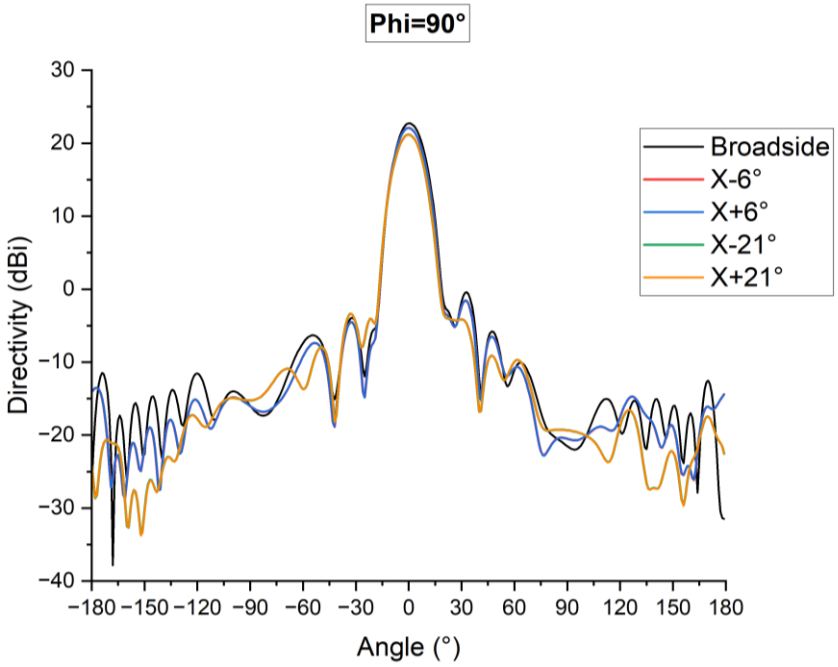

Figure 5. 51 Radiation patterns of X- direction beams of the 6x6 Ku- band array at 18.7 GHz and Phi=90° cut plane

5.3.2.3 Y- direction

As discussed in section 5.3.2 Coupling issue in the vertical power divider, although cutting out air slots around the input feedline improves the asymmetry, the ports are still imbalanced in the Y-direction. This is reflected in Figure 5. 53 and Figure 5. 54 as a distinct difference in radiation pattern that can be observed, as well as pointing angles that are different along the Y- direction. According to the results summarised in Table 5. 14 to Table 5. 16, the results in the Y- direction are still rather close from 18.6 to 18.8 GHz, hence this asymmetry does not cause a major issue.

Table 5. 8 Phase allocation for Y+6° in a 6x6 array

0°	0°	0°	0°	0°	0°
0°	0°	0°	0°	0°	0°
90°	90°	90°	90°	90°	90°
90°	90°	90°	90°	90°	90°
90°	90°	90°	90°	90°	90°
180°	180°	180°	180°	180°	180°

Table 5. 9 Phase allocation for Y-5° in a 6x6 array

180°	180°	180°	180°	180°	180°
90°	90°	90°	90°	90°	90°
90°	90°	90°	90°	90°	90°
90°	90°	90°	90°	90°	90°
0°	0°	0°	0°	0°	0°
0°	0°	0°	0°	0°	0°

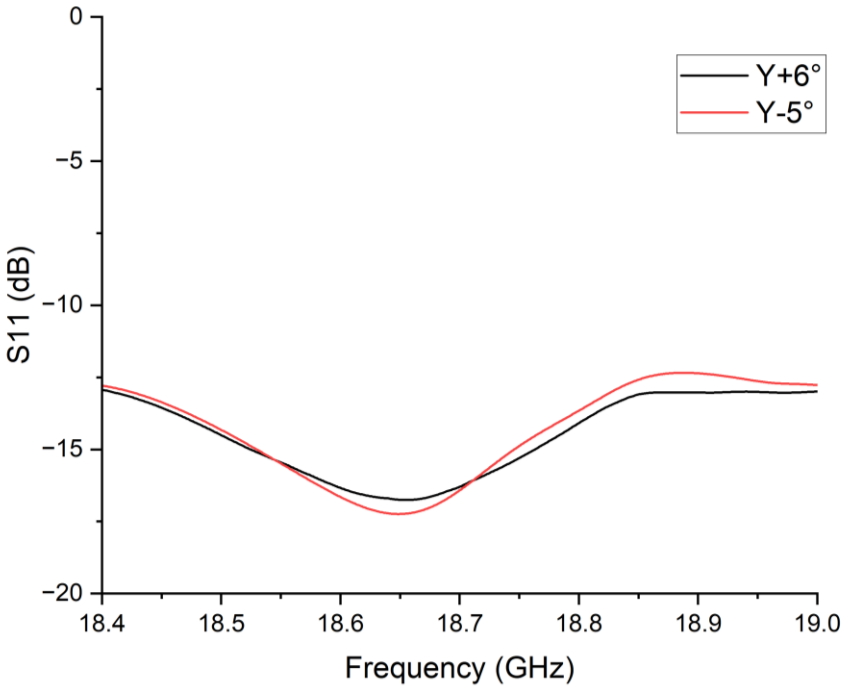

Figure 5. 52 |S11| of the Y- direction beams of the 6x6 Ku- band array

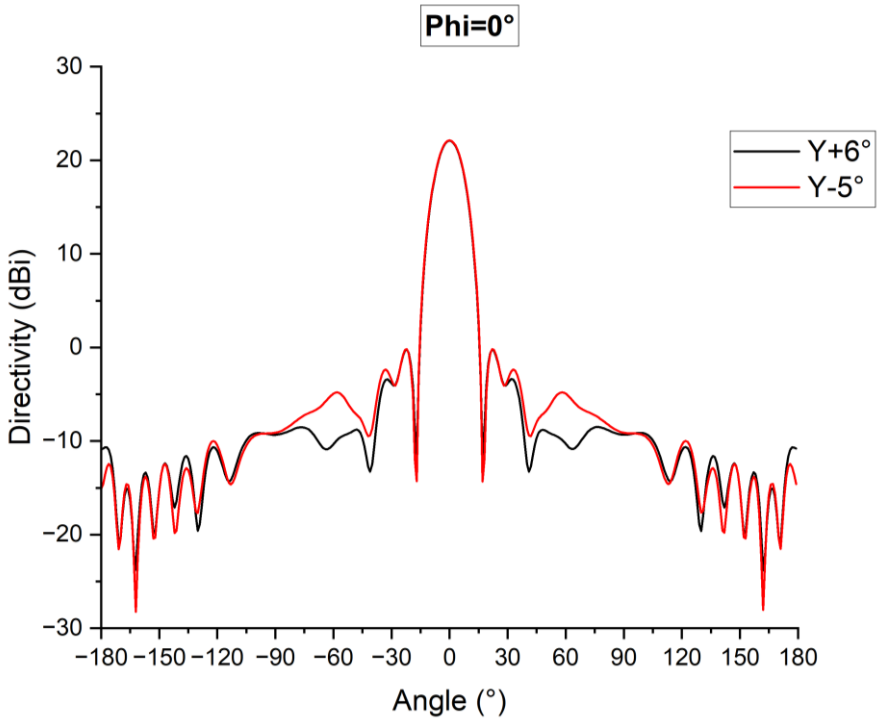

Figure 5. 53 Radiation patterns of Y- direction beams of the 6x6 Ku- band array at Phi=0° cut plane

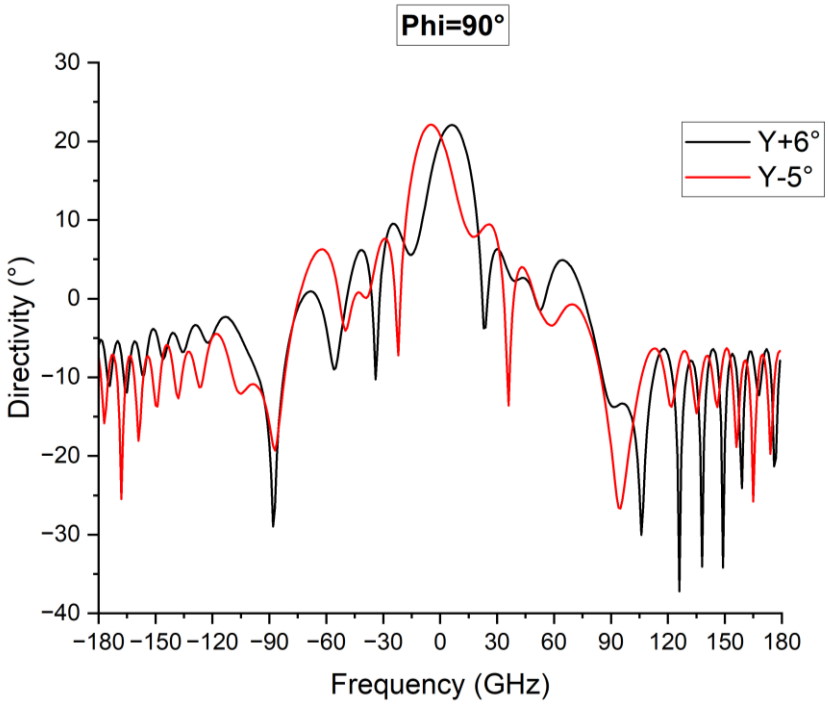

Figure 5. 54 Radiation patterns of Y- direction beams of the 6x6 Ku- band array at Phi=90° cut plane

5.3.3.4 Diagonal Scanning

In total, 8 diagonal beams can be generated by using the 2-bit phase shifter (hence 15 beams in total). As discussed in the previous two subsections, the beam patterns and antenna characteristics are highly symmetric in the X- direction, while they are asymmetric in Y- direction. In this sense, only the diagonal beams in +X half are presented and discussed in this chapter.

Table 5. 10 Phase allocation for [X+7°, Y+6°] in a 6x6 array

180°	270°	270°	0°	0°	0°
180°	270°	270°	0°	0°	0°
270°	0°	0°	90°	90°	90°
270°	0°	0°	90°	90°	90°
270°	0°	0°	90°	90°	90°
0°	90°	90°	180°	180°	180°

Table 5. 11 Phase allocation for [X+7°, Y-5°] in a 6x6 array

0°	90°	90°	180°	180°	180°
270°	0°	0°	90°	90°	90°
270°	0°	0°	90°	90°	90°
270°	0°	0°	90°	90°	90°
180°	270°	270°	0°	0°	0°
180°	270°	270°	0°	0°	0°

Table 5. 12 Phase allocation for [X+20°, Y+6°] in a 6x6 array

90°	270°	0°	90°	180°	270°
90°	270°	0°	90°	180°	270°
180°	0°	90°	180°	270°	0°
180°	0°	90°	180°	270°	0°
180°	270°	270°	0°	0°	0°
270°	90°	180°	270°	0°	90°

Table 5. 13 Phase allocation for [X+20°, Y-5°] in a 6x6 array

270°	90°	180°	270°	0°	90°
180°	0°	90°	180°	270°	0°
180°	0°	90°	180°	270°	0°
180°	0°	90°	180°	270°	0°
90°	270°	0°	90°	180°	270°
90°	270°	0°	90°	180°	270°

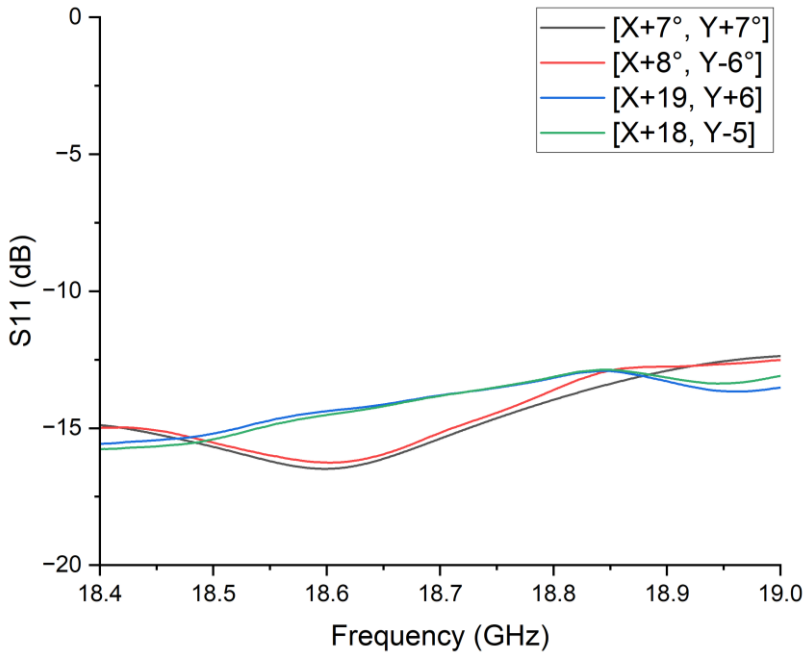

Figure 5. 55 |S11| of the diagonal beams of the 6x6 Ku- band array

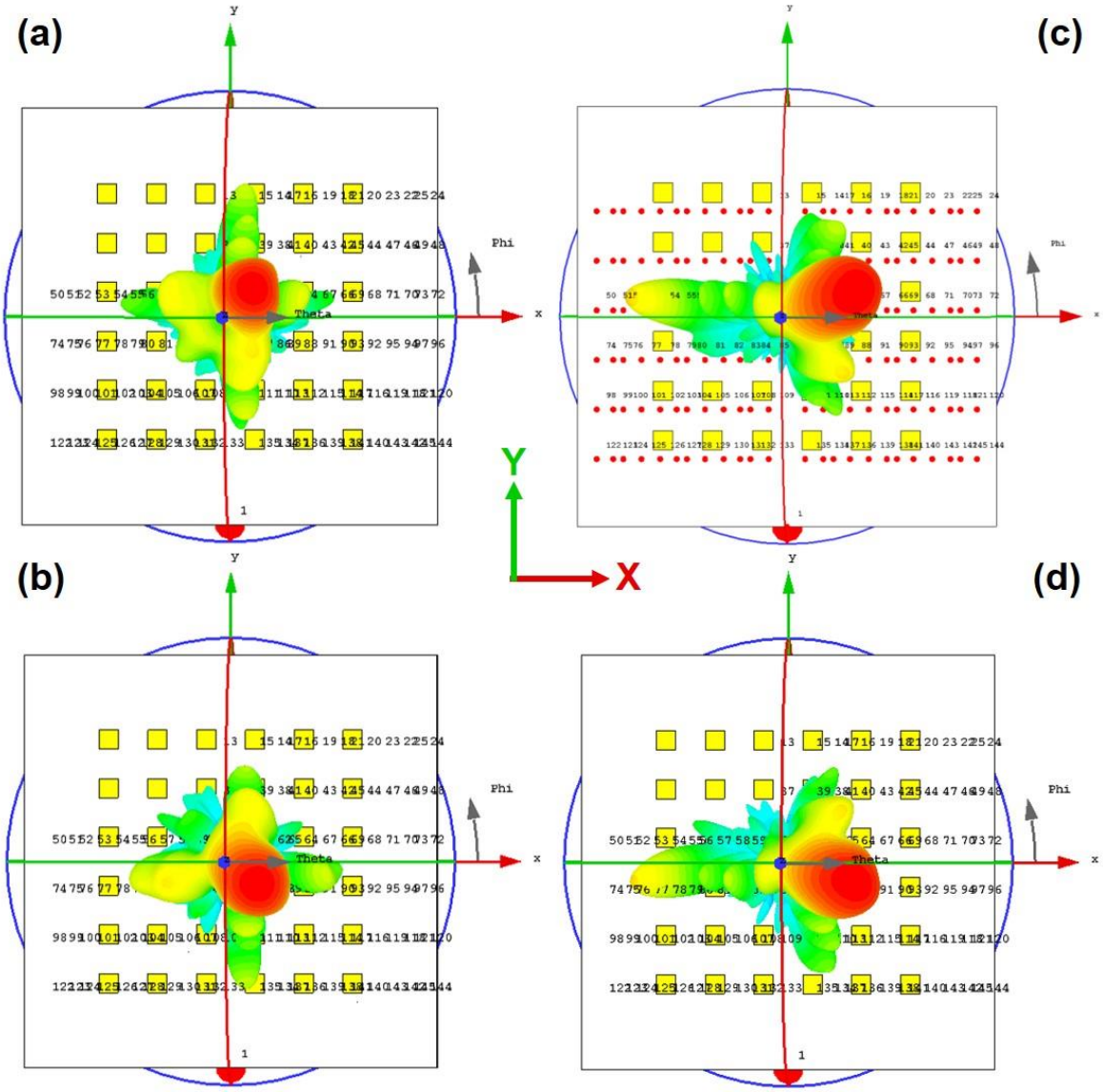

Figure 5. 56 Diagonal beams far field patterns of the 6x6 Ku- band array at 18.7 GHz

(a) [X+7°, Y+7°] (b) [X+8°, Y-6°] (c) [X+19°, Y+6°] (d) [X+18, Y-5°]

5.3.3.5 Summary and Discussion

Table 5. 14 Radiation pattern results summary at 18.6 GHz

Beam	Total loss (dB)	3-Dimensional Main Beam Efficiency (%)	Highest side lobe (dB)
0°	-5.055	96.95	-22.6
X-6°	-5.011	88.89	-11.8
X+6°	-5.011	88.90	-11.8
X-20°	-5.642	78.68	-9.1
X+20°	-5.643	78.69	-9.1
Y+6°	-5.085	86.52	-12.5
Y-5°	-5.125	88.38	-13.1
[X+8°, Y+7°]	-5.445	72.17	-11.5
[X+8°, Y-6°]	-5.461	73.76	-11.7
[X+19°, Y+7°]	-5.651	72.30	-10
[X+18°, Y-5°]	-5.683	72.40	-9.6

Table 5. 15 Radiation pattern results summary at 18.7 GHz

Beam	Total loss (dB)	3-Dimensional Main Beam Efficiency (%)	Highest side lobe (dB)
0°	-5.170	95.88	-22.1
X-6°	-5.250	87.92	-13.4
X+6°	-5.250	87.94	-13.4
X-21°	-5.816	75.59	-8.6
X+21°	-5.815	75.61	-8.6
Y+6°	-5.313	87.94	-12.6
Y-5°	-5.345	87.92	-12.7
[X+7°, Y+7°]	-5.610	69.30	-10
[X+8°, Y-6°]	-5.599	69.14	-9.7
[X+19°, Y+6°]	-5.595	72.63	-9.4
[X+18°, Y-5°]	-5.645	72.60	-9.4

Table 5. 16 Radiation pattern results summary at 18.8 GHz

Beam	Total loss (dB)	3-Dimensional Main Beam Efficiency (%)	Highest side lobe (dB)
0°	-5.573	95.59	-21.5
X-7°	-5.695	85.20	-11.6
X+7°	-5.695	85.28	-11.6
X-20°	-6.151	74.24	-8.3
X+20°	-6.151	74.24	-8.3
Y+7°	-5.671	84.95	-12.2
Y-5°	-5.715	84.03	-11.8
[X+7°, Y+7°]	-5.886	62.06	-8.6
[X+8°, Y-6°]	-5.865	61.62	-8.1
[X+19°, Y+6°]	-5.813	71.68	-9.4
[X+19°, Y-4°]	-5.855	70.88	-8.6

To summarise the diagonal scanning results in Table 5. 14 to Table 5. 16, the total efficiency of each beam is better than -5.683 dB, -5.816 dB and -6.151 dB at 18.6 GHz, 18.7 GHz and 18.8 GHz respectively. Furthermore, as shown in Figure 5. 46, the insertion loss of the two-bit phase shifter is flat over the radiometric bandwidth of the system. The lower total antenna efficiency at 18.8 GHz could be due to the fact that Ku- band array is tuned towards the lower half of the bandwidth as reflected in every impedance matching plot (Figure 5. 49 Figure 5. 52 Figure 5. 55), as well as the fact that this antenna has its best radiation efficiency at 18.6 GHz for most of the beams. In terms of 3-dimensional beam efficiency, all the one-dimensional beams have efficiencies better than 74.24% over the radiometric bandwidth. In the meantime, the diagonal scanning beams have efficiency around 70% owing to high side lobe levels in both X- and Y- directions.

Overall, the simulation results are considered as acceptable. The Ku- band phased array design is thereby ready for integration with the L- band phased array in the same aperture.

5.4 Shared aperture phased array

Due to the significant computational power required for running a full L-/Ku- band phased array, which could lead to an unacceptable simulation run time of over a month, the discussion of shared aperture phased array is divided into two parts: the first part being the simplified Ku- band array, and the second being a full model running only at L- band.

5.4.1 Simplified shared aperture Ku- band array

5.4.1.1 Simplified model and results comparison with discrete ports

Based on earlier simulation results of the fixed beam shared aperture array in section 5.1.4, the pattern distortion in the Ku- band array is minor within the same aperture. In this sense, the full model with the 4x4 array was simplified to just the centre 2x2 L- band patch surrounding the 6x6 Ku- band array as illustrated in Figure 5. 57. As depicted in Figure 5. 58, the feedline substrate and L- band metal back reflector were also removed, reducing the computational meshes to 14.3% of the full model.

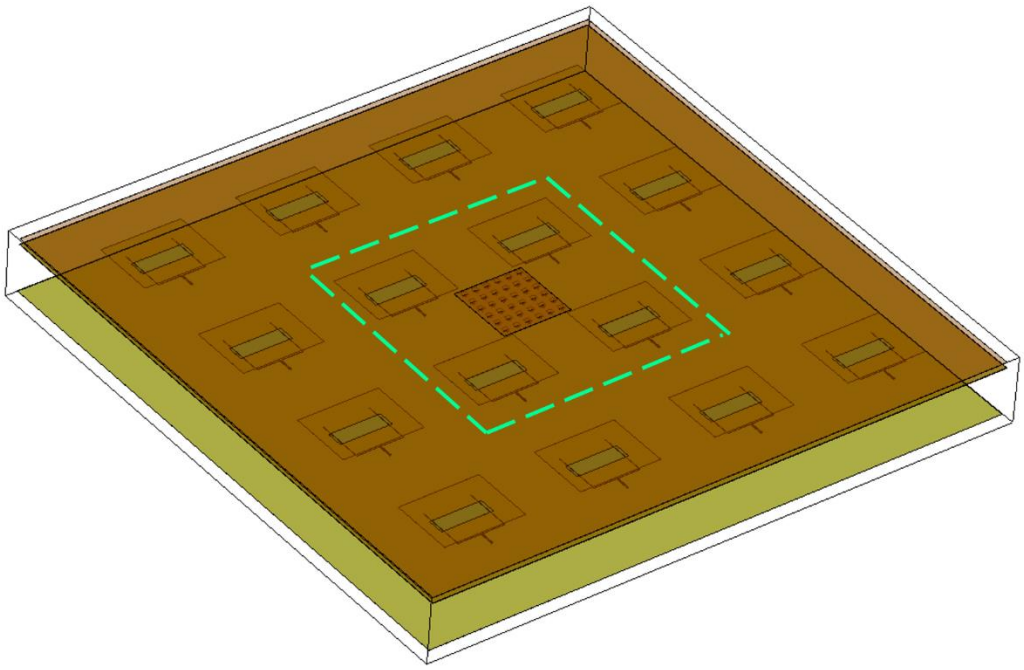

Figure 5. 57 Full shared aperture phased array model

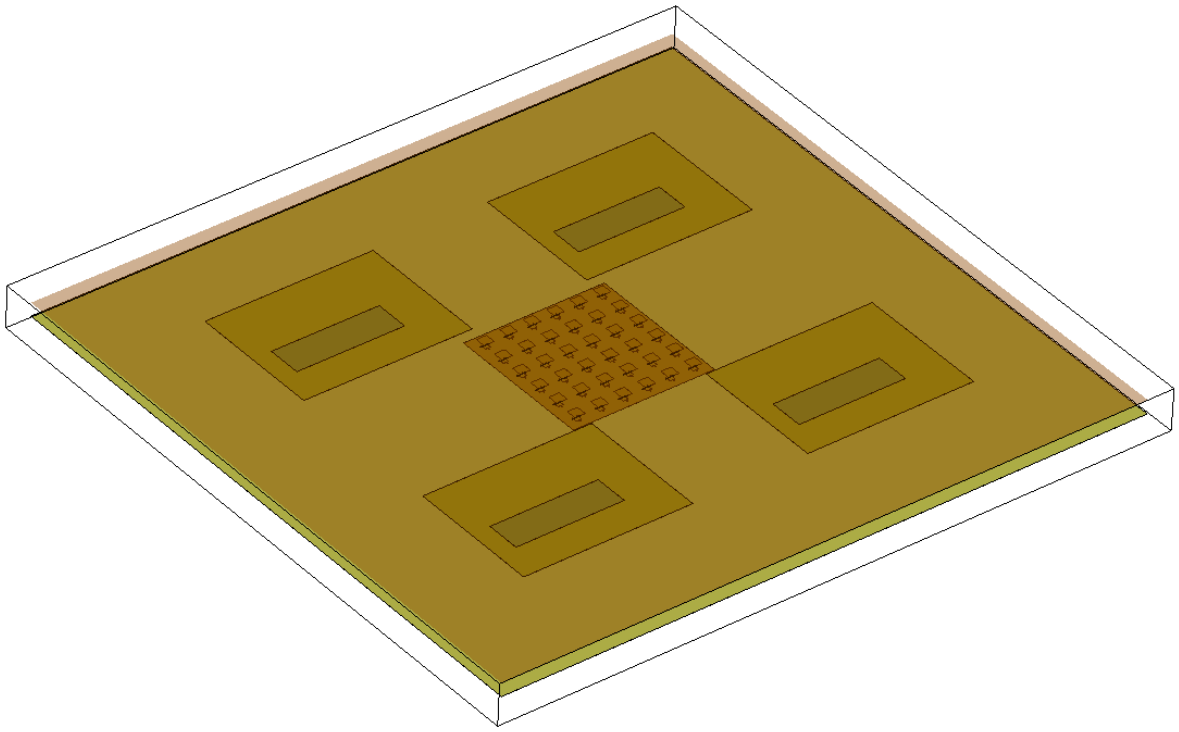

Figure 5. 58 Simplified shared aperture Ku- band phased array with discrete ports

To validate the accuracy of the simplified model, both X-20° and Y+7° were simulated in with a discrete port for each patch antenna as the initial assessment to test its accuracy in both X- and Y-directions. From Figure 5. 59 to Figure 5. 62 ,it can be observed that the radiation patterns of the full and simplified models are rather consistent for both beam steering cases, especially in the main beam and the major side lobes. As a result, the difference in 3-dimensional main beam efficiency is less than 0.69% between two models in both beam steering directions as summarised in Table 5. 17. Therefore, the simplified model can represent the full model for the Ku- band channel with high accuracy, while only requiring 14.3% of the computational workload. In the following parts of the section, the simplified radiation patch will be simulated with the developed Ku- band phased array feed network discussed in Section 5.2, which in this case is a feasible simulation time of a few days.

Table 5. 17 Comparison of 3-Dimensional Main Beam Efficiency between the simplified and full shared aperture Ku-band models

Beam/3-Dimensional Main Beam Efficiency (%)	Full Model	Simplified Model
X-20°	78.82	79.51
Y+7°	82.42	82.26

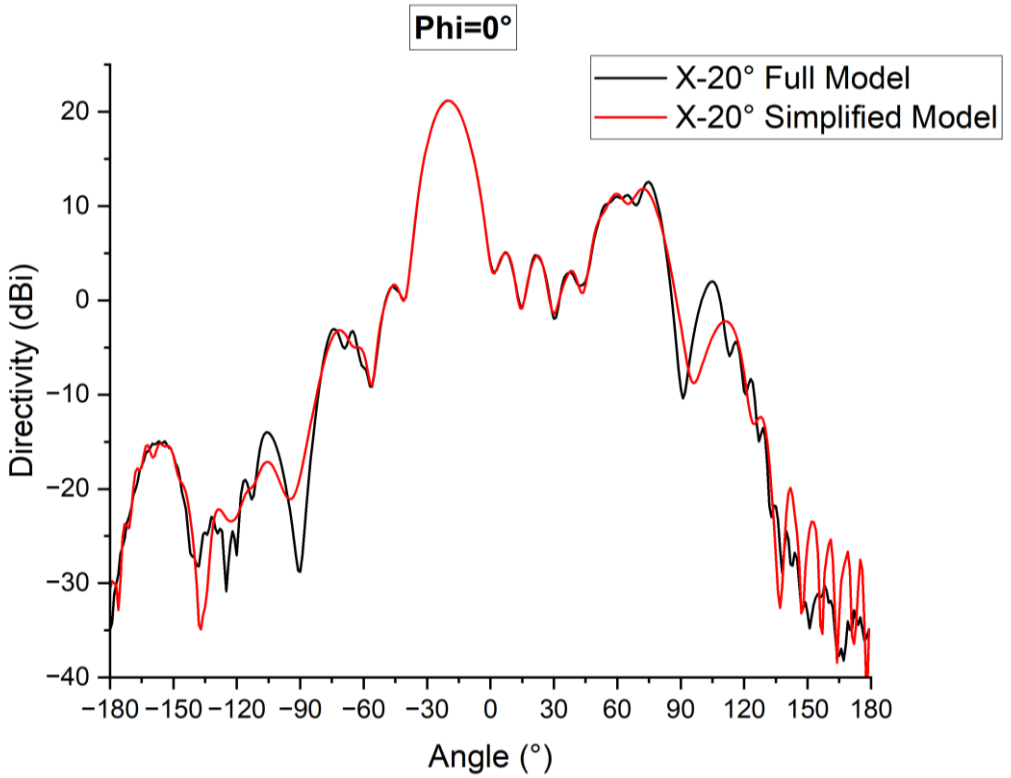

Figure 5. 59 Radiation patterns of the full and simplified model at X-20° in discrete port mode at Phi=0° cut plane

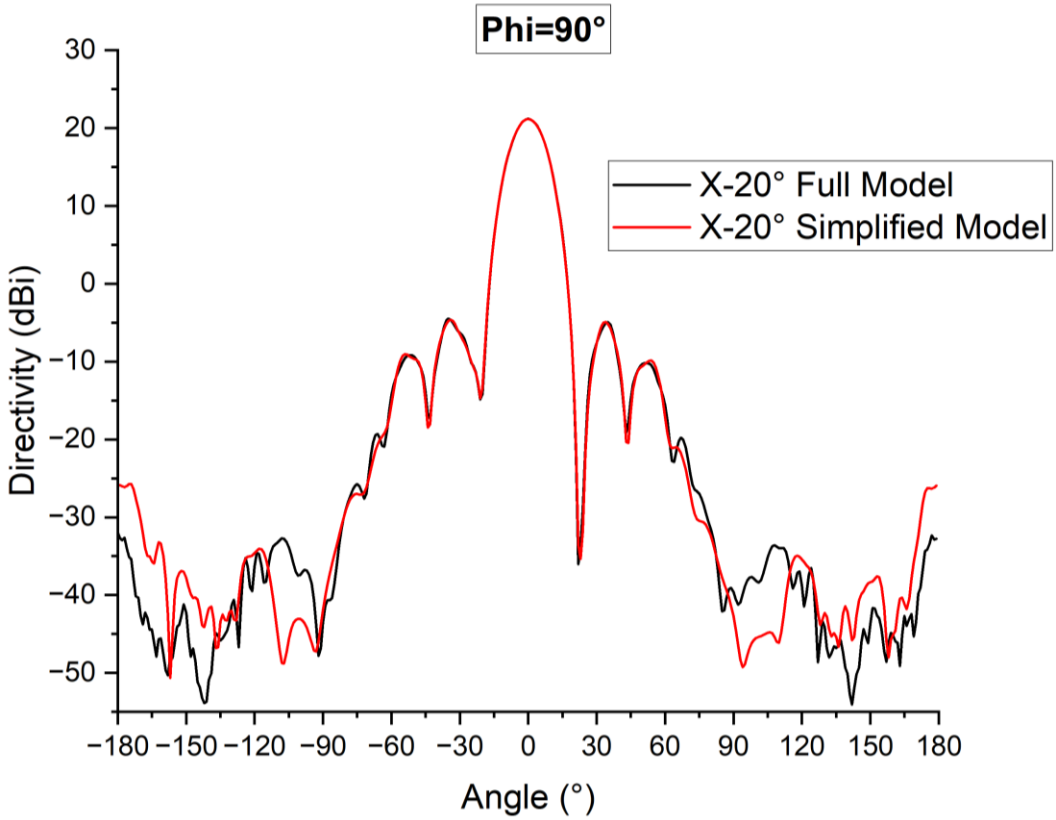

Figure 5. 60 Radiation patterns of the full and simplified model at X-20° in discrete port mode at Phi=90° cut plane

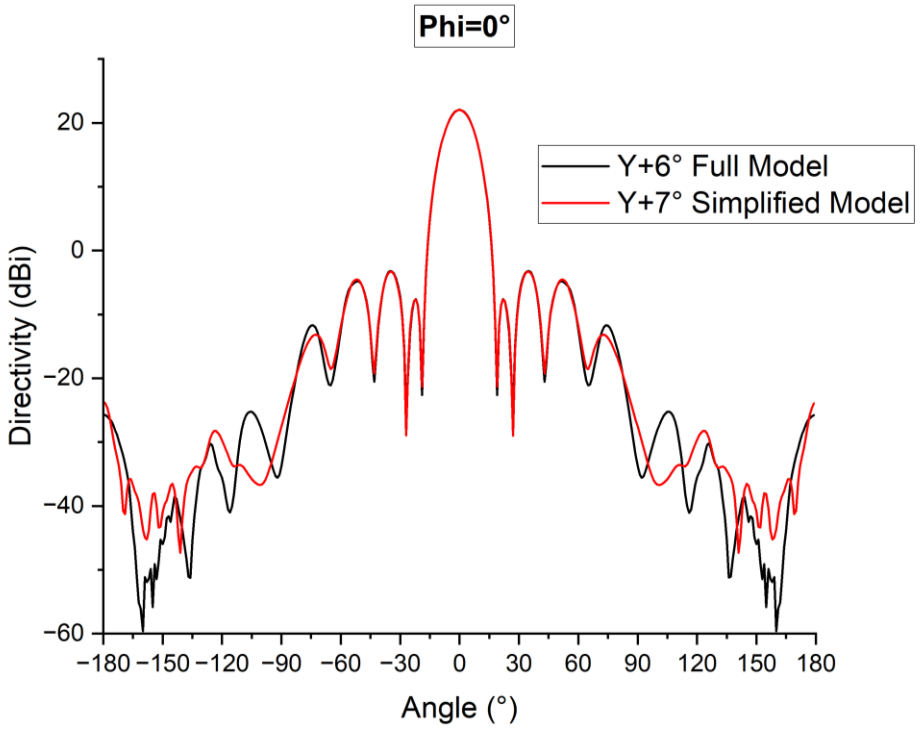

Figure 5. 61 Radiation patterns of the full and simplified model at Y+7° in discrete port mode at Phi=0° cut plane

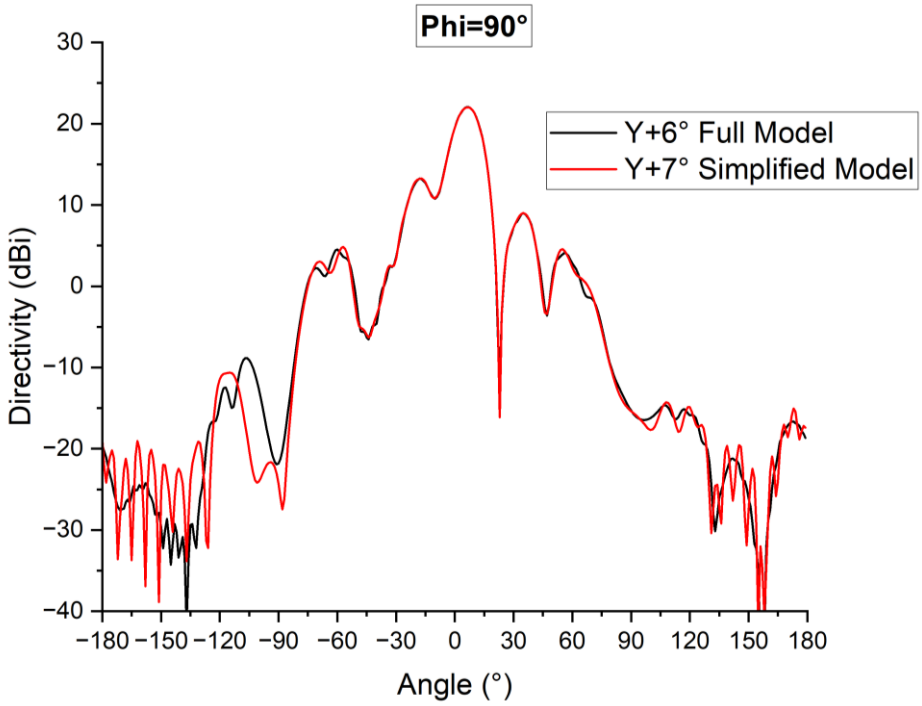

Figure 5. 62 Radiation patterns of the full and simplified model at Y+7° in discrete port mode at Phi=90° cut plane

Being similar the previous section, it can be observed that the shared aperture Ku- band array is still highly symmetrical in the X- direction (as reflected Figure 5. 63 and Figure 5. 65), while being slightly asymmetric in the Y- direction, which can be observed in Figure 5. 66 to Figure 5. 68. Likewise, only the diagonal beams in the positive X- directions are presented, followed by the results discussed in **5.4.1.5 Summary and discussion.**

5.4.1.2 X- Direction

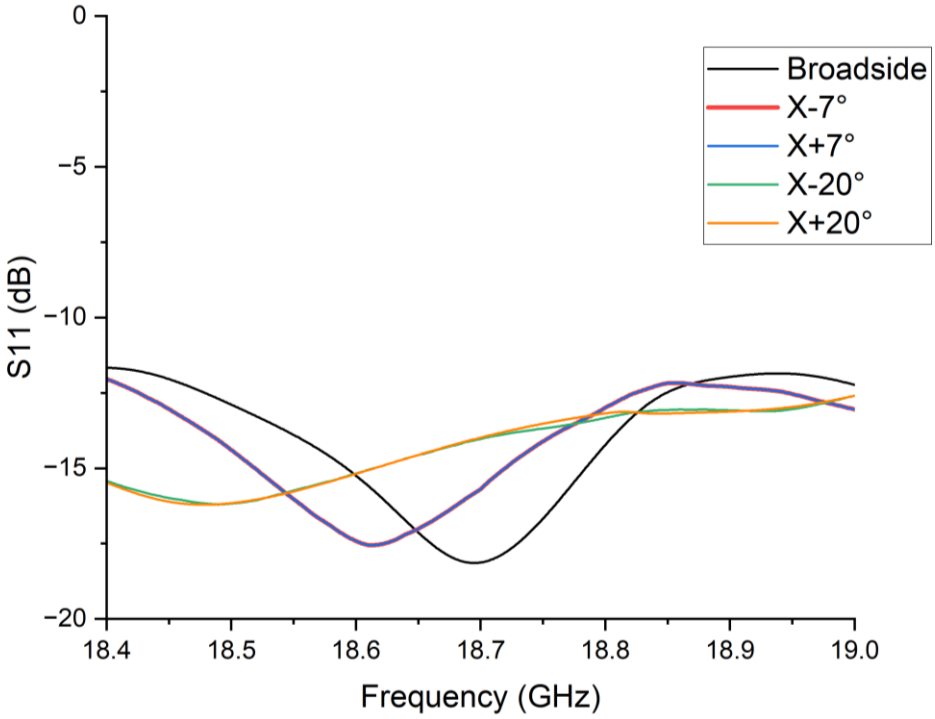

Figure 5. 63 |S11| of the X- direction beams of the simplified shared aperture Ku- band array

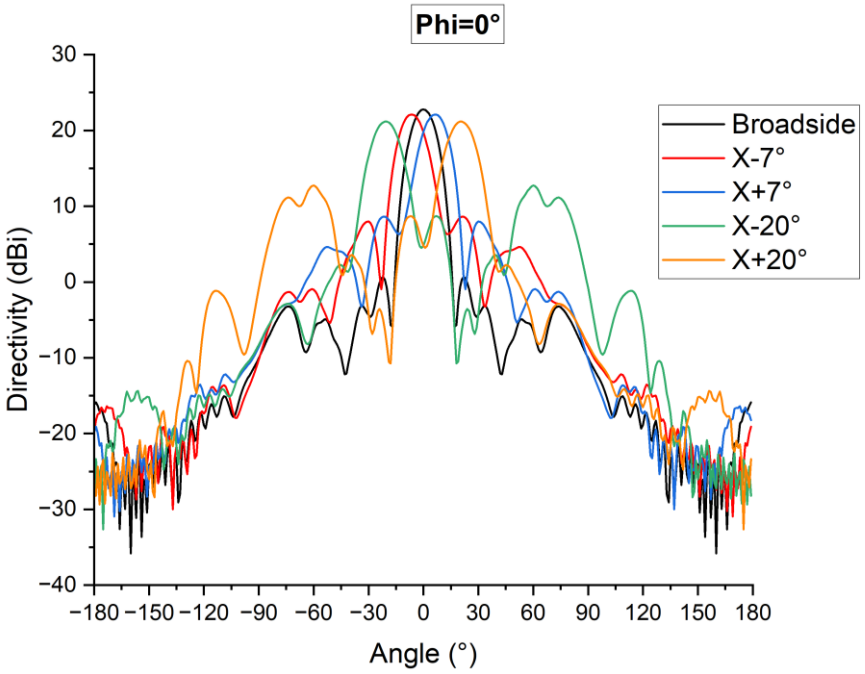

Figure 5. 64 Radiation patterns of X- direction beams of the simplified shared aperture Ku- band array at 18.7 GHz and Phi=0° cut plane

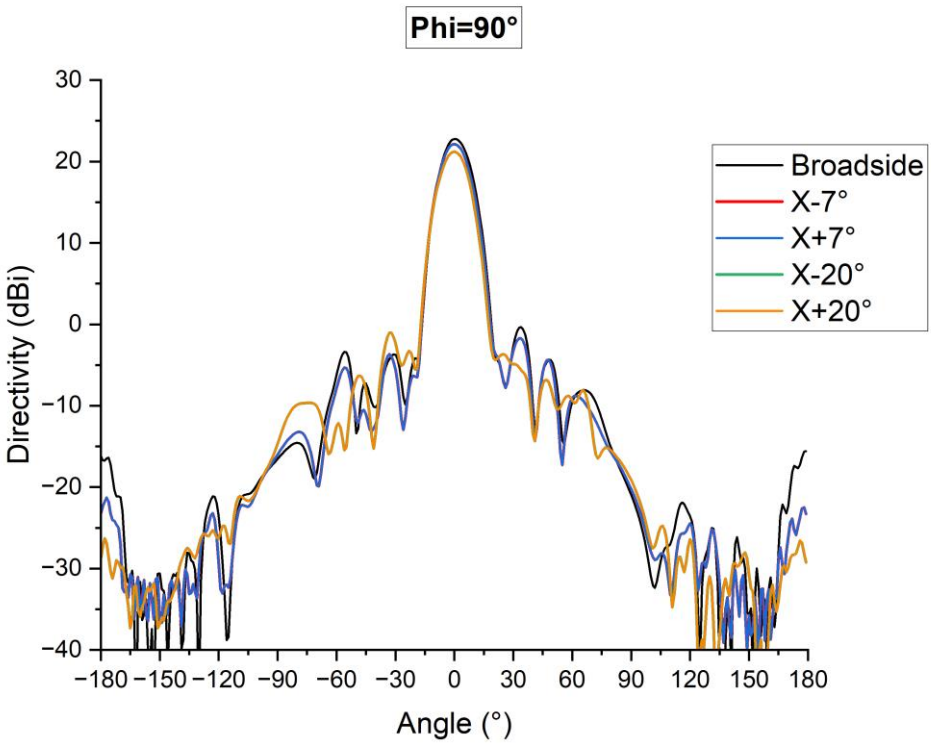

Figure 5. 65 Radiation patterns of X- direction beams of the simplified shared aperture Ku- band array at 18.7 GHz and Phi=90° cut plane

5.4.1.3 Y- Direction

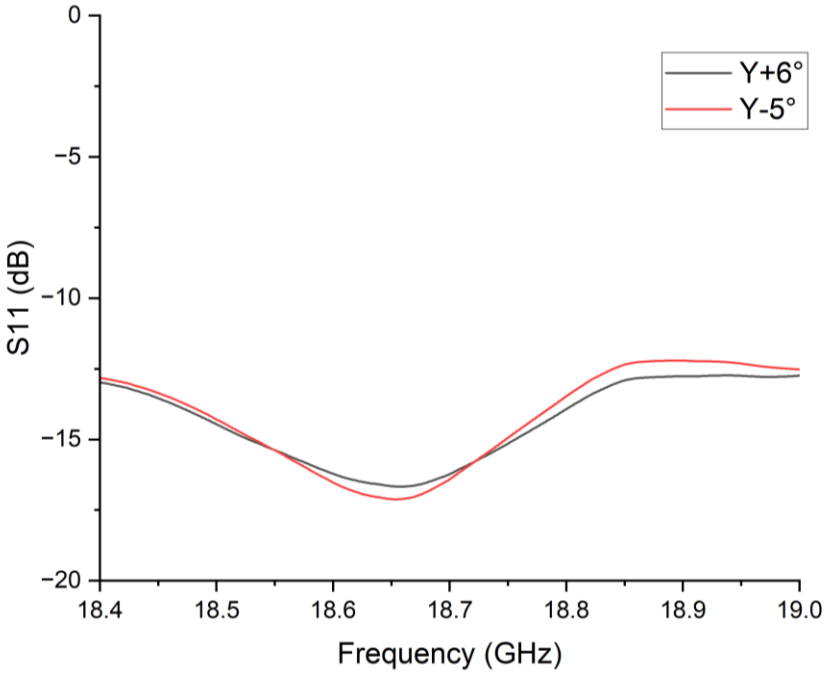

Figure 5. 66 |S11| of the Y- direction beams of the simplified shared aperture Ku- band array

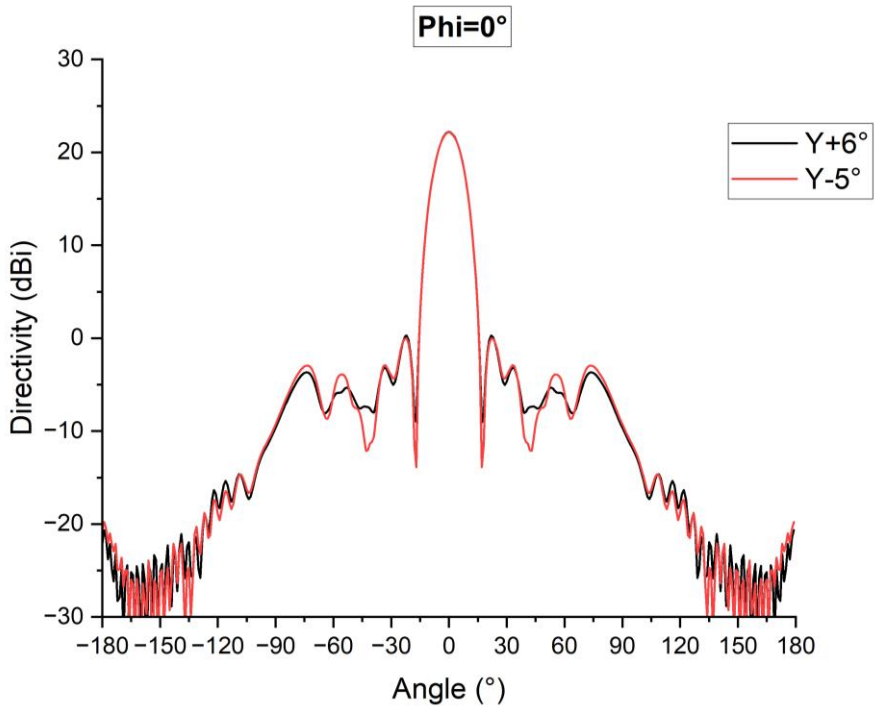

Figure 5. 67 Radiation patterns of Y- direction beams of the simplified shared aperture Ku- band array at Phi=0° cut plane

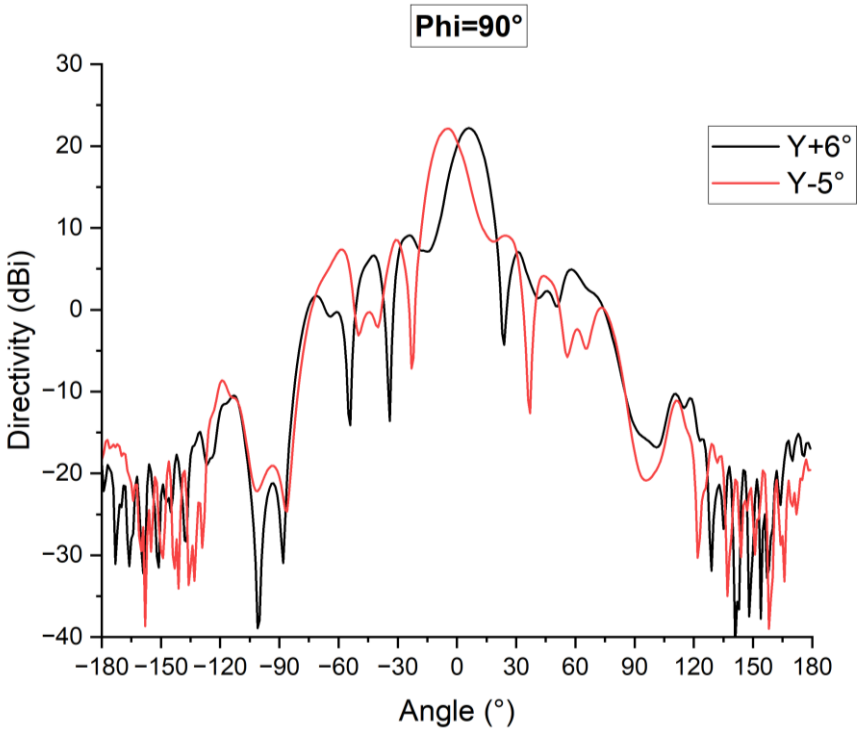

Figure 5. 68 Radiation patterns of X- direction beams of the simplified shared aperture Ku- band array at Phi=90° cut plane

5.4.1.4 Diagonal

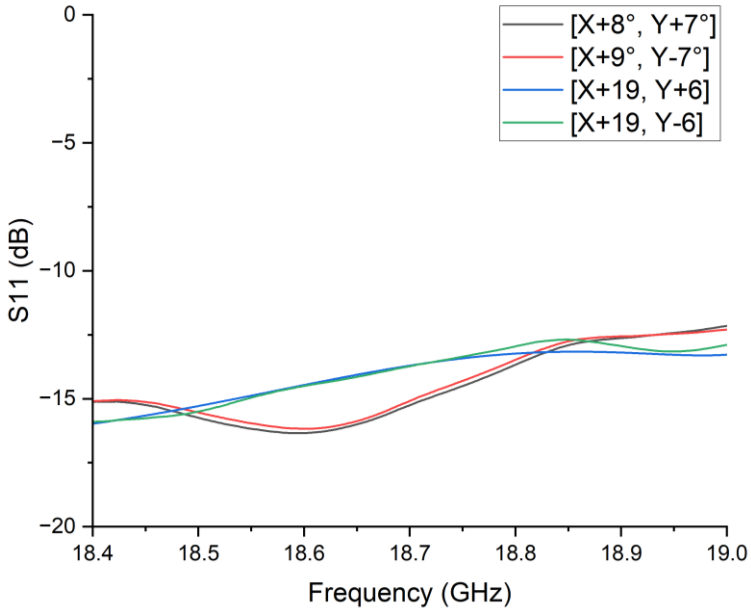

Figure 5. 69 |S11| of the diagonal beams of the simplified shared aperture Ku- band array

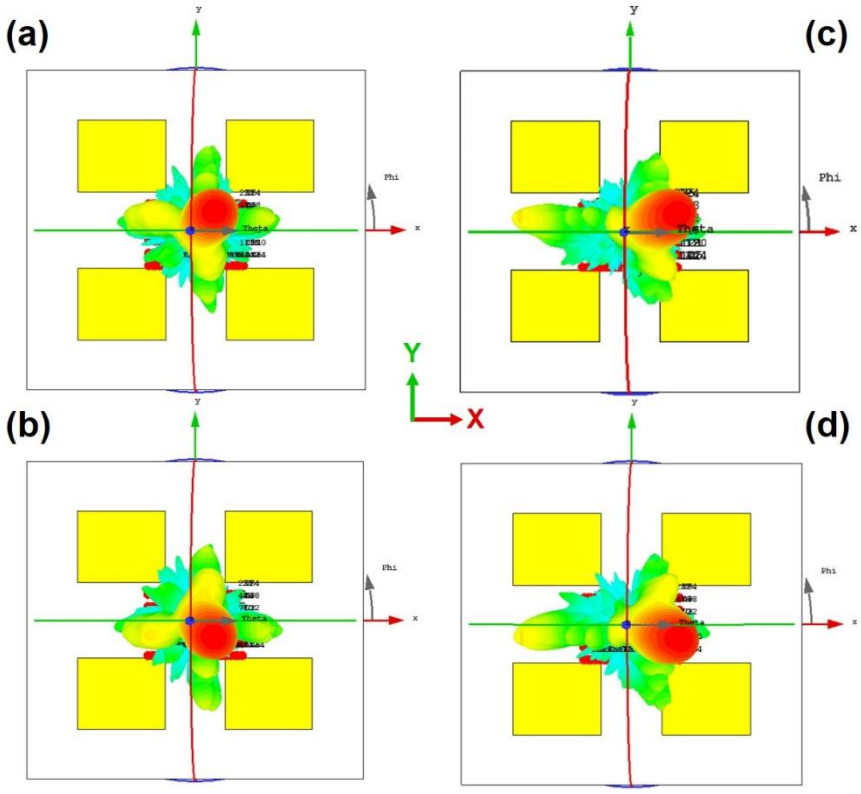

Figure 5. 70 Diagonal beams far field patterns of the simplified shared aperture Ku- band array at 18.7 GHz

(a) [X+8°, Y+7°] (b) [X+9°, Y-7°] (c) [X+19°, Y+6°] (d) [X+19°, Y-6°]

5.4.1.5 Summary and discussion

Table 5. 18 Radiation pattern results summary at 18.6 GHz

Beam	Total loss (dB)	3-Dimensional Main Beam Efficiency (%)	Highest side lobe (dB)
0°	-5.063	96.61	-22.8
X-6°	-5.015	88.27	-11.8
X+6°	-5.015	88.28	-11.8
X-20°	-5.647	77.18	-9
X+20°	-5.647	77.19	-9
Y+6°	-5.088	88.28	-13.3
Y-5°	-5.126	88.27	-13.6
[X+8°, Y+7°]	-5.443	71.78	-11.3
[X+8°, Y-6°]	-5.458	72.05	-11.2

[X+19°, Y+6°]	-5.647	70.34	-10.5
[X+19°, Y-6°]	-5.677	70.73	-9.9

Table 5. 19 Radiation pattern results summary at 18.7 GHz

Beam	Total loss (dB)	3-Dimensional Main Beam Efficiency (%)	Highest side lobe (dB)
0°	-5.173	95.47	-22.1
X-7°	-5.252	87.36	-13.5
X+7°	-5.252	87.35	-13.5
X-20°	-5.819	74.13	-8.4
X+20°	-5.819	74.13	-8.4
Y+6°	-5.308	85.88	-13.1
Y-5°	-5.337	86.65	-13.1
[X+8°, Y+7°]	-5.602	68.02	-9.9
[X+9°, Y-7°]	-5.589	68.51	-9.3
[X+19°, Y+6°]	-5.603	71.19	-10
[X+19°, Y-6°]	-5.644	70.46	-9.8

Table 5. 20 Radiation pattern results summary at 18.8 GHz

Beam	Total loss (dB)	3-Dimensional Main Beam Efficiency (%)	Highest side lobe (dB)
0°	-5.565	94.95	-22.1
X-7°	-5.694	84.81	-11.6
X+7°	-5.694	84.81	-11.6
X-20°	-6.153	72.94	-8.1
X+20°	-6.153	72.94	-8.1
Y+7°	-5.665	84.41	-12.6
Y-6°	-5.702	83.55	-12.3
[X+8°, Y+7°]	-5.876	60.93	-8.4
[X+9°, Y-7°]	-5.858	61.05	-8.1
[X+19°, Y+6°]	-5.826	69.64	-10.1
[X+19°, Y-6°]	-5.861	68.62	-9

In summary, as per Table 5. 18 to Table 5. 20, the total efficiency of each beam is better than -5.677 dB, -5.819 dB and -6.153 dB at 18.6 GHz, 18.7 GHz and 18.8 GHz respectively, which is similar to those of the isolated Ku- band phased array. Likewise, this antenna has its best radiation efficiency at 18.6 GHz, and lowest radiation efficiency at 18.8 GHz for most of the beams.

In terms of 3-dimensional beam efficiency, all the one-dimensional scanned beams are better than 72.94% over the radiometric bandwidth. While most of the diagonally scanned beams have efficiency around 70%. These values are also very similar to those of the isolated Ku- band array.

Overall, being similar to the fixed beam array, it can be observed that sharing the aperture with the L- band array does not have significant effect on the Ku- band phased array.

5.4.2. Shared aperture L- band array

In terms of the full shared aperture array in the L- band simulation, significant pattern distortion can be observed as shown in Figure 5. 71. This is because the extended Ku- band phased array feedline has become noticeably large and interferes with the coupling between the L- band patch and feedline. As illustrate in Figure 5. 72 one way to reduce this effect is to move the Ku- band patches and feedline off the centre where the patches have lower split power.

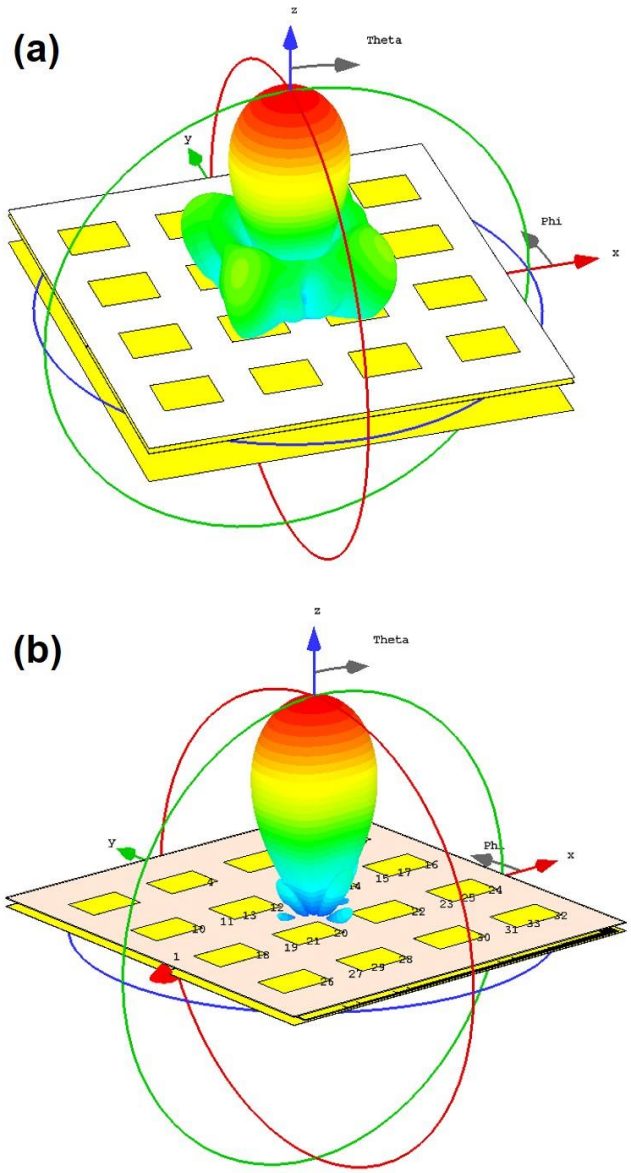

Figure 5. 71 (a) Broadside radiation pattern distortion at the L- shared aperture array (2) Reference broadside radiation pattern of the L- band phased array presented in Chapter 4

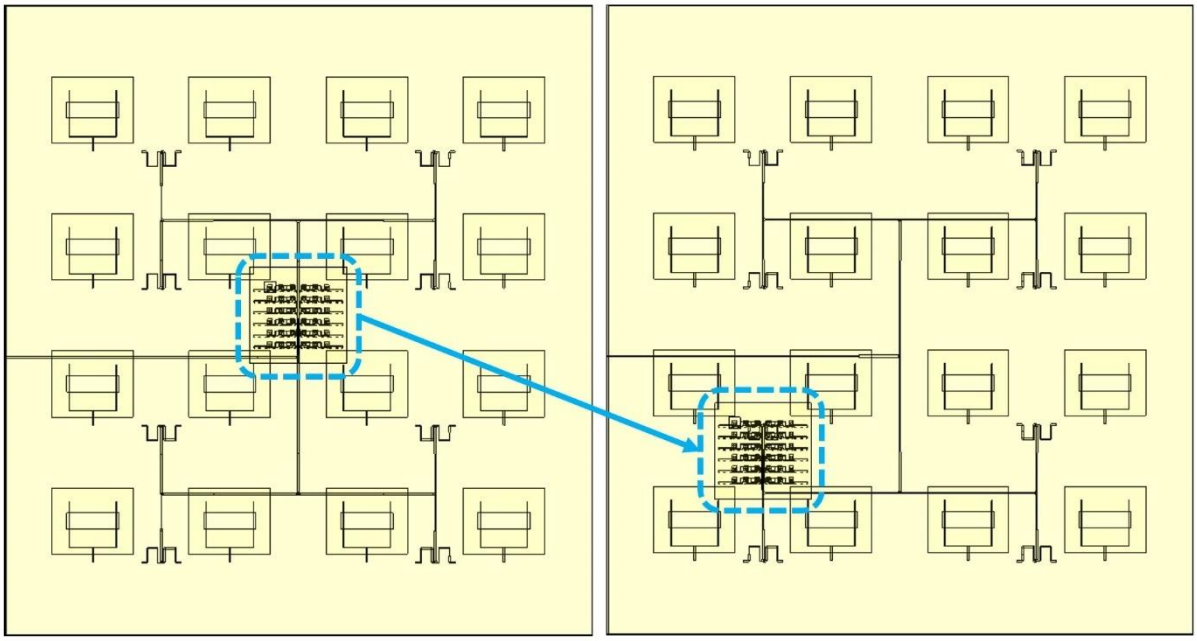

Figure 5. 72 Transparent view of the shared aperture phased array and moving the Ku- band phased array off the centre

As a result of shifting the Ku-band array, the level of pattern distortion at L-band has been reduced to moderate as suggested in Figure 5. 73. For a clear comparison, it can be observed from Figure 5. 74 to Figure 5. 76 that the side lobe levels are notably lower in all X- directional beams for the case of the offset Ku-band array. Likewise, over 12% improvement in 3-dimensional main beam efficiency can be observed by moving the Ku- band array off centre, resulting in an efficiency of better than 83% for all the required X- directional beam as summarised in Table 5. 21 and Table 5. 22. However, as a trade-off of interfering one quarter of the feed network rather than the centre area, a minor level of asymmetry in the X- direction can be observed by moving the Ku- band array to the side. This is reflected in very different |S11| curves of the X-19° and X+21° beams (in Figure 5. 77) along with the difference in pointing angles. Furthermore, as depicted in Figure 5. 75 and Figure 5. 76, the radiation patterns of the X-19° and X+21° beams are distinctly different, resulting in different highest side lobe levels as summarised in Table 5. 21 and Table 5. 22. Provided that positioning the Ku- band array in the centre results in significant radiation pattern distortion and poor main beam efficiencies, the improvements from moving the Ku- band elements away aside outweigh the minor effect of asymmetry. Overall, the results are considered to be demonstration of the proof of concept and simulation design work for the L-/Ku- band shared aperture design.

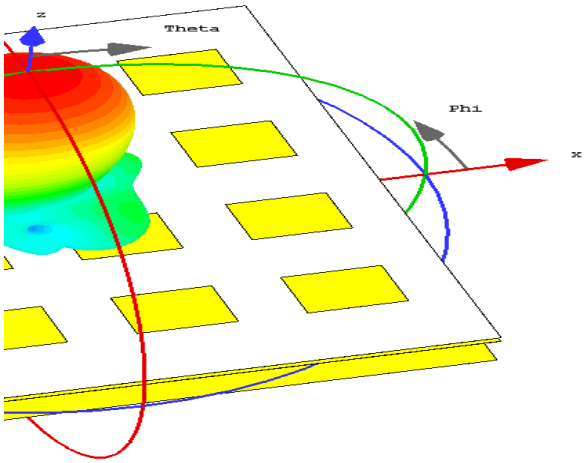

Figure 5. 73 Radiation pattern distortion at L- shared aperture array by moving the Ku- band array off the centre

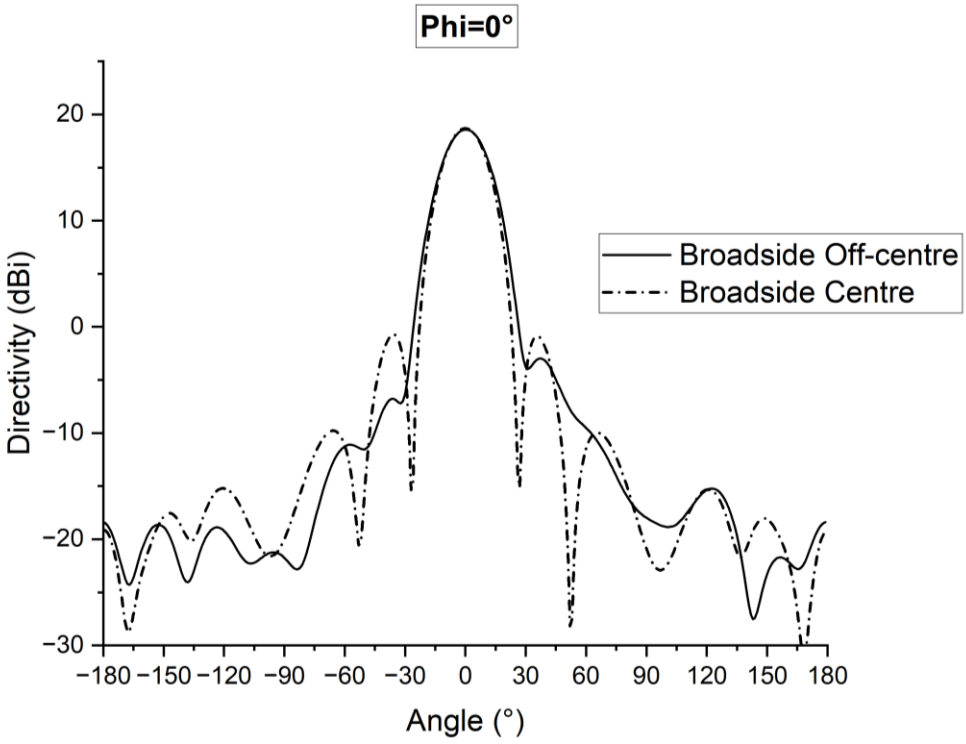

Figure 5. 74 Radiation patterns of the broadside shared aperture L- band beams at Phi=0° cut plane

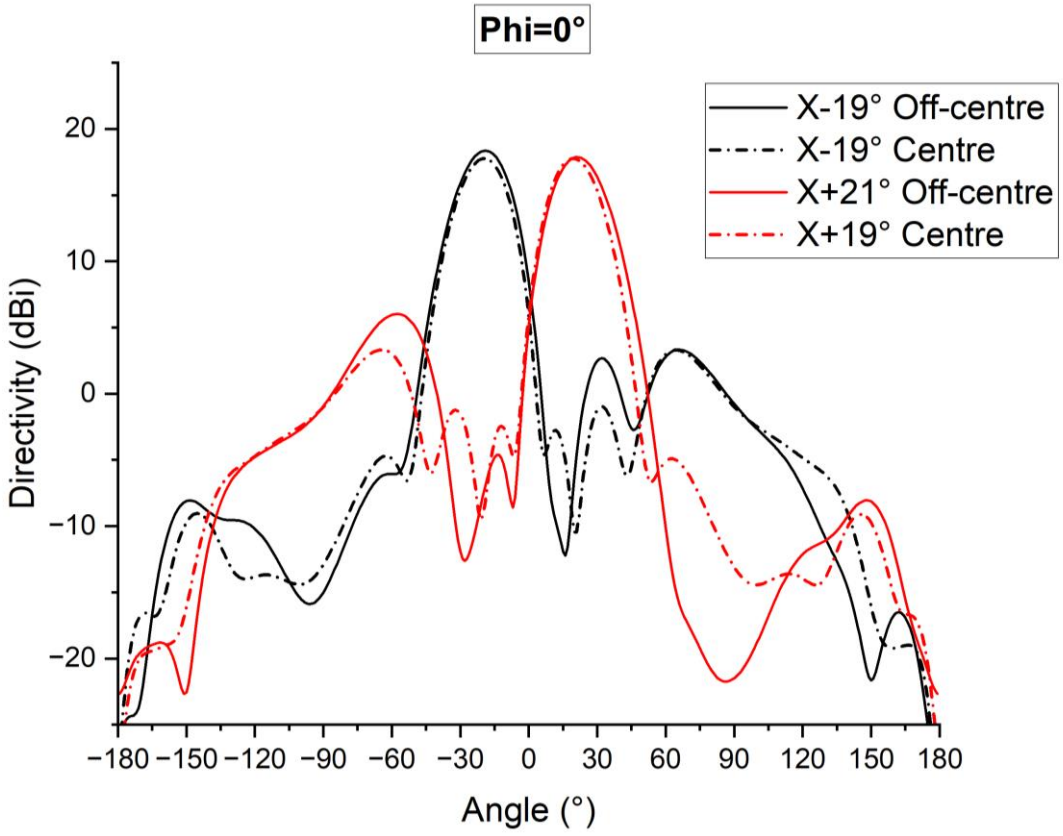

Figure 5. 75 Radiation patterns of the X±20° shared aperture L- band beams at Phi=0° cut plane

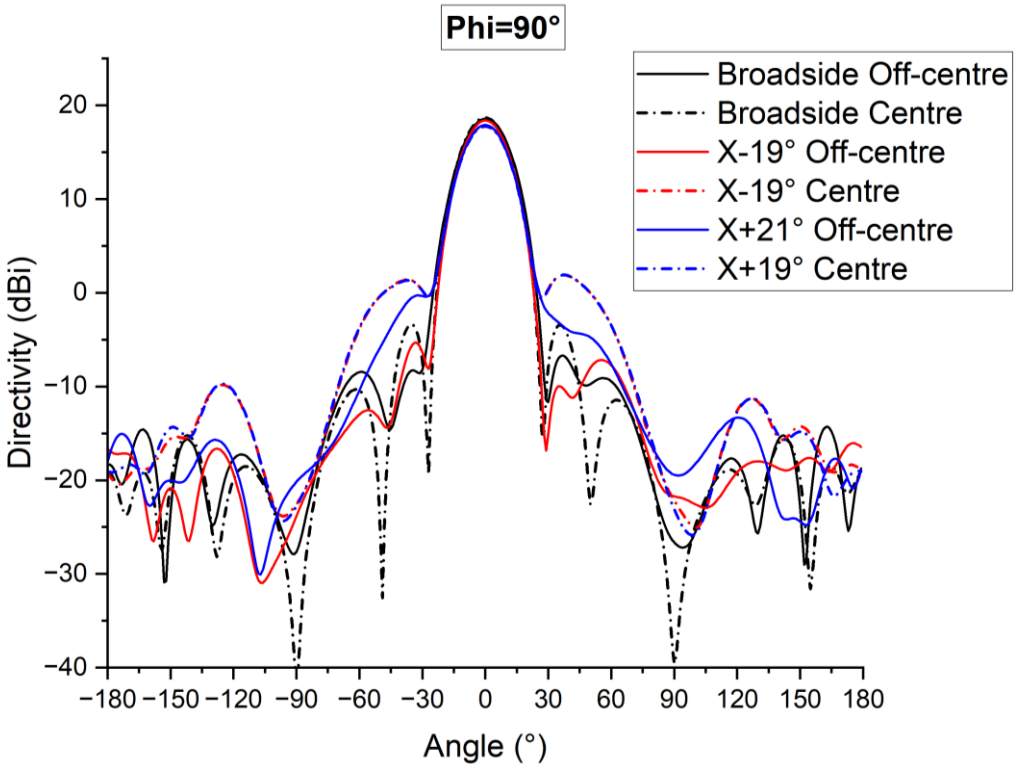

Figure 5. 76 Radiation patterns of the X- direction shared aperture L- band beams at Phi=90° cut plane

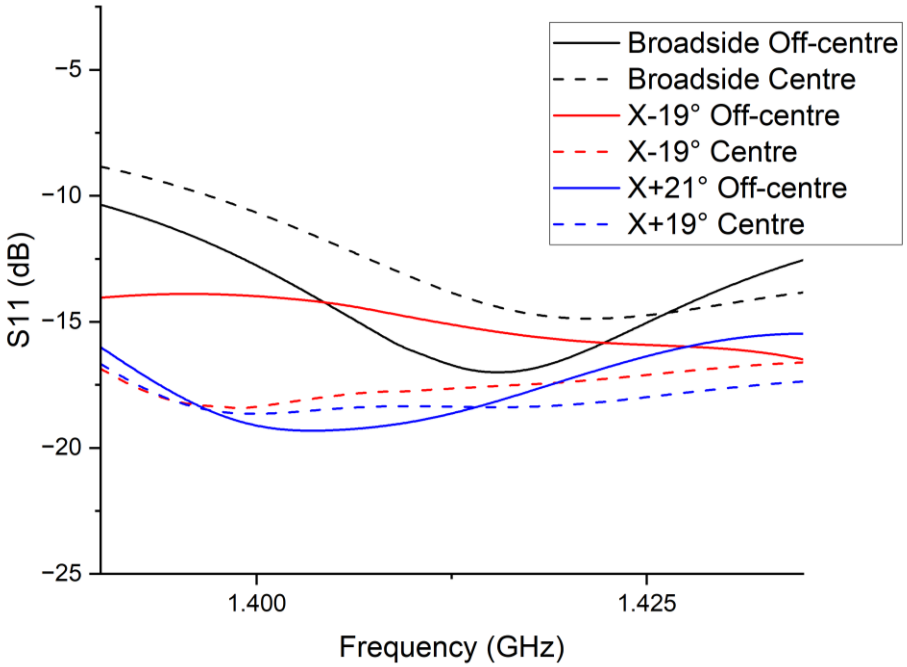

Figure 5. 77 |S11| of the X- direction beams of the L- band shared aperture phased arrays

Table 5. 21 Radiation pattern results summary at 1.4 GHz

Beam	Total loss (dB)		3-Dimensional Main Beam Efficiency (%)		Highest side lobe (dB)	
	Centre	Off-centre	Centre	Off-centre	Centre	Off-centre
0°	-1.800	-1.602	82.77	94.11	-19.4	-21.6
X-19°	-1.609	-1.777	72.69	86.40	-14.5	-15
X+19° (X+21° when off-centre)	-1.611	-1.649	72.59	85.64	-14.4	-11.8

Table 5. 22 Radiation pattern results summary at 1.425 GHz

Beam	Total loss (dB)		3-Dimensional Main Beam Efficiency (%)		Highest side lobe (dB)	
	Centre	Off-centre	Centre	Off-centre	Centre	Off-centre
0° (1° when off-centre)	-1.560	-1.572	75.86	93.05	-19.6	-23
X-20°	-1.635	-1.777	68.19	83.34	-13.2	-14.2
X+20°	-1.611	-1.724	67.95	83.93	-13.2	-12.8

5.5 Chapter summary

This chapter presents the simulation design of an unprecedented L-/Ku- band shared aperture phased array design. At the beginning of the chapter, a 6x6 Ku- band array is found to be the optimal configuration for the shared aperture design. In the next part, irregular three-way power dividers have been designed to reduce space consumption and feedline losses, leading to the tapered 6x6 Ku- band fixed beam array. For the shared aperture fixed beam array, the L- band ground plane has also been used as the metal back reflector of the Ku- band array, and by separating the feedline layers, excellent channel isolation can be observed, while pattern distortion is found to be minor in both channels. For the Ku- phased array, coupling issues in the vertical power divider have been investigated by cutting out air slots to reduce the port imbalance and correcting the pointing beam point angle. Radiation efficiency can also be improved by being careful to use only low loss bit states for the centre elements of the array. Finally, a simplified shared aperture model has been simulated at Ku- band for realistic simulation run time. Being similar to the shared aperture fixed beam array, pattern distortion is found to be minor at Ku- band. However, owing to the extend Ku- band phased array feedline layer, significant pattern distortion can be observed at L- band if the Ku- band array is place at the centre of the 4x4 L- band array.

Moving the Ku- band array off the centre can notably improve the L- band shared aperture radiation pattern, leading to overall satisfactory results to conclude this study.

At this point, the proof of concept and the antenna design work required for a novel L-/Ku- band shared aperture phased array has been completed. In here, the Ku- band phased array has the capability to generate overlapping high-resolution footprints to cover the low-resolution X-directional L- band footprints, which is the key concept for an unprecedented high-resolution dual-band airborne simulator to demonstrates the first-stage shared aperture phased array design for passive soil moisture remote sensing, and potentially new satellite design concept. Moreover, as compared to the conventional separate radiometer systems with bulky mechanical scanning parts, the proposed shared aperture electronic scanning design can also notably reduce airborne payload and hence make rooms for other sensors. The next chapter is to summarise and conclude this study, along with recommendations for future work. An initial proposal for a Ka- band phased array using 2-bit phase shifters to complete the blue print of tri-band beam scanning scheme will be presented in Appendix A.

Chapter 6. Conclusions and Future work

6.1 Conclusions

The ultimate goal of this study is complete the antenna design work of a novel L-/Ku- band shared aperture phased array radiometer antenna system for high resolution airborne remote sensing, and potentially to facilitate the simulation of a new satellite design concept in the airborne platform. The stage-by-stage design work to fulfil this goal has been presented following the sequence of earlier chapters. Along this journey, the original contributions can be summarised as followed:

(1) Chapter 2 presents a comprehensive review on the current development of satellite missions and downscaling approaches for passive high resolution global soil moisture mapping, radiometer antennas in the airborne platform, and thereby an unique perspective on the driven research gap of an L-/Ku- band shared aperture phased array radiometer antenna, with microstrip patch antenna array being the most suitable antenna type to meet compactness, shared aperture and beam steering requirements at the same time for the airborne platform.

(2) Chapter 3 and 4 presents a comprehensive hardware design flow of a compact and low-cost 4x4 L- band radiometer phased array system, from the fundamental single patch element design, to tapered feed network to suppress side lobe level, then beam scanning plan, phase shifter integration, driving electronics design, and at last assembly and measurements. By using a low-cost FR-4 as the substrate material for the radiating patch layer, the fabrication cost reduces for about $900 AUD per board as compared to that of using Taconic TLX-8 substrate. When comparing this design to the state of are PLMR radiometer which has one dimensional scanning capability [20, 83], although its scanning range is smaller, this phased array is capable of two dimensional scanning in both X- and Y- direction. Further, the measurement results of impedance matching and radiation patterns are considered to be satisfactory

(3) Chapter 5 presents the most important contributions of this study, which is the design of an unprecedented L-/Ku- band shared aperture phased array. This shared aperture phased array is able to demonstrate the key design concept which is to generate overlapping high-

resolution Ku- band footprints to cover the low-resolution L- band footprints, while the radiation pattern distortion is minimised by optimum array configuration and Ku- band array positioning. This design can also notably reduce airborne payload by removing the need of bulky mechanical scanning parts, and make rooms for other sensors to be deployed on board.

(4) Also included in this thesis, Appendix A presents a Ka- band beam scanning plan using 2-bit phase shifters, which is complete the blue print of tri-band overlapping beam scanning scheme to meet the essential requirements of the ARC Discovery Project. Appendix B presents the system level simulation of a Ka- band Dicke type radiometer which has been included in a joint publication [115], and the detailed development of an L- band total power receiver PCB prototype. This receiver prototype completes an L- band radiometer system with the phase array antenna discussed in (2), which are aimed to be deployed into linear irrigators for real time soil moisture monitoring upon further developments and integration.

6.2 Future work

6.2.1 Further development of the L-/Ku- band shared aperture phased array antenna and system prototype

Although all the required proof of concept and antenna design work for an unprecedented L-/Ku-band shared aperture phased array has been completed to fulfil the ultimate goal of this study, further developments are required to fabricate and deploy this antenna for field experiments, those include:

- Similar to Section 4.4 (in Chapter 4), developments of driving electronics for controlling the 2-bit Ku- band phase shifters are required.
    (1) Given this Ku- band phase shifter requires $\pm 10V$ for forward and reverse bias states [27], based on the author's limited knowledge, one feasible approach is a cascaded switch circuit using an NPN followed by a PNP as illustrated in *Figure 6. 1*.

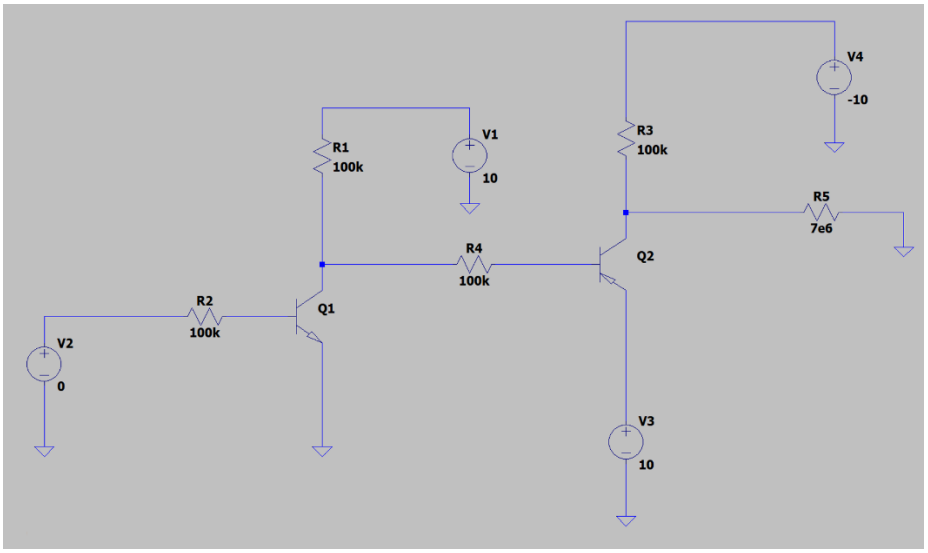

Figure 6. 1 Proposed switch structure for the Ku- band driving electronics

(2) Along with 2 x 36 digital outputs for the 6x6 Ku- band phased array, a further 2 x 16 digital outputs are required for the 4x4 L- band phased array in a shared aperture setting. This in turn requires a total number of 72+32=104 independent digital outputs to control this shared aperture phased array, which is beyond the digital output capability of any commercial microcontroller by itself. In this sense, adding general-purse input/output (GPIO) expansion modules to one microcontroller would be a viable option as compared to using multiple microcontrollers at the same time.

(3) Although preliminary hardware prototypes of the above two points have been developed and tested during the candidature of this PhD study, the levels of completion are not sufficient to be documented into this thesis.

(4) Upon fabrication, in the event of aperture distortion not being suppressed as simulated, higher side lobe level may be observed at the L- band array, leading to low main beam efficiency under 80% for X±20° beam. One alternative is to move the Ku- band array further away from the 4x4 L- band array as illustrate in Figure 6. 2, at a cost of expanding the overall shared aperture array size.

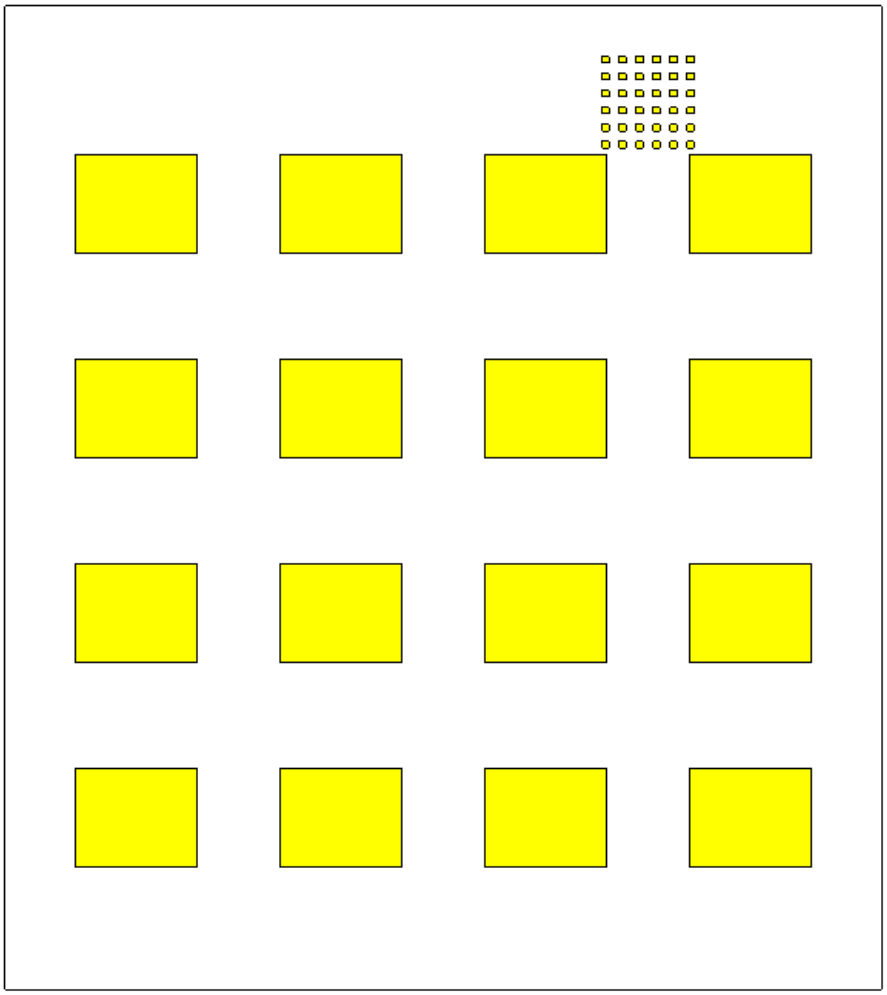

Figure 6. 2 Moving the 6x6 Ku- band array further away as an alternative approach to suppress pattern distortion

- Unlike the protected 1.4 – 1.425 GHz L- band, there are commercial down conversion modules and evaluation boards available at Ku- band. To the best of the author's understanding, those can be adopted as the radiometer receiver prototype for initial testing, rather than having to develop the receiver from scratch as presented in Appendix B.
- Upon successful testing of the radiometer system, radome design will be required for the dynamic airborne environments. Low loss, low dielectric constant, low moisture absorption and high mechanical strength materials, such as epoxy-based prepreg and quartz fabric composites should be considered [158, 159].

6.2.2 Development of the Ka- band aperture coupled patch antenna phased array

Provided that the beam scanning blue print using Ka- band 2-bit phase shifters have been proposed in Appendix A, similar to the design work flow presented in Chapter 4, the next steps shall be:

- Design of a fixed beam tapered power divider feed network for the 12x12 Ka- band antenna array
- Fabrication and measurements of the Ka- band 2-bit phase shifter developed by Dr. Trong Khoa Ho [29]
- Modifications to the feed network for the integration of phase shifters, importing phase shifter measurement results, and finalised the simulation design through iterations of fine tuning
- Design of driving electronics
- Fabrication, assembly and measurements.

Given the inter-element distance is only 6.4 mm for the Ka- band array, which is almost half to that of the Ku- band array at 12mm; while the feed network complexity would be notably higher for a 12 x12 array (as compared to that of the 6x6 Ku- band array), the author foresees that the development of the Ka- band phased array by itself would be a very challenging task with highly congested feed network design. Upon completion, helpful guidance for further shared aperture development could be referred to [26].

Appendix A. Ka- band phased array beam scanning proposal

A.1 Footprint size requirements

As per the ARC discovery project proposal (as illustrated in Figure A. 1), to achieve overlapped scanning footprints for high resolution soil moisture mapping, the footprint of the Ku- band antenna shall be half of L- band footprint; while Ka- band footprint shall be about half of Ku- band footprint. According to the current project development, Table A. 1 shows the half power beamwidths of the designed antennas, since the half power beamwidth of the 6x6 Ku- band phased array is 13.6°, it would be expected that the targeted half power beamwidth of the Ka- band shall in the range of 5-8° (i.e., 8° beamwidth would the maximum acceptable beamwidth).

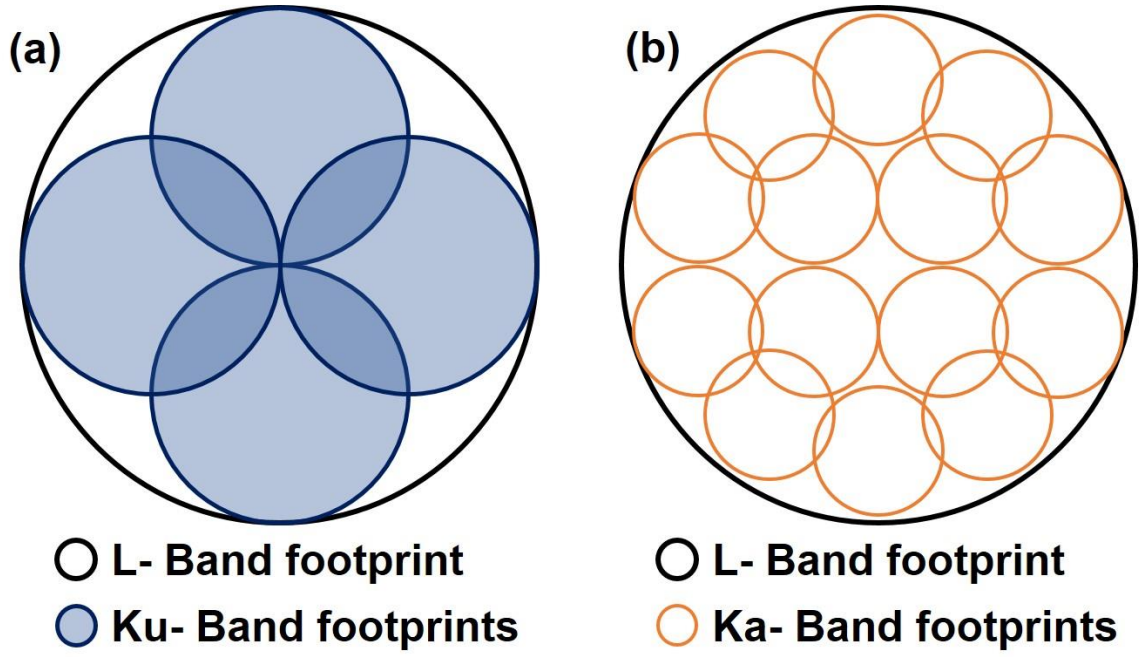

Figure A. 1 Scanning footprints concept referred to the ARC Discovery Project Proposal (a) L- and Ku- band (b)L- and Ka- band

Table A. 1 L- and Ku- band antenna 3dB beamwidth

Frequency	Array configuration	Half power beamwidth at Broadside beam and Phi=0° cut plane
1.4 GHz (L- band)	4x4	22.4°
18.7 GHz (Ku- band)	6x6	13.6°

A.2 CST pattern estimation of the Ka- band array

Based on the beamwidth requirement, antenna pattern synthesis has been conducted in CST Microwave Studio using a single Ka- band patch antenna. This single patch antenna is redesigned based on Dr. Muhsiul Hassan's work [28] , and has been modified to focus on single polarisation in this version.

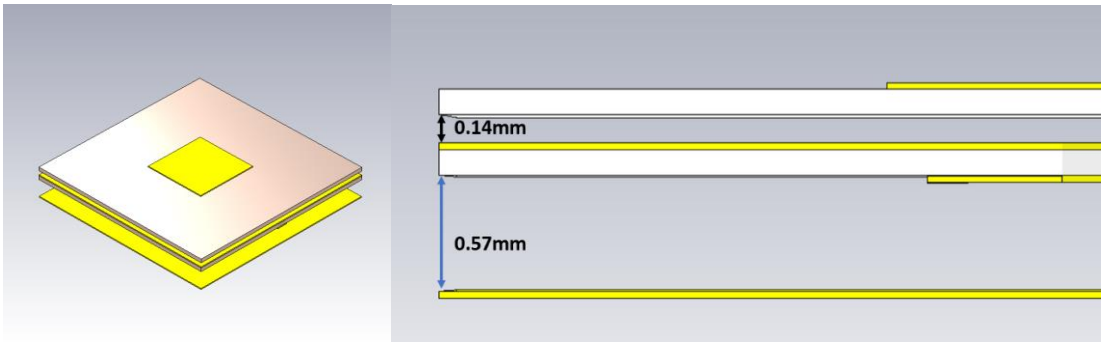

Figure A. 2Redesigned Ka- band single patch antenna

This antenna exhibits good matching at around 37 GHz, leading to a total loss of -0.3374 dB and a realised gain of 8.759 dBi. The antenna also shows a standard single patch antenna radiation pattern, with half power beamwidth at 69.4° and 58.4° at Phi=0° and Phi=90° cut plane respectively.

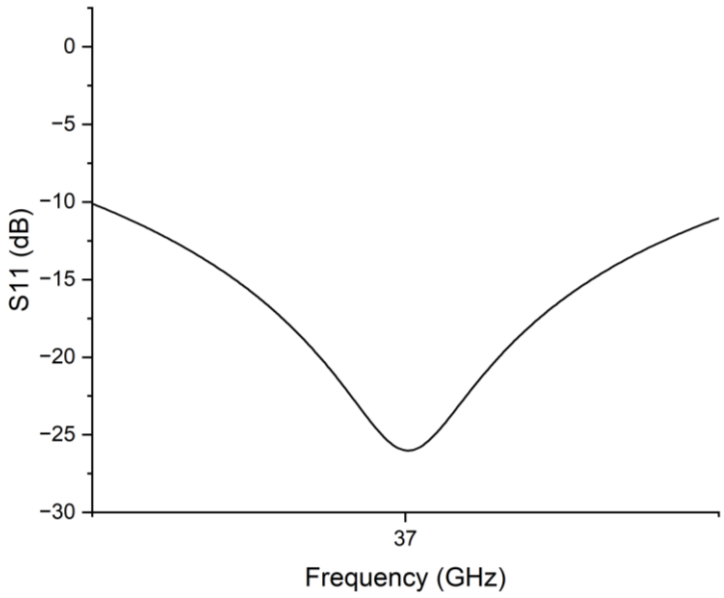

Figure A. 3 |S11| result of the single patch antenna

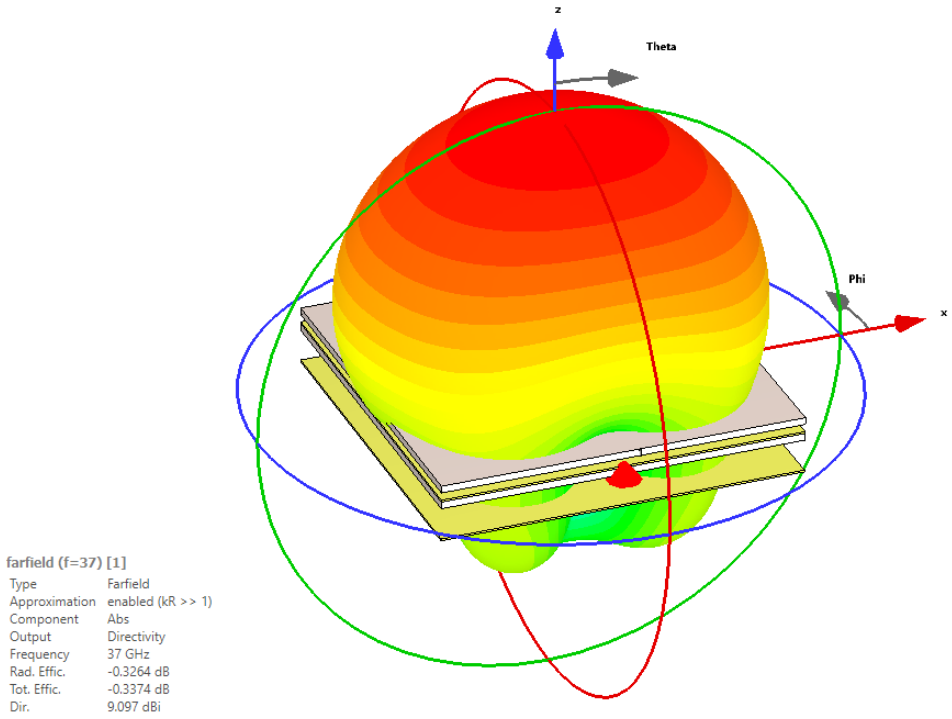

Figure A. 4 3D Farfield pattern of the single patch antenna

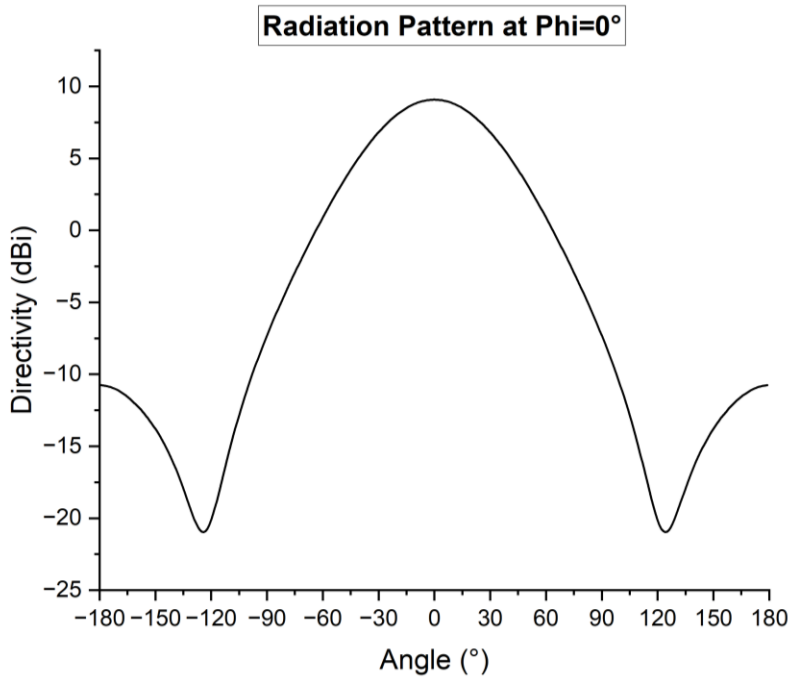

Figure A. 5 Radiation pattern of the single element at Phi=0° cut plane

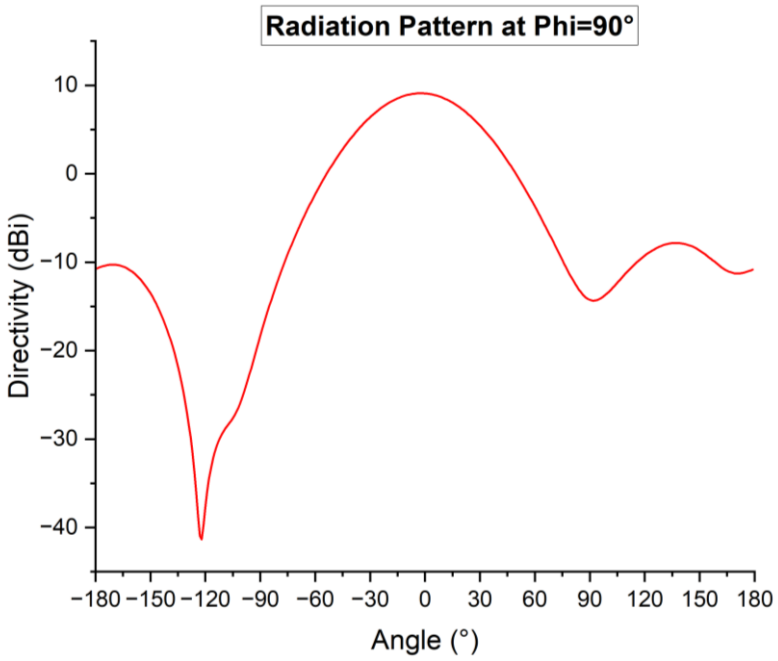

Figure A. 6 Radiation pattern of the single element at Phi=90° cut plane

Using the similar procedures for array synthesis discussed in Chapter 4, the designed single patch antenna pattern has been used to activate the Farfield Array function in CST Microwave Studio. For the initial set up, an 8x8 array configuration has been activated with an inter-element distance of 6.4 mm which corresponds to 0.79 λ_0 (free space wavelength) at 37 GHz. At this stage of estimation, only uniform excitation is considered. The same procure has been conducted for a 12x12, and a 16x16 configuration.

Table A. 2 summarises the synthesised beamwidths in 3 different array configurations (i.e. 8 x 8, 12 x 12 and 16 x 16). From the table, a notable beam narrowing from 8° to 5.2° by using a 12 x 12 array can be observed, while the improvement from 12 x 12 to 16 x 16 is rather insignificant weighting the added high complexity and cost. This observation is also illustrated in the summarised radiation plots in Figure A. 7 and Figure A. 8.

Overall, considering the cost of each phase shifter module is very high at Ka- band, a 12 x 12 array would be the optimal configuration to meet the half power beamwidth requirement (of 5° to 8°) with minimal cost. With 5.2° beamwidth in uniform excitation, this also leaves some headroom for beam widening with non-uniform excitation to suppress side lobe level.

Table A. 2 Ka- band Arrays synthesis with uniform excitation

Array configuration	Half power beamwidth at Phi=0° cut plane	Half power beamwidth at Phi=90° cut plane
8 x 8 (64 elements)	8°	8°
12 x 12 (144 elements)	5.2°	5.2°
16 x 16 (256 elements)	4°	4°

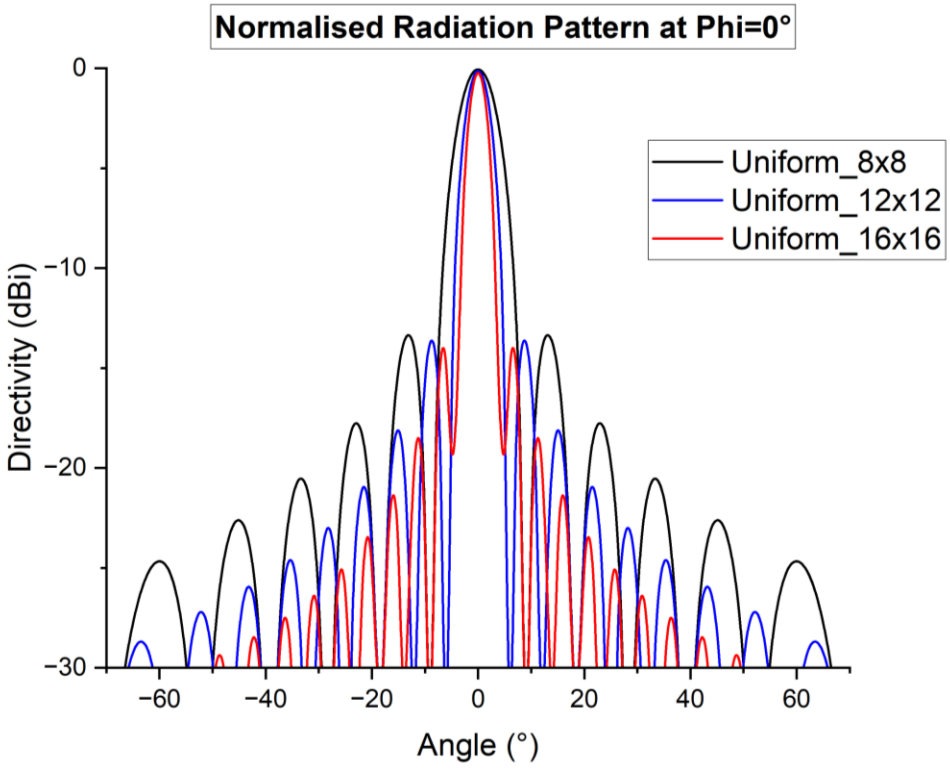

Figure A. 7 Normalised radiation pattern of the synthesised 8x8, 12x12 and 16x16 Ka- band array at Phi=0° cut plane

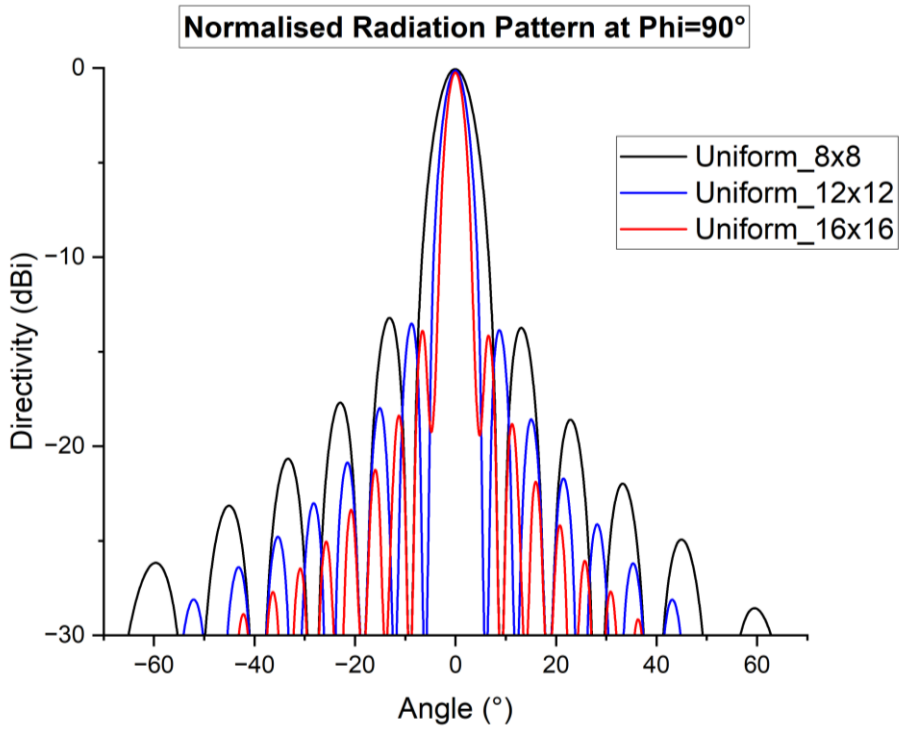

Figure A. 8 Normalised radiation pattern of the synthesised 8x8, 12x12 and 16x16 Ka- band array at Phi=90° cut plane

A.3 Proposal of using only two bits for beam steering

A.3.1 Beam scanning requirements (based on the designed L-/Ku- band shared aperture array)

Figure A. 9 illustrates an overlapped beam scanning scheme of the designed L- and Ku- band phased array antennas. The specific dimension of each beam is recorded in Table A. 3 and Table A. 4.

The requirements of the scanning range for the Ka- band phased array are established as followed:

1. Provided that the 0° beamwidth of the Ka- band 12x12 array is within 5 to 8°
2. The maximum L- foot reaches 31.7° (i.e. 20° + $\frac{23.4^\circ}{2}$ =31.7°) in X- direction, and 11° (i.e. $\frac{21.9^\circ}{2} \approx 11^\circ$) in Y- direction

3. The maximum Ku- band footprint reaches (i.e. 20°+ $\frac{17.9^\circ}{2}$ =29°) in X- direction, and (i.e. 7.81°+ $\frac{15.4^\circ}{2}$=15.5°)
4. Therefore, with all three factors considered, the minimum scanning range for the Ka- band array is:
    - X- direction: 29°-$\frac{8^\circ}{2}$=25°
        - Hence, it is envisioned that there will be 7 beams in the X- direction: 0°, ±8°, ±16°, ±24°
    - Y- direction: 15.5° - $\frac{8^\circ}{2}$ = 11.5°
        - Thereby, it is envisioned that there will be 5 beams in the Y- direction: 0°, ±12°, ±6°

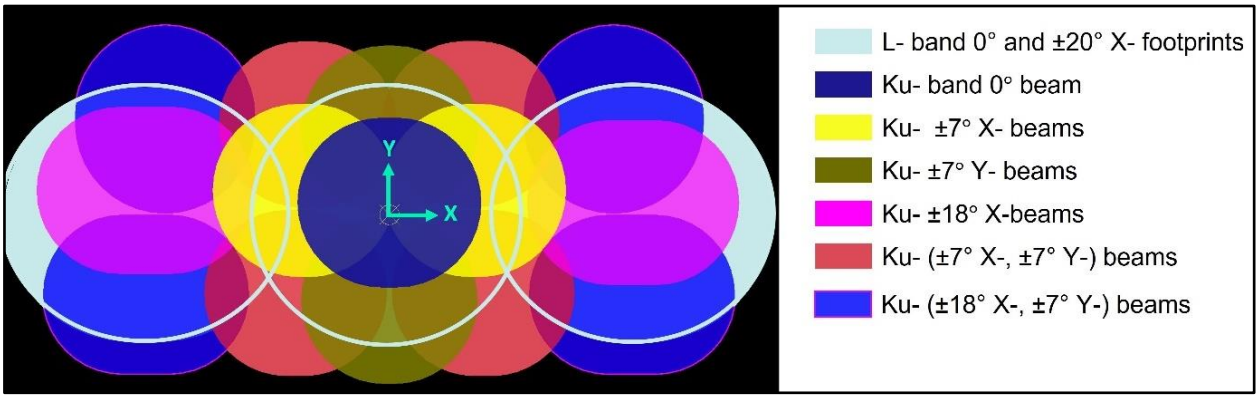

Figure A. 9 Overlapped beam scanning scheme of the designed L- and Ku- band phased array

Table A. 3 Footprint dimensions of the L- band phased array

Beam	Half power beamwidth at Phi=0° cut plane	Half power beamwidth at Phi=90° cut plane
0°	22.4°	21.9°
X-20°	23.4°	20.7°
X+20°	23.4°	20.8°

Table A. 4 Footprint dimensions of the Ku- band phased array

Beam	Half power beamwidth at Phi=0° cut plane	Half power beamwidth at Phi=90° cut plane
0°	15.1°	13.9°
X-7°	15°	14.2°
X+7°	15°	14.2°
Y+7°	13.7°	13.7°
Y-7°	14.5°	13.7°
X-20°	17.9°	13.7°
X+20°	17.9°	13.7°
[X-6.7°, Y+7.4°]	14.6°	13.6°
[X+6.7°, Y+7.4°]	14.6°	13.6°
[X-7.7°, Y-6.4°]	15°	13.6°
[X+7.7°, Y-6.4°]	15°	13.6°
[X-18.41°, Y+7.81°]	14.8°	15.4°
[X+18.41°, Y+7.81°]	14.8°	15.4°
[X-20°, Y-6.5°]	16.9°	13°
[X+20°, Y-6.5°]	16.9°	13°

A.3.2 Performance comparison of using four, three and two bits

Before beam scanning simulations, side lobe suppression has been applied with a -20dB Taylor distribution obtained from the phased array module of Keysight Pathwave System Design. The obtained excitation coefficients are applied according to the following Table A. 5:

Table A. 5 Side lobe suppression table in a 12x12 array

	1	2	3	4	5	6	7	8	9	10	11	12
1	0.06	0.08	0.11	0.15	0.20	0.22	0.22	0.20	0.15	0.11	0.08	0.06
2	0.08	0.10	0.14	0.19	0.25	0.28	0.28	0.25	0.19	0.14	0.10	0.08
3	0.11	0.14	0.19	0.27	0.34	0.39	0.39	0.34	0.27	0.19	0.14	0.11
4	0.15	0.19	0.27	0.37	0.48	0.54	0.54	0.48	0.37	0.27	0.19	0.15
5	0.20	0.25	0.34	0.48	0.61	0.70	0.70	0.61	0.48	0.34	0.25	0.20
6	0.22	0.28	0.39	0.54	0.70	0.79	0.79	0.70	0.54	0.39	0.28	0.22
7	0.22	0.28	0.39	0.54	0.70	0.79	0.79	0.70	0.54	0.39	0.28	0.22
8	0.20	0.25	0.34	0.48	0.61	0.70	0.70	0.61	0.48	0.34	0.25	0.20
9	0.15	0.19	0.27	0.37	0.48	0.54	0.54	0.48	0.37	0.27	0.19	0.15
10	0.11	0.14	0.19	0.27	0.34	0.39	0.39	0.34	0.27	0.19	0.14	0.11
11	0.08	0.10	0.14	0.19	0.25	0.28	0.28	0.25	0.19	0.14	0.10	0.08
12	0.06	0.08	0.11	0.15	0.20	0.22	0.22	0.20	0.15	0.11	0.08	0.06

The corresponding radiation pattern at Phi=0° and Phi=90° cut plane is depicted in Figure A. 10 and Figure A. 11 respectively. With side lobe level better than -25 dB, this yields a beam efficiency of 96.79%. Thereafter, the phase allocations for each scanning angle were obtained from Keysight PathWave System Design phased array module as recorded in Table A. 6 to Table A. 15, and applied in the Farfield Array synthesis function of CST Microwave Studio accordingly.

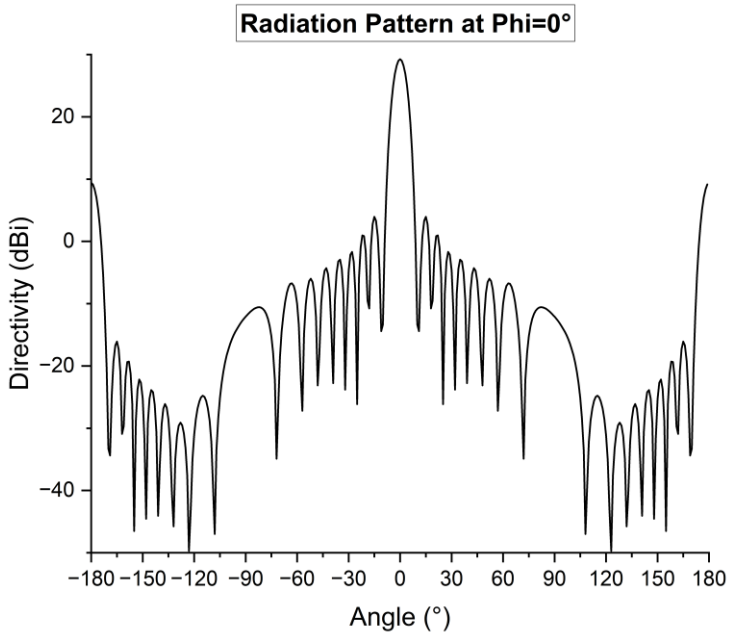

Figure A. 10 Radiation pattern of the 12x12 array with -20 dB Taylor distribution at Phi=0° cut plane

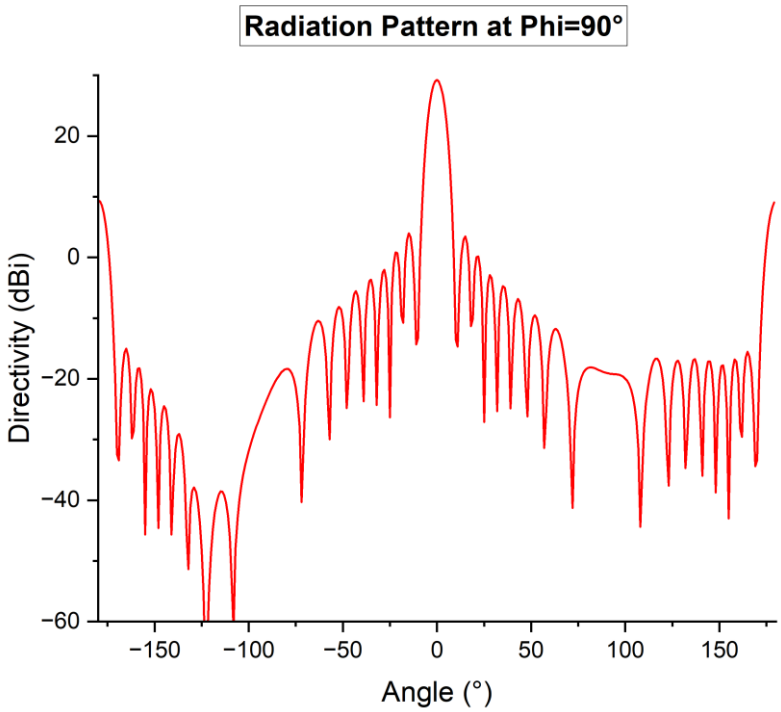

Figure A. 11 Radiation pattern of the 12x12 array with -20 dB Taylor distribution at Phi=90° cut plane

A.3.2.1 8° simulation

Table A. 6 7° Phase allocation using 4 bits in a 12x12 array

	1	2	3	4	5	6	7	8	9	10	11	12
1	0	0	0	0	0	0	0	0	0	0	0	0
2	-45	-45	-45	-45	-45	-45	-45	-45	-45	-45	-45	-45
3	-67.5	-67.5	-67.5	-67.5	-67.5	-67.5	-67.5	-67.5	-67.5	-67.5	-67.5	-67.5
4	-112.5	-112.5	-112.5	-112.5	-112.5	-112.5	-112.5	-112.5	-112.5	-112.5	-112.5	-112.5
5	-157.5	-157.5	-157.5	-157.5	-157.5	-157.5	-157.5	-157.5	-157.5	-157.5	-157.5	-157.5
6	-180	-180	-180	-180	-180	-180	-180	-180	-180	-180	-180	-180
7	-225	-225	-225	-225	-225	-225	-225	-225	-225	-225	-225	-225
8	-270	-270	-270	-270	-270	-270	-270	-270	-270	-270	-270	-270
9	-292.5	-292.5	-292.5	-292.5	-292.5	-292.5	-292.5	-292.5	-292.5	-292.5	-292.5	-292.5
10	-337.5	-337.5	-337.5	-337.5	-337.5	-337.5	-337.5	-337.5	-337.5	-337.5	-337.5	-337.5
11	-22.5	-22.5	-22.5	-22.5	-22.5	-22.5	-22.5	-22.5	-22.5	-22.5	-22.5	-22.5
12	-45	-45	-45	-45	-45	-45	-45	-45	-45	-45	-45	-45

Table A. 7 7° Phase allocation using 3 bits in a 12x12 array

	1	2	3	4	5	6	7	8	9	10	11	12
1	0	0	0	0	0	0	0	0	0	0	0	0
2	-45	-45	-45	-45	-45	-45	-45	-45	-45	-45	-45	-45
3	-90	-90	-90	-90	-90	-90	-90	-90	-90	-90	-90	-90
4	-90	-90	-90	-90	-90	-90	-90	-90	-90	-90	-90	-90
5	-135	-135	-135	-135	-135	-135	-135	-135	-135	-135	-135	-135
6	-180	-180	-180	-180	-180	-180	-180	-180	-180	-180	-180	-180
7	-225	-225	-225	-225	-225	-225	-225	-225	-225	-225	-225	-225
8	-270	-270	-270	-270	-270	-270	-270	-270	-270	-270	-270	-270
9	-315	-315	-315	-315	-315	-315	-315	-315	-315	-315	-315	-315
10	-315	-315	-315	-315	-315	-315	-315	-315	-315	-315	-315	-315
11	0	0	0	0	0	0	0	0	0	0	0	0
12	-45	-45	-45	-45	-45	-45	-45	-45	-45	-45	-45	-45

Table A. 8 8° Phase allocation using 2 bits in a 12x12 array

	1	2	3	4	5	6	7	8	9	10	11	12
1	0	0	0	0	0	0	0	0	0	0	0	0
2	0	0	0	0	0	0	0	0	0	0	0	0
3	-90	-90	-90	-90	-90	-90	-90	-90	-90	-90	-90	-90
4	-90	-90	-90	-90	-90	-90	-90	-90	-90	-90	-90	-90
5	-180	-180	-180	-180	-180	-180	-180	-180	-180	-180	-180	-180
6	-180	-180	-180	-180	-180	-180	-180	-180	-180	-180	-180	-180
7	-180	-180	-180	-180	-180	-180	-180	-180	-180	-180	-180	-180
8	-270	-270	-270	-270	-270	-270	-270	-270	-270	-270	-270	-270
9	-270	-270	-270	-270	-270	-270	-270	-270	-270	-270	-270	-270
10	0	0	0	0	0	0	0	0	0	0	0	0
11	0	0	0	0	0	0	0	0	0	0	0	0
12	-90	-90	-90	-90	-90	-90	-90	-90	-90	-90	-90	-90

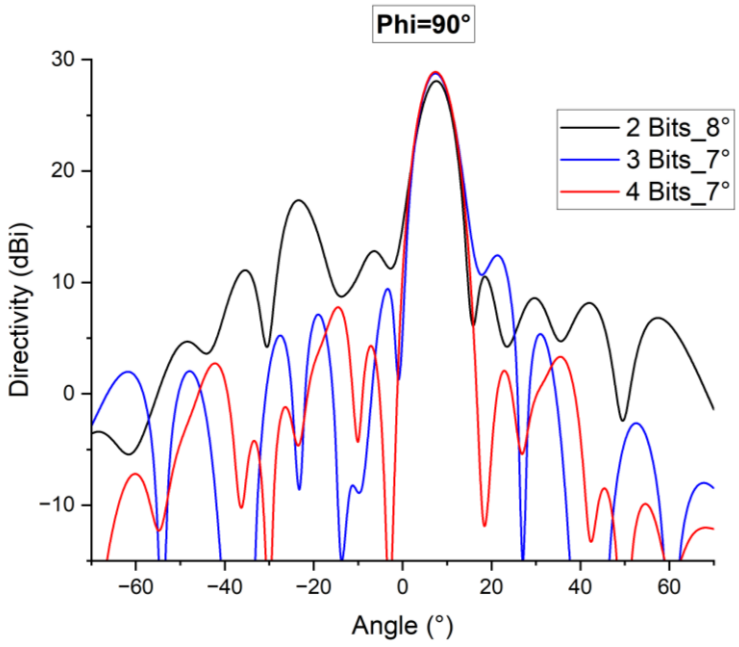

Figure A. 12 Radiation pattern of the synthesized 12x12 array at Phi=90° cut plane with target angle of 8°

A.3.2.2 14° simulation

Table A. 9 15° Phase allocation using 4 bits in a 12x12 array

	1	2	3	4	5	6	7	8	9	10	11	12
1	0	0	0	0	0	0	0	0	0	0	0	0
2	-67.5	-67.5	-67.5	-67.5	-67.5	-67.5	-67.5	-67.5	-67.5	-67.5	-67.5	-67.5
3	-157.5	-157.5	-157.5	-157.5	-157.5	-157.5	-157.5	-157.5	-157.5	-157.5	-157.5	-157.5
4	-225	-225	-225	-225	-225	-225	-225	-225	-225	-225	-225	-225
5	-292.5	-292.5	-292.5	-292.5	-292.5	-292.5	-292.5	-292.5	-292.5	-292.5	-292.5	-292.5
6	0	0	0	0	0	0	0	0	0	0	0	0
7	-90	-90	-90	-90	-90	-90	-90	-90	-90	-90	-90	-90
8	-157.5	-157.5	-157.5	-157.5	-157.5	-157.5	-157.5	-157.5	-157.5	-157.5	-157.5	-157.5
9	-225	-225	-225	-225	-225	-225	-225	-225	-225	-225	-225	-225
10	-292.5	-292.5	-292.5	-292.5	-292.5	-292.5	-292.5	-292.5	-292.5	-292.5	-292.5	-292.5
11	-22.5	-22.5	-22.5	-22.5	-22.5	-22.5	-22.5	-22.5	-22.5	-22.5	-22.5	-22.5
12	-90	-90	-90	-90	-90	-90	-90	-90	-90	-90	-90	-90

Table A. 10 14° Phase allocation using 3 bits in a 12x12 array

	1	2	3	4	5	6	7	8	9	10	11	12
1	0	0	0	0	0	0	0	0	0	0	0	0
2	-90	-90	-90	-90	-90	-90	-90	-90	-90	-90	-90	-90
3	-135	-135	-135	-135	-135	-135	-135	-135	-135	-135	-135	-135
4	-225	-225	-225	-225	-225	-225	-225	-225	-225	-225	-225	-225
5	-315	-315	-315	-315	-315	-315	-315	-315	-315	-315	-315	-315
6	0	0	0	0	0	0	0	0	0	0	0	0
7	-90	-90	-90	-90	-90	-90	-90	-90	-90	-90	-90	-90
8	-135	-135	-135	-135	-135	-135	-135	-135	-135	-135	-135	-135
9	-225	-225	-225	-225	-225	-225	-225	-225	-225	-225	-225	-225
10	-315	-315	-315	-315	-315	-315	-315	-315	-315	-315	-315	-315
11	0	0	0	0	0	0	0	0	0	0	0	0
12	-90	-90	-90	-90	-90	-90	-90	-90	-90	-90	-90	-90

Table A. 11 15° Phase allocation using 2 bits in a 12x12 array

	1	2	3	4	5	6	7	8	9	10	11	12
1	0	0	0	0	0	0	0	0	0	0	0	0
2	-90	-90	-90	-90	-90	-90	-90	-90	-90	-90	-90	-90
3	-180	-180	-180	-180	-180	-180	-180	-180	-180	-180	-180	-180
4	-180	-180	-180	-180	-180	-180	-180	-180	-180	-180	-180	-180
5	-270	-270	-270	-270	-270	-270	-270	-270	-270	-270	-270	-270
6	0	0	0	0	0	0	0	0	0	0	0	0
7	-90	-90	-90	-90	-90	-90	-90	-90	-90	-90	-90	-90
8	-180	-180	-180	-180	-180	-180	-180	-180	-180	-180	-180	-180
9	-270	-270	-270	-270	-270	-270	-270	-270	-270	-270	-270	-270
10	-270	-270	-270	-270	-270	-270	-270	-270	-270	-270	-270	-270
11	0	0	0	0	0	0	0	0	0	0	0	0
12	-90	-90	-90	-90	-90	-90	-90	-90	-90	-90	-90	-90

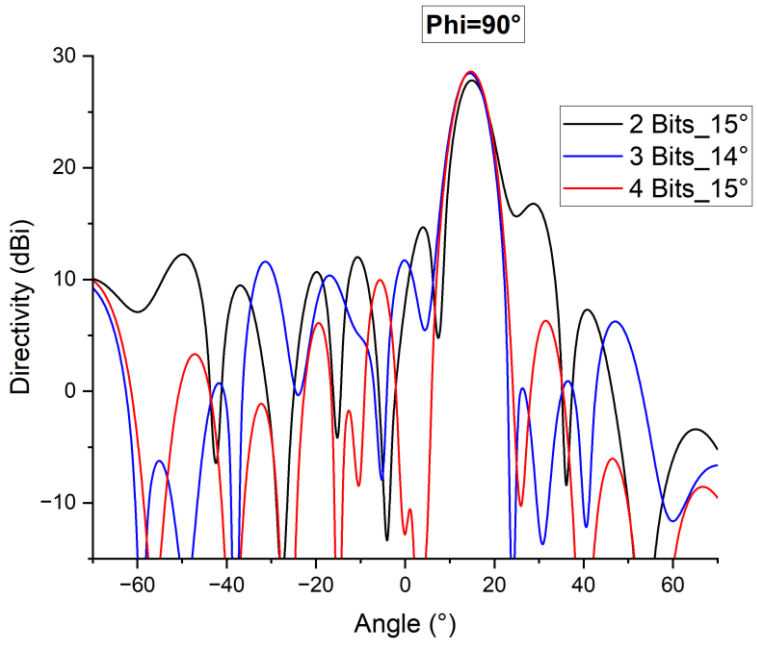

Figure A. 13 Radiation pattern of the synthesized 12x12 array at Phi=90° cut plane with target angle of 14°

A.3.2.3 24° simulation

Table A. 12 24° Phase allocation using 4 bits in a 12x12 array

	1	2	3	4	5	6	7	8	9	10	11	12
1	0	0	0	0	0	0	0	0	0	0	0	0
2	-112.5	-112.5	-112.5	-112.5	-112.5	-112.5	-112.5	-112.5	-112.5	-112.5	-112.5	-112.5
3	-225	-225	-225	-225	-225	-225	-225	-225	-225	-225	-225	-225
4	-337.5	-337.5	-337.5	-337.5	-337.5	-337.5	-337.5	-337.5	-337.5	-337.5	-337.5	-337.5
5	-112.5	-112.5	-112.5	-112.5	-112.5	-112.5	-112.5	-112.5	-112.5	-112.5	-112.5	-112.5
6	-225	-225	-225	-225	-225	-225	-225	-225	-225	-225	-225	-225
7	-337.5	-337.5	-337.5	-337.5	-337.5	-337.5	-337.5	-337.5	-337.5	-337.5	-337.5	-337.5
8	-90	-90	-90	-90	-90	-90	-90	-90	-90	-90	-90	-90
9	-202.5	-202.5	-202.5	-202.5	-202.5	-202.5	-202.5	-202.5	-202.5	-202.5	-202.5	-202.5
10	-315	-315	-315	-315	-315	-315	-315	-315	-315	-315	-315	-315
11	-67.5	-67.5	-67.5	-67.5	-67.5	-67.5	-67.5	-67.5	-67.5	-67.5	-67.5	-67.5
12	-202.5	-202.5	-202.5	-202.5	-202.5	-202.5	-202.5	-202.5	-202.5	-202.5	-202.5	-202.5

Table A. 13 24° Phase allocation using 3 bits in a 12x12 array

	1	2	3	4	5	6	7	8	9	10	11	12
1	0	0	0	0	0	0	0	0	0	0	0	0
2	-135	-135	-135	-135	-135	-135	-135	-135	-135	-135	-135	-135
3	-225	-225	-225	-225	-225	-225	-225	-225	-225	-225	-225	-225
4	0	0	0	0	0	0	0	0	0	0	0	0
5	-90	-90	-90	-90	-90	-90	-90	-90	-90	-90	-90	-90
6	-225	-225	-225	-225	-225	-225	-225	-225	-225	-225	-225	-225
7	-315	-315	-315	-315	-315	-315	-315	-315	-315	-315	-315	-315
8	-90	-90	-90	-90	-90	-90	-90	-90	-90	-90	-90	-90
9	-225	-225	-225	-225	-225	-225	-225	-225	-225	-225	-225	-225
10	-315	-315	-315	-315	-315	-315	-315	-315	-315	-315	-315	-315
11	-90	-90	-90	-90	-90	-90	-90	-90	-90	-90	-90	-90
12	-180	-180	-180	-180	-180	-180	-180	-180	-180	-180	-180	-180

Table A. 14 24° Phase allocation using 2 bits in a 12x12 array

	1	2	3	4	5	6	7	8	9	10	11	12
1	0	0	0	0	0	0	0	0	0	0	0	0
2	-90	-90	-90	-90	-90	-90	-90	-90	-90	-90	-90	-90
3	-270	-270	-270	-270	-270	-270	-270	-270	-270	-270	-270	-270
4	0	0	0	0	0	0	0	0	0	0	0	0
5	-90	-90	-90	-90	-90	-90	-90	-90	-90	-90	-90	-90
6	-180	-180	-180	-180	-180	-180	-180	-180	-180	-180	-180	-180
7	0	0	0	0	0	0	0	0	0	0	0	0
8	-90	-90	-90	-90	-90	-90	-90	-90	-90	-90	-90	-90
9	-180	-180	-180	-180	-180	-180	-180	-180	-180	-180	-180	-180
10	0	0	0	0	0	0	0	0	0	0	0	0
11	-90	-90	-90	-90	-90	-90	-90	-90	-90	-90	-90	-90
12	-180	-180	-180	-180	-180	-180	-180	-180	-180	-180	-180	-180

Table A. 15 21° Phase allocation using 2 bits in a 12x12 array

	1	2	3	4	5	6	7	8	9	10	11	12
1	0	0	0	0	0	0	0	0	0	0	0	0
2	-90	-90	-90	-90	-90	-90	-90	-90	-90	-90	-90	-90
3	-180	-180	-180	-180	-180	-180	-180	-180	-180	-180	-180	-180
4	-270	-270	-270	-270	-270	-270	-270	-270	-270	-270	-270	-270
5	-90	-90	-90	-90	-90	-90	-90	-90	-90	-90	-90	-90
6	-180	-180	-180	-180	-180	-180	-180	-180	-180	-180	-180	-180
7	-270	-270	-270	-270	-270	-270	-270	-270	-270	-270	-270	-270
8	0	0	0	0	0	0	0	0	0	0	0	0
9	-90	-90	-90	-90	-90	-90	-90	-90	-90	-90	-90	-90
10	-180	-180	-180	-180	-180	-180	-180	-180	-180	-180	-180	-180
11	-270	-270	-270	-270	-270	-270	-270	-270	-270	-270	-270	-270
12	-90	-90	-90	-90	-90	-90	-90	-90	-90	-90	-90	-90

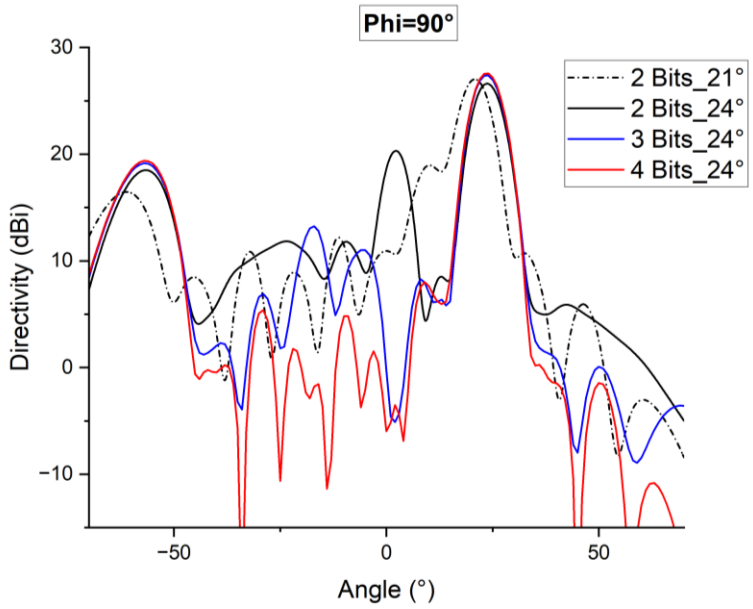

Figure A. 14 Radiation pattern of the synthesized 12x12 array at Phi=90° cut plane with target angle of 24°

A.3.3 Comparison and summary

In term of beam steering angle, it can be observed from the previous sections that using 4,3, or even 2 bits is capable of steering the antenna beam to the required angles of [8°, 14° and 24°] with acceptable tolerance.

The next critical aspect is side lobe level and resultant beam efficiency. By comparing the radiation patterns using different bits in Figure A. 12, Figure A. 13 and Figure A. 14, it is evident that using only 2 bits leads to higher maximum side lobe level, as well as more notable side lobes at every beam steering angle. This in turn results in a much lower beam efficiency, especially at lower angles as summarised in Figure A. 15. However, at larger angle over 20°, beam efficiencies drop rapidly for all cases. The results of 2-bit at 21° is comparable to using 3 and 4 bits at 24° degree. With this point considered, using 2 bits is still reasonable.

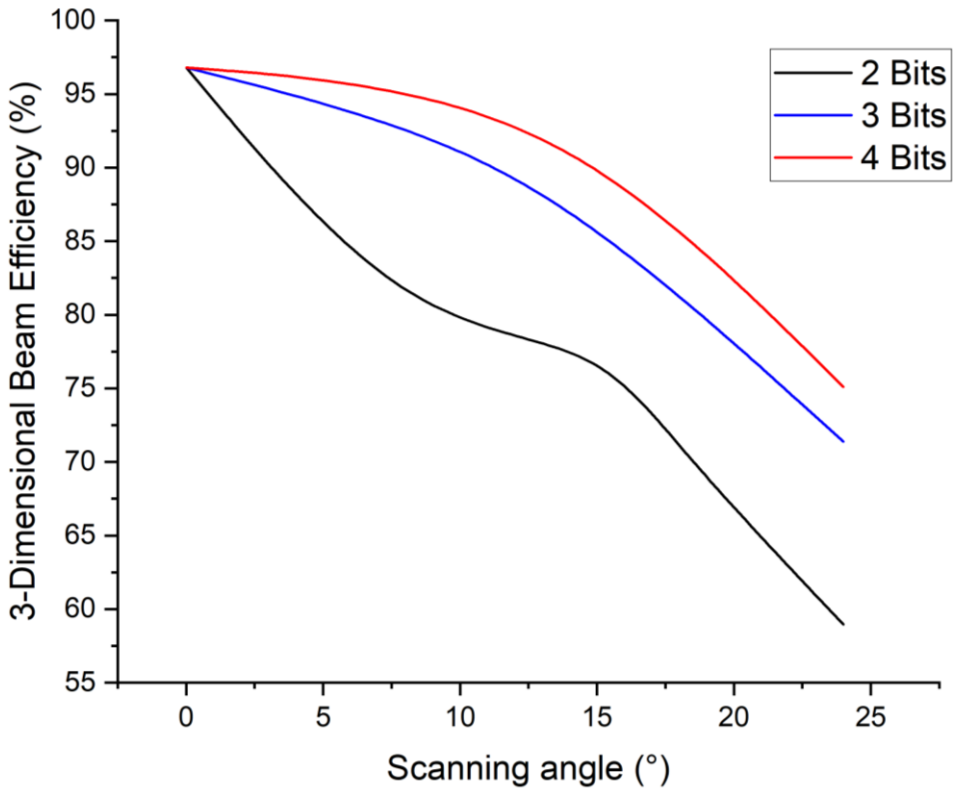

Figure A. 15 Beam efficiency vs Scanning angle for 2,3, and 4 Bits

Another crucial factor for consideration is the required space for phase shifters. As per discussion with the Ka- band phase shifter designer Dr. Trong Khoa Ho, the 3-bit phase shifter block requires a dimension of 15mm x 5mm, while a 2-bit phase shifter requires less than 10mm x 5mm. Since

each antenna patch has a dimension of 2.1 mm x 2.1 mm, and the inter-element distance in the array is 6.4 mm. illustrates the array with one phase shifter unit. Since the 3-bit unit has a length over 3 antenna patches, it is impossible to integrate this unit into a 12 x12 array in a single layer design; even with feedlines connected in different layers, the PCB board will be at least 3 times the size of a 12x 12 array. in comparison a 2-bit is significantly smaller and possible to fit into the array. Moreover, the 3-bit phase shifter has an estimated maximum insertion loss of -10 dB, while the maximum insertion loss for using 2 bits is -7.4 dB. Therefore, using 3 bits almost doubles the insertion loss as compared to using 2 bits.

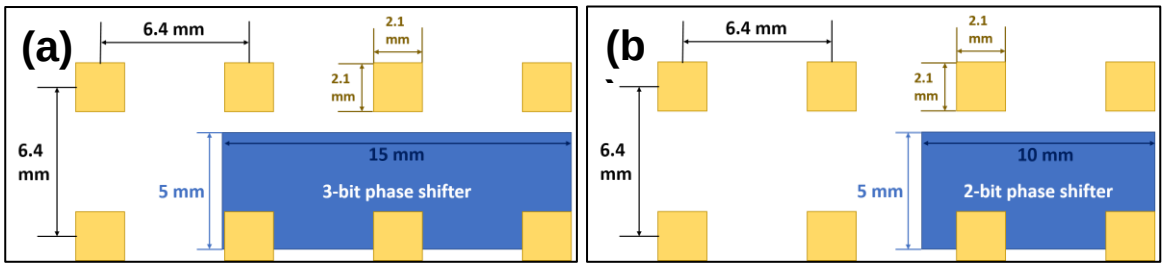

Figure A. 16 Illustration of one phase shifter unit integrated into the Ka- band patch array (a)a 3-bit unit (b)a 2-bit unit

With all these factors considered, as compared to using 2 bits, although using 3 bits leads to notably higher beam efficiencies at low steering angles, the added complexity and overall cost, as well as doubling the insertion losses outweigh its better performance. Therefore, 2-bit phase shifter unit shall be adopted.

A.4 Conclusion and Final beam scanning footprint

Based on earlier discussions, following the ARC discovery project requirements, it can be concluded that a 12x12 array using 2-bit phase shifters would be the optimum configuration to demonstrate overlapped beam scanning concept using L-, Ku- and Ka- band phased array antennas. To complete the Ka- band 2-dimensioal scanning scheme, the simulated Ka- band beams are summarised in the following Table A. 16:

Table A. 16 Summary of simulated beams using 2-bit phase shifter

	X- direction beamwidth (°)	Y- direction beamwidth (°)
0°	6.7	6.7
Y+7°	6.7	6.8
Y+12°	6.7	6.8
X+5°	6.7	6.7
X+8°	6.9	6.7
X+15°	6.9	6.7
X+21°	7.3	6.7

Based on the simulated beamwidths in the table, the full proposed overlapped scanning footprints are depicted in Figure A. 17. Although the outmost L- band footprints are not fully overlapped with either the Ku- or Ka- band footprint, according to the downscaling flight lines in The P- band Radiometer Inferred Soil Moisture Experiments 2019 Workplan [20], it is possible to narrow the track spacing such that the outmost L- band footprints are overlapping in each flight line. Therefore, the current scanning proposal will be sufficient to demonstrate the tri-band overlapped scanning concept.

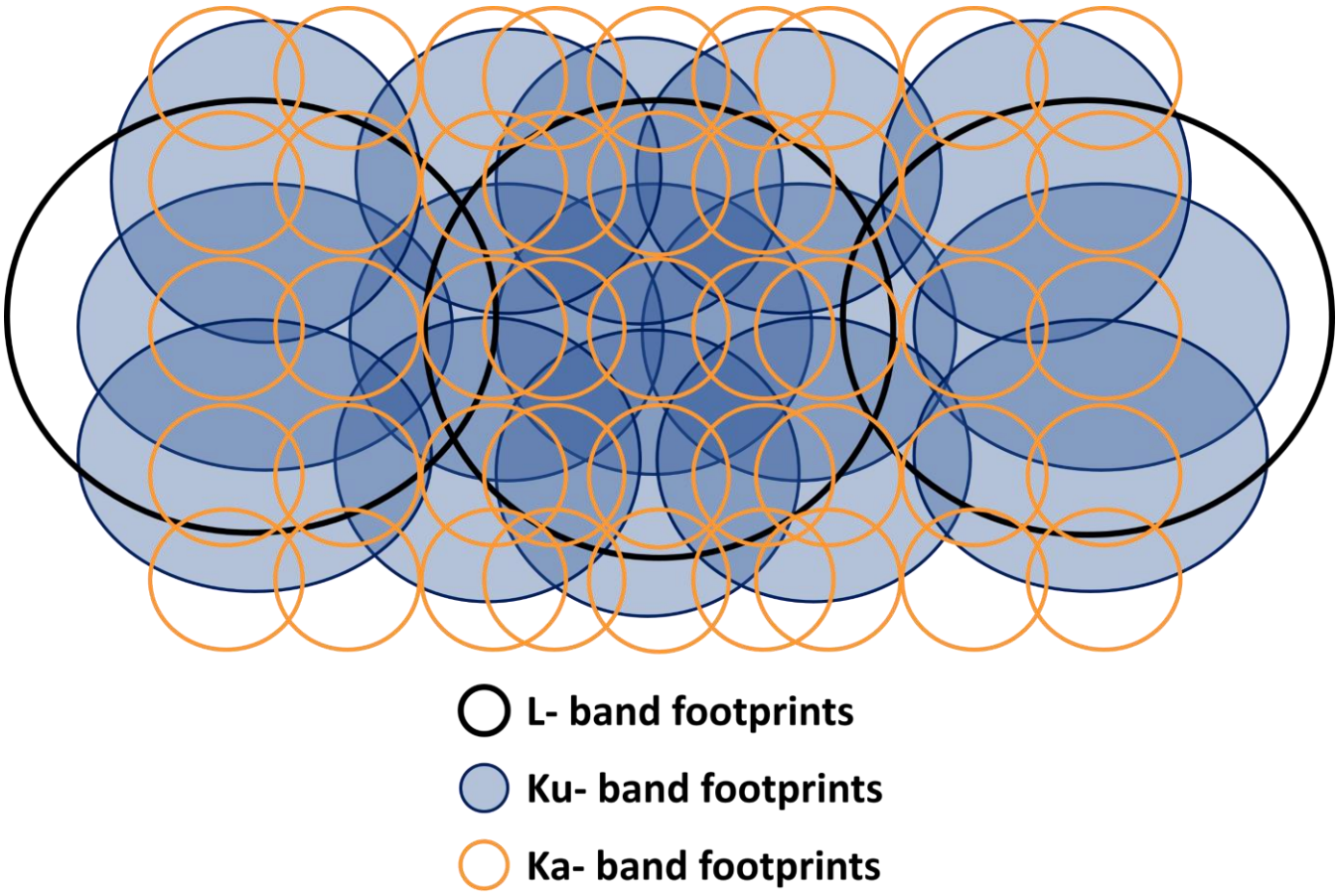

Figure A. 17 Full overlapped scanning footprints of L-, Ku- and Ka- band

Appendix B: Radiometer receivers simulation, fabrication and testing

B.1 Introduction

A radiometer system consists of an antenna and a radiometer receiver which converts the collected scene thermal radiation (according to radiation pattern weighting) from the antenna to readable system outputs. With the earlier chapters focusing on the design of radiometer antennas (which are the main objectives of this PhD study), to complete the whole picture of a radiometer system, this appendix is dedicated to the discussion on radiometer receivers as outlined in Figure B. 1. The first part is a system level Ka- band radiometer receiver simulation during early stage PhD candidature for fundamental study, and an L- band receiver frontend printed circuit board (PCB) prototype at late PhD candidature to develop a Low-cost L- band radiometer system along with the fabricated phased array antenna discussed in Chapter 4.

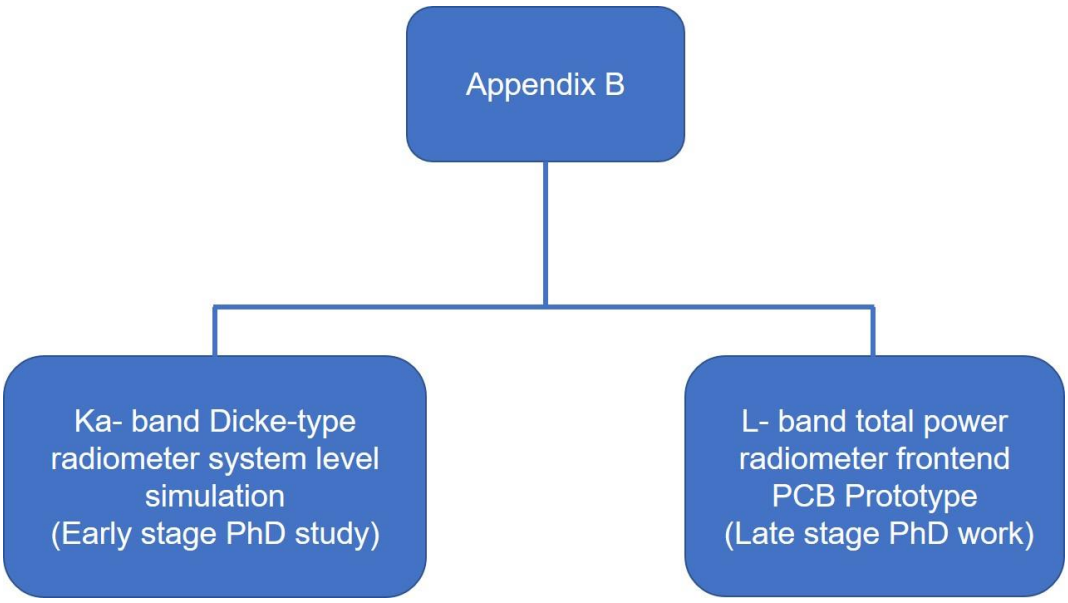

Figure B. 1 Road map of Appendix B

This appendix starts with a theoretical background of radiometric measurement, followed by a brief overview of 4 typical radiometer receiver topologies along with a discussion on the requirements for airborne soil moisture sensing application. Being a strong candidate for this application, a Dicke type radiometer receiver is simulated at the system level at Ka- band. Each stage of the system design

and considerations will be discussed in the following sections. Overall, the simulation results are consistent with those from the literature, and a sensitivity of 1.1° K has been obtained to meet the requirement of soil moisture measurement. This radiometer simulation work was included in the publication [115] along with the Ka- band substrate integrate waveguide (SIW) antenna array developed by Dr. Shahriar Hasan Shehab to demonstrate the early stage design concept of a Ka-band low-cost compact radiometer system. In the second part of this appendix, a low-cost L- band radiometer receiver has been fabricated and tested, with the first round focusing on hardware modification and experience learning, and successful outcome in the second round.

B.1.1 Theoretical background of radiometric measurement of soil moisture

Because of thermal radiation, any object with physical temperature higher that 0 K radiates energy. Emissivity(ε) is the term that addresses the capability of an object for absorbing and emitting radiation, it could be defined as the ratio between the physical temperature of the object and its brightness temperature. Where brightness temperature is the equivalent temperature that a blackbody (i.e. $\varepsilon = 1$) would emit the same amount of microwave radiation.

Soils are a mixture of solids, liquid and gases with different ratios. For the estimation of the emissivity and brightness temperature of soil, dielectric constant is the primary electrical property. This property is determined by the different compositions of solid, gas and liquid; roughness and physical temperature of the soil [63, 160]. Water and bare soil have a large difference in the dielectric constant, where water has large dielectric constant of around 80, and dry soil has low value of 5 [63] . Because of this contrast, different compositions of water and soil would result in different effective dielectric constants. Considering dielectric constant is a crucial factor for emissivity, this change in soil composition results in different emissivity, and hence different brightness temperatures. The dynamic range of land surface response is from 200 to around 300 k, where dry soils have a high emissivity (e.g. 0.95) and hence high brightness temperature, and wet soil yields low brightness temperature [161].

B.2 Brief Overview of the receiver topologies

There are four types of radiometer receiver structures that are commonly used. These are total power radiometer, Dicke Radiometer, the noise injection radiometer and the correlation radiometer. Each topology will be discussed in the following sections:

B.2.1 The Total Power Radiometer

A total power radiometer system diagram is depicted in Figure B. 2, and it has is the simplest topology. The receiver consists of gain blocks for amplifying the input thermal radiation collected from the antenna, bandpass filtering to pre-detection bandwidth, a square-law diode detector for converting the noise power into a noisy DC voltage, and finally an integrator to smooth the noisy DC voltage into a more stable DC level. However, as indicated in *Figure B. 2*, the system output V_{OUT} is a summing node of antenna measurement brightness temperature (T_A) and the system equivalent noise (T_{system}). This leads the system output being highly susceptible to gain and noise figure fluctuation of active components due to temperature variation. Therefore, very stable components (against voltage and temperature fluctuations) are required for this configuration, and this could incur a high practical cost.

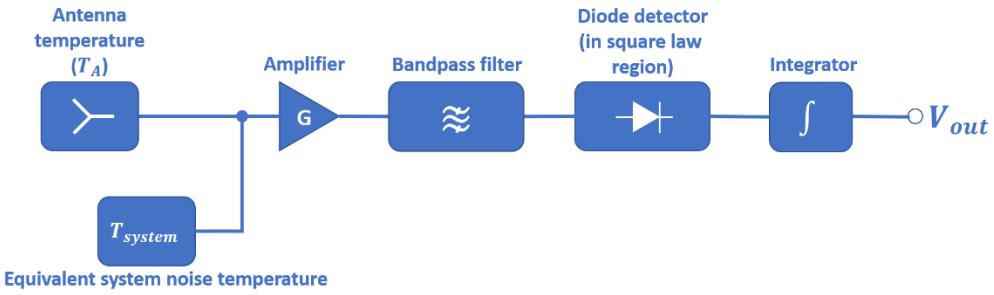

Figure B. 2 System diagram of a Total Power Radiometer

B.2.2 The Dicke radiometer

The Dicke radiometers adopt a frequent calibration (e.g. 1000 times in a second) to the total power radiometer in order to eliminate the effect of voltage and temperature drift in the active components. The system output is based on the temperature difference between a reference load at known brightness temperature and the antenna input; rather than a combination of system noise and

antenna temperature in the total power configuration. In this configuration, the instability in radiometer sensitivity due to gain and temperature fluctuation is greatly reduced.

As a trade-off, for the same amount of integration time, the sensitivity of the Dicke Radiometer is degraded by a factor of 2 due to the switching between a reference load and the antenna input, and the system structure is slightly more complex.

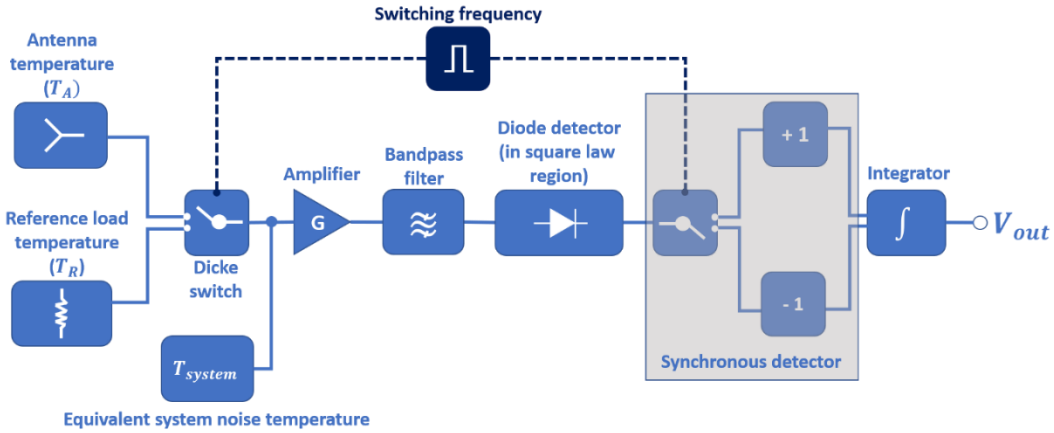

Figure B. 3 System diagram of a Dicke Radiometer

B.2.3 Noise Injection Radiometer

The concept of noise injection radiometer is based on the fact that reference load temperature (T_R) is generally larger than the antenna input temperature (T_A). In this sense, the noise injection radiometer further improves the stability of a Dicke radiometer by adding a feedback loop to control a variable noise generator (T_I) at the input of a Dicke radiometer receiver, such that the combined input of the Dicke radiometer (T_{AI}) is balanced to the temperature of the reference load in the Dicke radiometer; resulting in nearly zero system output (V_{out}). However, due to the adoption of feedback control, the system complexity is much higher.

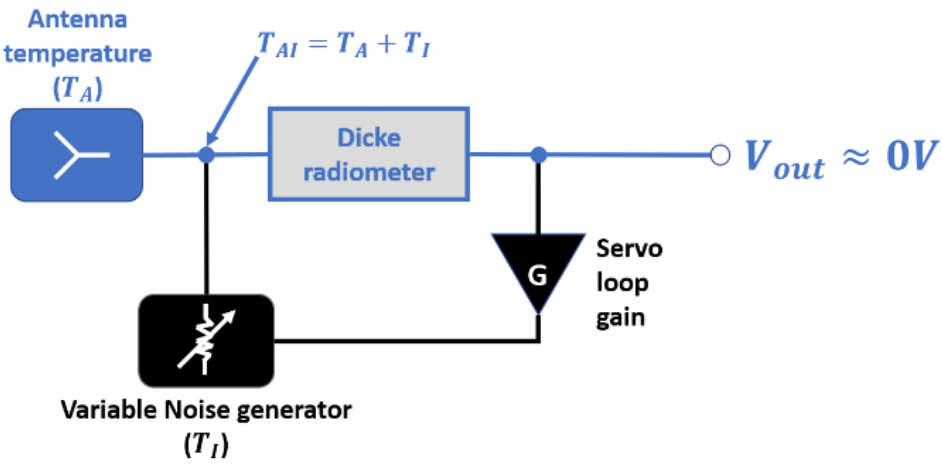

Figure B. 4 System diagram of a Noise Injection Radiometer

B.2.4 The Correlation Radiometer

A correlation radiometer has two channels with an ideally identical receiver in each channel. The receiver pair are typically total power or Dicke type in this topology. Before feeding the amplified and filtered noise signal to the diode detector, the noise signal is also input to the complex correlator for computing the real part and imaginary part of the cross-correlation. The correlation radiometer could be used for two applications. The first application is to measure the vertical and horizontal polarisation incident radiation, and calculate the real and imaginary part of their product as the Stokes parameters. Where Stokes parameters describe the polarisation state of the incidence microwave radiation. The most typical use of Stokes parameters in remote sensing is for wind vector retrieval by the harmonic characteristics in the 3rd and 4th stoke parameters over the periodic ocean surface. The other application for in synthetic aperture and interferometer.

Overall, in contrast to non-fully-polarimetric radiometers, the correlation radiometer requires stringent requirements on the stability of the local oscillator, and the required processing power would also be much higher

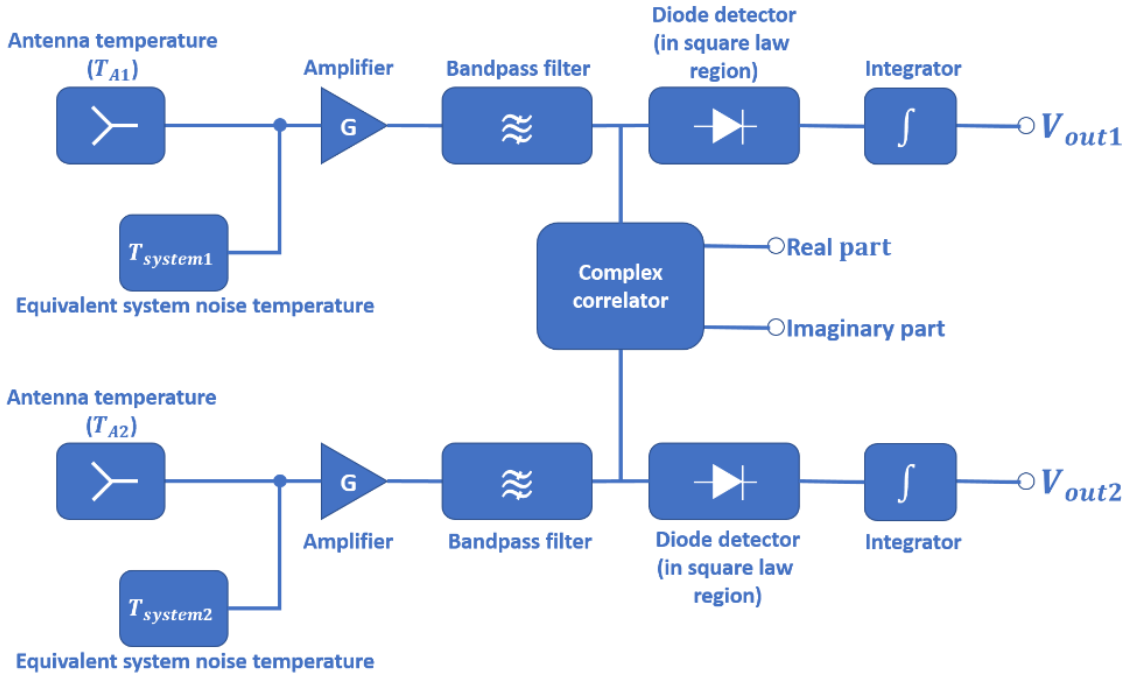

Figure B. 5 System Structure of a correlation radiometer

B.2.5 Requirement for airborne soil moisture measurement

For soil moisture measurement from an airborne platform, dual polarised signal would be required at the sensitivity of 1 K [162, 163]. The integration time of an airborne radiometer could not be extended for too long (e.g. in hundred milliseconds to about a second) considering the speed of flight. Based on literature survey, an integration time of up to 1 second would be acceptable [85, 164].

Polarimetric signature on the azimuth asymmetric of land surface could be obtained at low observation height, the signature depicts harmonic 3rd and/or 4th stokes parameter response on different azimuth viewing angles [163, 165]. However, by the research of [14], the azimuth signature from L- band radiometer at a measuring height of 3000m is insignificant, and the signature from finer observation (i.e. radar) would tend to cancel out at coarser resolutions. Therefore, non-fully-polarimetric radiometers on vertical and horizontal channels would be sufficient. Overall, for a low-cost dual-polarisation radiometer system with moderate sensitivity requirement, the Dicke radiometer would be a strong candidate.

B.3 System simulation of a Ka- band Dicke type radiometer

B.3.1 Simulation design flowchart

The system-level design and simulation could be divided into a few steps as illustrated in Figure B. 6.

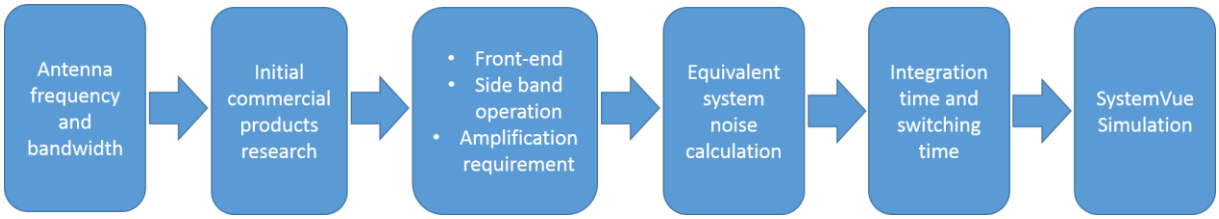

Figure B. 6 Flowchart of receiver system level design and simulation

1. Extract information on antenna frequency and bandwidth, the range of antenna thermal radiation power could then be computed, this will also be an important factor for designing pre-detection bandwidth
2. Initial research on the available commercial products, the important aspects would be
    a. Low noise and insertion losses
    b. Small size and planar form where possible
    c. Overall low system cost and equivalent noise, which will be further discussed
3. Based on this initial research, the key system configuration could be designed
    a. Considering the high overall amplification requirement (e.g. 50 dB), the front end is generally superheterodyne because of the high price of RF amplifiers (typically in Ka-Band)
    b. Single side band or double side band would be determined by the adoption of RF pre-amplifier. Considering the high insertion losses of commercial mixers, which will result in high system noise without an RF pre-amp, single side band operation with RF pre-amp would be preferred.
    c. After designing input bandwidth, the range of antenna noise power input could be finalised. By the requirement of -25 dBm power level for diode detector to work in a square–law region, the amplification requirements for RF and IF stage could be allocated

4. Equivalent noise calculation will then be performed as per B.3.5 System equivalent noise, this is to account for the insertion losses and noise contribution from the antenna input terminal to the IF stage output.
5. Based on the computed equivalent noise, and the designed bandwidth, the integration time can then be designed according to B.3.2 Simulation Overview to meet the requirement of 1° K sensitivity. The Dicke switching time shall then be determined such that $F_S \ll \tau$
6. With the input of component parameters (e.g. gain, bandwidth), a system-level simulation on SystemVue can then be performed for concept approval and initial system performance analysis

B.3.2 Simulation Overview

A system-level simulation of a Ka-band Dicke Radiometer receiver was performed in SystemVue. Figure B. 7 shows the overall receiver diagram, the simulation system is divided into 5 parts:

1. A Dicke Switch for alternating the thermal radiation input from the antenna, and a reference load that is enclosed at a reasonable electronics operating temperature of 313°K [34].
2. A superheterodyne front end for first-stage amplification, band filtering and frequency down-conversion
3. Intermediate frequency (IF) stage covers filtering for pre-detection bandwidth, and multistage amplification to boost the IF signal for square-law detection.
4. Diode detector block to model the square-law behaviour of a Schottky Diode, this is to convert the IF Stage noise input to DC voltages that are linear to the noise power.
5. Low frequency circuit to amplify, convert and smooth the fluctuating diode output into a more stable DC level corresponding to the brightness temperature of the target.
6. A square wave generator (Fswitch) to control the switching position of the Dicke Switch, and the synchronous detector in the low-frequency circuit.

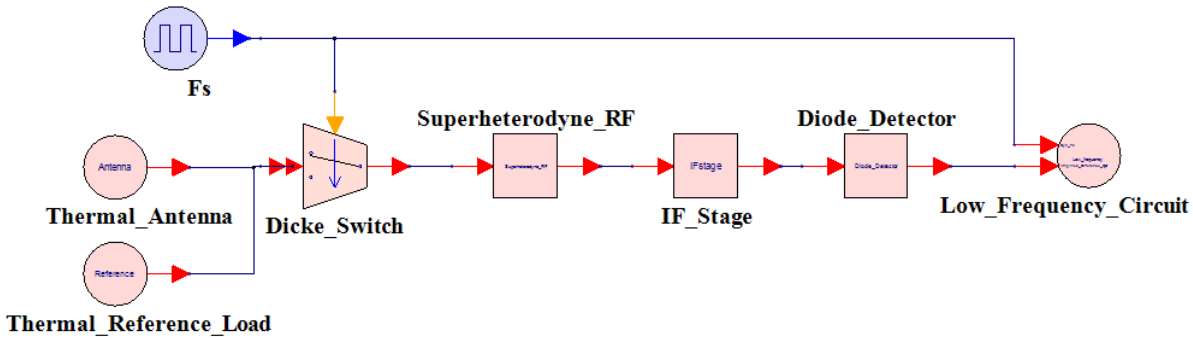

Figure B. 7 Overall system diagram of a Dicke Radiometer receiver

The key parameters of this design are summarised in Table B. 1, those parameters will be discussed along with each part of the radiometer. As an overview of the system performance, in a Dicke radiometer, its minimum detectable temperature variation is defined as sensitivity (ΔT), which could be computed as [34]:

$$\Delta T = 2 \times \frac{T_{SYS} + T_A}{\sqrt{B \times \tau}} = 1.1\ K\ (E.q.1)$$

Table B. 1 Radiometer system parameters

INPUT BANDWIDTH	35.7 – 36.7 GHz
PREDETECTION BANDWIDTH (B)	5 – 1000 MHz
SYSTEM NOISE TEMPERATURE(T_{SYS})	340 K
ANTENNA NOISE TEMPERATURE (T_A)	0 – 313 K
REFERENCE LOAD NOISE TEMPERATURE (T_R)	313 K
INTEGRATION TIME (τ)	1.4 ms
SENSITIVITY (ΔT)	1.1 K

B.3.3 Dicke Switch:

Considering the period of receiver gain variation is generally more than 1 second, this instability is eliminated by calibrating the system every short interval of time [166], so that system gain could be considered as constant during this short period (e.g. 1 ms). In this regard, switching frequency around 1 kHz range has been frequently reported [34]. Another consideration is that since the integrator filters the fluctuating component of the synchronous detector, but also the associated high frequency component superimposed by the square wave Fs [167]. In this regard, Fs shall be much higher than the integration time (e.g. around 10 times) [34, 167]. Given an integration time of 1.4 mS, the switching period is designed to be 0.2mS (i.e. switching frequency of 5000Hz), which is in a reasonable range.

B.3.4 Thermal radiation and noise density:

Thermal radiation occurs when objects with a physical temperature higher than 0° K at thermodynamic equilibrium, and this radiation follows Plank's law in the form of voltage V_n [168].

$$V_n = \sqrt{\frac{4hfBR}{e^{\frac{hf}{kT}} - 1}} \ (E.q.2)$$

Where: h is the Planck's constant: $6.626 \times 10^{-34} J - sec$

k is the Boltzmann's constant: $1.38 \times 10^{-23} J/°K$

T is the physical temperature of the object in Kelvin (K)

R is the terminal resistance in Ω

B is the bandwidth of the measuring system

F is the centre frequency of bandwidth

While Plank's law could be applied for all frequencies, in microwave domain, by Rayleigh-Jeans approximation, the thermal radiation can be simplified as:

$$V_n = \sqrt{4kTBR}\ (E.q.3)$$

In a matched load condition, the radiation power delivered to the system is:

$$Pn = \left(\frac{V_n}{2R}\right)^2 \times R = \frac{4kTBR}{4R} = TkB\ (E.q.4)$$

Where the power density of radiation is unchanged against frequency, which could be referred as white noise. E.q.3 depicts that the radiation power is proportional to the physical temperature of the object and system bandwidth [168].

In order to model a zero-mean white noise behaviour of this thermal radiation, a Gaussian Noise Generator is used. From the literature (e.g. [65, 169]), 200°K to 310 °K would be a reasonable temperature range of soil land surface. Within this temperature range, a temperature of 220°K was

chosen for modelling wet soil. In SystemVue, this temperature corresponds to noise power spectral density (NDensity) of:

$$NDensity = k \times T = 1.38 \times 10^{-23} \times 220 = 3.036 \times 10^{-21} \frac{W}{Hz} \ (E.q.5)$$

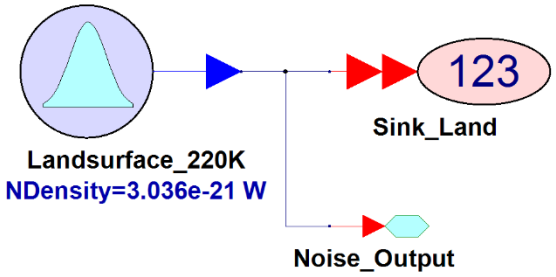

Figure B. 8 Thermal radiation model of Land surface

By applying an integration time of 1.4 ms, the sensitivity (ΔT) of a Dicke radiometer could be computed as [34] :

$$\Delta T = 2 \times \frac{T_{System} + T_A}{\sqrt{B \times \tau}} = 1.1 \ K \ (E.q.6)$$

This would be a reasonable sensitivity for soil moisture application [162].

B.3.5 System equivalent noise

Considering a microwave radiometer is a cascade system with different stages of filtering and amplification, and noise will be super-imposed with thermal radiation due to losses and internally generated noise from each component. In this regard, it is conventional to model a receiver system with a total equivalent noise and a noise-free system [66].

To start with a two-stage cascade system as in illustrated in Figure B. 9 (a), where Psi denotes the input signal power; $P_{n_{input}}$ is the input noise. $G1$, F_1 and T_{e1} are the gain, noise figure and effective input noise temperature of subsystem 1, and similar quantities apply to subsystem 2. Each stage of this noisy cascade system can be transformed into a noise-free subsystem with equivalent input noise as in Figure B. 9 (b).

To convert the cascade system into a simplified single-stage system (i.e. from Figure B. 9 (b) to Figure B. 9 (c)), it can be computed as:

$$P_{n_{output}} = G1G2(P_{n_{input}} + kT_{e1}B) + G2(kT_{e2}B)$$

$$= G1G2(P_{n_{input}} + k((T_{e1} + \frac{T_{e2}}{G_1})B)$$

$$= G1G2(P_{n_{input}} + k(T_eB)\ (E.q.7)$$

$$where: T_{e1} = (F_1 - 1) \times 290\ K\ (E.q.8\ )$$

$$T_e = T_{e1} + \frac{T_{e2}}{G_1}\ (E.q.9)$$

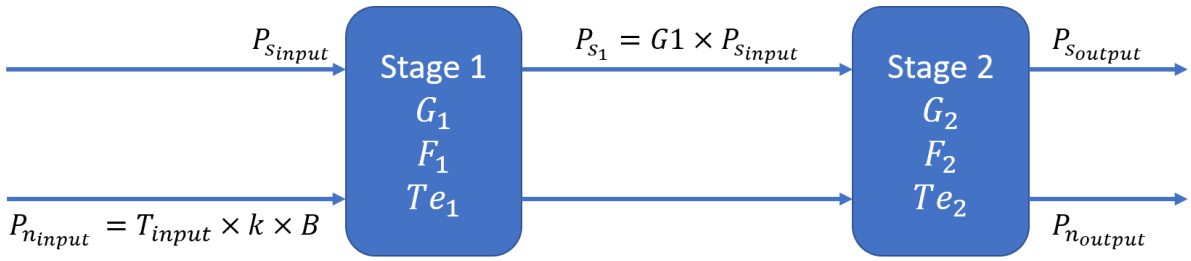

(a)

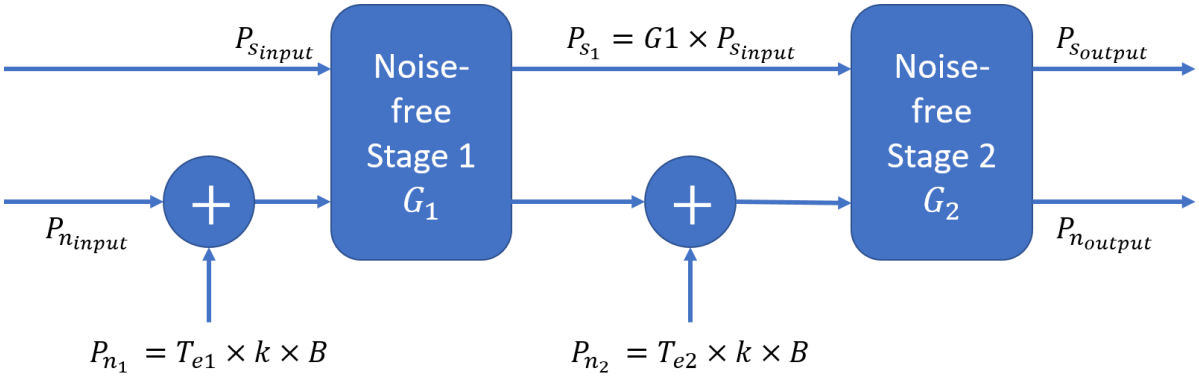

(b)

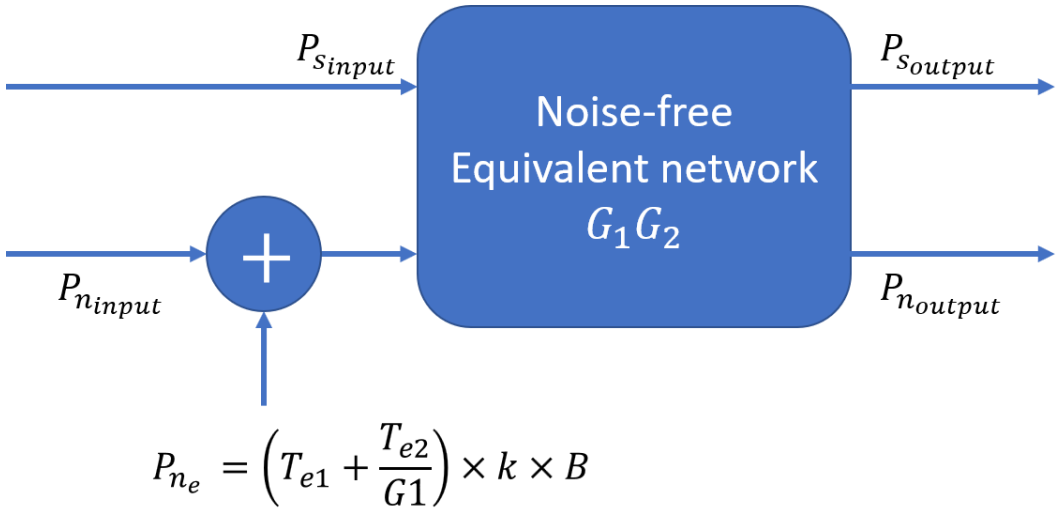

(c)

Figure B. 9 Equivalent noise of a two-stage cascade system [167]

This converting method is also valid for an N-stage cascade system, where E.q.9 could be expanded as:

$$T_e = T_{e1} + \frac{T_{e2}}{G_1} + \frac{T_{e3}}{G_1 G_2} + \frac{T_{e4}}{G_1 G_2 G_3} + \frac{T_{eN}}{G_1 G_2 G_3 \dots G_{N-1}} \quad (E.q.10)$$

Based on literature [34] and initial research of available commercial components, the equivalent system noise temperature was computed to be 340 K, where this noise temperature is to account for the components' loss and noise contribution, and this is primarily determined by the RF preamp and miscellaneous loss before RF amplification [34, 167], the detailed calculation could be found in System Noise calculation of the Appendix C.

B.3.6 Superheterodyne front end

In the radio frequency (RF) part of the radiometer, considering the availability of commercial low noise amplifier (LNA) at Ka band with moderate price, an RF preamplifier with single side band (SSB) operation is adopted for a low system noise figure and low susceptibility to other microwave interference. Given the antenna bandwidth is from 35.7 to 37.3 GHz, for an optimal system noise temperature, the RF filter (35.7 to 36.7 GHz) shall be placed after the RF preamplifier so that the insertion loss from this filter would have lower effective noise contribution; as well as to filter the noise from the preamplifier in the upper sideband [34, 164]. Frequency down conversion is performed by a local oscillator at 35.7GHz, and a mixer-preamp before IF pre-detection filtering.

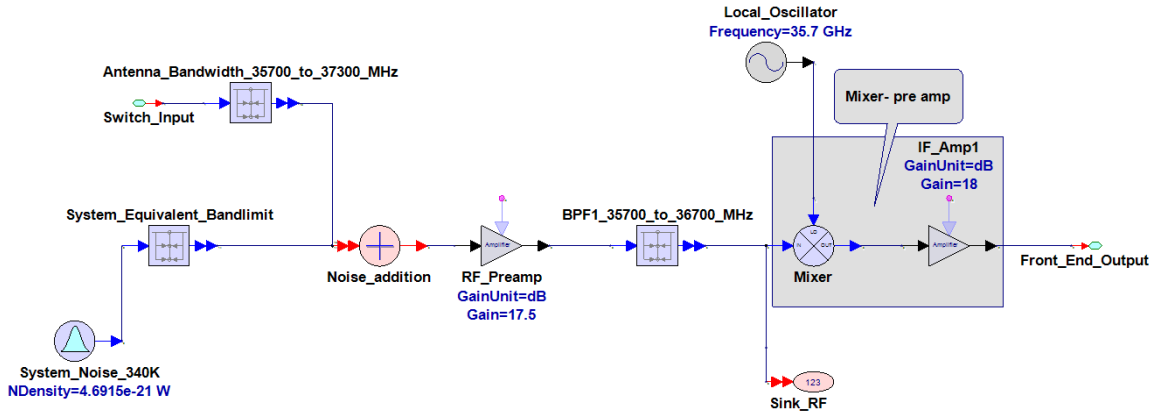

Figure B. 10 Block diagram of superheterodyne front end

B.3.7 IF stage

Substantial flicker (1/f) noise could be generated if the IF input frequencies to the diode detector is too low (e.g. including frequency components below 1000 Hz), this (1/f) noise will be superimposed at the output of the detector and hence degrade the sensitivity of receiver [170, 171]. In this regard, the pre-detection bandwidth is limited to 5-1000 MHz, so that the lower frequency boundary is well above a Schottky diode's corner frequency, where flicker noise becomes measurable below this

frequency. Most of the signal amplification is performed in IF part to boost the noise power to – 25 dBm level before power detection, such that the diode detector works in the square-law region.

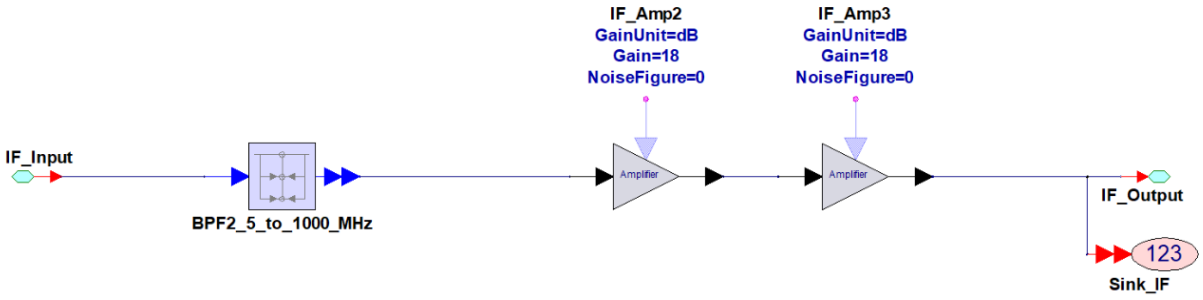

Figure B. 11 Block diagram of the IF stage

The power spectrum at receiver input, RF stage output IF stage output is depicted in Figure B. 12, from the wideband thermal radiation to the IF output, selective frequency filtering (35.7 to 36.7 GHz at RF; 5 to 1000 MHz at IF) and roughly an overall 58 dB gain can be observed. As the power spectrum is shown in dBm per MHz, a power spectrum level of -53 dBm means the total IF output power will be at $-53 + 10\,x\log_{10}(995) = -23\,dBm$ level, which is sufficient for square-law power detection. The time domain IF and RF results are shown in Figure B. 13, where IF output fluctuates in a much slower period and larger amplitude as compared to that of the RF output.

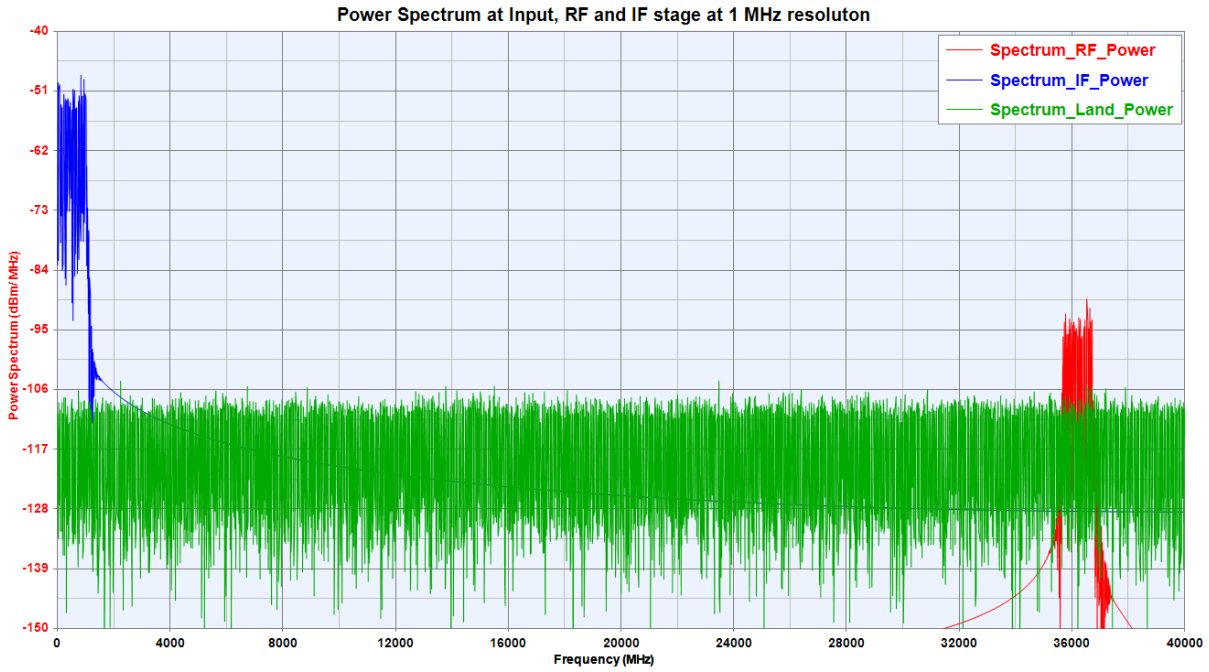

Figure B. 12 Power spectrum at Input, RF and IF stage

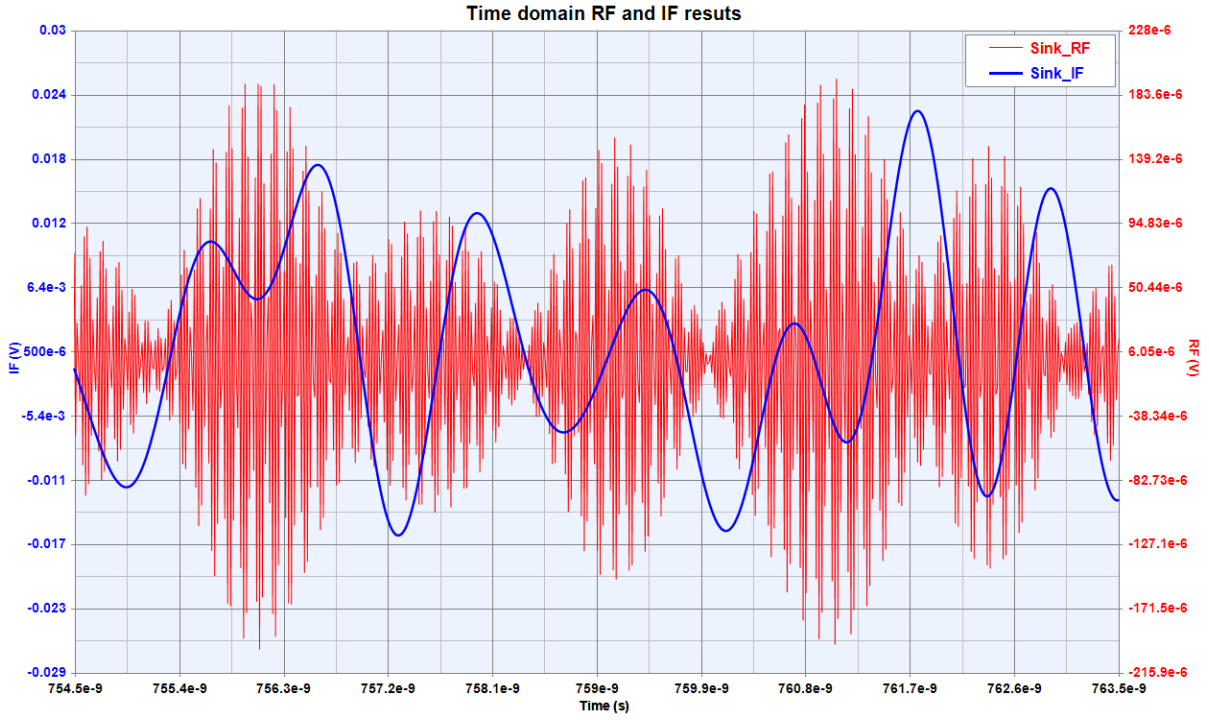

Figure B. 13 Time domain results at IF and RF stage

B.3.8 Diode detector

The diode detector response is modelled by a Log Video Detector and a Peak detector. The Log detector is for converting the noise power from the IF stage into noisy DC voltage in a linear manner.

Considering the input noise temperature ranges from 0 to 313 k, after total amplification of 54dB and bandwidth limiting, the dynamic range of IF stage output is thereby from -25 to -22 dBm. In this case, a linear slope is extracted from [171] to model the sensitivity of a HSMS-285x Schottky Diode. The peak detector is to model the behaviour of a capacitor, which is to extract the slope of noisy DC input, a time constant of 10 μs is chosen such that the response time is much higher compared to the switching frequency, but much slower than the IF input bandwidth [172]. The offset subtraction is to model the AC coupling of the peak detector output, its implication will be further discussed in results section. The AC component is then further amplified by 50dB to ensure a distinguishable voltage difference before synchronous demodulation.

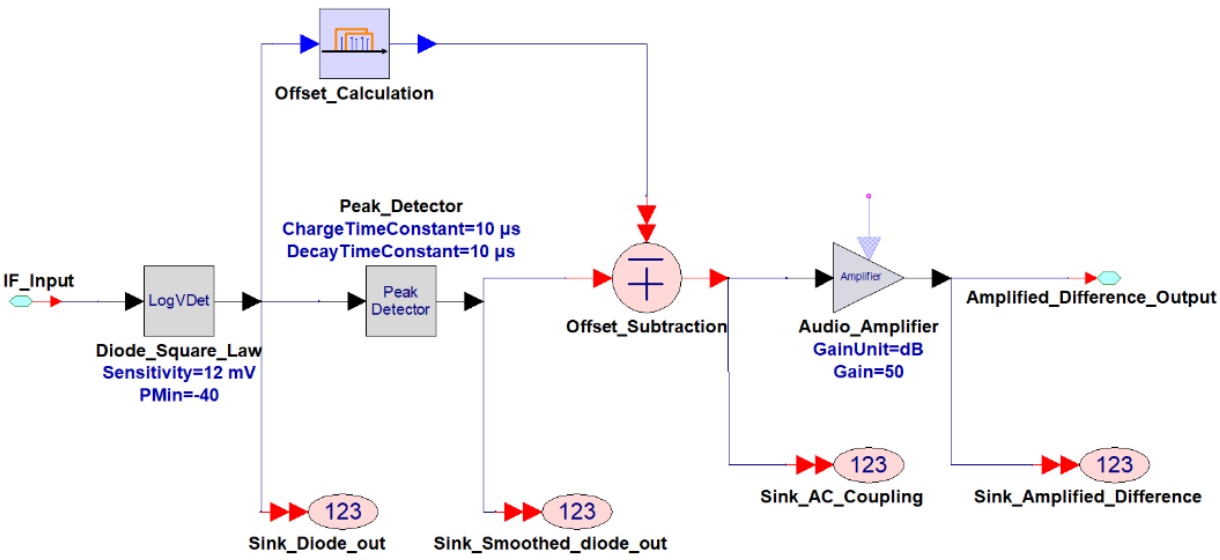

Figure B. 14 Simulation diagram of a Diode Detector

Figure B. 15 shows the simulation output from the IF stage and the diode detector. It could be observed the overall patter of the IF output is a noisy square wave to account for the switching between antenna temperature and reference load temperature. As the diode detector outputs voltage in portion to the IF noise power (i.e. in square-law region), hence diode detector output extracts the envelope of the IF noise output. As a result, two voltage levels corresponding to $T_R + T_{system}$ and $T_A + T_{system}$ could be observed, where T_{system} contributes to the DC offset of the detector output, and its AC component contains the information of temperature difference. This information could then be extracted by applying AC coupling to the detector output. The time domain results are

depicted in Figure B. 16, this temperature difference information is amplified by a factor of 316.2 in voltage (50 dB) for a distinguishable amplitude before being transformed to DC signal by the synchronous detector.

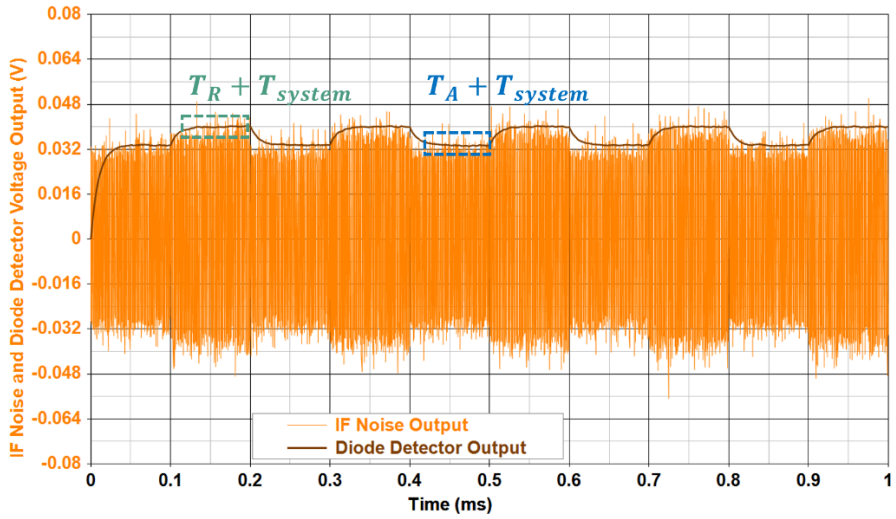

Figure B. 15 Simulation result of IF stage output and Diode detector output

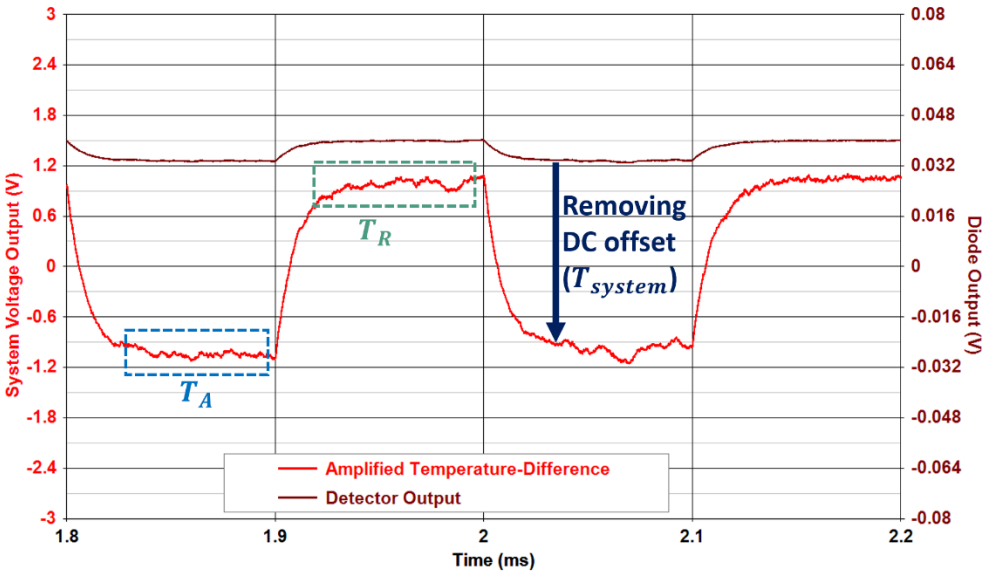

Figure B. 16 Diode detector output and Amplified Temperature difference after AC coupling

B.3.9 Low frequency circuit

In the Low Frequency Circuit stage, by adopting a synchronous detector, the AC component from the diode detector is transformed to a fluctuating DC voltage which still contains the information of temperature difference. As demonstrated in Figure B. 18, the negative voltage cycle of the AC

signal (e.g. 1.8 ms to 1.9 ms) is multiplied by a factor of -1, while the positive cycle (e.g. 1.9 ms to 2 ms) remains still.

The integrators work effectively as an averaging function to smooth the fluctuating DC voltage to a flatter level, hence reduce the uncertainty (i.e. ΔT) of the system output. Depending on the requirement of interfacing analogue to digital converter (ADC), further amplification may be performed by DC amplifier. As shown in Figure B. 19, the fluctuating synchronous detector output has been averaged (over 1.4 ms) to a more stable DC level.

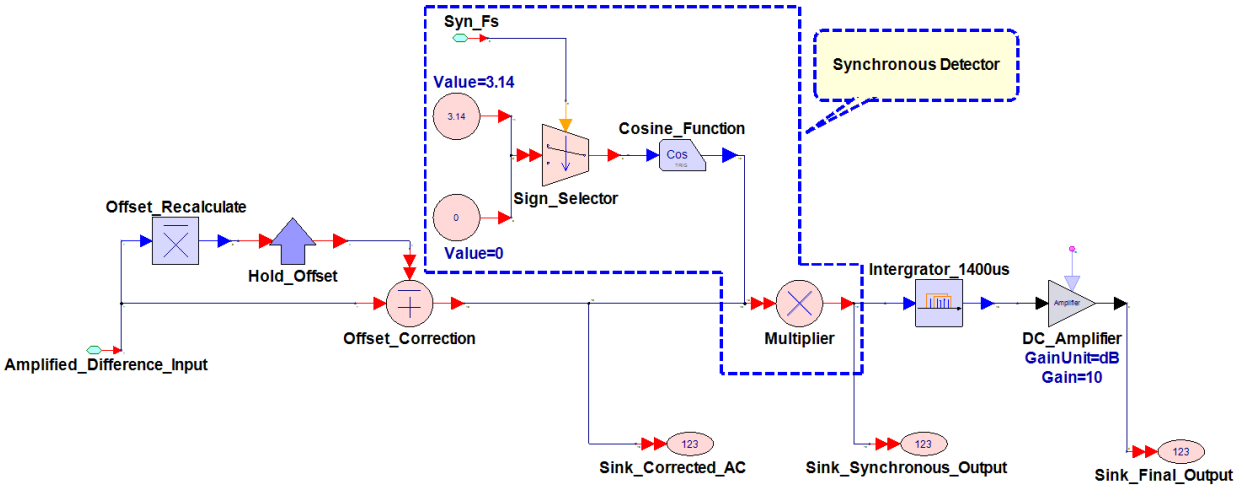

Figure B. 17 Simulation diagram of the low frequency circuit

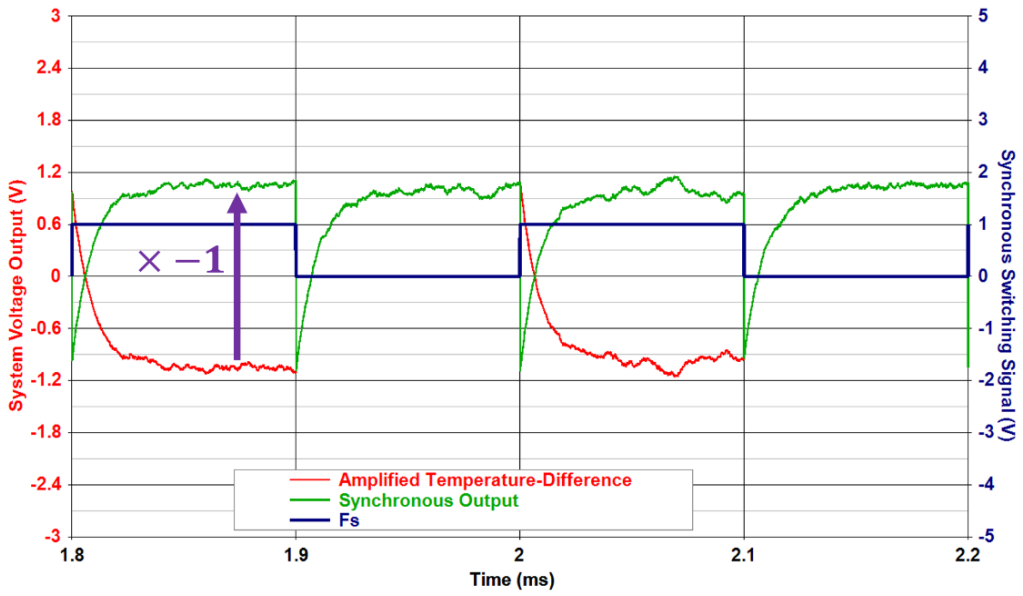

Figure B. 18 AC Temperature Difference being transforming to DC by the Synchronous Detector

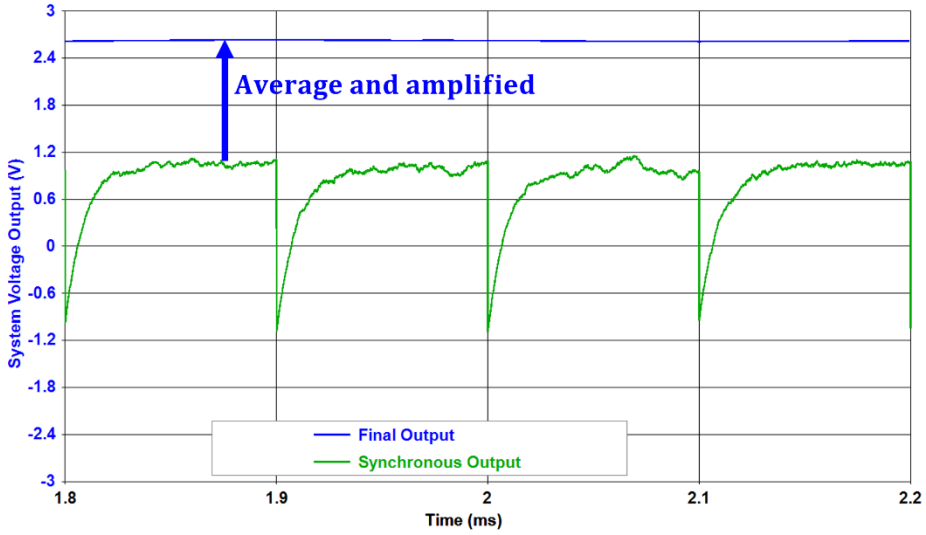

Figure B. 19 Synchronous Output being averaged and amplified by the integrator

B.3.10 Final simulation results

To validate the sensitivity of the system computed in B.3.2 Simulation Overview, brightness temperature of 220 K and 221.1 K are input to the system to model wet soil, it worth mentioning that sensitivity is slightly better than 1.1 K in 220K, since T_A contributes less deviation to the output compared to that from highest 313 K. Figure B. 20 shows the simulation results for system voltage output, where the solid and dotted blue line is the radiometer output for $T_A = 220\ K$ and $T_A = 221.1\ K$ respectively. As two distinct voltage levels could be observed to reflect the temperature difference between these two targets, the radiometer simulation system is working with sensitivity of 1.1 K. The voltage difference in tens of mV (a minimum of 16 mV in this case) should be adequate for interfacing with Analogue to Digital Converter (ADC) for counts output and further signal processing.

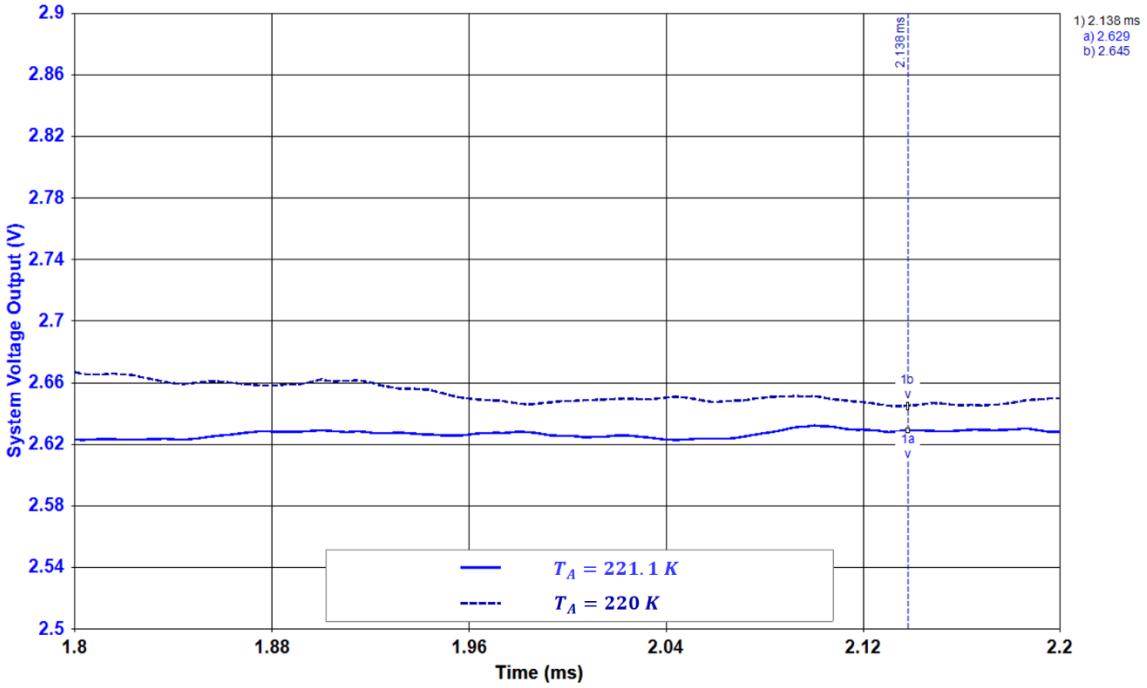

Figure B. 20 Radiometer system output for target temperature of 220° and 221.1° K

B.4 PCB development for an L- band radiometer front end

With the successful simulation of a Ka- band radiometer receiver, a Dicke type L- band radiometer frontend has been designed. The second part of this appendix focuses on the hardware development of an L- band radiometer receiver front end. Considering the RF components are relatively inexpensive at L- band, as well as to reduce overall system complexity, a direction conversion approach has been adopted, Figure B. 21 depicts the system diagram. Because of little experience in active RF circuits design, the radiometer receiver frontend is designed in blocks in one PCB, so that each part can be tested individually and connected with coaxial cables, Figure B. 22 illustrates the proposed design layout. It is also worth mentioning that pre-detection down conversion modules (i.e. amplifier, filter and mixer) are commercially available at both Ku- and Ka- band. In contrast, no commercial down conversion modules could be found for L- band at 1.4- 1.425 GHz, as being a protected bandwidth.

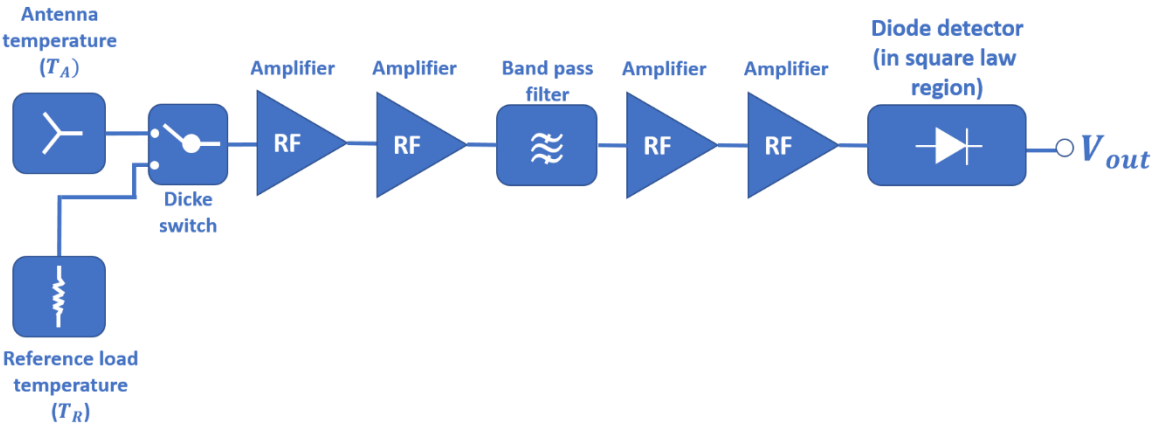

Figure B. 21 System diagram for the L- band radiometer receiver frontend

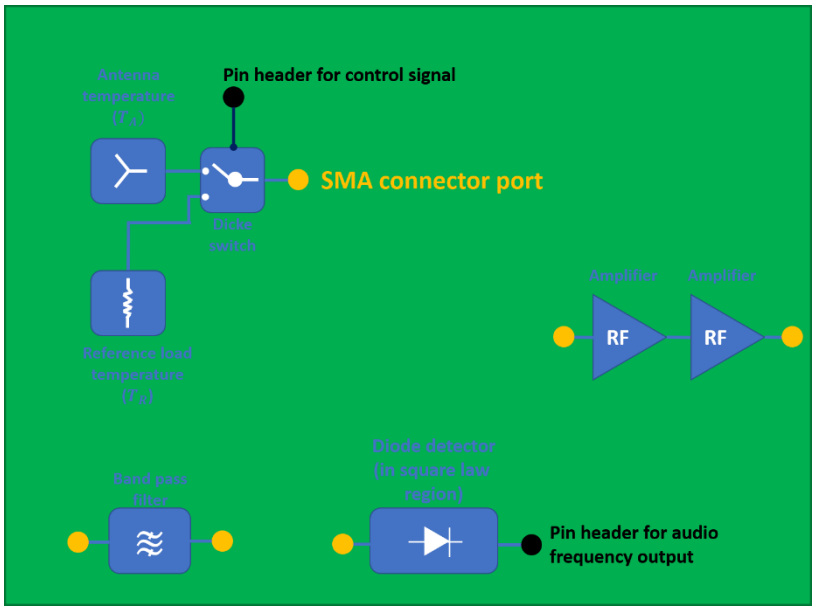

Figure B. 22 PCB design diagram

B.4.1 RF Switch testing

B.4.1.1 First iteration testing

The RF switch HMC574A is selected to be the Dicke switch of the radiometer receiver system; that is to frequently switch between a temperature-control matching load (usually at room temperature of 313° K) and the antenna input to subside the effect of temperature and voltage drift of active components.

Figure B. 23 shows the schematic of the RF switch, this is a single pole double throw (SPDT) switch, where Pin A and B are for digital high/low signal to control RFC selecting either RF1 or RF2.

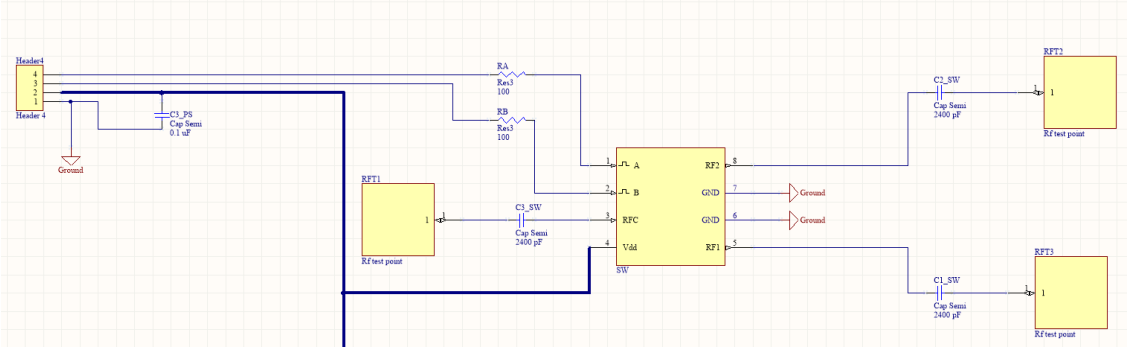

Figure B. 23 Schematic of the RF Switch HMC574A

Figure B. 24 shows the PCB hardware of the switch, with a label for each port. The measurements consist of 3 parts:

Input matching, transmission and isolation.

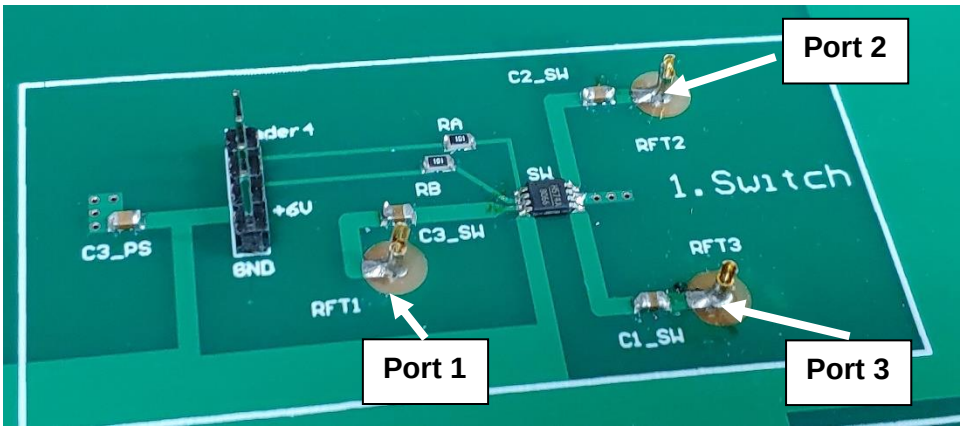

Figure B. 24 PCB hardware of HMC574A

Port 1 matching

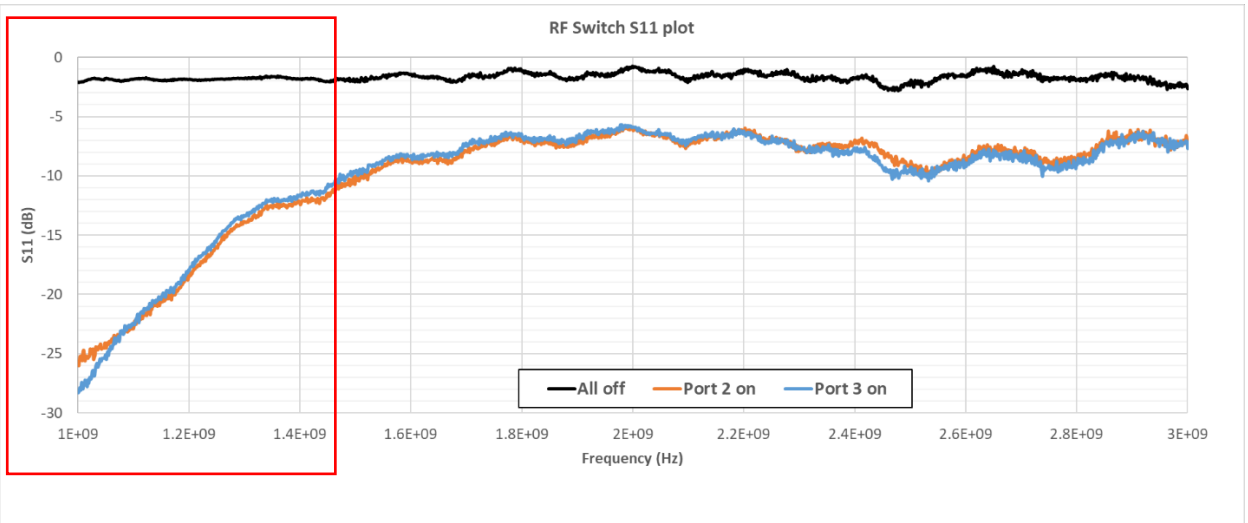

Figure B. 25 RF Switch input matching

Figure B. 25 shows the measurement results of RF switch input matching for both channels off and a single channel on. The matching conditions of activating only Port 2 and only Port 3 are very similar. Although the results do not exhibit a wide band matching, |S11| better than -10 dB within the required bandwidth of 1.4- 1.425 GHz will be sufficient.

Transmission and isolation

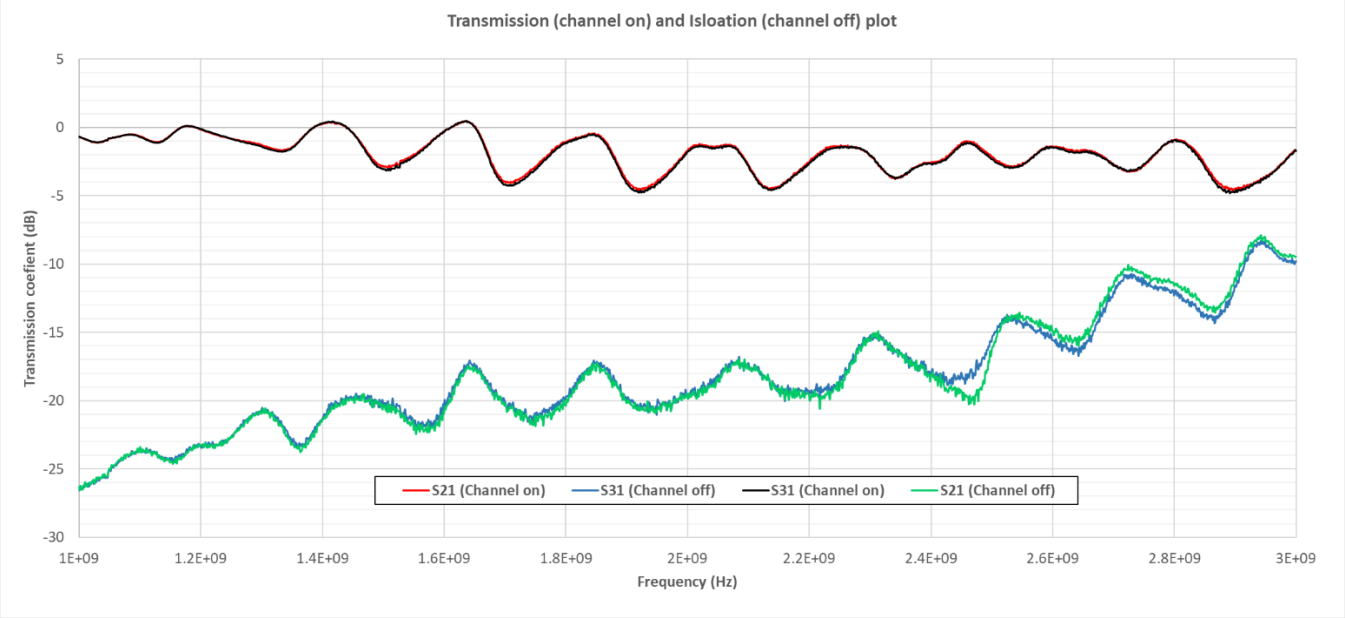

Figure B. 26 Transmission and isolation plot

Figure B. 26 depicts the transmission and isolation performance with each channel activated one at a time. Within the required frequency of 1.4 to 1.425 GHz, as transmission coefficients are close to 0 dB when the channel is on, and isolation is better than -20 dB when the channel is off, the performance is overall good.

Therefore, as the RF switch circuit exhibits satisfactory measurement results, no further design work is required for the next iteration.

B.4.1.2 Second iteration RF Switch testing

Since the switch design of the first iteration demonstrated sufficient performance, only the transmission line width was modified from the first design. Figure B. 27 shows the second iteration hardware of the switch, with a label for each port.

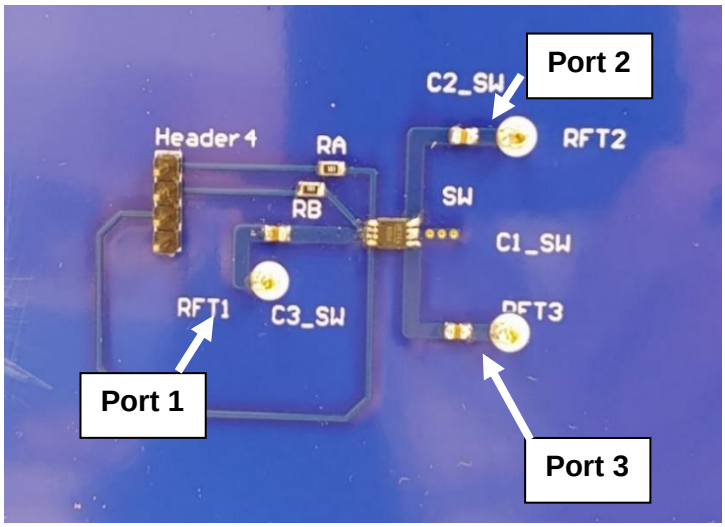

Figure B. 27 PCB hardware of HMC574A in the second iteration

Port 1 matching

Figure B. 28 shows the measurement results of RF switch input matching for both channels off and a single channel on. Likewise, the switch exhibits poor matching when both channels are off, while the matching conditions of activating only Channel 2 and only Channel 3 very similar. |S11| is better than -10 dB from 1 to 1.6 GHz, which is sufficient for the system.

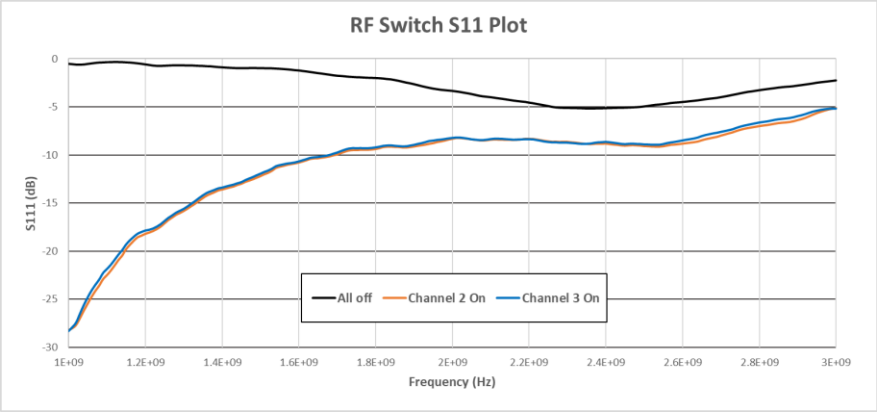

Figure B. 28 Second Iteration RF Switch input matching

Transmission and isolation

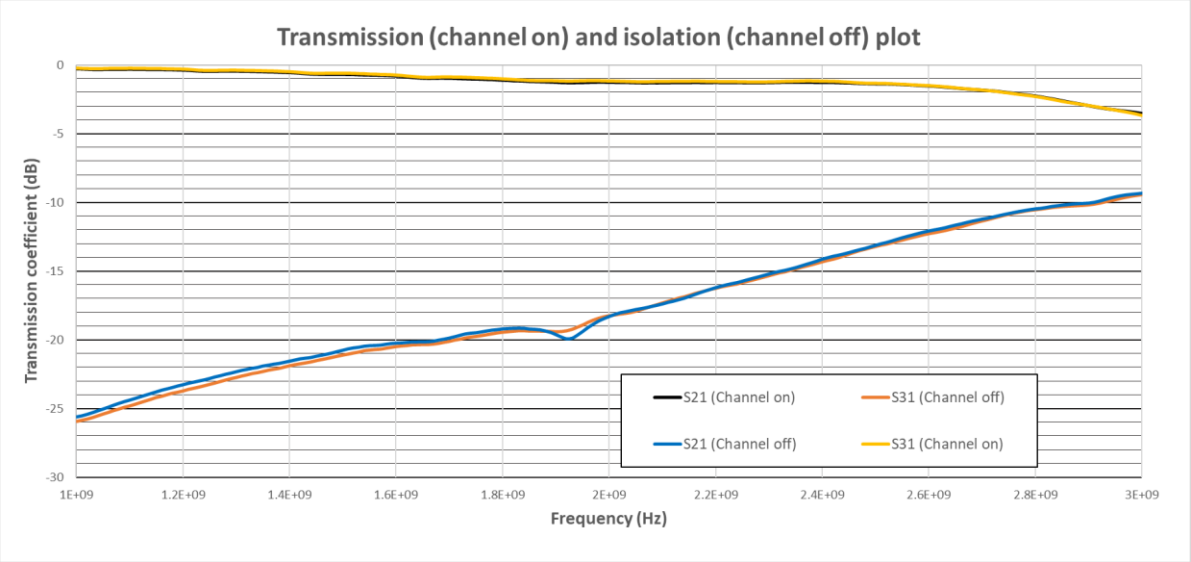

Figure B. 29 Second iteration switch transmission and isolation

Figure B. 29 depicts the transmission and isolation performance with each channel being activated one at a time. Within the required frequency band of 1.4 to 1.425 GHz, as transmission coefficients are close to 0 dB when the channel is on, and isolation is better than -20 dB when the channel is off, the performance is overall good.

B.4.2 Filter testing

Due to limited availability of commercial bandpass filters specified at 1400-1425 MHz, an interdigital microstrip bandpass has been designed with initial design parameters calculated from [173], and then fine tuned in simulation to meet the design requirements. A fifth-order Chebyshev topology was selected as suggested by [174], the filter design requirements for the simulation phase are listed in Table B. 2.

Table B. 2 Bandpass filter requirements

Centre frequency	1410MHz
1400-1425 MHz	Attenuation less than 1 dB
Outside 1375-1440 MHz	Attenuation over 1.5 dB (close to 2dB)

B.4.2.1 First iteration filter testing and modification

Initial testings for a single bandpass filter

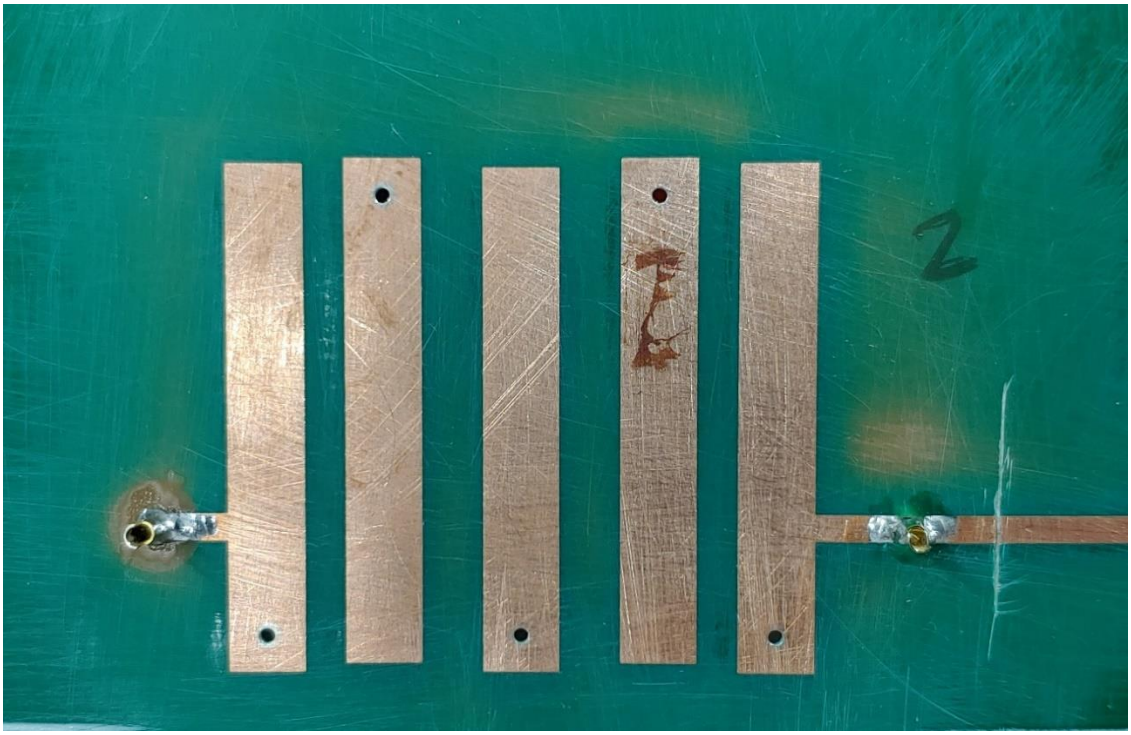

Figure B. 30 Bandpass filter single cut-out

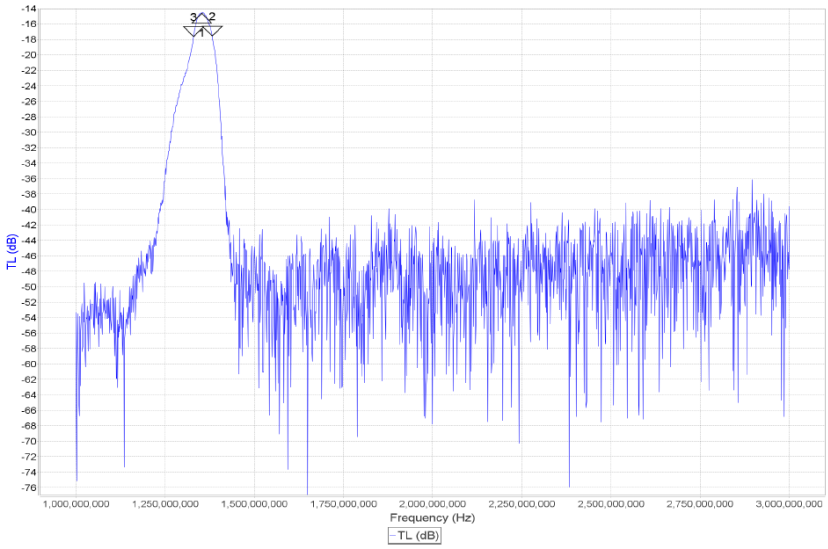

Marker	Freq. (Hz)	TL (dB)	TP (°)	|Z| ()	Rs ()	Xs ()	Theta	gr (ns)
1	1,352,715,304	-14.64	42.36	470.4	298.6	-363.5	0.0	15.7
2	1,382,108,246	-17.55	-139.09	682.0	470.1	-494.1	0.0	19.5
1-2	29,392,942	2.91	181.45	211.6	171.6	130.6	0.0	---
3	1,329,712,132	-17.63	149.93	676.5	558.7	381.4	0.0	9.8

Figure B. 31 Frequency response of a single bandpass filter

A single bandpass filter (in Figure B. 30) has been cut out for testing, the measured frequency response is shown in Figure B. 31. It can be observed that the filter has a sharp bandpass characteristic with a 3 dB bandwidth of 52 MHz, which would be acceptable for an L- band radiometer. However, the measurement result also flags two issues:

1. The centre frequency is at 1.35 GHz rather than between the required bandwidth of 1.4 – 1.425 GHz
    - In this regard, it is possible to cut out part of the filter length for tuning to a higher centre frequency. This modification will be discussed in the later section
2. Even a single filter is very lossy with -14.64 dB at its centre frequency, connecting two in series would in a total loss great than -29 dB. This is mostly due to using low-cost but lossy FR-4 material. Although it is possible to compensate for the high loss by using an RF amplifier, this will incur extra components cost for the amplifier block and also power consumption. Therefore, it would be a better approach to design the RF bandpass filters and consequently the radiometer receiver in Roger 4350B substrate which requires a slightly higher cost but much lower dielectric loss.

One RF amplifier connected with two bandpass filters in series

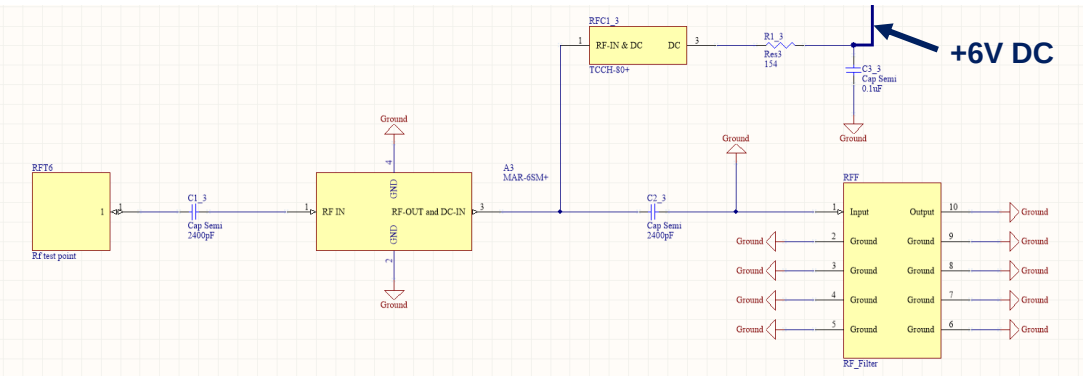

Figure B. 32 Schematic of an RF amplifier (MAR-6SM+) connected with two band pass filters

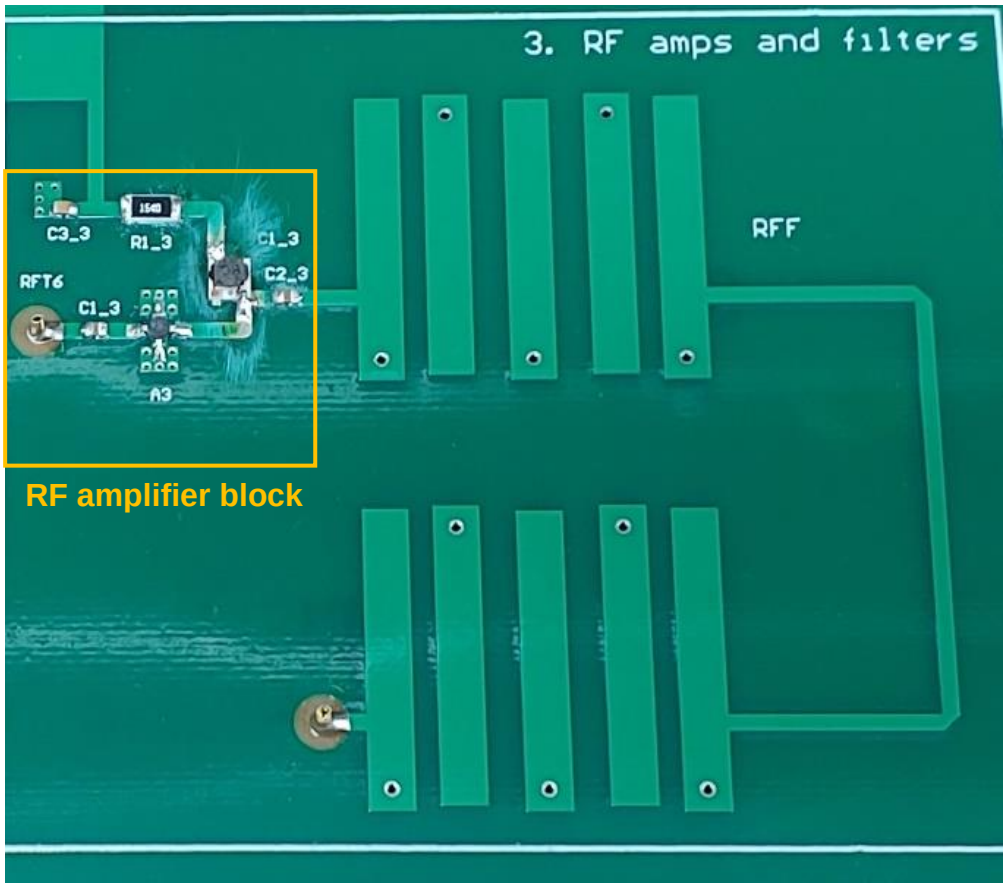

Figure B. 33 Hardware image of the module

To test the combined response for the RF amplifier MAR-6SM+ connected with two bandpass filters in series, a measurement for the combined module (as shown in *Figure B. 32* and *Figure B. 33*) has been conducted.

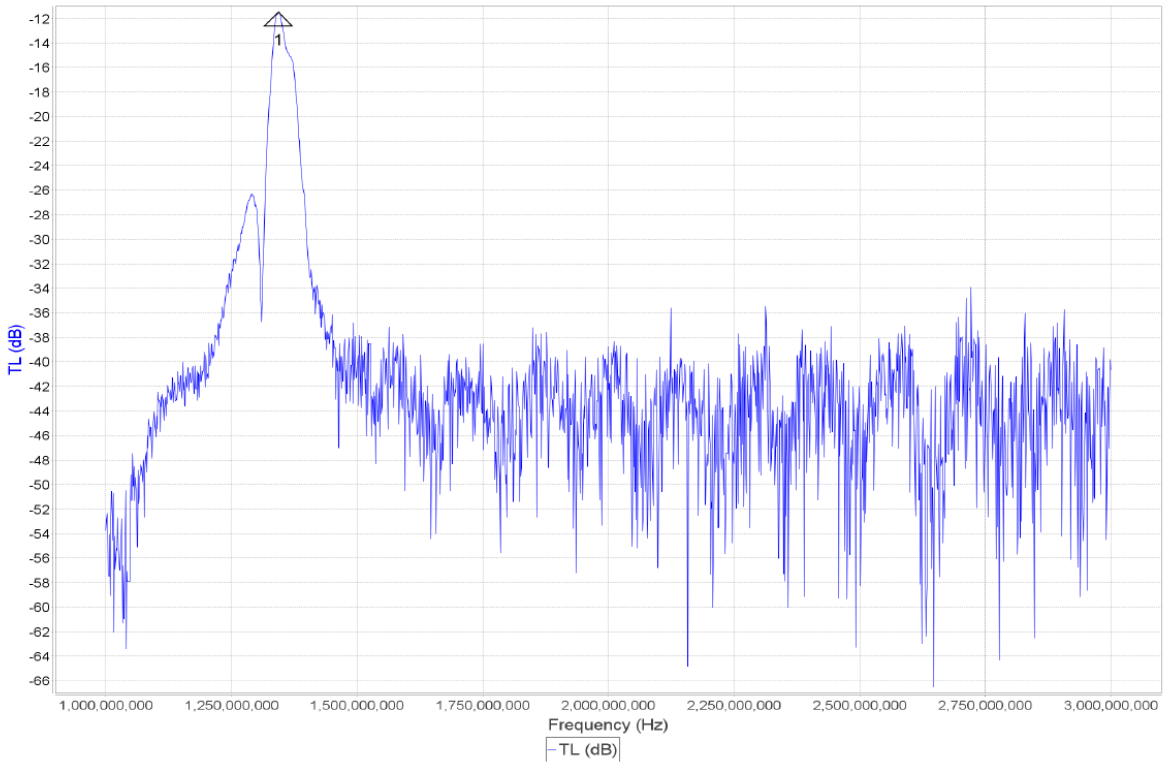

Marker	Freq. (Hz)	TL (dB)	TP (°)	|Z| ()	Rs ()	Xs ()	Theta	gr (ns)
1	1,343,330,887	-11.48	39.52	304.6	189.3	-238.6	0.0	26.9

Figure B. 34 Transmission coefficient for One RF amp connected with two RF filters in series

Figure B. 34 depicts the frequency response of the module. A sharper filtering response has been observed by connecting two filters in series. As discussed in the section Initial testings for a single bandpass filter, two bandpass filters in series would result in a total loss of -29 dB. Given the transmission coefficient is at -11.48 dB with one RF amplifier MAR-6SM+, the gain of this amplifier is about +17.5 dB which is consistent with expectation.

Modification to the filter

Figure B. 35 The single bandpass filter with final cutting

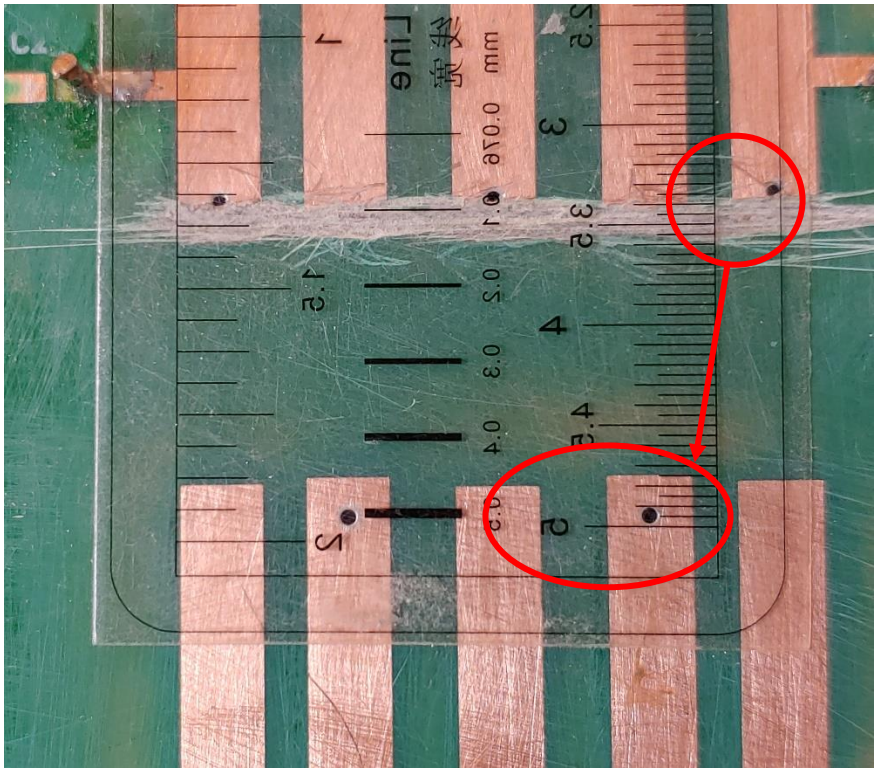

Figure B. 36 Final cutting length in mm

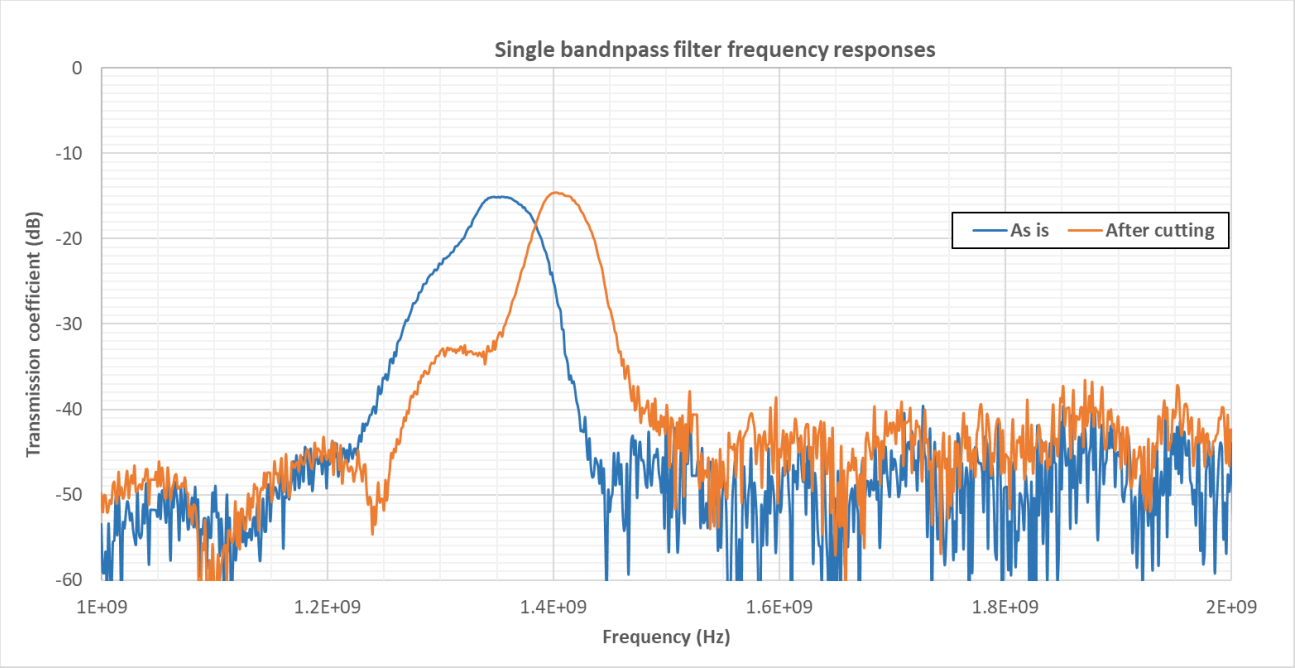

Figure B. 37 Filter responses before and after cutting

As discussed in the section Initial testings for a single bandpass filter, it is possible to increase the filter centre frequency by removing the solder mask cover and then cutting the length of each filter section.

After iterations of testing and cutting, the final cutting length is 3 mm as illustrated in *Figure B. 36*. As a result, the filter reached a centre frequency of 1.4 GHz preserving a sharp bandpass filtering response, the comparison of frequency responses before and after cutting is depicted in *Figure B. 37*.

Discussion for the deviation

To the best of the author's understanding, the main reason for this deviation is the difference in the Dielectric constant between the fabricated substrate and the one specified in simulations. During the design of the first radiometer receiver, one important factor being overlooked is the dielectric constant of FR-4: TG150 which is generally 4.6 at 1 GHz; while in the CST design, the dielectric constant is 4.3. With this difference in dielectric constant, a further simulation suggests a frequency shift of 45 MHz as depicted in *Figure B. 38* (where k stands for dielectric constant). This is very close to the frequency shift of about 60 MHz in the experimental observations. Therefore, for the next design, the substrate dielectric constant in simulation shall match with vendor's specification.

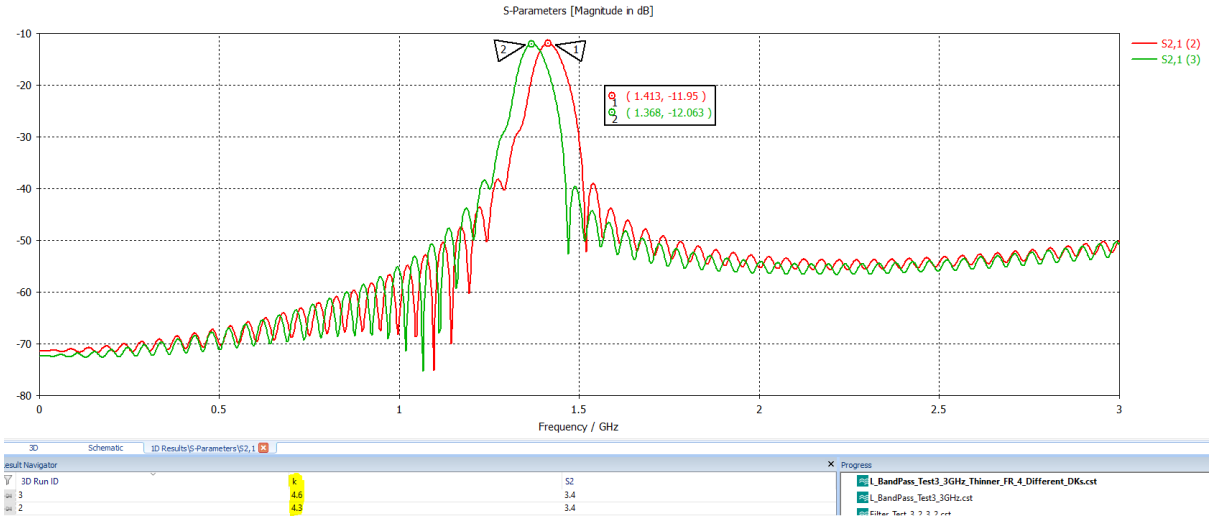

Figure B. 38 Frequency response of the same bandpass filter with different dielectric constants

New filters, substrate material and PCB design

As discussed earlier in Initial testings for a single bandpass filter, a single bandpass filter on Fr-4 substrate has an insertion loss of -14.64 dB, this is mostly due to the high substrate dielectric loss tangent of 0.025.

In order to reduce the insertion loss, widely available Roger materials have been selected. In particular, Roger RO4350B at 0.762mm has been selected due to its relatively lower fabrication cost (as compared to RO4003C); while its loss factor of 0.0037 is still much better than that of Fr-4.

With the experience learnt from the previous section, as per the specification of the dielectric constant for RO4350B on the vendor's website, the dielectric constant for RO4350B has been adjusted to 3.66 (which is 3.48 by default) in CST simulation.

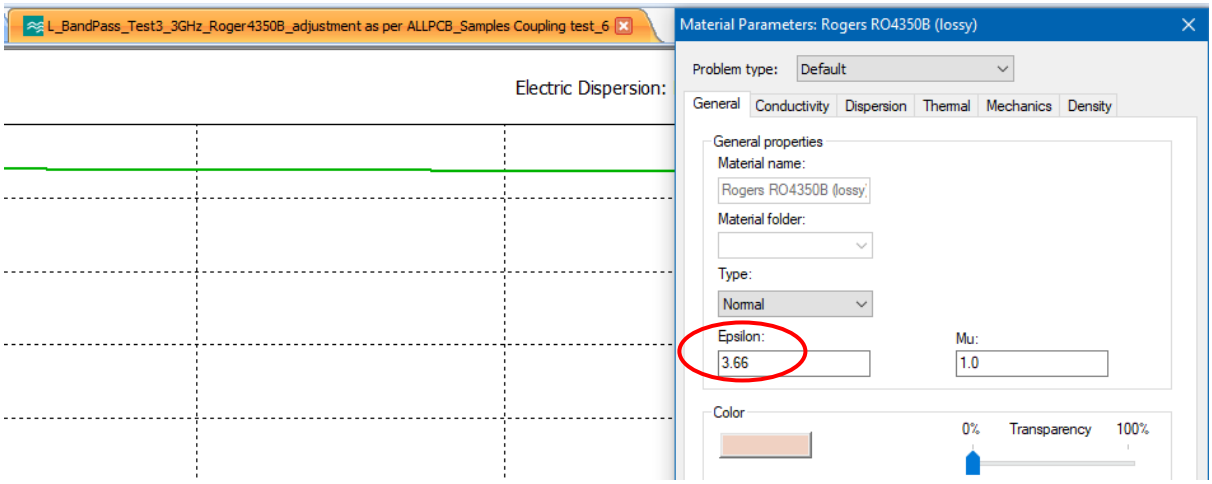

Figure B. 39 Dielectric constant adjustment in CST

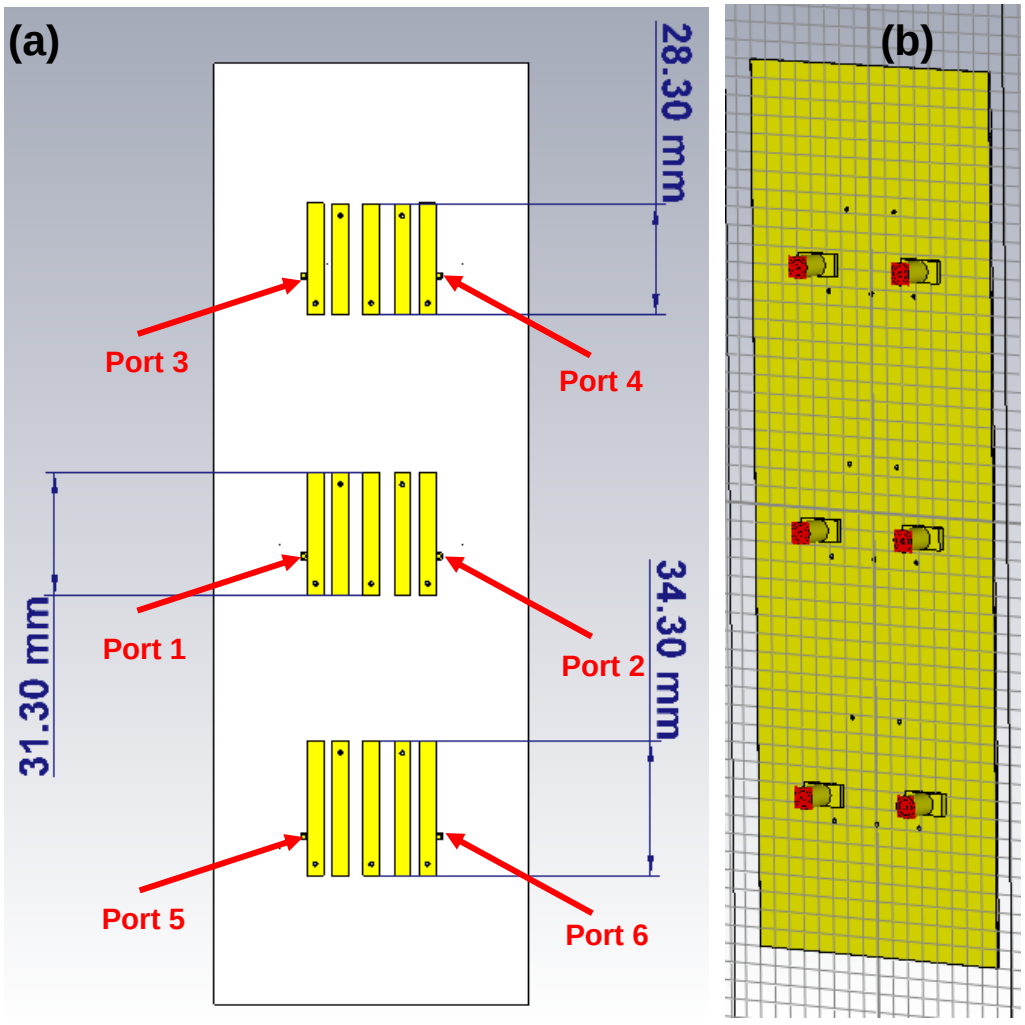

Figure B. 40 New filter design (a) Front facing side with Ports allocation (b) Back side with SMA connectors

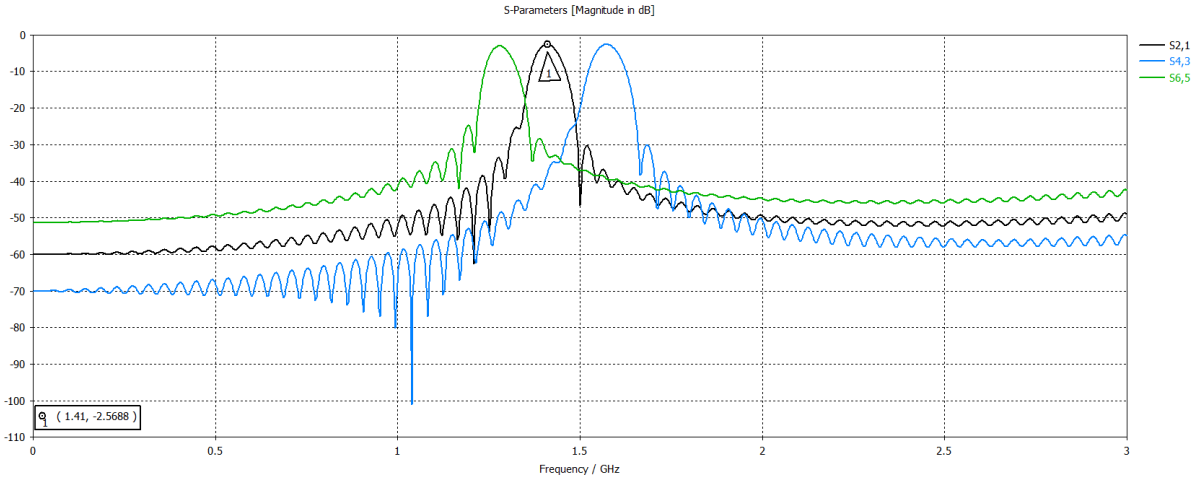

Figure B. 41 Simulated frequency response for all three filters

Further, in consideration of possible manufacturing errors, three bandpass filters with different lengths have been included in the new design for fabrication. The middle filter was optimised in simulation (with a length of 31.5 mm) to meet the required frequency band of 1.4 – 1.425 GHz, while the upper filter and the lower one has the optimised length decreased by 3 mm (i.e. 28.5 mm) and increased by 3 mm (i.e. 34.5 mm) respectively. Each filter is separated by 37 mm to minimise coupling effect, as *Figure B. 41* depicts that the centre frequency of the optimised middle filter stays at 1.41 GHz, this separation distance is sufficient.

It can also be observed that the Insertion loss of each filter Is less than -3dB at the centre frequency, which is much better than over -11 dB when using Fr-4 material (as shown in *Figure B. 38*).

B.4.2.2 Second iteration filter testing

Following the fabrication of the second iteration PCB, the transmission measurement of the middle bandpass filter (in *Figure B. 42*) has been conducted, the measured frequency response is shown in *Figure B. 43*. Being rather close to simulation results, the filter has a sharp bandpass response with a 3 dB bandwidth of 58.7 MHz, with the centre frequency at 1.402 GHz. The insertion loss of -3.52 dB is much lower than that of the first iteration (at -14.64 dB). Therefore, both the bandpass response and insertion loss are satisfactory.

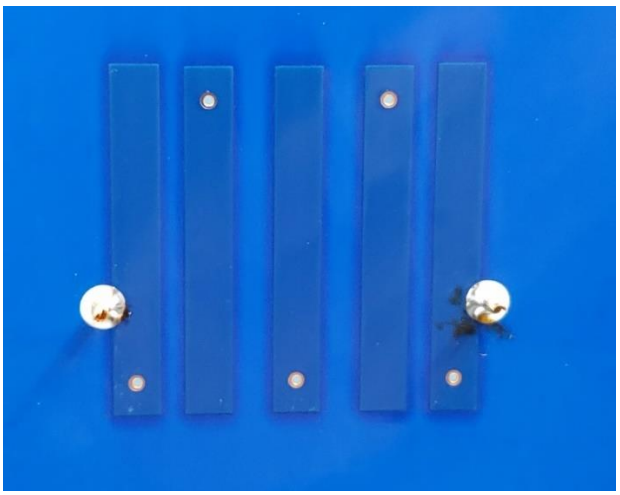

Figure B. 42 Middle bandpass filter in the second iteration PCB

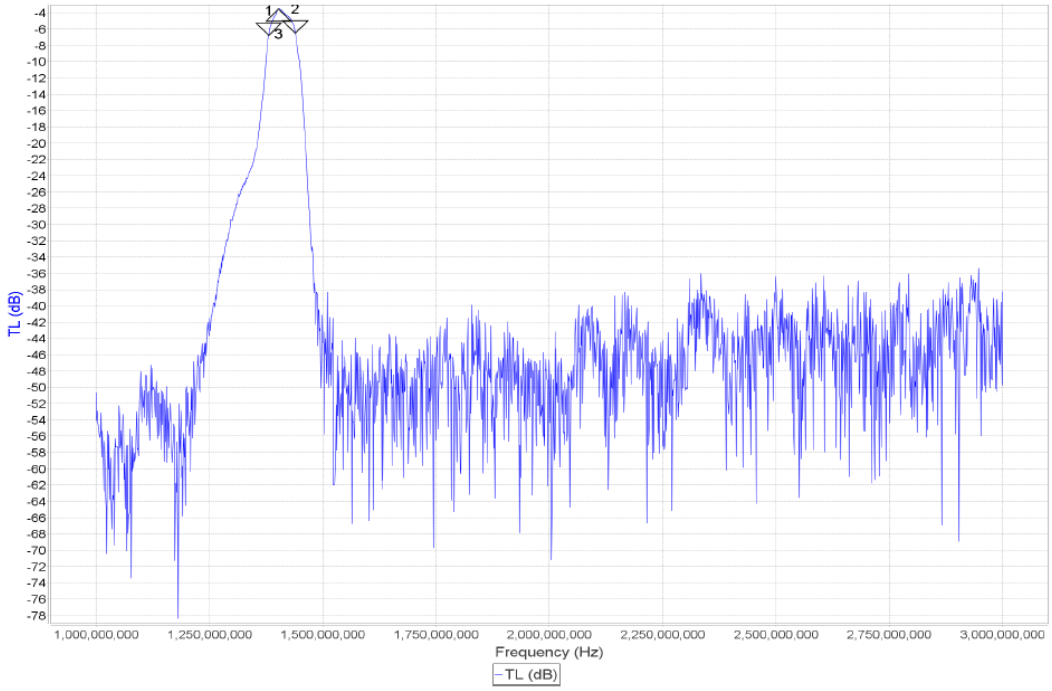

Marker	Freq. (Hz)	TL (dB)	TP (°)	|Z| ()	Rs ()	Xs ()	Theta	gr (ns)
1	1,380,343,956	-6.77	-163.28	125.5	108.7	-62.7	0.0	17.9
2	1,439,054,768	-6.51	-161.24	121.3	100.4	-68.1	0.0	19.4
1-2	58,710,812	0.25	2.04	4.2	8.3	5.4	0.0	---
3	1,402,041,430	-3.52	75.50	158.1	-62.4	-145.2	0.0	16.7

Figure B. 43 Frequency response of the middle bandpass filter

B.4.3 RF amplifiers testing

B.4.3.1 First iteration amplifiers testing and redesign:

Cascaded amplifiers testing

Considering an L- band radiometer receiver requires a total RF amplification of over 75 dB for boosting very weak thermal radiation (around -100 dBm) to the linear detection region (at least -25 dBm) of an RF detector diode, multiple amplifiers will be required. MAR-6SM+ has been selected for the RF amplifier because of its low cost, low noise figure and low current consumption. *Figure B. 44* shows two amplifiers MAR-6SM+ connected in series, yielding a total gain of 35 dB (thereby multiple blocks of cascaded amplifiers will be needed).

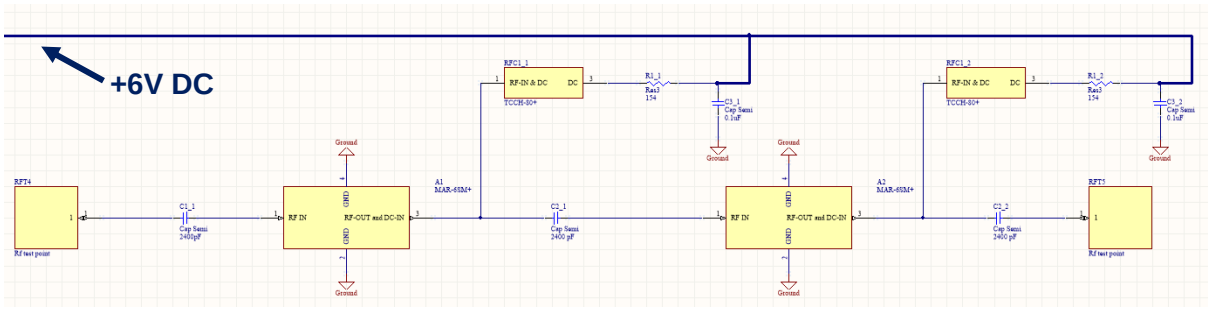

Figure B. 44 Schematic of the cascaded amplifiers MAR-6SM+

Figure B. 45 shows the PCB hardware of the amplifiers, where Port 1 is the amplifier input port; and Port 2 is the output port. Being the crucial factor, the measurement focuses on input impedance matching.

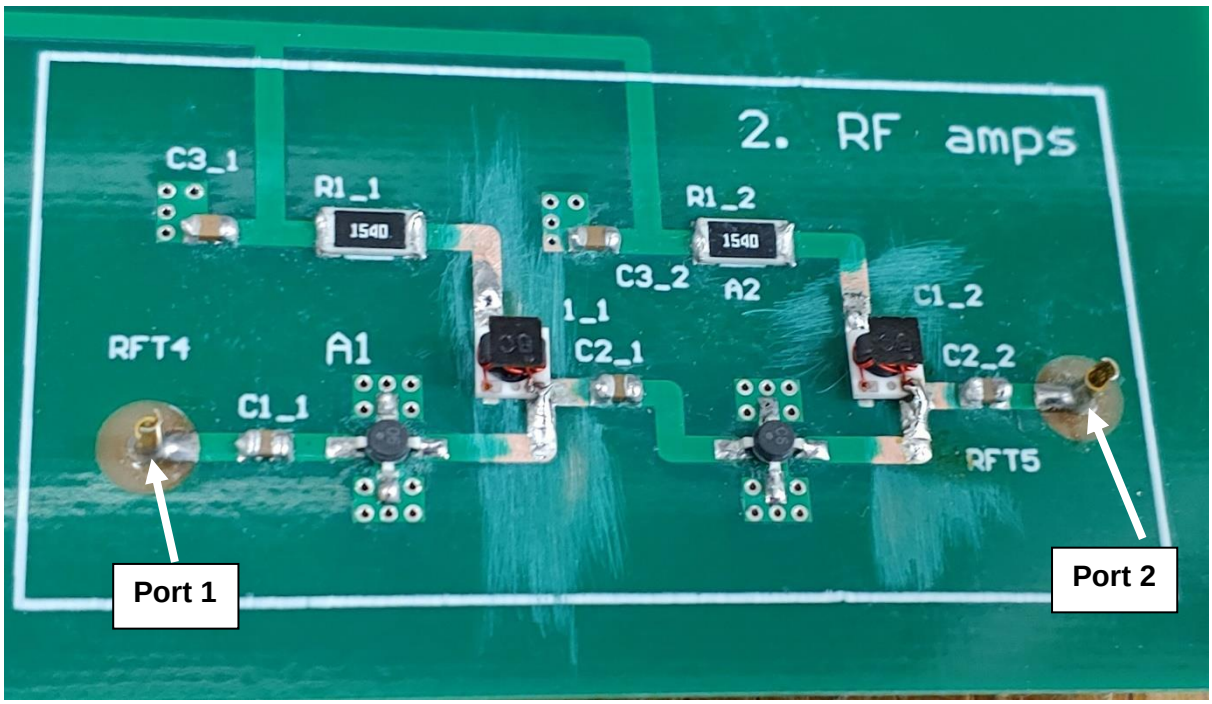

Figure B. 45 PCB hardware of cascaded amplifiers

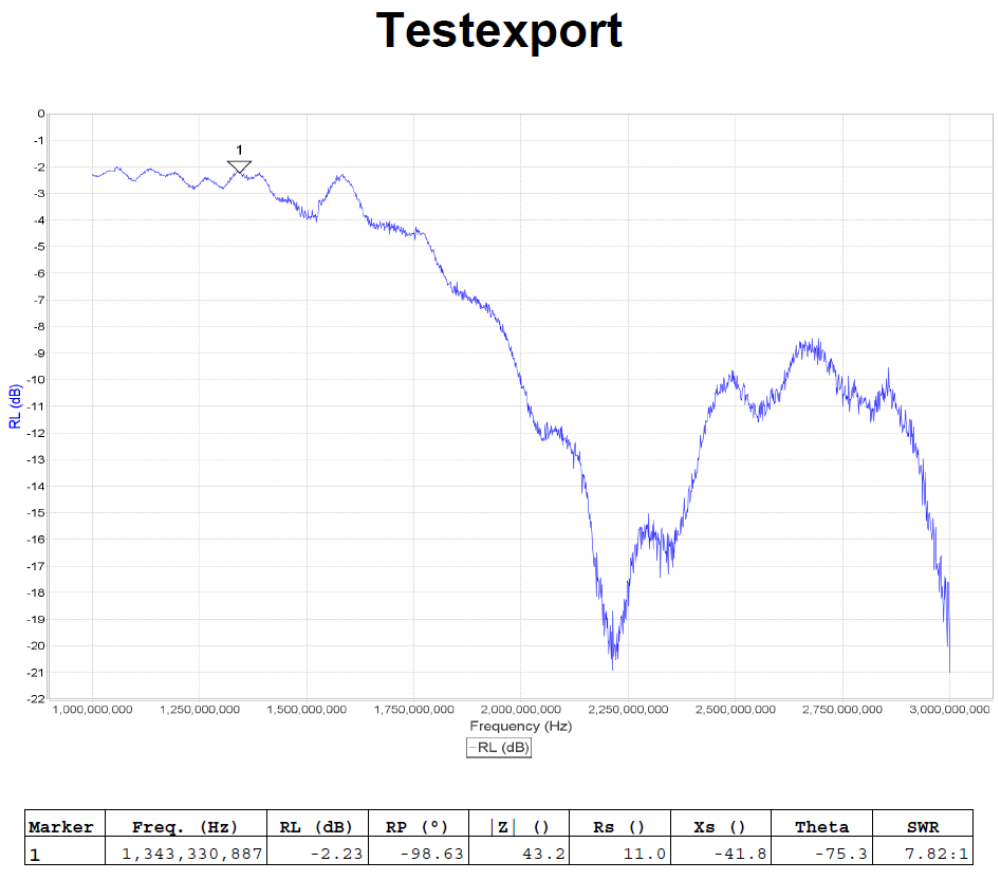

Marker	Freq. (Hz)	RL (dB)	RP (°)	|Z| ()	Rs ()	Xs ()	Theta	SWR
1	1,343,330,887	-2.23	-98.63	43.2	11.0	-41.8	-75.3	7.82:1

Figure B. 46 Input impedance matching measurement of the cascaded MAR-6SM+

Figure B. 46 shows the reflection coefficient measurement results of the amplifier input port. As |S11| is at -2 dB level within the target frequency of 1.4- 1.425 GHz, this exhibits very poor impedance matching results, further investigation is required.

Single-unit RF amplifier testing

To find out possible causes for the poor input matching, a single unit MAR-6SM+ has been cut and modified.

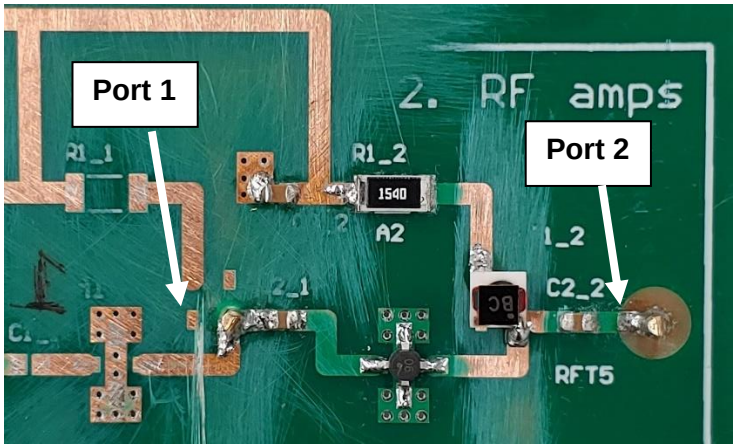

Figure B. 47 Front side of the single cut RF amplifier

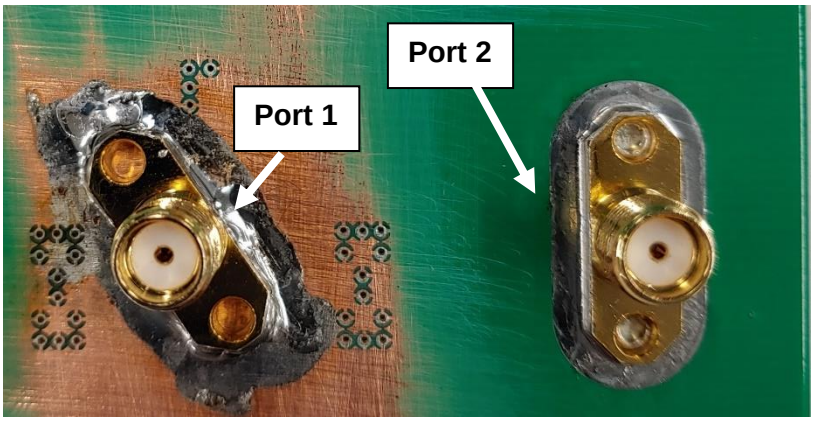

Figure B. 48 Backside of the single RF amplifier

Figure B. 47 and *Figure B. 48* show the modified cut-out RF amplifier after the required work of cutting, drilling, removing solder mask and soldering.

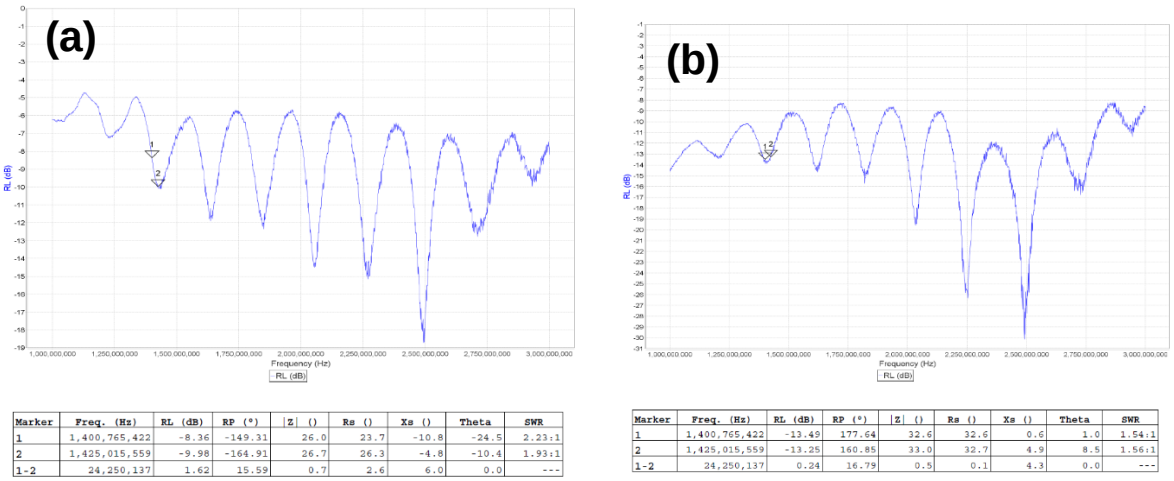

Marker	Freq. (Hz)	RL (dB)	RP (°)	|Z| ()	Rs ()	Xs ()	Theta	SWR
1	1,400,765,422	-8.36	-149.31	26.0	23.7	-10.8	-24.5	2.23:1
2	1,425,015,559	-9.98	-164.91	26.7	26.3	-4.8	-10.4	1.93:1
1-2	24,250,137	1.62	15.59	0.7	2.6	6.0	0.0	---

Marker	Freq. (Hz)	RL (dB)	RP (°)	|Z| ()	Rs ()	Xs ()	Theta	SWR
1	1,400,765,422	-13.49	177.64	32.6	32.6	0.6	1.0	1.54:1
2	1,425,015,559	-13.25	160.85	33.0	32.7	4.9	8.5	1.56:1
1-2	24,250,137	0.24	16.79	0.5	0.1	4.3	0.0	---

Figure B. 49 Impedance matching measurement of a single MAR-6SM+ block (a) Input matching |S11| (b) Output matching |S22|

Figure B. 49 (a) depicts the input impedance matching (|S11|) result of a single RF amplifier block, although |S11| is still not better than the required -10dB, this result indicates the amplifier is workable without significant input reflection loss. It can also be observed from *Figure B. 49* (b) that a single RF MAR-6SM+ has good output matching. Therefore, no significant design issue was found in a single RF amplifier block.

A further test was conducted to connect another single RF amplifier block from a different PCB boarding using an SMA cable, *Figure B. 50* shows the second cut-out unit.

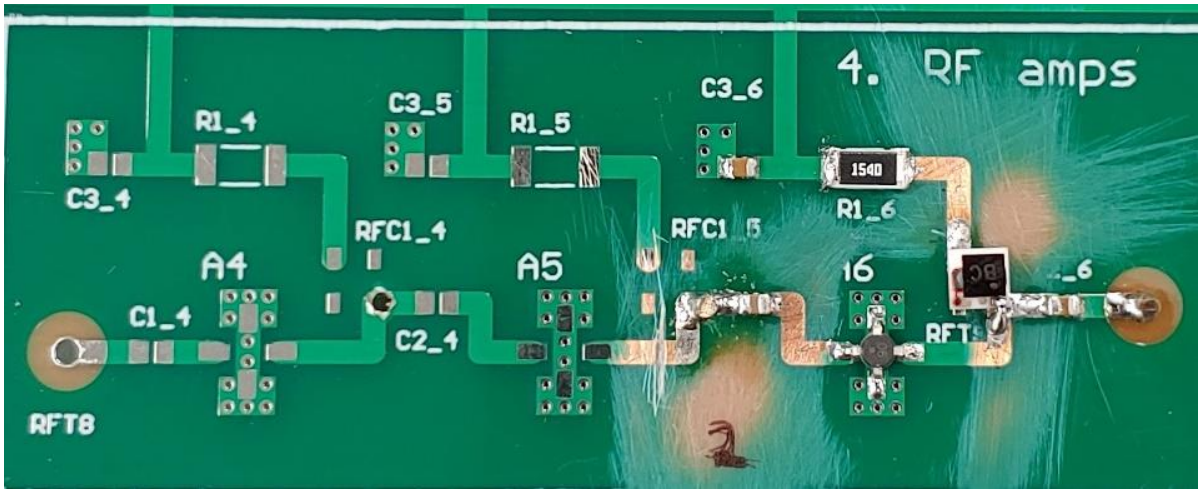

Figure B. 50 Second cut out MAR-6SM+ from another PCB board

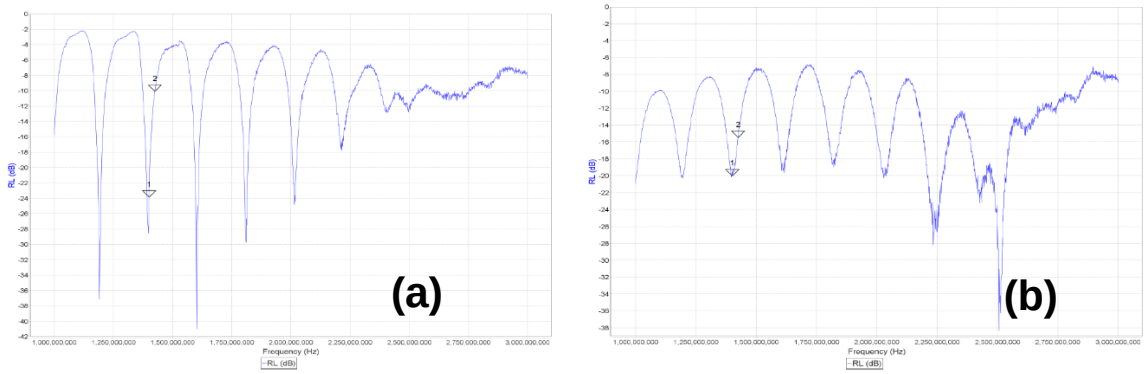

Marker	Freq. (Hz)	RL (dB)	RP (°)	|Z| ()	Rs ()	Xs ()	Theta	SWR
1	1,400,765,422	-23.85	-22.66	56.3	56.2	-2.8	-2.8	1.14:1
2	1,425,015,559	-10.08	-82.58	53.8	44.3	-30.5	-34.6	1.91:1
1-2	24,250,137	13.76	59.92	2.5	11.9	27.7	0.0	---

Marker	Freq. (Hz)	RL (dB)	RP (°)	|Z| ()	Rs ()	Xs ()	Theta	SWR
1	1,400,765,422	-20.01	-179.10	40.9	40.9	-0.1	-0.2	1.22:1
2	1,425,015,559	-15.48	-154.36	36.9	36.5	-5.5	-8.5	1.40:1
1-2	24,250,137	4.54	24.74	4.0	4.4	5.3	0.0	---

Figure B. 51 Impedance matching measurement of two separated MAR-6SM+ blocks connected with a SMA cable (a) Input matching (b) Output matching

Figure B. 51 shows the impedance matching results of two separated single RF amplifier units connected with an SMA cable, which exhibit good input and output impedance matching. This also narrows down the cause for the poor input matching in Cascaded amplifiers testing to be severe coupling issue between each amplifier block.

Simulation verification and new designs

To verify the coupling issue, a CST simulation of the cascaded amplifier has been conducted, and the measurement results from section Single-unit RF amplifier testing have also been imported into CST for a more accurate simulation. *Figure B. 52* shows the simulation in 3D view, where the components are connected accordingly with discrete edge ports in *Figure B. 53* (e.g. the measured amplifier results are connected from port 4 to port 5; port 8 to port 9). For comparison, measurement data with an ideal series connection has also been added to the simulation.

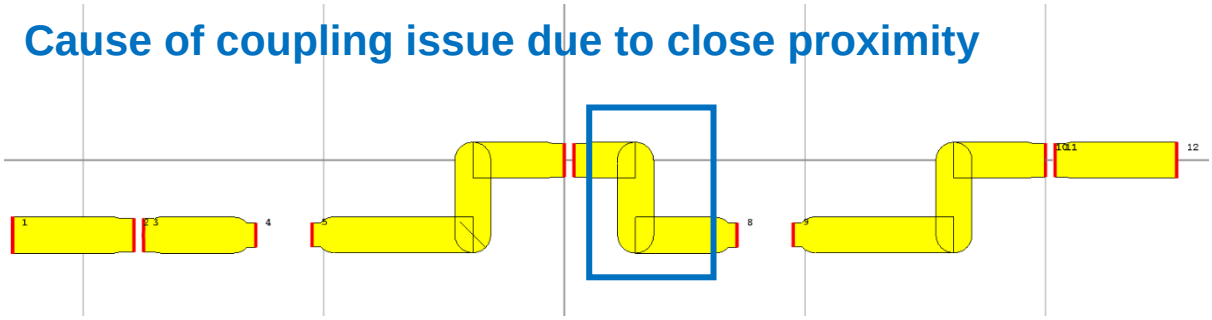

Figure B. 52 Cascaded amplifiers simulation in 3D view

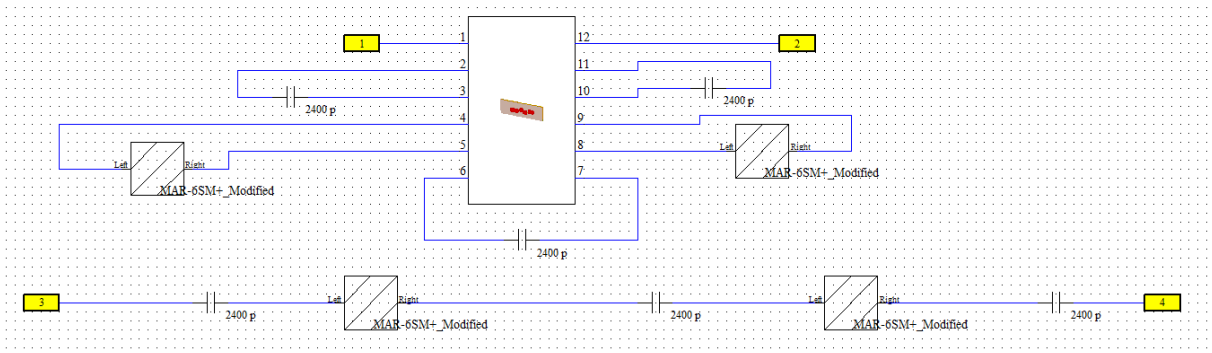

Figure B. 53 Cascaded amplifiers simulation in Schematic mode

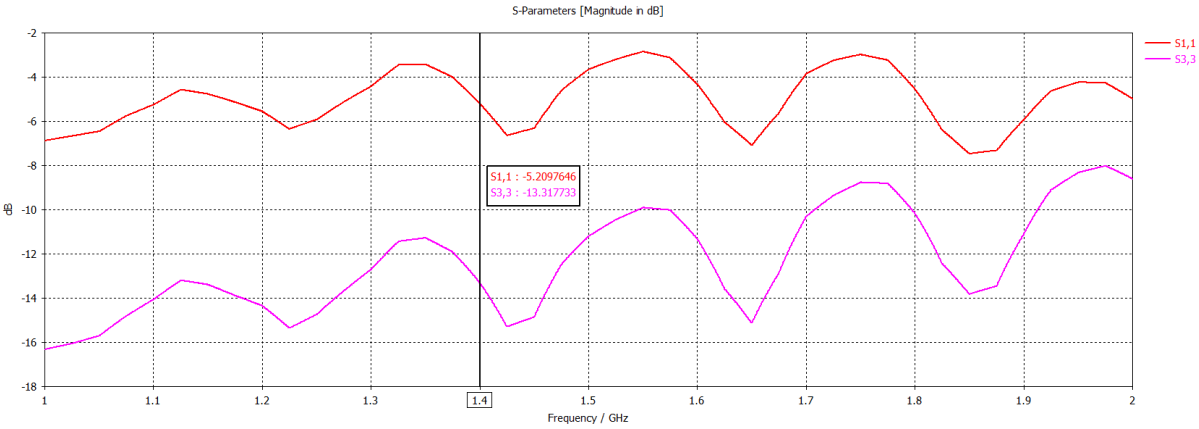

Figure B. 54 Simulation results of cascaded amplifiers input matching where |S11|: connection with microstrip lines in proximity; |S33|: ideal series connection

Figure B. 54 shows the simulated input matching results in both scenarios, where |S11| depicts the input matching with the first iteration amplifiers connection design; |S33| shows the results with an ideal series connection. Being consistent with experimental observations, due to severe coupling from two amplifiers connected in proximity, the input matching of the amplifier MAR-6SM+ has been significantly degraded. This coupling issue is now confirmed as the cause of poor input

matching results in Cascaded amplifiers testing, which was not well considered in the first iteration design.

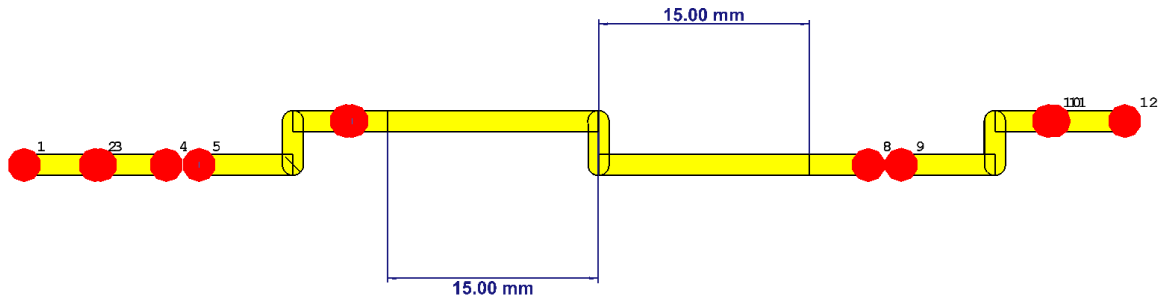

Figure B. 55 Amplifiers interconnection redesign to improve impedance matching

To reduce the coupling effect and improve impedance matching from the first iteration, the inter-amplifiers connection has been extended to around 30mm which is about a quarter guided wavelength at 1.4 GHz as depicted in *Figure B. 55*.

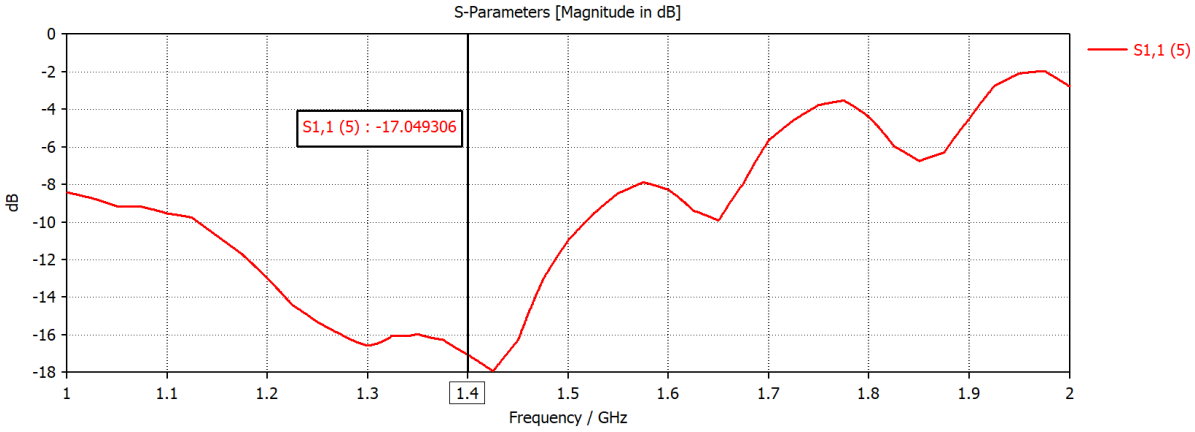

Figure B. 56 Simulated input matching results with the new design

Figure B. 56 shows the simulated input matching results with the new interconnection design, it can be observed that |S11| has been significantly improved from -5.2 dB (in the first iteration) to -17 dB in the new design.

As touched on in the section New filters, substrate material and PCB design, Roger RO4350B will be used as the substrate material. With the experience learnt, the cascaded amplifiers have been simulated with a long interconnection and specified dielectric constant of 3.66.

Figure B. 57 shows the cascaded amplifiers MAR-6SM+ design on Roger RO4350B substrate, the simulated impedance matching results are depicted in *Figure B. 58*. As both input and output reflection coefficients are better than -25 dB, this design is sufficient for the next iteration of PCB.

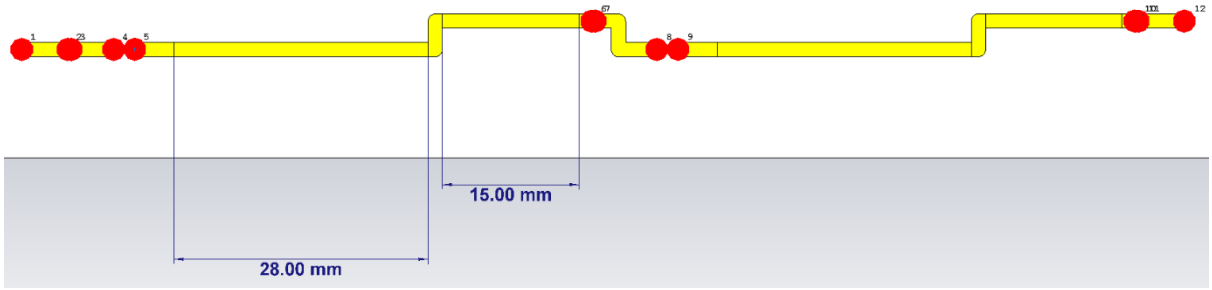

Figure B. 57 Cascaded RF amplifier design on Roger RO4350B

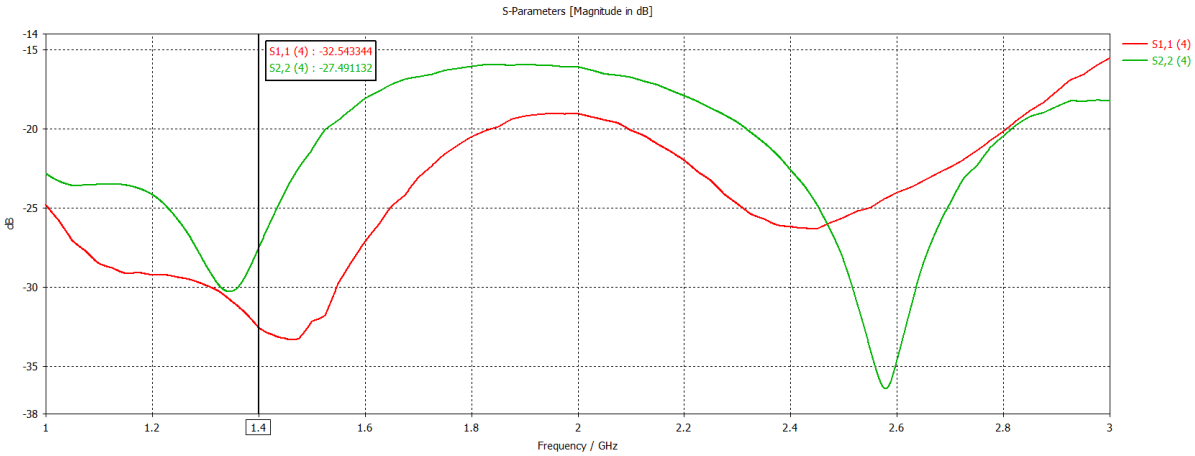

Figure B. 58 Simulated impedance matching results: |S11| for input matching; |S22| for output matching

B.4.3.2 Second iteration amplifiers testing

Single-unit RF amplifier testing

Before validating the new cascaded amplifier design, a single unit RF amplifier module (shown in *Figure B. 59*) of the iteration design has been tested. Acceptable input impedance matching result is depicted in *Figure B. 60* (a), as |S11| is better than -10 dB within the required bandwidth of 1.4 – 1.425 GHz. At the output end, this module exhibits good output matching with |S22| at -20dB level within the target frequency as shown in *Figure B. 60* (b).

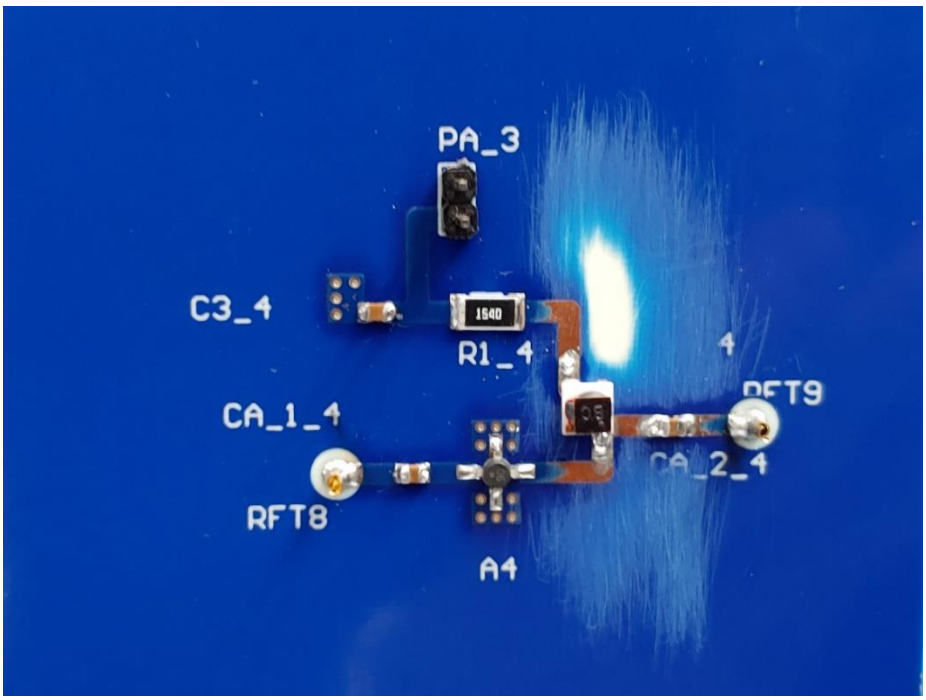

Figure B. 59 Single RF amplifier module in the second iteration

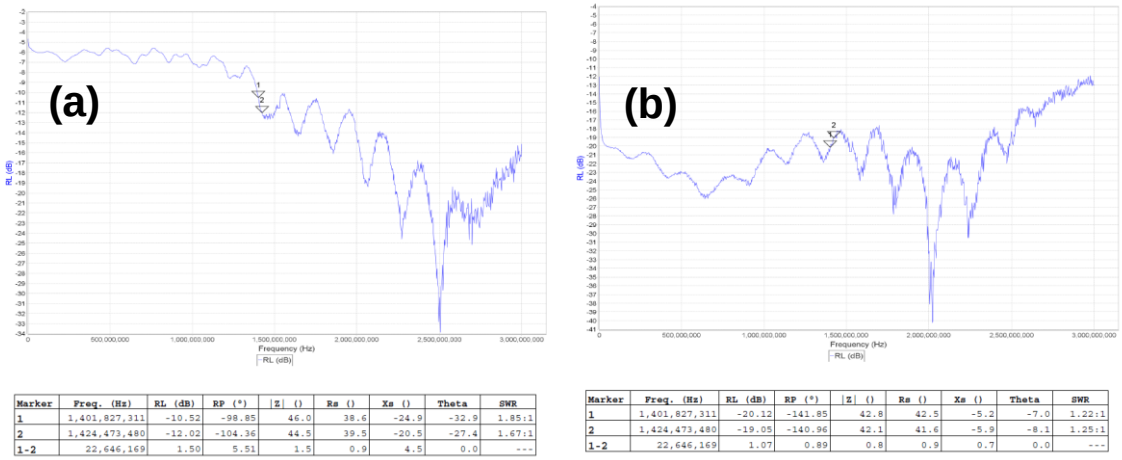

Marker	Freq. (Hz)	RL (dB)	RP (°)	|Z| ()	Rs ()	Xs ()	Theta	SWR
1	1,401,827,311	-10.52	-98.85	46.0	38.6	-24.9	-32.9	1.85:1
2	1,424,473,480	-12.02	-104.36	44.5	39.5	-20.5	-27.4	1.67:1
1-2	22,646,169	1.50	5.51	1.5	0.9	4.5	0.0	---

Marker	Freq. (Hz)	RL (dB)	RP (°)	|Z| ()	Rs ()	Xs ()	Theta	SWR
1	1,401,827,311	-20.12	-141.85	42.8	42.5	-5.2	-7.0	1.22:1
2	1,424,473,480	-19.05	-140.96	42.1	41.6	-5.9	-8.1	1.25:1
1-2	22,646,169	1.07	0.89	0.8	0.9	0.7	0.0	---

Figure B. 60 Impedance matching measurement of a single MAR-6SM+ block in the second iteration (a) Input matching |S11| (b) Output matching |S22|

Cascaded amplifiers testing

The fabricated new cascaded amplifier design is shown in *Figure B. 61*. The measurement results in *Figure B. 62* (a) shows acceptable input matching as |S11| is at -10.5 dB level within the required bandwidth; while a wide band output matching is depicted in *Figure B. 62* (b), with |S22| better than -14dB within the targeted frequency.

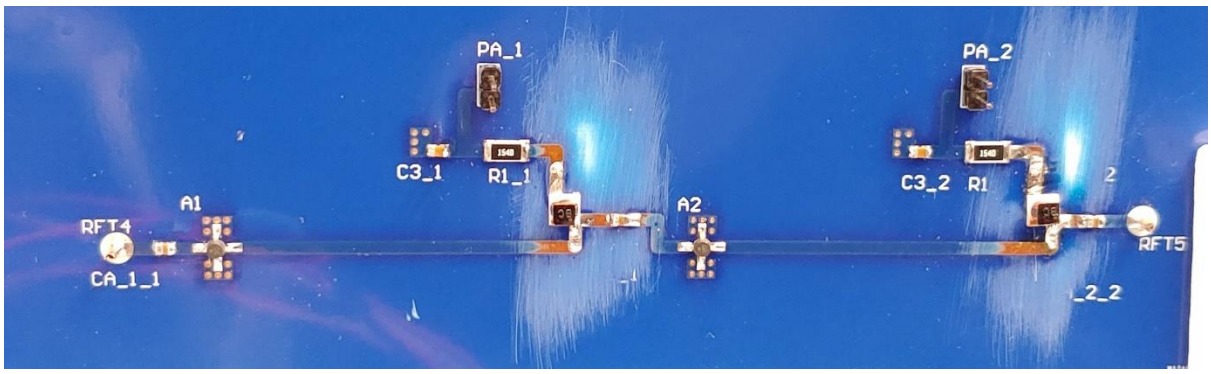

Figure B. 61 Cascaded amplifiers design in the second iteration

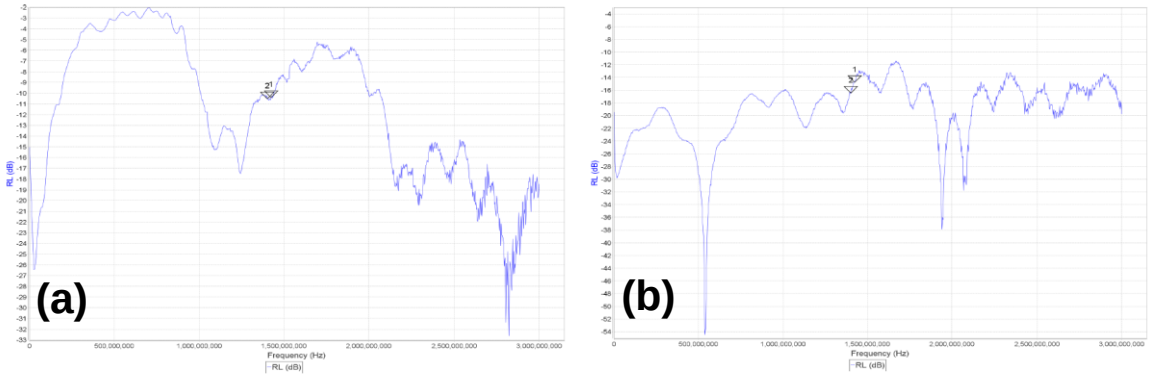

Marker	Freq. (Hz)	RL (dB)	RP (°)	|Z| ()	Rs ()	Xs ()	Theta	SWR
1	1,424,473,480	-10.40	-2.66	93.2	93.1	-2.9	-1.8	1.86:1
2	1,401,827,311	-10.52	13.10	90.6	89.6	13.3	8.4	1.85:1
1-2	22,646,169	0.12	15.76	2.6	3.5	16.1	0.0	---

Marker	Freq. (Hz)	RL (dB)	RP (°)	|Z| ()	Rs ()	Xs ()	Theta	SWR
1	1,424,473,480	-14.77	-128.18	40.0	38.4	-11.4	-16.5	1.45:1
2	1,401,827,311	-16.45	-129.26	41.4	40.3	-9.6	-13.4	1.35:1
1-2	22,646,169	1.68	1.08	1.4	1.9	1.8	0.0	---

Figure B. 62 Impedance matching measurement of the cascaded MAR-6SM+ amplifiers block (a)Input matching |S11| (b)Output matching |S22|

B.4.4 Rectifier testing

B.4.4.1 Rectifier circuit with modification from ECE3122 design project

After multiple failed attempts of using commercial RF power detectors, with available fabricated rectenna PCB designs from a teaching unit ECE3122 (in 2017), one of the PCB boards has been modified to extend the open circuit stub for matching a Schokty Detector Diode HSMS-2862 at 1.425 GHz as shown in Figure B. 63.

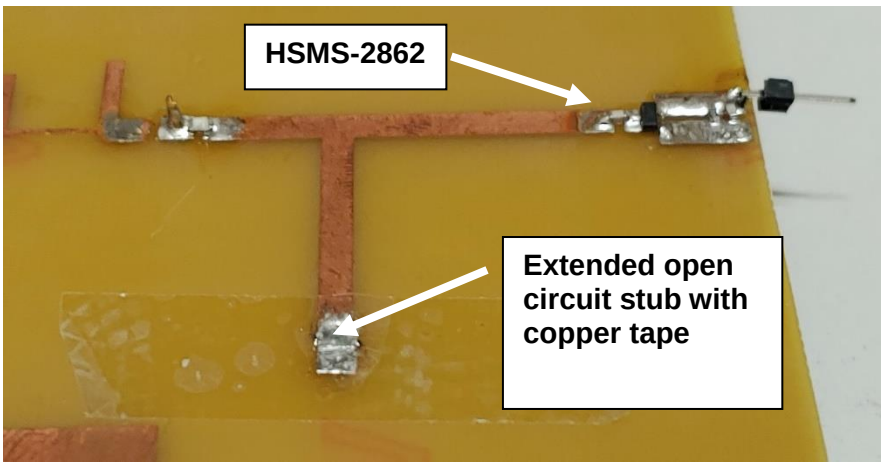

Figure B. 63 Modified rectifier circuit from ECE3022 Design Project

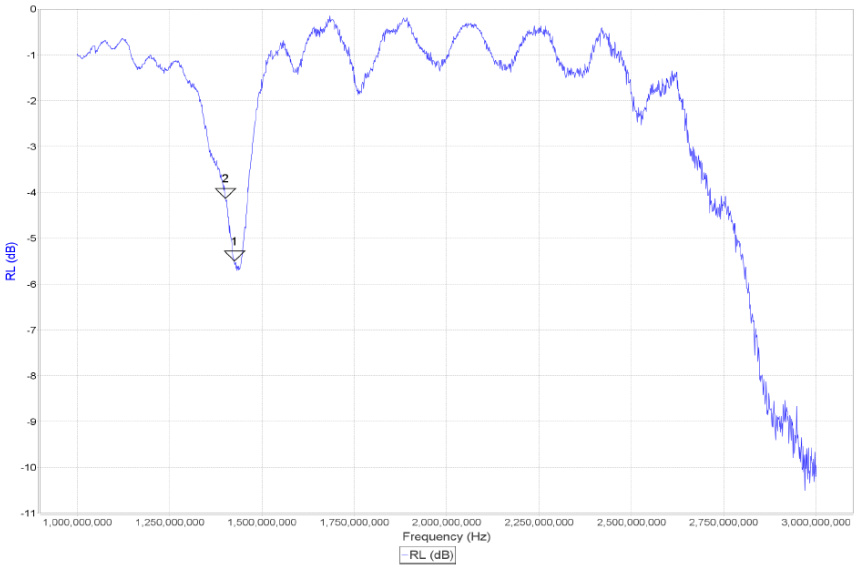

Marker	Freq. (Hz)	RL (dB)	RP (°)	|Z| ()	Rs ()	Xs ()	Theta	SWR
1	1,425,558,682	-5.50	84.71	54.0	30.3	44.6	55.8	3.26:1
2	1,401,277,556	-4.13	80.18	58.3	26.1	52.1	63.4	4.28:1
1-2	24,281,126	1.37	4.52	4.4	4.2	7.5	0.0	---

Figure B. 64 Input matching results of the modified ECE3022 rectifier

Figure B. 64 depicts the measurement matching result of the modified rectifier, although the input matching is still poor, a further RF Input to Voltage output test was encouraged by earlier experience of using testing this diode in 2017. *Figure B. 65* shows the experimental setup.

Figure B. 66 shows the RF Input to DC output plot of the modified rectifier. Overall, despite poor input matching, the diode detector is able to output DC voltages (according to different RF input power levels) in a nearly linear manner, better linearity can be achieved with RF input power

greater than -5 dBm. The author also believes improving input matching in the next iteration of PCB design will enhance the sensitivity of this rectifier.

The reason for not using this Detector Diode HSMS-2862 in the initial design is that this diode is obsolete, therefore it has very limited availability. However, with sufficient quantity available in the lab, it is envisioned that a working prototype can be developed with this diode, and thereby build confidence to work with newly available Schottky diodes.

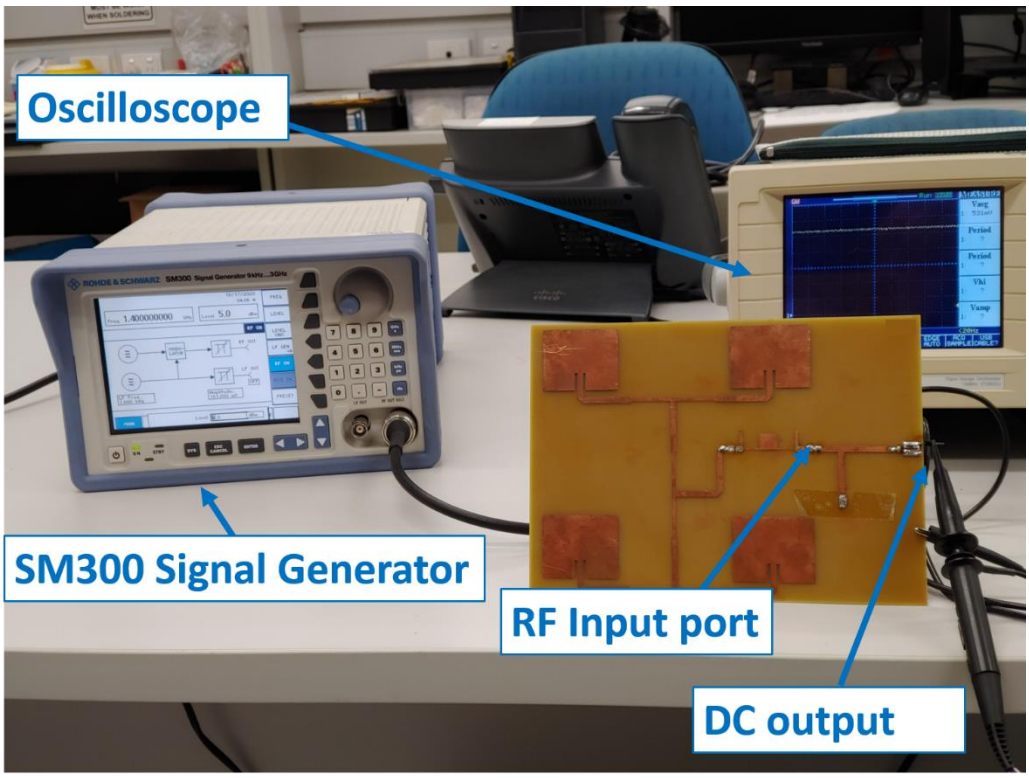

Figure B. 65 Output testing set up for the modified detector circuit

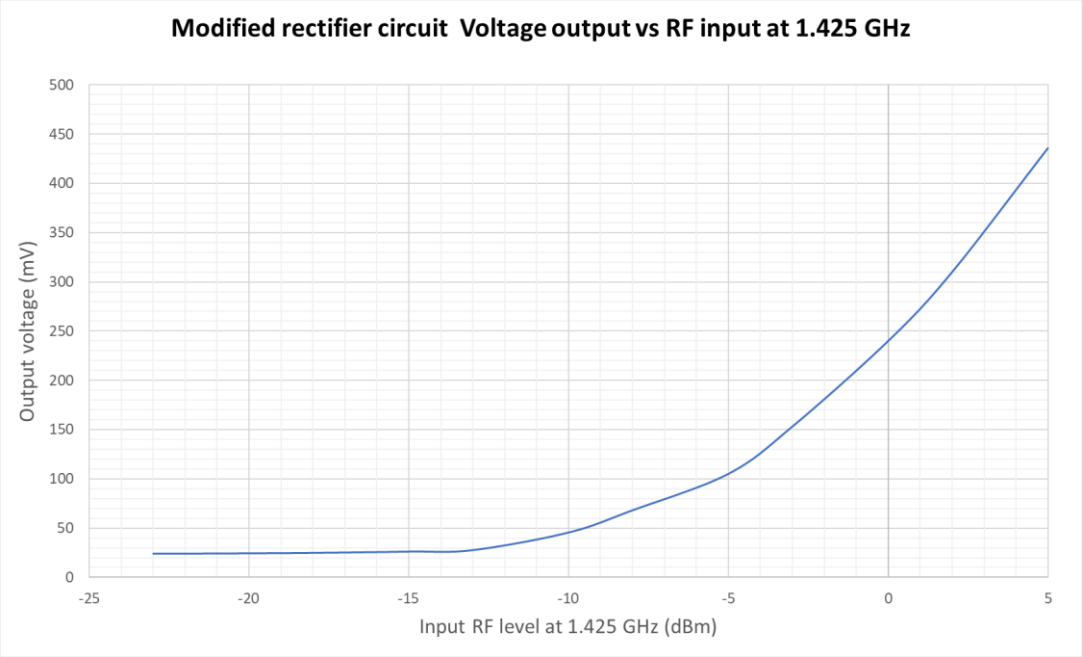

Figure B. 66 Voltage output vs RF Input curve of the modified rectifier

Rectifier circuit design on Roger RO4350B

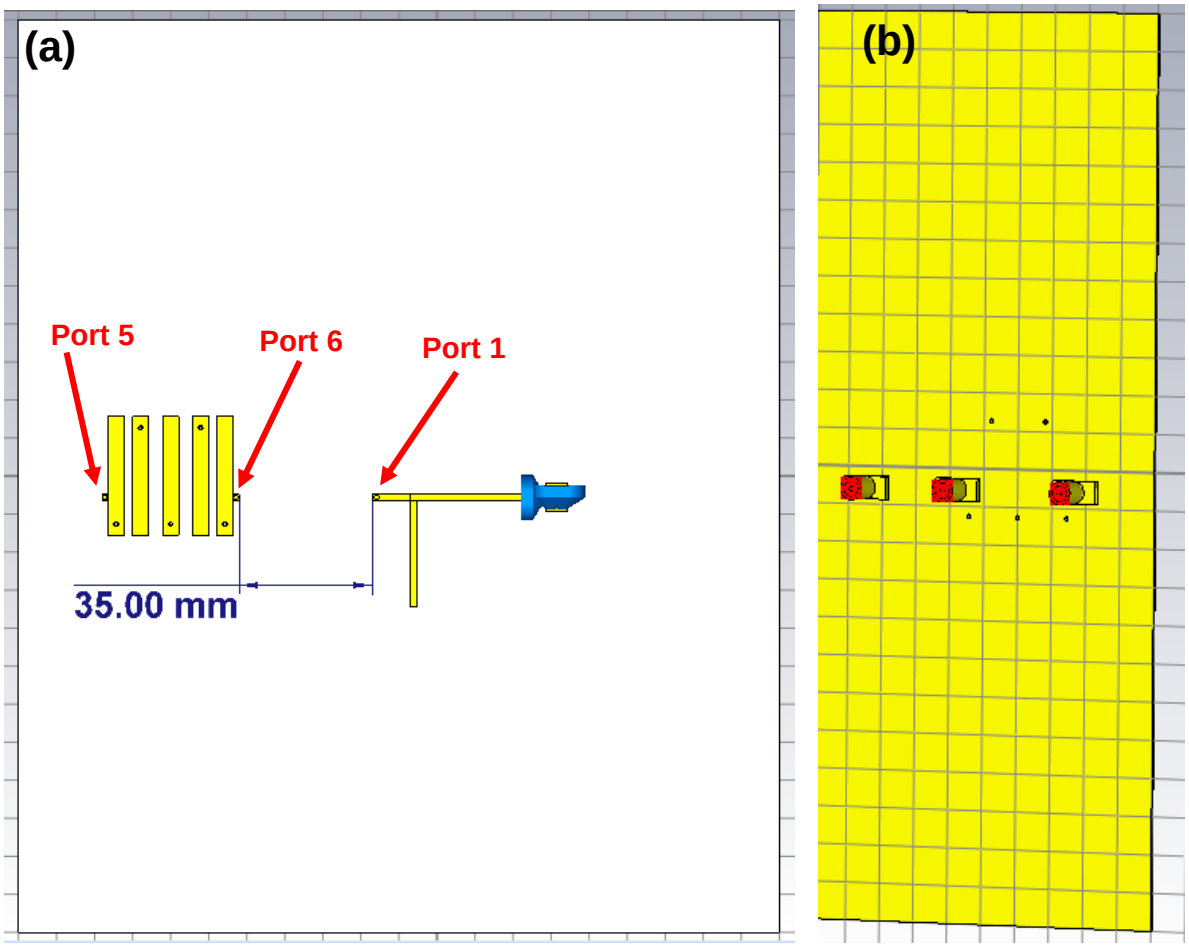

Figure B. 67 Simulation set up for the rectifier circuit and bandpass filter (a) Front facing side with ports allocation (b)backside with SMA connectors

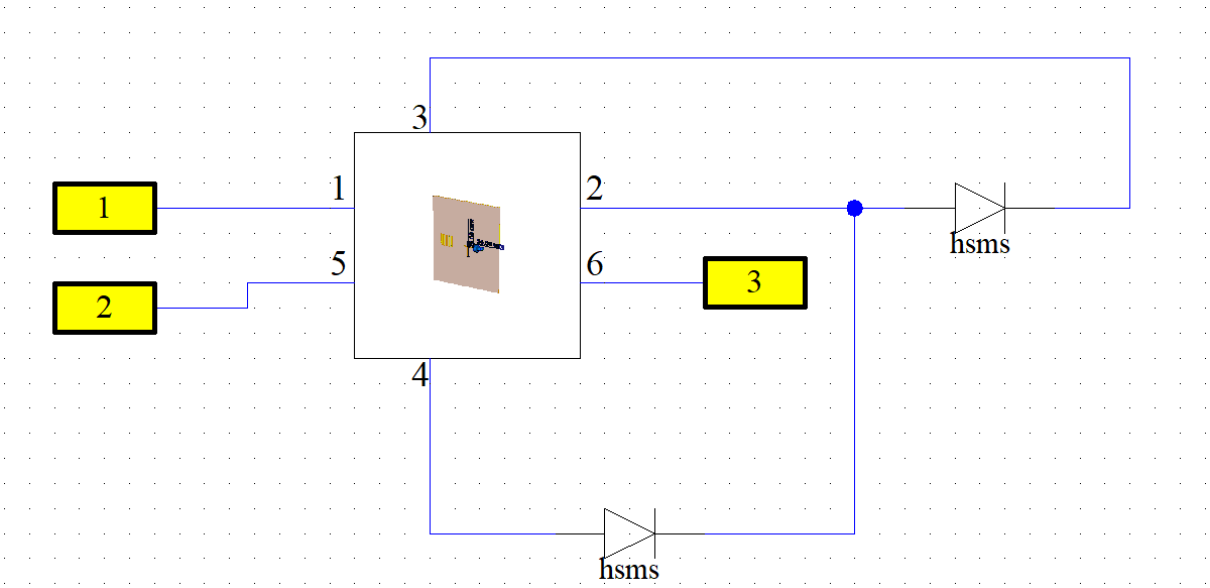

Figure B. 68 Simulation set up for the rectifier circuit and bandpass filter in Schematic mode

With sufficient demonstration of linearity to the RF input, a matching network for the detector diode has been designed in CST. In consideration of possible coupling effects with bandpass filters, a horizontal separation distance of 35mm was chosen for simulation. *Figure B. 67* and *Figure B. 68* show the simulation settings in CST.

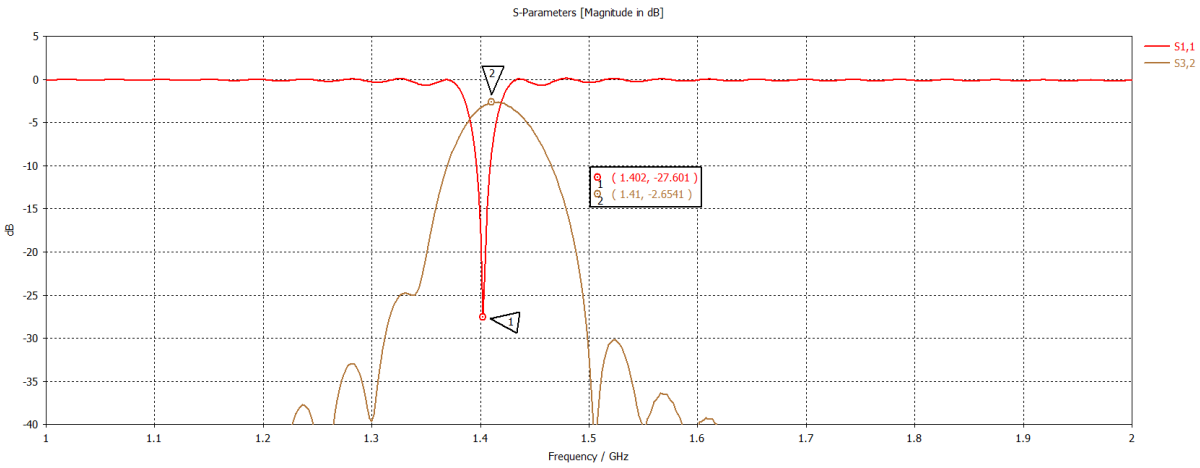

Figure B. 69 Simulation results: |S11| for input matching of the rectifier circuit; S32 for frequency response of the bandpass filter

The simulation results are depicted in *Figure B. 69*, where |S11| shows the input matching of the rectifier circuit, and S32 shows the bandpass filter frequency response. As the rectifier centre

frequency is at 1.4 GHz, while the bandpass filter has a centre frequency of 1.41 GHz, negligible coupling effect could be observed. Therefore, a separation distance of 35 mm between the bandpass filter and the rectifier circuit will be sufficient.

With possible manufacturing errors being considered, a similar approach for the bandpass filter (in the section New filters, substrate material and PCB design) has been applied here.

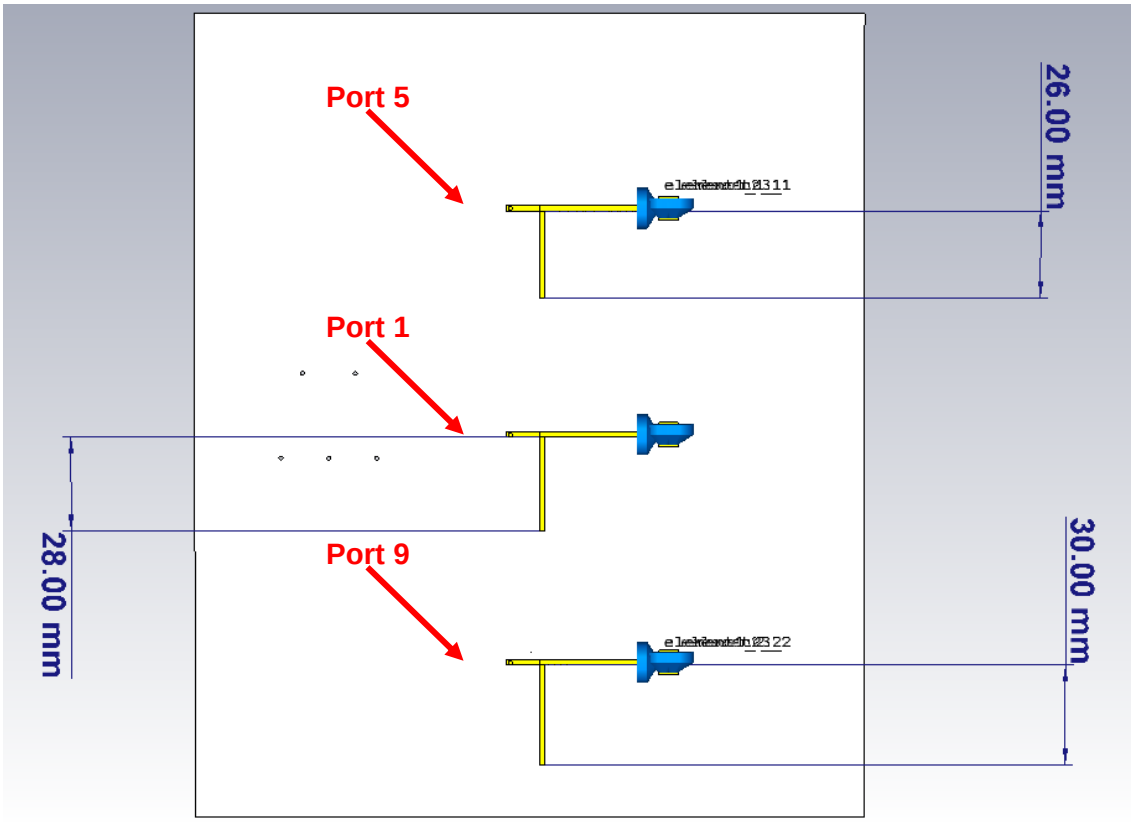

Figure B. 70 Simulation set up for the rectifier circuits in 3D view with ports allocation

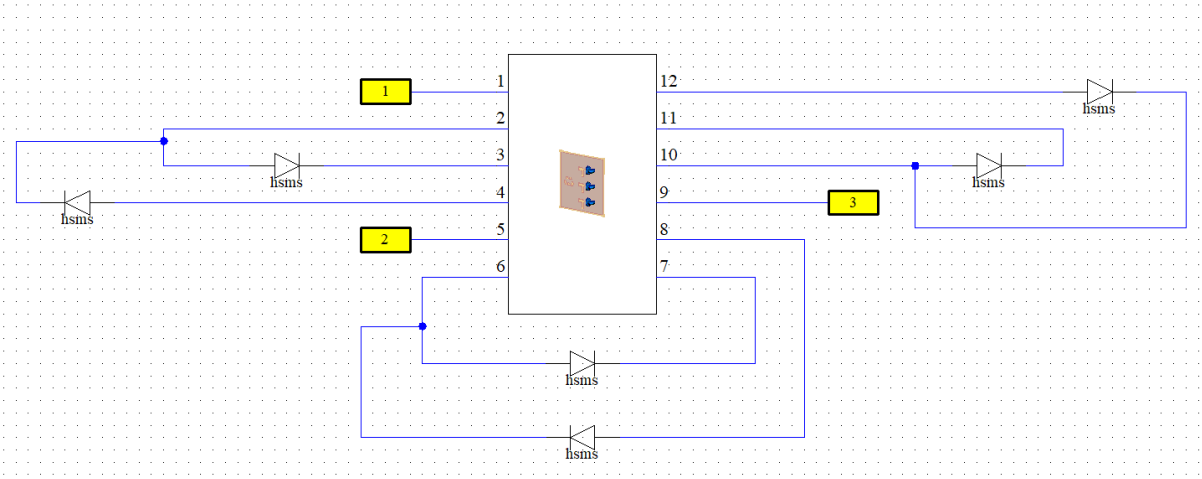

Figure B. 71 Rectifier circuits simulation set up in schematic mode

Figure B. 70 and *Figure B. 71* show the simulation set-up for HSMS-2862 diode rectifier circuits with multiple open circuit stub matching lengths, where the middle rectifier circuit has the optimised length of 28 mm for a good matching at 1.4 GHz, while the upper and lower circuits have the optimised length increased and decreased by 2mm respectively. Each filter is separated by a

vertical distance of 40mm to minimise possible coupling effects. *Figure B. 72* shows the simulated input matching results, as the centre frequency of the middle matching circuit (|S11|) stays at 1.4 GHz, 40mm vertical separation distance is adequate.

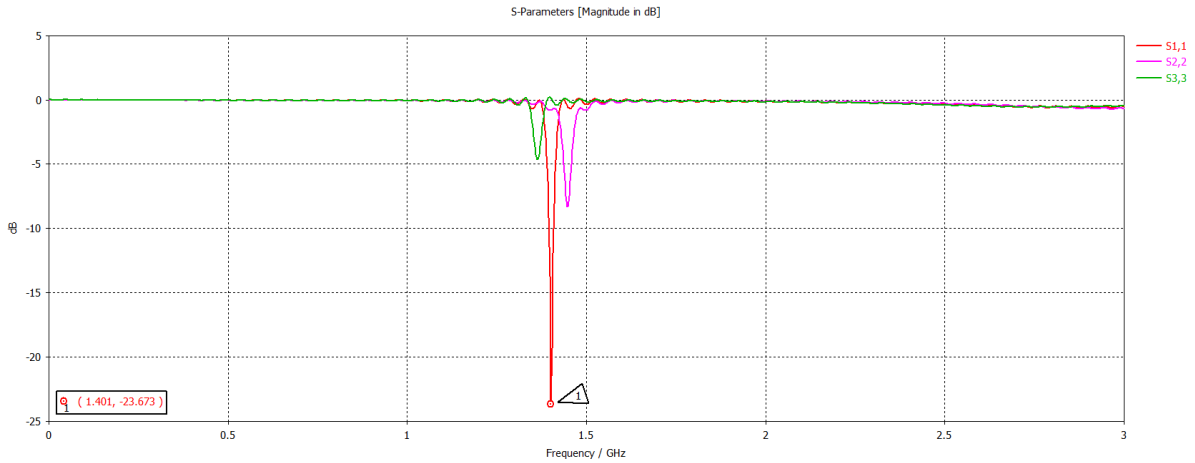

Figure B. 72 Simulated input matching results for the rectifier circuits: |S11| for the middle optimised matching circuit; |S22| for the upper circuit: |S33| for the lower circuit

B.4.4.2 Rectifier circuit in the second iteration

The fabricated rectifier circuit is shown in *Figure B. 73*. Its impedance matching results in *Figure B. 74* shows a narrow band matching with |S11| at -17.32 dB and centre frequency at 1.415 GHz which is the middle of the required bandwidth of 1.4-1.425 GHz. As the next step, the same experiment set up in *Figure B. 65* has been used for linearity test. *Figure B. 75* shows the RF Input to DC output plot of the modified rectifier. Overall, as compared to the poorly matched rectifier with linearity shown in *Figure B. 66*, a better sensitivity to RF input can be observed in this design.

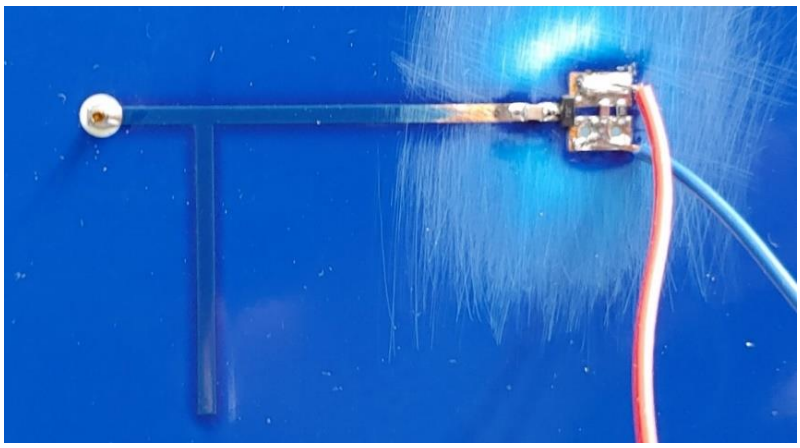

Figure B. 73 Middle rectifier in the second iteration PCB

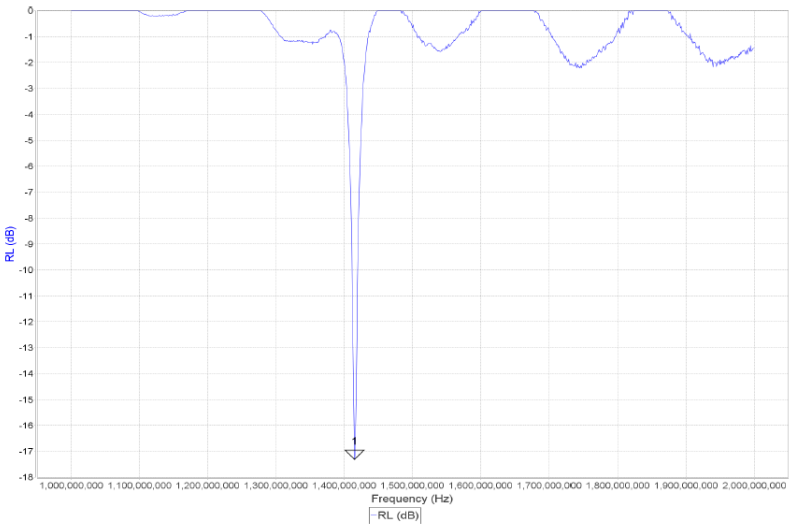

Marker	Freq. (Hz)	RL (dB)	RP (°)	|Z| ()	Rs ()	Xs ()	Theta	SWR
1	1,415,317,980	-17.32	-5.79	65.7	65.6	-1.8	-1.6	1.32:1

Figure B. 74 Input impedance matching results of the middle rectifier

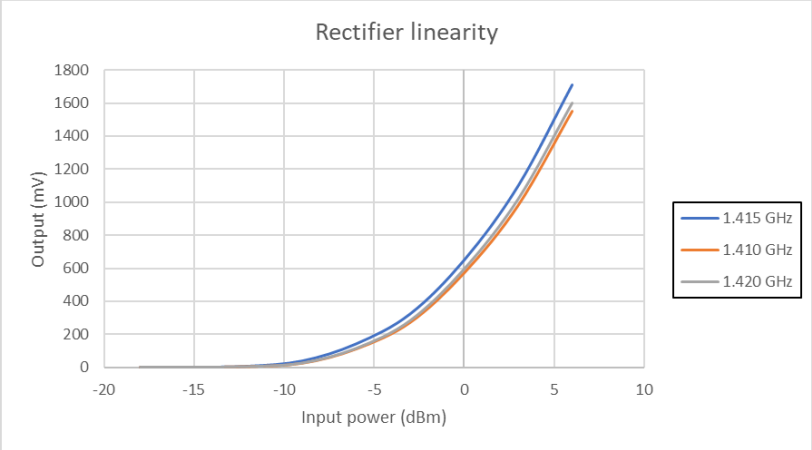

Figure B. 75 Voltage output vs RF Input curve of the middle rectifier circuit in the second iteration

B.4.5 System integration test

With each part of the radiometer receiver tested to be sufficient, the system has been connected in a total power topology for initial soil moisture experiments. The experiment set up and receiver system diagram are shown in *Figure B. 76* and *Figure B. 77* respectively.

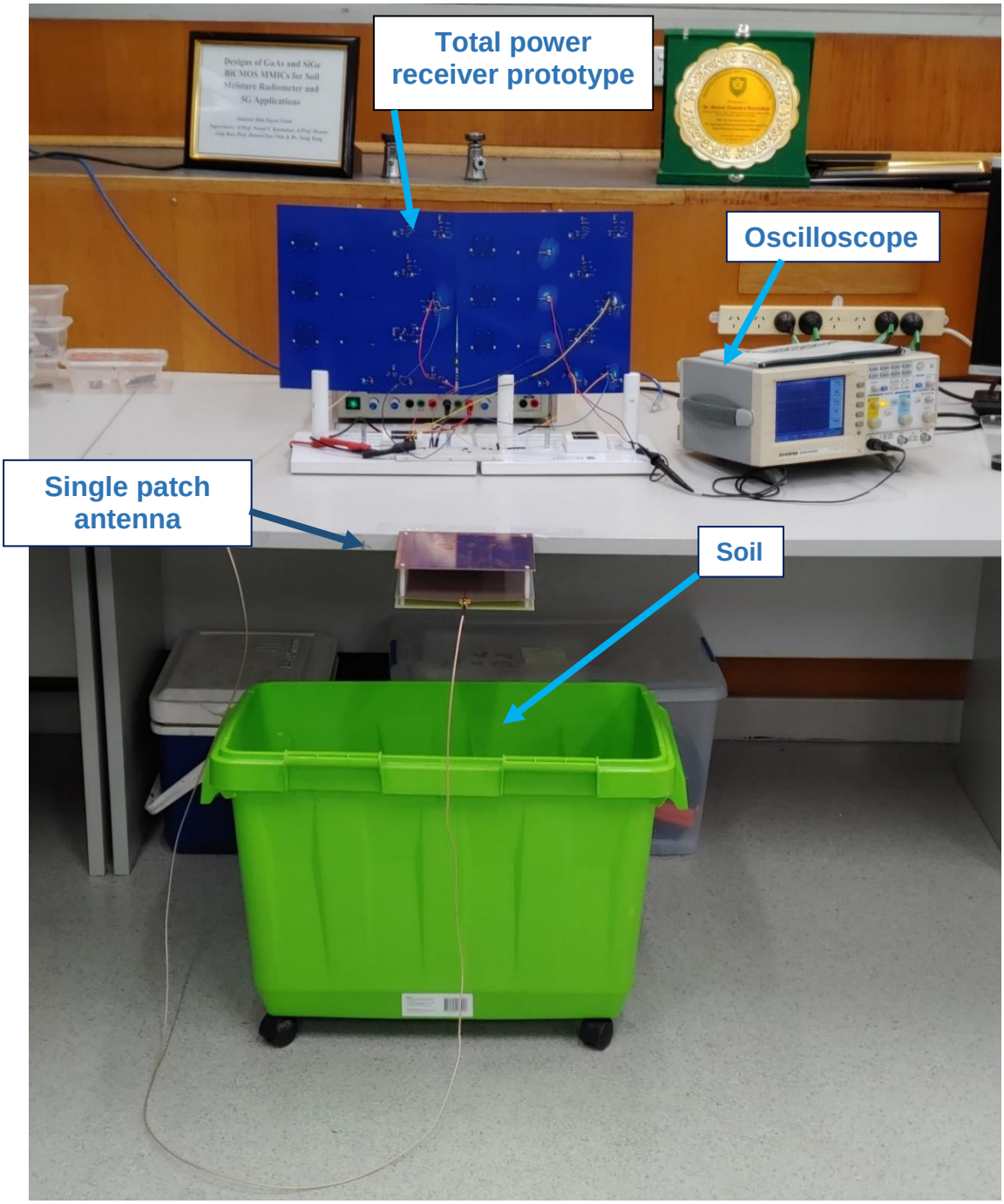

Figure B. 76 Initial soil moisture experiment set up

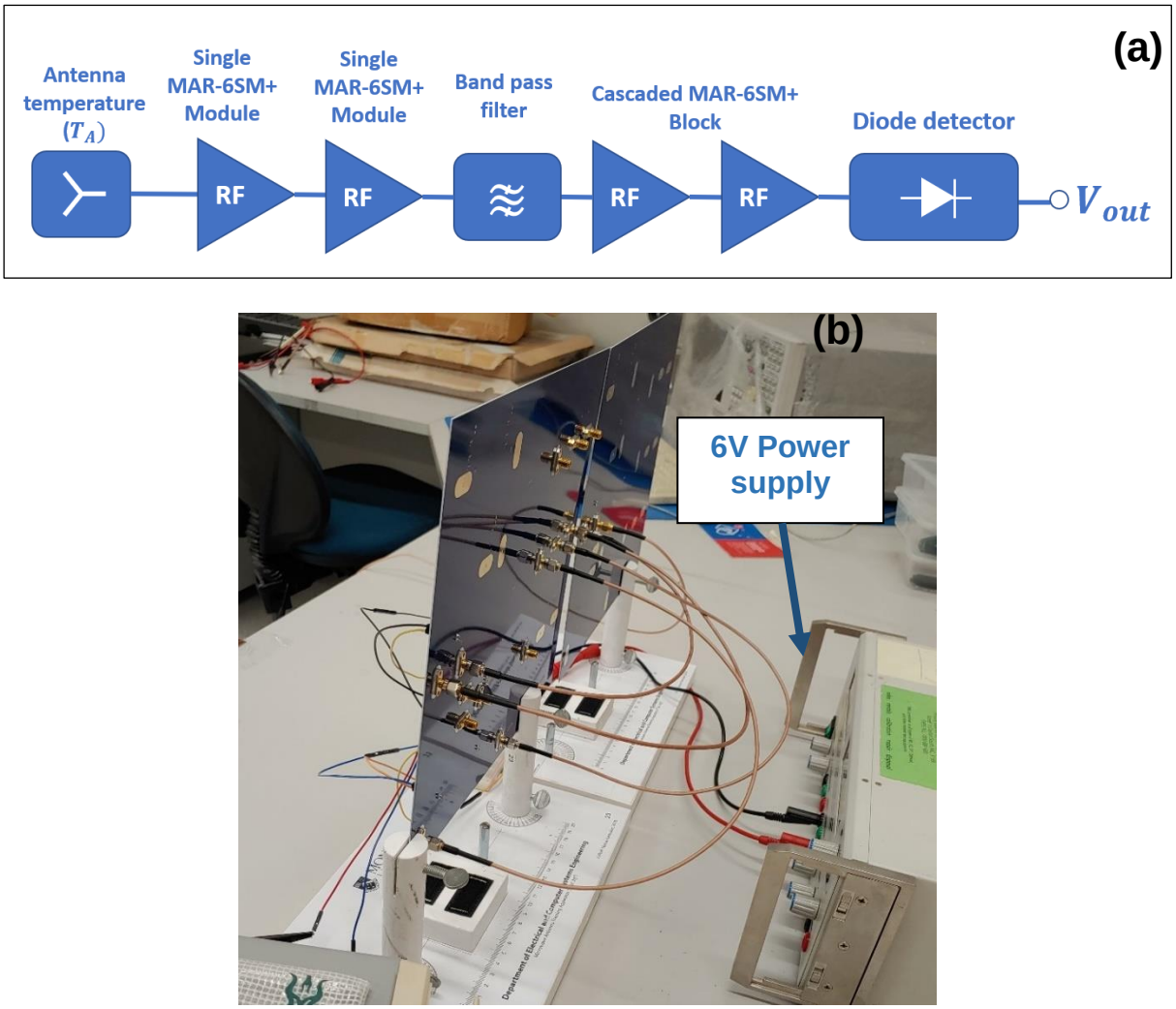

Figure B. 77 Integrated total power receiver (a) System diagram (b) PCB backside connection

Soil with three different soil moisture levels have been tested. Three different soil moisture levels were measured by a 3 in 1 Soil Meter for (1) top surface soil (in *Figure B. 78*), (2) near bottom soil (in *Figure B. 79*) and (3) bottom soil mixed with water (in *Figure B. 80*). The measurement results are also summarised in Table B. 3.

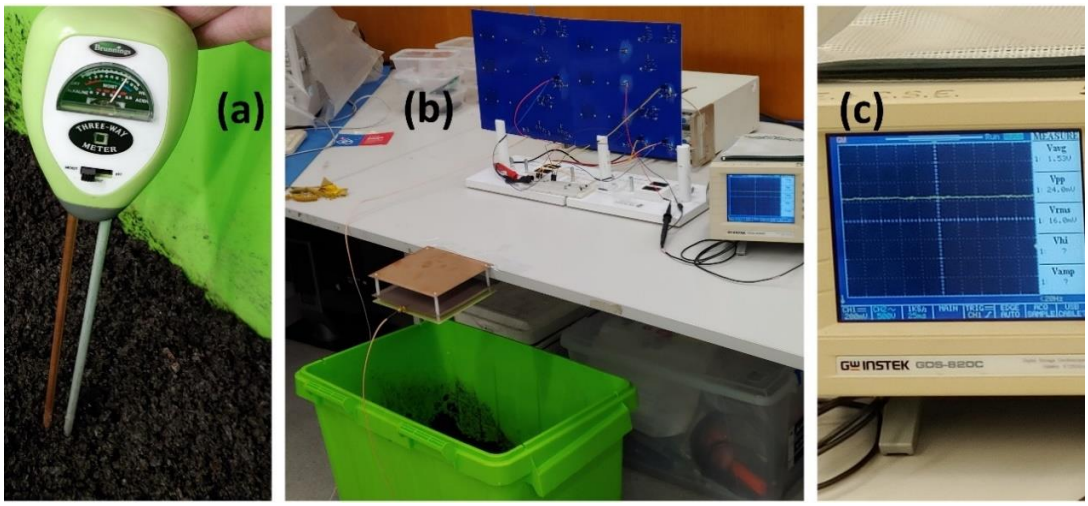

Figure B. 78 Top surface soil measurement (a) Soil meter reading (b) Experiment set up (c) Captured system voltage output

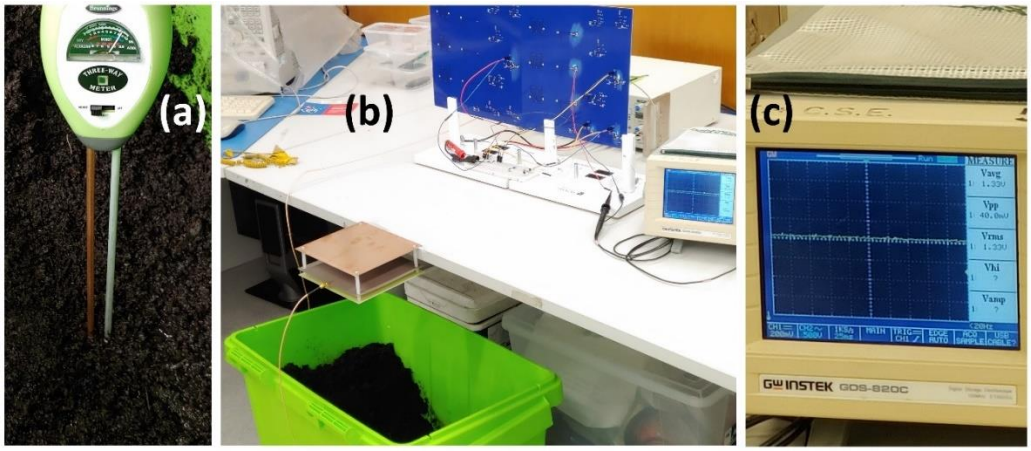

Figure B. 79 Wet soil measurement (a) Soil meter reading (b) Experiment set up (c) Captured system voltage output

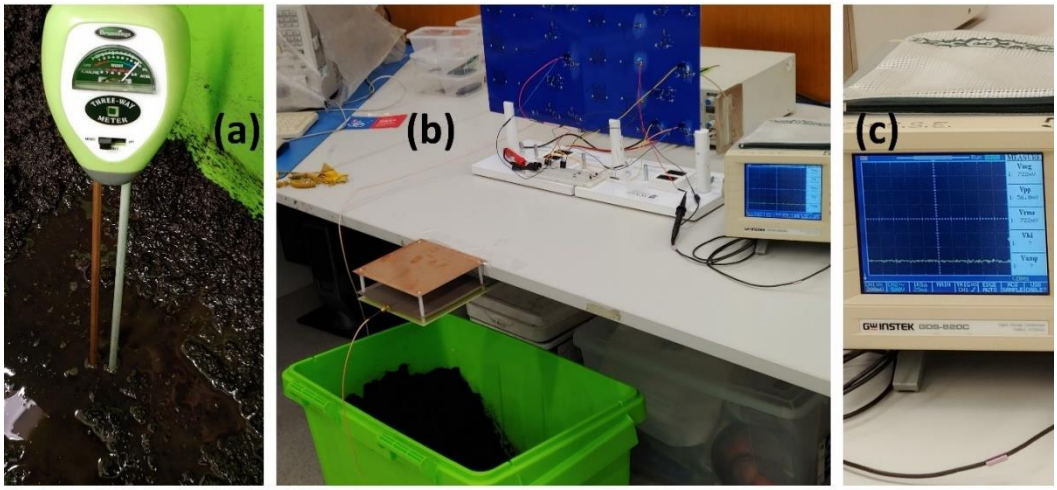

Figure B. 80 Soil mixed with water measurement (a) Soil meter reading (b) Experiment set up (c) Captured system voltage output

Table B. 3 Initial soil moisture experiment summary

Soil moisture level	Soil metre reading	Receiver voltage output (V)
Top surface moist soil	7.9	1.53
Near bottom wet soil	8.7	1.33
Bottom soil mixed with water	10	0.72

Through repeated measurements, a distinct voltage difference (in hundreds of millivolts) in the receiver output can be observed when the antenna is pointed at top surface moist soil and bottom soil with water, which signifies a successful implementation of an L- total power radiometer receiver prototype.

B.5 Conclusion

With earlier chapters focusing on the design of radiometer antennas, this is a complementary appendix to complete the understanding of a microwave radiometer system. In the first half of the appendix, 4 typical radiometer receiver topologies have been briefly reviewed, and the Dicke type radiometer receiver is found to be most suitable for airborne soil moisture sensing application.

In the following section, a system-level simulation of a Ka- band Dicke radiometer has been conducted. The design and calculation for 6 parts of the system: Dicke Switch, superheterodyne front end, IF Stage, Diode detector and Low frequency circuit has been discussed. The simulation results for frequency domain and time domain at each stage are consistent to those from literature [34, 166, 167]. A sensitivity of 1.1 k has been achieved in this design, and this sensitivity has been validated with typical brightness temperatures of wet soil [161]. Overall, this design could meet the requirement for airborne soil moisture sensing.

For the second part of this appendix, an L- band radiometer receiver frontend PCB has been developed through two iterations. In the second iteration, each block of the radiometer receiver has been tested with sufficient results. Lastly, a total power received has been implemented by

connecting each required block with coaxial cables. Through repeated measurements in the initial soil moisture experiments, a distinct difference in receiver voltage output (hence difference brightness temperatures) could be observed between moist soil and wet soil mixed with water, indicating a successful system prototype implementation. Further experiments and developments are required for a portable Dicke-type radiometer receiver, which could be expanded in the following areas:

(1) Dry up the moist soil, so that lower moisture level measurements could be observed

(2) Since total system current consumption of around 70 mA, it is possible to develop a portable system with batteries, so that outdoor experiment could be conducted.

- For receiver voltage output monitoring, a micro controller (e.g. Arduino) can be program to read the analog receiver output and display via a Laptop.

(3) Develop synchronise detector circuit, design square pulse generation circuit and integrate the designed RF switch circuit into the current total power system, so that the receive can be implemented in Dicke topology.

(4) Integrate the designed RF blocks into one compact radiometer frontend PCB design with microstrip transmission lines for interconnections

(5) Calibrate and characterise stability of the developed radiometer receiver, helpful guidelines could be referred to [175].

Appendix C: System noise temperature calculation example

System Noise calculation

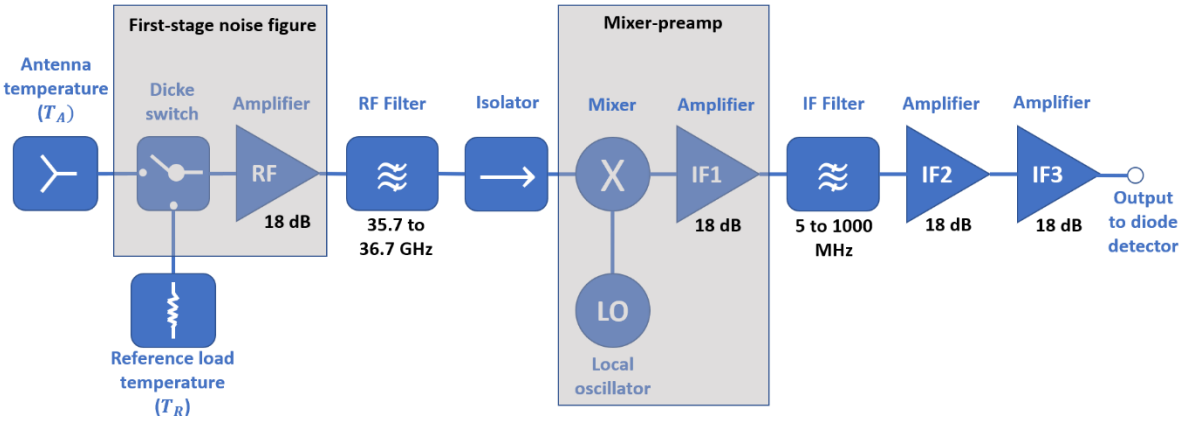

Figure C. 1 Ka- band Dicke radiometer schematic diagram

```
clc,

nf_1st_stage = 1.778 ;

g_1st_stage = 56.23 ;


nf_rf_fil = 1.32 ;

g_rf_fil = 0.76 ;


nf_iso = 1.07;

g_iso = 0.933;


nf_mixer = 10;

g_mixer = 0.1;


nf_if_amp1 = 1.62;

g_if_amp1 = 63.1;


nf_if_fil = 1.5;

g_if_fil = 0.666;


nf_if_amp2 = 1.62;

g_if_amp2 = 63.1;


nf_if_amp3 = 1.62;

g_if_amp3 = 63.1;
```

```
NF_system = nf_1st_stage + (nf_rf_fil-1)/g_1st_stage + (nf_iso-1)/(g_1st_stage * g_rf_fil) + (nf_mixer-1)/(g_1st_stage * g_rf_fil *g_iso) + (nf_if_amp1-1)/(g_1st_stage * g_rf_fil *g_iso*g_mixer) + (nf_if_fil-1)/(g_1st_stage * g_rf_fil *g_iso*g_mixer*g_if_amp1)+(nf_if_amp2-1)/(g_1st_stage * g_rf_fil *g_iso*g_mixer*g_if_amp1*g_if_fil)+(nf_if_amp3 - 1)/(g_1st_stage * g_rf_fil *g_iso*g_mixer*g_if_amp1*g_if_fil*g_if_amp2)
NF_system_dB = 10*log10(NF_system)
T_system = 290*(NF_system -1)

g_system = 10*log10(g_1st_stage * g_rf_fil * g_iso * g_mixer * g_if_amp1 * g_if_fil * g_if_amp2 * g_if_amp3)
```

NF_system = 2.1723

NF_system_dB = 3.3692

T_system =339.9668

g_system = 58.2423

System parameters calculation:

Input parameters

```
clc, clear all
BRF = 1e9;%Bandwidth of the Ka-Band antenna
BIF= 995e6; %Bandwidth of the IF stage
k = 1.38e-23; %Boltzman's constant
Tsys = 339.9668; %From "System_noies_calculation"
Tsoil = 220; %Brightness temperature of the soil (initial)
Tsoil_2 = 221.1; %For sensitivity testing
Tref = 313; %Brightness temperature of the reference load,considering a reasonable operating temperature of 40 Celcius(Refer to Microwave radiometer Systems:Design & Analysis)
t= 1.4e-3; %integration time
g_system = 58.2423; %Overall system gain
```

Noise Density calculation (for Gaussian Noise Input)

```
Dsoil = k*Tsoil;
Dsoil_2 = k*Tsoil_2;
```

```
Dsys = k*Tsys;
Dref = k*Tref;
```

Power calculation:

```
Psoil = BRF*k*Tsoil;
Psys = BRF*k*Tsys;
Pref = BRF*k*Tref;
```

Sensitivity of the overall radiometer

```
dT= 2* (Tref+Tsys)/sqrt(BIF*t)
```

dT = 1.1065 k

System power output

```
Pmax = Psys+Pref;
Ptest = Psys+Psoil;
Pmax_dBm = 10*log10(Pmax)+30;
Psys_dBm = 10*log10(Psys)+30;
Psoil_dBm = 10*log10(Psoil)+30;
Ptest_dBm = 10*log10(Ptest)+30;
P_det_max = Pmax_dBm + g_system
P_det_min = Psys_dBm + g_system
P_det_test = Ptest_dBm + g_system
```

P_det_max = -22.2100

P_det_min = -25.0445

P_det_test = -22.8773

References

[1] S. I. Seneviratne, T. Corti, E. L. Davin, M. Hirschi, E. B. Jaeger, I. Lehner, B. Orlowsky and A. Teuling, “Investigating soil moisture-climate interactions in a changing climate: A review,” *Earth-Science Reviews,* vol. 99, no. 3, pp. 125-161, 2010.

[2] B. Timbal, S. Power, R. Colman, J. Viviand and S. Lirola, “Does Soil Moisture Influence Climate Variability and Predictability over Australia?,” *Journal of Climate,* vol. 15, no. 10, pp. 1230-1238, 2002.

[3] Y. Kerr, “Soil moisture from space: Where are we?,” *Hydrogeology Journal,* vol. 15, no. 1, pp. 117-120, 2007.

[4] J. Leese, T. Jackson, A. Pitman and P. Dirmeyer, “Meeting summary: GEWEX/BAHC International Workshop on Soil Moisture Monitoring, Analysis, and Prediction for Hydrometeorological and Hydroclimatological Applications,” *Bulletin of the American Meteorological Society,* vol. 82, no. 7, pp. 1423-1430, 2001.

[5] V. Kumar, I. Dharssi, M. Yebra and P. Fox-Hughes, “Exploring the soil moisture-live fuel moisture relationship,” 2020. [Online]. Available: https://www.bnhcrc.com.au/sites/default/files/managed/downloads/nb09_fox-hughes_exploring_lfmc_smc_relationship_final_rt.pdf. [Accessed JUL 2023].

[6] G. Roth, G. Harris, M. H. Gillies, J. Montgomery and D. Wigginton, “Water-use efficiency and productivity trends in Australian irrigated cotton: A review,” *Crop and Pasture Science,* vol. 64, no. 12, pp. 1033-1048, 2014.

[7] L. Karthikeyan, I. Chawla and A. K. Mishra, “A Review of Remote Sensing Applications in Agriculture for Food Security: Crop Growth and Yield, Irrigation, and Crop Losses,” *Journal of Hydrology,* no. 4, p. 586, 2020.

[8] G. Ijjas, I. Juhasz and P. Zilahy, “Airborne microwave equiment for soil moisture investigation,” in *Microwave radiometry and remote sensing applications : proceedings of the specialist meeting held in Florence, Italy, 9-11 March, 1988*, P. Pampaloni, Ed., Utrecht, The Netherlands, VSP, 1989, pp. 321-328.

[9] J. P. Walker, G. Dumedah, A. Monerris, Y. Gao, C. Rüdiger, X. Wu, R. Panciera, O. Merlin, R. Pipunic, D. Ryu and M. Zreda, “High Resolution Soil Moisture Mapping,” *Digital Soil Assessments and Beyond - Proceedings of the Fifth Global Workshop on Digital Soil Mapping,* pp. 5-51, 2012.

[10] E. Anastasiou, A. T. Balafoutis and S. Fountas, “Trends in Remote Sensing Technologies in Olive Cultivation,” *Smart Agricultural Technology,* vol. 3, 2023.

[11] R. Koech and P. Langat, “Improving Irrigation Water Use Efficiency: A Review of Advances, Challenges and Opportunities in the Australian Context,” *Water,* vol. 10, no. 12, 2018.

[12] Y. Kerr, W. Philippe, J.-P. Wigneron and J. Martinuzzi, “Soil moisture retrieval from space: The Soil Moisture and Ocean Salinity (SMOS) mission,” *IEEE Transactions on Geoscience and Remote Sensing,* vol. 39, no. 8, pp. 1729-1735, 2001.

[13] D. Entekhabi, E. G. Njoku, P. E. O'Neill, K. H. Kellogg, W. T. Crow, W. N. Edelstein, J. K. Entin, S. D. Goodman, T. J. Jackson, J. Johnson, J. Kimball, J. R. Piepmeier, R. D. Koster, N. Martin, K. C. McDonald, M. Moghaddam, S. Moran, R. Reichle, J. C. Shi, M. W. Spencer,

S. W. Thurman, L. Tsang and J. Van Zyl, “The Soil Moisture Active Passive (SMAP) Mission,” *Proceedings of the IEEE,* vol. 98, no. 5, pp. 704-716, 2010.

[14] X. Wu, J. P. Walker, C. Rüdiger, R. Panciera and D. A. Gray, “Simulation of the SMAP Data Stream From SMAPEx Field Campaigns in Australia. Geoscience and Remote Sensing,” *IEEE Transactions on Geoscience and Remote Sensing,* vol. 53, no. 4, pp. 1921-1934, 2015.

[15] X. Wu, J. P. Walker and V. Wong, “Proximal Soil Moisture Sensing for Real-Time Water Delivery Control: Exploratory Study over a Potato Farm,” *Agriculture,* vol. 13, no. 7, 2023.

[16] G. Dumedah, J. Walker and C. Rüdiger, “Can SMOS data be used directly on the 15-km Discrete Global Grid?,” *IEEE Transactions on Geoscience and Remote Sensing,* vol. 52, no. 5, pp. 2538-2544, 2014.

[17] J. Chaubell, “SPL1BTB_E Algorithm Theoretical Basis Document [2016],” Dec 2016. [Online]. Available: https://nsidc.org/sites/default/files/smap_l1b_tb_e_product_atbd_d-56287.pdf. [Accessed Nov 2022].

[18] X. Wu, J. P. Walker, F. Jonard and N. Ye, “Inter-Comparison of Proximal Near-Surface Soil Moisture Measurement Techniques,” *IEEE Journal of Selected Topics in Applied Earth Observations and Remote Sensing,* vol. 15, pp. 2370-2378, 2022.

[19] X. Wu, J. Walker, C. Rüdiger, R. Panciera and Y. Gao, “Intercomparison of Alternate Soil Moisture Downscaling Algorithms Using Active–Passive Microwave Observations,” *IEEE Geoscience and Remote Sensing Letters,* vol. 14, no. 2, pp. 179-183, 2017.

[20] X. Wu, N. Ye, J. Walker, I.-Y. Yeo, T. Jackson, Y. Kerr, E. Kim and A. McGrath, “The P-band Radiometer Inferred Soil Moisture Experiment 2019 Workplan,” 2019. [Online]. Available: https://www.prism.monash.edu/Data/PRISM-19/PRISM_2019%20Workplan.pdf.

[21] M. Schwank, A. Wiesmann, C. Werner, C. Mätzler, D. Weber, A. Murk, I. Völksch and U. Wegmüller, “ELBARA II, an L-Band Radiometer System for Soil Moisture Research,” *Sensors,* vol. 10, no. 1, pp. 584-612, 2010.

[22] R. Bindlish, M. H. Cosh, T. J. Jackson, T. Koike, H. Fujii, S. K. Chan, J. Asanuma, A. Berg, D. D. Bosch, T. G. Caldwell, C. H. Collins, H. McNairn, J. Martínez-Fernández, J. Prueger, T. Rowlandson, M. Seyfried, P. Starks, M. Thibeault, R. Van Der Velde, J. P. Walker and E. Coopersmith, “GCOM-W AMSR2 Soil Moisture Product Validation Using Core Validation Sites,” *IEEE Journal of Selected Topics in Applied Earth Observations and Remote Sensing,* vol. 11, no. 1, pp. 209-219, 2018.

[23] L. Li, P. W. Gaiser, B.-C. Gao, R. M. Bevilacqua, T. J. Jackson, E. G. Njoku, C. Rüdiger, J.-C. Calvet and R. Bindlish, “WindSat Global Soil Moisture Retrieval and Validation,” *IEEE Transactions on Geoscience and Remote Sensing,* vol. 48, no. 5, pp. 2224-2241, 2010.

[24] M. Forkel, L. Schmidt, R.-M. Zotta, W. Dorigo and M. Yebra, “Estimating leaf moisture content at global scale from passive microwave satellite observations of vegetation optical depth,” *Hydrology and Earth System Sciences,* vol. 27, no. 1, p. 39–68, 2023.

[25] K. T. Trinh, J. Feng, S. H. Shehab and N. C. Karmakar, “1.4 GHz Low-Cost PIN Diode Phase Shifter for L -Band Radiometer Antenna,” *IEEE Access,* vol. 7, pp. 95274-95284, 2019.

[26] M. Hassan and N. Karmakar, “Design considerations of DP ACPA with higher isolation at Ku-band for soil moisture radiometer,” in *2017 IEEE Asia Pacific Microwave Conference (APMC)*, Kuala Lumpur, Malaysia, 2017.

[27] K. T. Trinh, J. Feng and N. C. Karmakar, “18.7 GHz 4-Bit PIN Diode Reflection Type Phase Shifter for Radiometer Phased Array Antenna,” in *2nd International Conference on Robotics, Electrical and Signal Processing Techniques (ICREST)*, DHAKA, Bangladesh, 2021.

[28] M. Hassan, “Shared Aperture Planar Array Antenna for Soil Moisture Radiometer,” Monash University, 2019.

[29] T. K. Ho, “Ka-band Phase Shifter for Tri-band (L-, Ku-, Ka-bands) Soil Moisture Smart Antenna Array,” Monash University, 2023.

[30] J.-C. Calvet, J. Noilhan and P. Bessemoulin, “Retrieving the root-zone soil moisture from surface soil moisture or temperature estimates: A feasibility study based on field measurements,” *Journal of Applied Meteorology,* vol. 37, no. 4, pp. 371-386, 1998.

[31] X. Wu, J. P. Walker, C. Rüdiger and R. Panciera, “Effect of Land-Cover Type on the SMAP Active/Passive Soil Moisture Downscaling Algorithm Performance,” *IEEE Geoscience and Remote Sensing Letters,* vol. 12, no. 4, pp. 846-850, 2015.

[32] S. Sabaghy, J. P. Walker, L. J. Renzullo and T. J. Jackson, “Spatially enhanced passive microwave derived soil moisture: Capabilities and opportunities,” *Remote Sensing of Environment,* vol. 209, pp. 551-580, 2019.

[33] P. Hildebrand, “Soil Moisture and Salinity using P-Band from Geostationary Orbit Final Report,” [Online]. Available: https://esto.nasa.gov/files/2004/Geo%20P-band%20Final%20Report1.pdf. [Accessed 05 02 2018].

[34] N. Skou and D. Le Vine, Microwave Radiometer Systems: Design and Analysis, Second Ediotion, Norwood, MA: Artech House, 2006.

[35] J. R. Piepmeier, P. Focardi, K. A. Horgan, J. Knuble, N. Ehsan, J. Lucey, C. Brambora, P. R. Brown, P. J. Hoffman, R. T. French, R. L. Mikhaylov, E.-Y. Kwack, E. M. Slimko, D. E. Dawson, D. Hudson, J. Peng, P. Mohammed, G. de Amici, A. Freedman, J. Medeiros, F. Sacks, R. Estep, M. W. Spencer, C. W. Chen, K. Wheeler, W. N. Edelstein, P. E. O'Neill and E. G. Njoku, “SMAP L-Band Microwave Radiometer: Instrument Design and First Year on Orbit,” *IEEE Transactions on Geoscience and Remote Sensing,* vol. 55, no. 4, pp. 1954-1966, 2017.

[36] A. Colliander, T. J. Jackson, S. K. Chan, P. O'Neill, R. Bindlish, M. H. Cosh, T. G. Caldwell, J. P. Walker, A. Berg, H. McNairn, M. Thibeault, J. Martínez-Fernández, K. H. Jensen, J. Asanuma, M. Seyfried, D. D. Bosch, P. Starks, C. H. Collins, J. H. Prueger, B. Su, E. Lopez-Baeza and S. Yueh, “An assessment of the differences between spatial resolution and grid size for the SMAP enhanced soil moisture product over homogeneous sites,” *Remote Sensing of Environment,* vol. 207, pp. 65-70, 2018.

[37] “NASA Soil Moisture Radar Ends Operations, Mission Science Continues,” Jet Propulsion laboratory, 02 09 2015. [Online]. Available: https://www.jpl.nasa.gov/news/news.php?feature=4710. [Accessed 29 01 2018].

[38] E. Santi, S. Paloscia, S. Pettinato, D. Entekhabi, H. Alemohammad and A. K. Konings, “Integration of passive and active microwave data from SMAP, AMSR2 and Sentinel-1 for

Soil Moisture monitoring," in *2016 IEEE International Geoscience and Remote Sensing Symposium (IGARSS)*, Beijing, 2016.

[39] S. Sabaghy, J. P. Walker, L. J. Renzullo, R. Akbar, S. Chan, J. Chaubell, N. N. Das, R. S. Dunbar, D. Entekhabi, A. Gevaert, T. Jackson, O. Merlin, M. Moghaddam, J. Peng, J. Piepmeier, M. Piles, G. Portal, C. Rüdiger, V. Stefan, X. Wu, N. Ye and S. Yueh, "Comparison of downscaling techniques for high resolution soil moisture mapping," in *2017 IEEE International Geoscience and Remote Sensing Symposium (IGARSS)*, Fort Worth, 2017.

[40] J. Peng, A. Loew, O. Merlin and N. Verhoest, "A review of spatial downscaling of satellite remotely sensed soil moisture," *Reviews of Geophysics,* vol. 55, no. 2, pp. 341-366, 2017.

[41] S. Sabaghy, J. P. Walker, L. J. Renzullo, R. Akbar, S. Chan, J. Chaubell, N. Das, R. S. Dunbar, D. Entekhabi, A. Gevaert, T. J. Jackson, A. Loew, O. Merlin, M. Moghaddam, J. Peng, J. Peng, J. Piepmeier, C. Rüdiger, V. Stefan, X. Wu, N. Ye and S. Yueh, "Comprehensive analysis of alternative downscaled soil moisture products," *Remote Sensing of Environment,* vol. 239, 2020.

[42] "SMAP Enhanced L3 Radiometer Global Daily 9 km EASE-Grid Soil Moisture, Version 1," National Snow and Ice Data Center, [Online]. Available: https://nsidc.org/data/SPL3SMP_E/versions/1. [Accessed 6 02 2018].

[43] "SMAP/Sentinel-1 L2 Radiometer/Radar 30-Second Scene 3 km EASE-Grid Soil Moisture, Version 1," National Snow and Ice Data Center, [Online]. Available: https://nsidc.org/data/SPL2SMAP_S/versions/1. [Accessed 06 02 2018].

[44] "LPRM_AMSR2_DS_SOILM2: AMSR2/GCOM-W1 downscaled surface soil moisture (LPRM) L2B V001," NASA GSFC, [Online]. Available: https://disc.gsfc.nasa.gov/datasets/LPRM_AMSR2_DS_SOILM2_V001/summary?keywords=Hydrology. [Accessed 06 02 2018].

[45] S. Park, S. Park, J. Im, J. Rhee, J. Shin and J. Park, "Downscaling GLDAS soil moisture data in east asia through fusion of multi-sensors by optimizing modified regression trees," *Water,* vol. 9, no. 5, 2017.

[46] E. Santi, S. Paloscia, S. Pettinato, L. Brocca, L. Ciabatta and D. Entekhabi, "On the synergy of SMAP, AMSR2 AND SENTINEL-1 for retrieving soil moisture," *International Journal of Applied Earth Observation and Geoinformation,* vol. 65, pp. 114-123, 2018.

[47] E. Santi, "An application of the SFIM technique to enhance the spatial resolution of spaceborne microwave radiometers," *International Journal of Remote Sensing,* vol. 31, no. 9, pp. 2419-2428, 2010.

[48] S. K. Chan, R. Bindlish, P. O'Neill, T. Jackson, E. Njoku, S. Dunbar, J. Chaubell, J. R. Piepmeier, S. Yueh, D. Entekhabi, A. Colliander, F. Chen, M. H. Cosh, T. G. Caldwell, J. P. Walker, A. Berg, H. McNairn, M. Thibeault, J. Martínez-Fernández, F. Uldall, M. Seyfried, D. D. Bosch, P. Starks, C. H. Collins, J. Prueger, R. van der Velde, J. Asanuma, M. A. Palecki, E. E. Small, M. Zreda, J.-C. Calvet, W. Crow and Y. Kerr, "Development and assessment of the SMAP enhanced passive soil moisture product," *Remote Sensing of Environment,* vol. 204, pp. 931-941, 2018.

[49] R. L. Ray, A. Fares, Y. He and M. Temimi, "Evaluation and Inter-Comparison of Satellite Soil Moisture Products Using In Situ Observations over Texas, U.S," *Water,* vol. 9, no. 6,

2017.

[50] M. S. Burgin, A. Colliander, E. G. Njoku, S. K. Chan, F. Cabot, Y. Kerr, R. Bindlish, T. J. Jackson, D. Entekhabi and S. H. Yueh, “A Comparative Study of the SMAP Passive Soil Moisture Product With Existing Satellite-Based Soil Moisture Products,” *IEEE Transactions on Geoscience and Remote Sensing,* vol. 55, no. 5, pp. 2959-2971, 2017.

[51] N. Ye, J. P. Walker, R. Bindlish, J. Chaubell, N. N. Das, A. I. Gevaert, T. J. Jackson and C. Rüdiger, “Evaluation of SMAP downscaled brightness temperature using SMAPEx-4/5 airborne observations,” *Remote Sensing of Environment,* vol. 221, pp. 363-372, 2019.

[52] E. Santi, S. Paloscia, S. Pettinato, L. Brocca, L. Ciabatta and D. Entekhabi, “Integration of microwave data from SMAP and AMSR2 for soil moisture monitoring in Italy,” *Remote Sensing of Environment,* vol. 212, pp. 21-30, 2018.

[53] J. Lu, R. Scarlat, G. Heygster and G. Spreen, “Reducing Weather Influences on an 89 GHz Sea Ice Concentration Algorithm in the Arctic Using Retrievals From an Optimal Estimation Method,” *Journal of Geophysical Research: Oceans,* vol. 127, no. 9, 2022.

[54] J. Lu, G. Heygster and G. Spreen, “Atmospheric Correction of Sea Ice Concentration Retrieval for 89 GHz AMSR-E Observations,” *IEEE Journal of Selected Topics in Applied Earth Observations and Remote Sensing,* vol. 11, no. 5, pp. 1442-1457, 2018.

[55] C. Galeazzi, C. Donlon, M. Sallusti, M. Triggianese, R. Midthassel, G. De Paris, A. Kornienko and B. Fiorelli, “The Copernicus Imaging Microwave Radiometer (CIMR) Mission: Project Status and System Overview,” in *IGARSS 2023 - 2023 IEEE International Geoscience and Remote Sensing Symposium*, Pasadena, CA, USA, 2023.

[56] C. Donlon, C. Galeazzi, R. Midthassel, M. Sallusti, M. Triggianese, B. Fiorelli, G. De Paris, A. Kornienko and I. Khlystova, “The Copernicus Imaging Microwave Radiometer (CIMR): Mission Overview and Status,” in *IGARSS 2023 - 2023 IEEE International Geoscience and Remote Sensing Symposium*, Pasadena, CA, USA, 2023.

[57] R. Midthassel, B. Fiorelli, C. Galeazzi, M. Sallusti and C. Donlon, “The Copernicus Imaging Microwave Radiometer (CIMR): Instrument Architecture and Performance,” in *IGARSS 2023 - 2023 IEEE International Geoscience and Remote Sensing Symposium*, Pasadena, CA, USA, 2023.

[58] C. Donlon, “Copernicus Imaging Microwave Radiometer (CIMR) Mission Requirements Document,” 11 February 2023. [Online]. Available: https://esamultimedia.esa.int/docs/EarthObservation/CIMR-MRD-v5.0-20230211_(Issued).pdf.

[59] M. S. Zhang, F. Alnasser and D. Entekhabi, “L-Band Disaggregation with C-Band Demonstration using SMAP and AMSR2 Data for Application to Forthcoming CIMR Measurements,” in *IGARSS 2023 - 2023 IEEE International Geoscience and Remote Sensing Symposium*, Pasadena, CA, USA, 2023.

[60] N. N. Das, A. Colliander, S. K. Chan, E. G. Njoku and L. Li, “Intercomparisons of Brightness Temperature Observations Over Land From AMSR-E and WindSat,” *IEEE Transactions on Geoscience and Remote Sensing,* vol. 52, no. 1, pp. 452-464, 2014.

[61] The European Space Agency, “Coriolis/WindSat,” [Online]. Available: https://www.eoportal.org/satellite-missions/coriolis#references. [Accessed 2023].

[62] “AMSR2 / AMSRE,” Remote Sensing Systems. [Online]. [Accessed 2018].

[63] T. J. Jackson and T. Schmugge, “Algorithm for the passive microwave remote sesing of soil moisture,” in *Microwave radiometry and remote sensing applications : proceedings of the specialist meeting held in Florence, Italy, 9-11 March, 1988*, Utrecht, The Netherlands, VSP, 1989, pp. 3-17.

[64] E. G. Njoku and J.-A. Kong, “Theory for passive microwave remote sensing of near-surface soil moisture,” *Journal of Geophysical Research,* vol. 82, no. 20, pp. 3108-3118, 1977.

[65] E. G. Njoku and D. Entekhabi, “Passive microwave remote sensing of soil moisture,” *Journal of Hydrology,* vol. 184, no. 1-2, pp. 101-129, 1996.

[66] F. T. Ulaby, R. K. Moore and A. K. Fung, “Introduction,” in *Microwave remote sensing : Active and passive, Volume 1, Microwave remote*, Reading, Mass, Addison-Wesley Pub., Advanced Book Program/World Science Division, 1981, pp. 1-57.

[67] B. Choudhury, “Reflectivities of Selected Land Surface Types,” *Remote Sensing of Environment,* vol. 46, no. 1, pp. 1-17, 1993.

[68] T. R. H. Holmes, R. A. M. de Jeu, M. Owe and A. J. Dolman, “Land surface temperature from Ka band (37 GHz) passive microwave observations.,” *Journal of Geophysical Research,* vol. 114, 2009.

[69] R. A. M. De Jeu and M. Owe, “Further validation of a new methodology for surface moisture and vegetation optical depth retrieval,” *International Journal of Remote Sensing,* vol. 24, no. 22, pp. 4559-4578, 2003.

[70] S. Paloscia, E. Santi, S. Pettinato, I. Mladenova, T. Jackson, R. Bindlish and M. Cosh, “A comparison between two algorithms for the retrieval of soil moisture using AMSR-E data,” *Frontiers in Earth Science,* vol. 3, 2015.

[71] R. Bindlish, T. J. Jackson, J. R. Piepmeier, S. Yueh and Y. Kerr, “Intercomparison of SMAP, SMOS and Aquarius L-band brightness temperature observations,” in *2016 IEEE International Geoscience and Remote Sensing Symposium (IGARSS)*, Beijing, 2016.

[72] I. Mladenova, V. Lakshmi, T. Jackson and J. Walker, “KU-Band Sensitivity to Soil Moisture. An Evaluation Study for Monitoring Temporal Soil Moisture Change Detection Over the NAFE06 Study Area,” in *IGARSS 2008 - 2008 IEEE International Geoscience and Remote Sensing Symposium*, Boston, 2008.

[73] J. Walker, R. Panciera and E. Kim, “High Resolution Airborne Soil Moisture Mapping,” in *Proceedings of the 14th Australasin Remote Sensing and Photogrammetry Conference*, Darwin, Australia, 2008.

[74] T. Jackson, J.-P. Wigneron, Y. Kerr, M. H. Cosh, A. Colliander, J. P. Walker and R. Bindlish, “Satellite-based soil moisture validation and field experiments; skylab to smap,” in *2016 IEEE International Geoscience and Remote Sensing Symposium (IGARSS)*, Beijing, 2016.

[75] H. McNairn, T. J. Jackson, G. Wiseman, S. Bélair, A. Berg, P. Bullock, A. Colliander, M. H. Cosh, S.-B. Kim, R. Magagi, M. Moghaddam, E. G. Njoku, J. R. Adams, S. Homayouni, E. R. Ojo, T. L. Rowlandson, J. Shang, K. Goïta and M. Hosseini, “IEEE Transactions on Geoscience and Remote Sensing,” *The Soil Moisture Active Passive Validation Experiment 2012 (SMAPVEX12): Prelaunch Calibration and Validation of the SMAP Soil*

Moisture Algorithms, vol. 53, no. 5, pp. 2784-2801, 2015.

[76] R. Panciera, J. P. Walker, T. J. Jackson, D. A. Gray, M. A. Tanase, D. Ryu, A. Monerris, H. Yardley, C. Rüdiger, X. Wu, Y. Gao and J. M. Hacker, "The Soil Moisture Active Passive Experiments (SMAPEx): Toward Soil Moisture Retrieval From the SMAP Mission," *IEEE Transactions on Geoscience and Remote Sensing,* vol. 52, no. 1, pp. 490-507, 2014.

[77] T. J. Jackson, R. Bindlish, A. J. Gasiewski, B. Stankov, M. Klein, E. G. Njoku, D. D. Bosch, T. L. Coleman, C. A. Laymon and P. Starks, "Polarimetric scanning radiometer C- and X-band microwave observations during SMEX03," *IEEE Transactions on Geoscience and Remote Sensing,* vol. 43, no. 11, pp. 2418-2430, 2005.

[78] K. Saleh, J.-P. Wigneron, J.-C. Calvet, E. Lopez-Baeza, P. Ferrazzoli, M. Berger, P. Wursteisen, L. Simmonds and J. E. Miller, "The EuroSTARRS airborne campaign in support of the SMOS mission: First results over land surfaces," *International Journal of Remote Sensing,* vol. 25, no. 1, pp. 177-194, 2004.

[79] S. Peischl, J. P. Walker, C. R¨udiger, N. Ye, Y. H. Kerr, E. Kim, R. Bandara and M. Allahmoradi, "The AACES field experiments: SMOS calibration and validation across the Murrumbidgee River catchment," *Hydrology and Earth System Sciences,* 2012.

[80] The National Aeronautics and Space Administration (NASA), "Soil Moisture Active Passive Validation Experiment 2016 (SMAPVEX16)," Jet Propulsion Laboratory, [Online]. Available: https://smap.jpl.nasa.gov/science/validation/fieldcampaigns/SMAPVEX16/. [Accessed 2023].

[81] S. K. Chan, R. Bindlish, P. E. O'Neill, E. Njoku, T. Jackson, A. Colliander, F. Chen, M. Burgin, S. Dunbar, J. Piepmeier, S. Yueh, D. Entekhabi, M. H. Cosh, T. Caldwell, J. Walker, X. Wu, A. Berg, T. Rowlandson, A. Pacheco, H. McNairn, M. Thibeault, J. Martínez-Fernández, Á. González-Zamora, M. Seyfried, D. Bosch, P. Starks, D. Goodrich, J. Prueger, M. Palecki, E. E. Small, M. Zreda, J.-C. Calvet, W. T. Crow and Y. Kerr, "Assessment of the SMAP Passive Soil Moisture Product," *IEEE Transactions on Geoscience and Remote Sensing,* vol. 54, no. 8, pp. 4994-5007, 2016.

[82] A. Colliander, M. H. Cosh, S. Misra, T. J. Jackson, W. T. Crow, J. Powers, H. McNairn, P. Bullock, A. Berg, R. Magagi, Y. Gao, R. Bindlish, R. Williamson, I. Ramos, B. Latham, P. O'Neill and S. Yueh, "Comparison of high-resolution airborne soil moisture retrievals to SMAP soil moisture during the SMAP validation experiment 2016 (SMAPVEX16)," *Remote Sensing of Environment,* vol. 227, pp. 137-150, 2019.

[83] ProSensing, "Polarimetric L-Band Microwave Radiometer," Prosensing, [Online]. Available: http://www.prosensing.com/crb-product/plmr/.

[84] D. M. Burrage, J. C. Wesson, M. A. Goodberlet and J. L. Miller, "Optimizing Performance of a Microwave Salinity Mapper: STARRS L-Band Radiometer Enhancements," *Journal of Atmospheric and Oceanic Technology,* vol. 25, no. 5, p. 776–793.

[85] S. S. Søbjærg, S. S. Kristensen, J. E. Balling and N. Skou, "The airborne EMIRAD L-band radiometer system," in *2013 IEEE International Geoscience and Remote Sensing Symposium - IGARSS*, Melbourne, 2013.

[86] M. Zribi, D. Hauser, M. Parde, P. Fanise, P. Leroy, M. Dechambre, A. Weill, J. Boutin, G. Reverdin, J. C. Calvet, J. P. Wigneron, N. Skou, S. S. Sobjaerg, N. Reul, A. Ruis and E. Cardellach, "Combined Airborne Radio-instruments for Ocean and Land Studies

(CAROLS)," in *IGARSS 2008 - 2008 IEEE International Geoscience and Remote Sensing Symposium*, Boston, 2008.

[87] M. Zribi, M. Pardé, J. Boutin, P. Fanise, D. Hauser, M. Dechambre, Y. Kerr, M. Leduc-Leballeur, G. Reverdin, N. Skou, S. Søbjærg, C. Albergel, J. C. Calvet, J. P. Wigneron, E. Lopez-Baeza, A. Rius and J. Tenerelli, "CAROLS: A New Airborne L-Band Radiometer for Ocean Surface and Land Observations," *Sensors,* vol. 11, no. 1, pp. 719-742, 2011.

[88] Jet Propulsion Laboratoty, "PALS | JPL's Earth Science Airborne Program," The National Aeronautics and Space Administration, [Online]. Available: https://airbornescience.jpl.nasa.gov/instruments/pals. [Accessed 2023].

[89] I. Ramos-Perez and S. Misra, "PALS instrument upgrade, a wide band radiometer," in *2017 IEEE International Geoscience and Remote Sensing Symposium (IGARSS)*, 2017.

[90] S. Yueh, "USER GUIDE: SMAPVEX08 PALS Brightness Temperature Data, Version 1," 2015. [Online]. Available: https://nsidc.org/sites/default/files/sv08pltb-v001-userguide.pdf. [Accessed 2023].

[91] E. Kim, A. Wu, H. Izadkhah and S. Abraham, "High-Resolution Soil Moisture—A European Airborne Campaign Using NASA Goddard's Scanning L-Band Active Passive (SLAP)," 2023. [Online]. Available: https://www.researchsquare.com/article/rs-2830042/v1. [Accessed 2023].

[92] J. R. Piepmeier, P. Focardi, K. A. Horgan, J. Knuble, N. Ehsan, J. Lucey, C. Brambora, P. R. Brown, P. J. Hoffman, R. T. French, R. L. Mikhaylov, E.-Y. Kwack, E. M. Slimko, D. E. Dawson, D. Hudson, J. Peng, P. N. Mohammed, G. De Amici, A. P. Freedman, J. Medeiros, F. Sacks, R. Estep, M. W. Spencer, C. W. Chen, K. B. Wheeler, W. N. Edelstein, P. E. O'Neill and E. G. Njoku, "SMAP L-Band Microwave Radiometer: Instrument Design and First Year on Orbit," *IEEE Transactions on Geoscience and Remote Sensing,* vol. 55, no. 4, pp. 1954-1966, 2017.

[93] "Polarimetric Scanning Radiometer - C/X Band (PSR/CX)," NASA, 27 01 2015. [Online]. Available: https://airbornescience.nasa.gov/instrument/PSR/CX.

[94] Physical Sciences Laboratory, "Polarimetric Scanning Radiometer (PSR) Instrument Information," National Oceanic and Atmospheric Administration, [Online]. Available: https://www.psl.noaa.gov/technology/psr/. [Accessed 2023].

[95] T. J. Jackson, R. Bindlish, A. J. Gasiewski, B. Stankov, M. Klein, E. G. Njoku, D. Bosch, T. Coleman, C. Laymon and P. Starks, "Polarimetric scanning radiometer C and X band microwave observations during SMEX03," in *2004 IEEE International Geoscience and Remote Sensing Symposium*, 2004.

[96] J. P. Bobak, D. J. Dowgiallo, N. R. McGlothlin and K. M. St Germain, "APMIR: airborne polarimetric microwave imaging radiometer," in *Scanning the Present and Resolving the Future. Proceedings. IEEE 2001 International Geoscience and Remote Sensing Symposium (Cat. No.01CH37217)*, 2001.

[97] J. P. Bobak, B. C. Hicks, L. A. Rose, N. R. McGlothlin, S. R. Quinn, D. J. Dowgiallo and T. E. vonRentzell, "APMIR: an airborne polarimeter designed for high accuracy," Oceans 2003. Celebrating the Past ... Teaming Toward the Future (IEEE Cat. No.03CH37492).

[98] "CORALYNN-17 (PKSR) Polarimetric K-Band Scanning Radiometer," Monash University, 2021. [Online]. Available: https://www.prism.monash.edu/CORALYN-17_PKSR.html.

[Accessed 2023].

[99] "CanEX-SM10 Canadian Experiment for Soil Moisture in 2010," 28 05 2010. [Online]. Available: http://canex-sm10.espaceweb.usherbrooke.ca/Experimental_plan_CANEx-SM10.pdf.

[100] J. Stroeve, V. Nandan, R. Willatt, R. Dadic, P. Rostosky, M. Gallagher, R. Mallett, A. Barrett, S. Hendricks, R. Tonboe, M. McCrystall, M. Serreze, L. Thielke, G. Spreen, T. Newman, J. Yackel, R. Ricker, M. Tsamados, A. Macfarlane, H.-R. Hannula and M. Schneebeli, "Rain on snow (ROS) understudied in sea ice remote sensing: a multi-sensor analysis of ROS during MOSAiC (Multidisciplinary drifting Observatory for the Study of Arctic Climate," *The Cryosphere,* vol. 16, no. 10, p. 4223–4250.

[101] K. Rautiainen, R. Butora, T. Auer, J. Kettunen, J. Kainulainen, J. Kainulainen, I. Mononen, D. Beltrami and M. Hallikainen, "Development of airborne aperture synthetic radiometer (HUT-2D)," in *IGARSS 2003. 2003 IEEE International Geoscience and Remote Sensing Symposium. Proceedings (IEEE Cat. No.03CH37477)*, 2003.

[102] J. Kainulainen, K. Rautiainen, S. Tauriainen, T. Auer, J. Kettunen and M. Hallikainen, "First 2-D Interferometric Radiometer Imaging of the Earth From an Aircraft," *IEEE Geoscience and Remote Sensing Letters,* vol. 4, no. 2, pp. 241-245, 2007.

[103] D. M. Le Vine, T. J. Jackson and M. Haken, "Initial Images of the Synthetic Aperture Radiometer 2D-STAR," *IEEE Transactions on Geoscience and Remote Sensing,* vol. 45, no. 11, pp. 3623-3632, 2007.

[104] eoPortal, "PSR - eoPortal," eoPortal, Jun 2012. [Online]. Available: https://www.eoportal.org/other-space-activities/psr#background. [Accessed Nov 2022].

[105] K. T. Ho, J. Feng, F. Bilawa, S. H. Shehab, K. T. Trinh, Y. Yang, C. Rüdiger, J. P. Walker and N. C. Karmakar, "Lightweight and Compact Radiometers for Soil Moisture Measurement: A review," *IEEE Geoscience and Remote Sensing Magazine,* vol. 10, no. 1, pp. 231-250, 2022.

[106] M. Zribi, M. Parde, P. Fanise, J. Boutin, J. C. Calvet, A. Clement, M. Dechambre, Y. Kerr, E. Lopez-Baeza, A. Matrin, A. Mialon, G. Reverdin, K. Saleh, J. P. Wigneron and N. Skou, "SMOS CAL/VAL campaigns 2010," 2010. [Online]. Available: https://earth.esa.int/eogateway/documents/20142/37627/carols-zribi.pdf. [Accessed 2023].

[107] "Polarimetric L-band Multibeam Radiometer (PLMR)," Monash University, 08 2010. [Online]. Available: http://www.moisturemap.monash.edu.au/aaces/aaces-1/plmr.php.

[108] A. Alonso-Arroyo, A. Camps, A. Monerris, C. Rüdiger, J. P. Walker, R. Onrubia, J. Querol, H. Park and D. Pascual, "On the Correlation Between GNSS-R Reflectivity and L-Band Microwave Radiometry," *IEEE Journal of Selected Topics in Applied Earth Observations and Remote Sensing,* vol. 9, no. 12, pp. 5862-5879, 2016.

[109] K. S. Kona, K. Bahadori and Y. Rahmat-Samii, "Stacked Microstrip-Patch Arrays as Alternative Feeds for Spaceborne Reflector Antennas," *IEEE Antennas and Propagation Magazine,* vol. 49, no. 6, pp. 13-23, 2007.

[110] D. Long, R. Bindlish, J. Piepmeier and M. Bailey, "The Global L-Band Observatory for Water Cycle Studies (GLOWS) - SMAP Continuity Mission," in *IGARSS 2022 - 2022 IEEE*

International Geoscience and Remote Sensing Symposium, 2022.

[111] S. H. Shehab and N. Karmakar, “SIW slot antennas for passive microwave radiometer system,” in *2017 IEEE Asia Pacific Microwave Conference (APMC)*, Kuala Lumpur, Malaysia, 2017.

[112] S. H. Shehab, M. Hassan and N. Karmakar, “SIW slot antenna at Ka-band for soil moisture radiometer system,” in *2017 Eleventh International Conference on Sensing Technology (ICST)*, Sydney, NSW, Australia, 2017.

[113] S. H. Shehab, J. Feng, N. Karmakar, E. M. Amin and J. Walker, “Improved wideband phase balancing SIW unequal power divider design for the low side-lobe array antennas,” *IET Microw. Antennas Propag,* vol. 15, pp. 115-122.

[114] S. H. Shehab, J. Feng and N. Karmakar, “Trends on Remote Sensing Technology: Receiver Architectures and Antenna Systems,” in *2019 International Conference on Robotics,Electrical and Signal Processing Techniques (ICREST)*, 2019.

[115] S. H. Shehab, J. Feng and N. Karmakar, “Ka-band Radiometer System Design Incorporated with SIW Slot Antenna for Soil Moisture Sensing,” in *2018 IEEE International Symposium on Antennas and Propagation & USNC/URSI National Radio Science Meeting*, Boston, MA, USA, 2018.

[116] U. K. Reddy, B. Kunooru, D. RamaKrishna, Z. Nazneen and A. Reddy, “Implementation of Phased Array Antenna for wide scan using SIW Technology in K-Band,” in *2019 IEEE Indian Conference on Antennas and Propogation (InCAP)*, 2019.

[117] J.-W. Lian, Y.-L. Ban, J.-Q. Zhu, J. Guo and Z. Chen, “Planar 2-D Scanning SIW Multibeam Array With Low Sidelobe Level for Millimeter-Wave Applications,” *IEEE Transactions on Antennas and Propagation,* vol. 67, no. 7, pp. 4570-4578, 2019.

[118] J.-W. Lian, X.-Y. Zhao, Y.-L. Ban, Y. Liu and Z. Nie, “Compact SIW 2-D Butler Matrix and Its Multibeam Application,” *IEEE Antennas and Wireless Propagation Letters,* vol. 20, no. 3, pp. 386-390, 2021.

[119] Y. Yang, W. Che, W. Yang and C. Fan, “Millimeter-wave multi-beam antenna based on 2-D SIW beam-scanning network,” in *2015 International Workshop on Electromagnetics: Applications and Student Innovation Competition (iWEM)*, 2015.

[120] H. Li, S. Li, B. Hou, X. Zhang, W. Wen and C. Hu, “A digital SIW-slot antenna array with FPGA implementation of beamforming,” *Scientific Reports,* vol. 12, 2022.

[121] Y. R. Ding and Y. J. Cheng, “Ku/Ka Dual-Band Dual-Polarized Shared-Aperture Beam-Scanning Antenna Array With High Isolation,” *IEEE Transactions on Antennas and Propagation,* vol. 67, no. 4, pp. 2413-2422, 2019.

[122] J. F. Zhang, Y. J. Cheng, Y. R. Ding and C. X. Bai, “A Dual-Band Shared-Aperture Antenna With Large Frequency Ratio, High Aperture Reuse Efficiency, and High Channel Isolation,” *EEE Transactions on Antennas and Propagation,* vol. 67, no. 2, pp. 853-860, 2019.

[123] J. F. Zhang, Y. J. Cheng and Y. R. Ding, “An S- and V-Band Dual-Polarized Antenna Based on Dual-Degenerate-Mode Feeder for Large Frequency Ratio Shared-Aperture Wireless Applications,” *IEEE Transactions on Antennas and Propagation,,* vol. 68, no. 12, pp. 8127-8132, 2020.

[124] C. X. Bai, Y. J. Cheng, Y. R. Ding and J. F. Zhang, “A Metamaterial-Based S/X -Band Shared-Aperture Phased-Array Antenna With Wide Beam Scanning Coverage,” *IEEE Transactions on Antennas and Propagation,* vol. 68, no. 6, pp. 4283-4292, 2020.

[125] L. L. Shafai, W. A. Chamma, M. Barakat, P. C. Strickland and G. Seguin, “Dual-band dual-polarized perforated microstrip antennas for SAR applications,” *IEEE Transactions on Antennas and Propagation,* vol. 48, no. 1, pp. 58-66, 2000.

[126] S. Liu, K. Jiang , G. Xu, X. Ding, K. Zhang , J. Fu and Q. Wu, “A Dual-Band Shared Aperture Antenna Array in Ku/Ka-Bands for Beam Scanning Applications,” *IEEE Access,* vol. 7, pp. 78794-78802, 2019.

[127] Australian Research Council, “DP160104233 — Monash University,” 2019. [Online].

[128] R. Acevo-Herrera, A. Aguasca, X. Bosch-Lluis, A. Camps, J. Martínez-Fernández, N. Sánchez-Martín and C. Pérez-Gutiérrez, “Design and First Results of an UAV-Borne L-Band Radiometer for Multiple Monitoring Purposes,” *Remote Sensing,* vol. 2, no. 7, pp. 1662-1679, 2010.

[129] D. Houtz, R. Naderpour and M. Schwank, “Portable L-Band Radiometer (PoLRa): Design and Characterization,” *Remote Sensing,* vol. 12, no. 17, 2020.

[130] E. Dai, A. J. Gasiewski, M. Stachura and E. M. McIntyre, “Microstrip Colinear Antenna Array for a Small Unmanned Aerial System Lobe Differencing Correlation Radiometer,” *IEEE Transactions on Antennas and Propagation,* vol. 66, no. 4, pp. 2135-2140, 2018.

[131] F. Babaeian and N. C. Karmakar, “4×4 Element UWB Dual-Polarized Aperture Coupled Microstrip Patch Antenna Array for Chipless RFID,” in *2020 IEEE International RF and Microwave Conference (RFM)*, Kuala Lumpur, Malaysia, 2020.

[132] F. Babaeian and N. C. Karmakar, “A High Gain Dual Polarized Ultra-Wideband Array of Antenna for Chipless RFID Applications,” *IEEE Access,* vol. 6, pp. 73702-73712, 2018.

[133] R. Bancroft, Microstrip and Printed Antenna Design, 2nd ed., Raleigh, NC: SciTech Pub, 2009.

[134] K. F. Lee and W. Chen, Advances in microstrip and printed antennas, New York: Wiley, 1997.

[135] D. M. Pozar, “Microstrip antennas,” *Proceedings of the IEEE,* vol. 80, no. 1, pp. 79-91, 1992.

[136] M. A. Islam and N. C. Karmakar, “A dual polarised universal reader for frequency domain-based chipless RFID tags and sensors,” *IET Microw. Antennas Propag,* vol. 15, no. 3, pp. 342-355, 2021.

[137] C. A. Balanis, Antenna theory : analysis and design, Fourth ed., Hoboken, New Jersey: Wiley, 2016.

[138] J. L. Volakis, “Chapter. 46 Radiometer Antennas,” in *Antenna Engineering Handbook*, 5th ed., New York, McGraw-Hill Education, 2019.

[139] M. Hassan and N. Karmakar, “Comparative study of different power distribution methods for array antenna beamforming for soil moisture radiometer,” in *2017 Eleventh International Conference on Sensing Technology (ICST)*, Sydney, NSW, Australia, 2017.

[140] T. T. Taylor, “Design of line-source antennas for narrow beamwidth and low side lobes,” *Transactions of the IRE Professional Group on Antennas and Propagation,* vol. 3, no. 1, pp. 16-28, 1955.

[141] A. Baki, K. Hashimoto, N. Shinohara, T. Mitani and H. Matsumoto, “New and improved method of beam forming with reduced Side Lobe Levels for microwave power transmission,” in *2008 International Conference on Electrical and Computer Engineering*, Dhaka, Bangladesh, 2008.

[142] C. L. Dolph, “A Current Distribution for Broadside Arrays Which Optimizes the Relationship between Beam Width and Side-Lobe Level,” *Proceedings of the IRE,* vol. 34, no. 6, pp. 335-348, 1946.

[143] The MathWorks, Inc, “chebyshevT,” The MathWorks, Inc, [Online]. Available: https://au.mathworks.com/help/symbolic/sym.chebyshevt.html. [Accessed 2024].

[144] P. J. Bevelacqua, “Dolph-Chebyshev Weights,” Antenna-Theory.com, [Online]. Available: https://www.antenna-theory.com/arrays/weights/dolph.php. [Accessed 2024].

[145] N. Ye, X. Wu, J. Walker, N. Boopathi, T. J. Jackson, Y. Kerr, E. Kim, A. McGrath, I.-Y. Yeo and M. Moghaddam, “Towards Multi-Frequency Soil Moisture Retrieval Using P- and L-Band Passive Microwave Sensing Technology,” in *IGARSS 2018 - 2018 IEEE International Geoscience and Remote Sensing Symposium*, Valencia, Spain.

[146] R. Wallace and K. Andreasson, Introduction to RF and Microwave Passive Components, Norwood: Artech House, 2015.

[147] Q. Qiao, Y. Dai and Z. Chen, “Signal integrity analysis on discontinuous microstrip line,” *Journal of Physics: Conference Series,* 2013.

[148] “M7886 • 9-36VDC to +/-15VDC Regulated Converter,” Altronics Distributors Pty Ltd, [Online]. Available: https://www.altronics.com.au/p/m7886-9-36vdc-to-15vdc-regulated-converter/. [Accessed October 2019].

[149] “MC7805CTMC7800 - 1.0 A Positive Voltage Regulators,” May 2013. [Online]. Available: https://au.mouser.com/datasheet/2/308/mc7800-d-1193434.pdf. [Accessed October 2019].

[150] “Arduino Mega 2560 Rev3,” Arduino, [Online]. Available: https://store.arduino.cc/usa/mega-2560-r3. [Accessed October 2019].

[151] “Mega with Wi-Fi,” jaycar, [Online]. Available: https://www.jaycar.com.au/mega-with-wi-fi/p/XC4421. [Accessed October 2019].

[152] “BC327 - PNP Epitaxial Silicon Transistor - Mouser Electronics,” October 2014. [Online]. Available: https://www.mouser.com/datasheet/2/149/BC327-30422.pdf. [Accessed November 2019].

[153] “ATmega640/1280/1281/2560/2561 datasheet,” February 2014. [Online]. Available: https://ww1.microchip.com/downloads/en/devicedoc/atmel-2549-8-bit-avr-microcontroller-atmega640-1280-1281-2560-2561_datasheet.pdf. [Accessed October 2019].

[154] N. C. Karmakar, P. Zakavi and M. Kambukage, “FPGA-Controlled Phased Array Antenna Development for UHF RFID Reader,” in *Handbook of Smart Antennas for RFID Systems*,

2010, p. 211–241.

[155] J. Malášek, “Understanding battery capacity: Ah is not A,” Pololu Corporation, 12 Nov 2010. [Online]. Available: https://www.pololu.com/blog/2/understanding-battery-capacity-ah-is-not-a. [Accessed Nov 2019].

[156] “2447-3050 - Rechargeable Battery, 11.1 V, Lithium Ion, 5.2 Ah, Wire Leads,” element14 Pty Ltd, [Online]. Available: https://au.element14.com/ansmann/2447-3050/rechargeable-batt-li-ion-11-1v/dp/2484238. [Accessed NOV 2019].

[157] L. Wang, Y.-X. Guo and W. Wu, “The substrate and ground plane size effect on radiation pattern of 60-GHz LTCC patch antenna array,” in *2013 Proceedings of the International Symposium on Antennas & Propagation*, Nanjing, China, 2013.

[158] Toray Advanced Composites, “Low Dielectric Composites for Radomes and Antennas,” AZoM, 17 Dec 2012. [Online]. Available: https://www.azom.com/article.aspx?ArticleID=7984.

[159] Toray Advanced Composities, “radome antenna systems,” [Online]. Available: https://www.toraytac.com/media/2f1ed017-889b-45e9-aadb-9d107078fe88/HNcupw/TAC/Documents/Selector%20Guides/Toray_Radome-Antenna-Systems_Advanced-Composite-Materials_Selector-Guide.pdf.

[160] M. Hassan and N. Karmakar, “Soil moisture measurement using smart antennas,” in *8th International Conference on Electrical and Computer Engineering*, Dhaka, Bangladesh, 2014.

[161] T. J. Jackson. and T. J. Schmugge, “Passive Microwave Remote Sensing of Soil Moisture,” in *Advances in Hydroscience*, vol. 14, B. C. Yen, Ed., Academic Press, 1986, pp. 123 - 159.

[162] N. Skou and D. Le Vine, “Second Example of a spaceborne Imager: A Sea Salinity/Soil Moisture Push-Broom Radiometer System,” in *Microwave Radiometer Systems: Design and Analysis, Second Ediotion*, Norwood, MA:, Artech House, 2006, pp. 171-194.

[163] N. Skou and S. S. Sobjaerg, “Polarimetric signatures from a crop covered land surface measured by an L-band polarimetric radiometer,” in *IGARSS 2003. 2003 IEEE International Geoscience and Remote Sensing Symposium. Proceedings*, 2003.

[164] J. Lahtinen, J. Pihlflyckt, I. Mononen, S. Tauriainen, M. Kemppinen and M. Hallikainen, “Fully polarimetric microwave radiometer for remote sensing,” *IEEE Transactions on Geoscience and Remote Sensing,* vol. 41, no. 8, pp. 1869-1878, 2003.

[165] S. V. Nghiem, M. E. Veysoglu, J. A. Kong, R. T. Shin, K. O'Neill and A. W. Lohanick, “Polarimetric Passive Remote Sensing of a Periodic Soil Surface: Microwave Measurements and Analysis,” *Journal of Electromagnetic Waves and Applications,* vol. 5, no. 9, pp. 997-1005, 1991.

[166] D. Pozar, “13.4 Radiometer Systems,” in *Microwave engineering* , Hoboken, NJ, John Wiley & Sons, 2005, pp. 665 - 669 .

[167] F. T. Ulaby, R. K. Moore and A. K. Fung, “Radiometer Systems,” in *Microwave remote sensing : Active and passive*, vol. 1, Reading, Mass:, Addison-Wesley Pub., Advanced Book Program/World Science Division, 1981, pp. 344-430.

[168] D. M. Pozar, “10.1 Noise in Microwave Circuits,” in *Microwave engineering*, Hoboken, NJ, John Wiley & Sons, 2005, pp. 487-491.

[169] S. Zhao, L. Zhang and Z. Zhang, “Design and Test of a New Truck-Mounted Microwave Radiometer for Remote Sensing Research,” in *IEEE International Geoscience & Remote Sensing Symposium, IGARSS 2008,*, Boston, Massachusetts, USA, 2008.

[170] H. E. Elder and V. J. Glinski, “Chapter 12 Detector a Mixer Diodes and Circuits,” in *Microwave semiconductor devices and their circuit applications*, New York, McGraw-Hill, 1969, pp. 370-389.

[171] “HSMS-285C, Zero bias small signal detector diode,” 5 2009. [Online]. Available: https://www.broadcom.com/products/wireless/diodes/schottky/hsms-285c. [Accessed 5 12 2017].

[172] H. J. De Los Santos, C. Sturm and J. Pontes, “Chapter 2 Modulation and Detection,” in *Radio Systems Engineering*, Cham, Springer, 2015, pp. 21-60.

[173] Marki Microwave, Inc., “Microstrip Filter Desgin Tool,” Marki Microwave, [Online]. Available: https://rf-tools.com/microstrip/.

[174] N. Skou and D. M. Le Vine, “Radiometer Receiver on a Block Diagram Level,” in *Microwave Radiometer Systems : Design and Analysis*, 2nd ed., Boston, Artech House, 2006, pp. 25-44.

[175] E. Chikando, J. R. Piepmeier, E. Levine and C. White, “Handheld L-Band Microwave Radiometer,” in *2006 IEEE MicroRad*, San Juan, 2006.